Micromechanical Signal Processors

by

Clark Tu-Cuong Nguyen

B.S. (University of California at Berkeley) 1988
M.S. (University of California at Berkeley) 1991

A dissertation submitted in partial satisfaction of the

requirements for the degree of

Doctor of Philosophy

in

Engineering-Electrical Engineering
and Computer Sciences

in the

GRADUATE DIVISION

of the

UNIVERSITY of CALIFORNIA at BERKELEY

Committee in charge:

Professor Roger T. Howe, Chair
Professor Paul R. Gray
Professor Albert P. Pisano

1994

Abstract

Micromechanical Signal Processors

by

Clark T.-C. Nguyen

Doctor of Philosophy in Electrical Engineering and Computer Sciences

University of California at Berkeley

Professor Roger T. Howe, Chair

Completely monolithic high-Q micromechanical signal processors constructed of polycrystalline silicon and integrated with CMOS electronics are described. The signal processors implemented include an oscillator, a bandpass filter, and a mixer+filter—all of which are components commonly required for up- and down- conversion in communication transmitters and receivers, and all of which take full advantage of the high Q of micromechanical resonators. Each signal processor is designed, fabricated, then studied with particular attention to the performance consequences associated with miniaturization of the high-Q element.

The fabrication technology which realizes these components merges planar integrated circuit CMOS technologies with those of polysilicon surface micromachining. The technologies are merged in a modular fashion, where the CMOS is processed in the first module, the microstructures in a following separate module, and at no point in the process sequence are steps from each module intermixed. Although the advantages of such modularity include flexibility in accommodating new module technologies, the developed process constrained the CMOS metallization to a high temperature refractory metal (tungsten metallization with $TiSi_2$ contact barriers) and constrained the micromachining process to long-term temperatures below 835°C. Rapid-thermal annealing (RTA) was used to relieve residual stress in the mechanical structures. To reduce the complexity involved with developing this merged process, capacitively transduced resonators are utilized.

The prototype high-Q oscillator uses a 16.5 kHz folded-beam, capacitive-comb transduced polysilicon microresonator in a series resonant oscillator architecture. The quality factor of the reference resonator has been measured to be 50,000 under a vacuum at 10 mTorr pressure. Its temperature coefficient is measured at -10 ppm/^{o}C, linearly and monotonically decreasing with increasing temperature over a 270K to 370K temperature range. Equivalent circuits for general multi-port capacitively transduced micromechanical resonators are proposed for design and noise analysis purposes. The oscillator sustaining amplifier is transresistance and is equipped with variable gain controls for future amplitude-level control.

The 16.5 kHz prototype oscillator generates an output signal with visibly low phase noise. Theoretical analysis shows that phase noise contributions due to superposed electronic noise (from the sustaining amplifier and Brownian noise of the resonator) are comparable to those in macroscopic high-Q oscillators, for similar carrier powers. However, theoretical considerations also predict that as the dimensions of the mechanical resonator shrink (i.e., as the frequency increases), the short-term stability of the resonator becomes increasingly susceptible to mass loading effects, where instantaneous differences in the rates of adsorption and desorption of contaminant molecules give rise to mass fluctuations, hence, frequency noise. At 100 MHz, theory predicts that mass loading noise dominates over superposed electronic noise at certain pressures and temperatures. One of the keys to avoiding mass loading-derived phase noise is to operate the resonator at pressures which minimize its effect—generally, extremely low pressures (< 1 μTorr).

High-Q single resonator and spring-coupled micromechanical resonator filters are also investigated, with particular attention to noise performance, bandwidth control, and termination design. The noise in micromechanical filters is found to be fairly high due to poor electromechanical coupling on the micro-scale with present-day technologies. Poor coupling leads to high series motional resistance in resonators, which implies large amounts of Brownian motion noise at resonance. Solutions to this high series resistance problem are suggested, including smaller electrode-to-resonator gaps to increase the coupling capacitance. Despite the high series resistance, micromechanical filters still have enough dynamic range to satisfy IF applications.

Active Q-control techniques are demonstrated which control the bandwidth of micromechanical filters and simulate filter terminations with little passband distortion. Noise analysis

shows that these active techniques are relatively quiet when compared with other resistive techniques.

Modulation techniques are investigated whereby a single resonator or a filter constructed from several such resonators can provide both a mixing and a filtering function, or a filtering and amplitude modulation function. These techniques center around the placement of a carrier signal on the micromechanical resonator. Mixing and filtering of signals from 200 MHz (RF) down to 20 kHz (IF) has been demonstrated.

Finally, micro oven stabilization is investigated in an attempt to null the temperature coefficient of a polysilicon micromechanical resonator. Here, surface micromachining procedures are utilized to fabricate a polysilicon resonator on a microplatform—two levels of suspension—equipped with heater and temperature sensing resistors, which are then imbedded in a feedback loop to control the platform (and resonator) temperature. Since excellent thermal isolation can be achieved on the micro-scale, only 2 mW of power was required to set the platform temperature at a reasonable bias point and control the temperature to stay there. Using micro oven control, the temperature coefficient of the resonance frequency is reduced from -10 ppm/°C to -2 ppm/°C.

Roger T. Howe December 14, 1994

Professor Roger T. Howe

Committe Chair

The dissertation of Clark Tu-Cuong Nguyen is approved:

Roger T. Howe — December 12, 1994

Professor Roger T. Howe, Chair — Date

Paul R. Gray — 12/15/94

Professor Paul R. Gray — Date

Albert P. Pisano — 14 DEC 94

Professor Albert P. Pisano — Date

University of California at Berkeley

1994

To my parents

Table of Contents

Acknowledgements

I would like to express, first, my deepest appreciation for the technical guidance and support given by my research advisor, Professor Roger T. Howe. His vast knowledge of numerous engineering disciplines, coupled with an unmatchable enthusiasm for the field of microsensors and microelectromechanics, will always be remembered.

Professors Richard Muller and Richard White also deserve great thanks for their interest in my research, their encouragement during research presentations, and for involving me in some of their projects. I also thank Professor Al Pisano for his advice and his enthusiasm for this field; he always knew how to liven up a meeting or two. I am grateful to Professor Paul Gray for his interest in my research and for his ever-practical perspective. Professor Ping Ko was a fountain of knowledge during the MICS development summer, and I greatly appreciate this. I thank Professor John Wawrzynek and John Lazzaro for their interest in my work as applied to speech processing systems.

To Katalin Voros I extend my utmost thanks for seeming to always be on my side whenever microlab decisions involving my research were required. UC Berkeley couldn't get a better microlab manager than Katalin.

Of the students and staff, I'd like to particularly thank Weijie Yun for all of those days and nights (weekends included) we spent together developing the MICS process in 1991. I'd like to thank Shenqing Fang for later taking away the need for me to run CMOS; he did such a good job of it! Early collaboration with Bill Tang, the inventor of the electrostatic-comb driven lateral microresonator, gave me hands on and instant knowledge of the workings and fabrication of this device. The early practical research advice of Jim Chung was greatly appreciated (despite his continued bad taste in music). Carlos Mastrangelo was also very helpful in my early years—what an amazing work ethic he had!

I'm grateful to all of the staff of the Berkeley Microfabrication Laboratory, especially Debra Hebert, for aiding the CMOS development efforts with parallel diagnostics of her own, and Marilyn Kushner, for churning out baseline CMOS mask sets ever so reliably. Thanks also to Jim Bustillo for much practical advice in the lab. Also, I'm grateful to Bob Hamilton and Dave Hebert for being so darn good at what they do. Thanks to Ron Wilson of the Materials Science Depart-

ment for all those SEM sessions; it's always more fun to take SEM's when the conversation's good. Also, many thanks to Alex Para and Ferenc Kovac for their assistance in equipment administration. Thanks to Rob McNicholas for assistance in computer administration.

In addition, stimulating technical and casual conversations from the aforementioned and from old generation students Reza Moazzami, Guochun Liang, Jian Chen, Martin Lim, Tim Hu, Chris Perleberg Stuart Wenzel, Leslie Field, Yu-Chong Tai, Dave Feld, Elyse Rosenbaum, Dave Burnett, and new generation students/post-docs Fariborz Assaderaghi, Clement Wann, Meng-Hsiung Kiang, Bob Ried, Peter Xiao, Crist Lu, Norman Tien, Olav Solgaard, Amit Lal, Rod Alley, Dennis Sinitsky, Gary Fedder, Mike Judy, Amy Wang, Annabel Nickles, Rich Moroney, Trey Roessig, Bill Clark, Chuck Bradley, Steve Parke, Khandker Quader, Greg Uehara, Jack Judy, Kirt Williams, and others who aren't mentioned only because this dissertation has a deadline.

Very special thanks to the crew of BSAC's administrative office.: Joel Nice, Sheila Kelly, and Barbara Barnes, for those fun conversations and for the life-saving snacks they gave on those "lunch-skipping" days. (And Joel, thanks for the ear-crunching jam sessions!)

I thank my family for their support and encouragement, and am especially grateful to my parents, for the upbringing and early attitude they instilled in me that led to all of this.

Last, but not least, I thank the undergraduate EE199 students who I've had the pleasure of working with: Kay Huang, Vadim Gutnik, and Justin Ward.

Finally, I would like to express my gratitude for having had the opportunity to be a member of the Berkeley Sensor and Actuator Center, and would like to thank all the individuals from member companies who I've had the pleasure of interacting and with whom, hopefully, I'll be able to continue interacting.

To end this, let me impose a little bit of the philosophy that has kept me going all these years. Like a true engineer, I express it in the form of an equation:

$$H = \frac{dE}{dt}, \tag{0.1}$$

where H is happiness and E is an event. (There can be no happiness in stagnation.)

CHAPTER 1 *Introduction*

Communication plays an integral role in every society. It permeates nearly every aspect of the average individuals everyday life and is perhaps the single most important activity in today's industrial society. Its ability to spread ideas and knowledge, and its governing role in efficiently allocating tasks to the proper resources, are paramount to the evolution of today's cultures around the world. The larger the scope of a given communication network (i.e., the more parties which may connect to and converse through a given network), the larger the volume and variety of information transferred, and thus, the larger the impact of such a network.

Among the many examples of how communications impacts our world can be seen through the already available wireless communication systems. To take the obvious examples, broadcast radio and television are perhaps the two most influential sources of information and entertainment for today's industrial cultures. Their huge influence is, of course, in large part a function of their scope (i.e., the size of their audiences), which in turn is a function of the technology they use: wireless communications. With just this simplistic view, the reasons for current interest in all forms of wireless communications, from single-building office-to-office systems, to cellular phone networks, to global satellite positioning systems, are clear.

Many technologies are currently available for implementing such wireless networks, as is obvious from the number of existing cellular phones, and the existing global satellite positioning systems already in operation. The available technologies, however, leave much to be desired. Firstly, they are expensive: Most contain discrete components, since many of the specifications for

the functions required for these systems cannot be adequately satisfied by present-day technologies and techniques. For example, to the author's knowledge, there are presently no integrated transistor-based filters or oscillators that can even vaguely match the performance of those based upon SAW resonators and quartz crystals. Whether an integrated version of these functions is necessary is in large part an issue of economics.

Gains through integration, however, are not limited to merely economic considerations. Size and power are equally important attributes These two are actually very much related when considering battery-operated wireless components; for example, integration is nice, but the product cannot be made compact unless it consumes low enough power to allow the use of small batteries. In the broader picture of global and cultural evolution of societies, availability and convenience may very well be among the most important attributes (right up there with economy), since they in large part determine the scope of a given communication system. Again, the importance of the scope in determining the societal impact of a communication system cannot be overemphasized. Since convenience and availability are often congruent with small size, complete integration of communication products is an important area for research.

Several approaches to implementing fully monolithic communication systems are currently being pursued, including some based upon traditional heterodyning methods but using integrated transistor-based filters and some attempting single-heterodyning to the baseband (eradication of the IF filter). This dissertation considers an approach based upon traditional heterodyning implementations of receivers and transmitters, but replacing the off-chip passive components (quartz crystals, ceramic filters, SAW resonators) with monolithically integrated versions, fabricated using the planar integrated circuit processing techniques of both CMOS and surface micromachining.

1.1 The Target Application

Miniaturized (micro-scale) mechanical devices, fabricated using a variety of bulk or surface micromachining technologies, have been predominately directed towards the field of sensors. Among the many microsensors achieved via micromachining technologies are pressure sensors for medical and tactile applications [1,2], accelerometers and gyroscopes for inertial navigation [3],

and a myriad of chemical and biological sensors [4,5]. Today, several sensor products are currently on the market which utilize micromachined components.

When used in sensors, mechanical elements are generally utilized as transducers. For example, an accelerometer uses a mechanical proof mass to sense acceleration in the mechanical domain and transduce it to voltage or charge in the electrical domain, where it can then be amplified and processed by subsequent stages of electronics. In this example application, the mechanical properties of most importance are the density of the material (the total attainable mass) and the resonance frequency of the effective mass-spring-damper system. In addition, temperature and aging stability of the structural material is also of utmost importance. If the accelerometer in question were a resonant accelerometer, then the quality factor of both the material and design would be a very important parameter.

It is well known that the quality factor of mechanical resonators is generally orders of magnitude higher than achievable by discrete or integrated LCR tank circuits. For this reason, many of the high-Q filters and local oscillators required in communication systems are implemented using off-chip macroscopic mechanical components, which interface with the integrated amplifying and discriminating electronics on the board level. The use of off-chip components, although relatively inexpensive, makes production of such communications products cumbersome and prevents the realization of a truly compact product (such as a wristwatch cellular phone).

There is great incentive, then, to replace high-Q macroscopic (off-chip) elements with integrated versions, since this could potentially lead to a fully monolithic, batch fabricated transmitter or receiver system. One of the aims of this dissertation is to investigate the possibility of replacing the crystal, ceramic, and SAW components currently used in today's communications equipment with (nearly) equivalent miniaturized and integrable micromechanical versions.

To get an idea of which components are replaceable, we refer to Fig. 1.1, which presents the highly simplified schematic of a broadcast FM receiver. The first component in this receiver is the front end RF image rejection filter, which gathers and amplifies the information in the desired channel and directs it to a subsequent mixer. This mixer heterodynes the information signal down to the much lower IF frequency, where further filtering, amplification, and discrimination can be performed at a much lower cost. The main purpose of the RF filter is to reject signals at the image frequency (shown as a lightly shaded triangle in Fig. 1.1), which may also get mixed down to the

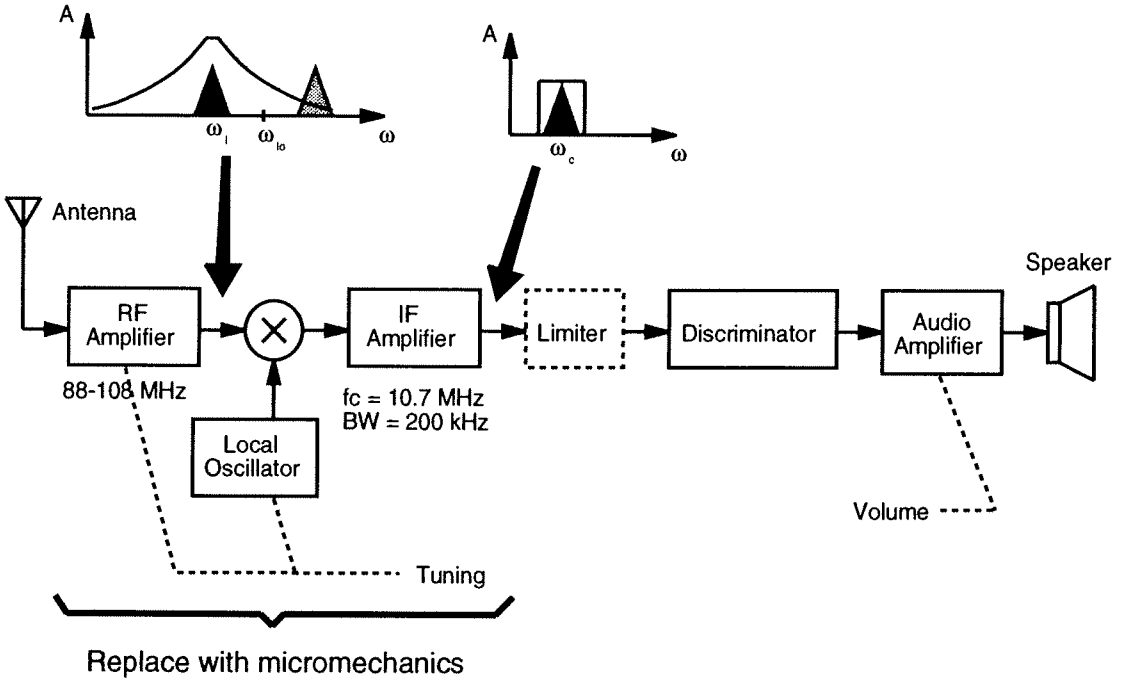

Fig. 1.1: Simplified schematic of a broadcast FM receiver.

IF frequency. The degree to which the RF filter can reject the image signal determines how high the IF frequency must be. Thus, the RF filter should be highly selective (i.e., should have high-Q) to insure a reasonably low IF frequency. Among filters suitable for RF applications (i.e., filters which have high Q at high RF frequencies) are SAW and cavity resonator filters, both passive off-chip components.

The signal processed by the RF filter/amplifier is next directed to a mixer, which multiplies the signal with a local oscillator signal (with frequency equal to $f_i + f_{lo}$), mixing it down to the IF frequency. In order to maximize the range of this receiver, noise in the signal path must be minimized. For this reason, the local oscillator which mixes with the information signal must be generated by a high quality, low phase noise oscillator, usually referenced to a quartz crystal blank (another off-chip component).

The mixer output is then fed to the IF filter/amplifier, which must also have high-Q. This filter is usually a crystal or ceramic off-chip, passive filter. The rest of the receiver, after the IF filter, can be implemented using integrated electronics.

The target components which can potentially be replaced by micromechanics, then, include all off-chip high-Q components used in the IF amplifier, the local oscillator, and perhaps the RF filter (if micromachined resonators can reach such frequencies). Whether such components are replaceable by micromechanics depends upon the specifications of the system and on the material and design properties of the micromechanical elements, in particular the quality factor. For example, recent measurements of polysilicon microresonator Q in the range of over 10,000 at 30 MHz [6] suggest that the broadcast FM receiver of Fig. 1.1 is feasible using micromachining technologies to replace off-chip components. For applications such as wireless communications, where RF frequencies from 1.2 to 4 GHz are used with IF frequencies from 70 to 200 MHz, it is presently not clear whether micromachined resonators can achieve the RF frequency.

Once the off-chip components are miniaturized, a technology which then merges these devices with amplifying and discriminating electronics is all that is required to realize a fully monolithic receiver or transmitter. The bulk of this dissertation is devoted to the design, fabrication, and testing of micromechanical signal processors, for which one of the target applications is communication systems. Before proceeding, however, it is instructive to first review present-day macroscopic and integrated technologies which have similar functions. The remainder of this chapter centers on this task.

1.2 Macroscopic Mechanical Signal Processors

Mechanical resonators are widely used for precision and high performance applications, from simple but accurate wrist watch time keepers, to ultra-low phase noise oscillators for satellite communications, to IF and RF filters in wireless communications technologies. The workhorse material of choice the macroscopic domain has been quartz, which in crystalline form achieves extremely high quality factors, very low aging rates, and extremely low temperature coefficients. The frequency range of this material starts as low as 400 Hz for quartz tuning forks to as high as 125 MHz for AT cut quartz operating at a higher overtone. Via frequency-multiplication, quartz is even used for applications beyond this frequency range. The quality factor ranges from 20,000 to over 1,000,000, depending upon the frequency, type or cut of quartz resonator, and manufacturing quality. Unaided temperature coefficients in the range of from 0.2 to 2 ppm/^{o}C are achievable, again, dependent upon the type or cut of resonator.

TABLE 1.1. Quartz Frequencies

Mode	Frequency Range
Flexure	0.4 — 100 kHz
Extensional	40 — 15 000 kHz
Shear	100 — 200 000 kHz

As mentioned, bulk-mode quartz is very useful in the LF to VHF frequency ranges for oscillator and filtering applications. When used as a surface acoustic wave (SAW) device, its frequency range even extends into the UHF range. Other common materials used for macroscopic mechanical filters include various iron-nickel alloys, which, when constructed properly, exhibit acceptable temperature coefficients and slow aging rates [7]. They have typically been used for mechanical filter applications in the 400 Hz to 700 kHz frequency range [8].

This section briefly covers the advantages and disadvantages, performancewise and economically, for both of these materials. Of course, other materials are also available for similar purposes, including PZT, and various ceramics. However, the intent of this section is to provide background for comparison when micromechanical signal processors are discussed. Thus, a comprehensive description of all such macroscopic mechanical signal processors will not be provided.

1.2.1 Quartz Resonators

As discussed, crystal resonators, due to their stability, frequency range, and manufacturability, are among the most commonly used macroscopic signal processors. A variety of crystal resonator geometries have been used, from anchor-balanced tuning forks which resonate in a flexural mode and implement the lower frequency range, to quartz blanks, which typically operate in a shear mode and are commonly used for the high frequency applications. The frequency ranges of typically used modes for quartz crystals are summarized in Table 1.1.

Actuation of these modes is most commonly achieved using the piezoelectric property of properly cut quartz. The magnitude of the piezoelectric effect is governed by the cut of the crystal, which determines the degree of lattice asymmetry in a given direction. This lattice asymmetry gives rise to the formation of charge dipoles when a stress is applied in the direction of asymmetry,

i.e. the piezoelectric effect. This dipole distribution of charge gives rise to a voltage across the quartz blank, which can then be sensed to provide motional information for the crystal. In similar fashion, application of a voltage across the crystal and in the direction of lattice asymmetry gives rise to displacement in the crystal. A single crystal, thus, provides its own input and output transduction. When designing crystal filters, the mechanical resonance properties of the crystal must be considered in conjunction with the piezoelectric properties.

1.2.1.1 Quartz Crystal Manufacturing

Quartz is basically crystalline silicon dioxide (SiO_2), which crystallizes in the trigonal trapezohedral class of the trigonal system. There are two types of raw quartz crystals: natural and cultured. Natural quartz occurs naturally and is mined, primarily in Brazil. Cultured quartz is synthetically grown in a process analogous to that for cultured pearls. Although more expensive, cultured quartz crystals are usually better formed than natural quartz, having fewer impurities. This results in a higher yield of quality plates per crystal.

Once the raw crystals are formed, they must be cut into plates or blanks to give them particular piezoelectric properties. By slicing the raw quartz at various angles with respect to its axes, it is possible to obtain a variety of blanks having different temperature characteristics. In addition, the dimensions of the quartz blank, as well as the mode of vibration, determine the frequency of the resonator. Thus, the lower frequency limit is set by the dimensions of the largest usable plates obtainable from the raw crystal. The upper frequency limit is reached when the quartz plate becomes so small and thin that it is difficult to handle and likely to shatter during normal usage. Some of the more common crystal cuts used are summarized, along with frequency ranges, in Table 1.2 [9,10].

The AT-cut thickness-shear-mode crystal is the most popular for two main reasons: first, it is the most temperature stable; and second, it can be mounted in such a manner as to decouple the dominant mode of vibration from the supports. The latter characteristic is a result of a phenomenon called energy trapping [11], in which mechanical energy is confined to the area underneath the plated electrodes used for transduction,. The exact frequency of the crystal is, thus, determined by the *electrode* dimensions and the thickness of the plate, rather than by the overall plate dimensions. Crystal areas outside of the electrode regime can then be used for crystal support and electri-

TABLE 1.2. Quartz Crystal Freq. Range

Cut	Frequency Range [kHz]
X	40 - 20 000
Y	1000 - 20 000
AT	500 - 200 000
BT	1000 - 75 000
GT	100 - 550

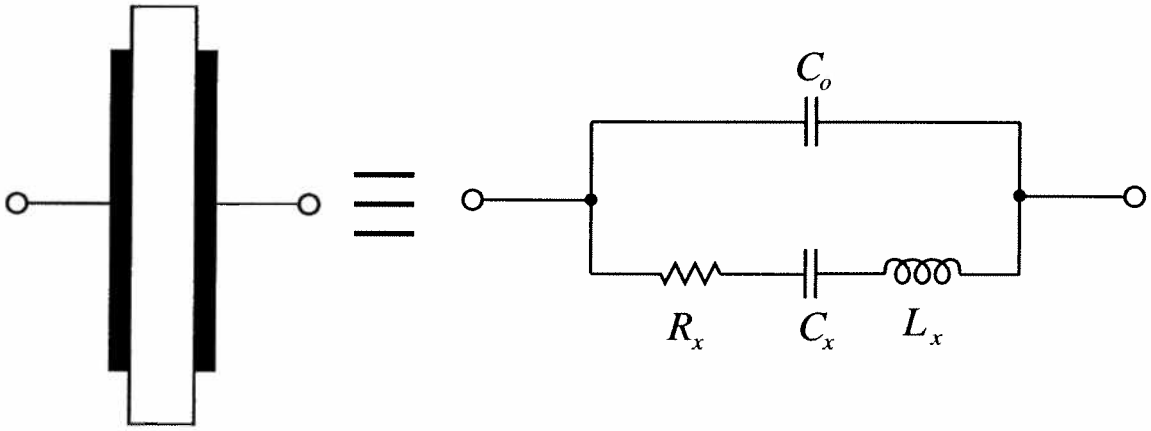

Fig. 1.2: Equivalent circuit for a quartz crystal.

cal connections, which, due to energy trapping, now have very little influence on the resonance frequency of the crystal unit.

1.2.1.2 Quartz Signal Processors

Quartz crystals are most commonly used as a one-port devices. A typical equivalent electrical circuit for a crystal is shown in Fig. 1.2. The element values of the circuit are determined largely by the efficiency of the electromechanical transducer which couples electrical to mechanical energy, and vice versa. The transducer efficiency is most commonly measured using the electromechanical coupling coefficient k_e, defined (in circuit terms) by

$$k_e^2 = \frac{C_x}{C_o}. \tag{1.1}$$

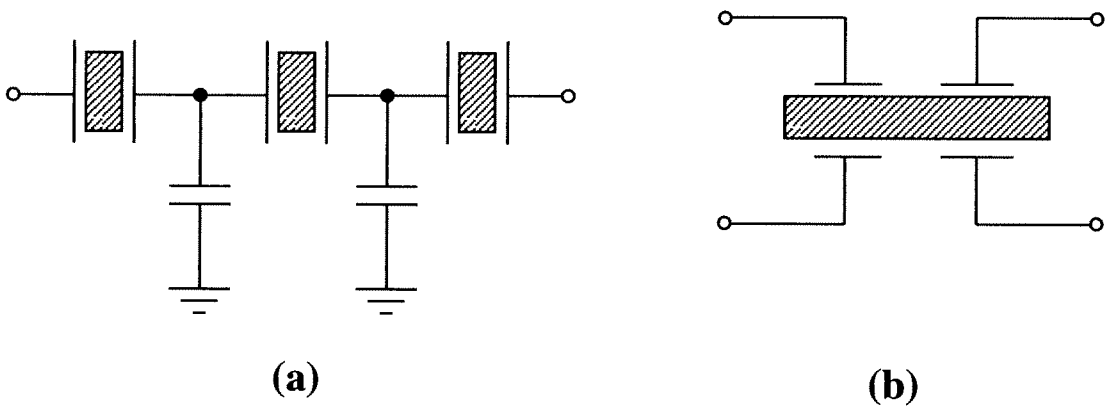

Fig. 1.3: Schematics of crystal filters. (a) A discrete crystal filter, electrically coupled. (b) A single crystal filter, with acoustically coupled resonators.

The value of the k_e, the larger the amount of coupling.

In oscillator applications, the use of quartz crystals is generally well known. For filter applications, two approaches are popular: (1) discrete crystal resonators coupled by electrical elements (usually capacitors); and (2) single crystal filters in which resonators are implemented by metal plating over the crystal and are coupled acoustically. Pictorial representations for each of these are given in Fig. 1.3. The advantage of the type (2) filters is compactness and the availability of monolithic fabrication techniques. These filters, however, suffer from the presence of spurious modes, which place resonance peaks at undesirable locations. For this reason, discrete crystal filters (type 1), in which spurious modes are often suppressed via electronic coupling, are widely used, as well.

1.2.2 Iron-Nickel Alloy-Based Resonators

As will be seen, the filters of this work are closer in design to macroscopic mechanical filters based upon spring-coupled resonators. A pictorial representation of such a filter is presented in Fig. 1.4, in which flexural mode disk resonators are coupled via longitudinal mode wires. Electromechanical transduction is provided at the end resonators in this design. Fig. 1.4 shows magnetostrictive transduction, which is commonly used in macroscopic mechanical filters. The design of micromechanical versions of such filters will be detailed in Chapter 5 of this dissertation.

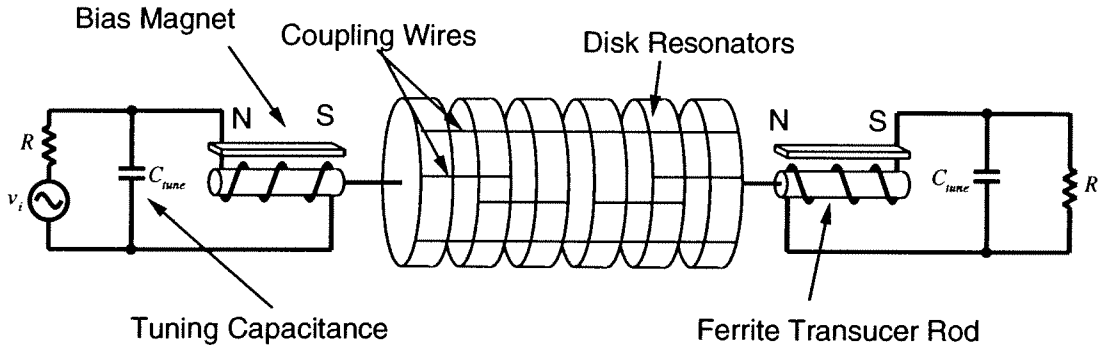

Fig. 1.4: A spring-coupled resonator mechanical filter.

Various iron-nickel alloys are commonly used to realize the resonators and coupling springs in macroscopic mechanical filters. Each such alloy has its own construction procedure and consequent material properties. A commonly used material is Ni-Span C (Thermelast 4002), which has longitudinal and shear mechanical Q's of over 20,000 (for frequencies up to 700 kHz) and a resonance frequency temperature variation of around 80 ppm over a temperature range from -25°C to 75°C. In order to achieve these characteristics, the construction of such resonators involves cold working and heat treatment procedures.

Mechanical filters generally cover the frequency range from hundreds of Hertz to almost 700 kHz. The frequency is limited by the mass of the macroscopic resonators. By miniaturizing the resonators (thus, reducing their mass) such as done in this work, one expects to be able to achieve much higher frequencies.

1.2.3 Important Resonator Properties

Macroscopic mechanical resonators are extremely popular in the communications industry due to three basic properties: an extremely high quality factor, low temperature coefficient, and a very low aging rate. They are also quite inexpensive in large quantities. In addition, the electromechanical transduction mechanism and geometric vibration characteristics of quartz crystals make them easy to design with. For example, the low series resistance in the equivalent motional circuit for an AT-cut quartz crystal makes the design of sustaining amplifiers in oscillators much simpler, and it allows the design of crystal or mechanical filters much simpler in terms of filter termination.

These are some of the properties that are desirable in the miniaturized integrated circuit mechanical resonators proposed in this dissertation. It is these properties that dictate the type of material used in this work, and the specific geometric design strategies implemented for these microresonators.

1.3 Miniaturization of High-Q Oscillators and Filters

To be sure, there have been many previous attempts to miniaturize the high-Q oscillators and bandpass filters used in communication systems. Over the years, macroscopic mechanical filters, with frequency ranges up to about 700 kHz, have been replaced in a wide variety of applications by new integrated filter technologies. These transistor-based integrated filters can achieve the frequencies, and often the bandwidths, of macroscopic mechanical filters in much smaller area and through cost effective batch fabrication processes. Some examples of these filters include switched-capacitor [12,13], MOSFET-C [14], and g_m-C [15,16] filters.

These filters generally use high-Q on-chip capacitors (with Q's on the order of 10,000), resistors (MOSFET or switched-capacitor types) or transconductors, and operational amplifiers to actively synthesize the required bandpass response. Unfortunately, however, the Q of high-frequency bandpass filters in these active filter technologies is limited by the dc gain of the operational amplifiers used in the integrators. In brief, it is much easier to implement high-Q low pass filters than high-Q high pass filters in these active technologies. To implement a low pass filter with a dominant pole quality factor equal to Q_{LP}, integrators with $Q = Q_{LP}$ are required. On the other hand, to implement a high pass filter with the same bandwidth, the required integrator Q is given by $(2\omega_o/B)\,Q_{LP}$, where ω_o is the center frequency and B is the filter bandwidth. Thus, for high center frequencies, much higher Q is required to implement bandpass filters with a given bandwidth than lowpass filters. This translates to the requirement for much higher dc gain in the operational amplifiers implementing the integrators.

On top of the above drawback, it has been shown [12,13] that there is a dynamic range-to-Q trade-off. In other words, to attain high Q using active techniques, one must sacrifice dynamic range. For these reasons, highly selective filters have so far not been implemented in these technologies. Even modulation-based filters in these technologies, such as n-path filters, which can achieve effective filter Q's as high as 400, have insufficient dynamic range [17]. Thus, an inte-

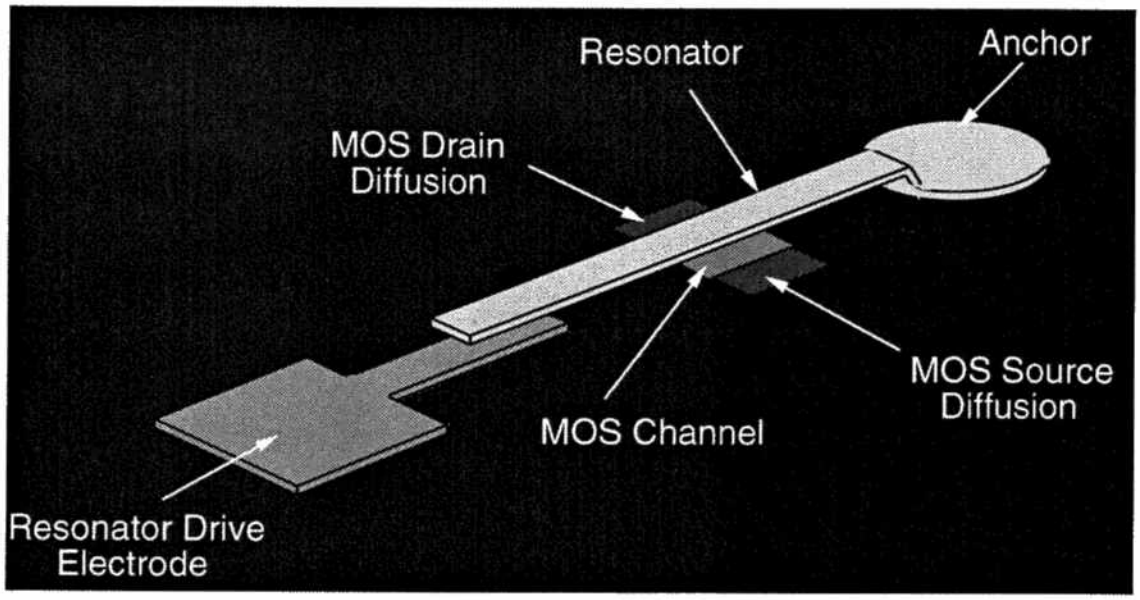

Fig. 1.5: Schematic of the resonant gate transistor.

grated technology based upon transistors, which can achieve high-Q filtering in the MF to UHF range, is still unavailable.

There are, however, integrated passive mechanical technologies currently under development, which are based upon the same passive miniaturization ideas of this dissertation. These are thin-film bulk-acoustic resonator devices, commonly referred to as FBARs [18]. They operate at frequencies above 1 GHz, and can have quality factors as high as 2,000. They have potential for use as RF front-end filters.

1.4 A Previous Micromechanical Attempt: The Resonant Gate Transistor

The resonant gate transistor [19], depicted in Fig. 1.5, was one of the very first planar processed micromechanical elements, and was actually aimed at signal processing, not sensor applications. The device was conceived and fabricated by Nathanson and coworkers from Westinghouse as far back as 1967. As shown in the figure, this device consisted of a conductive cantilever beam suspended above a silicon substrate over a channel situated between two heavily-doped junctions. As is evident from the figure, the cantilever served as the gate of a FET transistor. Any motion of the biased cantilever perpendicular to the substrate results in corresponding modulation of the drain current. Thus, with proper circuit design, positive feedback can be implemented,

and self-sustaining oscillation of the cantilever could be achieved. Since the cantilever has high intrinsic mechanical Q, a completely monolithic oscillator with higher Q than any currently available on-chip device could be achieved.

Unfortunately, the device suffered from some fundamental flaws. First, the cantilever was constructed of evaporated gold, which at the time, was difficult to deposit with reasonable amounts of vertical stress. Cantilever beam lengths were, thus, greatly limited, which in turn, limited the lowest manufacturable frequencies. In addition, the temperature coefficient of the resonance frequency for the gold beam was quite high, much higher than that for quartz. Finally, fundamental device design problems existed, such as interface charge on the exposed channel, which made device threshold voltages unpredictable.

Due to the above reasons, the resonant gate transistor project was scrapped shortly after 1967. Integrated mechanical resonator work would not resurface until the early 1980's when Howe began researching resonant sensor applications of polycrystalline silicon mechanical resonators [4].

1.5 Conclusions

Since the impact of a given communication system is very much dependent upon its scope, or the number of individuals it reaches, convenience and availability are two important attributes which must be considered when designing the components making up a given system. Since convenience and availability often translate to compactness, miniaturization of the transmitters and receivers used in wireless communication systems is desirable.

Miniaturization of present-day communication devices is limited mainly by the need for high-Q signal processing, which is generally performed using off-chip passive components, such as quartz or ceramics. The advent of micromachining technologies, whereby integrated high-Q micromechanical devices are now possible, makes replacement of these off-chip components via micromechanical substitutes an interesting proposition. The design, fabrication, and testing of such replacements, as well as proposals for future directions in this area, is the aim of this dissertation.

1.6 Overview

This dissertation will focus upon design issues of high-Q oscillators and filters utilizing micromechanical resonators. It begins in Chapter 2 with an in depth discussion of micromechanical resonators, from design, to material properties, to circuit modelling. Next, in Chapter 3, the technology which merges CMOS electronics with surface micromachined polysilicon mechanical resonators is discussed, both from both philosophical and procedural viewpoints. Chapter 4 discusses the first application of this technology: high-Q fully integrated micromechanical resonator oscillators with sustaining CMOS electronics. The design of the prototype oscillator of this work will be detailed, and issues concerning the limitations of miniaturized resonators will be discussed. In particular, phase noise limitations due to Brownian motion noise and mass loading of resonators will be addressed in detail. Chapter 5 then discusses the high-Q filtering application of this technology, where one of the major consequences of miniaturization—high series motional resistance—will be seen to limit the noise performance and dynamic range of micromechanical filters. Chapter 6 then details yet another application of this technology, in which a single micromechanical resonator may be used simultaneously as a mixer and a filter for heterodyning purposes in both transmitters and receivers. Finally, Chapter 7 addresses one of the more fundamental material constraints of this technology: thermal stability. A micro-scale oven-control method will be demonstrated which significantly nulls out the temperature coefficient of the resonance frequency for a micromechanical resonator. Chapter 8 finishes with some conclusions. Experimental measurement and verification is interspersed throughout each of these chapters.

CHAPTER 2 *Micromechanical Resonators*

Since every mechanical structure has an infinite number of resonance frequencies. The problem of emphasizing a particular resonance frequency is generally approached through consideration of resonator geometry and the properties of its structural material. Since planar and bulk micromachining fabrication technologies can realize a large variety of geometries, usually in single masking steps, these technologies provide substantial design flexibility for resonators. In addition, the list of available materials to construct microresonators is also quite large. A wide variety of publications are available which describe different resonator geometries and materials [4,20,22,26,27,34], both macroscopic and microscopic. Even so, the design of micromechanical resonators and the materials used are still not optimized, and much work remains to improve the performance of devices based upon these elements.

The focus of this dissertation is on signal processing using micromechanical elements, and therefore, only a small subset of possible resonator topics will be addressed in this chapter. This chapter, thus, concentrates on the material properties and geometric designs which determine the resonance frequency of resonators, their temperature coefficients and aging characteristics, and their circuit performance (i.e. equivalent circuits and linearity).

2.1 Micromechanical Resonator Geometrical Design

Because they are lithographically-based, planar integrated circuit processing methods provide tremendous flexibility for construction of micromechanical resonators. In a single lithogra-

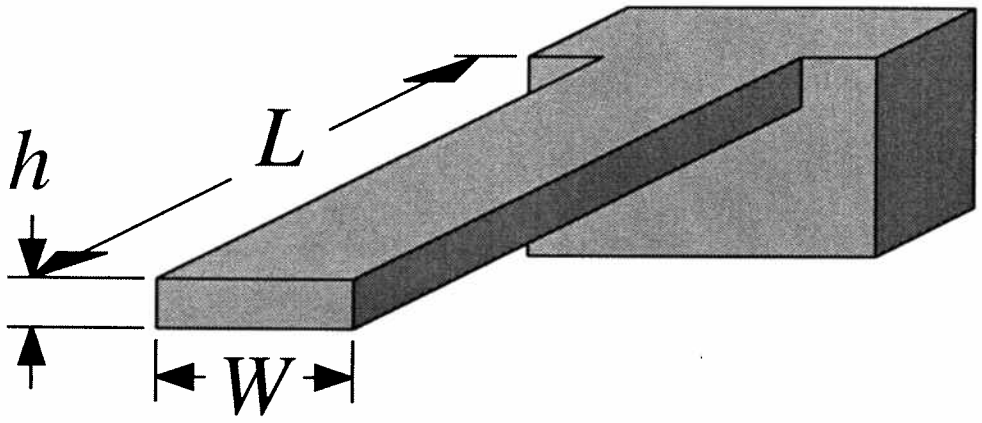

Fig. 2.1: A cantilever resonator.

phy-and-etch process module, many complex geometries in a single plane may be patterned in a variety of materials. With several planes of structural material, of course, the possibilities for additional complexity or optimization greatly increase. For example, mechanical or thermal isolation of a mechanical resonator and bridging between indirectly coupled resonators become possible.

2.1.1 Single Beam Resonators

Some of the simplest micromechanical resonators available are single beam cantilevers or clamped-clamped resonators, depicted schematically in Figs. 2.1 and 2.2. Analytical expressions for the fundamental vertical mode frequency of these resonators may be obtained through a variety of techniques [20], and are given as follows:

Cantilever Beam:

$$f_n = \frac{(k_n L)^2}{2\pi L^2}\sqrt{\frac{EI}{\rho S}} \quad , \quad \cos k_n L = \frac{1}{\cosh k_n L}$$
$$\text{(Fundamental mode: } k_1 L = 1.875) \Rightarrow \quad f_1 = 0.1615\sqrt{\frac{E}{\rho}}\left(\frac{h}{L^2}\right) \tag{2.1}$$

Clamped-clamped Beam:

$$f_n = \frac{(k_n L)^2}{2\pi L^2}\sqrt{\frac{EI}{\rho S}} \quad , \quad \cos k_n L = \frac{1}{\cosh k_n L}$$
$$\text{(Fundamental mode: } k_1 L = 4.730) \Rightarrow \quad f_1 = 1.03\sqrt{\frac{E}{\rho}}\left(\frac{h}{L^2}\right) \tag{2.2}$$

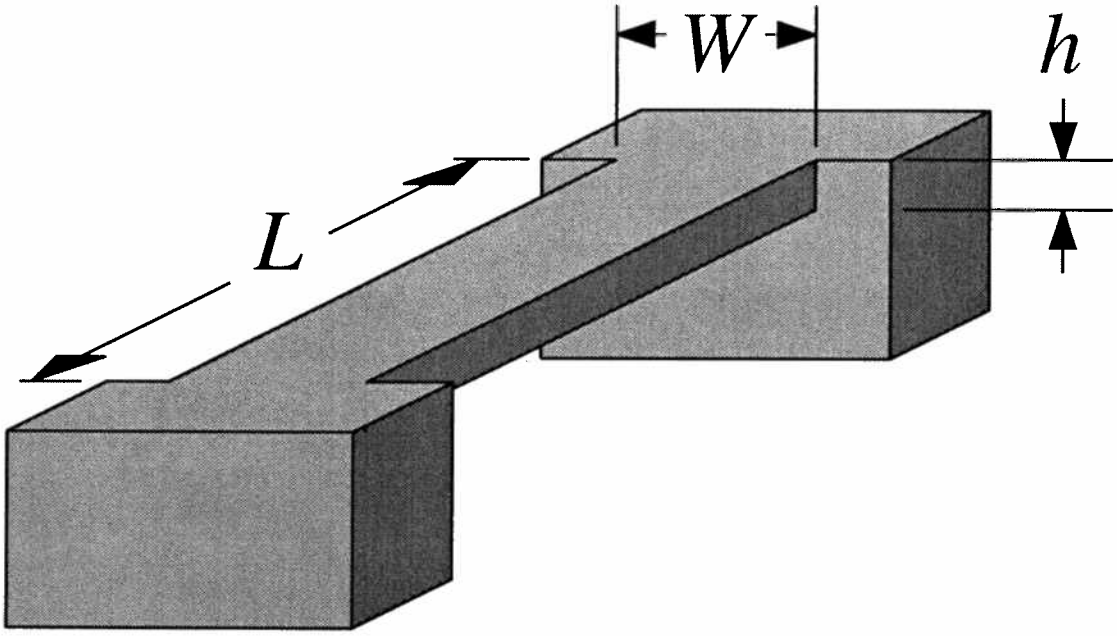

Fig. 2.2: A clamped-clamped beam resonator.

where $S = Wh$ is the cross-sectional area of the beam, E is the Young's modulus of the resonator material, ρ is its density, and the geometric quantities L and h are given in Figs. 2.1 and 2.2. Thus, the resonance frequencies of these resonators are functions of material properties and geometry.

From Eqs. (2.1) and (2.2), the clamped-clamped beam is seen to be longer than its cantilever counterpart for a given frequency. Thus, a low frequency resonator, which requires a large L, is more easily attainable using the cantilever design. If the beam has a compressive stress after fabrication, then the cantilever is the much better design than the clamped-clamped beam, which may buckle under the stress. Since the total buckling force is proportional to the beam length L, the longer the clamped-clamped beam (lower the resonator frequency), the higher the probability of buckling.

For high frequencies, however, buckling under compressive stress is no longer a problem, since the required beam length of the clamped-clamped resonator will be much smaller (but still larger than the length of the cantilever, of course). In fact, lithography becomes a major limitation at high frequencies, since required beam lengths become small enough that length variations due to lithography and etching may degrade the matching tolerance of identical or ratioed resonators.

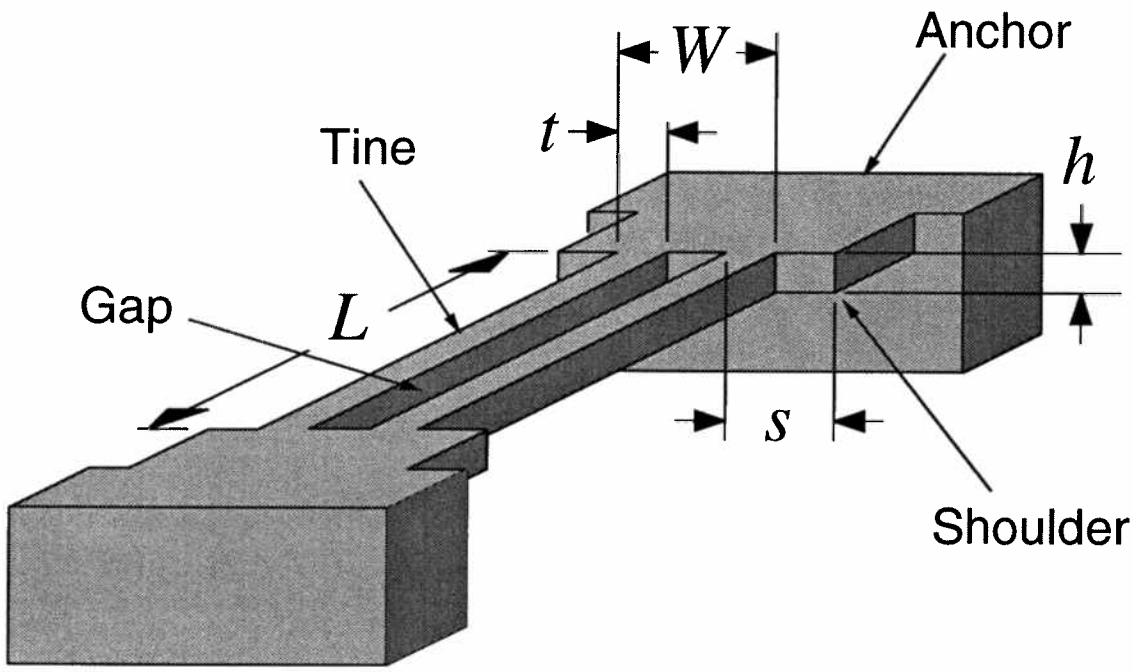

Fig. 2.3: Schematic of a double-ended tuning fork (DETF) resonator designed to resonate laterally.

As will be seen later, matching of resonators is extremely important when implementing high-Q filters. Thus, the longer clamped-clamped beam is the preferred resonator embodiment at high frequency.

2.1.2 Tuning Fork Resonators

At high frequencies, the simple clamped-clamped resonator design of Fig. 2.2 may still not be the optimum design, because of possible degradation of the quality factor of the resonator. Some of this Q loss is attributable to energy dissipation in the material, which may or may not increase with frequency [21]. Another fraction of the loss might be attributable to dissipation through the anchors of the resonator. A more balanced resonator design, such as the laterally resonant tuning fork shown in Fig. 2.3, could be used to minimize energy dissipation at the resonator anchors when the DETF operates in the antisymmetric mode. The equation for the resonance frequency of the double-ended tuning fork (DETF) shown in Fig. 2.3 is [22,23]

$$f_{1,DETF} = 2.06\sqrt{\frac{E}{\rho}}\frac{h}{L^2} \tag{2.3}$$

TABLE 2.1. Constraint Equations Insuring Minimum Loss in DETF Anchors

Mode	Long Tuning Fork Arm Length	Short Tuning Fork Arm Length
1st	$\frac{2s}{W} = 0.141$	$\frac{2s}{W} = 0.141$
2nd	$\frac{2s}{W} = 0.182$	$\frac{2s}{W} = 0.228$
3rd	$\frac{2s}{W} = 0.231$	$\frac{2s}{W} = -0.192$

where L and t are geometries as shown in Fig.2.3. Note that the resonance frequency is twice as high as that for a clamped-clamped beam.

The design of Fig.2.3 takes advantage of a special shoulder design which minimizes displacement at the anchors [24]. The optimum dimensions of the shoulders have been determined through finite element simulation [24], and the constraint equations resulting from these simulations are summarized in Table 2.1 for several different modes and for both long- and short-beam cases. Again, the geometric dimensions are shown pictorially in Fig. 2.3. The SEM of a fabricated DETF is shown in Fig. 2.4.

2.1.3 Folded-Beam Resonators

Of the above resonator designs, the only one which relieves axial stress is the cantilever design. For resonators that require a clamped-clamped design, a simple folding of the beams can greatly relieve stresses. Such a folded-beam resonator is depicted in Fig. 2.5, where a shuttle mass is supported by two folded-beam suspensions. In this scheme, if all beams expand or contract by the same amount (which will likely be the case in a planar process technology), there will be minimal residual axial compressive or tensile stresses. Any induced stresses will be caused by mismatches in the expansion or contraction of the beams after release.

In addition to post fabrication stress relief, the linearity of the resonator is greatly enhanced when its supporting beams are folded. Folding the beams allows nearly stress-free expansion of the beams, which greatly reduces nonlinearity due to spring stiffening. The range of Duffing-free displacements is much larger for a folded-beam resonator than for an unfolded

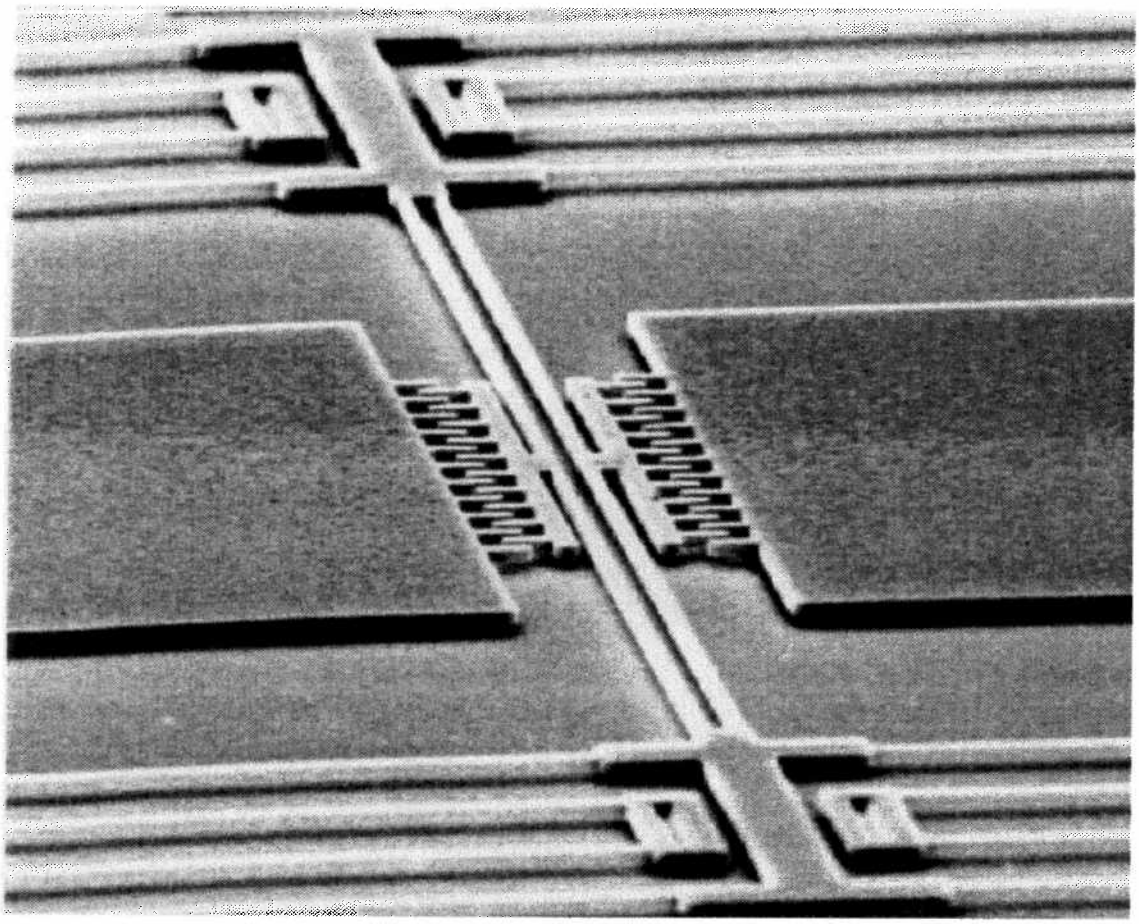

Fig. 2.4: SEM of a fabricated polysilicon DETF with a 1 MHz fundamental mode frequency.

clamped-clamped resonator. As will be seen, however, even with folding, the Duffing phenomenon is still observable at very high Q's.

The fundamental lateral mode resonance frequency of the folded-beam resonator of Fig. 2.5 is given by the expression [38]

$$f_1 = \frac{1}{2\pi}\left[\frac{2Eh(W/L)^3}{\left(M_P + \frac{1}{4}M_t + \frac{12}{35}M_b\right)}\right]^{1/2}, \tag{2.4}$$

where M_P is the shuttle mass, M_t is the mass of the folding trusses, and M_b is the total mass of the suspending beams.

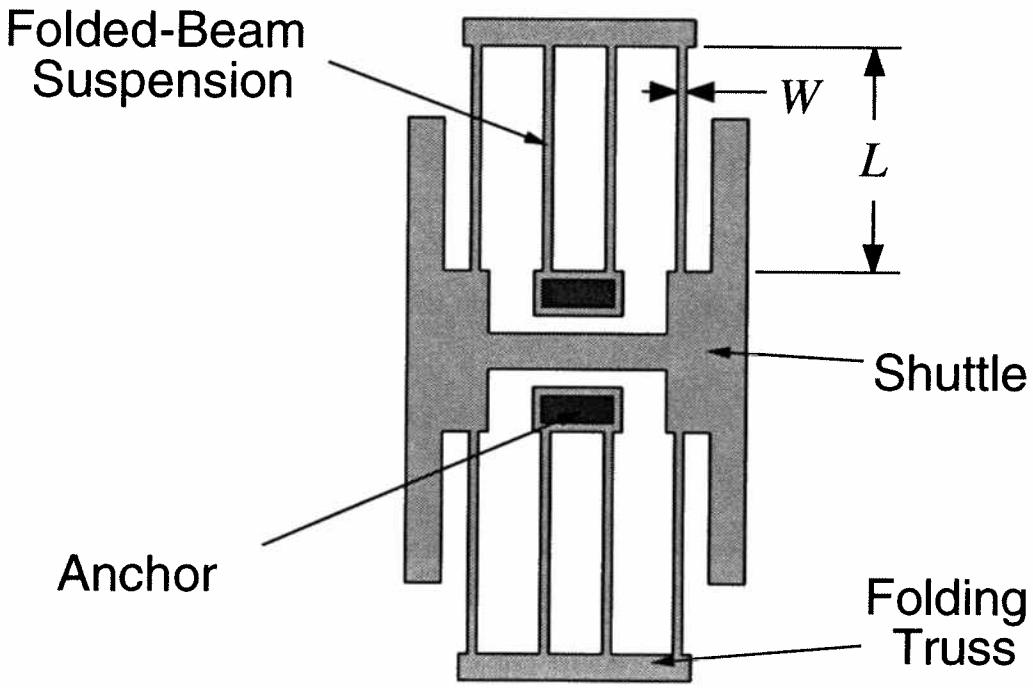

Fig. 2.5: Overhead view schematic for a folded-beam micromechanical resonator. Here, the darkly shaded regions are anchored to the substrate, while the lightly shaded regions are suspended 2 μm above the substrate.

For the case of low frequency DETF's, beam buckling may again pose a problem if the resonator is under compressive stress. If this is the case, then beam folding may be used to advantage here, as well. Figure 2.6 shows the SEM of a DETF design in which the anchors are actually plates, which are suspended themselves by folded-beams, which are then finally anchored to the substrate. This design not only relieves post fabrication residual stress, it also may even help to further decouple the tuning fork anchors from the substrate, possibly further minimizing Q-degradation due to anchor losses.

2.2 Quality Factor

As mentioned, the main advantage provided by an integrated mechanical resonator is high-Q. Figure 2.7 presents the measured transconductance spectrum for an 18.8 kHz polysilicon micromechanical resonator operated under 20 mTorr pressure. The quality factor extracted from this curve is close to 50,000.

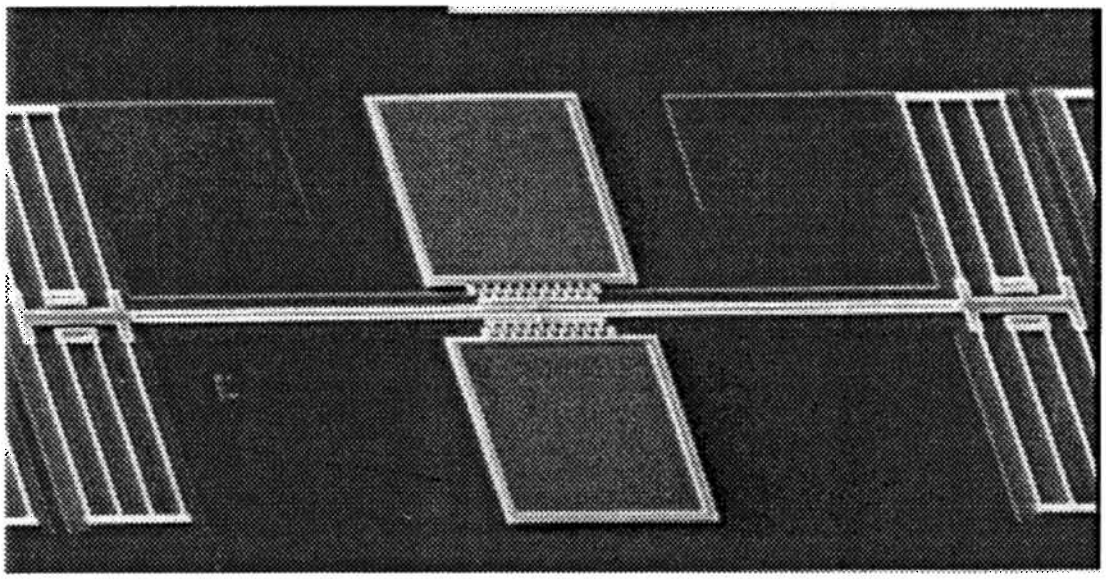

Fig. 2.6: SEM of a DETF utilizing folded-beam anchor suspensions.

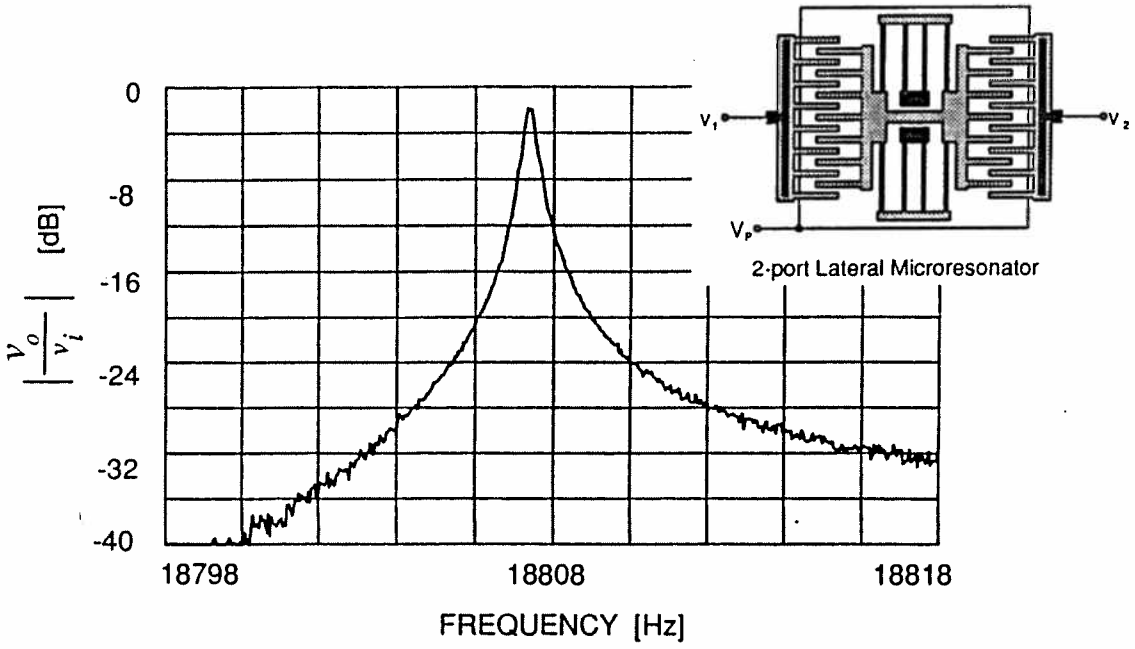

Fig. 2.7: Measured transconductance spectrum for an 18.8 kHz folded-beam polysilicon micromechanical resonator operated under 20 mTorr pressure. The quality factor extracted from this curve close to 50,000. The experimental set-up used to measure this spectrum is shown in the insert.

The quality factor of a micro-scale resonator is a function of many variables, among which are environmental conditions, such as pressure and temperature; design variables, such as

anchor losses; and intrinsic material-based variables, such as thermoelastic friction and surface roughness.

Among the mentioned variables, pressure dominates at the lower Q's, in the range of about 1 mTorr on up [26]. When pressure determines Q, fluidic dissipation mechanisms, such as squeeze-film damping [4] of vertically resonant beams or Couette flow in laterally resonant plates [27,28], are dominant. Measured curves of quality factor versus pressure for silicon and polysilicon resonators can be found in [26]. These show a logarithmic increase in Q with decreasing frequency, leveling off at a pressure around 1 mTorr. Below this pressure, anchor dissipation or intrinsic-material dissipation determines Q.

A wide variety of intrinsic dissipation mechanisms are possible, including thermoelastic friction, surface roughness, and possible anharmonic effects [21,26]. Thermoelastic friction has been studied to some extent for silicon resonators [29], and can be modelled via the expression:

$$\zeta = \Gamma(T)\,\Omega(f) = \frac{1}{2Q}, \tag{2.5}$$

where

$$\Gamma(T) = \frac{a^2 TE}{4\rho C_p} \tag{2.6}$$

$$\Omega(f) = 2\left[\frac{f_o f}{f_o^2 + f^2}\right] \tag{2.7}$$

and where

$$\begin{aligned} \zeta &= \text{thermoelastic critical damping fraction} \\ a &= \text{thermal expansion} \\ T &= \text{beam temperature} \\ E &= \text{Young's Modulus} \\ \rho &= \text{density of the structural material} \\ C_p &= \text{thermal conductivity} \\ f &= \text{resonance frequency of the beam} \\ t &= \text{beam thickness} \\ f_o &= \text{characteristic damping frequency} \end{aligned} \tag{2.8}$$

Using Eq. (2.5), we see that the Q is minimized (i.e., the loss is maximized) at the characteristic damping frequency, given by

$$f_o = \frac{\pi k}{2\rho C_p t^2} \tag{2.9}$$

where k is the thermal conductivity of the material. Thus, to maximize the quality factor, one must design the frequency of the resonator away from the characteristic frequency.

Again, thermoelastic friction is only one of several internal mechanisms which cause dissipation (thus, Q-reduction) in mechanical resonators. Many other intrinsic dissipation mechanisms exist for every degree of freedom in a mechanical system, at the molecular or macrosopic levels [21]. Given the strong incentive for increasing the frequency of micromechanical resonators, the topic of dissipation mechanisms is of central importance and must be investigated to ensure a high quality factor at high frequencies.

2.3 Micromechanical Resonator Materials

Several materials have been successfully utilized to implement mechanical devices on the micro-scale, including polycrystalline silicon [4,25,27,28,32], single crystal silicon [1,43,44,45,46], silicon nitride [47,48], polyimide [49], nickel [50,51], aluminum [53], and even silicon dioxide [52]. Of the present integrated material choices, silicon or polycrystalline silicon are excellent choices for the needs of micromechanical signal processors. This is due mainly to their instrinsic high quality factor, low aging rate, and relatively low temperature coefficient:[1] the same properties that make quartz so popular in the macroscopic domain.

For technological reasons having to do mainly with integration of CMOS electronics with surface-micromachined mechanics, the resonators of this work are constructed of *in situ* phosphorous-doped polycrystalline silicon, low-pressure chemical vapor deposited (LPCVD'ed) at 610°C at 300 mTorr pressure with flow rates of 100 sccm SiH_4 and 1 sccm PH_3. The Young's modulus of this material, extracted from resonance curves [27,31], is in the range of from 140 to 170 GPa. A plot of the measured fractional frequency change versus temperature for an 18 kHz polysilicon

[1]Although not as low as quartz.

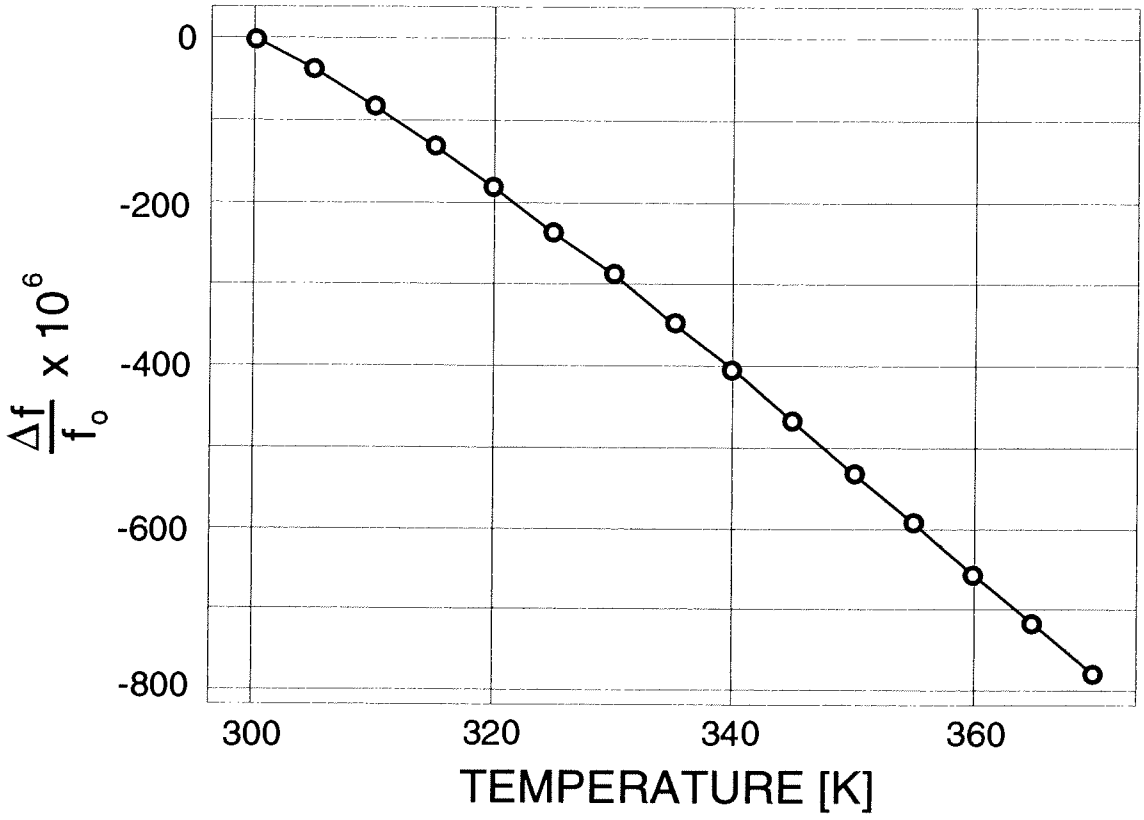

Fig. 2.8: Plot of the measured fractional frequency change versus temperature for an 18 kHz polysilicon folded-beam resonator.

folded-beam resonator is presented in Fig. 2.8. From the slope of this curve, the temperature coefficient of the resonance frequency, TC_{fr} for this device is -10 ppm/°C.

From the value of TC_{fr} and the expression for the resonance frequency of a folded-beam resonator (Eq. (2.4)), the temperature dependence of the Young's modulus for the polycrystalline silicon used for this work may now be determined. First, use (2.4) to find the expression for TC_{fr}:

$$TC_{fr} = \frac{1}{f_r}\frac{\partial f_r}{\partial T} = \frac{1}{2}\left[\frac{1}{E}\frac{\partial E}{\partial T} + \frac{1}{h}\frac{\partial h}{\partial T} + \frac{3}{W}\frac{\partial W}{\partial T} - \frac{3}{L}\frac{\partial L}{\partial T}\right]$$
$$TC_{fr} = \frac{1}{2}[TC_E + TC_h] \tag{2.10}$$

where TC_E is the temperature coefficient of the Young's modulus and TC_h is the temperature coefficient of the thickness, which is the same as the thermal expansion coefficient for polycrystalline

silicon. (2.5 ppm/°C). The final form of Eq. (2.10) was obtained by using the fact that the thermal (expansion) coefficients of the beam width and length are equivalent.

Rearranging (2.10), we have

$$TC_E = 2TC_{fr} - TC_h . \tag{2.11}$$

Using the measured value of TC_{fr} = -10 ppm/°C, Eq. (2.11) yields TC_E = -22.5 ppm/°C. This value is considerably smaller than a previously reported number [32], and it is stated tentatively pending a more systematic study of other factors which can effect the TC_{fr}, such as packaging stress due to thermal mismatches.

2.4 Transduction for Micromechanical Resonators

Several transduction methods are available for resonator actuation and motion sensing, among which are capacitive [4,27], piezoelectric [54,55], piezoresistive [56], thermal [57], and magnetic [58] techniques. Some of the common piezoelectric and piezoresistive materials that have been successfully used on the micro-scale include ZnO, PZT, AlN, and implanted silicon. Each material-transduction mechanism pair comes with its own advantages and disadvantages with respect to performance and fabrication complexity.

Again, due to technology considerations, the structural material used in this work is poly-crystalline silicon. Of the available transduction mechanisms, capacitive, piezoelectric, and piezoresistive have been the most common for this material. Magnetic transduction has been less frequently used than electrostatic or piezoelectric in the micromechanical world, perhaps due the increased fabrication complexity that it introduces. This contrasts sharply with macroscopic mechanical filters, which very commonly use magnetostrictive transduction [33,34,35].

Piezoelectric or piezoresistive transduction methods may entail excessive fabrication complexity. For the case of piezo-transduction, a piezoelectric material is usually deposited onto the resonator, then patterned to reside at a designed location. This complicates the material, introducing a more complex stress topology and altering the resonance frequency of the device. Since the uniformity of deposited piezoelectrics is presently difficult to control from die-to-die, repeatability and matching of resonance frequencies may be compromised. Furthermore, the temperature

behavior of the resonator now takes on the characteristics of the piezoelectric, which in the majority of cases where the piezoelectric is deposited, are worse than that of silicon or polycrystalline silicon. Thus, process complexity for piezoelectrically transduced resonators is increased due to requirements for stress control, and designability is compromised due to unpredictable resonance frequency (i.e. matching tolerances, absolute tolerances, etc...) and temperature characteristics. Note, however, that despite these drawbacks, there is a significant advantage in using a multiple-layer material if the temperature characteristics of the resonator could be accurately tailored to reduce the total frequency excursion over a given temperature range. Zero TC_{fr} points in the frequency versus temperature curve are also useful, since they make excellent bias points for oven control stabilization techniques (Chapter 7).

Piezoresistively sensed microresonators are commonly implemented by implanting an impurity into a designed location on the resonator. Thus, they may suffer from similar problems to that of piezoelectrically transduced resonators, namely postfabrication residual stress and temperature effects. In addition, a piezoresistance cannot be used to actuate the resonator. Oftentimes, piezoresistively sensed resonators are actuated by capacitive methods.

Capacitive transduction methods are the most forgiving in terms of fabrication complexity and impact on microresonator characteristics. From a fabrication point of view, film thicknesses or lithographic resolution determine practical strengths of capacitive transduction. From a resonator property point of view, there is no added material to the structural silicon or polysilicon, so no additional stress is introduced, and no additional temperature coefficients are imposed. Design of micromechanical signal processors can usually proceed with consideration of the properties of a single material, rather than a sandwich of them. (Note that other materials in contact with a capacitively transduced resonator may still impose second order constraints on resonator design. For example, differences in thermal expansion between the structural and substrate materials may influence a design.)

Given that the fabrication of micromechanical signal processors already requires the additional complexity for merging both CMOS and micromachining technologies, this work focuses upon capacitively transduced microresonators. Next generation processes may include piezoelectric transduction mechanisms. Whether piezoelectrics are required or not, is an issue based mainly on the required value of electromechanical coupling coefficient for filters and oscillators.

2.4.1 Capacitive Parallel-Plate Transduced Microresonators

The earliest capacitively transduced microresonators consisted of cantilevers, like the resonant-gate transistor, or clamped-clamped beams, which were driven perpendicular to the substrate surface by parallel-plate capacitive electrostatic forces. The overhead and cross-sectional views of a typical clamped-clamped vertically driven resonator, along with a typical bias and excitation configuration, are shown in Fig. 2.9. Here, a dc-bias voltage V_P is applied to the resonator, while an ac excitation voltage is applied to a drive electrode. Both the dc and ac voltages are required to excite resonance at the frequency of the ac excitation voltage. The dc-bias V_P effectively acts to create and amplify force components *at the frequency of the ac excitation voltage* v_i. This can be seen by deriving the equation for the drive force f_d as follows:

$$\begin{aligned} f_d &= \frac{1}{2}(V_{PD} - v_i)^2 \frac{\partial C_d}{\partial x} \\ &= \frac{1}{2}(V_{PD} - |v_i|\cos\omega t)^2 \frac{\partial C_d}{\partial x} \\ &= \frac{1}{2}\{V_{PD}^2 - 2|v_i|V_{PD}\cos\omega t + |v_i|^2\cos^2\omega t\}\frac{\partial C_d}{\partial x} \\ &= \frac{1}{2}\left\{V_{PD}^2 + \frac{|v_i|}{2} - 2|v_i|V_{PD}\cos\omega t + \frac{|v_i|^2}{2}\cos 2\omega t\right\}\frac{\partial C_d}{\partial x} \end{aligned} \tag{2.12}$$

where $V_{PD} = V_P - V_D$. (This will be the convention of this dissertation; i.e., $V_{AB} = V_A - V_B$. The resultant drive force consists of a dc component, a component at the drive frequency ω, and one at twice the drive frequency, 2ω. If the frequency of the excitation voltage is at the resonance frequency of the beam, then the component at the drive frequency is amplified by the quality factor of the beam, as well as by the dc-bias voltage, V_P, applied to the resonator. The dc and second harmonic components do not receive Q-amplification, and in many cases, may be neglected when compared with the drive frequency component. Note from Eq. (2.12) that with no dc-bias voltage, there is no component of force at the frequency of the drive voltage.

An expression for the resonance frequency of the resonator of Fig. 2.9 was given as Eq. (2.2). If the ac excitation occurs at a frequency close enough to the resonance frequency of the resonator, the beam will, of course, oscillate, creating a time-varying capacitance between the beam and the electrodes. The dc-bias $V_{PS} = V_P - V_S$ is effectively applied across the time-varying

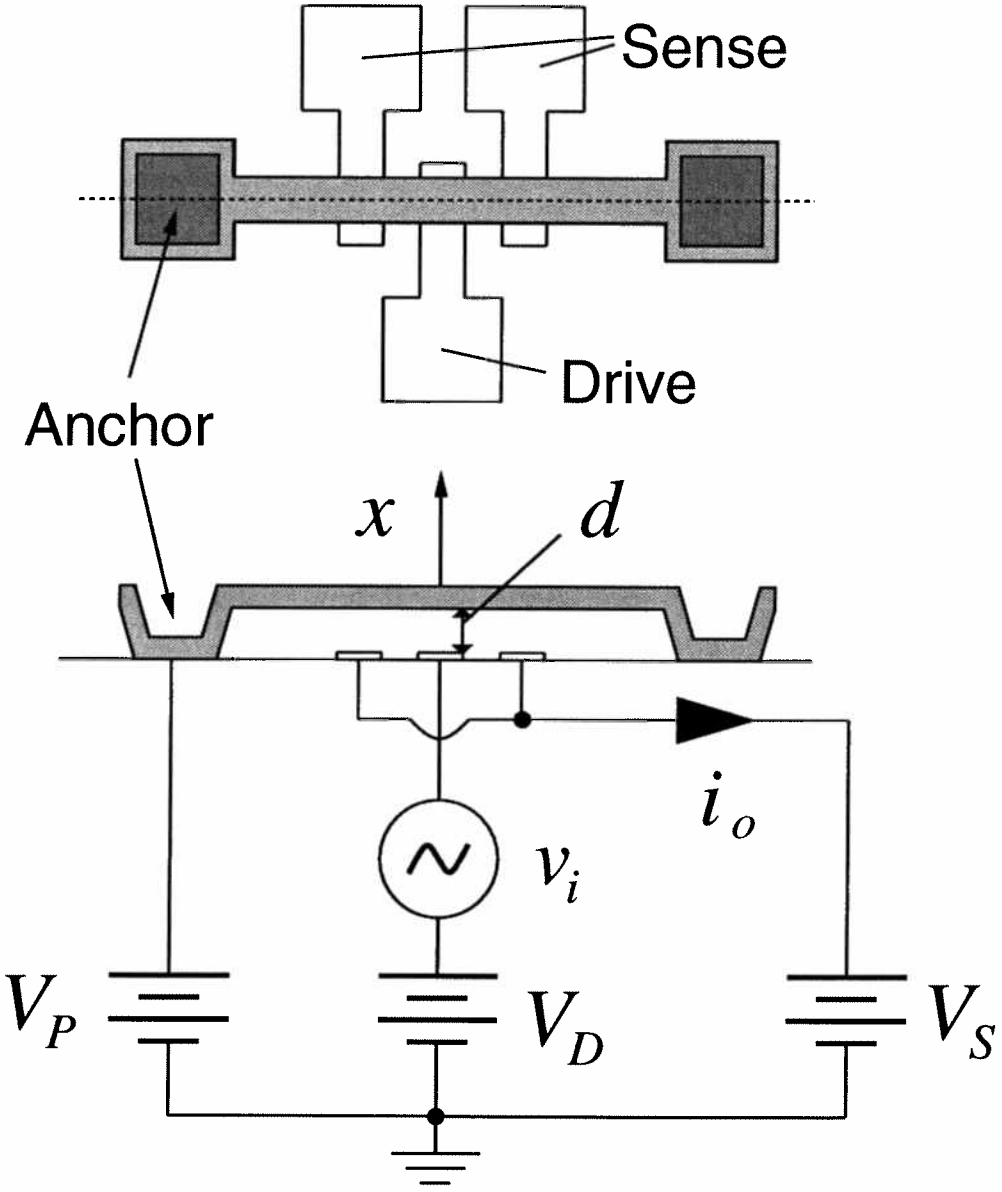

Fig. 2.9: Overhead and cross-sectional views of a typical clamped-clamped vertically driven resonator, along with a typical bias and excitation configuration.

capacitance at the sense electrode, which results in a motional output current (going *into* the sense electrode by convention) given by

$$i_o = -V_{PS}\frac{\partial C_s}{\partial t} = -V_{PS}\frac{\partial C_s}{\partial x}\frac{\partial x}{\partial t}, \tag{2.13}$$

which in phasor form becomes

$$I_o = -j\omega V_{PS}\frac{\partial C_s}{\partial x}X. \tag{2.14}$$

In Eqs. (2.13) and (2.14), $V_{PS} = V_P - V_S$, and $\partial C_s/\partial x$ is the incremental change in beam-to-sense electrode capacitance C_s with beam displacement x. For the resonator of Fig. 2.9, the value of beam-to-sense electrode capacitance as a function of displacement is approximately (ignoring fringing fields and assuming the capacitor plates are flat) given by

$$C_s(x) = \frac{\varepsilon_o A_{os}}{(d+x)} = C_{os}\left(1+\frac{x}{d}\right)^{-1} \tag{2.15}$$

where A_{os} is the beam to sense electrode overlap area, and C_{os} is the static capacitance between the sense electrode and beam. Differentiating (2.15) we obtain for $\partial C_s/\partial x$

$$\frac{\partial C_s}{\partial x} = -\frac{C_{os}}{d}\left(1+\frac{x}{d}\right)^{-2} \tag{2.17}$$

If beam displacements are small, then the approximation x=0 holds in Eq. (2.17). For this case, and for the typical values A_{os} = 400 μm^2 and d = 2 μm, $\partial C_s/\partial x$ = 8.85 x 10^{-11} F/m. For a 455 kHz clamped-clamped beam biased with V_{PS} = 10 V and driven into resonance with a displacement amplitude of 0.1 μm, the expected magnitude of motional current is 2.5 nA. This value of motional current could be increased with increased amplitude of motion or an increase in the dc-bias voltage, V_P. Unfortunately, however, for the resonator of Fig. 2.9, a larger dc-bias voltage V_P may pull the resonator down to the substrate, where it may short to the drive or sense electrodes and be destroyed [19,36]. In addition, increasing the amplitude of motion may introduce spring stiffening nonlinearity, which would distort a filter passband, or degrade the short-term stability of an oscillator.

---

[2]Note that both Eqs. (2.15) and (2.17) are approximations in that they neglect the actual shape of the resonator over the electrode. (It's not exactly flat.) A more accurate treatment would take the mode shape of the beam into account by replacing x with $x(y)$ and integrating over the width of the electrode:

$$C_s(x) = \int_{W_e}\frac{\varepsilon_o W_b dy}{(d+x(y))} \tag{2.16}$$

where W_b is the width of the beam and W_e is the width of the electrode. To simplify the form of results, however, we will neglect this for the remainder of this chapter. This approximation is most applicable to cases where the electrode is thin compared with the length of the beam.

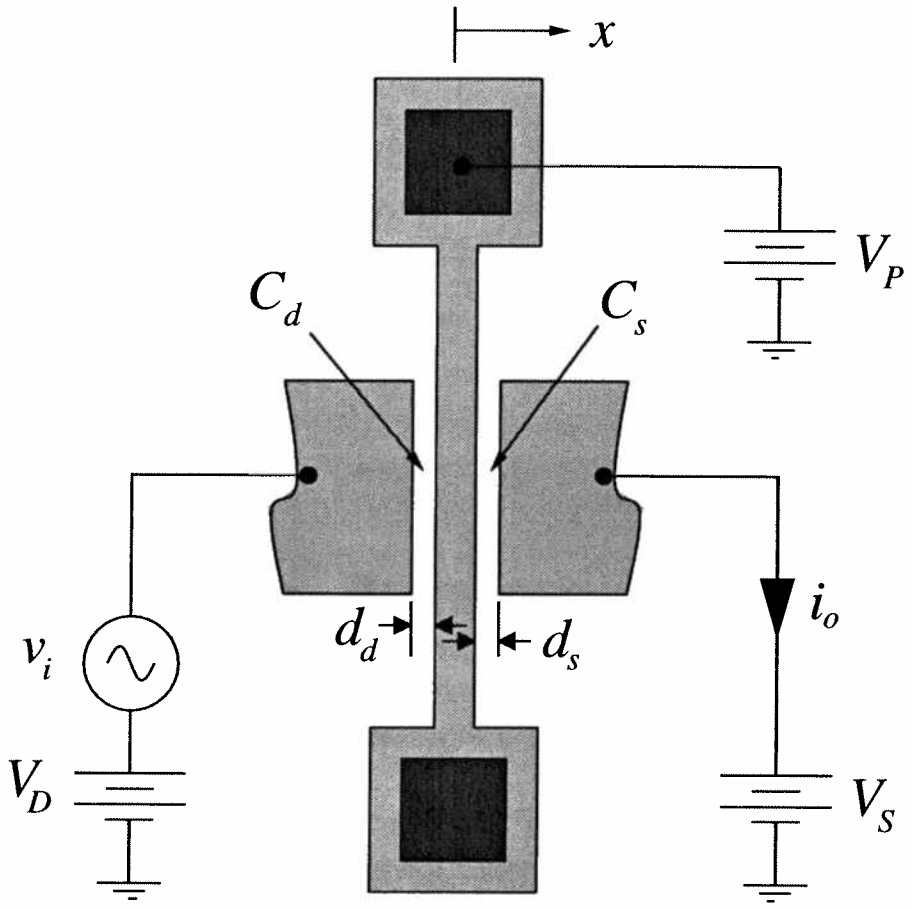

Fig. 2.10: Overhead view of a typical clamped-clamped laterally driven resonator with balanced electrodes, including a typical bias and excitation configuration.

2.4.1.1 Balanced Parallel-Plate Capacitive Transduction for Single-Beam Resonators

To increase the output motional current for a clamped-clamped beam resonator, the allowable value of dc-bias voltage V_P which avoids pull-in must be increased. This can be achieved with the design of Fig. 2.10, where the beam now moves in a direction parallel to the substrate (in the plane of this paper), and the drive and sense electrodes are placed in symmetrically opposing locations. If $V_D = V_S$, then a large value of V_P would now impose equal and opposite electrostatic forces from the symmetrically placed electrodes, ideally leaving no net dc force component. The limit on V_P is determined by the matching tolerance between drive and sense capacitances.

The equation for output current at the sense port (again, with the convention that currents always go into a node) for this symmetrically transduced design is still given by Eq. (2.13). The

capacitance between beam and sense electrode, however, now decreases with increasing x. The expressions for $C_s(x)$ and $\partial C_s/\partial x$ are now

$$C_s(x) = C_{os}\left(1 - \frac{x}{d_s}\right)^{-1} \quad \Rightarrow \quad \frac{\partial C_s}{\partial x} = \frac{C_{os}}{d_s}\left(1 - \frac{x}{d_s}\right)^{-2}, \tag{2.18}$$

where C_{os} is the static sense electrode-to-beam capacitance, and d_s is the gap distance between sense electrode and resonator beam, which can now be different from that between drive electrode and resonator beam.

Taking, now, a typical lateral clamped-clamped beam microresonator, with $A_{os} = 100\ \mu m^2$, $d = 1\ \mu m$, $f_o = 455$ kHz, and $V_{PS} = 50$ V, the value of $\partial C_s/\partial x = 8.854 \times 10^{-10}$ F/m and the output motional current magnitude for a 0.1 μm displacement magnitude is $i_o = 12.6$ nA. This magnitude is even larger for higher frequency resonators with the same peak displacement amplitude.

2.4.1.2 Nonlinearity in Parallel-Plate Driven Resonators

Parallel-plate capacitive transduction methods generally yield nonlinear transconductance transfer functions, since the drive and sense capacitors are nonlinear functions of displacement (Eq. (2.15)). This nonlinearity gives rise to several phenomena in parallel-plate capacitively driven resonators: (1) a dc-bias voltage dependence in the center frequency of the resonator; (2) distortion in the frequency response of the resonator; and (3) harmonic distortion in the resonator output current. Each of these can drastically affect the performance of both oscillators and filters constructed of these microresonators.

Each of these phenomena will now be addressed in sequence. The following analyses will focus on the two-port parallel-plate resonator shown in Fig. 2.11, which presents geometric and dynamic data, and shows a general bias and excitation configuration for a multi-port resonator (and ac signal is now included at port 2).

2.4.1.2.1 Frequency-Pulling in Parallel-Plate Driven Resonators

As indicated by Eqs. (2.17) and (2.18), if the electrode-to-resonator capacitance $C(x)$ is a nonlinear function of displacement x, then the corresponding $\partial C/\partial x$ is a function of x. Consequently, the drive force f_d, which depends upon $\partial C/\partial x$ (Eq. (2.12)), is dependent on not only the

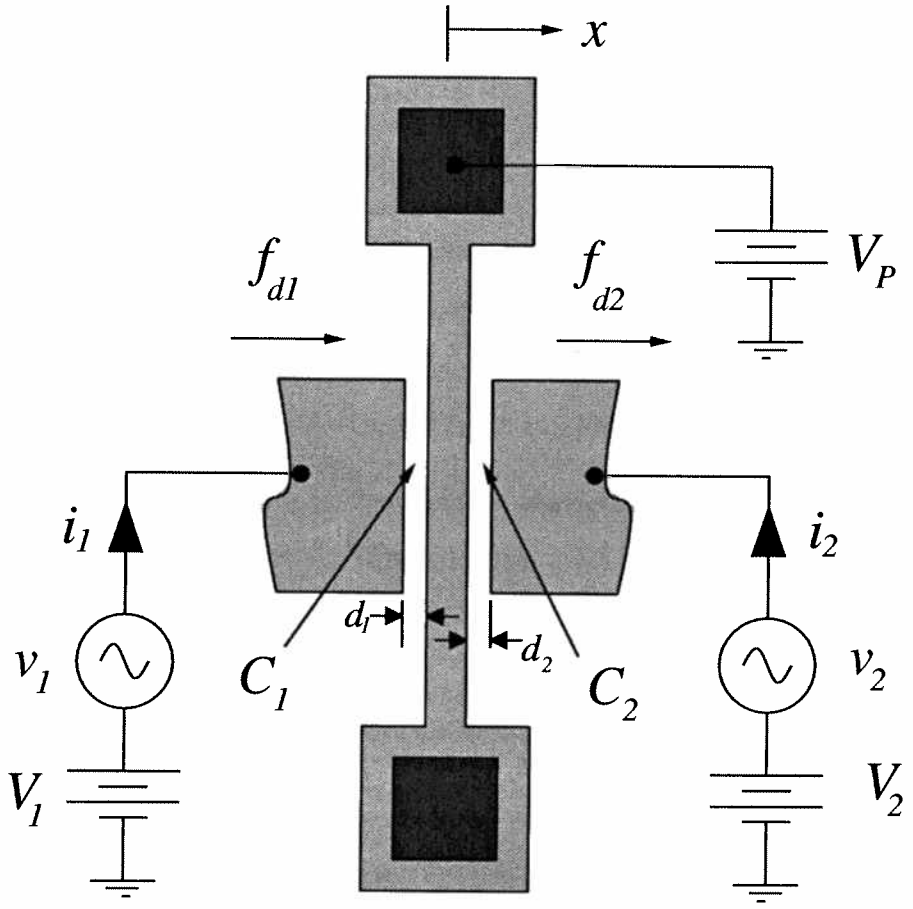

Fig. 2.11: Clamped-clamped laterally driven resonator with balanced electrodes in a general bias and excitation configuration.

drive voltage v_i, but also on the beam displacement x. This latter dependence leads to an effective electrostatic spring constant that adds to the mechanical spring constant, and thus, pulls the frequency of the resonator.

To show this explicitly, we refer to Fig. 2.11, and assume for the moment that there is only one port: port 1. The expression for the change in capacitance per unit displacement at this port is given by Eq. (2.17) (and note footnote 1). (Note that the direction for positive displacements is given in Fig. 2.11.) If displacements are small, a Taylor series expansion may be performed on Eq. (2.17), yielding

$$\frac{\partial C_1}{\partial x} = -\frac{C_{o1}}{d_1}(1 + A_1 x + A_2 x^2 + A_3 x^3 + \ldots)$$

where (2.19)

$$A_1 = -\frac{2}{d_1} \quad , \quad A_2 = \frac{3}{d_1^{\,2}} \quad , \quad A_3 = -\frac{4}{d_1^{\,3}} \quad , \quad \ldots$$

Inserting (2.19) into (2.12), assuming small displacements (thus, retaining only the first two terms of (2.19)) we have

$$f_{d1} = -\frac{1}{2}\frac{C_{o1}}{d_1}\{V_{P1}^2 - 2V_{P1}v_1 + v_1^2 + A_1 V_{P1}^2 x - 2A_1 V_{P1} x v_1 + A_1 x v_1^2\} \,, \tag{2.20}$$

where the displacement at resonance $x = |x|\sin\omega_r t$ is quadrature phase-shifted from the drive voltage $v_1 = |v_1|\cos\omega_r t$. Retaining only terms at the drive frequency and using (2.19), (2.20) becomes

$$f_{d1}\big|_{\omega_o} = V_{P1}\frac{C_{o1}}{d_1}|v_1|\cos\omega_o t + V_{P1}^2\frac{C_{o1}}{d_1^2}|x|\sin\omega_o t \,, \tag{2.21}$$

where ω_o is the radian center frequency of the resonator. The first term in (2.21) represents the drive force arising from the input excitation voltage at the frequency of this voltage. Note that this force acts to oppose the dc force component (given by the first term of Eq. (2.20)), which is expected, since when v_1 increases, $(V_P - v_1)$ decreases (i.e the voltage difference between the resonator and electrode 1 decreases). The second term represents an additional force component that has a displacement dependence. At resonance, this second component is quadrature phase-shifted from the input voltage (force), similar to the mechanical spring restoring force of the resonator. However, while the mechanical spring restoring force generally acts to oppose an input force, this force acts to increase the input force. The second term in Eq. (2.21), in fact, can be interpreted as an electrical spring constant,

$$k_e = V_{P1}^2\frac{C_{o1}}{d_1^{\,2}}, \tag{2.22}$$

which subtracts from the mechanical spring constant of the beam, k_m, changing its resonance frequency. Accounting for this electrical spring constant, the center frequency for the resonator is now

$$f_o' = \sqrt{\frac{k_m - k_e}{m}} = \sqrt{\frac{k_m}{m}}\sqrt{1 - \frac{V_{P1}^2 C_{o1}}{k_m \, d_1^{\,2}}} = f_o\left(1 - \frac{V_{P1}^2 C_{o1}}{k_m \, d_1^{\,2}}\right)^{\frac{1}{2}}, \tag{2.23}$$

where f_o is the original mechanical center frequency of the resonator and f_o' is the new center frequency, adjusted by the electrical spring constant k_e.

Thus, for a parallel-plate driven resonator, the resonance frequency may be conveniently adjusted by adjustment of the dc-bias voltage V_P. Using the binomial approximation, Eq. (2.23) may be rearranged to give the fractional frequency change as a function of V_P for small frequency excursions:

$$\frac{\Delta f}{f_o} = -\frac{1}{2}\frac{V_{PD}^2 C_{od}}{k_m d^2}. \tag{2.24}$$

Note that the fractional frequency change is proportional to $\partial C/\partial x$, inversely proportional to the square of the gap distance d, and inversely proportional to the value of mechanical spring constant k_m.

Equations (2.22) through (2.24) were derived assuming only one electrode at a different potential from the resonator. If there are other electrodes (e.g. the sense electrode, or other ports in a multi-port resonator), then these will also contribute electrical spring constants, which must be added to the expression in Eq. (2.23). Any additional port on the same side of the resonator as port 1 will contribute a force component at resonance with a form similar to Eq. (2.21). The sine terms in the force expressions from ports on the same side as port 1 will, thus, all add, adding to the total electrical spring constants.

One might wonder whether the electrical spring constant contributed by port 1 could be cancelled by the k_{e2} resulting from a dc-bias across port 2. Applying an analysis similar to the above, but for port 2 (with all the polarity changes intact), the force due to port 2 is given by

$$f_{d2}\big|_{\omega_o} = -V_{P2}\frac{C_{o2}}{d_2}|v_2|\cos\omega_o t + V_{P2}^2\frac{C_{o2}}{d_2^2}|x|\sin\omega_o t. \tag{2.25}$$

As shown in Fig. 2.11, the total force on the resonator is given by the sum of f_{d1} and f_{d2}. As expected, the drive voltage force component subtracts from the one due to port 1. The spring force

component, however, adds, even if V_{P2} is negative. Thus, all electrodes in a multi-port resonator will *add* to the total electrical spring constant, no matter the placement of electrodes or their respective bias polarities. (i.e. It doesn't matter if they are placed to balance each other, or if their dc-bias values are opposite in polarity.)

For a typical 20 kHz parallel-plate driven resonator, with a nominal V_P = 10 V, d = 2 μm, and C_o = 1.77 fF, the predicted fractional frequency change using (2.23) is -3600 ppm/V. The frequency variability governed by (2.23) makes parallel-plate driven resonators useful in VCO applications.

However, (2.23) also suggests that oscillators referenced to parallel-plate capacitively driven microresonators are less stable against power supply variations, due to electronic noise or changes in temperature. For example, if V_P = 10 V is supplied by a Zener diode reference, which typically varies 250 mV over a 0°-100° range, the corresponding fractional frequency variation for a 20 kHz microresonator is -864 ppm over this temperature range. If a bandgap voltage reference is used (3 mV variation over a 0°-100° range), the $\Delta f/f_o$ variation is -10 ppm, which may still be considered excessive for some applications.

2.4.1.2.1 Spring Softening in Parallel-Plate Transduced Resonators

In the previous section, capacitive nonlinearity was shown to result in a frequency pulling phenomenon arising from an additive electrical spring constant. The analysis in that section can be taken a step further to obtain higher order terms for electrical spring constant, which can cause spring-softening distortion in the resonator's transfer function. Proceeding with this analysis, we start by including the higher order terms of Eq. (2.19) when evaluating (2.12). Doing so yields

$$\begin{aligned} f_d &= -\frac{1}{2}\frac{C_{o1}}{d_1}\left(V_{P1}^2 - 2V_{P1}v_1 + v_1^2\right)\left(1 + A_1x + A_2x^2 + A_3x^3 + \ldots\right) \\ &= -\frac{1}{2}\frac{C_{o1}}{d_1}\left(V_{P1}^2 - 2V_{P1}v_1 + v_1^2 + V_{P1}^2A_1x - 2V_{P1}A_1v_1x^2 + A_1xv_1^2\right. \\ &\quad \left. + V_{P1}^2A_2x^2 - 2V_{P1}A_2v_1x^2 + A_2x^2v_1^2 + V_{P1}^2A_3x^3 - 2V_{P1}A_3v_1x^3 + A_3x^3v_1^2\right) \end{aligned} \tag{2.26}$$

Retaining only terms at the drive frequency, and using $v_1 = |v_1|\cos\omega_o t$ and $x = |x|\sin\omega_o t$ at resonance to include phase information in each term, yields

$$f_d = V_{P1}\frac{C_{o1}}{d_1}|v_1|\cos\omega_o t - \frac{1}{2}\frac{C_{o1}}{d_1}V_{P1}^2 A_1|x|\sin\omega_o t - \frac{1}{8}\frac{C_{o1}}{d_1}A_1|x||v_1|^2\sin\omega_o t + \frac{1}{4}\frac{C_{o1}}{d_1}A_2 V_{P1}|v_1||x|^2\cos\omega_o t$$
$$-\frac{1}{4}\frac{C_{o1}}{d_1}A_3 V_{P1}^2|x|^3\sin\omega_o t + \frac{1}{8}\frac{C_{o1}}{d_1}A_3 V_{P1}^2|x|^3\cos\omega_o t - \frac{1}{16}\frac{C_{o1}}{d_1}A_3|v_1|^2|x|^3\sin\omega_o t \quad (2.27)$$

The terms associated with the effective spring constant are those which are 90° phase-shifted from the drive signal at resonance. After inserting the values for A_1, A_2, and A_3 from Eq. (2.19), these components are

$$\begin{aligned}|f_d|_{90^o} &= V_{P1}^2\frac{C_{o1}}{d_1^{\,2}}|x| + \frac{1}{4}\frac{C_{o1}}{d_1^{\,2}}|x||v_1|^2 + V_{P1}^2\frac{C_{o1}}{d_1^{\,4}}|x|^3 + \frac{1}{4}\frac{C_{o1}}{d_1^{\,4}}|x|^3|v_1|^2 \\ &= \left(V_{P1}^2\frac{C_{o1}}{d_1^{\,2}} + \frac{1}{4}\frac{C_{o1}}{d_1^{\,2}}|v_i|^2\right)|x| + \left(V_{P1}^2\frac{C_{o1}}{d_1^{\,4}} + \frac{1}{4}\frac{C_{o1}}{d_1^{\,4}}|v_1|^2\right)|x|^3 \\ &= k_{e1}|x| + k_{e3}|x|^3\end{aligned} \quad (2.28)$$

From (2.28), we have

$$\begin{aligned}k_{e1} &= V_{P1}^2\frac{C_{o1}}{d_1^{\,2}} + \frac{1}{4}\frac{C_{o1}}{d_1^{\,2}}|v_1|^2 \approx V_{P1}^2\frac{C_{o1}}{d_1^{\,2}} \\ k_{e3} &= V_{P1}^2\frac{C_{o1}}{d_1^{\,4}} + \frac{1}{4}\frac{C_{o1}}{d_1^{\,4}}|v_1|^2 \approx V_{P1}^2\frac{C_{o1}}{d_1^{\,4}}\end{aligned} \quad (2.29)$$

The third order component, k_{e3}, gives rise to nonlinear Duffing behavior in the resonator transfer function, which distorts the passband as shown in Fig.2.12. Note that since the electrical spring constant subtracts from the total system spring constant, this is a softening spring nonlinearity. Even a tiny nonlinearity will induce noticeable distortion under conditions where the resonator Q is very large. Such distortion would of course be detrimental to very high Q mechanical filters. It could also be a cause of short-term frequency instability in oscillators referenced to micromechanical resonators (that are not automatic-level controlled).

In order to design high-Q mechanical filters utilizing micromachined parallel-plate capacitively driven beams, the spring-softening Duffing nonlinearity contributed by the nonlinear electrical spring must be minimized. Such minimization may already be conveniently present for resonators which show nonlinearity due to mechanical spring stiffening [31,30]. For this case, the electrical spring constants subtract from the mechanical spring constants associated with the mechanical resonator, leading to a force-displacement relationship given by

Fig. 2.12: Transconductance spectrum for a resonator such as that of Fig. 2.11, showing spring softening Duffing behavior caused by nonlinearity in port capacitance as a function of displacement.

$$f_d = (k_{m1} - k_{e1})x + (k_{m3} - k_{e3})x^3 \tag{2.30}$$

Equations (2.29) and (2.30) imply that through proper choice of the dc-bias voltage V_P, the third order spring nonlinearity in parallel-plate driven mechanical resonators may be minimized.

An extend analysis similar to the above, but using port 2, reveals that all sine force components add, independent of the side of the resonator at which electrodes are placed. In other words, the spring softening restoring force cannot be cancelled by symmetry, nor can the electrical spring constant (as shown in the previous section).

2.4.1.3 Output Current Distortion in Parallel-Plate Transduced Resonators

Since a vacuum-operated micromechanical resonator is fundamentally a high-Q bandpass biquad filter when operated in a two-port mode (Fig.2.10), any harmonic distortion in the input excitation voltage signal gets filtered away when passing through the filter. However, because the $\partial C/\partial x$ between the sense electrode and resonator beam is nonlinear, the output current will still be distorted. This output distortion determines the upper signal bound when calculating the dynamic range of filters, and thus, its value is of utmost importance.

The harmonic distortion components as a function of displacement x may be obtained by applying Volterra series analysis to the expression for output current as a function of displacement. To this end, we again refer to Fig. 2.11, this time allowing the existence of only ports 1 and 2, with port 1 driving the resonator into linear, sinusoidal resonance and port 2 sourcing the output current to be measured ($v_2 = 0$). The Taylor series-expanded expression for the current i_2 flowing into port 2, given a sinusoidal variation in beam displacement, is obtained through combination of Eqs. (2.13) and (2.18) as follows:

$$\begin{aligned} i_2 &= -V_{P2}\left(\frac{\partial C}{\partial x}\right)_2 \frac{\partial x}{\partial t} = -V_{P2}\frac{C_{o2}}{d_2}\left(1-\frac{x}{d_2}\right)^{-2}\frac{\partial x}{\partial t} \\ &= -V_{P2}\left(\frac{C_{o2}}{d_2}\right)(1 - A_1 x + A_2 x^2 - A_3 x^3 + \ldots)\frac{\partial x}{\partial t} \\ &= -V_{P2}\frac{C_{o2}}{d_2}\frac{\partial x}{\partial t} + \frac{1}{2}V_{P2}\frac{C_{o2}}{d_2}A_1\frac{\partial x^2}{\partial t} - \frac{1}{3}V_{P2}\frac{C_{o2}}{d_2}A_2\frac{\partial x^3}{\partial t} + \frac{1}{4}V_{P2}\frac{C_{o2}}{d_2}A_3\frac{\partial x^4}{\partial t} + \ldots \end{aligned} \tag{2.31}$$

Nonlinearity in i_2 may be expressed as a function of displacement x through a Volterra series expansion as follows:

$$i_2 = A_1(j\omega) \bullet x + A_2(j\omega_a, j\omega_b) \bullet x^2 + A_3(j\omega_a, j\omega_b, j\omega_c) \bullet x^3 + \ldots \tag{2.32}$$

Equating first order terms, the first Volterra coefficient is found to be

$$A_1(j\omega) \bullet x = -V_{P2}\frac{C_{o2}}{d_2} j\omega \bullet x \quad \Rightarrow \quad A_1(j\omega) = -j\omega V_{P2}\frac{C_{o2}}{d_2}. \tag{2.33}$$

Equating second order terms, the second Volterra coefficient is found to be

$$A_2(j\omega_a, j\omega_b) = -j(\omega_a + \omega_b) V_{P1}\frac{C_{o2}}{d_2^2}. \tag{2.34}$$

And finally, equating third order terms, the third Volterra coefficient is

$$A_3(j\omega_a, j\omega_b, j\omega_c) = j(\omega_a + \omega_b + \omega_c) V_{P1}\frac{C_{o2}}{d_2^3}. \tag{2.35}$$

For bandpass filters, third-order intermodulation distortion (IM_3) is perhaps the most important, since it may occur at frequencies within the passband. For two signals at frequencies, ω_1 and ω_2, the expression for IM_3 is

$$IM_3 = \frac{3}{4}\frac{|A_3(j\omega_2, j\omega_2, -j\omega_1)|}{|A_1(j\omega_1)||A_1(j\omega_2)|^2}\hat{S}_o^2, \tag{2.36}$$

where $\hat{S}_o$ is the average magnitude of the output variable, in this case, i_3. Using Eqs. (2.33) and (2.35) in (2.36), the IM_3 as a function of output current amplitude is

$$IM_3 = \frac{3}{4}\frac{(2\omega_2 - \omega_1)}{\omega_1\omega_2^2}\frac{1}{d_2^2}\frac{1}{\eta^2}\hat{i}_3^2$$
$$\text{where } \eta = V_{P2}\frac{C_{o2}}{d_2} \tag{2.37}$$

The mean output current, however, is given by Eq. (2.14). Given two input signals, $|x_1|\sin\omega_1 t$ and $|x_2|\sin\omega_2 t$, the mean square value of their combined outputs is (using Eq. (2.14))

$$\hat{i}_3^2 = V_{P2}^2\left(\frac{C_{o2}}{d_2}\right)^2(\omega_1^2\hat{x}_1^2 + \omega_2\hat{x}_2^2) \tag{2.38}$$

Using (2.38) in (2.37), IM_3 may be expressed as a function of mean displacement amplitude as follows:

$$IM_3 = \frac{3}{4}\frac{(2\omega_2 - \omega_1)^3}{\omega_1\omega_2^2}\frac{1}{d_2^2}(\omega_1^2\hat{x}_1^2 + \omega_2\hat{x}_2^2)\ . \tag{2.39}$$

Some insight into the maximum allowable resonator displacement amplitude with acceptable IM_3 distortion may be obtained by taking $\omega_1 = \omega_2 = \omega_o$ and $\hat{x}_1 = \hat{x}_2 = \hat{x}$ in Eq. (2.39), yielding

$$IM_3 = \frac{3}{4}\frac{1}{d_2^2}\hat{x}^2\ . \tag{2.40}$$

Solving for $\hat{x}$ yields

$$\hat{x} = \left[\frac{4}{3}(IM_3)\right]^{1/2}d_2\ . \tag{2.41}$$

For IM_3 = -40 dB, Eq. (2.41) indicates that the displacement amplitude should be no larger than 11% of the gap distance d_2.

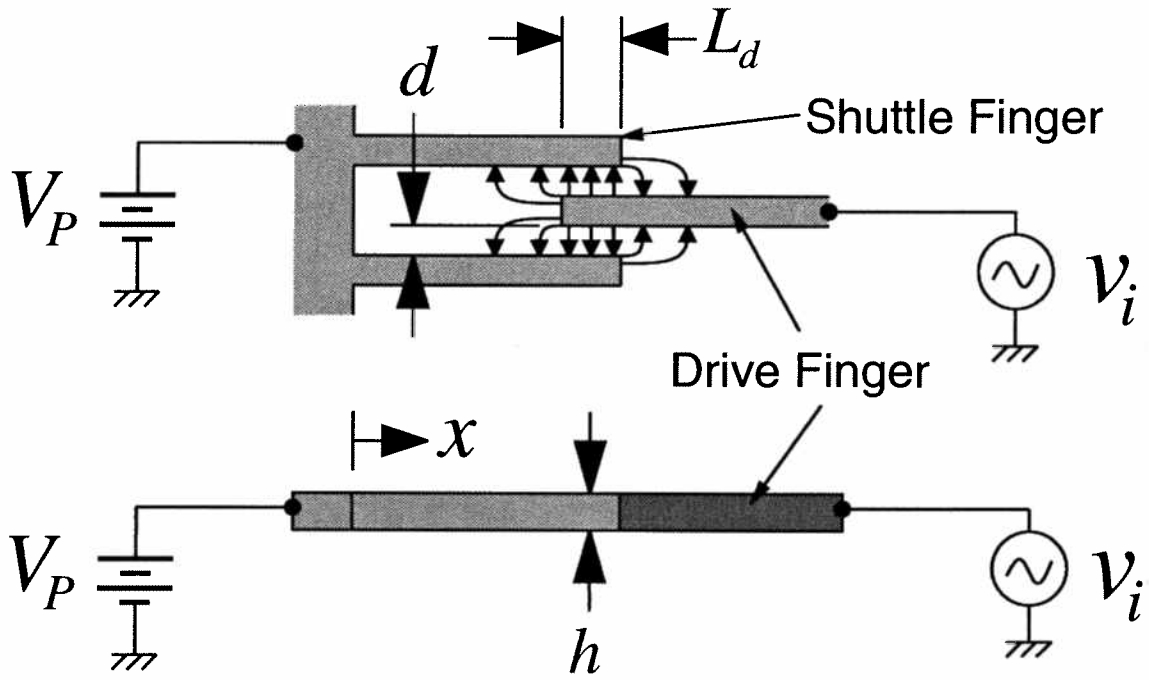

Fig. 2.13: Interdigitated-comb finger capacitive transduction.

Note that differential drive of the resonator may reduce even ordered harmonics, but will not cancel out odd ordered harmonic distortion, including IM_3 distortion.

2.4.2 Electrostatic-Comb Driven Resonators

As discussed in the previous section, a drive capacitance that varies nonlinearly with displacement leads to the undesirable consequences of frequency instability, transfer function distortion, and transfer function nonlinearity. To eliminate these drawbacks, the electrode-to-resonator capacitance must be made to vary linearly with resonator displacement. This may be achieved by using interdigitated-comb finger drive and sense capacitors first introduced by Tang [27], and depicted in Fig. 2.13. This capacitive-comb structure consists of fingers attached to an anchored electrode interdigitated with fingers attached to a moveable resonator shuttle.

Ignoring fringing fields and levitation effects, the approximate[3] value for the finger-gap capacitance for a single electrode-to-resonator finger pair as a function of displacement is given by

[3]The degree to which this is an approximation is discussed in the next section.

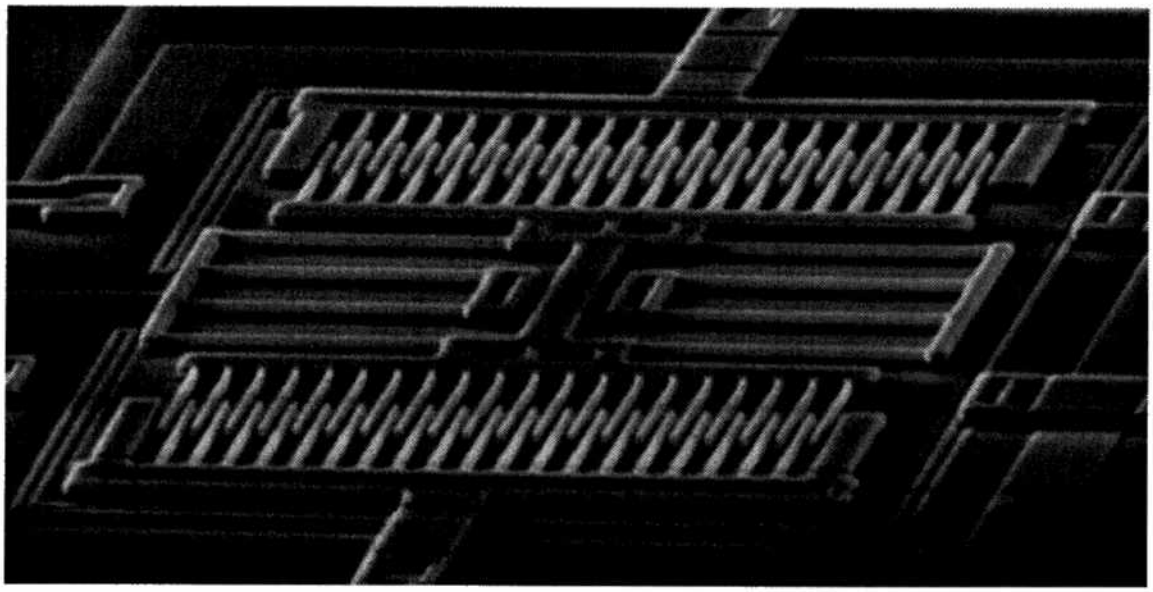

Fig. 2.15: SEM of a fabricated polysilicon folded-beam comb-transduced resonator.

$$C_{fg}(x) \approx \frac{\varepsilon_o h}{d}(L_o + x) \,. \tag{2.42}$$

For N finger-gaps, then, the change in electrode-to-resonator capacitance per displacement is approximately given by

$$\frac{\partial C}{\partial x} \approx \frac{N\varepsilon_o h}{d} \,. \tag{2.43}$$

Note that (2.43) has no dependence on displacement. The force, then, following a similar analysis to that for Eq. (2.17), is given by

$$f_d = V_{P1}\frac{\partial C}{\partial x}v_i \approx V_{P1}\frac{N\varepsilon_o h}{d}v_i \,, \tag{2.44}$$

which does not depend upon displacement, x. Here, V_{P1} is defined by $V_{P1} = V_P - V_I$. Thus, ideally there is no electrical spring constant, and the resonance frequency of the comb-driven resonator is independent of the dc-bias voltage, V_P. Resonator nonlinearity is dominated by the mechanical spring, which with careful design, could be minimized.

Combining this feature with that of linearizing folded-beams, the resonator of Fig. 2.14 results. An SEM of a fabricated polysilicon resonator with this design is shown in Fig. 2.15. This

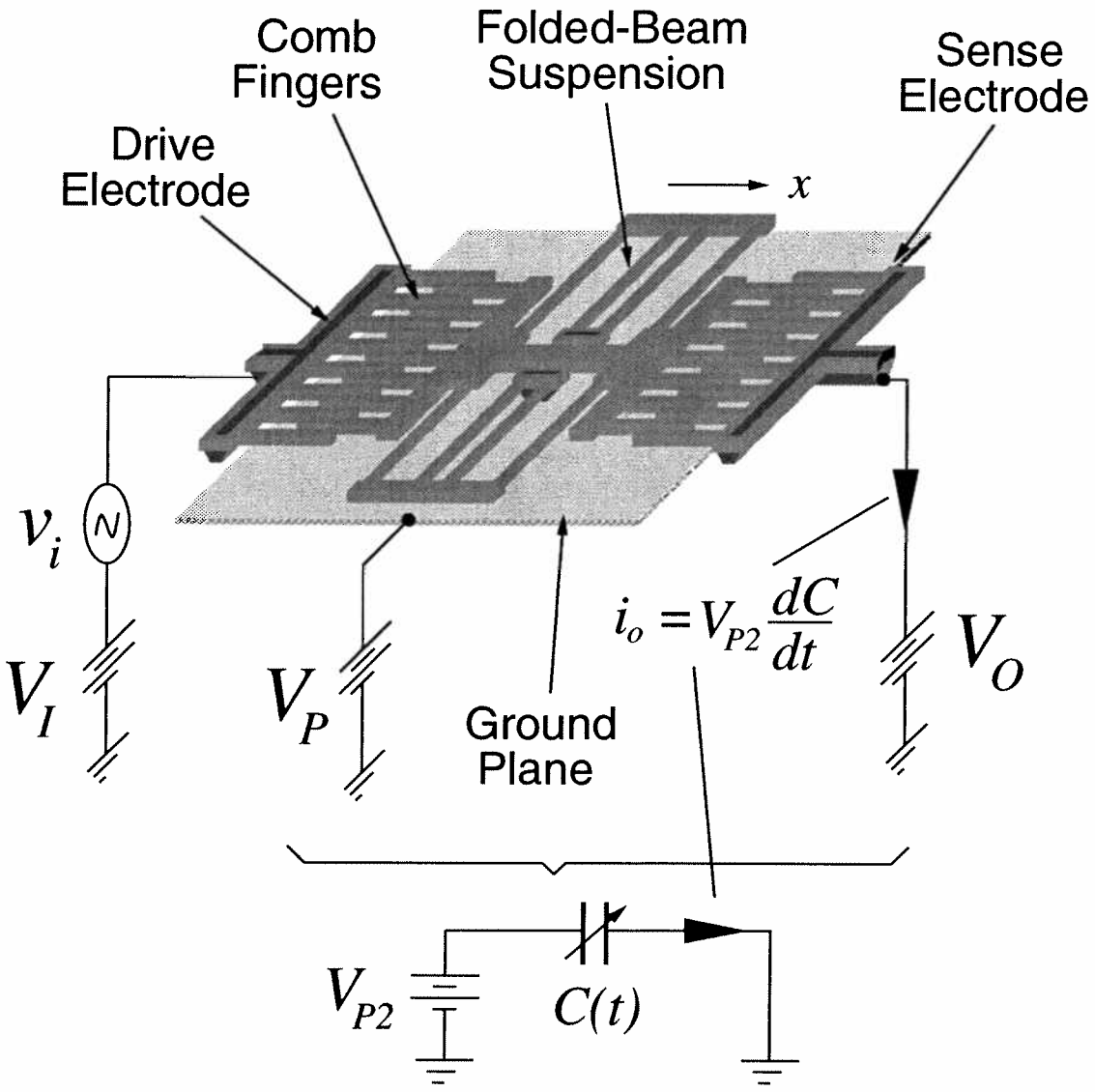

Fig. 2.14: A folded-beam comb-transduced micromechanical resonator in a common bias and excitation configuration.

resonator consists of a movable shuttle suspended a few microns (usually, 2 μm, in this work) above the substrate by the folded-beam flexures. The flexures are anchored near the center of the structure to an underlying ground plane, which may cover the resonator completely (a blanket ground plane); or which may cover every part of the resonator except the spaces between the fingers (sliced ground plane). The ground plane is necessary; if it is not present, the resonator may pull-in to the substrate with even small (0.5 V) voltage differences, since now the area coupling resonator and substrate is much larger. One reason for using a sliced ground plane rather than a blanket type is that the former reduces levitation of the shuttle, caused by an imbalance of verti-

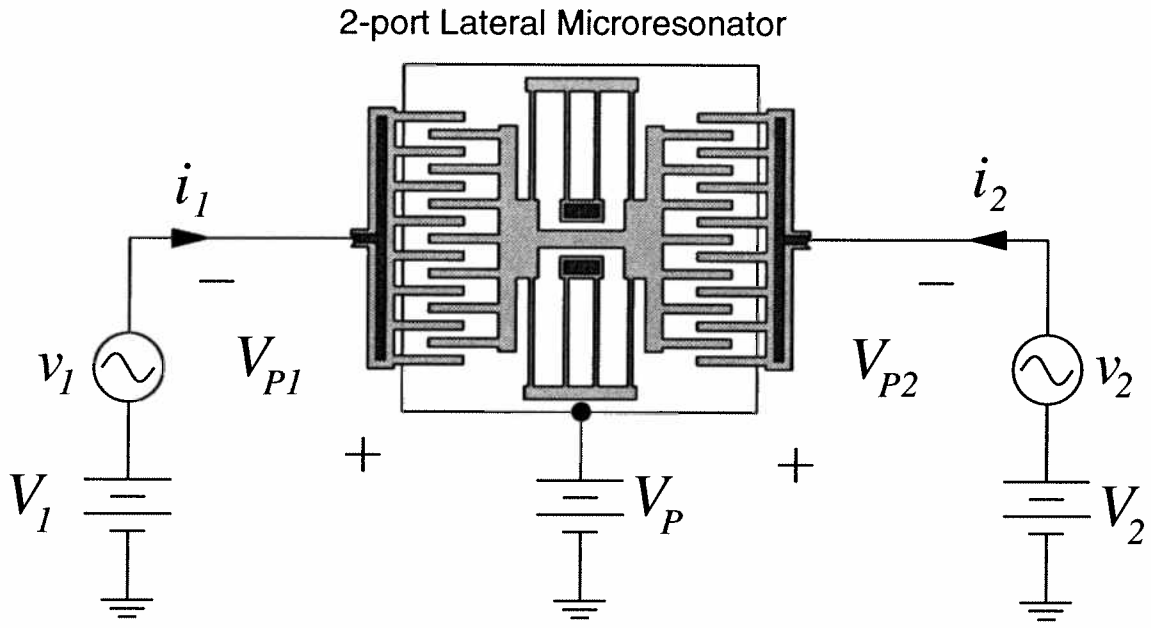

Fig. 2.16: A folded-beam comb-transduced micromechanical resonator with general bias and excitation configuration.

cally directed forces between shuttle and electrode fingers. This is discussed in more detail in the next section.

Figure 2.14 also shows a common bias and excitation configuration for a two-port, folded-beam, comb-driven resonator. A general bias and excitation configuration is shown in Fig. 2.16, where the possibility of an ac signal at the second port, as well as port 1, is included. (Later, we will investigate the possibility of an ac signal applied to the resonator itself; i.e., added to V_P.) The most preferred configuration is one where $V_{P1} = V_{P2}$, since in this configuration, there is ideally no net dc force acting on the resonator shuttle (at least for this symmetrical resonator, with an equal number of fingers at its ports), which allows the application of very large $V_{P1} = V_{P2}$. As will be seen, large values of electrode-to-resonator dc-bias are sometimes required to minimize the series motional resistance of an electrostatically driven microresonator.

In an ideal situation, the output current, which is still given by Eq. (14), will be linear, as long as the finger-gap capacitance varies linearly with displacement x. For a 100 kHz folded-beam, comb-driven resonator, biased with $V_P = 50$ V, and with $d = 1$ μm, $N_s = 25$, and $h = 2$ μm, the output current using this approximate theory for a peak displacement of 1 μm is 13.9 nA.

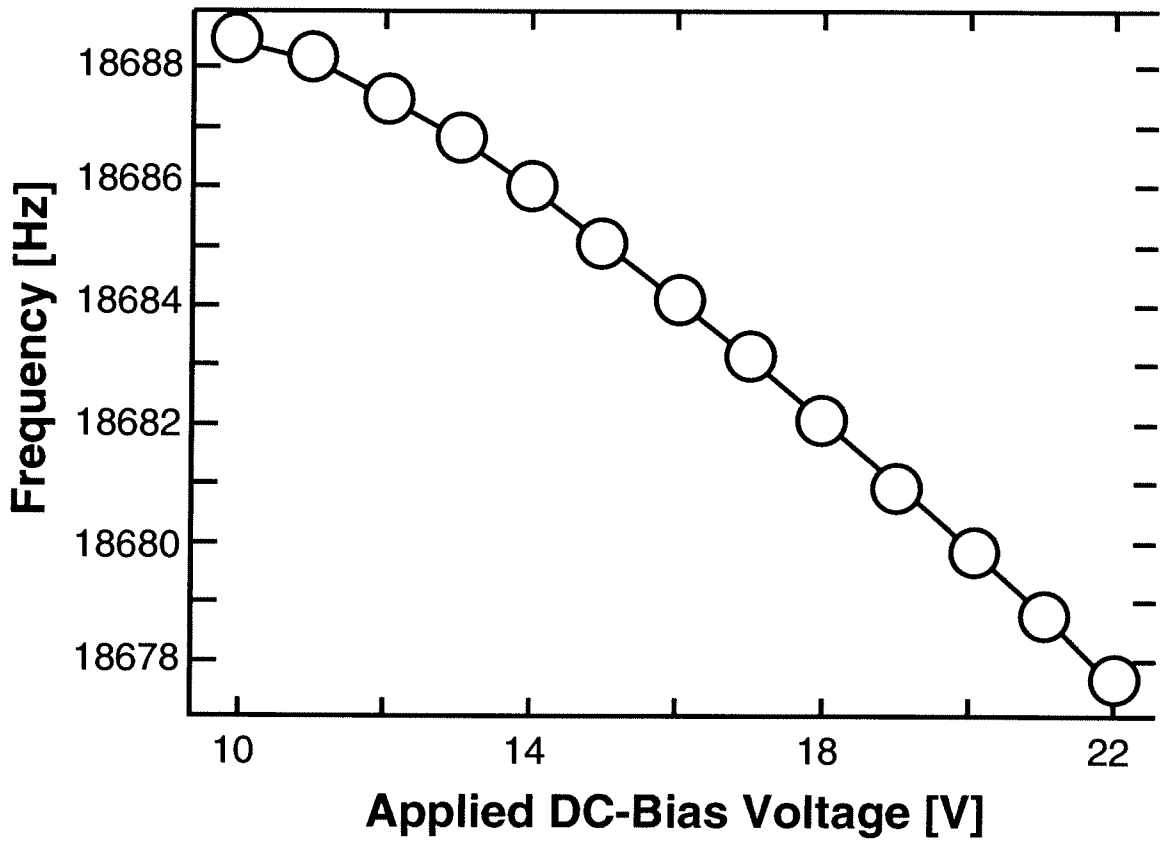

Fig. 2.17: Measured plot lot of center frequency vs. dc-bias for a folded-beam comb-driven microresonator.

Another advantage of capacitive-comb transduction is that it allows a large displacement of the resonator, which usually translates to a larger output current for low frequency resonators. At first glance, this appears to be a tremendous advantage for comb-driven resonators when compared with parallel-plate. However, a large range of motion cannot generally be used for most signal processing applications, even for folded-beam resonators, since it introduces increased spring-stiffening nonlinearity, which distorts filter passbands and adds intermodulation distortion.

2.4.2.1 Second-Order Nonlinearity in Comb-Driven Resonators

For actual comb-driven μresonators, nonidealities do not permit absolute cancellation of k_e, and some variation of frequency with V_P is observed. Figure 2.17 shows a plot of center frequency vs. dc-bias for a micromachined comb-driven resonator. The frequency variation is about -

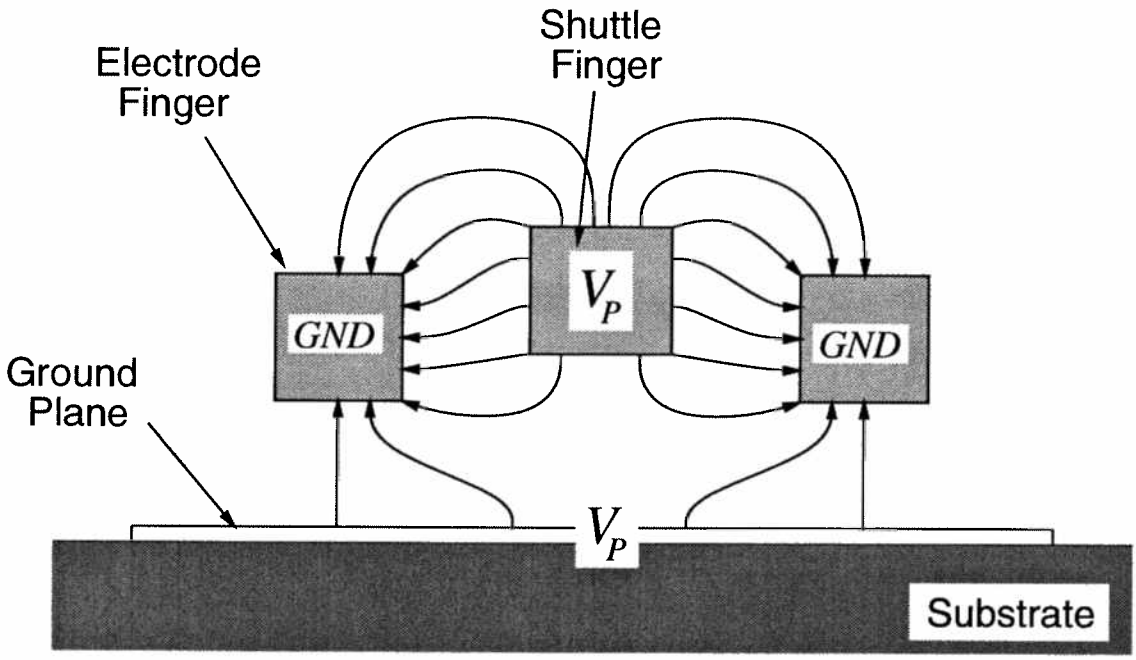

Fig. 2.18: Cross-section of interdigitated electrode and shuttle fingers over a uniform ground plane, showing an imbalance of vertically directed electric fields which cause levitation of the shuttle.

54 ppm/V , corresponding to 14 ppm and 0.2 ppm fractional frequency variations over a 0°-100°C range for a Zener diode and a bandgap reference, respectively.

One of the mechanisms for nonlinearity in the $\partial C/\partial x$ of comb-transduced structures is levitation [37]. The previous section mentioned that levitation of comb-transduced structures arises from an imbalance of vertically directed electric fields (or forces) acting on the movable shuttle, caused by a blanket ground plane underneath the interdigitated fingers. Figure 2.18 presents a pictorial depiction of this imbalance. As shown, some of the shuttle-to-electrode electric field lines below the structure are stolen by the underlying ground plane. A net force in the vertical direction results, which is a function of the voltage between shuttle and electrode (i.e., a function of the drive voltage v_d, as well as the dc-bias V_P) The simultaneous lateral and vertical motion of the resonator caused by levitation forces leads to a $\partial C/\partial x$ that depends slightly on displacement, and thus, introduces a second-order electrical spring constant. More detailed analyses of levitation can be found in [37], [38], and [39].

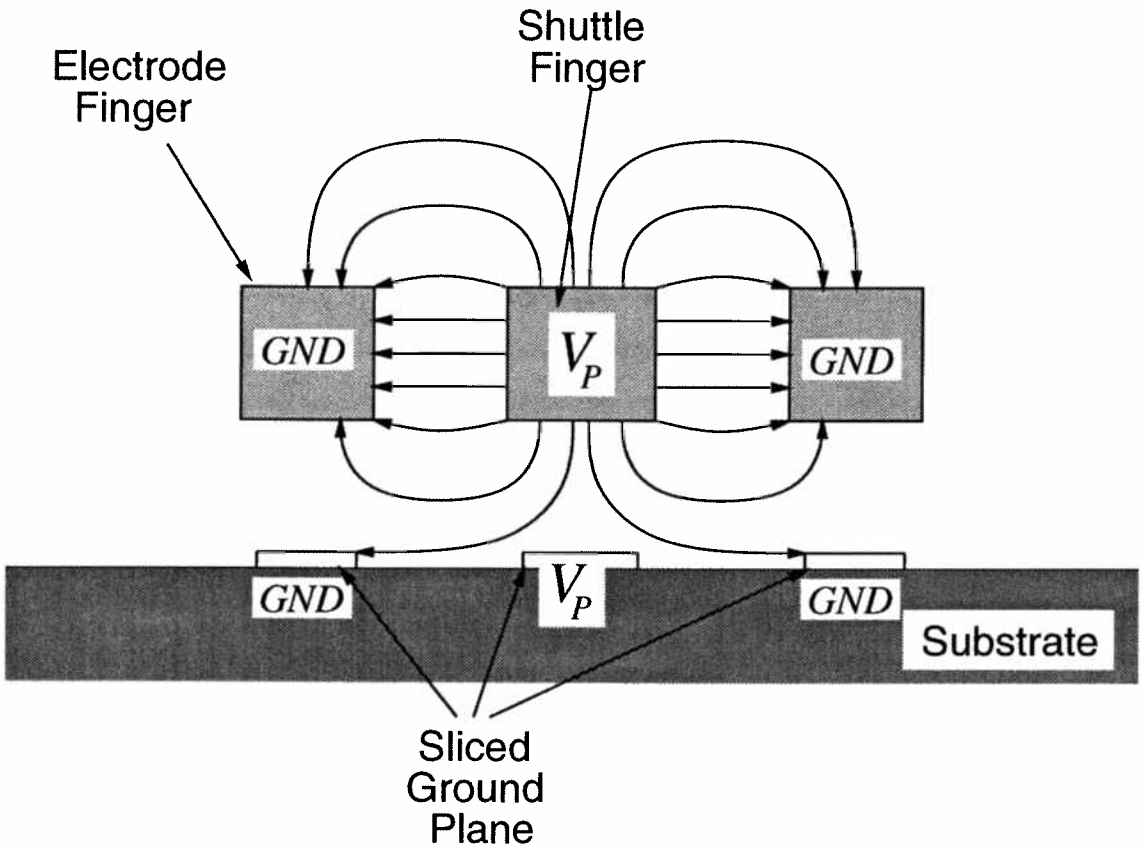

Fig. 2.19: Cross-section of interdigitated electrode and shuttle fingers over a sliced ground plane, showing a more balanced distribution of vertically directed electric fields which decreases levitation of the shuttle relative to that of Fig. 2.18

One way to alleviate this nonlinearity is to place a V_P-biased blanket conductor above the resonator, with the same gap distance as the lower blanket conductor. This strategy could be used if the resonator is encapsulated in a conducting shell.

Without a third polysilicon layer or shell, levitation can be minimized via a sliced ground plane [37], shown in Fig. 2.19. As biased, this strategy minimizes the number of lost shuttle-to-electrode fields lines, thus, helping to balance out vertically directed forces. Another, even more effective strategy, is discussed in [37], where drive voltages of opposite polarity are applied to adjacent electrode fingers over a sliced ground plane.

Note that levitation not only introduces nonlinearity in the force to displacement transfer function of a comb-transduced resonator, it also lowers the effective value of $\partial C/\partial x$. As will be

seen, this parameter should be maximized for best performance of micromechanical signal processors, and thus, the above strategies for reducing levitation may play an important role for future designs based upon comb-transduced resonators.

2.5 Small Signal Equivalent Circuits for Micromechanical Resonators

The equivalent circuit describing microresonator performance under ac electrostatic excitation can be derived through consideration of the electromechanical transduction mechanism and the details of resonator construction (i.e. geometry and structural material). As mentioned, the focus of this work is on capacitively driven and sensed resonators, and therefore, the majority of details in this section will concentrate on these. Other transduction methods, however, will also be briefly addressed towards the end for comparison purposes. Particular attention will focus on the question of which transduction techniques are most suitable for micromechanical resonator applications.

Since the electrostatic-comb configuration offers several advantages over other approaches, it is of the most interest for the present work and will be the focus of the detailed derivation in the following subsection. The methods of derivation, however, apply equally well to other capacitive transduction geometries.

2.5.1 Equivalent Circuit for a Two-Port Electrostatic-Comb Driven and Sensed Lateral Microresonator

The equivalent circuit for the folded-beam comb-driven resonator of Figs.2.14 and 2.16 will now be derived. We first consider the input drive admittance at port 1 of the microresonator, defined (in phasor form) by

$$Y_i(j\omega) = \frac{I_i(j\omega)}{V_i(j\omega)}. \tag{2.45}$$

To start, we define explicitly the bias and excitation parameters of interest:

$$\begin{aligned} v_i(t) &= |v_i|\cos\omega t \\ v_D(t) &= V_I + v_i(t) - V_P = -V_{P1} + v_i(t) \\ V_{P1} &= V_P - V_I \\ V_{P2} &= V_P - V_O \end{aligned} \tag{2.46}$$

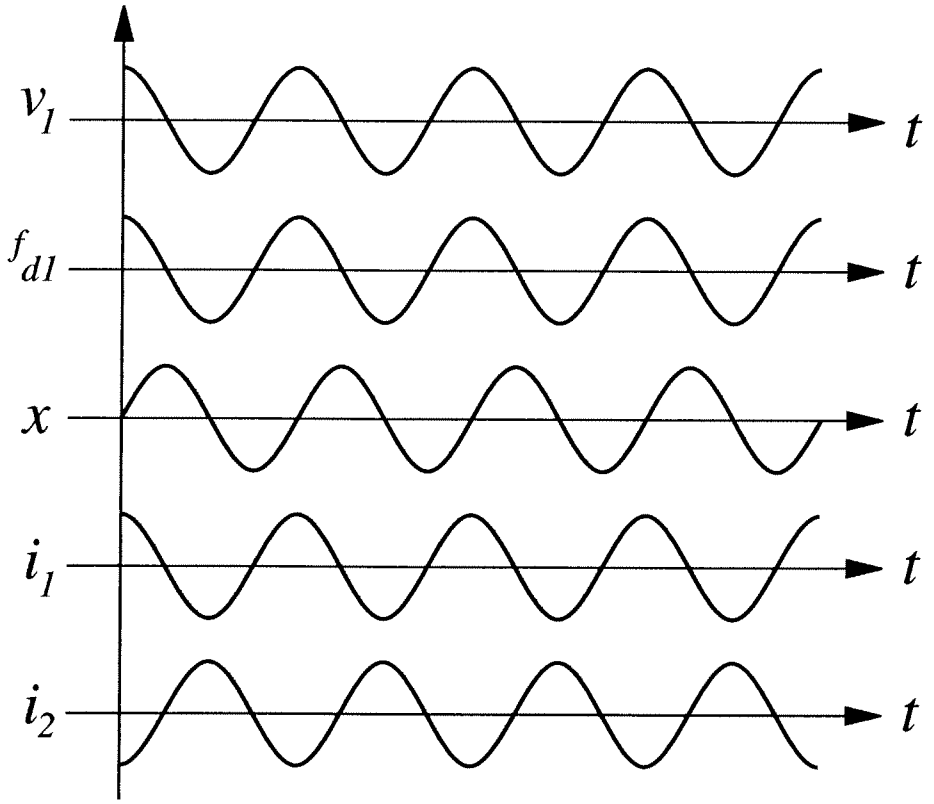

Fig. 2.20: Waveforms showing the respective phases of the signals defined in Fig. 2.14.

where $v_D(t)$ is the effective drive voltage applied at port 1. In addition, the total electrode-to-shuttle finger-gap capacitance will be lumped into a single time-variable capacitor

$$C_1(t) = \begin{cases} \approx C_{o1} & \text{off resonance} \\ C_{o1} + C_{m1}(t) & \text{at resonance} \end{cases} \tag{2.47}$$

$$C_{m1}(t) = |C_{m1}| \sin\omega_r t \tag{2.48}$$

where $C_1(t)$ represents the total capacitance at the drive port (port 1), C_{o1} is the total dc capacitance (i.e. the value of capacitance for a motionless shuttle), and $C_{m1}(t)$ is the total (ac) motional capacitance at port 1 with peak amplitude $|C_{m1}|$. Note that the motion of the microresonator as measured by x lags the excitation force f_d by 90° at resonance, therefore the capacitance $C_1(t)$ must lag the excitation voltage v_i by 90°. Waveforms showing the respective phases of the signals defined in Fig. 2.14 are shown in Fig. 2.20 for reference.

With this, let us proceed to find an expression for the input current $i_i(t)$. A general expression for $i_i(t)$ at resonance can be written

$$i_i(t) = C_1(t)\frac{\partial v_D(t)}{\partial t} + v_D(t)\frac{\partial C_1(t)}{\partial t}. \tag{2.49}$$

Using the relations

$$\frac{\partial C_1(t)}{\partial t} = \frac{\partial C_1(x,t)}{\partial x}\frac{\partial x}{\partial t} \quad \text{and} \quad C_{m1}(t) = x(t)\frac{\partial C_1(x,t)}{\partial x} \tag{2.50}$$

and dropping notation which shows explicit dependencies, (2.49) reduces to

$$\begin{aligned} i_i(t) &= C_{o1}\frac{dv_i}{dt} + x\frac{\partial C_1}{\partial x}\frac{dv_i}{dt} - V_{P1}\frac{\partial C_1}{\partial x}\frac{\partial x}{\partial t} + v_i\frac{\partial C_1}{\partial x}\frac{\partial x}{\partial t} \\ &= C_{o1}\frac{dv_i}{dt} + x\left(\frac{\partial C}{\partial x}\right)_1\frac{dv_i}{dt} - V_{P1}\left(\frac{\partial C}{\partial x}\right)_1\frac{\partial x}{\partial t} + v_i\left(\frac{\partial C}{\partial x}\right)_1\frac{\partial x}{\partial t} \end{aligned} \tag{2.51}$$

where the second line applies to the specific case of a comb-driven resonator, for which $\partial C/\partial x$ is constant. Converting to phasor form,

$$I_i(j\omega) = C_{o1}j\omega V_i + 2\left(\frac{\partial C}{\partial x}\right)_1 j\omega V_i X - V_{P1}\left(\frac{\partial C}{\partial x}\right)_1 j\omega X. \tag{2.52}$$

The first term in Eq. (2.52) represents the feedthrough current arising from an ac excitation voltage v_i across an effective dc capacitor with value C_{o1}. The second represents a modulation component at dc and at twice the excitation frequency. It results from multiplicative interaction between the microresonator ac capacitance $C_1(t)$ and the excitation voltage v_i. The third component is the motional current arising from the dc-biased microresonator time-varying capacitor $C_1(t)$. In practice, the microresonator will be biased such that $V_P \gg |v_i|$. For example, in air, typical bias and excitation voltages are V_P = 80 V and $|v_i|$ = 5 to 10 V; while in vacuum, V_P = 5 V and $|v_i|$ = 10 mV are typical. Thus, in practice, the modulation component (second term of Eq. (2.52)) will generally be the smallest of the three i_i constituents. With this in mind, the modulation component will be neglected in the derivation of the drive admittance given by Eq. (2.45). It, however, will be reconsidered in a later chapter as a possible means for detection of microstructure resonance in environments where parasitic feedthrough dominates.

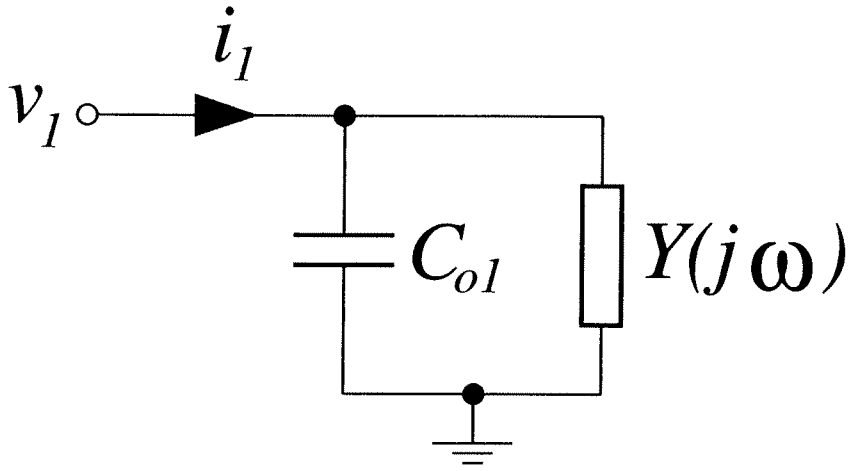

Fig. 2.21: Block element equivalent circuit looking into port 1 of Fig. 2.14.

Equation (2.52), after neglecting the second component, can be seen to have an equivalent circuit comprised of the parallel combination of the capacitor C_{o1} and the drive admittance due to motional current

$$Y_{x1}(j\omega) = \frac{I_{x1}(j\omega)}{V_i(j\omega)}. \tag{2.53}$$

where $I_x(j\omega)$ is the phasor motional current representing the third component of Eq. (2.52)

$$I_{x1}(j\omega) = -V_{P1}\left(\frac{\partial C}{\partial x}\right)_1 j\omega X. \tag{2.54}$$

The equivalent circuit is shown in Fig. 2.21.

Using (37), (2.53) may be expanded as

$$Y_{x1}(j\omega) = \frac{I_{x1}(j\omega)}{V_i(j\omega)} = -V_{P1}\left(\frac{\partial C}{\partial x}\right)_1 j\omega\frac{X(j\omega)}{V_i(j\omega)} = -j\omega V_{P1}\left(\frac{\partial C}{\partial x}\right)_1\frac{X(j\omega)}{F_d(j\omega)}\frac{F_d(j\omega)}{V_i(j\omega)}. \tag{2.55}$$

where $F_d(j\omega)$ is the phasor drive force imposed by v_i. From Eq. (2.12), the phasor drive force over input voltage transfer function is

$$\frac{F_d(j\omega)}{V_i(j\omega)} = -V_{P1}\left(\frac{\partial C}{\partial x}\right)_1 . \tag{2.56}$$

The displacement over drive force mechanical transfer function is given by

$$\frac{X(j\omega)}{F_d(j\omega)} = \frac{k^{-1}}{1-(\omega/\omega_r)^2 + j(\omega/Q\omega_r)}, \tag{2.57}$$

where ω_r is the resonance frequency, k is the system spring constant, and Q is the loaded quality factor of the resonator system. Note that Eq. (2.57) correctly indicates that at resonance the resonator displacement x lags the force by 90°. From (2.56) and (2.57), the *electromechanical* admittance is

$$\frac{X(j\omega)}{V_i(j\omega)} = \frac{X(j\omega)}{F_d(j\omega)}\frac{F_d(j\omega)}{V_i(j\omega)} = \frac{-k^{-1}V_{P1}\left(\frac{\partial C}{\partial x}\right)_1}{1-(\omega/\omega_r)^2 + j(\omega/Q\omega_r)} . \tag{2.58}$$

At this point, the reader may be disturbed by the negative sign in Eq. (2.58), since displacement should lag the excitation voltage by 90°, not -90°. Equation (2.58) is, in fact, consistent with this, since $(\partial C/\partial x)_1$ is negative with the x-direction convention taken in Fig. 2.14. Inserting (2.56) and (2.57) in (2.55) yields, finally, the motional electrical admittance:

$$Y_{x1}(j\omega) = \frac{I_{x1}(j\omega)}{V_i(j\omega)} = \frac{j\omega k^{-1}V_{P1}^2\left(\frac{\partial C}{\partial x}\right)_1^2}{1-(\omega/\omega_r)^2 + j(\omega/Q\omega_r)} . \tag{2.59}$$

Equation (2.59) indicates that the current entering port 1 $I_x(j\omega)$ is in phase with the excitation voltage $V_i(j\omega)$ at resonance. From Eq. (2.59), the block element in Fig. 2.21 may now be recognized as a series LCR circuit with elements given by

$$C_{x1} = \frac{\left[V_{P1}\left(\frac{\partial C}{\partial x}\right)_1\right]^2}{k} = \frac{\eta^2}{k} \tag{2.60}$$

$$L_{x1} = \frac{k}{\omega_r^2\left[V_{P1}\left(\frac{\partial C}{\partial x}\right)_1\right]^2} = \frac{m}{\eta^2} \tag{2.61}$$

$$R_{x1} = \frac{k}{\omega_r Q\left[V_{P1}\left(\frac{\partial C}{\partial x}\right)_1\right]^2} = \frac{\sqrt{km}}{Q\eta^2} \tag{2.62}$$

where

$$\eta = V_{P1}\left(\frac{\partial C}{\partial x}\right)_1 . \tag{2.63}$$

In Eqs. (2.60) through (2.63), m is effective mass of the resonator evaluated at the point of transduction (read on), and η is the electromechanical coupling factor. These equations indicate that the equivalent circuit element values for capacitively transduced microresonators are strong functions of resonator dc-bias V_P and the capacitance per displacement ratio $\partial C/\partial x$ at the transduction ports.

Of the three elements that dictate motional current in micromechanical resonators, the series motional resistance R_x is arguably the most convenient to work with in both oscillator and filter design. For these applications, design becomes easier as the value of R_x is reduced, suggesting that the optimum resonator designs are those where the km product is minimized, the Q is maximized, and the electromechanical coupling is maximized.

In Fig 2.14, the output current is sensed at port 2 of the resonator, which is biased with a dc voltage. This output current i_o arises purely from the dc-biased time varying capacitance at port 2, and from Eqs. (14) and (2.58), is given (in phasor form) by

$$I_o(j\omega) = j\omega V_{P2}\left(\frac{\partial C}{\partial x}\right)_2 \frac{X(j\omega)}{V_i(j\omega)} = \frac{j\omega k^{-1} V_{P1} V_{P2}\left(\frac{\partial C}{\partial x}\right)_1\left(\frac{\partial C}{\partial x}\right)_2}{1-(\omega/\omega_r)^2 + j(\omega/Q\omega_r)} V_i(j\omega) \ . \tag{2.64}$$

where $(\partial C/\partial x)_2$ is the capacitance change per unit displacement at port 2. The input motional current $I_{xI}(j\omega)$ follows from Eq. (2.59)

$$I_{x1}(j\omega) = \frac{j\omega k^{-1} V_{P1}^2\left(\frac{\partial C}{\partial x}\right)_1^2}{1-(\omega/\omega_r)^2 + j(\omega/Q\omega_r)} V_i(j\omega) \ . \tag{2.65}$$

Thus, $I_{xI}(j\omega)$ and $I_o(j\omega)$ are related by

$$\phi_{21} = \frac{I_o(j\omega)}{I_{x1}(j\omega)} = \frac{V_{P2}\left(\frac{\partial C}{\partial x}\right)_2}{V_{P1}\left(\frac{\partial C}{\partial x}\right)_1} \tag{2.66}$$

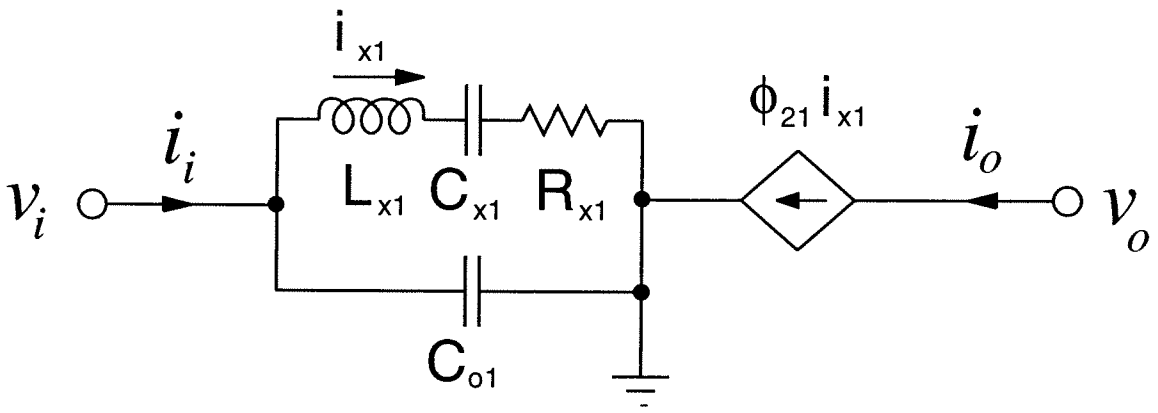

Fig. 2.22: Equivalent circuit for a two-port capacitively transduced resonator hooked as in Fig. 2.14. The circuit element equations are also given.

when port 2 is connected to a dc-bias. The equivalent circuit for the two-port resonator connected as in Fig. 2.14 can now be presented as in Fig. 2.22, where a current-controlled current source describes the electrical behavior of the microresonator at port 2. Note that the sign of Eq. (2.66) will be negative, since the change in finger overlap capacitance for a given change in x will have the opposite sign at the port 2 from that at the port 1.

In the general case, the microresonator might be used as a two-port device, where there are excitation signals at both ports, as shown in Fig. 2.16. By symmetry, the equivalent circuit and the corresponding equations defining the elements for this general case are those summarized in Fig. 2.23. Also shown in the figure is the explicit equivalence between this circuit and an LCR circuit when the resonator is port-symmetrical (i.e., $(\partial C/\partial x)_1 = (\partial C/\partial x)_2$).

A note on sign conventions for ϕ_{mn} is in order. As a general rule of thumb, the value of ϕ_{mn} is positive if ports m and n are on the same side of the resonator, and negative if they are on opposite sides. This is a simple enough rule to remember. However, rather than grapple with signs, it is sometimes much more convenient to simply reverse the direction of the current-controlled current source if ports m and n are on opposite sides, and use $\phi_{mn}' = |\phi_{mn}|$ instead. This converts the equivalent circuit of Fig. 2.23to that of Fig. 2.24. The general rule of thumb here is that the current-controlled current source is directed into ground if ports m and n are on the same side of the resonator, and away from ground if they are on opposite sides.

2.5.2 Typical Element Values

Equations (2.60) through (2.63) indicate that the element values are directly determined by the value of the electromechanical coupling factor, which in turn is determined by the value of dc-bias between electrode-and-resonator and by the value of $\partial C/\partial x$. For parallel-plate-transduced resonators, $\partial C/\partial x$ is proportional to the electrode-to-resonator overlap capacitance. For comb-transduced resonators, $\partial C/\partial x$ is proportional to thickness and inversely proportional the gap spacing between fingers.

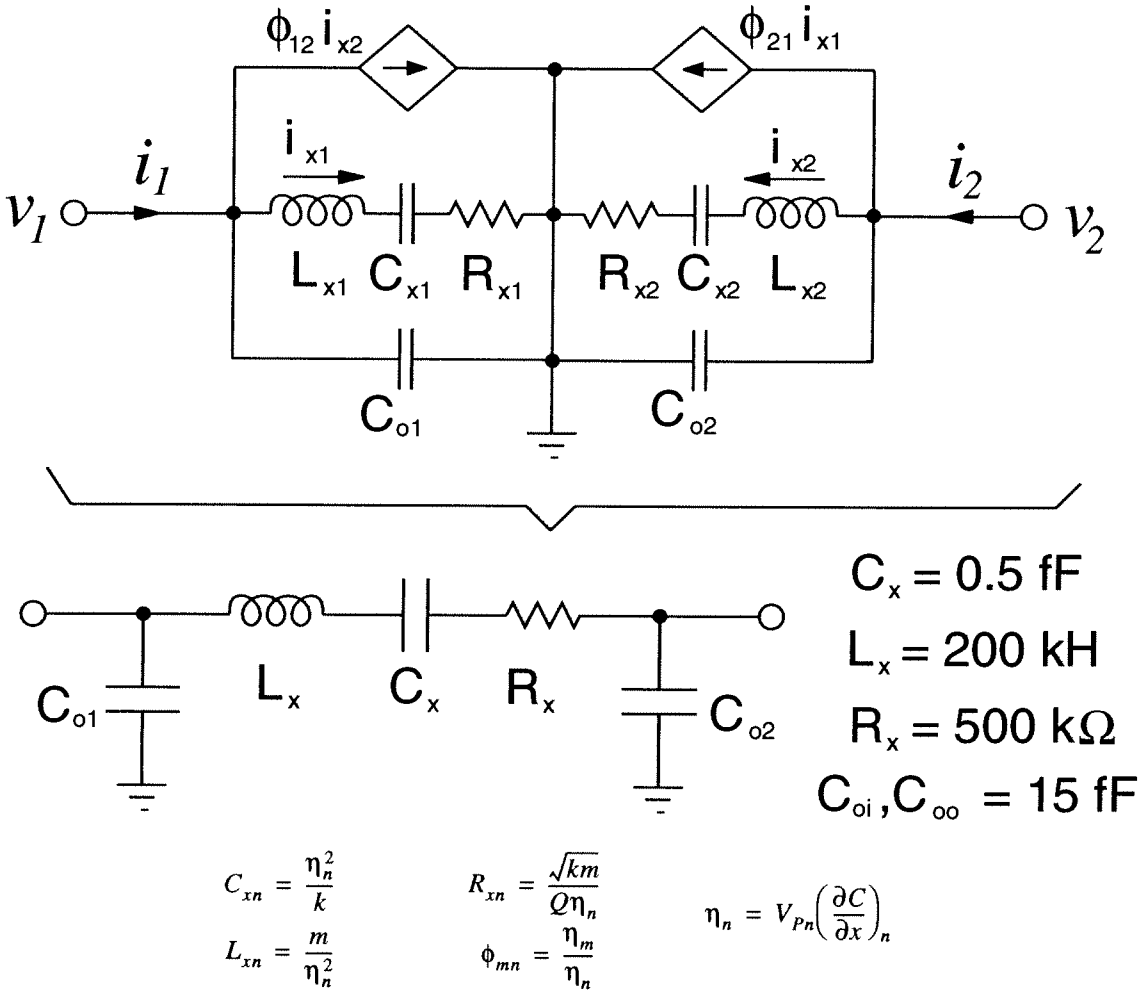

Fig. 2.23: Equivalent circuit for a two-port capacitively transduced resonator, driven at ports 1 and 2. The equivalence between this circuit and a series LCR when the resonator is port-symmetrical is explicitly shown, and typical element values are given. The circuit element equations are also given.

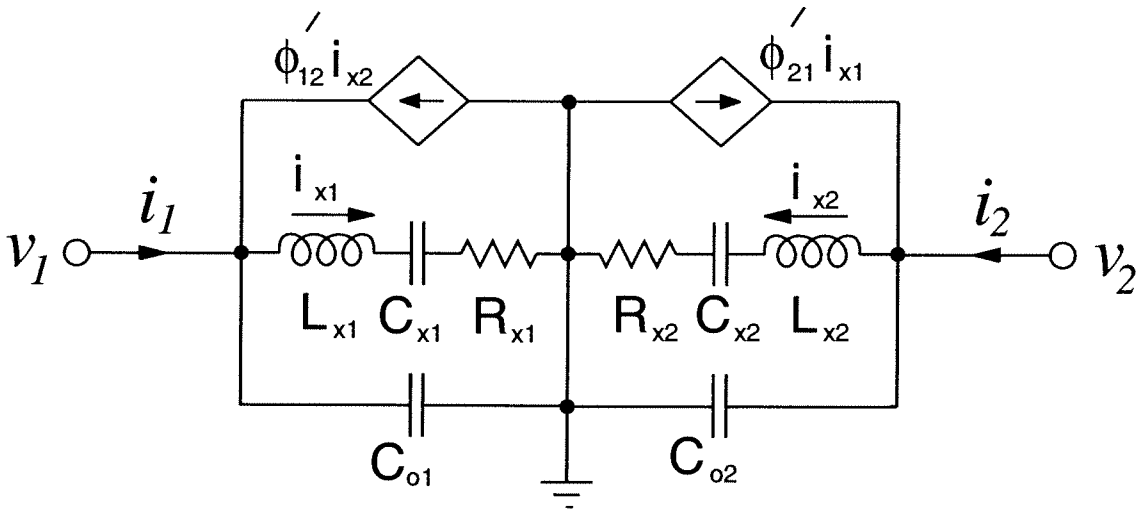

Fig. 2.24: Alternative to the equivalent circuit of Fig. 2.23, where $\phi_{mn}' = |\phi_{mn}|$ is always positive.

A design for a typical folded-beam capacitive-comb-transduced resonator is summarized with equivalent element values in Table 2.2. In this table, the symbols correspond to those discussed in the previous section, and summarized in Figs. 2.5 and 2.16. (As a reminder, h is thickness.) For this calculation, $\partial C/\partial x$ was calculated using the approximate Eq. (2.43), which neglected fringing fields and levitation. The element values in Table 2.2 are, thus, off by a fudge factor (generally less than a factor of 2), but convey the correct order of magnitude.

As will be seen, the series resistance R_x of a micromechanical resonator is of particular importance when designing both oscillators and filters. In general, for both designability and noise considerations, this resistance must be made small. To reduce R_x, the most obvious tweaking parameters are the dc-bias voltage V_P, the number of finger overlaps N, and the gap spacings between fingers. Reducing R_x by increasing N is not a very efficient technique, since this adds to the mass of the resonator (which increases R_x as seen in Eq. (2.62)). Increasing V_P or decreasing d are technology limited techniques. Figures 2.25 and 2.26 plot R_x versus V_P and d, respectively, for the resonator of Table 2.2. Note that these plots neglect fringing field and levitation nonidealities, and thus, their magnitudes must be adjusted by an appropriate fudge factor. However, the trends they depict are informative.

TABLE 2.2. 455 kHz Comb-Transduced Resonator (Figs. 2.5 and 2.16)

Parameter	Value	Units
E	150	GPa
W	2	μm
L	26.4	μm
h	2	μm
d	1	μm
N	40 (20 shuttle fingers)	—
M_p	3.1×10^{-11}	kg
f_o	455	kHz
Q	50 000	—
V_P	30	V
R_x	4.0	MΩ
C_x	70 768	H
L_x	1.7	aF
C_o	7.1	fF

As seen in Table 2.2, for a 455 kHz comb-transduced resonator, the folded-beam length is already in the range of 25 μm. Higher frequencies would require even shorter folded-beam lengths, which entails extremely stiff springs. The springs may become so stiff that the lowest frequency mode may no longer be the designed mode; rather, the comb truss may resonate first.[4] The reason why the springs need to be so stiff is that the mass of the resonator is relatively large, due to the requirement for supporting the comb-fingers.

A balanced parallel-plate-transduced resonator, however, requires much less mass than its comb-transduced counterpart. With some degradation in linearity, a balanced parallel-plate-transduced resonator, such as shown in Figs. 2.2 and 2.11, may be the design of choice for HF or VHF (or UHF?) range resonators. For such a resonator, the design data and element values corresponding to a 10 MHz design are summarized in Table 2.3. (Here, some of the results of Section 2.5.4

[4]This, in fact, has been observed several times for 2 MHz comb-driven resonators.

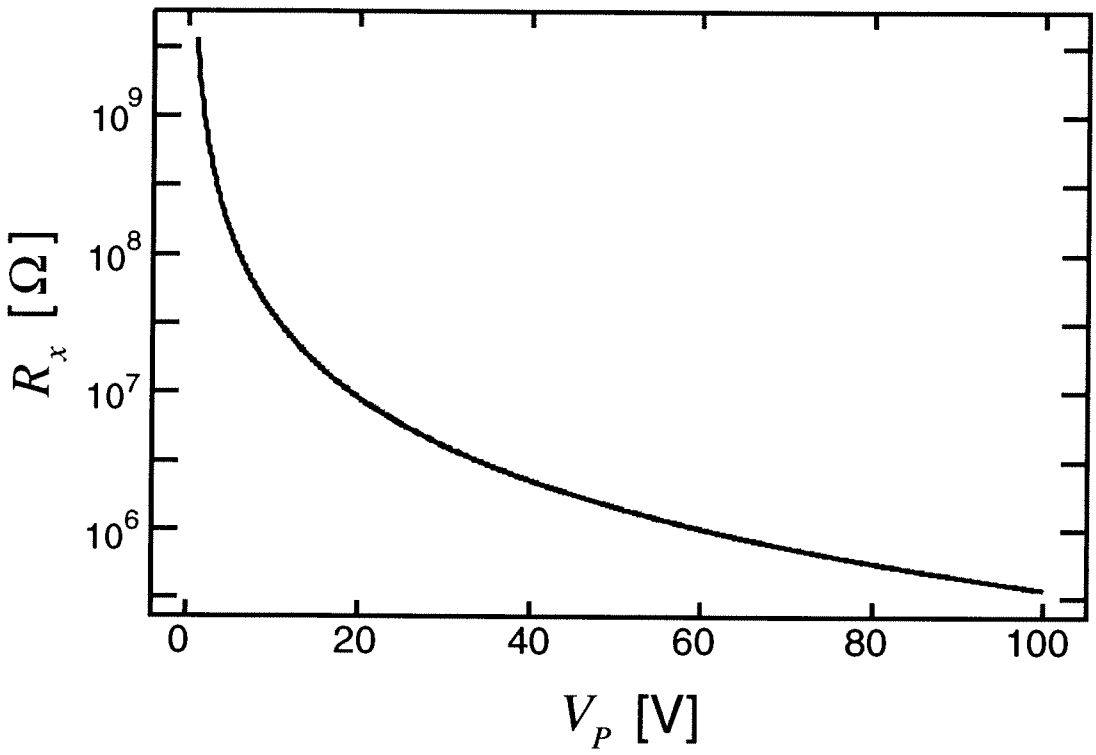

Fig. 2.25: Plot of resonator series motional resistance R_x versus the dc-bias voltage applied to the microresonator for the comb-transduced resonator of Table 2.2. For the simulation, the finger gaps are taken to be 1 μm.

were utilized.) Note that for a gap spacing of only 0.1 μm and a dc-bias voltage of 20 V, a very reasonable value of series motional resistance in the kiloohm range is attained. This gap spacing should be attainable even in today's technology, where 40 Å CMOS gate oxide thicknesses are already attainable. Thus, 10 MHz resonators should be feasible.

It is instructive to investigate a 100 MHz clamped-clamped resonator. Such a design (with an assumed value of Q = 10,000) is summarized in Table 2.3. Here, the electrode-to-resonator overlap area have been reduced to account for the shorter beam length. Note that the beam length of 12.9 μm is still very lithographically reasonable. Thus, geometrically, the 100 MHz design is feasible. Whether the Q is actually 10,000 is the important question, here, which can only be answered via further research. The series resistance for this resonator is 81 kΩ, which is somewhat excessive. It can be reduced through either increasing V_P or decreasing d. For example, if d were reduced to 500 Å, and keeping all other parameters the same, the series resistance would be

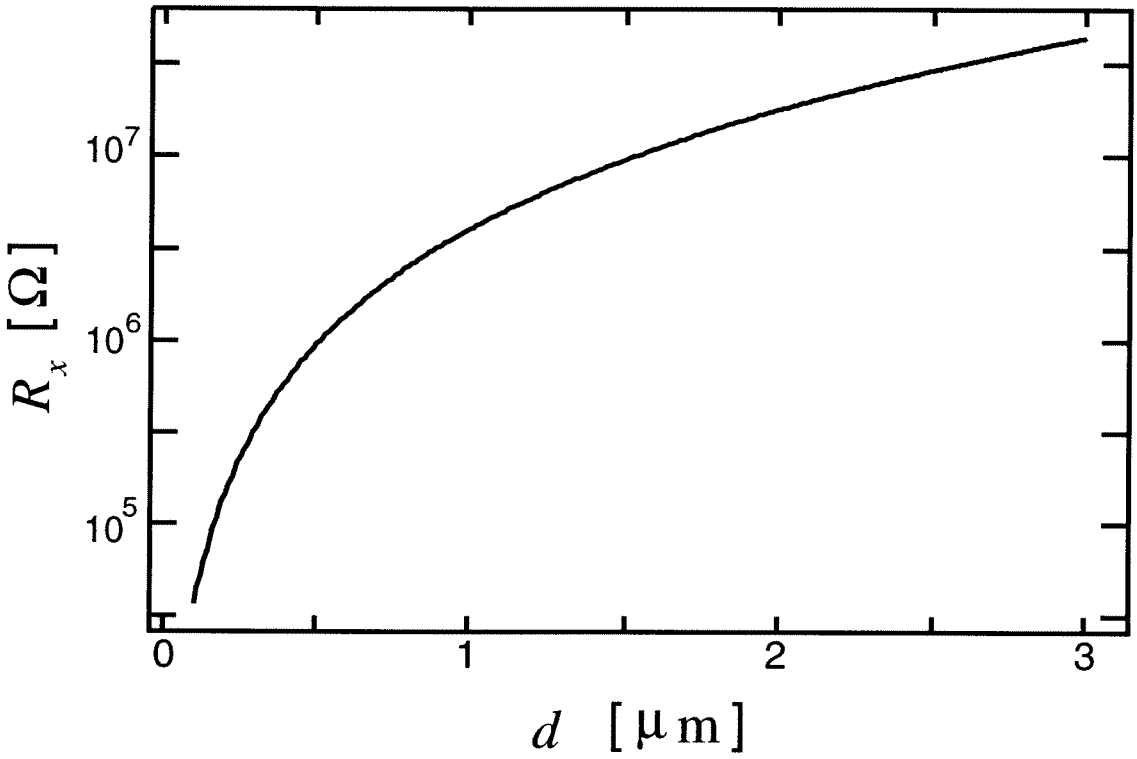

Fig. 2.26: Plot of resonator series motional resistance R_x versus finger gap spacing d for the comb-transduced resonator of Table 2.2. For the simulation, the dc-bias voltage is taken to be 30 V.

5.1 kΩ, which is quite adequate for design purposes. Note that a 500 A gap should be feasible, as well, even in today's technology, if sidewall technologies [40] are utilized.

2.5.3 Equivalent Circuits for Multi-Port Resonators

The equivalent circuit for any multi-port resonator can be obtained through extension of the results of Section 2.5.1. For each additional port added, a parallel combination of a static capacitance C_o, a series LCR, and $(n-1)$ current-controlled sources is required. In addition, the current-controlled current source modelling the influence of this port on the other ports must be added to each of the other resonator ports. The generalized equivalent circuit for an n-port capacitively transduced mechanical resonator is presented in Fig. 2.27.

TABLE 2.3. 10 MHz Parallel-Plate Resonator (Figs. 2.2 and 2.11)

Parameter	Value	Units
E	150	GPa
W	2	μm
L	40.8	μm
h	2	μm
d	0.1	μm
$A_{overlap}$	20×2	μm^2
f_o	10	MHz
Q	20 000	—
V_P	20	V
R_x	1.6	kΩ
C_x	0.5	fF
L_x	0.5	H
C_o	3.5	fF

2.5.4 General Equivalent Circuits for Resonators

Section 2.5.1 showed the detailed derivation for the specific case where the input and output coupling were both taken at a central location (the shuttle mass) of the resonator. In general, the elements in the equivalent circuit are functions of the velocity distribution across the resonator, and thus, a given location on a resonator will yield a unique set of element values. An understanding of this will be necessary for the design of mechanical filters, where spring-coupling between resonators can occur at arbitrary locations.

The derivation of the equivalent circuit can be generalized to all resonator locations by first defining an equivalent mass M_{eq}, then selecting an equivalent spring constant K_{eq} which resonates M_{eq} at the resonance frequency ω_o. One method for finding the equivalent mass of a resonator [7] is based upon the fact that the kinetic energy of the resonator is invariant; i.e., it is not dependent upon the point or direction chosen for calculating the equivalent mass. Thus, to calcu-

TABLE 2.4. 100 MHz Parallel-Plate Resonator (Figs. 2.2 and 2.11)

Parameter	Value	Units
E	150	GPa
W	2	μm
L	12.9	μm
h	2	μm
d	0.1	μm
$A_{overlap}$	7×2	μm^2
f_o	100	MHz
Q	10 000	—
V_P	20	V
R_x	82.0	kΩ
C_x	1.9	aF
L_x	1.3	H
C_o	1.2	fF

late the equivalent mass, we first equate the total kinetic energy in the spring mass system to that in the resonator. For a one-dimensional resonator of length l,

$$\frac{1}{2}\, {}_{eqx}V_x = \frac{1}{2}\int_0^l (V(x))^2 \rho A\, dx \tag{2.67}$$

which reduces to

$$M_{eqx} = \frac{\frac{1}{2}\int_0^l (V(x))^2 \rho A\, dx}{\frac{1}{2}V_x} \tag{2.68}$$

where M_{eqx} is the equivalent mass at a point x as related to the velocity V_x in the x-direction. ρ is density of the material and A is the cross-sectional area (assumed constant for the one-dimensional example). Thus, the procedure for obtaining the equivalent mass at any location on a resonator is to calculate the total kinetic energy in the bar at resonance, and then divide this number by one-

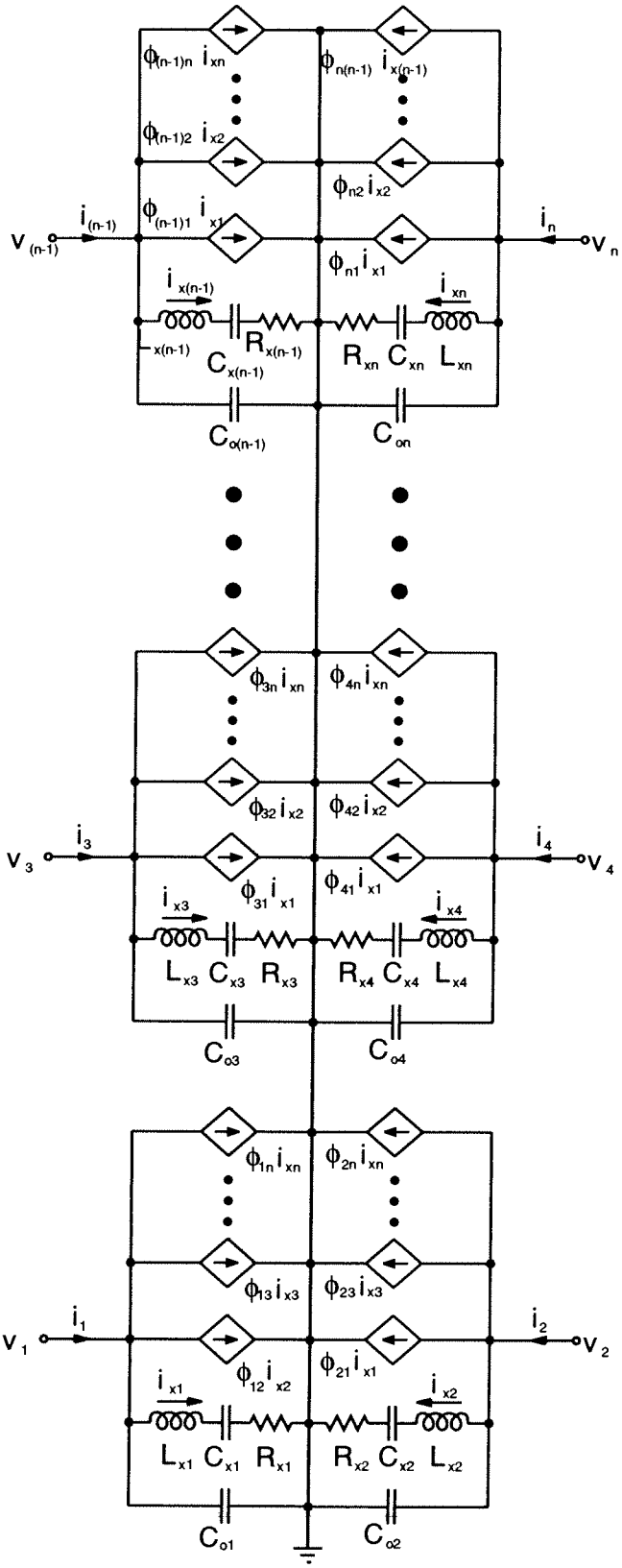

Fig. 2.27: The generalized equivalent circuit for an *n*-port capacitively transduced mechanical resonator with equations for the circuit elements.

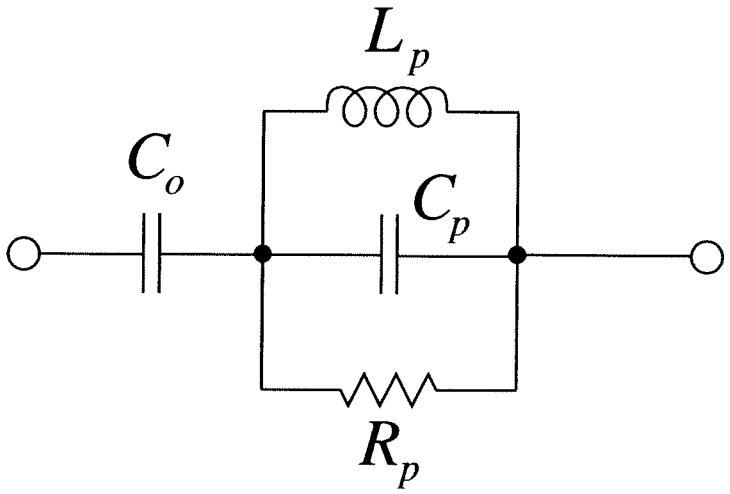

Fig. 2.28: Mobility analogy equivalent circuit for a micromechanical (end) resonator.

half the squared velocity at a given point and direction. Then, given the equivalent mass M_{eqx}, the equivalent spring constant K_{eq} which resonates this mass at ω_o can be found via $K_{eq} = \omega^2 M_{eqx}$. Then, Eqs. (2.60) through (2.63) can be used with $m = M_{eqx}$ and $k = K_{eq}$ to obtain equivalent circuit elements.

2.5.5 Parallel Resonator Equivalent Circuits: The Mobility Analogy

Thus far, we have focused on series LCR circuits to represent microresonator behavior. This is consistent with the current analogy, where force is equated to voltage and velocity to current. However, in some filtering applications, it may be more useful to model a resonator using a parallel LCR topology, as shown in Fig. 2.28. This circuit comes about when velocity is equated to voltage and force to current. For this circuit, the element values are given as follows:

$$L_p = \frac{\eta^2}{k} \tag{2.69}$$

$$C_p = \frac{m}{\eta^2} \tag{2.70}$$

$$R_p = \frac{Q_p}{\omega_o C_p} \tag{2.71}$$

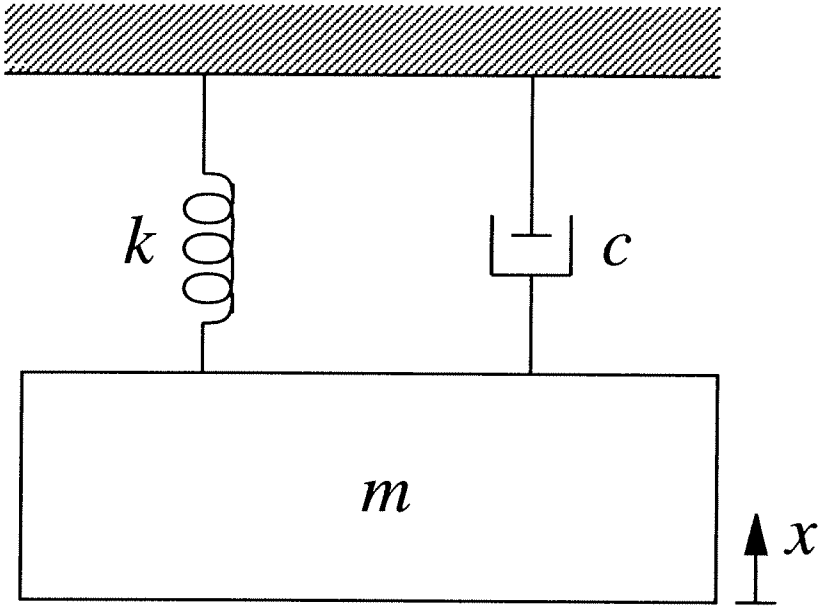

Fig. 2.29: A simple mass-spring-damper system with no applied input force. This schematic violates the Second Law of Thermodynamics.

where

$$\eta = V_P \frac{\partial C}{\partial x}. \tag{2.72}$$

In these equations, k is the equivalent system spring constant, m is the equivalent mass, ω_o is the resonance frequency, Q_p is the quality factor, $\partial C/\partial x$ is the change in capacitance per unit displacement at the capacitive-transduction port, and V_P is the dc-bias applied to the resonator. As shown, the equivalent circuit of Fig.2.28 models an end resonator in a spring-coupled filter.

Chapter 5, which focuses upon microelectromechanical filters, will address both the electromechanical analogies in greater detail.

2.6 Brownian Motion Noise

The expression modelling a free (no applied input force) mass-spring-damper system, such as shown in Fig. 2.29, is commonly given as

$$m\ddot{x} + c\dot{x} + kx = 0. \tag{2.73}$$

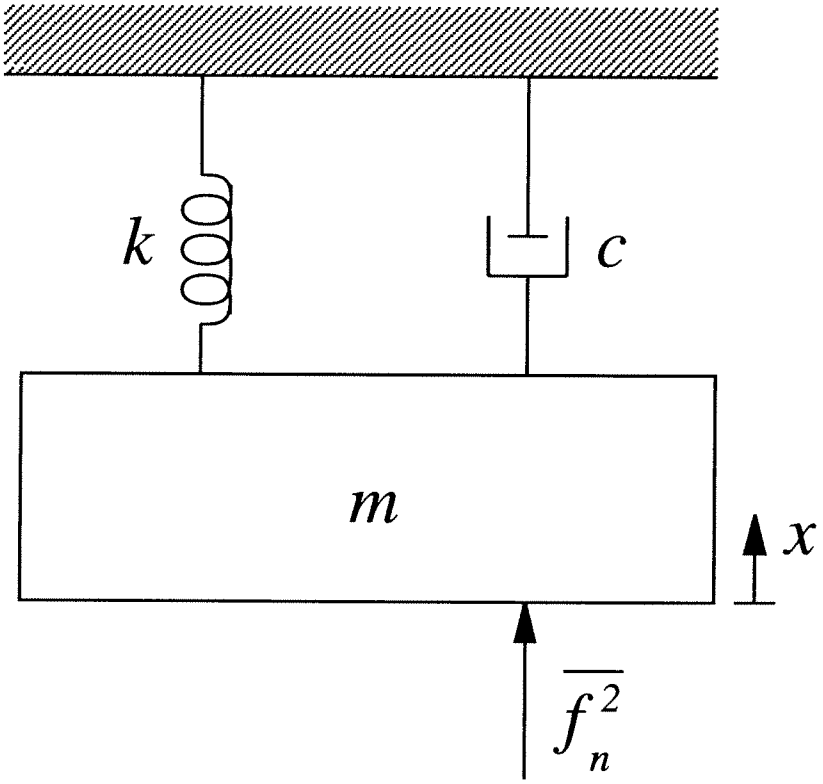

Fig. 2.30: The correct representation of a mass-spring-damper system with no externally applied input force. The addition of the noise force $\overline{f_n^2}$ establishes the equilibrium criterion governed by the Second Law of Thermodynamics.

The presence of the damping term $c\dot{x}$ suggests that any oscillation would continue to decrease in amplitude forever, including vibration of the molecules making up the structure. Since temperature is a measure of molecular motion, Eq. (2.73) implies that the temperature of the resonator would decrease to 0 Kelvin. However, the temperature of the resonator cannot drop below that of the surroundings; otherwise, the Second Law of Thermodynamics would be violated!

Thus, the correct model for a damped simple harmonic oscillator must include a force generator with sufficient amplitude to bring the system into thermal equilibrium. The correct equation is then

$$m\ddot{x} + c\dot{x} + kx = f_n(t)\,, \tag{2.74}$$

which is pictorially depicted in Fig. 2.30.

An expression for the noise force f_n can be obtained using the Equipartition Theorem [41,42], which states that any mode of a system in thermal equilibrium has an average noise energy of $\frac{1}{2}k_BT$, where k_B is Boltzmann's constant (1.38×10^{-23} J/K) and T is the temperature in Kelvin. Through equilibrium arguments [42], the action of all modes (including molecular vibrations, velocity, etc...) may be combined into the action of an "ordered" mode, such as vibration of a mass-spring system. The average noise displacement of the mass in a mass-spring-damper oscillator system, assuming one designed dominant mode in the x-direction, is given by

$$\frac{1}{2}k\langle x_n^2\rangle = \frac{1}{2}k_BT, \tag{2.75}$$

where $\langle x_n^2\rangle$ is equal to the integral of $|x_n|^2$ over all frequencies. Inserting the expression for $|x_n|^2$, Eq. (2.75) becomes:

$$\frac{\overline{f_n^2}}{2\pi k}\int_0^\infty \frac{1}{(1-(\omega/\omega_r)^2)^2 + (\omega/Q\omega_r)^2}d\omega = k_BT \tag{2.76}$$

Integrating and rearranging (2.76) yields

$$\frac{\overline{f_n^2}}{\Delta f} = \frac{4kk_BT}{\omega_o Q} = \frac{4\sqrt{km}k_BT}{Q}. \tag{2.77}$$

Note that this noise force is white over the thermal bandwidth. In converting from force to displacement, the noise is shaped by the force-to-displacement transfer function of the mechanical resonator, given by Eq. (2.57). This is depicted in Fig. 2.31, which shows a simulated Brownian noise density spectrum. The displacement noise $\overline{x_n^2}$ peaks at the resonance frequency (where filters and oscillators operate). Note that this noise is Q times larger than that for mechanical devices operating below resonance, such as accelerometers. From (2.77), an expression for noise displacement at resonance may be obtained as follows:

$$\frac{\overline{x_n^2}}{\Delta f} = \frac{Q^2}{k^2}\frac{\overline{f_n^2}}{} = \frac{4Q\sqrt{m}k_BT}{k^{3/2}}. \tag{2.78}$$

Using Eq. (2.78) and the expression for output current as a function of displacement for a capacitively transduced resonator (Eq. (2.14)), the noise current at resonance is given by

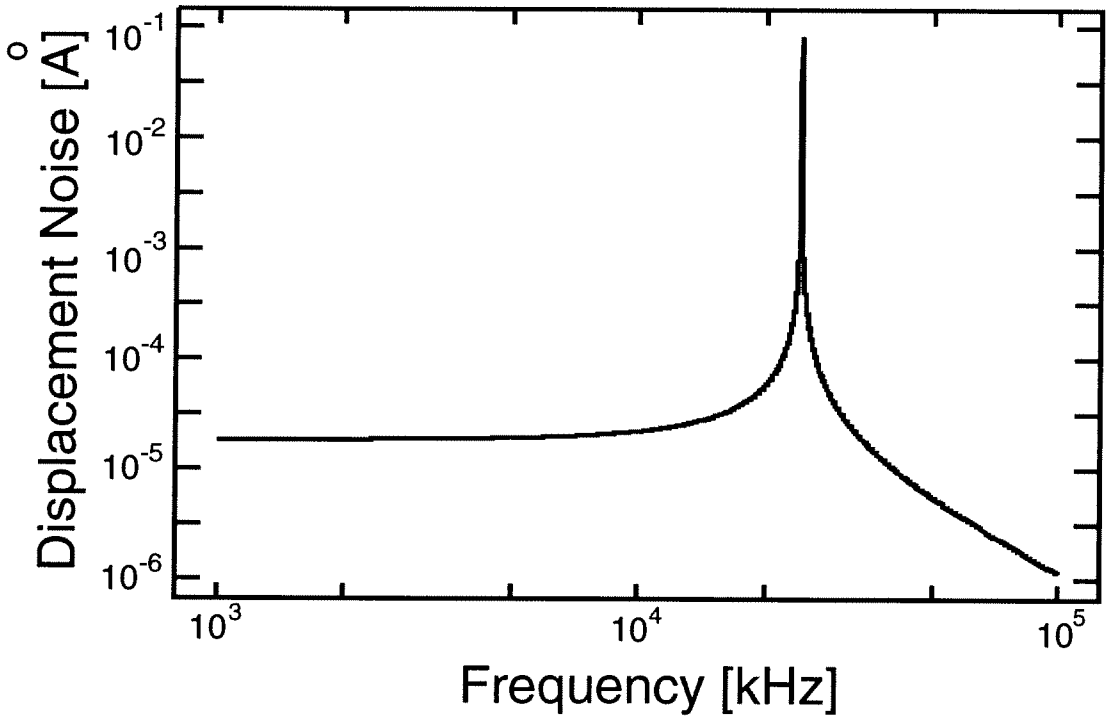

Fig. 2.31: Simulated Brownian noise density spectrum for a typical 20 kHz folded-beam, comb-driven microresonator.

$$\frac{\overline{i_n^2}}{\Delta f} = \omega_o^2 V_P^2 \left(\frac{\partial C}{\partial x}\right)^2 \frac{\overline{x_n^2}}{\Delta f} = \frac{4k_B T \omega_o Q V_P^2 \left(\frac{\partial C}{\partial x}\right)^2}{\sqrt{km}} = \frac{4k_B T}{R_x} \tag{2.79}$$

where R_x is the series motional resistance of the microresonator seen at resonance at the port in question. Off resonance, this noise is shaped by the resonator frequency characteristic. Thus, the thermal noise performance of a micromechanical resonator is modelled completely by the noise performance of its equivalent circuit. Thus, for a port-symmetric resonator (i.e., $\eta_1 = \eta_2$), one need only add a noise generator corresponding to the resistor R_x in the equivalent LCR circuit. Two versions of this are shown in Fig 2.32.

When using the generalized equivalent circuit for multi-port resonators, shown in Fig. 2.27, only one of the resistors should be given a noise source, since the current-controlled current sources will distribute this noise proportionately to the other ports. The other resistors should be considered noiseless. They are present only to model the distribution of power in the multi-port resonator. This will be applied in detail in Chapter 5.

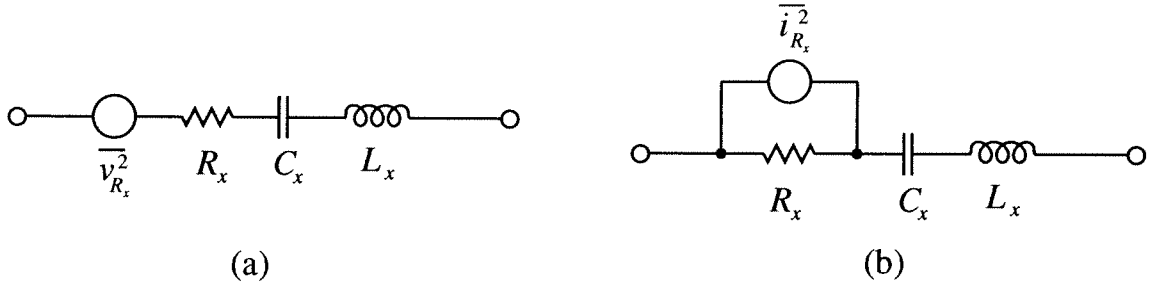

Fig. 2.32: Noise circuits modelling Brownian noise in port-symmetric micromechanical resonators. (a) Circuit with voltage noise generator. (b) Alternative circuit with current noise generator.

2.7 Motional Sensing Techniques for Resonators

The majority of integrated methods for electronically detecting the motion of micromechanical resonators can be lumped into two categories: capacitive or resistive. These two approaches are summarized in Figs. 2.33 and 2.34.

As shown, capacitive detection senses the displacement of the resonator, and thus, yields a lowpass biquad transfer function given by the expression:

$$\frac{v_o}{v_i}(s) = \frac{\omega_o}{QC}\frac{1}{s^2 + \left(\frac{\omega_o}{Q}\right)s + \omega_o^2}. \tag{2.80}$$

On the other hand, resistive detection senses the velocity of the resonator, and thus, yields a symmetrical bandpass biquad transfer function, given by the expression:

$$\frac{v_o}{v_i}(s) = \frac{\omega_o}{QR}\frac{s}{s^2 + \left(\frac{\omega_o}{Q}\right)s + \omega_o^2}. \tag{2.81}$$

Both of the above transfer functions are very useful in filter and oscillator design and will be addressed in more detail in subsequent chapters.

2.8 Matching Tolerance of the Resonance Frequency

From the experience of this work, the absolute tolerance of the resonance frequency of a

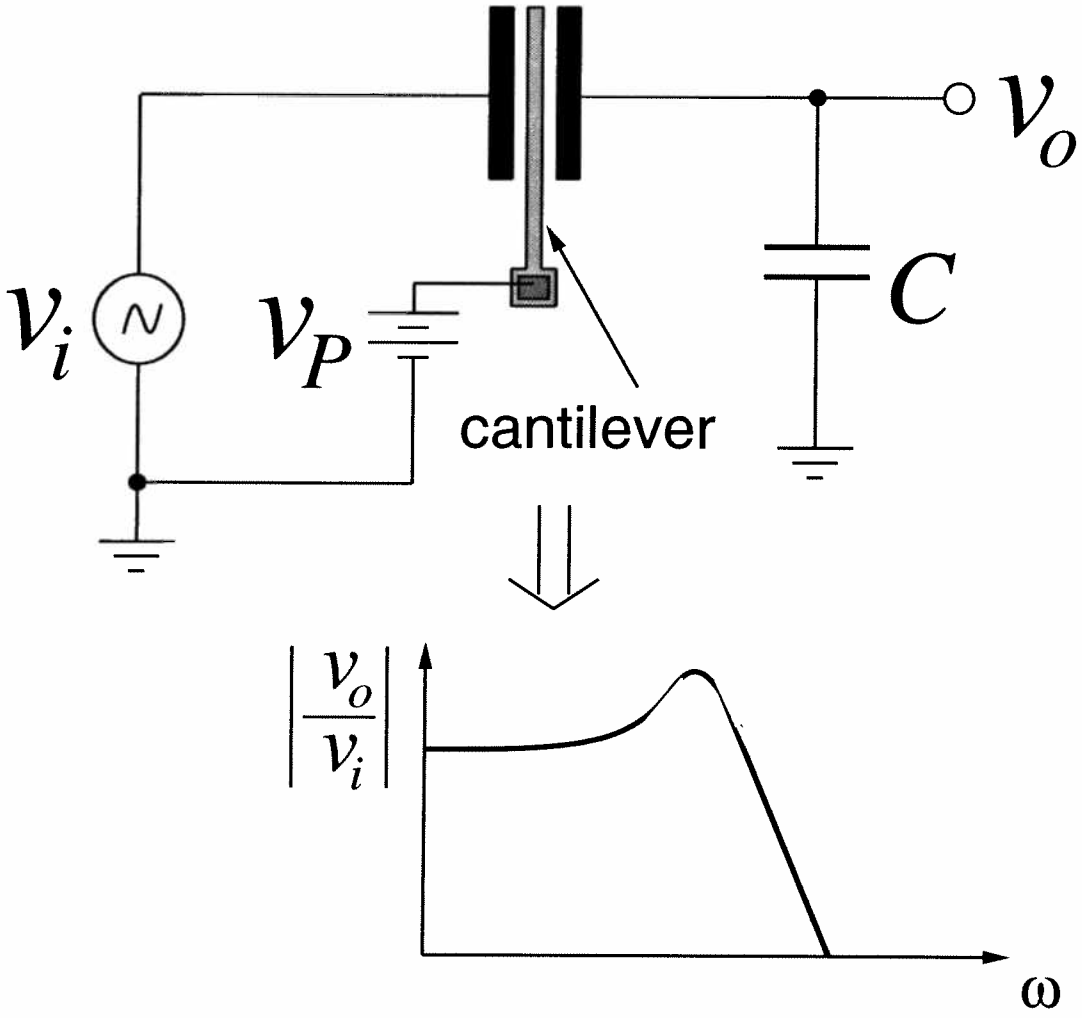

Fig. 2.33: Capacitive detection of capacitively transduced resonator motion.

Chapter 3 and in the Appendices, is on the order of 3%. For both filter and oscillator applications, this must be trimmed to the target frequency. Perhaps more advanced processes could decrease this tolerance specification.

For micromechanical filters, the matching tolerance, as well as the absolute tolerance, of a resonator is important. Briefly, poor resonator matching leads to passband distortion in many filter architectures. Fortunately, planar integrated technologies are much better at achieving low matching tolerances than absolute tolerances. For this reason, many integrated circuit designs rely on ratioed elements, rather than single elements. Generally, the closer two identical elements are on a

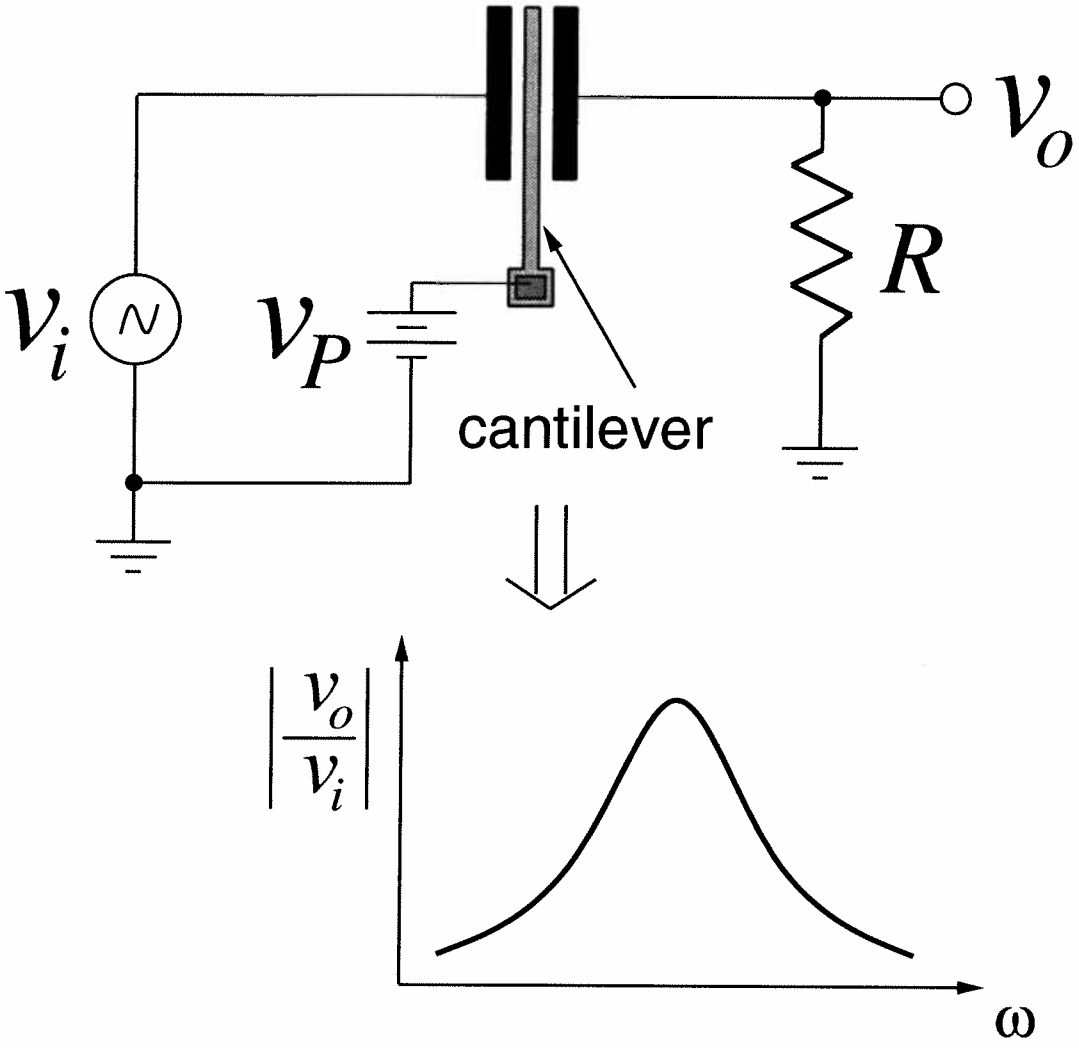

Fig. 2.34: Resistive detection of capacitively transduced resonator motion.

chip, the better the matching tolerance. Capacitance matching using IC technologies has been achieved to 0.1% without trimming [12].

The matching tolerance of folded-beam, comb-driven micromechanical resonators was investigated by fabricating several of them in close proximity. The measured spread of resonance frequencies is summarized in Table 2.5. From the table, the matching tolerance of the resonance frequency is seen to be 0.4%. This is fairly good. Strategies to improve matching might involve attaining better thickness uniformity over each die and improving etch uniformity.

TABLE 2.5. Identical Resonators in Close Proximity

Resonator#	Frequency [Hz]
1	18298.25
2	18166.50
3	18397.25
4	18318.75
5	18422.25

2.9 Conclusions

The advent of surface micromachining technologies provide new methods for integrating stable high-Q resonators on-chip. With (LF) Q's of over 80,000 under vacuum and center frequency temperature coefficients in the range of -10 ppm/°C (several times less with nulling techniques), polycrystalline silicon micromechanical resonators may serve reasonably well as miniaturized substitutes for crystals in a variety of high-Q oscillator and filtering applications.

When considering fabrication complexity, temperature stability, designability, and repeatability, capacitive transduction methods are relatively attractive. Other means for transduction, such as piezoelectric or magnetostrictive, are also available. These, however, usually complicate the resonator, since they generally require multi-layered structures, which may lead to poor thermal stability and inadequate frequency tolerances (absolute and matching). For a first attempt at integrating micromechanics with electronics, the simpler capacitive transduction was, thus, chosen.

Of the many topologies possible for capacitive transduction, parallel-plate and comb-transduction are the most common. Capacitive-comb transduction provides more linear transfer characteristics than parallel-plate, and thus, usually has a larger dynamic range and minimizes such phenomena as the electrical spring constant and spring softening Duffing effects. Parallel-plate transduction, on the other hand, is inherently nonlinear, and thus, has dynamic range limitations at low frequencies. At high frequencies, however, the magnitude of displacement at resonance will be quite small, so parallel-plate techniques are quite viable. In fact, they make high

frequency design simpler, since they generally have much less mass than their comb-transduced counterparts.

The equivalent circuit for a micromechanical resonator plays a central role in the design of applications utilizing this element. The noise performance of a micromechanical resonator is completely determined by the equivalent circuit. The circuit is similar in function to that modelling quartz crystals, the main difference being element values; on a micro-scale, motional capacitors are much smaller and motional resistors are much larger than their macroscopic (quartz) counterparts. This is somewhat unfortunate, since the design and (noise) performance of oscillators and filters are both optimum when the series resistance is small. As shown, the series resistance for capacitively transduced resonators is inversely proportional to the dc-bias voltage applied between the resonator and electrode, and inversely proportional to the capacitance change per unit displacement at the resonator-to-electrode interface. Thus, obtaining smaller series resistances should be feasible through technology improvements which increase the range of usable dc-biases, or which increase the electrode-to-resonator capacitance (such as smaller gap spacings). These will most likely be upcoming research directions.

CHAPTER 3 *Fabrication Technology*

The miniaturization of electronic components via planar integrated circuit technologies has revolutionized electronics industry, in both volume and capability. Because of miniaturization and the advantages that come with it—speed, compactness (higher complexity), low power, low price—the electronics industry has changed societies across the world. Given the enormous number of applications for which macroscopic mechanical devices are essential—from quartz timekeepers and communications oscillators to a wide variety of navigation, chemical, and pressure sensors, to the mirrors and lenses of optical receivers and relays—the ability to miniaturize these mechanical elements could very likely have a similar effect. A technology which then integrates micromechanics with electronics should have implications beyond any of this.

As will be seen in later Chapters, the performance of systems based upon micromechanical structures, especially resonators, is heavily dependent upon the amount of stray capacitance coupling drive or sense nodes to ground. This is most readily understood when considering the relative sizes of the capacitors in the microresonator equivalent circuits (on the order of femtoFarads, or attoFarads for the motional element) to those of bonding parasitics (picoFarads). This, coupled with the large series resistances characteristic of micro-scale mechanical resonators, makes integration of electronics with micromechanics a near necessity when using micromechanics as signal processors. All of the above effects will be detailed thoroughly in subsequent chapters.

This chapter begins with a brief overview of technologies capable of realizing micromechanical structures, then focuses upon the specific technique used in this work: surface microma-

chining. The options and issues related to integration of surface-micromachined mechanical structures are then investigated. Finally, a complete process description for the Modular Integration of CMOS and μStructures (MICS) process, which merges surface-micromachined mechanics with CMOS electronics, is provided.

3.1 Micromachining

The several micromachining technologies which may realize micromechanical structures can be categorized into two main groups: bulk micromachining or surface micromachining.

In bulk micromachining, a silicon (or other material; quartz, for example) wafer is patterned, then etched using anisotropic etchants, such as KOH or ethylenediamine pyrocatechol (EDP) Dissolved wafer technologies [45] are also bulk technologies. Often, double-sided alignment is required for bulk micromachined devices. Many variants of this technology have been used successfully for a variety of devices, including pressure sensors [1], accelerometers [44], resonators [59], and lamb wave sensors [48}. The technology is well developed, and integration with electronics has been successfully achieved [47,60].

Surface micromachining, on the other hand, is relatively new in comparison. It realizes micromechanical structures through the same processing procedures used for standard CMOS processes. It involves a sequence of depositions and patternings to achieve a structure in which the film-to-be-suspended sits upon a sacrificial film, which is exposed to the surface and can be accessed by isotropic etchants. A sacrificial etch then removes the sacrificial layer, freeing the structure in the process. Recently, this technique has been used to fabricate a wide variety of mechanical devices, including resonators [4,27,56], accelerometer proof masses and suspensions [3,61,62], miniaturized optical mirrors [53], and micromotors [25], to name a few.

3.1.1 Surface-Micromachining

Since this work utilizes surface micromachined polycrystalline silicon mechanical resonators, the focus here will be on surface-micromachining. Simple cross-sections which very quickly convey the idea of surface-micromachining are presented in Fig. 3.1. Details of the process flow are given in Section 3.3.1, so we will defer process details, such as temperature or flow rates, to this later section.

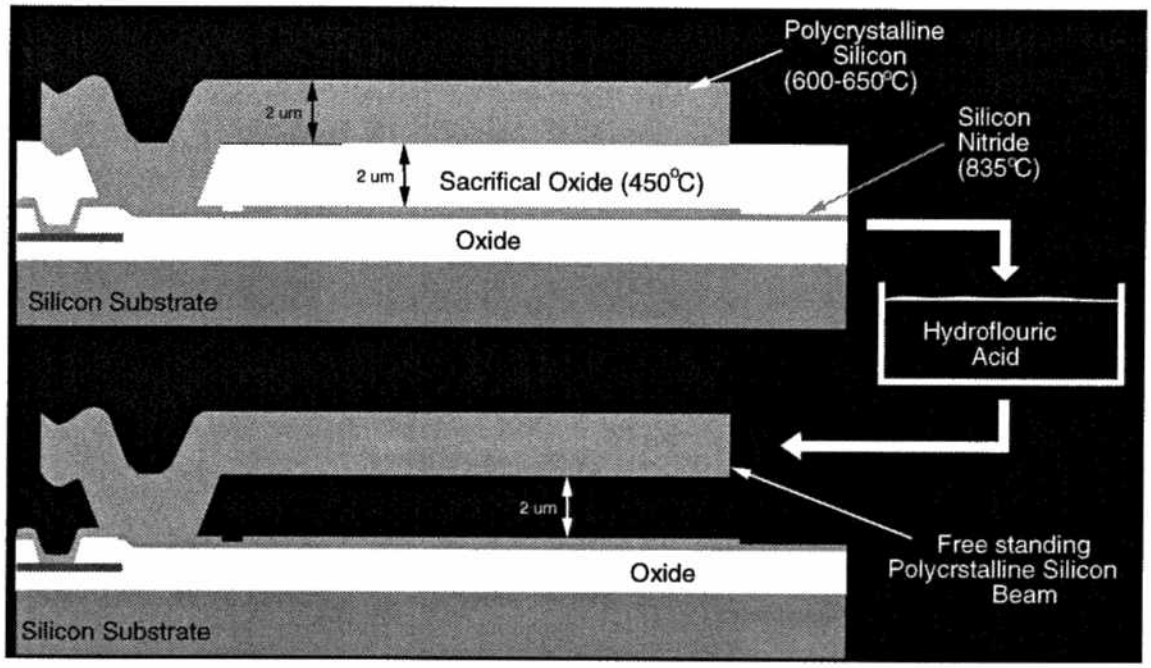

Fig. 3.1: Cross-sections describing surface-micromachining of polycrystalline silicon structures. (a) The wafer cross-section immediately before the release etch. (b) The cross-section after the HF release etch.

Figure 3.1(a) shows the wafer cross-section required just before the sacrificial release etch. This structure consists of layers of different materials, strategically placed to serve specific functions for both device performance and for release etch protection. The first oxide layer above the silicon substrate serves as a structural buffer which reduces the capacitance from structure to the substrate. As will be seen in Chapter 6, capacitance from structure (anchor) to substrate may seriously degrade the performance of filters based upon micromechanical resonators. Thus, this oxide layer should be as thick as possible.

The silicon nitride layer directly above the oxide protects the oxide from the sacrificial etchant, which is most often hydroflouric acid. The etch rate selectivity of oxide to silicon nitride is very large for all available concentrations of hydroflouric acid (for example, 100:1 for 5:1 buffered HF).

The thin (3500 Å) layer of polycrystalline silicon (heretofore referred to as poly1) over the silicon nitride has two purposes: first, it serves as a ground plane connected to the resonator (not shown; what's shown is a suspended electrode) which prevents the resonator from pulling into the

substrate due to voltage differences; secondly, it serves as interconnect between the structural polysilicon (in this case, the electrode) and the electronics beneath it. (The layer to which this polysilicon attaches on the left side of the cross-section is CMOS gate polysilicon, as will be seen shortly.) In addition, the polysilicon is comparatively resistant to HF attack when compared with oxide (also, 100:1 oxide vs. polysilicon selectivity), and thus, it protects the oxide in the poly1-to-gate poly contact.

The next layer of oxide, between poly1 and the structural polysilicon, serves as a sacrificial oxide layer. It temporarily supports the structural polysilicon (to be freed) until the sacrificial etch. It is generally deposited thick, on the order of 1 to 3 μm. The structural polysilicon (heretofore referred to as poly2) above the sacrificial oxide and anchored to the poly1 layer is usually from 1 to 3 μm thick, although much thinner or thicker polysilicon films are possible. For resonator applications, the structural polysilicon is usually deposited *in situ* phosphorous-doped, which slows the deposition process enormously, and thus, often puts a practical limit on the thickness of the structural layer. (Note, though, that the use of a boron-dopant would not suffer from this problem.)

The oxide layer (5000 Å) above the structural polysilicon is used as a "hard mask", which helps to achieve straight sidewalls when etching the thick structural polysilicon layer, and which also allows for thinner lithographical gaps, since it eliminates the need for a thick photoresist.

To relieve residual stress (usually compressive for phosphorous-doped polysilicon), the completed structure shown in Fig. 3.1(a) is usually annealed, either in a furnace or in a rapid thermal annealer. Then, as shown in Fig. 3.1, the wafer in (a) is dipped in hydroflouric acid, which etches away the sacrificial oxide layer and leaves all other layers intact. The released structure is as shown in Fig. 3.1(b).

Perhaps the most difficult step of the process occurs last: drying. The problem, here, is the tendency of microstructures with compliant springs to stick to the surface. This occurs because capillary forces in drying liquids between the structure and substrate can be strong enough to pull compliant structures down to the surface, where they remain indefinitely, until probed up. Surface-micromachining literature is tattered with articles on this phenomenon and on methods by which it may be avoided [63-66]. Many of the methods attempt to minimize or eliminate liquid surface tension, which gives rise to capillary forces.

One of the more successful techniques [66] for preventing sticking is one in which microstructures are first immersed in liquid carbon dioxide, which is then taken to its supercritical point, where it is neither a liquid, nor a gas, and thus, has no surface tension. The carbon dioxide is then flushed from the container, leaving freely suspended structures. This "supercritical CO_2" method for drying micromechanical structures was used in this work.

3.2 Merging CMOS and Micromechanics

The decision to merge CMOS and micromechanics to realize a given product is one based largely on economics and performance. From the economic side, one cannot blindly make the assumption that products will be cheaper just because they are batch fabricated in a planar process, especially when development costs could be enormous. From the performance side, if the required specifications can also be met without integration, then one must return to the question of economics. If, however, the performance specifications (such as product size, sensitivity, or frequency range) cannot be met without integration, then one has no choice. As previously mentioned, the relative sizes of micro-scale motional capacitance versus parasitic bonding capacitance justifies integration for this work.

Once the decision to integrate has been made, a myriad of different strategies must be considered. For example, it makes the most economic sense to develop a technology which uses an infrastructure that can be used for several different product lines, and which can easily keep up with advances in technology. In addition, the technology should be flexible enough to satisfy a wide range of performance specifications, preferably without the need for special equipment dedicated to only one product line.

The many choices for integration of electronics with micromechanics can be broken down into three basic categories, defined by where in the process flow the micromechanics are done: (1) post-CMOS; (2) pre-CMOS; and (3) mixed. These three choices are described schematically in Fig. 3.2.

3.2.1 Post-CMOS

As shown in Fig. 3.2, post-CMOS is a modular approach to integration, where the CMOS is processed first in one module, then the microstructures are processed in a following module, and

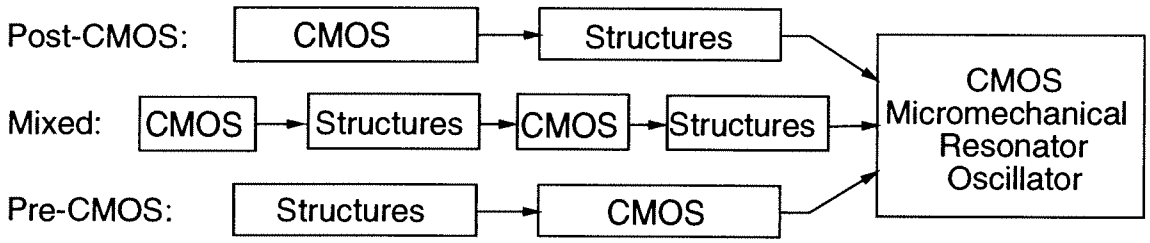

Fig. 3.2: Schematic description of the three basic approaches available for merging of CMOS and micromachining technologies.

at no point in the process are CMOS and micromachining steps intermixed. The advantages of this modular approach are tremendous in the ideal case: Modularity ideally allows the flexibility to use just about any CMOS circuit technology in the first module, and nearly any surface-micromachining technology in the second. This means that products which require high-speed circuits and those which do not can share the same merging technology. Also, the individual modules may advance at independent rates, i.e. if a faster CMOS line becomes available, this does not effect the structural process or the merging process. Finally, much less development time is required for new products, since one need only select which CMOS process and which micromechanics process are to be used, without worrying too much about merging

Unfortunately, this attractive idea is accompanied by many technical problems. To begin, if the temperature ceiling of the microstructural process is above 450°C (which is the case for polysilicon microstructures), then aluminum metallization, which is so popular in CMOS technologies, cannot be used. A metal with a higher melting temperature, such as a refractory metal must be used instead. The use of a refractory metal would not only increase interconnect resistance, but might also suffer from adhesion problems.

Assuming a suitable metal is found, there are additional problems. First, the temperature ceiling of the microstructural process cannot be over 1000°C, since such temperatures would induce junction diffusion. A further constraint on the temperature ceiling arises from the metal contacts, which will require a contact barrier to prevent spiking of metal into the junctions at high temperatures. The contact barrier, which could be $TiSi_2$, for example, will have a temperature limit of its own. For tungsten over $TiSi_2$, this limit is from 800 to 850°C, for limited times (under 3 hours). All of these temperature limits, of course, compromise the true modularity of this process.

For the case of this work, a process which realizes polycrystalline silicon micromechanical resonators is required. A surface-micromachined polysilicon microstructural process which satisfies an 850°C temperature ceiling is quite feasible up to the annealing step, which is commonly done in a furnace at 1050°C for one hour. Some other method of annealing will then be required—perhaps rapid thermal annealing.

3.2.2 Pre-CMOS

Like post-CMOS, a pre-CMOS process is also modular, but this time the microstructures are fabricated first, followed by the CMOS module. In the ideal case, all the advantages of modularity mentioned in Section 3.2.1 apply here, as well. As with post-CMOS, however, pre-CMOS is accompanied by technical problems, perhaps even more difficult to solve.

First and foremost is topography. Since micromechanical structures are usually designed to be thick (1 to 2 μm) relative to the layers in CMOS, some way to alleviate stringer and photoresist welling problems incurred during CMOS processing must be found. With today's chemical-mechanical polishing technologies, perhaps this problem could be solved by recessing the micromechanics, polishing down any residual humps, then proceeding with CMOS.

Even if the topography problem is solved, there will be a temperature limit for the finished polysilicon microstructure and surrounding sacrificial/protection layers. Since many of the process steps in CMOS use high temperatures (e.g. well drive-in), the CMOS process used must adhere to the temperature ceiling of the finished microstructures. This, of course, compromises the modularity of the process.

3.2.3 Mixed

As shown in Fig. 3.2, this approach is not modular, rather the process steps of CMOS and micromachining are intermixed in one process flow. The advantage of this technique is that usually a process can be designed such that all high temperature steps can be done first, before any low temperature materials are present. The disadvantage is that the process is not modular; in other words, each new product with dissimilar technological requirements would require a significant amount of design investment.

In addition, mixed processes usually require more processing steps than the modular alternatives, since many additional steps must be taken to protect/passivate the layers of one technology from the processing steps of the other. Thus, mixed processes can be much more expensive.

3.3 Modular Integration of CMOS and μStructures (MICS)

For this work, post-CMOS was chosen, since of the two modular choices, it was deemed most feasible within the existing technology base at the University of California at Berkeley. A mixed process was not considered due to the disadvantages explained above.

To solve the interconnect problem, tungsten metallization is used. Tungsten has a very high melting temperature (3410°C) and very low coefficient of thermal expansion, which is close in value to that of silicon. Nevertheless, tungsten suffers from oxide adhesion problems at excessive temperatures (over 1050°C, as will be seen). $TiSi_2$ contact barriers are utilized to prevent spiking of tungsten into the silicon at high temperatures. Residual stress in the micromechanical structures is relieved via rapid thermal annealing (RTA), rather than a furnace anneal, to reduce the *Dt* constant (hence, preserve the metal contacts).

The cross-section for the Modular Integration of CMOS and μStructures (MICS) process [3,67,68,69,75] used to merge CMOS and surface micromachining technologies is shown in Fig. 3.3. The details of the process flow will now be presented.

3.3.1 Process Outline

A cross-sectional outline of the MICS process sequence is presented in Fig. 3.4. The fabrication process begins with standard CMOS up to and including the contact cut for the first metallization (Fig. 3.4(a)). At this point, a thin film of titanium is sputter deposited onto the wafer surface, and then rapid-thermal annealed (RTA) for 30 seconds at 600°C in a nitrogen ambient to form $TiSi_2$ at points where titanium contacts silicon. Unreacted titanium is then etched away using a 3:1 $NH_4OH:H_2O_2$ solution, and another RTA is performed for 10 seconds at 1000°C. At this point, the cross-section appears as in Fig. 3.4(b). A 6000 Å film of tungsten is then sputter deposited and patterned to form the single-level interconnect (Fig. 3.4(c)). Subsequent low-pressure

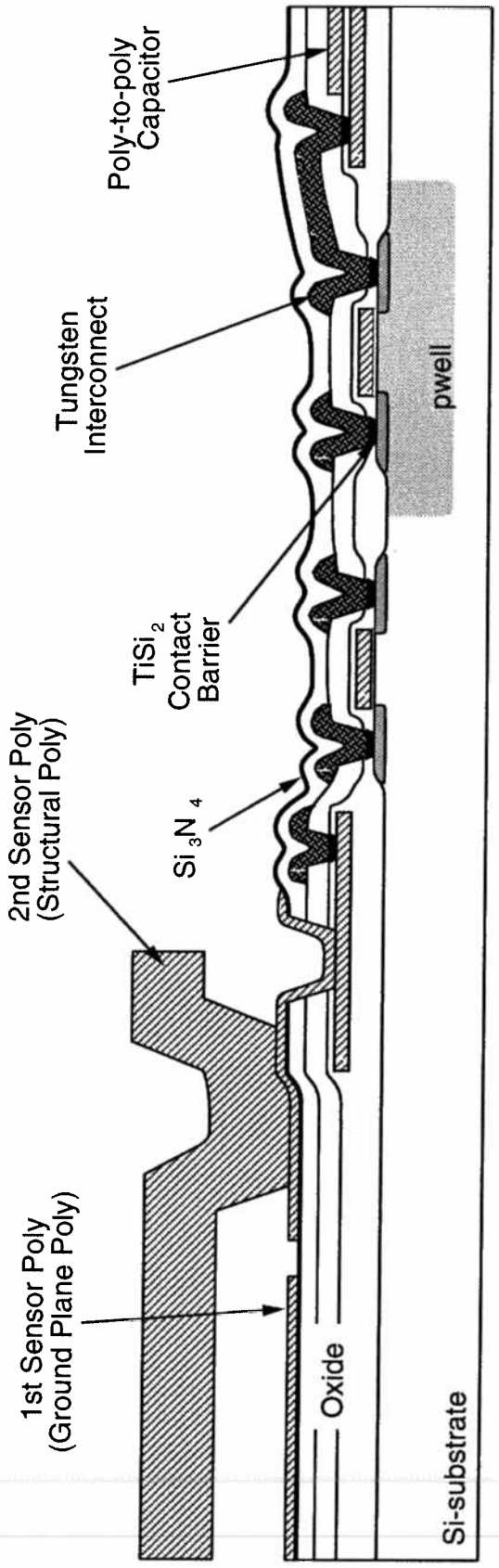

Fig. 3.3: Cross-section of the MICS technology for integration of CMOS and microstructures.

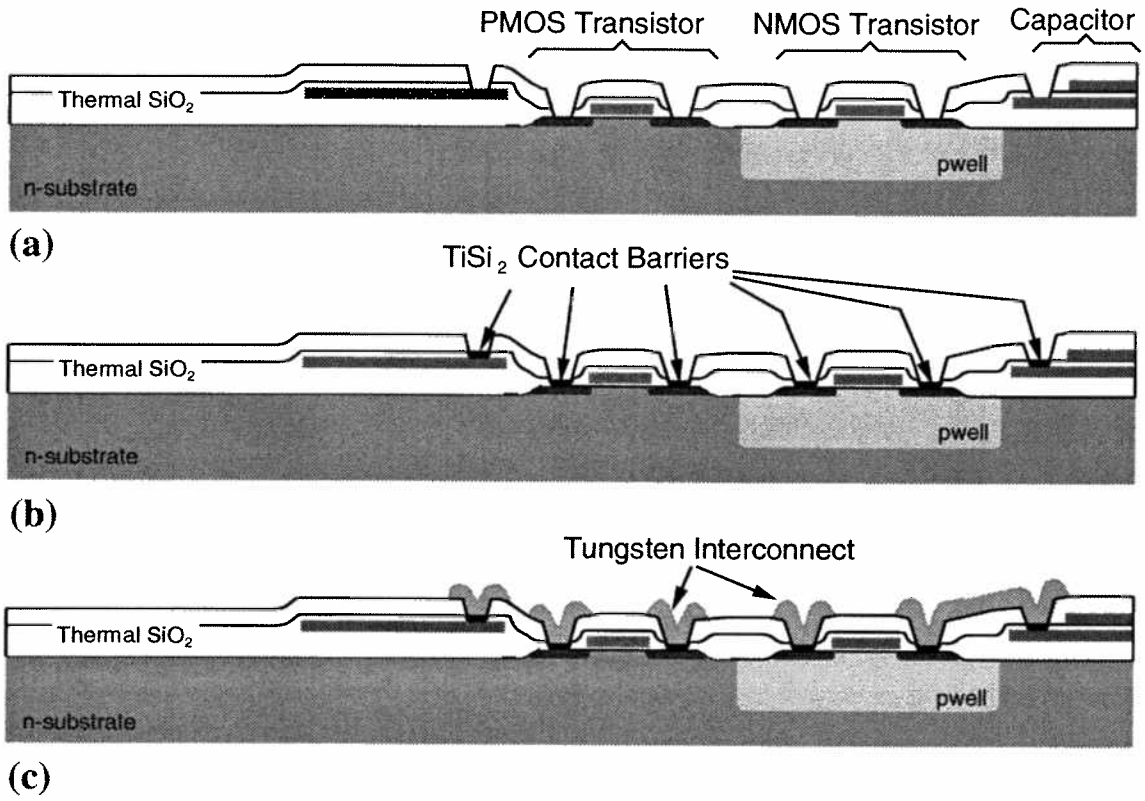

Fig. 3.4: Cross-sectional process flow for the CMOS plus microstructure fabrication technology. (a)-(c) constitute the metallization steps.

chemical vapor depositions (LPCVD) of 5000 A of low-temperature oxide (LTO) and 1500 A of silicon-rich nitride, at 450°C and 835°C, respectively, serve to passivate the metal (Fig. 3.4(d)).

Vias are then plasma etched through the nitride and underlying oxide to expose gate polysilicon runners that were formed during CMOS processing (Fig. 3.4(e)). These runners serve as an intermediate conductive level that joins the CMOS tungsten interconnect with the structural polysilicon interconnect. Direct contact between the first structural (ground plane) polysilicon and tungsten metal never occurs. This originally was a precaution to prevent contamination of the polysilicon deposition system by tungsten.

Next, 3000 Å of *in situ* phosphorous-doped LPCVD polysilicon is deposited at 610°C and patterned to define the interconnect and ground plane polysilicon for the microstructures (Fig. 3.4(f)). This is followed by a 2 μm LPCVD deposition (450°C) of phosphosilicate glass (PSG) that serves as a sacrificial layer to be removed when releasing the mechanical structures.

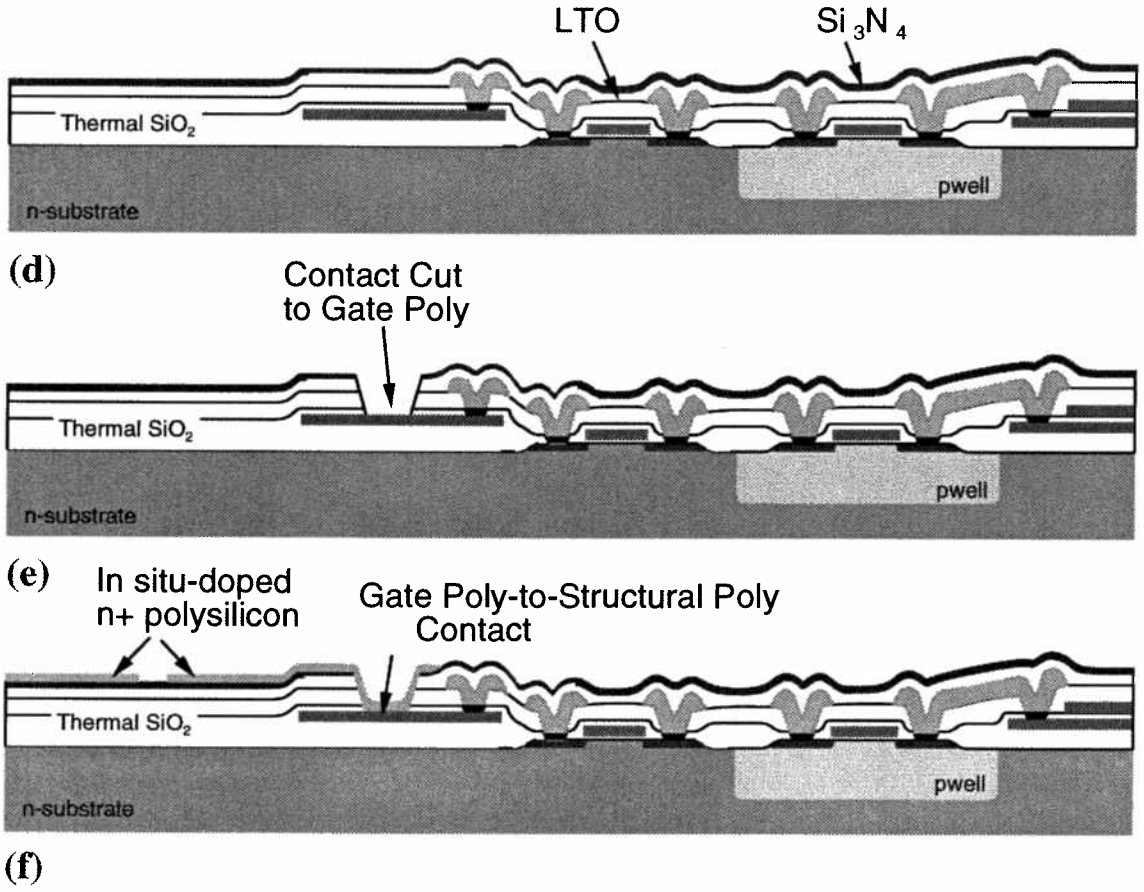

Fig. 3.4: (continued) (d)-(f) constitute the metallization steps.

Next, a contact cut in the PSG defines the anchor points for resonators and electrodes (Fig. 3.4(g)), and 2 μm of *in situ* phosphorous-doped LPCVD polysilicon is deposited at 610°C to serve as the structural material.

The structural material is then capped with a 5000 Å film of LTO, which deposits conformally onto the polysilicon. A thin layer of photoresist is applied and patterned with a single mask that defines resonator geometries, including interdigitated-comb fingers. The oxide cap is first plasma etched using a CF_4/C_2F_6-based chemistry, which is very selective towards oxide, but which etches silicon very slowly. The oxide then serves as a hard mask for the ensuing plasma etch that patterns the structural polysilicon. This etch is done using a Cl_2-based chemistry that attacks silicon, but etches oxide very slowly. At this point, the structural polysilicon is fully patterned, and the cross-section of Fig. 3.4(h) results.

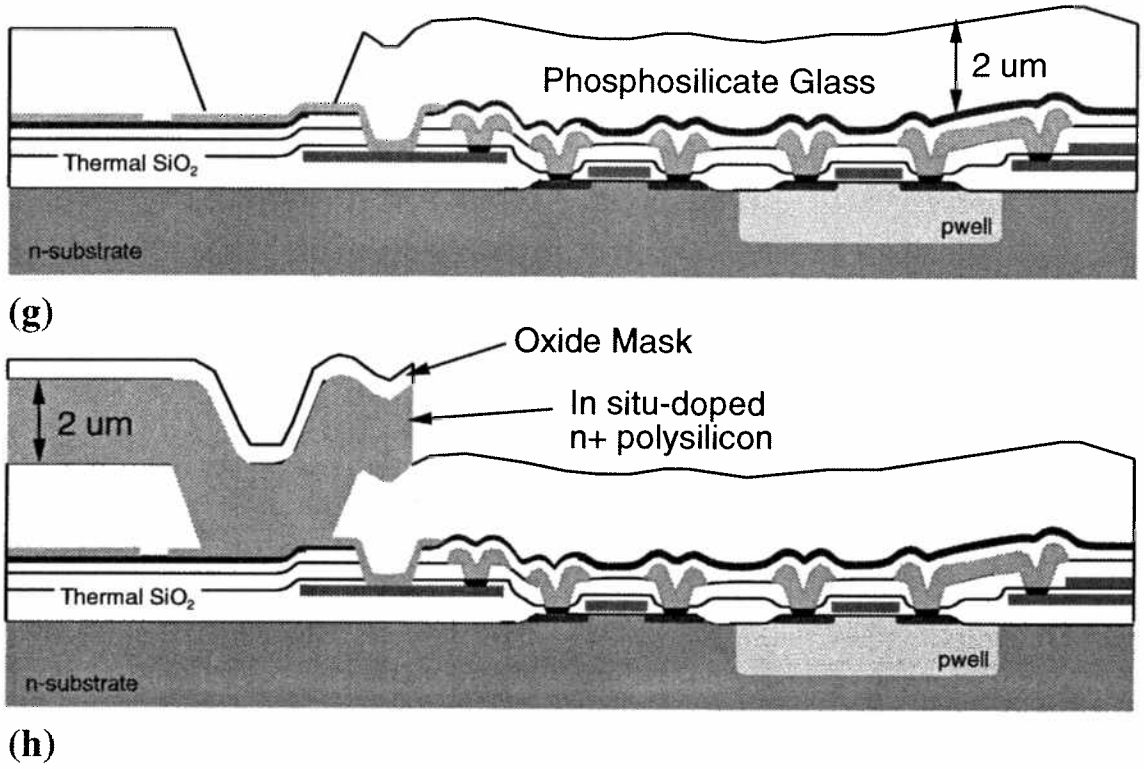

Fig. 3.4: (continued) (g)-(h) show the micromachining steps.

Use of this oxide mask greatly enhances the resolution with which finger gaps may be defined. Without the oxide mask, a double or triple layer of photoresist would be required to insure proper coverage of large steps, which occur around the anchors of the resonators and electrodes. With an oxide mask, however, the photoresist is no longer required to cover large steps, since now oxide protects the underlying polysilicon. During the oxide mask etch, the oxide along the step slopes may be attacked, since the photoresist is very thin along the steep slopes. However, as illustrated in Fig. 3.5, the vertical thickness of the conformal oxide layer is much larger along the these slopes, so oxide will remain to protect polysilicon even after long anisotropic overetches during oxide mask patterning. Thus, a much thinner film of photoresist may be used when an oxide mask is present, which leads to improved lithographic resolution. High resolution is extremely important for oscillator or signal processing applications of capacitively transduced resonators, since the degree of electromechanical coupling achievable via capacitive transduction is directly related to the gap spacings between interdigitated fingers.

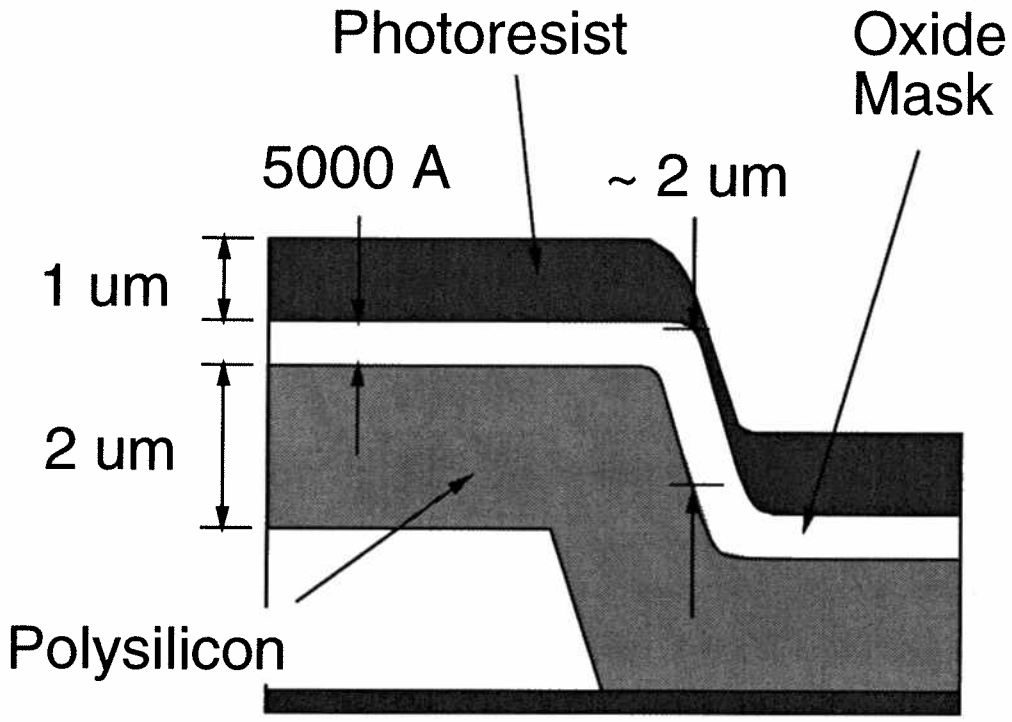

Fig. 3.5: Cross-section illustrating how a conformal oxide mask can reduce photoresist thickness requirements over large steps, thus, enhancing lithographic resolution. The oxide is much thicker vertically in the regions were the photoresist is thin.

Continuing with the process flow, a stress anneal is performed via RTA for 1 minute at 950°C, followed by a sequence of etches to expose the conductive backside of the silicon wafer. Finally, the wafer is dipped in 5:1 buffered hydrofluoric acid to remove the sacrificial PSG and free the microstructures. The wafers are dried using a supercritical carbon dioxide technique, which prevents sticking of the structures to the substrate by eliminating surface tension forces during drying [66]. The final cross-section is shown in Fig. 3.3.

Although quite different from the traditional 1 hour at 1050°C furnace stress anneal [28], which cannot be used here due to the presence of CMOS electronics, the rapid thermal stress anneal performs comparably. However, due to the heavy phosphorous concentration in the polycrystalline silicon, the residual compressive stress in the polysilicon films of this work is still quite large and is difficult to anneal away. Thus, stress-relaxing designs, such as cantilevers or folded-beam resonators, are required for the current process. The aforementioned stress problems may be alleviated in the future by lowering the phosphorous content in the μresonators, or by using *in situ*

boron-doped polysilicon. The latter solution has the additional advantage of substantially reducing the polysilicon deposition rate.

3.3.2 Limitations of MICS

Throughout the development of the MICS process, there were several problems with the process. Obviously, since this dissertation has yielded working devices, these problems are not debilitating in a research environment. In an industrial environment, however, there much reason for concern.

The main problems with the MICS process that achieved the oscillator of this work are listed as follows:

1. *Nonlinear contact resistance in boron-doped p+ junctions.* This phenomenon is attributed to consumption of silicon and resultant outdiffusion of boron during the rapid-thermal anneal silicidation process for the $TiSi_2$ contact barriers. The p+ junction contact resistance was not uniform over the wafer. It was highly nonlinear, with contact resistance as high as 2 kΩ at low voltages in some areas of the oscillator wafer, and as low as 7 Ω on one edge of the wafer, which little discernible nonlinearity. This latter result implies that a simple solution to the nonlinear p+-junction problem must be possible. Thus far, the only technique that has truly linearized the p+-junctions in this author's MICS experience has been an extra boron implant step, immediately after silicidation formation, and before the 1000°C activation anneal.
2. *Poor adhesion of tungsten to the oxide.* This problem limited microstructural RTA annealing temperatures to under 1050°C. At 1050°C or higher, catastrophic blistering of the tungsten occurred. Fortunately, RTA temperatures lower than 1050°C were found to be adequate.
3. *Nonideal release procedure required.* One of the supposed advantages of the MICS process was its release cleanliness; in other words, during the microstructural HF release etch, no photoresist is necessary in the ideal case. Rather, circuits and underlying oxides should be protected by the silicon nitride and polysilicon layers at the wafer surface. Wafer cleanliness may have advantages in preventing future device failure due to sticking on the wafer surface. Unfortunately, this was not the case. The thin silicon nitride layer—which had to be thin to reduce the time spent over 800°C—was found to be porous or cracked at the end of

the first MICS run, and it allowed HF to attack the underlying circuits. Thus, the release etch for MICS presently requires photoresist to protect the underlying circuits. The use of photoresist further requires the use of buffered hydroflouric acid, since unbuffered HF will attack most photoresists.

4. *Compressive stress in deposited in situ phosphorous-doped polycrystalline silicon films.* Due to this compressive stress, folded-beam suspensions were required by all designs, except the highest frequency ones. An eye-opening example of the degree to which the polysilicon films are compressive is shown in Fig. 3.6, which shows a buckled double-ended tuning fork with 250 μm-long tines. Solutions to this problem are currently under investigation by researchers within the Berkeley Sensor and Actuator Center.

3.4 Conclusions

From an economic viewpoint, a modular process is most desirable when attempting to merge two dissimilar technologies. This philosophy has led to development of the Modular Integration of CMOS and μStructures (MICS) process, which merges planar CMOS fabrication technologies with those of surface micromachining to yield fully integrated microelectromechanical systems. Here, CMOS electronics are fabricated in a first module, then micromechanical structures are fabricated in a following module, and at no point in the process are any steps from the two modules intermingled.

In the truest sense of the word, modularity implies freedom of choice of constituent modules. The process described here attempts to approach this ideal condition as closely as possible, with as few constraints from one module to another, while maintaining a completely planar process with low parasitic interfaces between microstructures and CMOS. In the MICS process, the metallization in the CMOS is constrained to be able to withstand temperatures up to 835°C, while the micromechanics are constrained to be deposited *in situ* doped, and constrained to use folded-beam designs to relieve residual stress.

Despite these constraints, a working process was achieved, and the designs implemented using this process will be detailed throughout the rest of this dissertation. Scanning electron micrographs will be presented accordingly in later chapters.

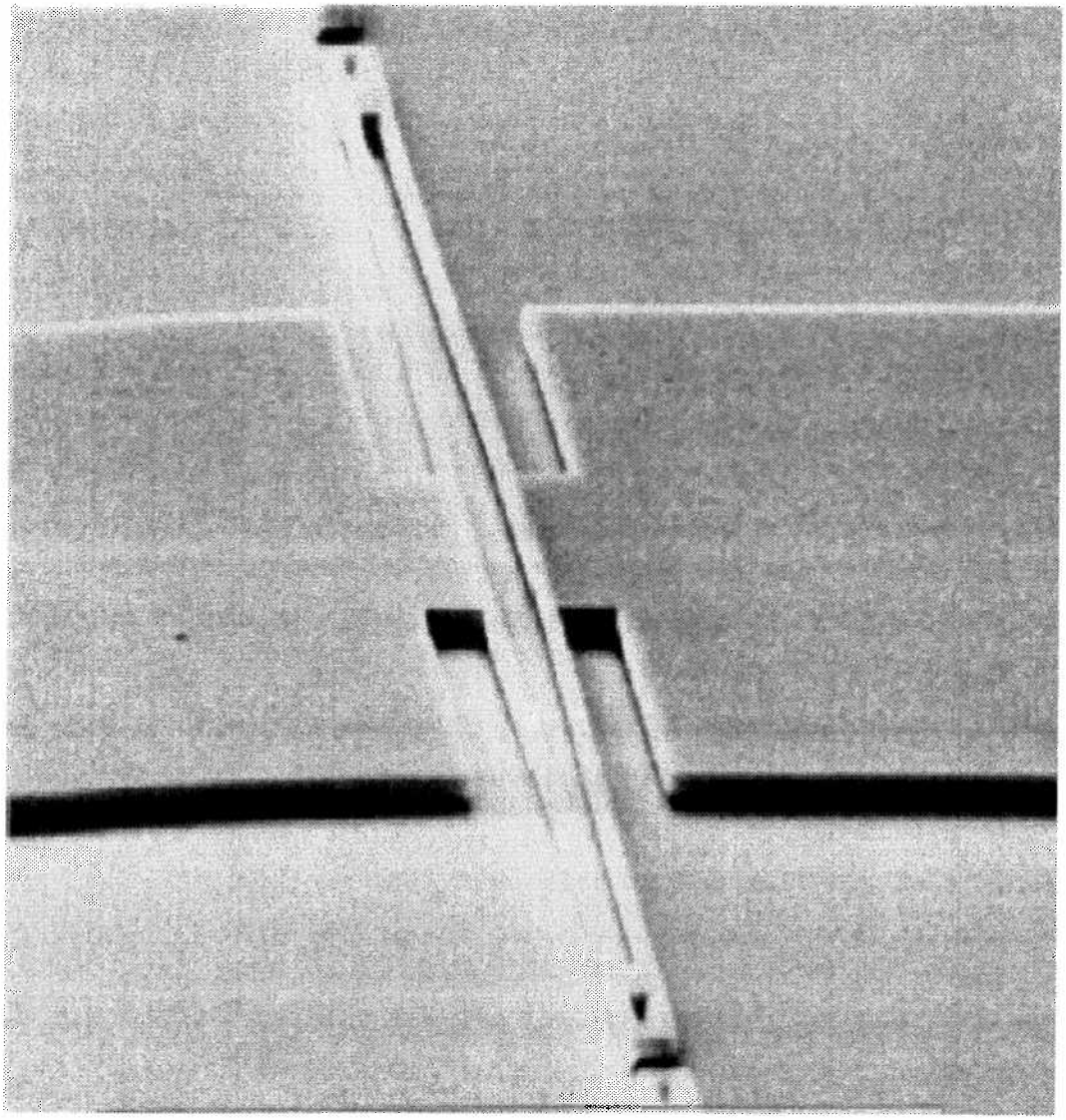

Fig. 3.6: SEM of a buckled double-ended tuning fork constructed of *in situ* phosphorous-doped polycrystalline silicon, deposited at 610°C via LPCVD.

CHAPTER 4 *High-Q CMOS Micromechanical Resonator Oscillators*

Crystal oscillators are widely used to generate precision frequency standards for complex integrated circuits. They are utilized in a wide range of applications: from wrist watches and digital computers, where their extremely stable frequencies make them useful as precise timekeepers; to local oscillators in a wide variety of communication links and radar detection schemes, where low oscillator phase noise is paramount in setting the minimum detectable signal in heterodyning receivers. As interest in wireless, mobile communications grows, so does the incentive to include increasing amounts of a total system on a single silicon chip. Designers have, in fact, already begun to include the oscillator function, except for the crystal, on the silicon die [70]. A fully monolithic high-Q oscillator, which includes the "crystal" element as well as sustaining CMOS electronics on-chip, is thus desirable.

As described in Chapter 2, polycrystalline silicon micromechanical resonators, with Q's of over 80,000 [71] under vacuum at audio frequencies and center frequency temperature coefficients in the range of -10 ppm/°C (several times less with nulling techniques) [72], can serve reasonably well as miniaturized substitutes for crystals in a variety of high-Q oscillator and filtering applications. Several approaches to integrating such micromechanical resonators with sustaining monolithic electronics are available [4,73,74,75]; one of these was discussed at length in Chapter 3. Although much work is still required from a technological standpoint to increase the frequency range of both transistor and mechanical devices in a merged technology, the process of Chapter 3 is quite sufficient to implement initial designs of a fully monolithic high-Q oscillator.

Miniaturization of the high-Q element of an oscillator is a challenging prospect in view of stringent phase noise requirements imposed by sensitive radar and communication systems [76,77]. The prospects for maintaining adequate oscillator performance after miniaturization is complicated by a general decrease in electromechanical coupling due to decreased transduction area. In addition, as the mass of the high-Q element decreases, such phenomena as Brownian motion and mass loading noise [78] have greater influence on oscillator short-term stability and may limit the ultimate stability of micro-scale resonators, unless design strategies which minimize these effects are implemented.

After an initial focus on the phase noise requirements of present-day communication systems, this chapter proceeds with a discussion of the specifics of microresonator oscillator design and with analyses aimed at quantifying oscillator amplitude limiting and oscillator phase noise performance. During these discussions, performance limiting effects, such as Brownian motion and mass loading, as well as amplifier bandwidth limitations, will be addressed in detail.

4.1 System Phase Noise Requirements

Often, for initial system design, a signal source is viewed as having an output at a single frequency, i.e., its spectrum is an infinitely narrow line (delta function) in the frequency domain. This view, however, is often inadequate in predicting the performance of many of today's communication systems. In practice, if only because an oscillator is not switched on for an infinite amount of time, the actual spectral line will have a finite bandwidth. In addition, even the most high quality signal sources will have other imperfections, leading to unwanted amplitude and phase modulation of the carrier.

For communication systems, such as shown in Fig. 1.1, such noise modulation can be severely detrimental to the overall system performance (i.e., range, required transmission power). For example, if a carrier with unwanted amplitude or phase modulation is modulated, either in amplitude or in phase, by an information carrying baseband signal, then the signal quality or error rate of the communications link will be worsened as a result of the unwanted carrier modulation. Because the majority of high capacity communication systems use angle modulation, spurious phase modulation is usually more technically and economically important than amplitude modulation.

In describing the effect of spurious angle modulation on a given system, such as FM, one may choose to represent the noise as either a phase modulation or a frequency modulation. The two, in fact, are practically equivalent representations, and are related by the equation [76]

$$(\delta f_o)^2_{f_m} = \left(\frac{2N_{op}}{C}\right)_{f_m} f_m^2, \tag{4.1}$$

where $(\delta f_o)^2_{f_m}$ is the frequency power variation at a frequency f_m offset from the carrier, and $\frac{2N_{op}}{C}$ is the corresponding double-sideband phase noise density to carrier ratio (single sideband is half this). Phase noise density to carrier ratio is more commonly used to specify oscillator short-term stability, even for FM systems. For example, the specification for the first local oscillator of present-day cellular telephones is -50 dBc/Hz at 50 Hz offset from the carrier. (The temperature stability specification is ±1.5 ppm over -20°C to 70°C.)

To illustrate the economic importance of phase noise, take for example a very expensive satellite communication system. A 3 dB degradation in performance (due to phase noise) would halve the traffic capacity of this system. To restore full capacity, several options are available, among which are: (1) duplicate the communication system for the other half of the required capacity (ridiculously expensive solution); (2) increase transmitting power; and (3) increasing receiving capacity (increase the sizes of satellite dishes). All three of the above are extremely expensive solutions. Thus, from a cynical point of view, performance degradation due to phase noise performance could be equated to "money lost".

The above presents one of the overriding reasons, in addition to temperature and aging stability, for using high quality oscillators, such as crystal oscillators, as local oscillators in communication systems. The same reasons, plus the potential for economic and performance enhancements (through use of systems of many oscillators), fuel this research on miniaturized high quality oscillators.

4.2 Oscillator Design

The equivalent circuit for the two-port μmechanical resonator of Fig. 2.16, shown transformed to an equivalent LCR representation, was presented in Fig. 2.23, of Chapter 2, along with typical element values. As discussed in Chapter 2, due to the present difficulty in achieving suffi-

cient electromechanical coupling on the micro-scale, the motional element values are quite different from those for quartz crystal units (which typically have R_x=50Ω, C_x=0.04 pF, L_x=0.25 H), and this dictates differing strategies in the design of μresonator oscillators versus macroscopic crystal oscillators.

4.2.1 Minimal Q-Loading

Design of a high-Q oscillator often requires specific attention to preservation of the quality factor of the high-Q element [9]. In this respect, the best high-Q oscillator designs are those for which degradation of resonator Q by the sustaining electronics is minimized, or at least balanced with requirements for maximum power transfer. With this in mind, oscillator architectures may be subdivided into two broad categories: series resonant or parallel resonant. Schematic examples of both of these categories are presented in Fig. 4.1, where for both cases, the two-port resonator is represented by an equivalent LCR circuit, as previously done in Chapter 2.

In the series resonant architecture of Fig. 4.1 (a), the input impedance of the sustaining (transresistance) amplifier is in series with the resonator's motional resistance, resulting in an effective oscillator Q given by

$$Q = \frac{\omega L_z}{(R_x + R_{ia} + R_{oa})} = \frac{Q_{ul}}{1 + ((R_{ia} + R_{oa})/R_x)}, \tag{4.2}$$

where R_{ia} and R_{oa} are the input and output resistances of the sustaining amplifier, respectively, and $Q_{ul} = \omega L_x/R_x$ is the unloaded resonator quality factor. Eq. (4.2) indicates that a series resonant oscillator architecture offers minimum Q-loading of the resonator when the series motional resistance of the resonator R_x is much larger than the sum of the input and output resistances of the sustaining amplifier, i.e., where $R_x \gg R_{ia} + R_{oa}$.

For the parallel resonant architecture of Fig. 4.1(b), the transformed input impedance and the output impedance of the sustaining (transconductance) amplifier are in parallel with that of the parallel motional resistance R_p of the resonator, yielding an effective oscillator Q given by

$$Q = \frac{Q_{ul}}{1 + (R_p/(n^2 R_{ia} \| R_{oa}))}. \tag{4.3}$$

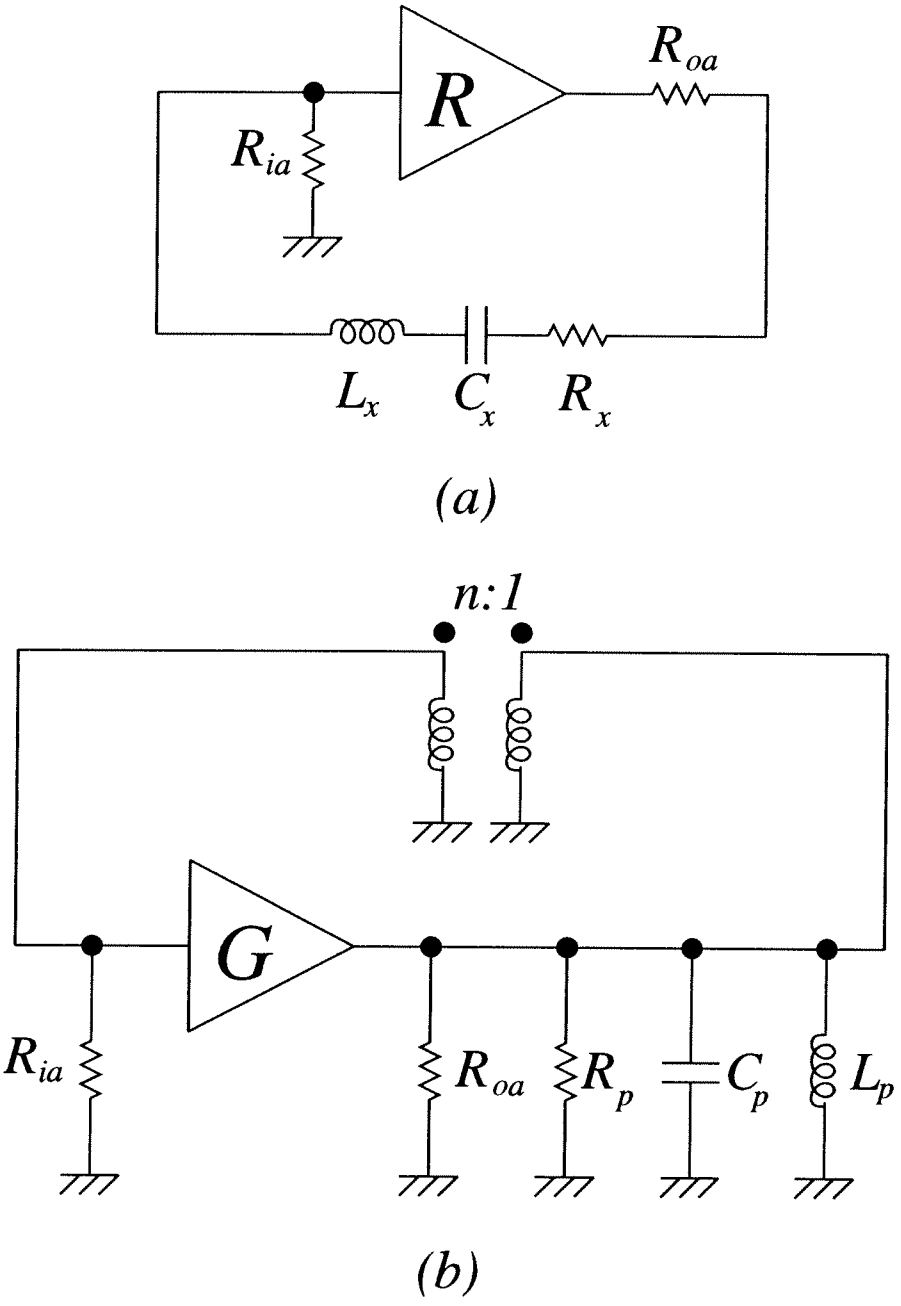

Fig. 4.1: Schematic examples of (a) a series resonant oscillator architecture; and (b) parallel resonant oscillator architecture.

Here, loading of the resonator Q is minimized when $R_p \ll R_{ia} \| R_{oa}$. For most cases, if the series motional resistance R_x of a resonator is small, then the parallel motional resistance R_p will be large. (This, however, is not always the case.)

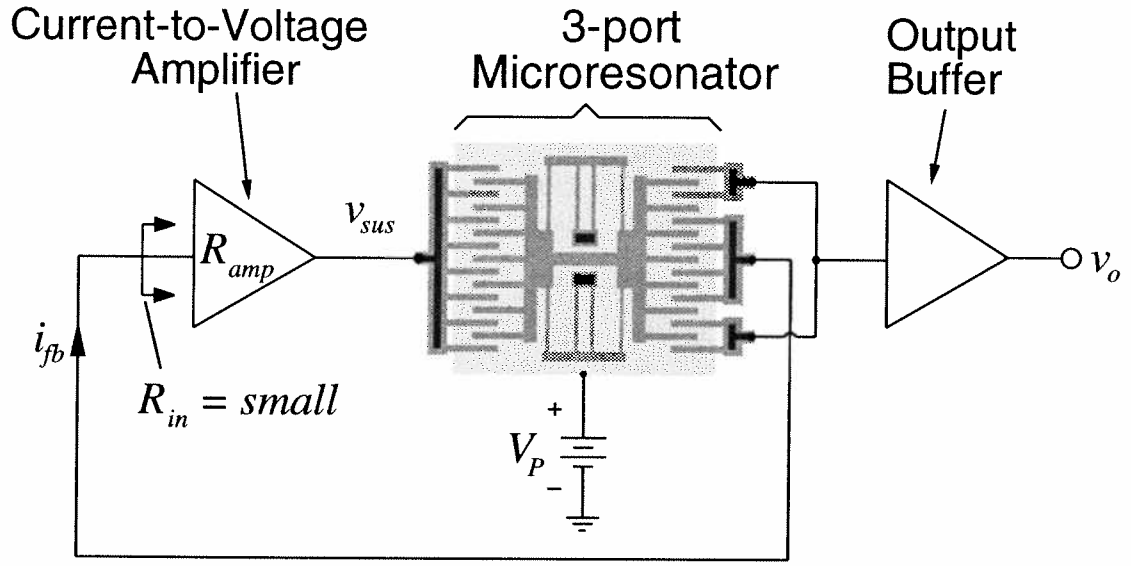

Fig. 4.2: System level schematic showing the basic series resonant architecture used for the CMOS micromechanical resonator oscillator of this work.

4.2.2 Prototype Oscillator Design

As explained in Chapter 2, the motional resistance of a micromechanical resonator is usually quite large for typical values of resonator dc-bias voltage and present-day lithographic capabilities. Thus, for the prototype micromechanical resonator oscillator of this work, a series resonant oscillator architecture will be used. However, it should be understood that parallel architectures, such as the popular Pierce design, could be advantageous for low series resistance resonator designs.

4.2.2.1 System-Level Design

Figure 4.2 shows a system-level schematic describing the basic architecture used for this oscillator. Since the motional resistance of the μresonator is large (Fig. 2.23), a series resonant oscillator architecture is utilized to minimize Q-loading, as explained in the previous section. As shown, the system consists of a three-port micromechanical resonator, for which two ports are embedded in a positive feedback loop with a sustaining transresistance amplifier, while a third port is directed to an output buffer. The equivalent circuit for the three-port micromechanical resonator is an extension of that for the two-port and is shown in Fig. 4.3, along with expressions for the elements. The use of a third port effectively isolates to some extent the sustaining feedback loop from

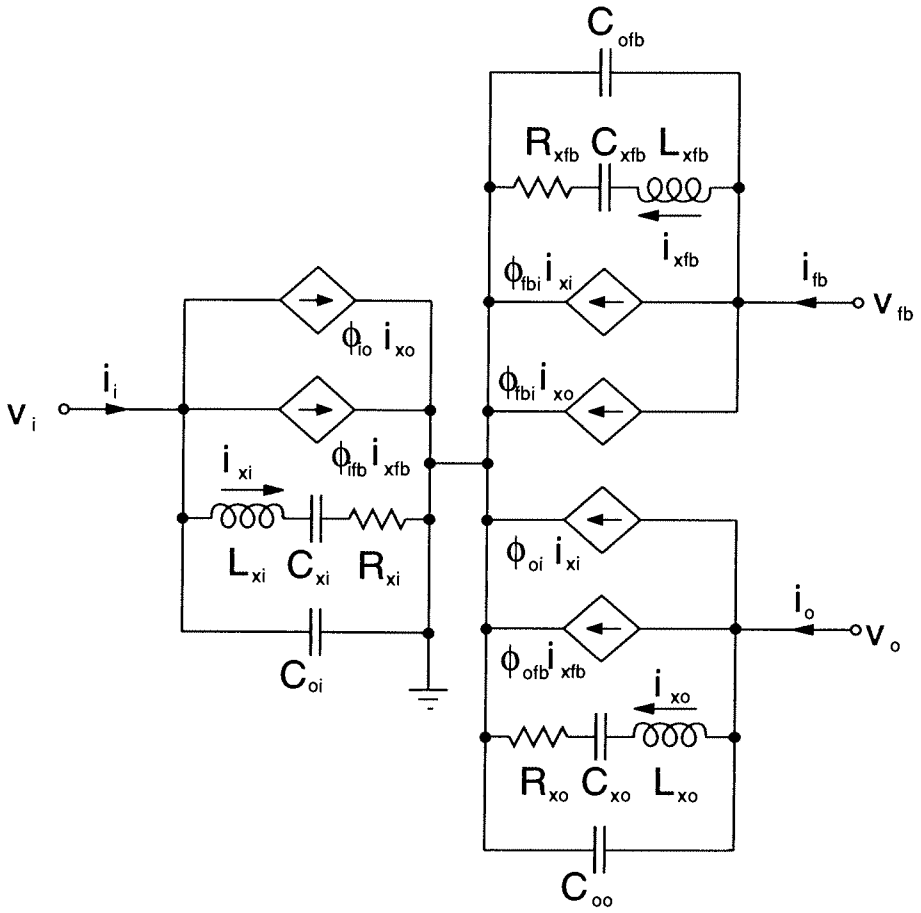

$$C_{xn} = \frac{\eta_n^2}{k} \qquad R_{xn} = \frac{\sqrt{km}}{Q\eta_n} \qquad \eta_n = V_{Pn}\left(\frac{\partial C}{\partial x}\right)_n$$

$$L_{xn} = \frac{m}{\eta_n^2} \qquad \phi_{mn} = \frac{\eta_m}{\eta_n}$$

Fig. 4.3: Equivalent circuit for a three-port micromechanical resonator with expressions for the elements.

variations in output loading. This is the case because any output loading variation must be reflected through the effective motional series resistance connecting the input and output (third) port, which can be very large. Equivalently, power losses to the output load are reduced when taking the output from a resonator port.

Conceptually, the sustaining amplifier and μmechanical resonator comprise negative and positive resistances, respectively. During start-up, the negative resistance of the amplifier R_{amp} is larger in magnitude than the positive resistance of the resonator R_x, and oscillation results. Oscilla-

tion builds up until either some form of nonlinearity or a designed automatic-level control circuit alters either or both resistors so that, $R_{amp} = R_x$, at which point the oscillation amplitude limits.

4.2.2.2 Transistor-Level Design

To maximize the short- and long-term stability performance of an oscillator, the sustaining amplifier should be made as simple as possible [80]. This is part of the logic behind the popular Pierce design, which uses a single transistor to invoke oscillation around quartz crystals, and which is one of the more stable oscillator designs available. Use of a simple sustaining amplifier is usually also accompanied by larger bandwidth capability, as well. The Pierce design is a parallel resonant oscillator architecture, and as such, is not optimum for the present high resonator series resistance design [79,80].

Figure 4.4 shows the detailed circuit schematic for the oscillator of Fig. 4.2. The sustaining amplifier design is transresistance, using shunt-shunt feedback to achieve a low input resistance, and therefore, minimal Q-loading. M_4 and M_5 serve as replica biasing for gain stages M_1-M_2 and M_6-M_7. M_3 is biased in the linear region by control voltage V_{GC} and serves as an MOS resistor with resistance given approximately by

$$R_3 = \left[\mu_n C_{ox}\left(\frac{W}{L}\right)_3 (V_{GS} - V_t - V_{DS})\right]^{-1}, \tag{4.4}$$

where μ_n is the electron mobility in silicon, C_{ox} is the gate oxide capacitance per unit area, W and L are the MOS channel width and length, respectively, and V_t is the transistor threshold voltage. The low-frequency transresistance gain R_{amp} of the amplifier is given by

$$R_{amp} = g_{m7}(r_{o7} \parallel r_{o6}) R_3, \tag{4.5}$$

where g_{m7} is the transconductance of M_7, and r_{o6} and r_{o7} are the output resistances of M_6 and M_7, respectively. To insure start-up of oscillation, the gain R_{amp} should be chosen three or more times larger than the effective series resistance of the microresonator.

M_{3A} is included in the design for automatic-level control purposes, as will be explained later. The capacitors C_{c1} and C_{c2} are compensation capacitors to be explained in detail in Section 4.2.2.4.

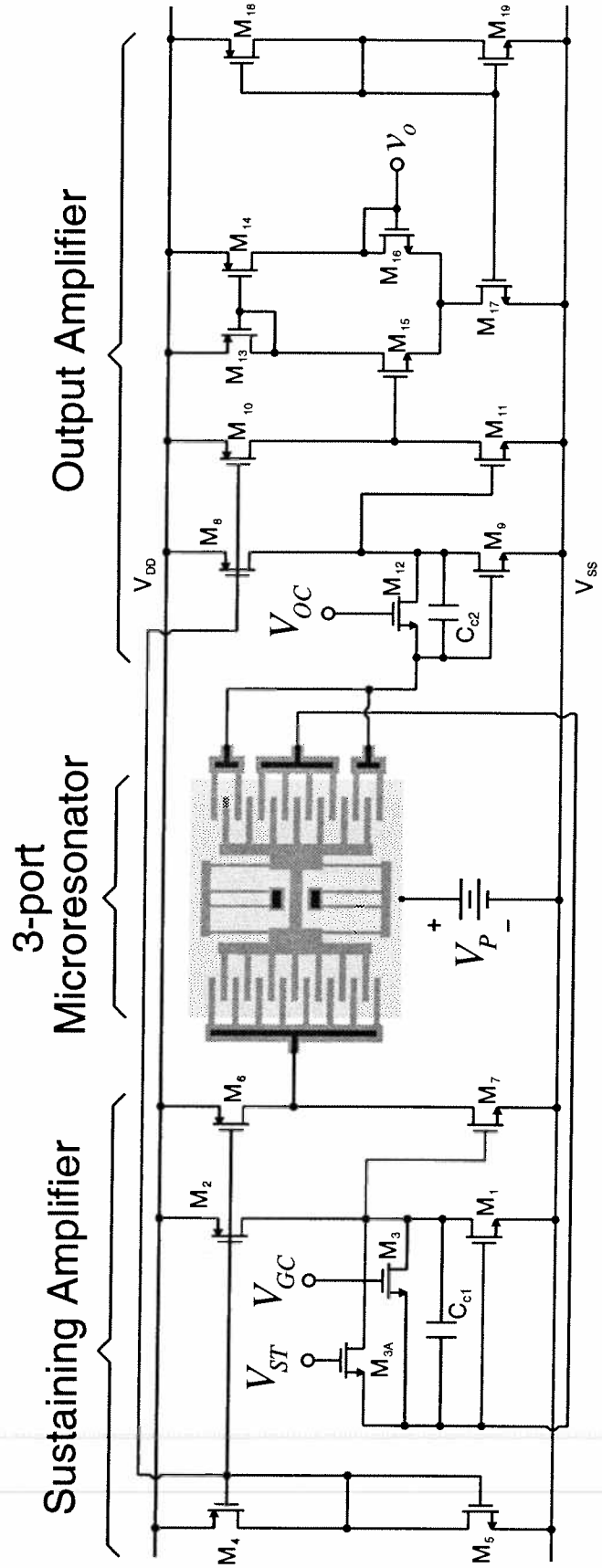

Fig. 4.4: Detailed circuit schematic for the CMOS micromechanical resonator oscillator of this work.

4.2.2.3 Replica Biasing

For purposes of robustness, the sustaining amplifier circuit is biased such that all nodes in the signal path have the same dc level. This is conveniently achieved through devices M_4 and M_5, which are replicas of M_1 and M_2, and M_6 and M_7. The device sizes of M_4 and M_5 for a specified value of bias current I_D and signal path dc-level V_B can be derived using the equation for current in a saturated MOS transistor

$$I_D = \frac{1}{2}\mu C_{ox}\left(\frac{W}{L}\right)(V_{GS} - V_t)^2, \tag{4.6}$$

where μ is the channel mobility, C_{ox} is the gate capacitance, (W/L) is the gate width over length ratio, V_{GS} is the gate-to-drain voltage, and V_t is the threshold voltage. Using (4.6), the equations for the bias device sizes, given a specific bias current I_D and signal path dc-level V_B, and assuming that $V_{tn} = |V_{tp}| = V_t$ are

$$\begin{aligned}\left(\frac{W}{L}\right)_4 &= \frac{2I_D}{\mu_n C_{ox}(V_B - V_{SS} - V_t)^2} \\ \left(\frac{W}{L}\right)_5 &= \frac{2I_D}{\mu_p C_{ox}(V_{DD} - V_B - V_t)^2}\end{aligned} \tag{4.7}$$

For the actual design, a 50% duty cycle output waveform was specified. This requires a signal path dc-level equal to one-half the full supply voltage. In this case, the device sizes are given by

$$\begin{aligned}\left(\frac{W}{L}\right)_4 &= \frac{2I_D}{\mu_n C_{ox}\left(\frac{1}{2}V_{supply} - V_t\right)^2} \\ \left(\frac{W}{L}\right)_5 &= \frac{\mu_n}{\mu_p}\left(\frac{W}{L}\right)_4\end{aligned}. \tag{4.8}$$

The advantage of this biasing scheme is its simplicity and robustness, characteristics that are especially important considering the experimental nature of the technology used to integrate CMOS electronics with polysilicon resonators in this work.

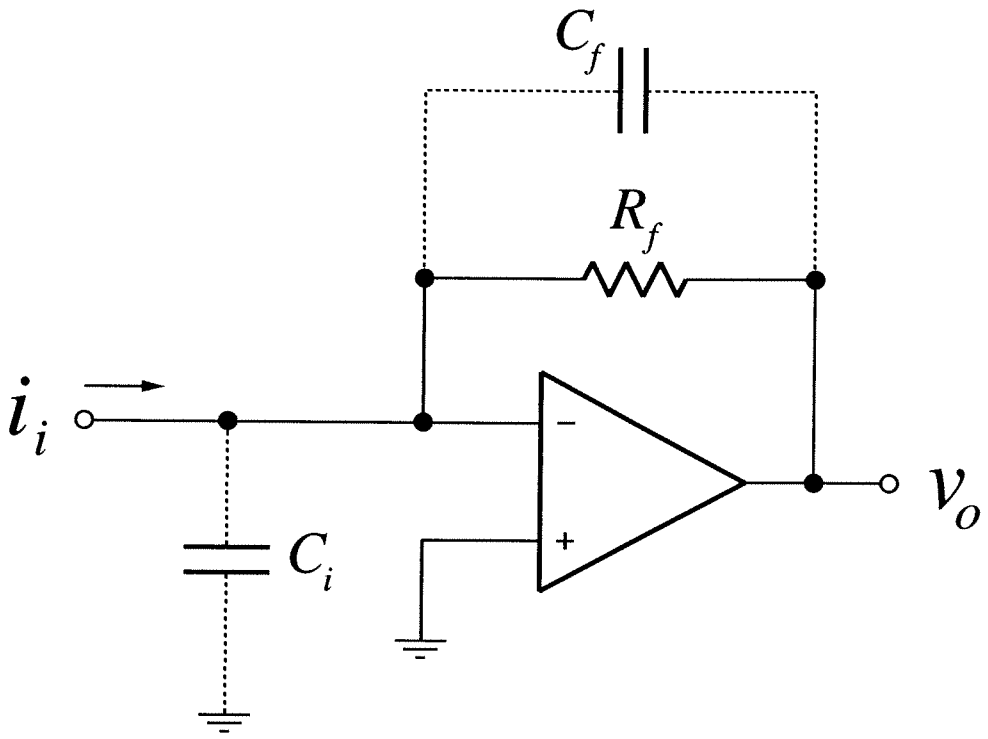

Fig. 4.5: Transresistance amplifier based on shunt-shunt feedback around an operational amplifier.

4.2.2.4 Transresistance Amplifier Bandwidth

The general schematic of an op amp-based shunt-shunt feedback transresistance amplifier is shown in Fig. 4.5. The bandwidth and stability for the amplifier of Fig. 4.5 is determined largely by the capacitance at the input of the amplifier, C_i, and across the feedback resistor, C_f. Before deriving quantitative relationships for the influence of these capacitors on the frequency response, the transfer function for the ideal case (no capacitors) will first be derived.

4.2.2.4.1 The Ideal Case: $C_i = 0$, $C_f = 0$

To derive the transfer function for the ideal case, where there is no input or shunt capacitance, we use the equivalent feedback loading diagram [80] for the circuit of Fig. 4.5 (with $C_i = 0, C_f = 0$), shown in Fig. 4.6. A simple one-pole model will be used for the operational amplifier, where the voltage-to-voltage transfer function is given by

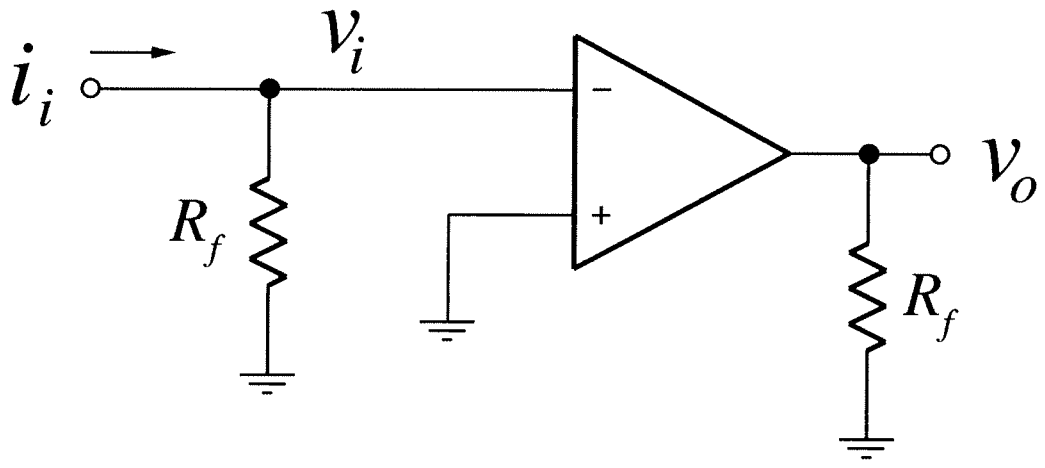

Fig. 4.6: Equivalent feedback loading diagram for the op amp transresistance amplifier of Fig. 4.5 with no input or shunt capacitance.

$$A_v = \frac{a_v}{1 + \frac{s}{\omega_b}}. \tag{4.9}$$

Recognizing that the voltage seen at the input to the amplifier under the loading shown in Fig. 4.6 is $v_i = i_i R_i$, where R_i is the input resistance of the operational amplifier, the open-loop transresistance gain of the amplifier is determined to be

$$v_o = -\frac{i_i a_v R_f}{1 + \frac{s}{\omega_b}} \quad \Rightarrow \quad r_m = \left.\frac{v_o}{i_i}\right|_{OL} = -\frac{a_v R_f}{1 + \frac{s}{\omega_b}}. \tag{4.10}$$

Shunt-shunt feedback provides a feedback transconductance given by $g_f = -1/R_f$, which leads to a transresistance gain

$$R_{amp} = \frac{r_m}{1 + r_m g_f} = -\frac{a_v}{1 + a_v}\frac{R_f}{1 + (s/\omega_T)} \approx -\frac{R_f}{1 + (s/\omega_T)}, \tag{4.11}$$

where the unity gain radian frequency of the operational amplifier, $\omega_T = a_v \omega_b$, has been inserted, and the last expression holds when $a_v \gg 1$. Equation (4.11) implies that with no capacitance, the 3 dB bandwidth for this transresistance amplifier is equal to the $f_T = \omega_T/(2\pi)$ of the operational

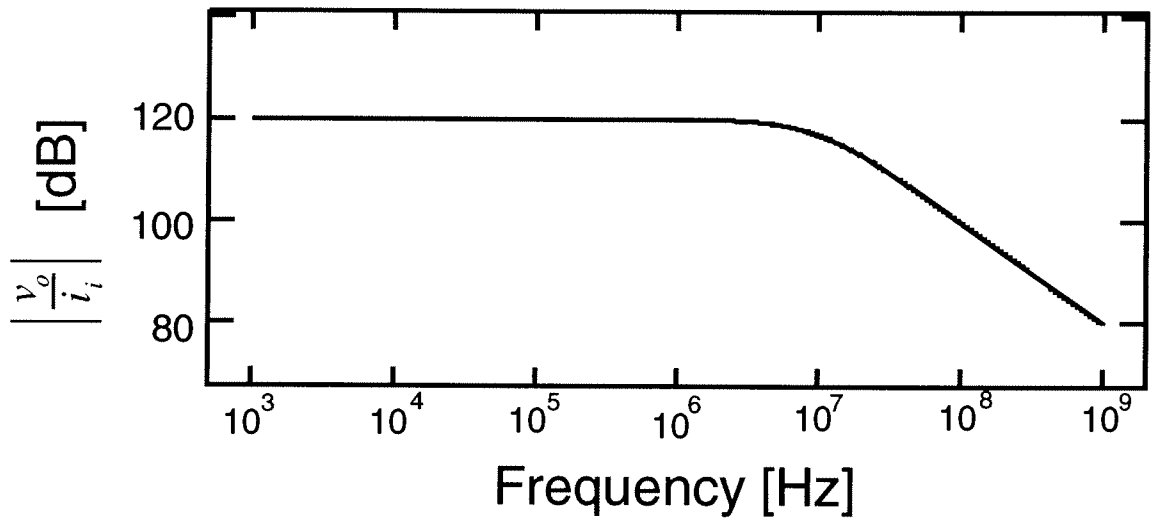

Fig. 4.7: Transfer function for the transresistance amplifier of Fig. 4.5, assuming one op amp pole, f_T = 10 MHz, and no input or shunt capacitance.

amplifier, which could be quite high. The transfer function corresponding to Eq. (4.11) is presented in Fig. 4.7. Note that the magnitude of the loop gain, given by $A_l = r_m g_f = a_v/(1+s/\omega_b)$, is frequency dependent, yielding an equivalent input impedance

$$Z_i = \frac{R_i|_{OL}}{1+A_l} = \frac{R_f}{1+a_v}\frac{1+(s/\omega_b)}{1+(s/\omega_T)}, \tag{4.12}$$

which also depends upon frequency, rising 20 dB/decade in the frequency range from f_b to f_T.

4.2.2.4.1 The Effect of Input Capacitance, C_i

The addition of input capacitance C_i greatly reduces the 3 dB-down frequency of the amplifier. In Fig. 4.8, the feedback loading schematic is again shown, this time including the input capacitance C_i. The voltage at the input of the amplifier is now $v_i = i_i(R_f \| (1/(sC_i))$, which leads to an open loop transresistance gain

$$v_o = -\frac{i_i a_v\left(R_f \| \frac{1}{sC_i}\right)}{1+\frac{s}{\omega_b}} \quad \Rightarrow \quad r_m = \left.\frac{v_o}{i_i}\right|_{OL} = -\frac{a_v R_f}{\left(1+\frac{s}{\omega_b}\right)\left(1+\frac{s}{\omega_i}\right)}, \tag{4.13}$$

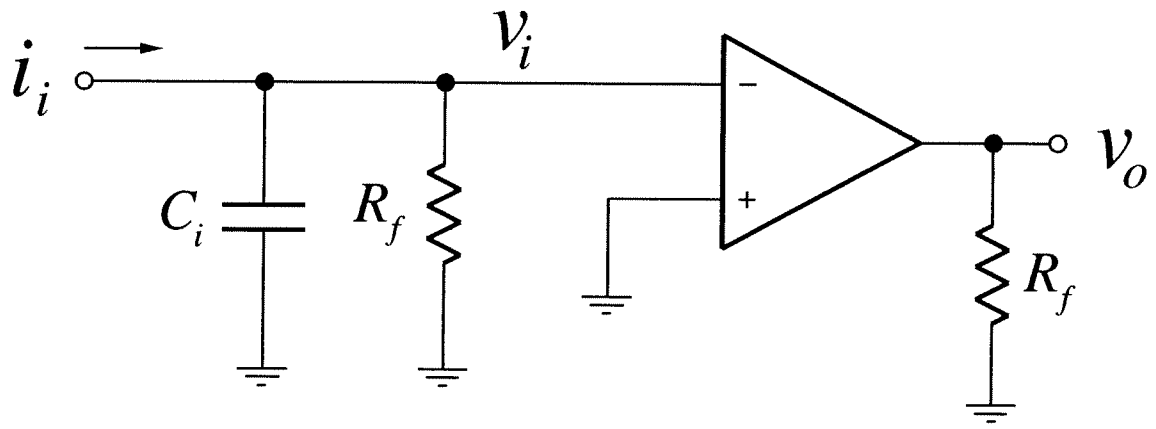

Fig. 4.8: Feedback loading diagram for the shunt-shunt feedback op amp transresistance amplifier with input capacitance C_i.

where $\omega_i = 1/(R_f C_i)$. Again, the feedback factor is $g_f = -1/R_f$, and this along with Eq. (4.13), yields for the transresistance gain

$$R_{amp} = \frac{r_m}{1 + r_m g_f} = \frac{a_v R_f \omega_i \omega_b}{s^2 + s(\omega_i + \omega_b) + \omega_t \omega_i} = \frac{R_f \omega_{pk}^2}{s^2 + s\frac{\omega_{pk}}{Q} + \omega_{pk}^2} \tag{4.14}$$

where $\omega_{pk} = \sqrt{\omega_i \omega_t}$

$\omega_i = 1/(R_f C_i)$

$\omega_T = a_v \omega_b$ = op amp unity gain frequency

Equation (4.14) has the form of a lowpass biquad transfer function, with dc gain $R(0) = R_f$ and peak frequency ω_{pk}. This transfer function is plotted in Fig. 4.9, against that for the amplifier without input capacitance for comparison. Note that ω_{pk} is now the effective roll-off frequency, and its value is substantially less than the ω_T of the op amp (which was the roll-off frequency for the amplifier without C_i.) The degree of peaking can be characterized via the quality factor Q of the lowpass biquad. The Q of the lowpass biquad can be calculated from Eq. (4.14):

$$\frac{\omega_{pk}}{Q} = \omega_i + \omega_b \quad \Rightarrow \quad Q = \frac{\omega_{pk}}{\omega_i + \omega_b} = \frac{\sqrt{\omega_i \omega_T}}{\omega_i + \omega_b}. \tag{4.15}$$

A plot of Q versus ω_i (with ω_b and ω_T held constant) is shown in Fig. 4.10. Note that the Q peaks (i.e. the amplifier is most unstable) when $\omega_i = \omega_b$, for which the value of Q is

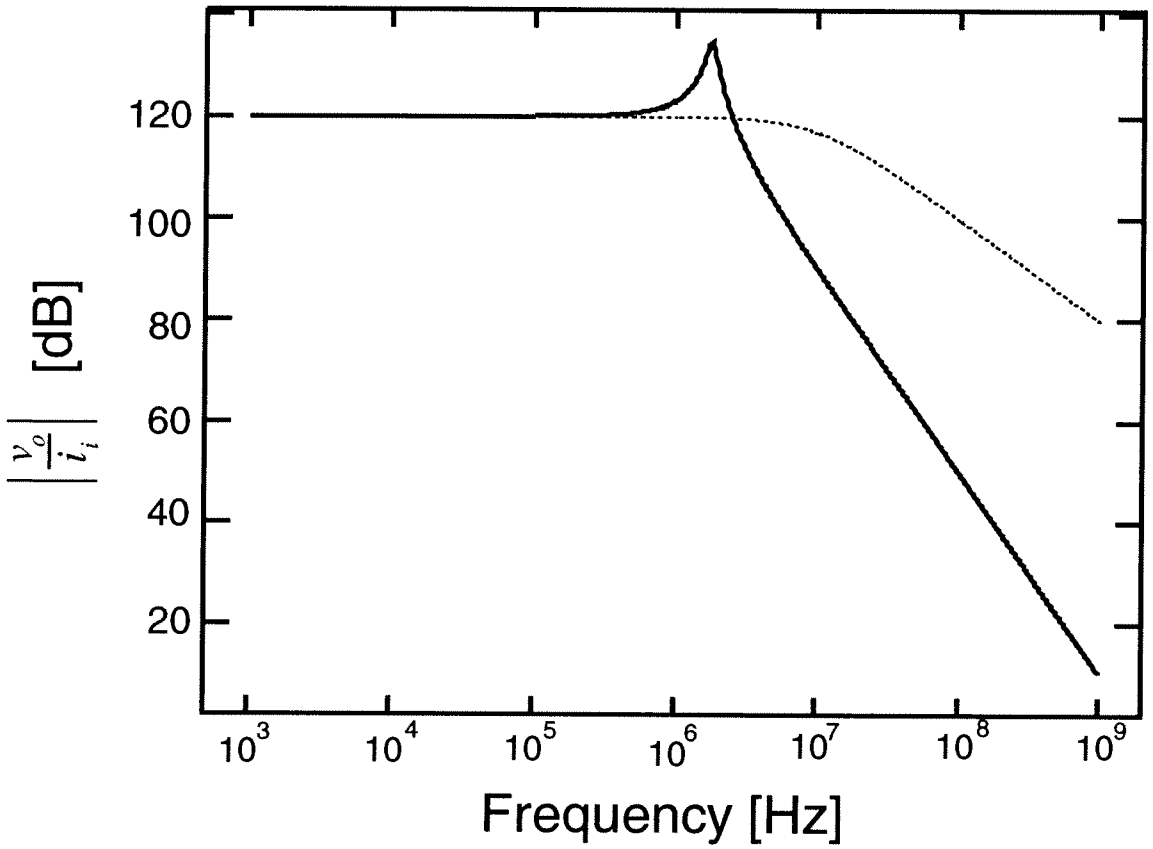

Fig. 4.9: Comparison of transfer functions for the transresistance amplifier of Fig. 4.5, with C_i = 500 fF (solid line) and C_i = 0 fF (and using the op amp with the characteristics of that used in Fig. 4.7).

$$Q_{max} = \frac{1}{2}\sqrt{\frac{\omega_T}{\omega_b}}, \tag{4.16}$$

which can be very large. For proper amplifier stability, the Q should be kept low, since the Q of a second-order closed-loop lowpass biquad system can be directly transformed to a value of stability phase margin. A phase margin of 45° is generally accepted as a value which insures sufficient amplifier stability. 45° phase margin corresponds to a peak height of 2.3 dB. (For reference, 90° phase margin corresponds to $Q = 0.707$ and no peaking, i.e., critically damped.)

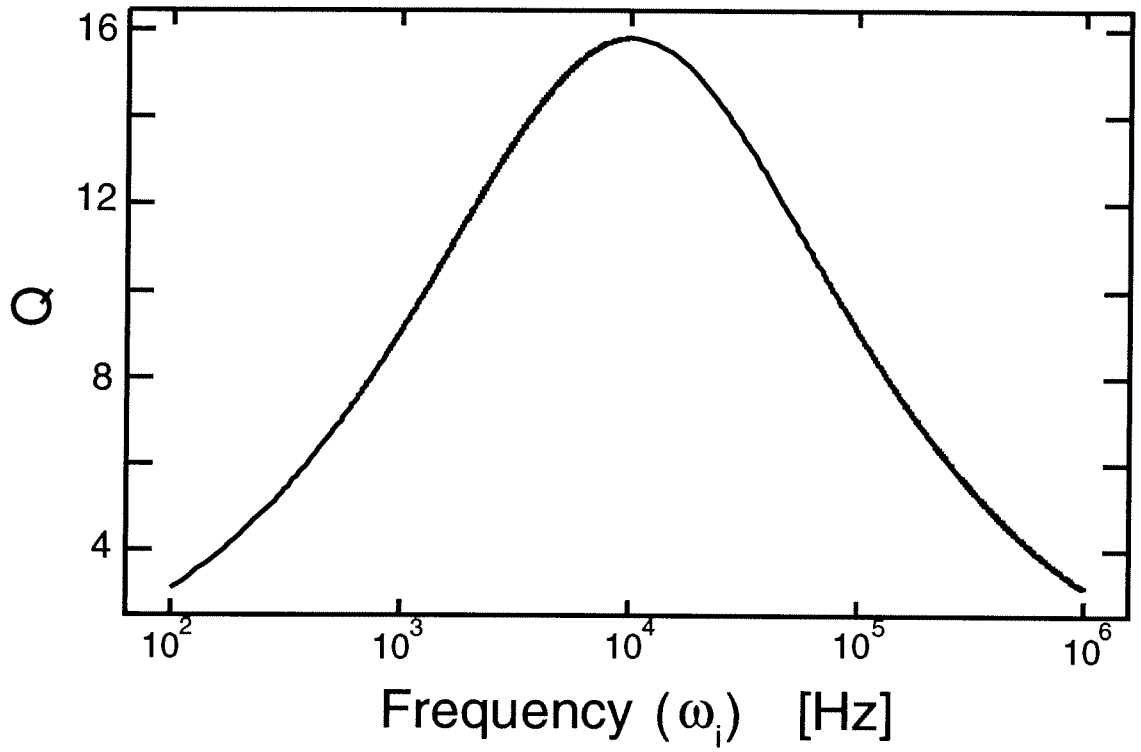

Fig. 4.10: Plot of Q versus ω_i (with ω_b = 10 kHz and ω_T = 10 MHz held constant) for the transresistance amplifier of Fig. 4.5 with $C_f = 0$. (Variables are defined in the text.)

4.2.2.4.1 Compensation Via Shunt Capacitance, C_f

To compensate for C_i-induced instability, a capacitor C_f can be added in parallel with the feedback resistor R_f. The feedback loading diagram for the circuit of Fig. 4.5, now including both C_i and C_f is shown in Fig. 4.11. With the addition of C_f, the feedback factor now becomes

$$g_f = -\left(R_f \| \frac{1}{sC_f}\right)^{-1} = -\frac{1 + (s/\omega_f)}{R_f}, \tag{4.17}$$

where $\omega_f = 1/(R_f C_f)$. Using (4.13) and (4.17), the transresistance transfer function is now found to be

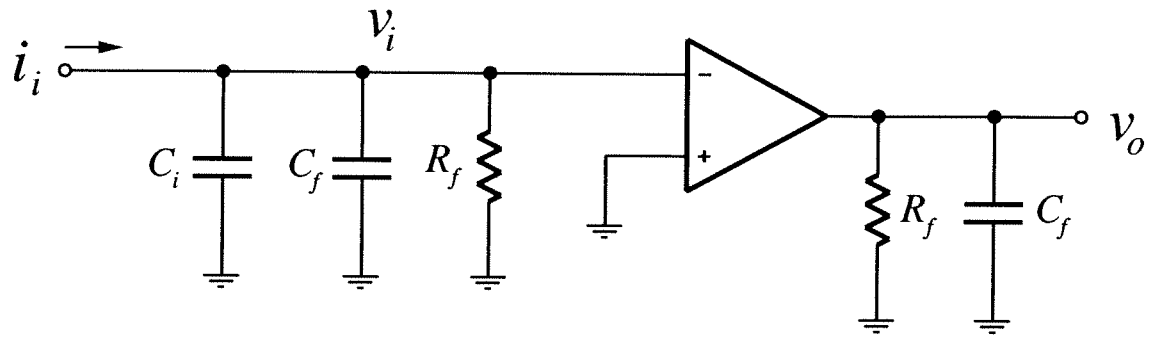

Fig. 4.11: Feedback loading diagram for a shunt-shunt feedback op amp transresistance amplifier with input capacitance C_i and compensating shunt capacitor C_f.

$$R_{amp} = \frac{r_m}{1 + r_m g_f} = \frac{a_v R_f \omega_i \omega_b}{s^2 + s\left(\omega_i + \omega_b + \dfrac{a_v \omega_b \omega_i}{\omega_f}\right) + \omega_T \omega_i} = \frac{R_f \omega_{pk}^2}{s^2 + s\dfrac{\omega_{pk}}{Q} + \omega_{pk}^2}$$

where $\omega_{pk} = \sqrt{\omega_i \omega_t}$

$\omega_i = 1/[R_f(C_i + C_f)]$

$\omega_f = 1/(R_f C_f)$

$\omega_T = a_v \omega_b$ = op amp unity gain frequency

$$Q = \frac{\omega_{pk}}{\omega_i + \omega_b + \dfrac{\omega_{pk}^2}{\omega_f}} \qquad (4.18)$$

Equation (4.18) indicates that the quality factor Q of the system decreases as ω_f decreases. From the dependence of ω_f on C_f, and using (4.18), the feedback capacitance C_f required to achieve a given quality factor Q (and thus, a given phase margin) is

$$C_f = \frac{(\omega_{pk}/Q) - \omega_i - \omega_b}{\omega_{pk}^2 R_f} \qquad (4.19)$$

As expected, to reduce Q (enhance stability) one must increase C_f. The compensated transfer function for the amplifier of Fig. 4.9 is shown in Fig. 4.12.

4.2.3 Bandwidth and Stability of the Designed Sustaining Amplifier

The above results may now be applied to the actual sustaining amplifier design of Fig. 4.4. The theory applies particularly to the first stage, comprising transistors M_1 - M_3. This stage is a

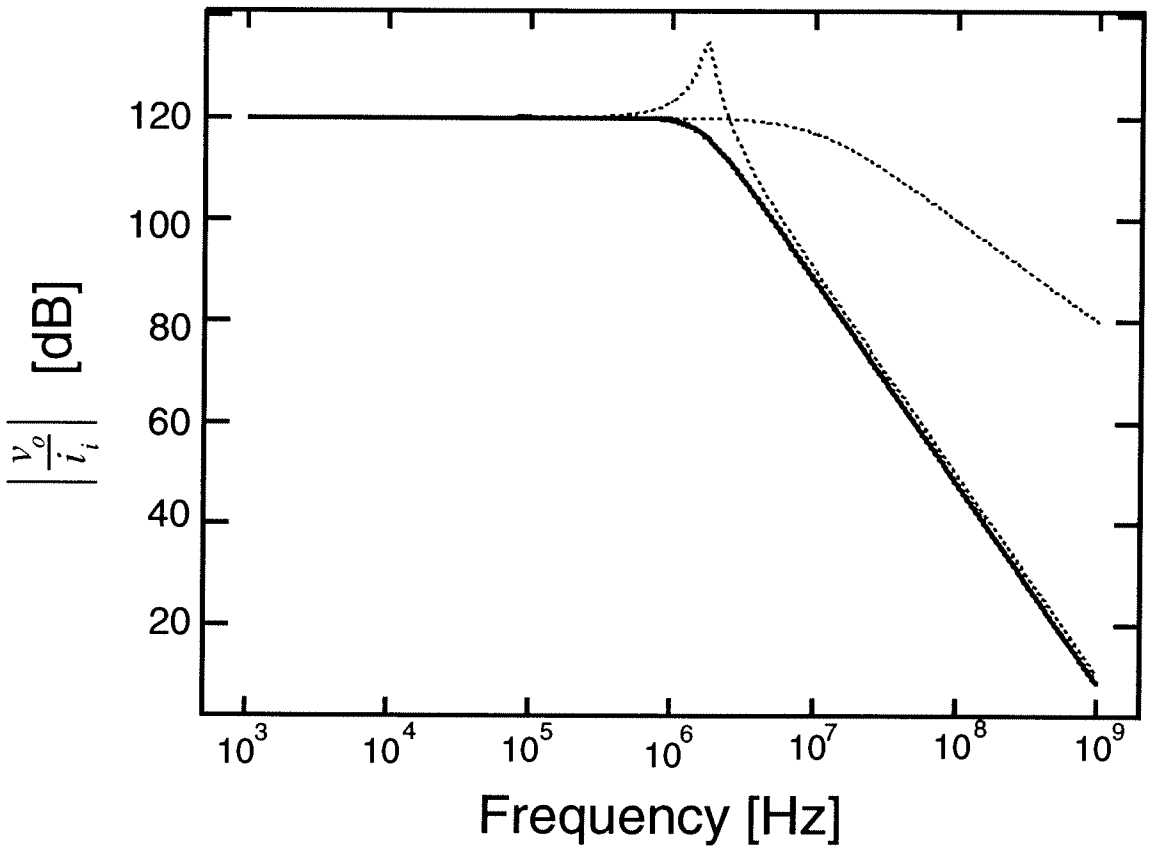

Fig. 4.12: Transfer function for the transresistance amplifier of Fig. 4.9 compensated via a shunt capacitor C_f = 124 fF.

simple transresistance amplifier, where M_1 and M_2 make up a voltage amplifier, and M_3 serves as an MOS resistor, connected in a shunt-shunt feedback configuration and biased in the linear region. An MOS resistor is used rather than a thin-film polysilicon resistor, since in the technology of this work, MOS resistors can achieve large values of resistance in smaller area and with less distributed capacitance. MOS resistors, however, suffer from nonlinearity, which can pose a problem for filtering applications, which often require linearity. For an oscillator application, the sustaining amplifier need not be extremely linear, especially when automatic-level control is utilized for amplitude limiting.

The linearly operated MOS transistor, M_3, can be modelled using a distributed resistance and capacitance as shown in the equivalent circuit of Fig. 4.13. The channel resistance for M_3, as biased in Fig 4.13, is approximately given by

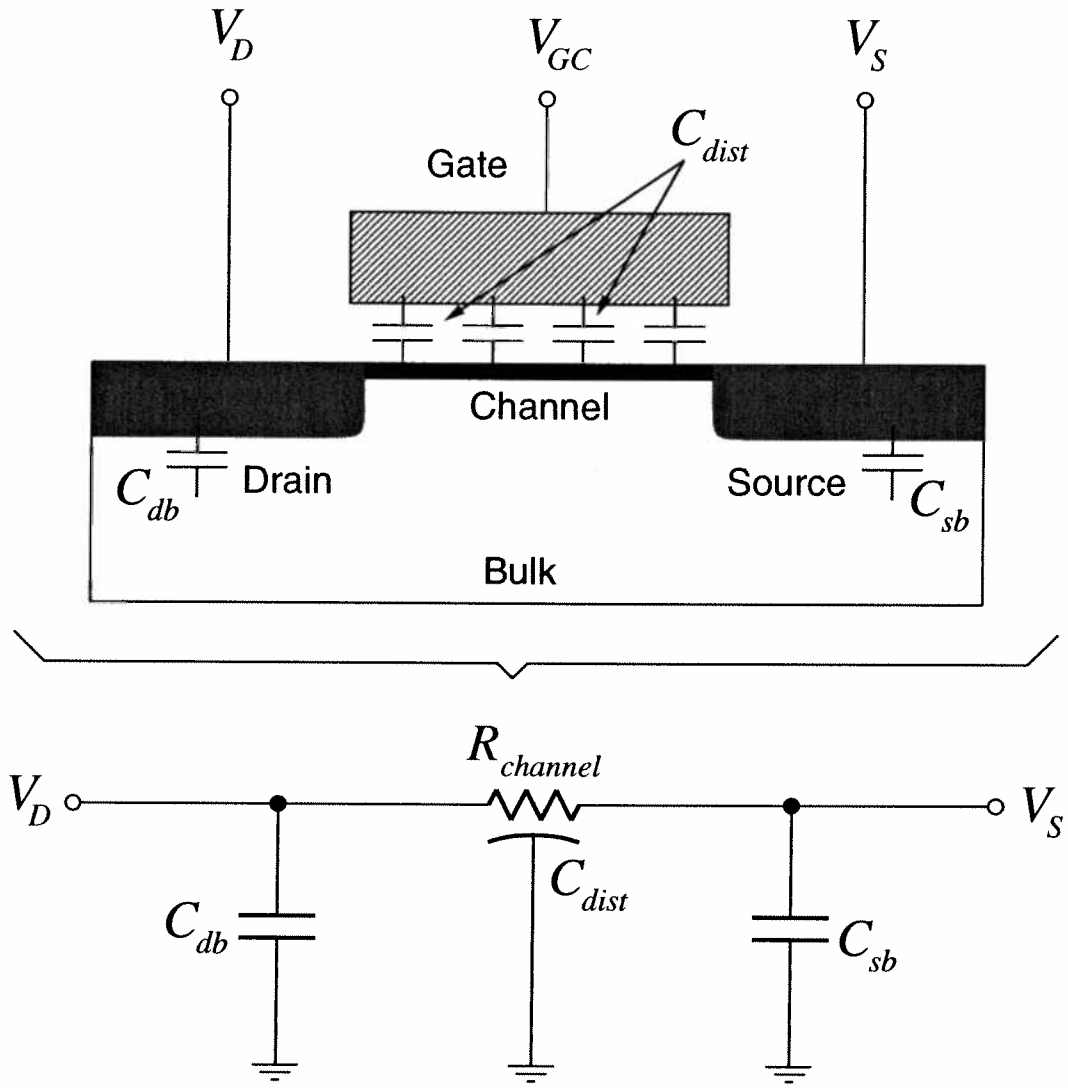

Fig. 4.13: Cross section of an MOS resistor and the equivalent circuit schematic which approximates its behavior. For the text, $R_{channel} = R_3$.

$$R_3 = \frac{1}{\mu_n C_{ox}\left(\frac{W}{L}\right)_3 (V_{GC} - V_t)}, \tag{4.20}$$

which is correct only to first order. More accurately, the resistance is quite nonlinear, and this will be addressed in Chapter 5, which details the design of micromechanical filters. For a given minimum channel width W, the channel length L required for a desired value of resistance R_3 is

$$L_3 = \mu_n C_{ox} W_3 R_3 [V_{GC} - V_t] . \tag{4.21}$$

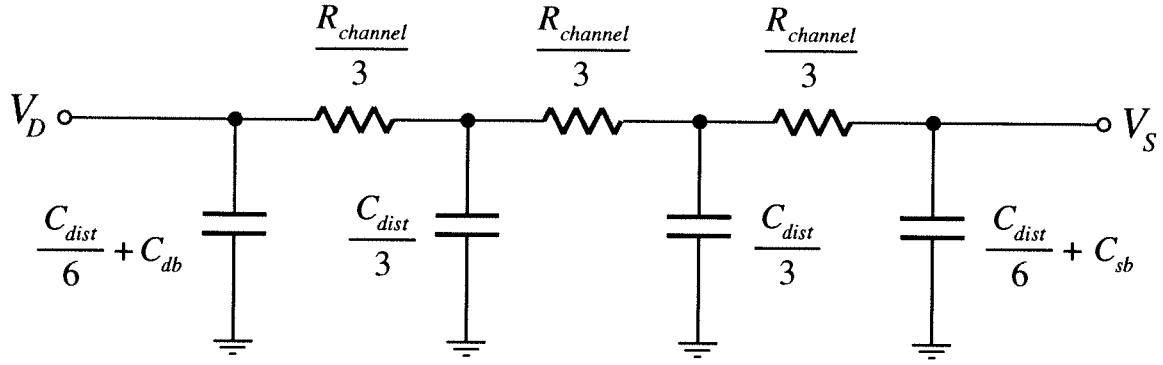

Fig. 4.14: Triple-π approximation to the circuit of Fig. 4.13.

The capacitance depicted in the equivalent circuit of Fig. 4.13 arises mainly from gate-to-channel capacitance C_g, and also from junction capacitance in the source and drain, C_{db} and C_{sb}. Since this parallel capacitance contributes to amplifier instability as described in the previous section, its value is of great importance. The values for the component capacitors are given by

$$C_g = WLC_{ox} \quad , \quad C_{db} = \frac{C_{db0}}{\left(1 + \frac{V_{DB}}{\psi_o}\right)^{1/2}} \quad , \quad C_{sb} = \frac{C_{sb0}}{\left(1 + \frac{V_{SB}}{\psi_o}\right)^{1/2}} \quad , \tag{4.22}$$

$$\text{where } C_{db0} = C_j WL_{drain} + C_{jsw}(W + 2L_{drain})$$
$$C_{sb0} = C_j WL_{source} + C_{jsw}(W + 2L_{source})$$

where C_{db0} is the zero-bias drain-to-bulk junction capacitance, C_{sb0} is the zero-bias source-to-bulk junction capacitance, ψ_o is the built-in potential across the drain-to-bulk or source-to-bulk junctions, C_j is the zero-bias junction capacitance per area, and C_{jsw} is the zero-bias sidewall capacitance per length of junction. For typical values of resistance, C_g is commonly the dominant component, even after distribution along the channel resistance. Because of this, and for ease of design, it is useful to define both a sheet resistance R_S and a sheet capacitance C_S (corresponding to gate-to-channel capacitance):

$$R_S = [\mu_n C_{ox}(V_{GS} - V_t)]^{-1} \tag{4.23}$$

$$C_S = W^2 C_{ox} \tag{4.24}$$

The effect of distributed capacitance on the stability of the amplifier is more easily seen through the triple-π model for Fig. 4.13, shown in Fig. 4.14, which approximates the action of a

distributed RC line[5]. Here, a substantial amount of the distributed capacitance is effectively translated to the input terminal of the resistor. This capacitance then contributes to the total C_i and reduces amplifier stability as described in Section 4.2.2.4.

Given this detailed description of the MOS resistor, M_3, the frequency characteristics of the designed amplifier of Fig. 4.4 may now be calculated. For the first stage (which is transresistance), and with reference to Fig. 4.4, the loop gain, 3 dB frequency, and unity gain frequency are as follows

$$\begin{aligned} A_l &= g_{m1}R_o \\ \omega_b &= [R_oC_o]^{-1} \\ \omega_T &= a_v\omega_b = \frac{g_{m1}}{C_o} \quad , \\ \text{where } R_o &= r_{o1} \parallel R_3 \parallel r_{o2} \\ C_o &= C_{db1} + C_{db2} + C_{gs7} + (1 + a_{v2})\, C_{\mu 7} + C_{g3} \end{aligned} \tag{4.25}$$

where r_{on} is the output resistance of transistor M_n, C_{dbn} is the drain-to-bulk capacitance of transistor M_n, $C_{gsn} = (2/3)W_nL_nC_{ox}$ is the gate-to-source capacitance of M_n, C_{g3} is the effective gate capacitance from M_3 (lumped by the triple-π model or a more accurate equivalent) at the output node, a_{v2} is the gain of the second stage (M_6 and M_7), R_3 is the equivalent channel resistance of M_3, and g_{m1} is the transconductance of M_1, given by

$$g_{m1} = \sqrt{2\mu_n C_{ox}\left(\frac{W}{L}\right)_1 I_{D1}} = \mu_n C_{ox}\frac{W}{L}(V_{GS} - V_t) \, . \tag{4.26}$$

The pole contributed by the capacitance at the input node of M_1 is given by

$$\omega_i = \frac{1}{R_3C_i} = \frac{1}{R_3(C_{gs1} + C_{sb3} + C_{g3})} \, , \tag{4.27}$$

---

[5]Note that the triple-π model functions best when used to obtain transient solutions, as in problems where digital waveforms are determined. It is less accurate when used for bandwidth and stability calculations, but is useful for illustration. To simulate a distributed RC line correctly for frequency purposes, one should use a line of ten resistors and ten capacitors for best results.

where C_{g3} is the effective amount of the distributed capacitance from M_3 at the source node. The frequency of the peak in the uncompensated transfer function for the amplifier of Fig. 4.4 is then given by

$$\omega_{pk} = \sqrt{\omega_i \omega_t} = \sqrt{\frac{g_{m1}}{R_3 (C_{db1} + C_{db2} + C_{gs7} + (1 + a_{v2}) C_{\mu 7} + C_{g3}) (C_{gs1} + C_{sb3} + C_{g3})}}. \tag{4.28}$$

Inserting (4.20) and (4.26), Eq. (4.28) becomes

$$\omega_{pk} = \frac{\mu_n C_{ox} (W/L)_1 (W/L)_3 \sqrt{(V_{GS1} - V_{t1}) (V_{GS3} - V_{t3})}}{\sqrt{(C_{db1} + C_{db2} + C_{gs7} + (1 + a_{v2}) C_{\mu 7} + C_{g3}) (C_{gs1} + C_{sb3} + C_{g3})}} \tag{4.29}$$

For the case where the gate-to-source capacitors dominate, Eq. (4.28) proportionately reduces to

$$\begin{aligned} \omega_{pk} &= \frac{\mu_n C_{ox}}{\sqrt{C_{gs}^2}} \sqrt{(W/L)_1 (W/L)_3 (V_{GS1} - V_{t1}) (V_{GS3} - V_{t3})} \\ &= \frac{\mu_n C_{ox}}{(2/3) W_1 L_1 C_{ox}} \sqrt{(W/L)_1 (W/L)_3 (V_{GS1} - V_{t1}) (V_{GS3} - V_{t3})} \\ &= \frac{3}{2} \mu_n W_1^{-1/2} L_1^{-2/3} \sqrt{(W/L)_3 (V_{GS1} - V_{t1}) (V_{GS3} - V_{t3})} \end{aligned} \tag{4.30}$$

where $W_7 = W_1$ and $L_7 = L_1$ has been used. (In this replica-biased design, M_1 and M_7 have identical sizes.) Equation (4.30) implies that in cases where the gate-to-source capacitance dominates, the peak frequency ω_{pk} is increased when the channel widths and lengths of M_1 (or M_7) are decreased.

Due to the large series motional resistance of capacitively driven micromechanical resonators, the effective channel resistance of M_3 must usually be made equally large. This requires a long channel length L_3, as specified by Eq. (4.21), which in turn leads to a large distributed capacitance C_{g3}. Thus, it is usually the case that C_{g3} dominates over C_{gs}, and the peak frequency is then given by the expression:

$$\begin{aligned}\omega_{pk} &= \frac{\mu_n C_{ox}}{\sqrt{C_{g3}^2}}\sqrt{(W/L)_1\,(W/L)_3\,(V_{GS1}-V_{t1})\,(V_{GS3}-V_{t3})} \\ &= \frac{\mu_n C_{ox}}{KW_3L_3C_{ox}}\sqrt{(W/L)_1\,(W/L)_3\,(V_{GS1}-V_{t1})\,(V_{GS3}-V_{t3})}\,. \\ &= \frac{3}{2}\mu_n W_3^{-1/2}L_3^{-2/3}\sqrt{(W/L)_1\,(V_{GS1}-V_{t1})\,(V_{GS3}-V_{t3})}\end{aligned} \tag{4.31}$$

Equation (4.31) suggests that the peak frequency ω_{pk} increases with the square root of W_1.

For noise reduction purposes[6], the first stage (M_1, M_2, and M_3) of the designed amplifier of Fig. 4.4 usually has much higher gain than the second stage (M_6 and M_7), which usually has a gain of around 10 or less. In addition, the load capacitance offered by the input of a micromechanical resonator, connected to the drains of M_6 and M_7, is usually very small . Thus, the first stage is most often the bandlimiting stage. For cases where the load capacitance is large, however, the second stage can very quickly become the limiting stage. In this case, a buffer amplifier may be used to alleviate the loading.

4.2.4 Amplifier Gain, Input, and Output Resistance

The total dc gain for the amplifier of Fig. 4.4 is given simply by a combination of the gains of the two stages. Doing so, yields

$$R_{amp} = g_{m2}\,(r_{o6} \parallel r_{o7})\,R_f, \tag{4.32}$$

which is a positive quantity, and which thus requires a 0° phase shift across the resonator in an oscillator configuration.

The input resistance R_{in} follows from Eq. (4.12)

$$R_{in} = \frac{R_f}{1+a_v}\frac{1+(s/\omega_b)}{1+(s/\omega_t)} = \frac{R_f}{1+g_{m1}R_{o1}}\frac{1+(s/\omega_b)}{1+(s/\omega_t)}, \tag{4.33}$$

where R_{o1} is the output resistance of the feedback-loaded first stage in Fig. 4.4 and $g_{m1}R_{o1}$ can be recognized as the loop gain of the first stage.

---

[6]Specifically, oscillator phase noise reduction, as will be seen.

TABLE 4.1. Transresistance Amplifier Design Data

Parameter	Value	Units
$\mu_n C_{ox}$	35	$\mu A/V^2$
$\mu_p C_{ox}$	15	$\mu A/V^2$
t_{ox}	500	Å
$(W/L)_n$	7/7	μm/μm
$(W/L)_p$	8/4	μm/μm
$(W/L)_3$	3/80	μm/μm
V_{supply}	±2.5	V

The output resistance of the sustaining amplifier is given by

$$R_{oa} = (r_{o6} \| r_{o7}) , \tag{4.34}$$

where r_{o6} and r_{o7} are the resistances looking into the drains of M_6 and M_7, respectively.

Devices sizes and other relevant data pertaining to the designed transresistance amplifier are summarized in Table 4.1. The device sizes were chosen more to optimize (with reasonable power consumption) the gain and bandwidth of the second stage of the amplifier than the first. In addition, very conservative channel lengths were chosen to offset the uncertainty of the CMOS technology. The simulated (via SPICE) transresistance transfer function for this amplifier is shown in Fig. 4.15. In addition, Fig. 4.16 presents the simulated input impedance as a function of frequency.

Note that although M_3 is presently operated in the linear region, it may also be operated in the weak inversion region to achieve much higher values of transresistance. Designs using this strategy, however, must address increased nonlinearity in the effective resistor.

---

[7] I'm referring to the first MICS CMOS process that was run when I say "uncertainty." Weijie Yun and I basically (re)developed the CMOS in the summer of 1991, and it took several trials to get the threshold voltages near correct. The current process at UC Berkeley, thanks to concentrated development by the microlab, is running very well today.

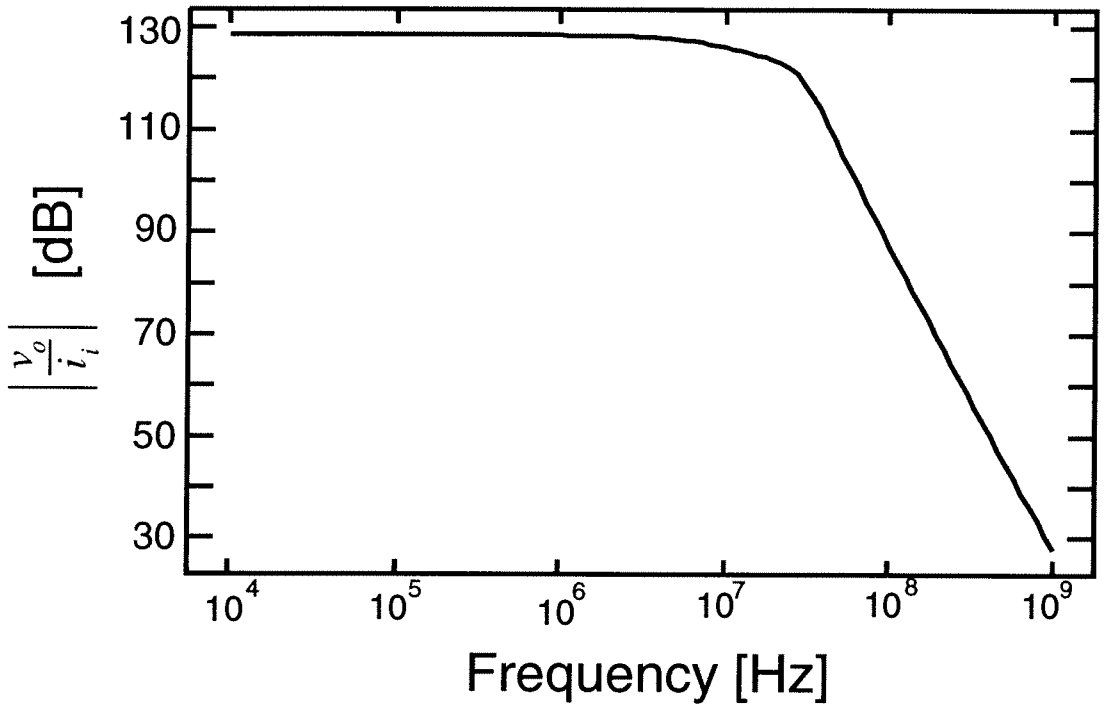

Fig. 4.15: Simulated (via SPICE) Bode plot for the transresistance amplifier used in Fig. 4.4. Here, V_{GC} = 2.5 V and a load capacitance of 20 fF is assumed.

4.3 Amplitude Limiting

As mentioned in Section 4.2.2.1, steady-state oscillation is reached when some form of nonlinearity or a designed automatic-level control circuit alters either the gain of the sustaining amplifier or the series resistance of the resonator such that the loop gain equals (or is slightly above) unity. For oscillators controlled by quartz crystals without automatic-level control, the nonlinearity usually appears in the sustaining circuit, where transistors enter the triode region at large voltage amplitudes, reducing effective device transconductances until the loop gain drops to unity. Limiting due to crystal nonlinearity, in which the series resistance in the crystal is increased until it equals the effective transresistance gain of the sustaining amplifier, is rare, since for crystals the starting value of R_x is small (~ 50Ω) and would have to increase by orders of magnitude to cause the loop gain to drop to unity.

On the other hand, even though comb-driven, folded-beam μmechanical resonators are only slightly less linear than crystals [82], limiting due to nonlinearity in flexural-mode μresona-

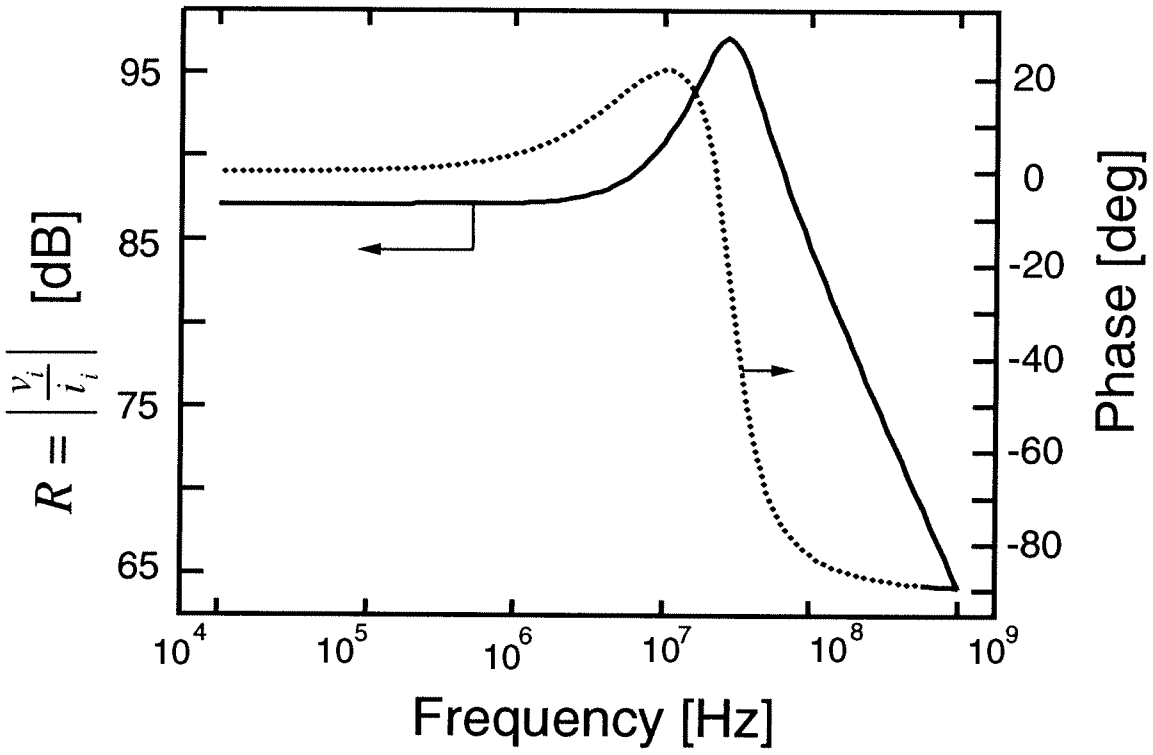

Fig. 4.16: Input impedance as a function of frequency for the transresistance amplifier used in Fig. 4.4. Again, V_{GC} = 2.5 V and a load capacitance of 20 fF is assumed. Note that the plot follows the prediction of Eq. (4.33) only for low frequencies; at high frequencies, the effect of high frequency poles, which was not modelled, begins to come in.

tors is quite practical through adjustment of the dc-bias voltage V_P. As seen from the equations of Fig.4.3, the values of the motional circuit elements representing the capacitively driven μmechanical resonator are strongly dependent upon the dc-bias voltage V_P applied to the resonator. In particular, the value of motional resistance R_x is inversely proportional to the square of V_P, and thus, it can be set to just under R_{amp} at the start of oscillation by proper selection of V_P. As oscillation builds up, stiffening nonlinearities in the resonator springs then increase the effective R_x of the μresonator until R_x=R_{amp}, when the loop gain equals one and the amplitude limits. The steady-state amplitude of oscillation is thus a function of the initial separation between R_x and R_{amp}, which is in turn a function of V_P.

4.3.1 Quasi-Linear Analysis

To quantify this limiting process, we first write an expression describing the spring nonlinearity. Since at resonance, the force is amplified by the Q, we have

$$Qf = k_1 x + k_2 x^2 + k_3 x^3 + \ldots, \tag{4.35}$$

where k_1 is the small displacement system spring constant, and k_2 and k_3 model the spring nonlinearity. A series reversion then yields

$$x = b_1 Qf + b_2 (Qf)^2 + b_3 (Qf)^3 + \ldots, \tag{4.36}$$

where $b_1 = k_1^{-1}$, $b_2 = -k_2 k_1^{-3}$, and $b_3 = 2k_2^2 k_1^{-5} - k_3 k_1^{-4}$. Retaining only those components at resonance, the phasor form for displacement X is then given by

$$X = b_1 QF + \frac{3}{4} b_3 Q^3 F^3. \tag{4.37}$$

Expressions for current I_x as a function of X and force F in terms of input voltage V_i were derived in Chapter 2, and are repeated here for the case of a symmetrical μresonator, with equal numbers of drive and sense fingers and equal dc-biases across the drive and sense ports:

$$I_x = \omega_o V_P \frac{\partial C}{\partial x} X \tag{4.38}$$

$$F = V_P \frac{\partial C}{\partial x} V_i \tag{4.39}$$

where $\partial C/\partial x$ applies to both drive and sense ports, ω_o is the oscillation frequency, and V_P is the dc-bias across the ports.

Inserting these expressions into (4.37), assuming a Duffing nonlinearity in the resonator springs (k_2=0), and differentiating, we have

$$\frac{\partial I_x}{\partial V_i} = \frac{Q}{k_1} \omega_o V_P^2 \left(\frac{\partial C}{\partial x}\right)^2 - \frac{9}{4} \frac{k_3 Q^3}{k_1^4} \omega_o V_P^4 \left(\frac{\partial C}{\partial x}\right)^4 V_i^2 = \frac{1}{R_{ss}} \tag{4.40}$$

Equation (4.40) shows that as the amplitude of oscillation V_i grows, the small-signal series resistance R_{ss} increases until it equals the transresistance of the sustaining amplifier, R_{amp}, at which

point the loop gain is unity, and V_i settles at a steady-state value. From (4.40), the steady-state V_i is clearly controllable through the resonator dc-bias voltage V_P.

4.3.2 Exact Nonlinear Analysis

The analysis of Section 4.3.1 presented a quasi-linear treatment of this limiting behavior in that Eq. (4.35) is a quasi-linear approximation to a nonlinear problem. The treatment, however, is conceptually revealing and gives reasonable predictions to actual oscillator limiting.

A more complete analysis may be performed by considering the Duffing behavior of the resonator under viscous damping. For this problem, the equation of motion may be written as:

$$\ddot{x} + \frac{\omega_o}{Q}\dot{x} + \omega_o^2 (x \pm \mu x^3) = |f_d| \cos \omega t , \tag{4.41}$$

where x is resonator displacement, ω_o is the natural frequency of the resonator, Q is its quality factor, $|f_d|$ is the amplitude of the applied force, and μ is related to the third-order restoring force term (of Eq. (4.35)) by the equation:

$$\mu = \frac{k_3}{k_1}. \tag{4.42}$$

To solve Eq. (4.41),. the Ritz averaging method may be used as done in [83]. In applying the Ritz method, the solution to (4.41) is first approximated by a series

$$x = a_1\phi_1(t) + a_2\phi_2(t) + a_3\phi_3 + \ldots = \sum_{i=1}^{n} a_i\phi_i(t) , \tag{4.43}$$

where $\phi_1(t)$, $\phi_2(t)$, etc., are selected functions of time, and the a_1, a_2, etc., are weighting factors to be determined. For this case, a good choice for the approximate solution is

$$\begin{aligned} x &= |x| \cos(\omega t - \psi) = a_1 \cos \omega t + b_1 \sin \omega t \\ \text{where} \quad |x| &= \sqrt{a_1^2 + b_1^2} \quad \text{and} \quad \psi = \tan^{-1}\left(\frac{b_1}{a_1}\right) \end{aligned} \tag{4.44}$$

The Ritz averaging method is based upon the postulate that if a system is subjected to a virtual displacement, δx, the work done by the forces acting upon the system must be equal to zero. Thus,

$$[\ddot{x} + f(\dot{x}) + g(x)]\,\delta x = 0. \tag{4.45}$$

The weighting factors in Eq. (4.43) must be determined in such a manner that the virtual work per cycle vanishes. To do this, virtual displacements are taken in the form

$$\delta x_i = \delta a_i \phi_i(t)\ , \tag{4.46}$$

and by integrating the work over one cycle, n equations in n unknowns (the weighting factors, a_i) are obtained of the form

$$\int_o^\tau [\ddot{x} + f(\dot{x}) + g(x)]\,\phi_i(t) = 0, \tag{4.47}$$

which can then be solved simultaneously to determine the values of $a_1, a_2, \ldots, a_n$.

Using Eqs. (4.41) and (4.44), the simultaneous equations for the Duffing problem are

$$\begin{aligned} \int_0^\tau \left[\ddot{x} + \frac{\omega_o}{Q}\dot{x} + \omega_o^2(x \pm \mu x^3) - |f|\cos\omega t\right]\cos\omega t\,dt &= 0 \\ \int_0^\tau \left[\ddot{x} + \frac{\omega_o}{Q}\dot{x} + \omega_o^2(x \pm \mu x^3) - |f|\cos\omega t\right]\sin\omega t\,dt &= 0 \end{aligned} \tag{4.48}$$

Solving Eq. (4.48), using (4.44), we have [83]

$$\left(-\omega^2 + \omega_o^2 \pm \frac{3\omega_o^2\mu|x|^2}{4}\right)^2 + \left(\frac{\omega_o}{Q}\right)^2\omega^2 = \left(\frac{|f_d|}{|x|}\right)^2 \tag{4.49}$$

$$\psi = \tan^{-1}\left(\frac{\left(\frac{\omega_o}{Q}\right)\omega}{-\omega^2 + \omega_o^2 \pm \frac{3\omega_o^2\mu|x|^2}{4}}\right) \tag{4.50}$$

which can be solved for the displacement amplitude $|x|$ and phase angle ψ given a force amplitude $|f_d|$ and frequency ω.

For the series resonant oscillator design of this work, the electronic phase shift across the resonator is 0^o, and thus, the force-to-displacement phase shift is 90^o. Using $\psi = 90^o$ and for a given $|f_d|$, Eqs. (4.49) and (4.50) may be solved to obtain the oscillation frequency ω_{osc} and displacement amplitude $|x|_{osc}$:

$$\omega_{osc} = \omega_o\left[1 \pm \frac{3\mu|x|_{osc}^2}{4}\right]^{1/2} \tag{4.51}$$

$$\text{Hardening Spring:} \quad |x|_{osc} = \left[\frac{1}{2}\left(-\frac{4}{3\mu}\left(\frac{\omega_o^2}{Q}\right)^2 + \sqrt{\frac{16}{9\mu^2}\left(\frac{\omega_o^2}{Q}\right)^4 + \frac{16}{3\mu}|f_d|^2}\right)\right]^{1/2} \tag{4.52}$$

$$\text{Softening Spring:} \quad |x|_{osc} = \left[\frac{1}{2}\left(\frac{4}{3\mu}\left(\frac{\omega_o^2}{Q}\right)^2 + \sqrt{\frac{16}{9\mu^2}\left(\frac{\omega_o^2}{Q}\right)^4 - \frac{16}{3\mu}|f_d|^2}\right)\right]^{1/2}. \tag{4.53}$$

The drive force f_d as a function of input voltage was given previously as Eq. (2.56). Inserting this in (4.52) and (4.53), we have the steady-state displacement as a function of steady-state oscillator output voltage v_o and dc-bias V_P:

$$\text{Hardening Spring:} \quad |x|_{osc} = \left[\frac{1}{2}\left(-\frac{4}{3\mu}\left(\frac{\omega_o^2}{Q}\right)^2 + \sqrt{\frac{16}{9\mu^2}\left(\frac{\omega_o^2}{Q}\right)^4 + \frac{16}{3\mu}V_P^2\left(\frac{\partial C}{\partial x}\right)^2|v_o|_{osc}^2}\right)\right]^{1/2} \tag{4.54}$$

$$\text{Softening Spring:} \quad |x|_{osc} = \left[\frac{1}{2}\left(\frac{4}{3\mu}\left(\frac{\omega_o^2}{Q}\right)^2 + \sqrt{\frac{16}{9\mu^2}\left(\frac{\omega_o^2}{Q}\right)^4 - \frac{16}{3\mu}V_P^2\left(\frac{\partial C}{\partial x}\right)^2|v_o|_{osc}^2}\right)\right]^{1/2} \tag{4.55}$$

Going one step further, the equation for current as a function of displacement (Eq. (2.54)) may be inserted in (4.54) and (4.55) to yield motional current as a function of steady-state oscillation voltage:

Hardening Spring:

$$|i_x|_{osc} = \left[\frac{1}{2}\left(-\frac{4}{3\mu}\left(\frac{\omega_o^2}{Q}\right)^2 + \sqrt{\frac{16}{9\mu^2}\left(\frac{\omega_o^2}{Q}\right)^4 + \frac{16}{3\mu}V_P^2\left(\frac{\partial C}{\partial x}\right)^2|v_o|_{osc}^2}\right)\right]^{1/2}\left[\omega_{osc}V_P\left(\frac{\partial C}{\partial x}\right)\right]^{-1} \tag{4.56}$$

Softening Spring:

$$|i_x|_{osc} = \left[\frac{1}{2}\left(\frac{4}{3\mu}\left(\frac{\omega_o^2}{Q}\right)^2 + \sqrt{\frac{16}{9\mu^2}\left(\frac{\omega_o^2}{Q}\right)^4 - \frac{16}{3\mu}V_P^2\left(\frac{\partial C}{\partial x}\right)^2|v_o|_{osc}^2}\right)\right]^{1/2}\left[\omega_{osc}V_P\left(\frac{\partial C}{\partial x}\right)\right]^{-1} \tag{4.57}$$

The small-signal series motional resistance of the resonator may be obtained by differentiating (4.56) and (4.57):

$$\frac{\partial|i_x|_{osc}}{\partial|v_o|_{osc}} = \frac{1}{R_{SS}}, \tag{4.58}$$

(where I won't put in the result of the differentiation to save a few pages). The value of $|v|_{osc}$ for a given V_P for which $R_{SS} = R_{amp}$ is the steady-state oscillation voltage amplitude. Note that this

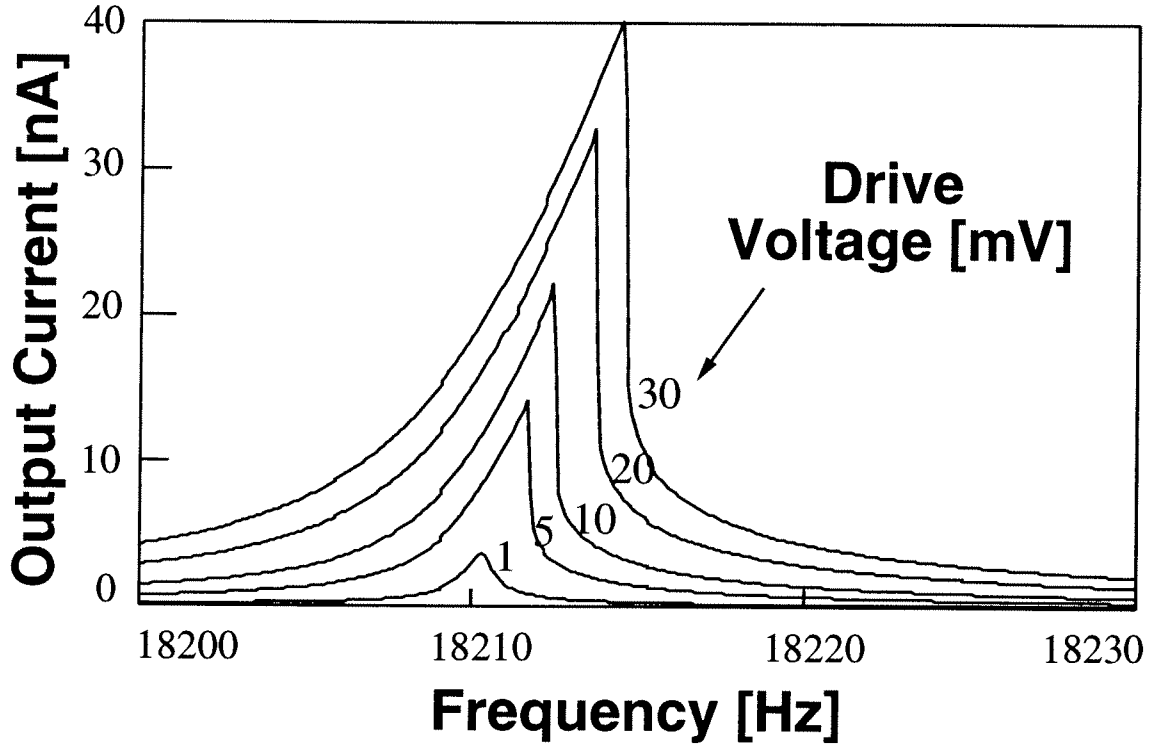

Fig. 4.17: Measured transconductance versus frequency curves for varying drive voltage amplitudes for the folded-beam, comb-driven resonator used in the prototype oscillator.

value depends upon the dc-bias V_P, verifying once again that the oscillation amplitude is controllable through V_P.

4.3.3 Measurement Versus Theory

Duffing curves (displacement versus frequency) for a folded-beam comb-driven micromechanical resonator used for the prototype oscillator were measured for several values of input voltage at a constant dc-bias voltage and are presented in Fig. 4.17. These curves show a hardening spring in this case. From these curves, the Duffing stiffening term, k_3, may be determined by identifying the critical amplitude $|x|_{crit}$ and critical frequency ω_{crit} of a Duffing curve at the point where the slope of the curve is infinite (the critical point), and using the equation

$$\frac{9\mu|x|_{crit}^2}{4} = \frac{\omega_{crit}^2}{\omega_o^2} - 1, \tag{4.59}$$

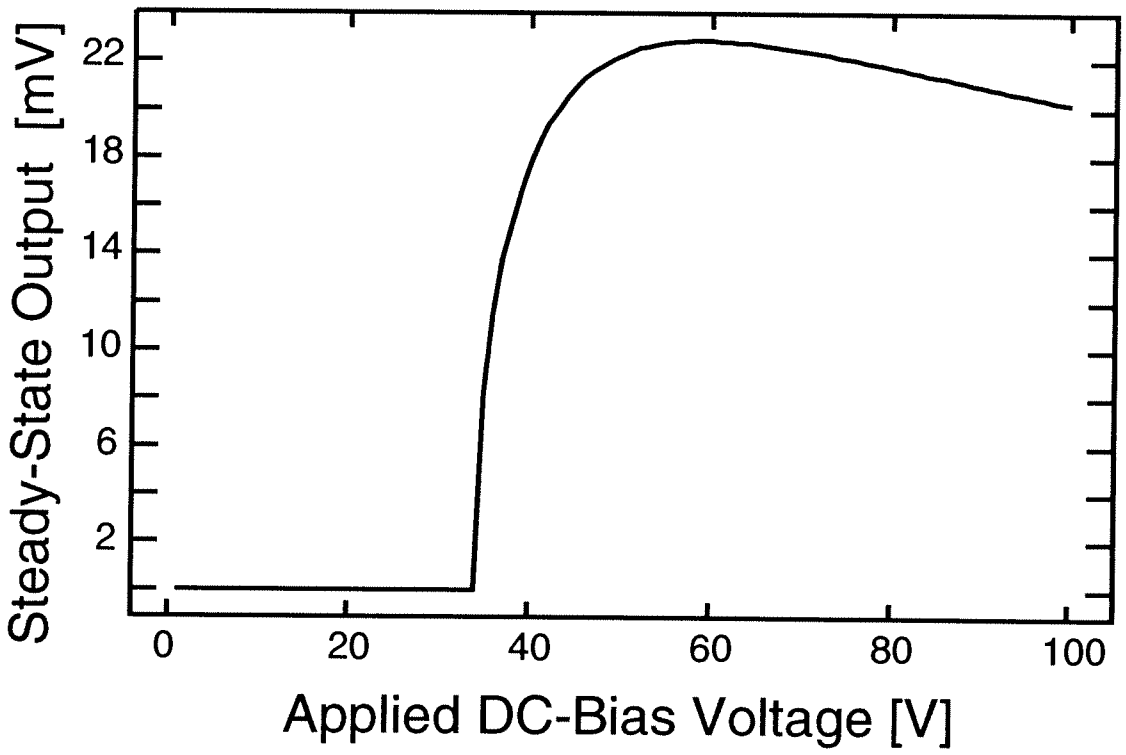

Fig. 4.18: Theoretical plot of oscillation voltage amplitude versus resonator dc-bias voltage. The dependence of oscillation amplitude on V_P is clearly seen.

which holds at the critical point. From Eq. (4.59) μ may be extracted, then (4.42) may be used to obtain k_3, assuming k_1 is known. Doing so, the measured curves in Fig. 4.17 yield 9.8×10^6 N/m^3.

Using a combination of Eqs. (4.58), (4.56), and (4.51), the value of $|v_o|_{osc}$ may be plotted against the dc-bias voltage V_P applied to the resonator. Such a plot is presented in Fig. 4.18. For this plot, an amplifier transresistance gain of 1 MΩ and a loaded quality factor of 5000 were used, with the value of k_3 calculated above. For comparison, the measured output voltage versus dc-bias voltage curve for the fabricated oscillator is shown in Fig. 4.19. The discrepancy in output voltage amplitude for the two plots is in part due to the fact the measured curve was obtained using an off-chip buffer amplifier. (The on-chip one was blown out after a power surge.) However, the curves have the same relative positions and shapes.

Both the theoretical and experimental plots show a decrease in slope at around 50 V dc-bias. The theoretical curve actually shows the amplitude peaking, then settling to a constant value

as V_P increases. This, however, does not occur experimentally. In the experiment, the increase in oscillation amplitude slows around V_P = 50 V, but then rises quickly again, indicating that phenomena unaccounted for by the present theory are taking place at higher dc-bias voltages. There, in fact, are some high dc-bias points at which chaotic [84] behavior is observed, where the resonator is visibly seen to switch oscillation amplitudes in a seemingly random fashion. Such chaotic behavior is not at all unexpected, given the nonlinear nature of this closed-loop system.

4.4 Short-term Frequency Stability

As discussed in Section 4.1, short-term frequency stability is of utmost importance for oscillators used as carriers or local oscillators in communications and radar systems. Short-term stability is typically measured in terms of close to carrier phase noise power density, which is directly related to frequency noise power. Typical phase noise requirements range from -100 dBc/Hz at 270 kHz deviation from the carrier for the local oscillator in FDM/FM satellite communications networks [76] to -150 dBc/Hz at 67 kHz carrier deviations in Doppler-based radar systems [85].

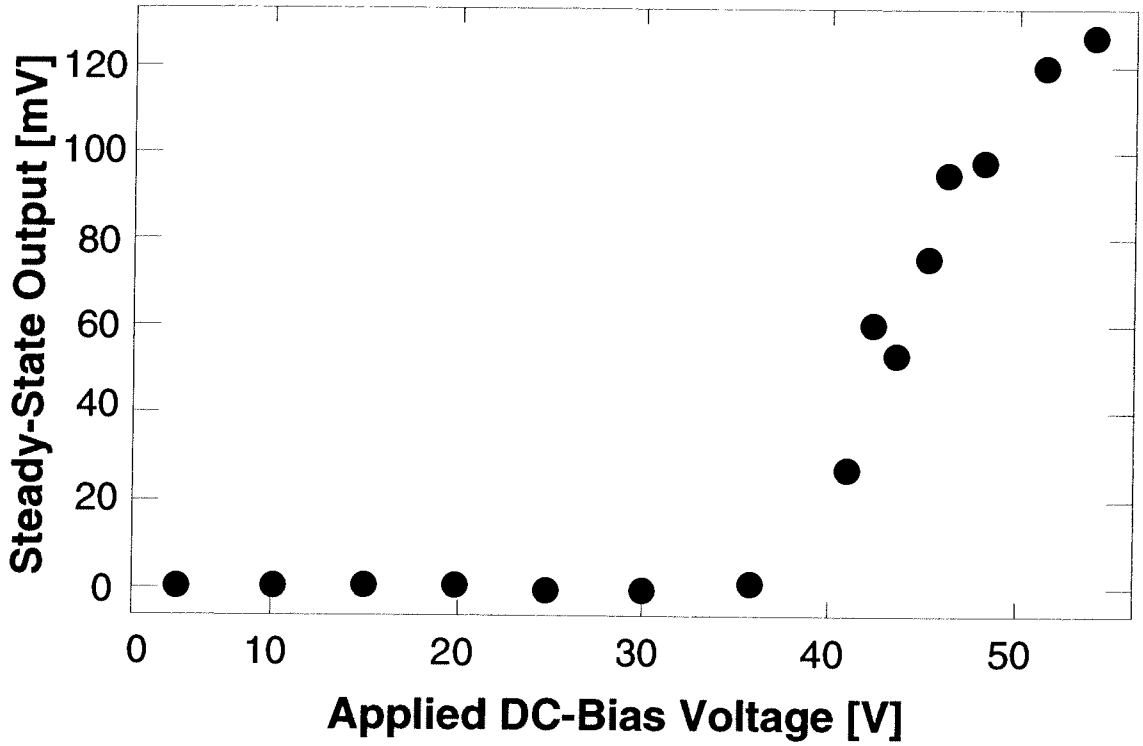

Fig. 4.19: Measured output voltage versus dc-bias voltage for the fabricated CMOS micoresonator oscillator.

Many phenomena contribute to phase noise in oscillators. The most commonly recognized phenomenon is superposed electronic noise from the sustaining amplifier. In the micromechanical domain, however, noise due to Brownian motion and mass loading have increased influence and may actually dominate among mechanisms which cause phase noise. These noise mechanisms will be addressed in detail in this section.

4.4.1 Superposed Electronic Noise

The phase noise power due to superposed electronic noise from the sustaining amplifier may be predicted theoretically using a procedure similar to that in [10]. Since this noise power is derived from noise in the sustaining amplifier, the noise figure of this amplifier must first be established.

4.4.1.1 Amplifier Noise Figure

The equivalent noise power reflected to the input of an amplifier is dominated by noise components from the first stage of the amplifier, provided the gain of this first stage is substantial. This is the case for the transresistance amplifier of this design. Thus, the noise diagrams for the for this amplifier, shown in Fig 4.20, includes only the first transresistance stage.

Using Fig. 4.20, shorting inputs of circuits (a) and (b), and equating noise, the equivalent input noise voltage generator is found to be

$$\overline{v_i^2} = \overline{v_{ia}^2}, \tag{4.60}$$

Opening inputs and equating noise, the equivalent input noise current generator is

$$\overline{i_i^2} = \overline{i_f^2} + \overline{i_{ia}^2} + \frac{\overline{v_{ia}^2}}{R_f}. \tag{4.61}$$

The expressions for $\overline{v_{ia}^2}$ and $\overline{i_{ia}^2}$ for the gain amplifier in the feedback loop of Fig. 4.4 can be found through a similar analysis applied to Fig. 4.21. Here, the relevant noise generators associated with each transistor are included in (a), and the equivalent noise schematic with input-referred noise generators is shown in (b). The current noise generators for M_2, M_4, and M_5 are not included,

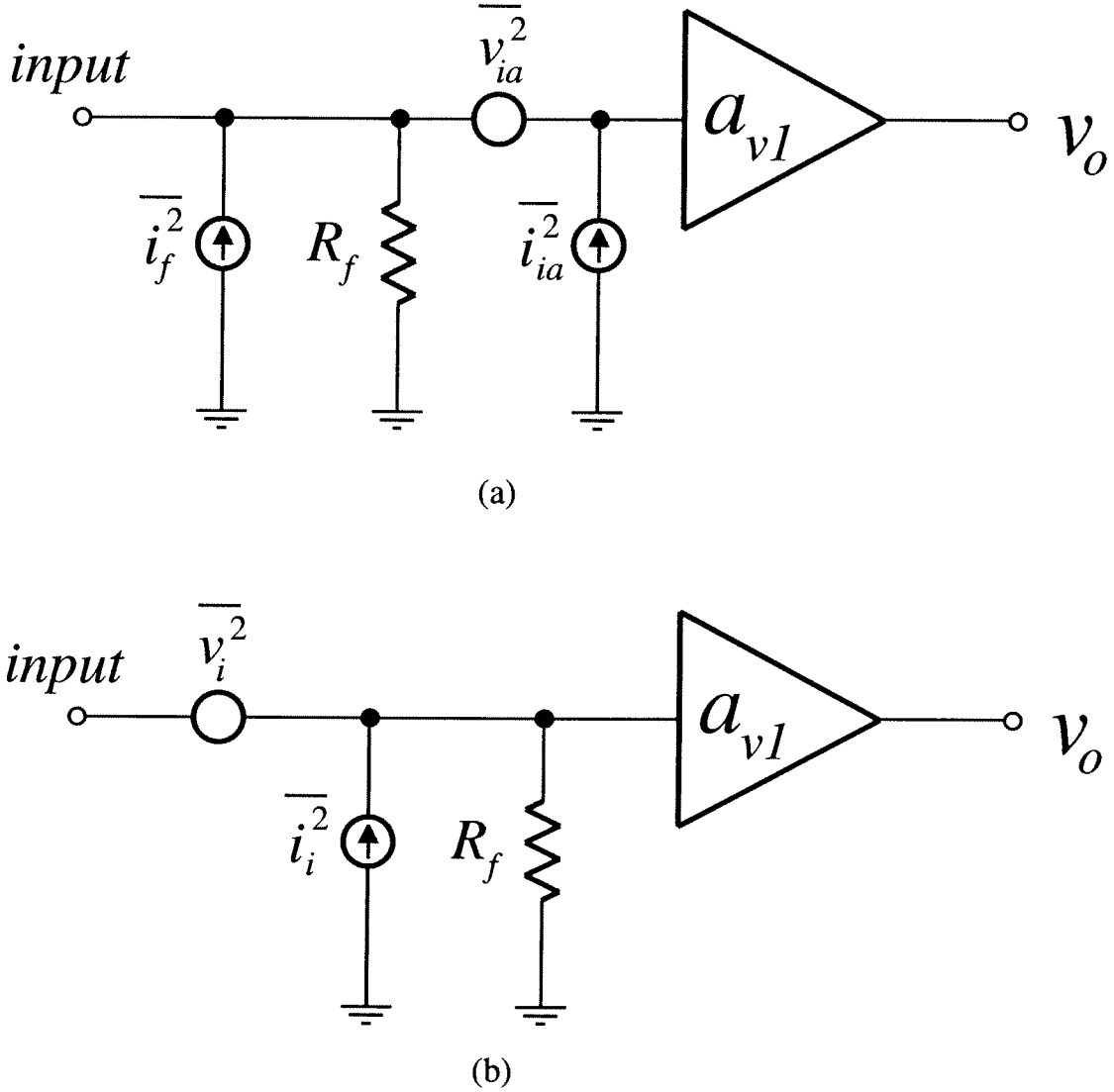

Fig. 4.20: Noise diagrams for the transresistance sustaining amplifier of Fig. 4.4. (a) shows the circuit schematic with the noise generators associated with each element. (b) shows the noise diagram when all noise generators have been referred to equivalent input noise generators.

since the gates of these transistors are attached to a low impedance node. Shorting inputs and equating output voltages for the circuits of (a) and (b) yields

$$\overline{v_{ia}^2} = 4\left[4kT\frac{2}{3}\frac{1}{g_m} + \frac{K_f}{WLC_{ox}f}\right]\Delta f \tag{4.62}$$

where the factor of four comes from the fact the g_m's of all the transistors are identical when biasing is designed for a 50% duty cycle output. Opening inputs and equating outputs yields

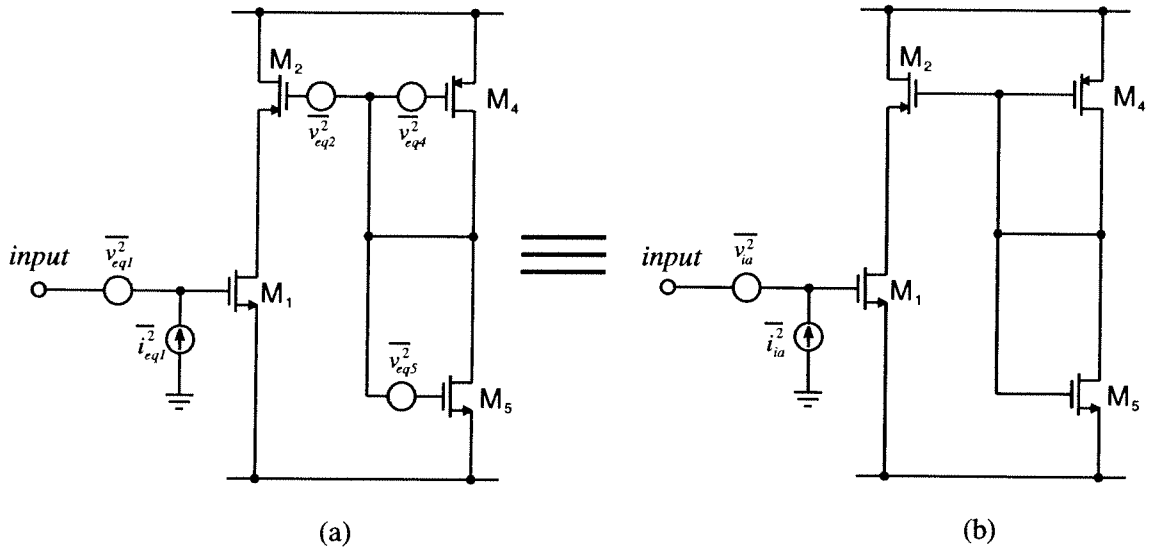

Fig. 4.21: Noise diagrams for the gain amplifier in the feedback loop of Fig. 4.4. (a) shows the circuit schematic with the relevant noise generators associated with each transistor. (b) shows the noise diagram when all noise generators have been referred to equivalent input noise generators.

$$\overline{i_{ia}^2} = \left(\omega^2 C_{gs}^2 + \frac{1}{R_f^2}\right)\overline{v_{ia}^2}, \tag{4.63}$$

where the fact that the input current into the gate of an MOS transistor is zero has been used.

Using Eqs. (4.60) through (4.65), the spot noise figure may be determined as follows:

$$\begin{aligned} F &= 1 + \frac{\overline{v_i^2}}{4kTR_S\Delta f} + \frac{\overline{i_i^2}}{4kT(1/R_S)\Delta f} \\ &= 1 + \frac{2}{3}\frac{4}{g_m R_S} + \frac{R_S}{R_f} + \frac{R_S}{R_f^2}\frac{2}{3}\frac{4}{g_m} + \left[\frac{1}{4kTR_S} + \frac{R_S}{R_f}\frac{1}{4kT}\right]\left(\frac{4K_f}{WLC_{ox}}\right)\frac{1}{f}. \\ &\quad + \left(\frac{4\pi^2 C_{gs}^2 R_S}{4kT}\frac{4K_f}{WLC_{ox}}\right)f + \left(4\pi^2 C_{gs}^2 R_S \frac{2}{3}\frac{4}{g_m}\right)f^2 \end{aligned} \tag{4.64}$$

For most resonator circuits, the source resistance, R_S, in Eq. (4.64) will be the series motional resistance of the resonator, R_x. The effect of R_x is, thus, included in the noise figure formulation, which in turn means that Brownian motion is accounted for in Eq. (4.64). If $1/f$, f, and f^2 noise are neglected (i.e. if the oscillator is of intermediate frequency), Eq. (4.64) reduces to

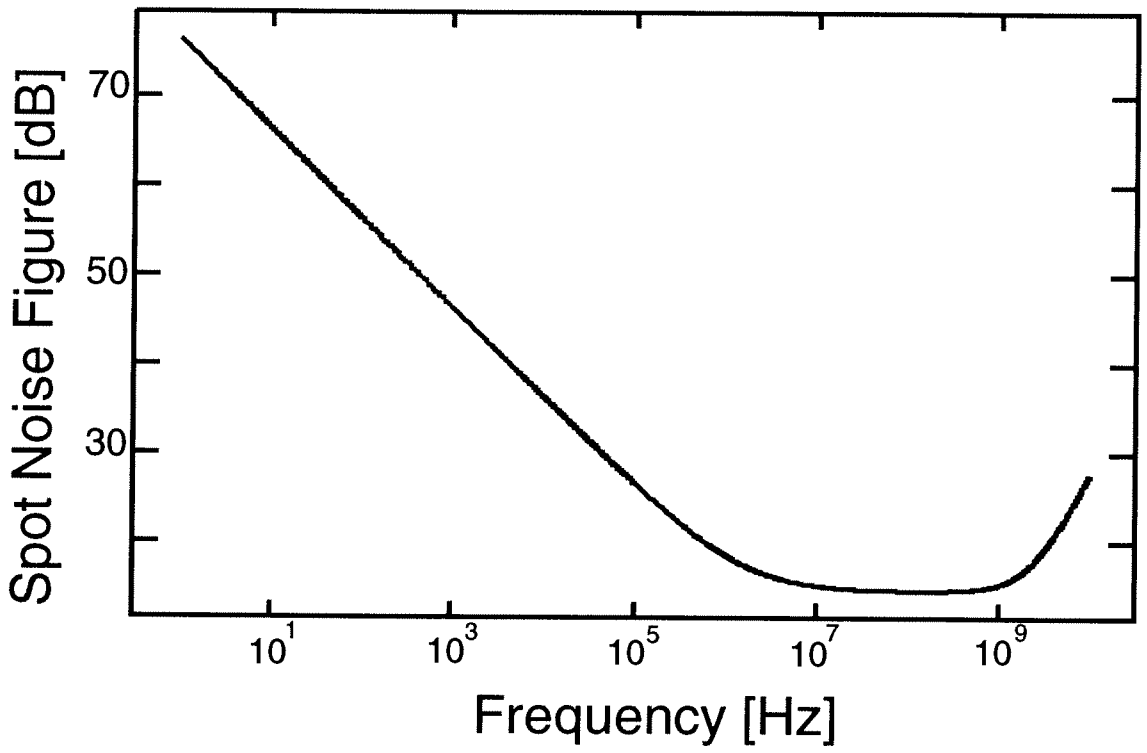

Fig. 4.22: Simulated spot noise figure versus frequency curve for the sustaining amplifier circuit of Fig. 4.4.

$$F = 1 + \frac{2}{3}\frac{4}{g_m R_S} + \frac{R_S}{R_f} + \frac{R_S}{R_f^2}\frac{2}{3}\frac{4}{g_m}. \tag{4.65}$$

Under steady-state oscillation conditions, when the loop gain is close to unity, the third term usually dominates F as given by Eq. (4.65). The fourth term, however, can become significant if the transconductance of M_1 is small.

Using the design data summarized in Table 4.1, and using $R_S = 100\ \text{k}\Omega$, $R_f = 20\ \text{k}\Omega$, and $K_f = 3 \times 10^{-24}\ \text{V}^2/\text{F}$, the simulated spot noise figure for the transresistance amplifier design of this work can be plotted against frequency using Eq. (4.64). This is presented in Fig. 4.22.

4.4.1.2 Phase Noise Due to Superposed Electronic Noise

Equations for oscillator phase noise will now be derived following a procedure similar to that used by Robins [76]. For this analysis, the following assumptions will be made:

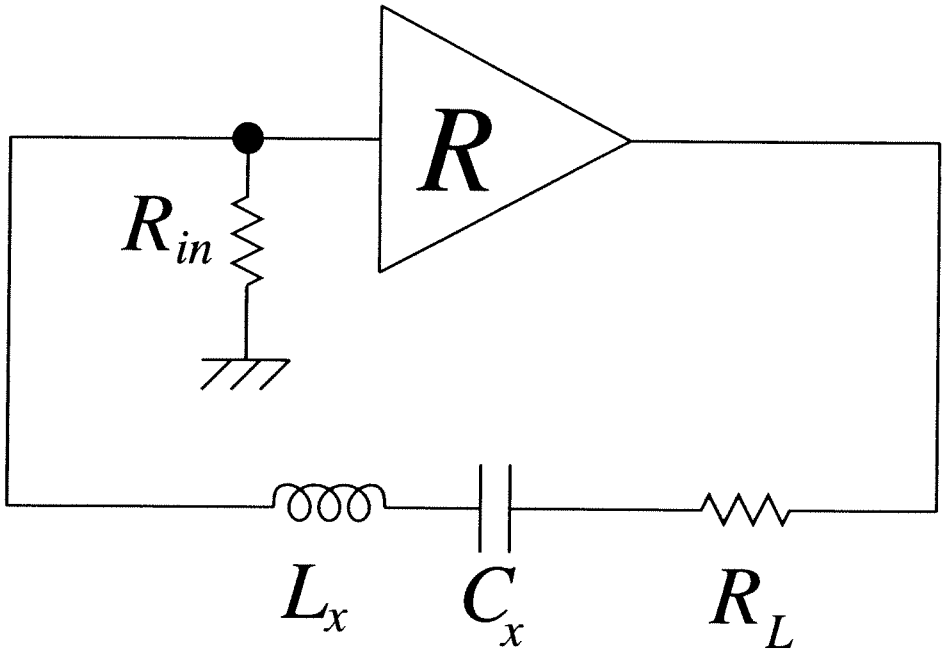

Fig. 4.23: Simplified schematic of the series microresonator oscillator for phase noise derivation purposes.

5. The oscillator is linear. This is a reasonably good assumption for a high quality oscillator except when used to predict carrier/noise ratios for very small offset frequencies.
6. The output power of an oscillator consists only of noise amplified by the positive feedback and filtered by the effective (boosted) quality factor achieved via positive feedback

Assumption (1) is especially relevant for automatic-level controlled oscillators, but is also reasonable even for oscillators which limit through sustaining amplifier nonlinearity [76]. One might question the validity of assumption (2) by arguing that oscillation could have been instigated by a sizable "switch-on" transient, which could make up a sizable contribution to the output power of the oscillator. This, however, is not usually the case, since the electronic noise of the amplifier is present for the whole time that the oscillator is switched on, and its total energy is therefore large compared with any "switch-on" transient.

With these assumptions, we now begin the analysis with a simplified schematic of the oscillator, shown in Fig 4.23. Here, an ideal sustaining amplifier with transresistance R is repre-

sented by a box imbedded in a series feedback loop with the equivalent circuit of the resonator, represented by the elements R_L, C_x, and L_x. R_L represents not only the resonator motional resistance, but also the output resistance of the amplifier and any other losses, perhaps associated with coupling to the final output. R_i represents the input resistance of the sustaining amplifier. The noise figure for the amplifier under steady-state oscillation conditions is given by Eq. (4.64), where now the source resistance $R_S = R_L$, and where, as before, R_f is the shunt resistance across the first stage of the transresistance amplifier.

Since the oscillator output is just noise amplified over many cycles in a tiny bandwidth, the output current fed back to the input and the input noise current that created it can be considered correlated. Thus, currents add at the input. With this in mind, an expression for the output voltage v_o in terms of the rms input noise current i_a at resonance may be derived as follows:

$$\begin{aligned} i_{in} &= i_a + \frac{v_o}{R_L + R_{in}} = i_a + \frac{v_o}{R_L'} \\ \therefore \quad v_o &= \left(i_a + \frac{v_o}{R_L'}\right)R \\ v_o &= \frac{Ri_a}{1 - (R/R_L')} \quad \text{at resonance} \end{aligned} \tag{4.66}$$

where $R_L' = R_L + R_{in}$. Removing the restriction to resonance, (4.66) becomes

$$\begin{aligned} v_o &= \frac{Ri_a}{1 - \frac{R}{R_L'} + 2jQ\left(\frac{\delta f}{f_o}\right)} = \left[\frac{R}{1 - \frac{R}{R_L'}}\right]\left[\frac{i_a}{1 + 2j\left(\frac{Q}{1 - (R/R_L')}\right)\left(\frac{\delta f}{f_o}\right)}\right] \\ \therefore \quad v_o &= \left[\frac{R}{1 - \frac{R}{R_L'}}\right]\left[\frac{i_a}{1 + 2jQ'\left(\frac{\delta f}{f_o}\right)}\right] \end{aligned} \tag{4.67}$$

where due to positive feedback, the effective quality factor Q' and effective bandwidth B' are given by

$$\begin{aligned} Q' &= \frac{Q}{1 - (R/R_L')} \\ B' &= B\left(1 - \frac{R}{R_L'}\right) \end{aligned} \tag{4.68}$$

The quantity $(1 - R/R_L')$ in steady-state oscillation will have a value very close to zero, since the loop gain, $A_l = R/R_L'$, will have a magnitude very close to, but slightly larger than, unity. Thus, the effective quality factor is greatly amplified through positive feedback, by orders of magnitude. The corresponding bandwidth is in turn greatly reduced by the same factor. The degree of increase in Q is governed by the amount that the loop gain A_l deviates from unity, and this in turn, is determined by the losses in the oscillator circuit.

The value of $(1 - R/R_L')$ can be estimated by equating the power gain from the input resistance of the amplifier to the load resistance, $PG_{internal}$, with the total power gain, including output power and all losses, PG_{total}. Proceeding first with the derivation of $P_{internal}$, the power in R_L at resonance is

$$P_L = \frac{v_o^2 R_L}{(R_L')^2} = \frac{R^2 R_L \overline{i_a^2}}{(1 - R/R_L')^2 (R_L')^2} \tag{4.69}$$

The power into the amplifier is given by $P_{in} = \overline{i_a^2} R_{in}$. The internal power gain is then

$$PG_{internal} = \frac{P_L}{P_{in}} = \frac{R^2 R_L}{(1 - R/R_L')^2 (R_L')^2 R_{in}}. \tag{4.70}$$

The total power gain can be found in a similar fashion by first recalling that the output of an oscillator is just amplified noise in a very narrow band. The input power is given by FkT times the effective noise bandwidth, which for a bandpass biquad circuit with a 3 dB bandwidth B' is given by $(\pi/2)B'$. Thus, the input power is

$$P_{in} = FkTB' \frac{\pi}{2}. \tag{4.71}$$

Letting P be the total power generated, including output power and all losses, the total power gain is

$$PG_{total} = \frac{P}{FkTB'(\pi/2)} \tag{4.72}$$

Equating (4.70) and (4.72) and solving for the quantity $(1 - R/R_L')$ yields

$$\left(1-\frac{R}{R_L'}\right)=\frac{\pi}{2}\frac{FkTB}{P}\frac{R^2R_L}{(R_L')^2R_{in}}. \tag{4.73}$$

Equation (4.68) may now be expressed as

$$\begin{aligned} Q' &= Q\frac{2}{\pi}\frac{P}{FkTB}\frac{(R_L')^2R_{in}}{R^2R_L} \\ B' &= B\frac{\pi}{2}\frac{FkTB}{P}\frac{R^2R_L}{(R_L')^2R_{in}} \end{aligned} \tag{4.74}$$

Since the output power is amplified noise in a narrow bandwidth, the output power density is really a noise density given by

$$N_o=\frac{P}{(\pi/2)B'}\frac{1}{\left|1+2jQ'(\delta f/f_o)\right|^2}, \tag{4.75}$$

where the second factor accounts for the shape of the effective bandpass filter of the oscillator. From Eq. (4.75), the noise density-to-carrier ratio is

$$\frac{N_o}{P}=\frac{2}{\pi}\frac{1}{B'}\frac{1}{\left|1+2jQ'(\delta f/f_o)\right|^2}=\frac{2}{\pi}\frac{1}{B'}\frac{1}{1+4Q'^2(\delta f/f_o)^2}. \tag{4.76}$$

For points sufficiently far from resonance so that $4Q'^2(\delta f/f_o)^2 \gg 1$, using (4.74) and substituting the carrier power (C) for output power (P) (but remembering to evaluate F at the output power level P), the noise density-to-carrier ratio is

$$\frac{N_o}{C}=\frac{FkT}{C}\frac{1}{4Q^2}\frac{R^2R_L}{(R_L')^2R_{in}}\left(\frac{f_o}{f_m}\right)^2=\frac{FkT}{C}\frac{1}{4Q^2}\frac{R^2R_L}{(R_L+R_{in})^2R_{in}}\left(\frac{f_o}{f_m}\right)^2, \tag{4.77}$$

where the frequency deviation from the carrier symbol f_m has been substituted for δf. As shown in Section 4.1, the phase noise density is one-half of the total noise density, and is thus given by

$$\frac{N_{op}}{C}=\frac{FkT}{C}\frac{1}{8Q^2}\frac{R^2R_L}{(R_L')^2R_{in}}\left(\frac{f_o}{f_m}\right)^2=\frac{FkT}{C}\frac{1}{8Q^2}\frac{R^2R_L}{(R_L+R_{in})^2R_{in}}\left(\frac{f_o}{f_m}\right)^2 \tag{4.78}$$

4.4.1.3 Minimizing Phase Noise

Eq. (4.78) shows that the phase noise density is inversely proportional to the square of the resonator quality factor Q (before positive feedback amplification). At first glance, this would imply that for lowest phase noise density, one should minimize Q-loading by the sustaining electronics. For this series resonant architecture, the loaded Q of the resonator is given by

$$Q = Q_{ul}\left(\frac{R_x}{R_L + R_{in}}\right) = Q_{ul}\left(\frac{R_x}{R_L'}\right), \tag{4.79}$$

where R_x is the motional resistance of the mechanical resonator and Q_{ul} is its unloaded quality factor. Equation (4.79) suggests that for minimum Q-loading the input and output resistances of the sustaining amplifier should be minimized, i.e. $R_{in} + R_o \ll R_x$. However, the effect of Q-loading must be balanced with that of the third term in Eq. (4.78), which also depends upon R_L', and with the noise figure F, which may depend upon R_L.

Using Eq. (4.79) in (4.78), the phase noise density in terms of the unloaded resonator Q_{ul} is

$$\frac{N_{op}}{C} = \frac{FkT}{C}\frac{1}{8Q_{ul}^2}\frac{R^2 R_L}{R_x^2}\frac{1}{R_{in}}\left(\frac{f_o}{f_m}\right)^2. \tag{4.80}$$

In steady-state, the loop gain must be near unity, which means $R \approx R_L + R_{in}$ must hold. (Note that either R decreases or R_L increases to make this true in steady-state.) Inserting this in (4.80) yields

$$\frac{N_{op}}{C} = \frac{FkT}{C}\frac{1}{8Q_{ul}^2}\frac{(R_L + R_{in})^2 R_L}{R_x^2}\frac{1}{R_{in}}\left(\frac{f_o}{f_m}\right)^2. \tag{4.81}$$

The value of R_{in} which minimizes (4.81) for a given value of R_L is obtained by differentiating (4.81) with respect to R_{in}, setting the result equal to zero, then solving for R_{in}. Doing so yields

$$\begin{aligned} \frac{\partial (N_{op}/C)}{\partial R_{in}} &= \frac{2(R_L + R_{in})R_{in} - (R_L + R_{in})^2}{R_{in}^2} = 0 \\ \Rightarrow \quad & R_{in}\big|_{opt} = R_L \end{aligned} \tag{4.82}$$

Thus, phase noise density for this circuit is minimized when the input resistance is matched to the load (source) resistance. This is intuitively agreeable, since matched impedances is also the condition for maximum power transfer.

For the particular sustaining amplifier circuit used in this work (Fig. 4.4), the amplifier input resistance R_{in} cannot be matched to the source resistance $R_S = R_L$ during steady-state oscillation. (This will in general be the case for oscillators which do not use transformers to match impedances.) This can be seen through a steady-state analysis of oscillator operation.

Under steady-state oscillation conditions, the loop gain is very nearly unity, and thus, $R = R_L + R_{in}$. For the designed sustaining amplifier of Fig. 4.4, the value of the shunt resistance R_f may be determined from the gain equation as follows:

$$\begin{aligned} R = R_f a_{v2} \quad \Rightarrow \quad R_f = \frac{R}{a_{v2}} = \frac{R_L + R_{in}}{a_{v2}} &= \frac{R_L}{a_{v2}} + \frac{R_f}{a_{v2}(1+a_{v1})} \\ R_f\left[1 - \frac{1}{a_{v2}(1+a_{v1})}\right] &= \frac{R_L}{a_{v2}} \\ \therefore \quad R_f &\approx \frac{R_L}{a_{v2}} \end{aligned} \tag{4.83}$$

where Eq. (4.12) has been used ($R_{in} = R_f/(1+a_{v1})$) has been used. Using (4.83) and (4.12), the low-frequency input resistance of the amplifier during steady-state oscillation is found to be

$$R_{in} = \frac{R_f}{1+a_{v1}} = \frac{R_L}{a_{v2}(1+a_{v1})}, \tag{4.84}$$

which is in general not equal to R_L.

Since for this oscillator, the source and input impedances cannot in general be matched, it makes sense to instead find the optimum value of resonator series resistance, $R_x|_{opt}$, that minimizes the phase noise density-to-carrier ratio. To do this, the influence of R_x on the noise figure of the sustaining amplifier must first be addressed. For the case where $1/f$, f, and f^2 noise can be neglected, the noise figure F for the circuit of Fig. 4.4 is given by Eq. (4.65), which, since $R_S = R_L$, now has the form

$$F = 1 + \frac{2}{3}\frac{1}{g_m R_L} + \frac{R_L}{R_f} + \frac{R_L}{R_f^2}\frac{2}{3}\frac{1}{g_m}. \tag{4.85}$$

Inserting (4.83) in (4.85), the noise figure neglecting $1/f$, f, and f^2 noise is

$$F = 1 + \frac{2}{3}\frac{1}{g_m R_L} + a_{v2} + \frac{a_{v2}^2}{R_L}\frac{2}{3}\frac{1}{g_m} = 1 + a_{v2} + \frac{K}{R_L}, \quad \text{where } K = \frac{2}{3}\frac{1}{g_m}(1 + a_{v2}^2) = \text{constant} \tag{4.86}$$

Using Eq. (4.86) in (4.81), the expression for the phase noise density-to-carrier ratio becomes

$$\frac{N_{op}}{C} = \frac{kT}{C}\frac{1}{8Q_{ul}^2}\left(1 + a_{v2} + \frac{K}{R_x}\right)\frac{(R_L + R_{in})^2 R_L}{R_x^2}\frac{1}{R_{in}}\left(\frac{f_o}{f_m}\right)^2. \tag{4.87}$$

where Eq. (4.83) has been used. Inserting (4.84) in (4.87) yields

$$\begin{aligned}\frac{N_{op}}{C} &= \frac{kT}{C}\frac{1}{8Q_{ul}^2}\left(1 + a_{v2} + \frac{K}{R_x}\right)\frac{R_L^2\,[1 + 1/a_{v2}(1 + a_{v1})]^2}{R_x^2}a_{v2}(1 + a_{v1})\left(\frac{f_o}{f_m}\right)^2 \\ &\approx \frac{kT}{C}\frac{1}{8Q_{ul}^2}\left(1 + a_{v2} + \frac{K}{R_x}\right)\frac{R_L^2}{R_x^2}a_{v2}(1 + a_{v1})\left(\frac{f_o}{f_m}\right)^2\end{aligned} \tag{4.88}$$

The value of resonator series resistance R_x that minimizes the phase noise density for a given R_{in} may be derived using a similar procedure to that used to obtain Eq. (4.82). To simplify the expression, the analysis will be carried out assuming that the output resistance of the amplifier is negligible compared with the resonator series resistance, i.e. $R_L \approx R_x$. With this assumption, Eq. (4.88) becomes

$$\frac{N_{op}}{C} = \frac{kT}{C}\frac{1}{8Q_{ul}^2}\left(1 + a_{v2} + \frac{K}{R_x}\right)a_{v2}(1 + a_{v1})\left(\frac{f_o}{f_m}\right)^2, \tag{4.89}$$

which is a minimum for values of resonator series resistance

$$R_x\big|_{opt} > \frac{\frac{2}{3}\frac{1}{g_m}(1 + a_{v2}^2)}{1 + a_{v2}} \approx \frac{2}{3}\frac{a_{v2}}{g_m}. \tag{4.90}$$

For values of R_x that satisfy Eq. (4.90), the minimum phase noise density-to-carrier ratio for the oscillator circuit of Fig. 4.4, in the range of frequencies where $1/f$, f, and f^2 noise components are negligible, is

$$\left.\frac{N_{op}}{C}\right|_{min} = \frac{kT}{C}\frac{1}{8Q_{ul}^2}\underbrace{(1+a_{v2})}_{\text{noise figure}}\underbrace{a_{v2}(1+a_{v1})}_{\text{Q-loading/matching}}\left(\frac{f_o}{f_m}\right)^2. \tag{4.91}$$

As indicated, the $(1+a_{v2})$ term in Eq. (4.91) results from the noise figure for this particular sustaining amplifier, and the $a_{v2}(1+a_{v1})$ term arises from a combination of Q-loading and impedance mismatches.

4.4.2 Phase Noise in the Prototype Microresonator Oscillator

Using the expressions from Section 4.4.1, the phase noise density, assuming noise contributions from only superposed electronic noise, many now be determined for the designed prototype micromechanical resonator oscillator. Data associated with the noise calculations for the prototype oscillator of Fig. 4.4 are presented in Table 4.2. A plot of the phase noise density-to-carrier ratio versus frequency deviation from the carrier for a 10 MHz microresonator oscillator with an unloaded Q = 20,000, is shown in Fig. 4.24.

Figure 4.25 presents a plot of phase noise density-to-carrier ratio at 100 Hz deviation from the carrier as a function of resonator R_x for the same oscillator. Although the plot clearly shows a dependence upon R_x, it does not match Eq. (54) exactly. This is because the output resistance of the amplifier of Fig. 4.4 is not negligible, as was assumed when deriving Eq. (54).

The phase noise density-to-carrier ratio versus frequency for the oscillator of Fig.4.4 using a 16.5 kHz micromechanical resonator with Q = 80 000 is graphed in Fig. 4.26. These very low phase noise densities are expected at this low frequency.

4.4.3 Mass Loading Noise

In addition to superposed electronic noise, any physical phenomenon which causes instantaneous frequency deviations in the resonator will contribute to the total phase noise power. Given that the typical mass of a μmechanical resonator is on the order of 10^{-11} kg, mass loading noise is

TABLE 4.2. Noise Calculation Data for the Oscillator

Parameter	Value	Units
g_m	6.3×10^{-5}	mhos
K_f	3×10^{-24}	V^2/F
R_o	200	kΩ
R_x	200	kΩ
R_f	$(R_o + R_x + R_{in}) / a_{v2}$	Ω
R_{in}	$R_f / (1 + a_{v1})$	Ω
a_{v1}	20	—
a_{v2}	10	—
C	0.5	mW
Q_{ul} (10 MHz)	20 000	—
Q_{ul} (16.5 kHz)	80 000	—

expected to make a sizable contribution. Mass loading noise [6] arises from instantaneous differences in the rates of adsorption and desorption of contaminant molecules to and from the resonator surface, which cause mass fluctuations, and consequently, frequency fluctuations. Figure 4.27 shows a pictorial representation of mass loading of a micromechanical resonator.

Some of the factors which determine the magnitude of mass loading noise include the adsorption/desorption rate of contaminant molecules, contaminant molecule size and weight, pressure, and temperature. Using a procedure similar to that in [78], expressions describing mass loading noise for micromechanical resonators will now be derived.

4.4.3.1 Rates of Contamination

The rate of arrival of molecules at the surface of a resonator may be described by the equation [86]

$$r_o = 3.51 \times 10^{22} \frac{P}{(TM)^{1/2}} \text{ molecules/cm}^2\text{/s}, \tag{4.92}$$

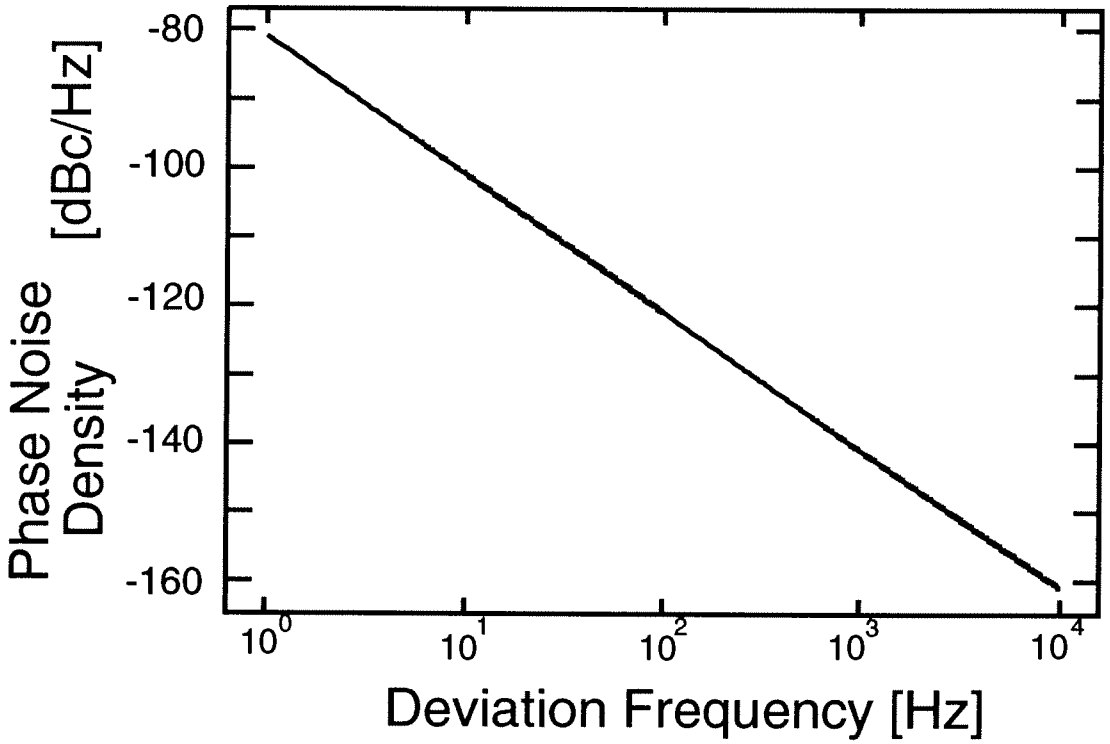

Fig. 4.24: Plot of phase noise density-to-carrier ratio as a function of frequency deviation from the carrier for a 10 MHz oscillator with the architecture of Fig. 4.4 and with a micromechanical resonator with Q = 20,000, for varying values of microresonator series resistance, R_x.

where P is the pressure in Torr, T is the temperature in Kelvin, and M is the molecular weight of the contaminant molecule. The molecular interarrival time is given by the reciprocal of (4.92), $\tau_o = 1/r_o$.

Once they adhere to a surface, the contaminant molecules reside on the surface for a finite amount of time. The mean residence time is given by [86]

$$\tau_1 = \alpha \exp\left(\frac{E_d}{RT}\right), \tag{4.93}$$

where $R = 1.987 \times 10^{-3}$ kcal/(mol K) is the gas constant and E_d is the desorption energy in kcal/mol. Some desorption energies for gas molecules on various surfaces are usually in the range of 10 to 30 kcal/mol. α in Eq. (4.93) is usually from 10^{-11} to 10^{-14} s.

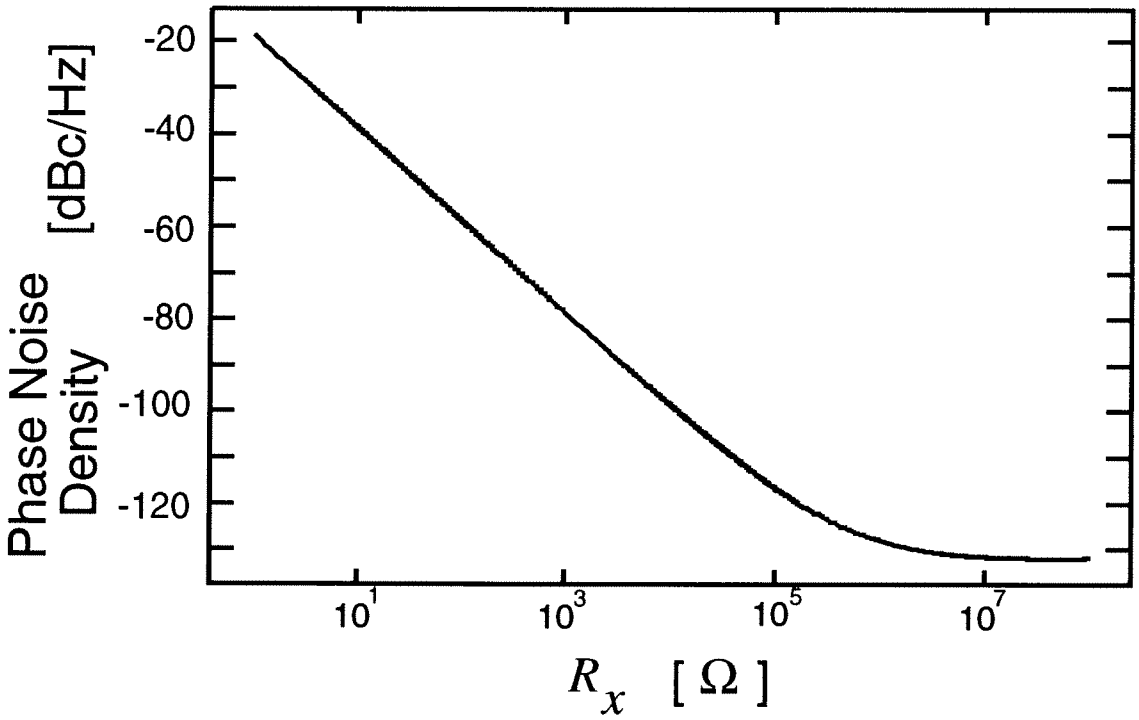

Fig. 4.25: Plot of phase noise density-to-carrier ratio as a function of microresonator series resistance R_x for a 100 Hz deviation from the carrier for the oscillator described in the caption of Fig 4.24.

In this analysis, the adsorption/desorption of contaminant molecules will be modelled by the filling or evacuation of sites on the resonator surface. It will be assumed that only a monolayer of molecules is possible, i.e. that the sticking probability for a contaminant molecule on a filled site is zero. The sticking probability for an uncontaminated (unfilled) site, however, will be assumed to be a finite number between 0 and 1. This simplification reduces the number of states to

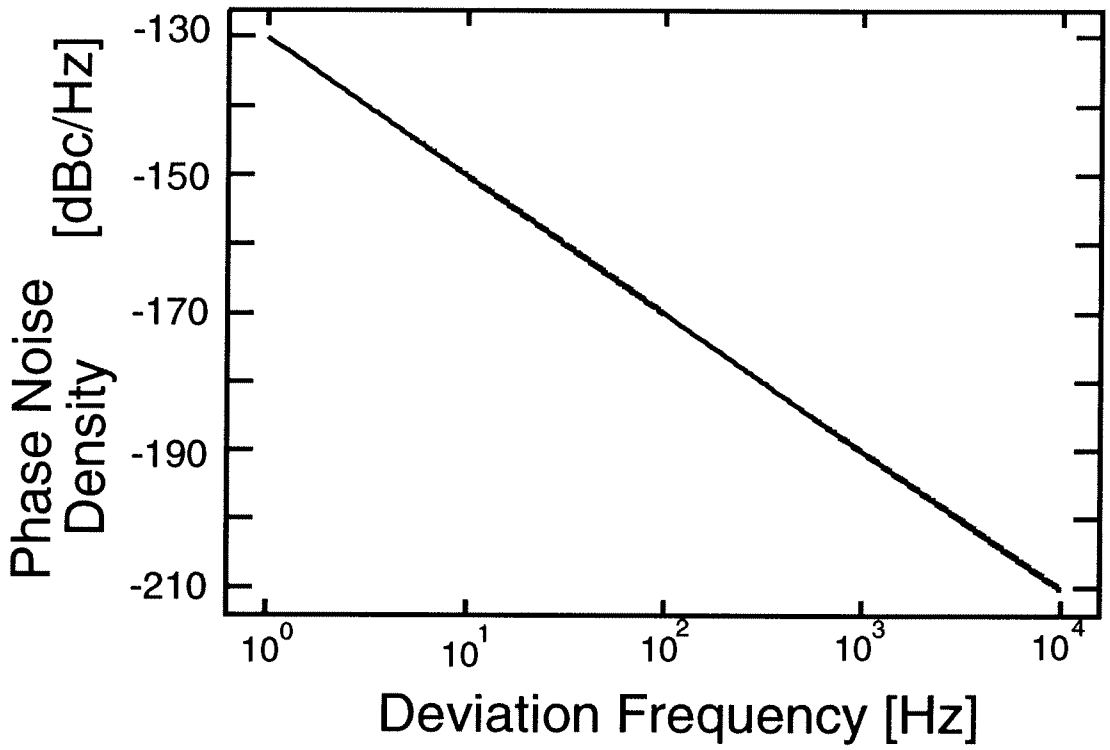

Fig. 4.26: Plot of phase noise density-to-carrier ratio versus frequency deviation from the carrier for the oscillator of Fig.4.4 using a 16.5 kHz folded-beam, comb-driven micromechanical resonator.

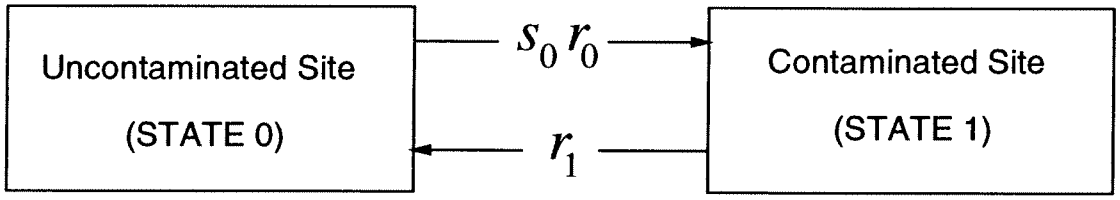

Fig. 4.28: Schematic representation of a two-state system model for the flux of particles to and from a surface.

two: (1) site uncontaminated (state 0) and (1) site contaminated (state 1). Figure 4.28 schematically represents the two state system model.

When the system of contaminant gas and resonator surface settles down to a steady-state dynamic equilibrium, the states of contaminant sites can be described by steady-state probabilities. Let p_0 and p_1 denote the steady-state probabilities that a site is uncontaminated and contaminated, respectively. In addition, let s_0 denote the sticking probability at a given uncontaminated site.

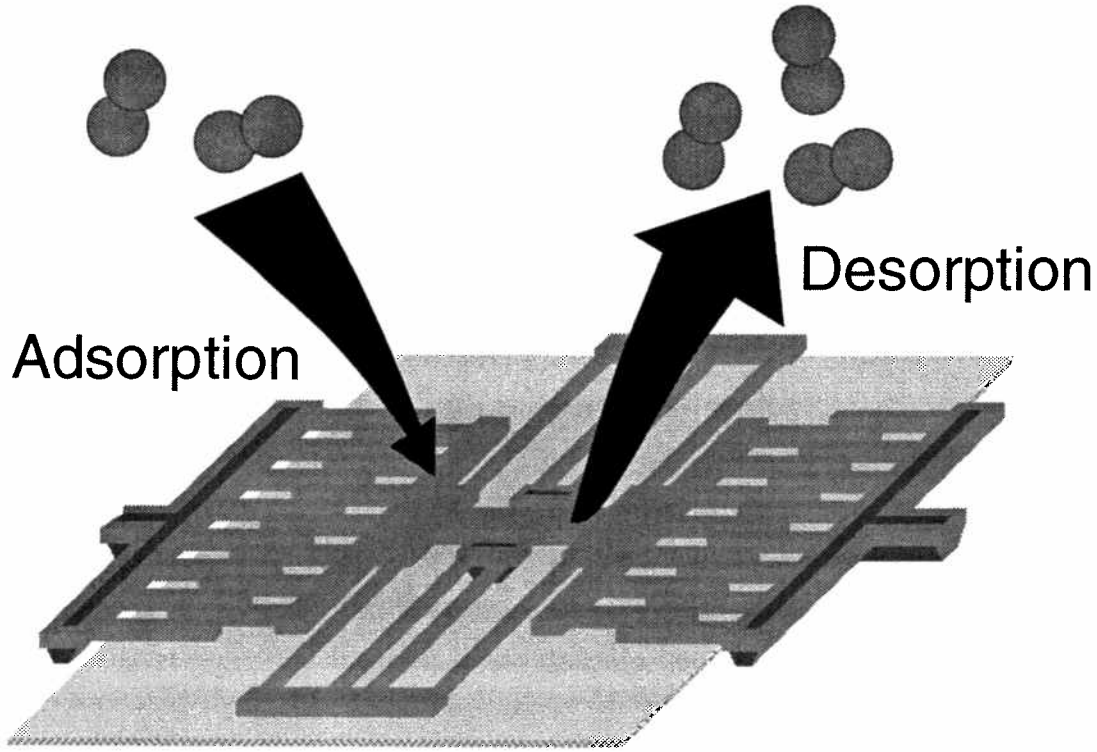

Fig. 4.27: Pictorial representation of mass loading of a folded-beam, comb-driven micromechanical resonator.

Then, under steady-state conditions, the rate at which a site enters a particular state must be equal to the rate at which it leaves. The rate balance equations may be written as follows:

TABLE 4.3. Absorption/Desorption Rates

State	Rate Entering (R_o)	Rate Leaving (R_l)
0	$p_1 r_1$	$s_0 p_0 r_0$
1	$s_0 p_0 r_0$	$p_1 r_1$

Since in this analysis we consider only two states, the probabilities for state 0 and state 1 must sum to one:

$$p_0 + p_1 = 1 . \tag{4.94}$$

From Table 4.3 and Eq. (4.94), expressions for the probabilities for each state may be written:

$$p_0 = \frac{r_1}{r_1 + s_0 r_0} \quad \text{and} \quad p_1 = \frac{s_0 r_0}{r_1 + s_0 r_0} . \tag{4.95}$$

The probability p_1 can be interpreted as the ratio of contaminated area to total surface area, i.e. the fraction of the area contaminated. A highly contaminated, or "dirty" surface would have a value of p_1 close to unity.

4.4.3.2 Frequency Deviation Due to Mass Loading

The amount of resonator center frequency deviation Δf resulting from mass loading is a function of both the amount of mass added and the location on the resonator surface. For the case of a folded-beam, comb-driven microresonator, such as shown in Fig. ,2.15, the expression for frequency change can be greatly simplified if the shuttle mass is much greater than the mass of the support springs. For this case, mass loading of the springs may be neglected, and all mass loading may be considered to add to the shuttle, which may be considered a rigid body with a constant peak velocity at all points.

With these assumptions, the frequency change for a comb-driven (shuttle-based) resonator is found to be

$$f_o \approx \sqrt{\frac{k}{mA_s}} \quad \Rightarrow \quad \Delta f \approx -\frac{f_o}{2}\frac{m'}{m}, \tag{4.96}$$

where f_o is the center frequency of the resonator, k is the system spring constant, A_s and m are the top surface area and the mass per unit area, respectively, of the resonator shuttle, and m' is the total mass per unit area of contaminant molecules added to the shuttle mass. To arrive at Eq. (4.96), the binomial approximation has been used, since in most cases the ratio of contaminant mass to shuttle mass is tiny.

For other resonators which cannot be adequately approximated by a spring-mass system, the dependence of frequency on mass loading is not so simple, since the effective mass at each point of the resonator varies with the peak velocity at each location. As will be seen, mass loading has the most impact on the less massive resonators, and thus, these effects become most significant for high frequency resonators, which are commonly designed to minimize mass. For these resonators, frequency variations due to mass loading can be conveniently displayed by plotting the frequency influence curve (frequency change versus position of added mass) [78], then incorporating a positional dependence in the analyses which follow in subsequent sections. For tractability, however, the following analyses will assume a flat frequency influence curve, in which the frequency

change upon occupation by a contaminant from each location on the resonator's surface is assumed independent of position. The consequence of this assumption will be a lower predicted noise level than the actual noise level (by perhaps, 3 dBc [78]).

For a flat frequency influence curve (i.e. Δf is independent of position), then, the frequency change per site is constant and is given by

$$\xi_i = \frac{\Delta f}{N} \quad \text{where } i = 1, 2, \ldots, N, \tag{4.97}$$

where N is the number of sites in the active area of the resonator.

4.4.3.3 Stochastic Modelling

Each contaminant site yields a stochastic process that is assumed stationary and mutually independent of other sites. The stochastic process of frequency fluctuations per site i can be written as

$$f_i(t) = \xi_i b_i(t) \quad i = 1, 2, \ldots, N \ , \tag{4.98}$$

where $b_i(t)$ is a Bernoulli random variable with a value of one if the site is contaminated and zero otherwise. The mean or expected value of $b_i(t)$ is simply

$$E[b_i(t)] = p_1 . \tag{4.99}$$

The combined effect of all contaminant sites can be modelled by summing the stochastic processes $f_i(t)$ over $2N$ sites to obtain

$$f(t) = \sum_{i=1}^{2N} f_i(t) = \sum_{i=1}^{2N} \xi_i b_i(t) . \tag{4.100}$$

The summation is taken over $2N$ sites to account for both the top and bottom surfaces of the resonator.

4.4.3.4 Autocorrelation and Spectral Density Functions

The spectral density function modelling the frequency noise induced by mass loading may be derived by first finding the autocorrelation function for $f(t)$, then using the Wiener-Klintchine

relation to obtain the one-sided spectral density. Doing so, the autocorrelation function for $f(t)$ is found as follows:

$$\begin{aligned} R(\tau) &= E[f(t+\tau)f(t)] \\ &= \sum_{i=0}^{N-1} \xi_i^2 E[b_i(t+\tau)\,b_i(t)] + \left(\sum_{i=0}^{2N-1} \sum_{j=0}^{i} \xi_j \xi_{i-j} - \sum_{i=0}^{N-1} \xi_i^2 \right) p_1^2 \\ &= \sum_{i=0}^{N-1} \xi_i^2 E[b_i(t+\tau)\,b_i(t)] + K_\xi p_1^2 \end{aligned} \tag{4.101}$$

In Eq. (4.101), statistical independence between surface sites was assumed. If the value of ξ_i is constant and equal to ξ, which is the case for a comb-driven shuttle-based resonator, Eq. (4.101) reduces to

$$R(\tau) = 2N\xi^2 \sum_{i=0}^{N-1} E[b_i(t+\tau)\,b_i(t)] + (4N-1)N\xi^2 p_1^2 \tag{4.102}$$

Equation (4.101) calls for the autocorrelation of the Bernoulli random variable $b_i(t)$. As expressed in Eq. (4.101), the autocorrelation is merely the mean of the product $b_i(t+\tau)b_i(t)$, which may be expanded as

$$\begin{aligned} E[b_i(t+\tau)\,b_i(t)] &= 0 \cdot 0 \cdot P[B_i(t+\tau) = 0 \cap B_i(t) = 0] \\ &\quad + 0 \cdot 1 \cdot P[B_i(t+\tau) = 0 \cap B_i(t) = 1] \\ &\quad + 1 \cdot 0 \cdot P[B_i(t+\tau) = 1 \cap B_i(t) = 0] \\ &\quad + 1 \cdot 1 \cdot P[B_i(t+\tau) = 1 \cap B_i(t) = 1] \\ \therefore\ E[b_i(t+\tau)\,b_i(t)] &= 1 \cdot 1 \cdot P[B_i(t+\tau) = 1 \cap B_i(t) = 1] \end{aligned} \tag{4.103}$$

or

$$E[b_i(t+\tau)\,b_i(t)] = P[B_i(t+\tau) = 1 | B_i(t) = 1]\,P[B_i(t) = 1]\,. \tag{4.104}$$

From Eq. (4.99), the probability that $b_i(t) = 1$ at time t is simply

$$P[B_i(t) = 1] = p_1\,. \tag{4.105}$$

The probability that $b_i(t+\tau) = 1$ given that $b_i(t) = 1$ can be found through the following reasoning: First, the Bernoulli random variable $b_i(t)$ takes on values of either 0 or 1 in random fashion, at ran-

dom time intervals. The number of transitions between 0 and 1 in time τ can be modelled via a Poisson process, with a probability density function given by [87]

$$P(A_n) = \frac{(\lambda|\tau|)^n}{n!} e^{-\lambda|\tau|} , \tag{4.106}$$

where

$$A_n = \text{probability that } n \text{ transitions have occurred in time } \tau . \tag{4.107}$$

In Eq. (4.106), λ is the mean occurrence rate of transitions; that is, the average number of transitions per unit time. For the case where $b_i(t)$ is initially 1, $b_i(t+\tau) = 1$ when there have been an even number of transitions. Using Eq. (4.106), the probability that there has been an even number of transitions in time τ can be expressed by

$$P(n = \text{even}) = \sum_{n=0}^{\infty} \frac{(\lambda|\tau|)^{2n}}{(2n)!} e^{-\lambda|\tau|} = \frac{1}{2}(e^{\lambda|\tau|} + e^{-\lambda|\tau|}) . \tag{4.108}$$

Using (4.105) and (4.108) in (4.104) yields

$$\begin{aligned} E[b_i(t+\tau)\, b_i(t)] &= \frac{p_1}{2}(e^{\lambda|\tau|} + e^{-\lambda|\tau|})\, e^{-\lambda|\tau|} \\ &= \frac{p_1}{2}(1 + e^{-2\lambda|\tau|}) \end{aligned} . \tag{4.109}$$

Using Eq. (4.101), the autocorrelation of frequency fluctuations is

$$R(\tau) = \sum_{i=0}^{N-1} \xi_i^2 \frac{p_1}{2}(1 + e^{-2\lambda|\tau|}) + K_\xi p_1^2 . \tag{4.110}$$

If $\xi_i = \xi$ = constant, then the autocorrelation may be written

$$\begin{aligned} R(\tau) &= N\xi^2 \frac{p_1}{2}(1 + e^{-2\lambda|\tau|}) + (4N-1) N\xi^2 p_1^2 \\ &= N\xi^2 \frac{p_1}{2} e^{-2\lambda|\tau|} + N\xi^2 p_1 \left[\frac{1}{2} + (4N-1)\, p_1\right] \end{aligned} \tag{4.111}$$

Taking the Fourier transform of Eq. (4.111), the one-sided spectral density of frequency fluctuations is given by

$$S_{\Delta f}(f) = \frac{2Np_1\xi^2\lambda}{(2\lambda)^2 + 4\pi^2 f^2} + N\xi^2 p_1\left[\frac{1}{2} + (4N-1)p_1\right]\delta(f)\,, \tag{4.112}$$

where f is the Fourier frequency. The second term in Eq. (4.112) models the dc frequency shift of the resonator due to mass loading, and thus, it has no frequency dependence. Only the first term in (4.112) models frequency noise.

In the steady-state dynamic equilibrium of one species of contaminant molecule and one type of site on the resonator surface, there is one adsorption rate $s_0 r_0$ and one desorption rate r_1. Thus, the mean occurrence rate can be expressed as

$$\lambda = \frac{1}{2}(s_o r_0 + r_1)\,. \tag{4.113}$$

Using (4.113) and ignoring the second (dc) term of (4.112), the one-sided spectral density of frequency fluctuations for the case where the frequency influence curve is flat becomes

$$S_{\Delta f}(f) = \frac{s_o r_0 (\Delta f)^2 / N}{(s_o r_0 + r_1)^2 + 4\pi^2 f^2}\,. \tag{4.114}$$

Note that mass loading-derived frequency noise as given by Eq. (4.114) (1) depends upon the rates of adsorption and desorption of contaminant molecules to and from the resonator surface; (2) is proportional to the square of frequency change due to a monolayer of contaminant molecules; and (3) is inversely proportional to the number of sites. The last of these points suggests that mass loading derived frequency instability may be reduced by increasing the surface area of the mechanical resonator.

The frequency noise as given by Eq. (4.114) is graphed in Fig. 4.29 for the case of a 10 MHz clamped-clamped beam resonator in a nitrogen ambient with a sticking probability of 1. Figure 4.29 shows two regimes with different frequency dependencies:

$$\begin{aligned} f \ll \frac{s_o r_o + r_1}{2\pi}: &\qquad [S_{\Delta f}(f) = \text{constant}] \Rightarrow \text{ white noise} \\ f \gg \frac{s_o r_o + r_1}{2\pi}: &\qquad [S_{\Delta f}(f) \propto 1/f^2] \Rightarrow \text{ random walk in frequency} \end{aligned} \tag{4.115}$$

The spectral density of phase fluctuations follows immediately from Eq. (4.114):

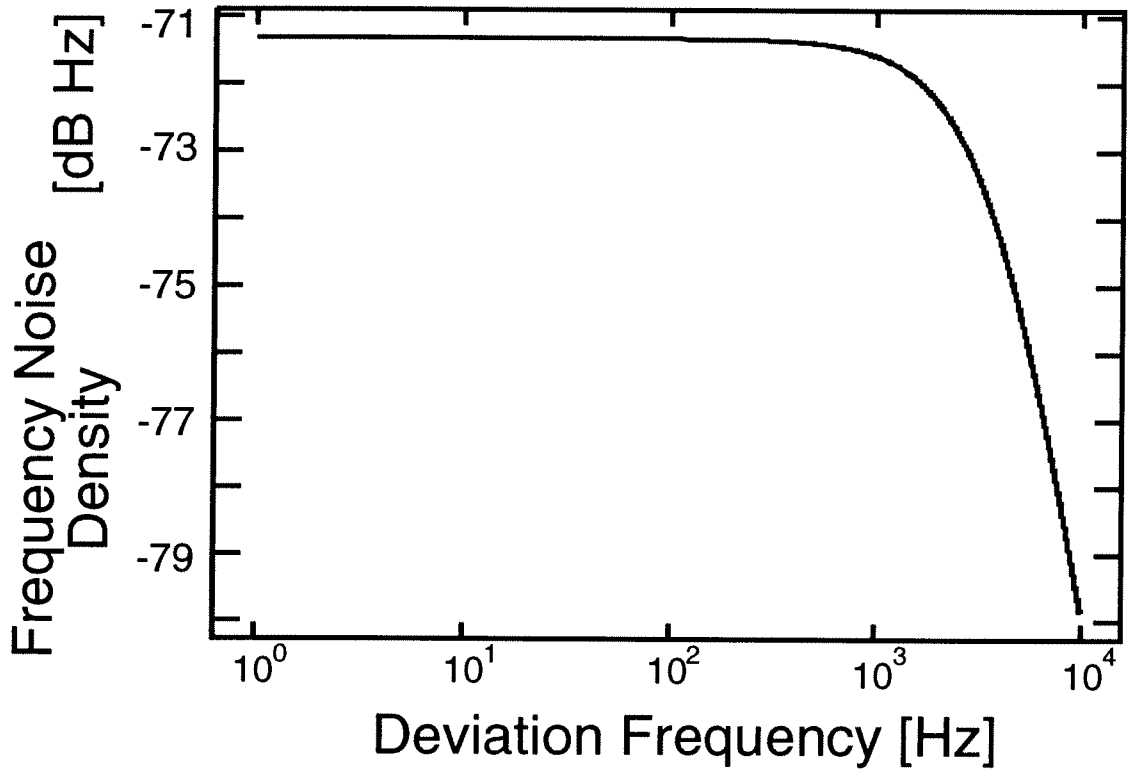

Fig. 4.29: Plot of frequency noise as a function of frequency deviation from the carrier as predicted by Eq. (4.114) for the case of a 10 MHz clamped-clamped beam resonator in a nitrogen ambient with a sticking probability of 1.

$$S_\phi(f) = (S_{\Delta f}(f))/f^2 = \frac{s_o r_0 (\Delta f)^2/N}{(s_o r_0 + r_1)^2 + 4\pi^2 f^2} \cdot \frac{1}{f^2} \tag{4.116}$$

Equation (4.116) is plotted versus frequency deviation from the carrier in Fig. 4.30 for the case of a 10 MHz clamped-clamped beam resonator in a nitrogen ambient at 300 K and at the pressure of 10 mTorr (which maximizes phase noise; see next section).

The dependence of phase and frequency fluctuations on the rates of adsorption and desorption of contaminant molecules in Eqs. (4.114) and (4.116) suggests a strong dependence of these noise sources on the temperature and pressure of the system wherein the resonator operates. These will now be investigated in detail for the case of micromechanical resonators.

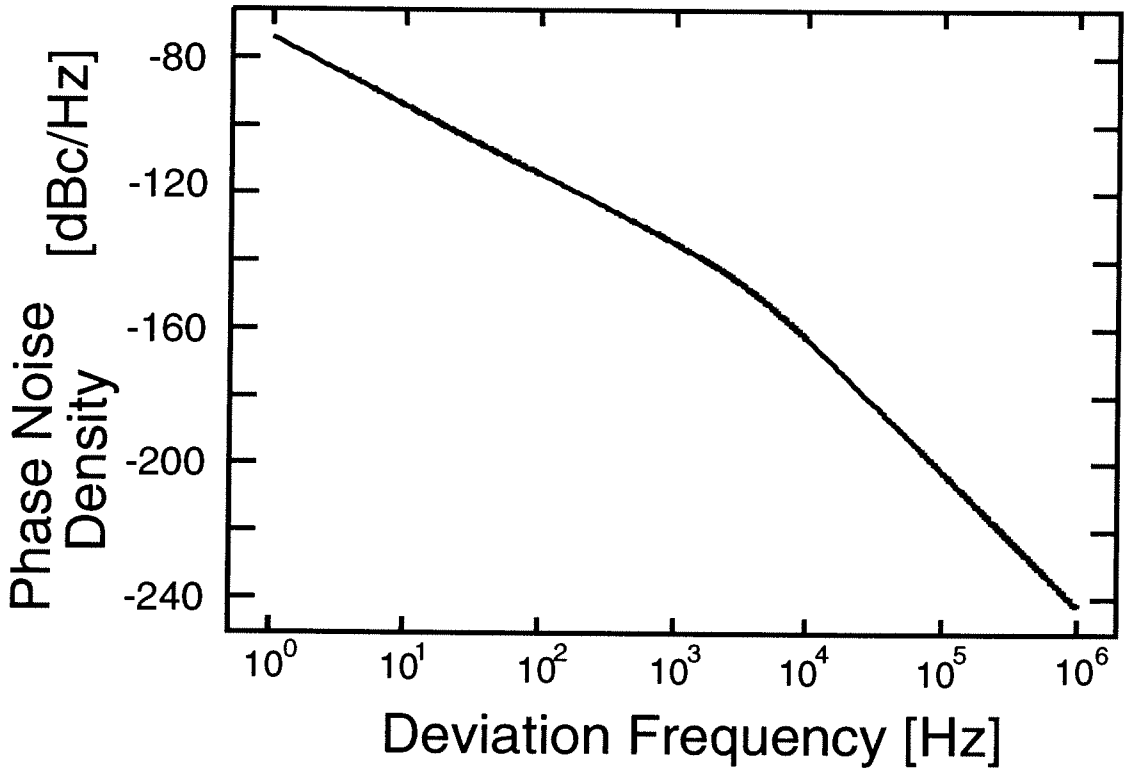

Fig. 4.30: Plot of phase noise density-to-carrier ratio versus frequency deviation from the carrier for a 10 MHz clamped-clamped beam resonator in a nitrogen ambient at 300 K and at the pressure of 10 mTorr. The oscillator carrier power is assumed to be 0.5 mW to be consistent with Section 4.4.2.

4.4.3.5 Pressure Dependence of Mass Loading

The design data for the 16.5 kHz polysilicon folded-beam comb-driven micromechanical resonator used in the prototype oscillator are summarized in Table 4.4. In this analysis, the resonator will be approximated by a single mass-single spring system, so the frequency change per filled site will be assumed given by Eq. (4.96). Since nitrogen is a common gas present after many microresonator encapsulation methods [88], a gas with its molecular weight (M = 28) will be used for this analysis. In addition, since typical desorption energy values for gases on solid surfaces range from 10 to 30 kcal/mol [89], this range will be considered. Then, setting the temperature constant at T = 300 K, and using Eqs. (4.92), (4.93), (4.96), and (4.116), curves for mass loading phase noise density in the 16.5 kHz micromechanical resonator versus pressure are plotted for this spread of desorption energies, and assuming a sticking probability of 1, in Fig. 4.31 for a 100 Hz frequency deviation from the carrier.

TABLE 4.4. Resonator Design Data for the Prototype Oscillator)

Parameter	Value	Units
W	2	μm
L	164.9	μm
h	2	μm
d	2	μm
N_d	24 (12 shuttle fingers)	—
N_s	40 (20 shuttle fingers)	—
N_o	16 (8 shuttle fingers)	—
M_p	3.3×10^{-11}	kg
f_o	16.5	kHz
Q	25 000 to 80 000	—

In both curves, a strong dependence on the desorption activation energy is seen. In addition, for each of the curves, the mass loading phase noise density is largest at an intermediate value of pressure and smallest at the higher and lower pressures. This is reasonable when one considers that at high pressures, the resonator may be saturated with contaminant molecules and little transfer to and from the surface occurs. At extremely low pressures, very few contaminants are present, and the flux of contaminant molecules is likewise small. It is at intermediate pressures where transfer of contaminant molecules is maximized, and consequently, mass loading-derived phase noise peaks.

As seen when comparing Figs. 4.26 and 4.31, the phase noise density contributed by mass loading via a nitrogen-sized molecule can, depending on the value of E_d, be larger than that contributed by superposed electronic noise for the comb-driven resonator of the prototype oscillator. The situation gets even worse as the frequency of the resonator increases. As discussed in Chapter 2, high frequency resonators are easier to achieve when resonator mass is decreased. This decrease in mass combined with a corresponding decrease in surface area increases the frequency instability of the resonator as predicted by Eq. (4.114), in turn, increasing phase noise density.

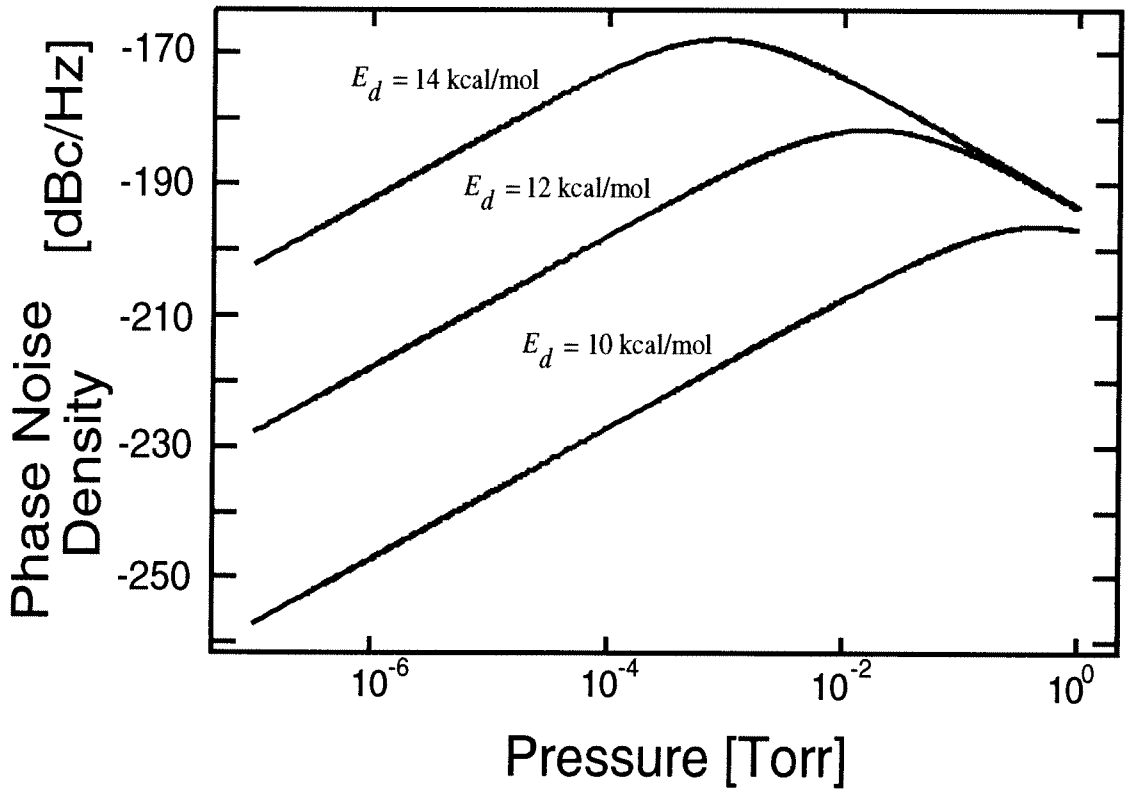

Fig. 4.31: Plot of mass loading-derived phase noise density (at a 100 Hz deviation from the carrier) versus pressure for a 16.5 kHz folded-beam, comb-driven micromechanical resonator at a constant temperature of 300K for contaminant molecules with the molecular weight of nitrogen and varying values of desorption activation energy. The carrier power is assumed to 0.5 mW

The design data for a 10 MHz resonator was presented in Table 2.3 of Chapter 2. For the same nitrogen-sized contaminant used for the 16.5 kHz resonator, and at a constant temperature of 300 K, the phase noise density due to mass loading of this high frequency resonator is plotted versus pressure in Fig. 4.32 for 100 Hz frequency deviation from the carrier. The phase noise contribution from mass loading of contaminants is substantially higher now, and appears to be the dominant source of phase noise when comparing with Fig. 4.24 (provided that our assumption of Q = 20,000 in generating Fig. 4.24 is correct.)

4.4.3.6 Temperature Dependence of Mass Loading

The dependence of mass loading-derived phase noise on temperature arises mainly from the temperature dependence of the rates of adsorption and desorption of contaminants, as given in

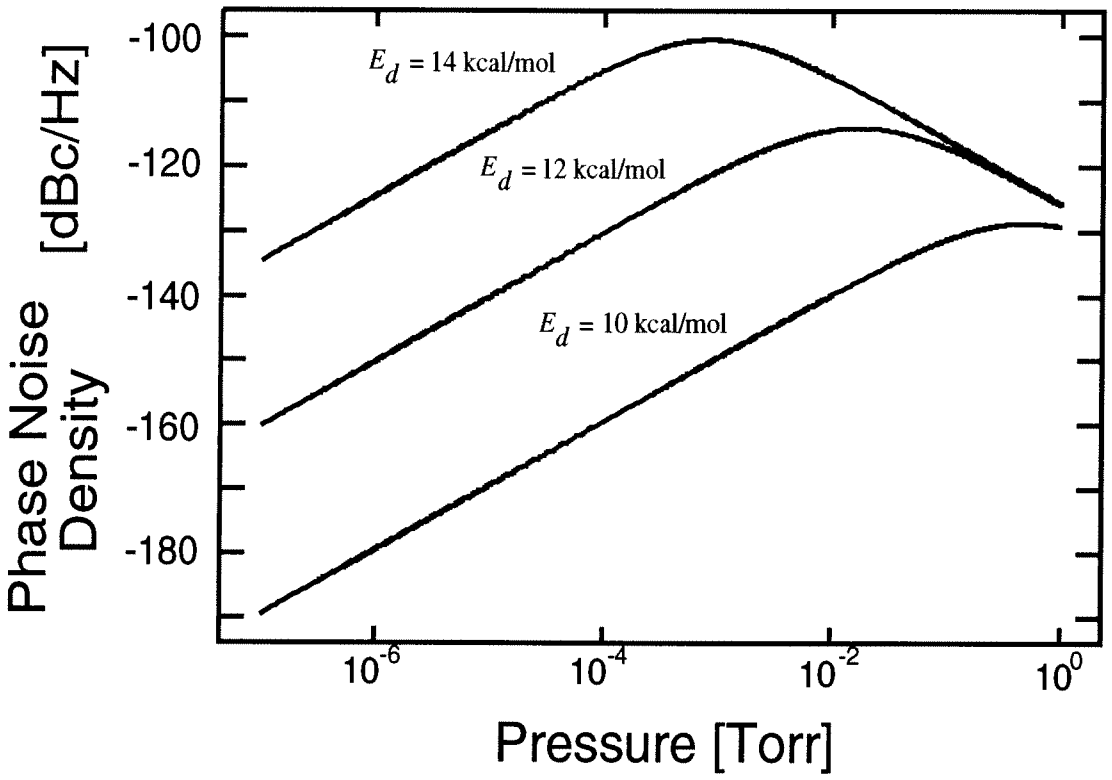

Fig. 4.32: Plot of mass loading-derived phase noise density (at a 100 Hz deviation from the carrier) versus pressure for a 10 MHz clamped-clamped beam micromechanical resonator at a constant temperature of 300K for contaminant molecules with the molecular weight of nitrogen and varying values of desorption activation energy. The carrier power is assumed to 0.5 mW.

noise density for the 10 MHz parallel-plate clamped-clamped beam resonator of Fig. 4.32 at 100 Hz frequency deviation from the carrier and for the pressure where mass loading noise peaks (1 mTorr), is shown in Fig. 4.33 as a function of temperature.

As seen in the plot, the effect of mass loading on the short term frequency stability of a resonator should taper off as temperatures increase. Perhaps a low power micro-oven, such as described in Chapter 7, could be used to substantially reduce phase noise contributions due to mass loading.

4.4.3.7 Minimizing Mass Loading Noise

As seen in the plots of the previous sub-sections, the magnitude of phase noise density caused by mass loading of a micromechanical resonator is heavily dependent upon both pressure

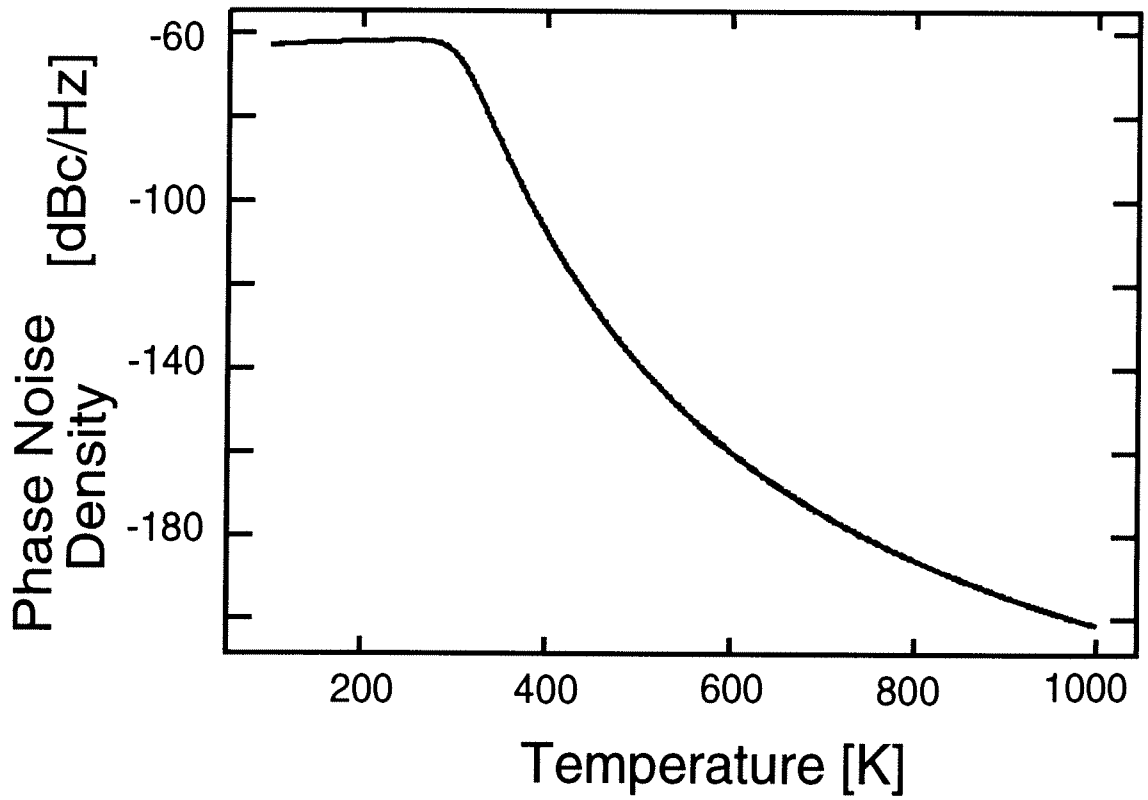

Fig. 4.33: Plot of phase noise density caused by mass loading versus temperature for the 10 MHz parallel-plate clamped-clamped beam resonator of Fig. 4.32 at 100 Hz frequency deviation from the carrier and for the pressure where mass loading noise peaks (1 mTorr).

and temperature, where for both parameters, it peaks at some intermediate value; i.e., it is minimized at high and low values of both pressure and temperature. In addition, it is heavily dependent upon the rate of desorption of contaminant molecules, on the surface area and mass of the resonator, and on the molecular weight of the contaminant molecules.

Several approaches to minimizing phase noise due to mass loading of resonators may now be suggested:

1. Encapsulate the microresonator under very low pressure vacuum ($< 10^{-6}$ Torr). (Note that high pressures are unreasonable, since these will severely degrade the quality factor of the mechanical resonator.)
2. Operate the microresonator under more optimal temperatures as determined by curves such as Figs. 1.37 and 1.38. One low power method for doing this could be through the micro-oven techniques of Chapter 7.

3. Treat the surface of the resonator to tailor the desorption energies of contaminant molecules such that the peaks of mass loading occur at pressures and temperatures far removed from the operating point.
4. Tailor an encapsulation process such that only contaminants with molecular weights and desorption energies that create mass loading-derived phase noise peaks far removed from the operating point are used.
5. Increase the surface area of the resonator, perhaps by using porous silicon [90].

This list is certainly not complete, but it does convey the idea that there are many methods available for minimizing, if not eliminating, phase noise contributions due to mass loading of micromechanical resonators.

4.4.3.8 Total Microresonator Oscillator Phase Noise

By comparison of the data and simulations in Sections 4.4.1 and 4.4.3, mass loading noise is very frequently the dominant source of phase noise in high-Q microresonator oscillators. In the general case, whether mass loading noise or superposed electronic noise dominates the short-term stability of microresonator oscillators is largely dependent upon the types of contaminants involved—each with its own molecular weight, activation energy of desorption, and sticking probability—and the types of resonators involved—each with its own surface characteristics, quality factor, etc...

One point, however, can be made in general: If the microresonator oscillator can be operated under very low pressure (< 1 μTorr), then its short-term stability should be very good, since mass loading noise is minimized at low pressures, and resonator Q is maximized. The importance of vacuum-encapsulating technologies [64,91,88,92,93], whether integrated or not, cannot be overemphasized when designing micromechanical signal processors.

4.5 Experimental Results

Figure 4.34 presents a scanning electron micrograph of the prototype oscillator, fabricated using the technology detailed in Chapter 3. The phosphorous-doped, polysilicon, folded-beam, comb-transduced mechanical resonator used has a center frequency of 16.5 kHz with a quality fac-

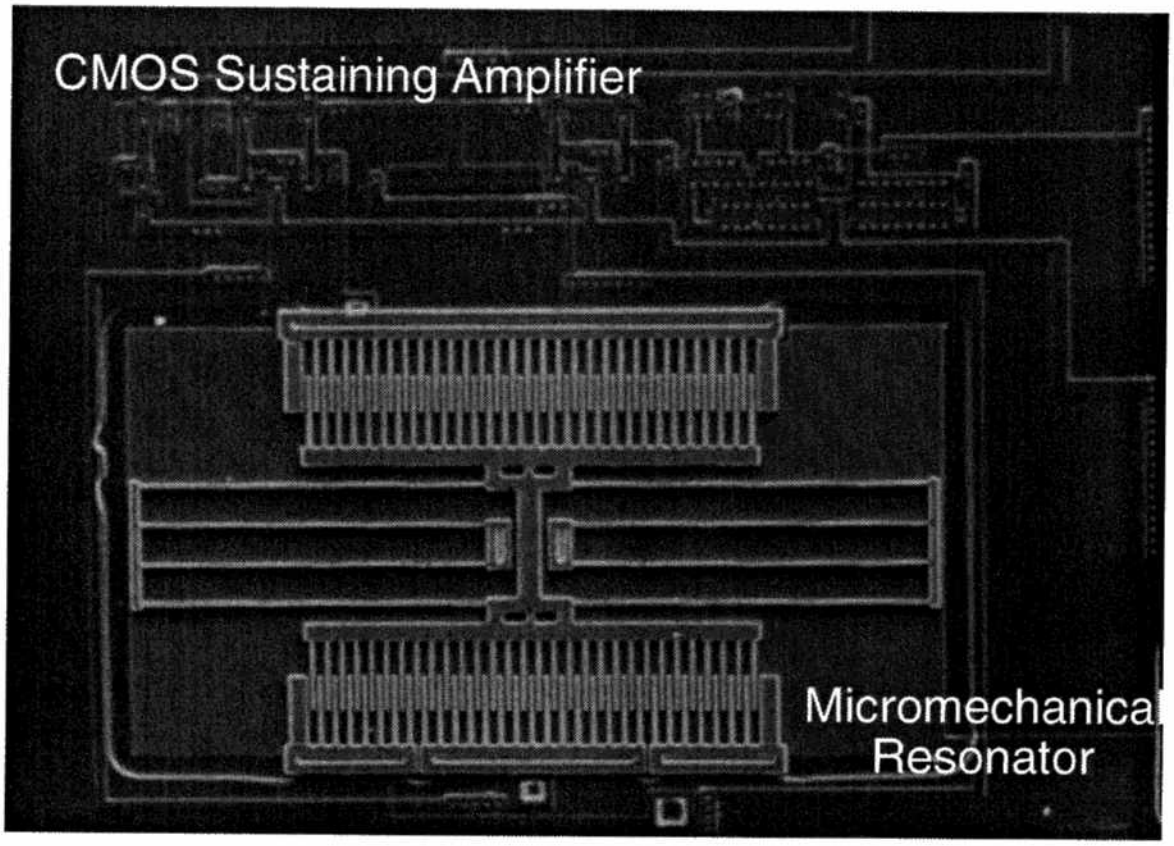

Fig. 4.34: Scanning electron micrograph of the 16.5 kHz prototype CMOS micromechanical resonator oscillator.

tor of over 80 000 under 50 μTorr pressure. Other design details for this resonator were summarized in Table 4.4.

The fabricated oscillator was bonded up in a dual-in-line package and tested under a variable pressure vacuum probe station. Figure 4.35 shows a typical oscilloscope plot for a 16.5 kHz version of this oscillator. The amplitude of oscillation was visibly controllable through adjustment of V_P, consistent with the discussion of Section 4.3. A measured plot of steady-state oscillator output voltage versus μresonator dc-bias was presented in Fig. 4.19 Over most of the range of V_P, the oscillation was visibly and measurably clean. However, over about a 5 V range some chaotic behavior of the resonator was visible under microscope. This indicates that in a finite range of dc-bias voltage, the oscillator may be exhibiting second-order nonautonomous behavior when limiting through resonator nonlinearity [84].

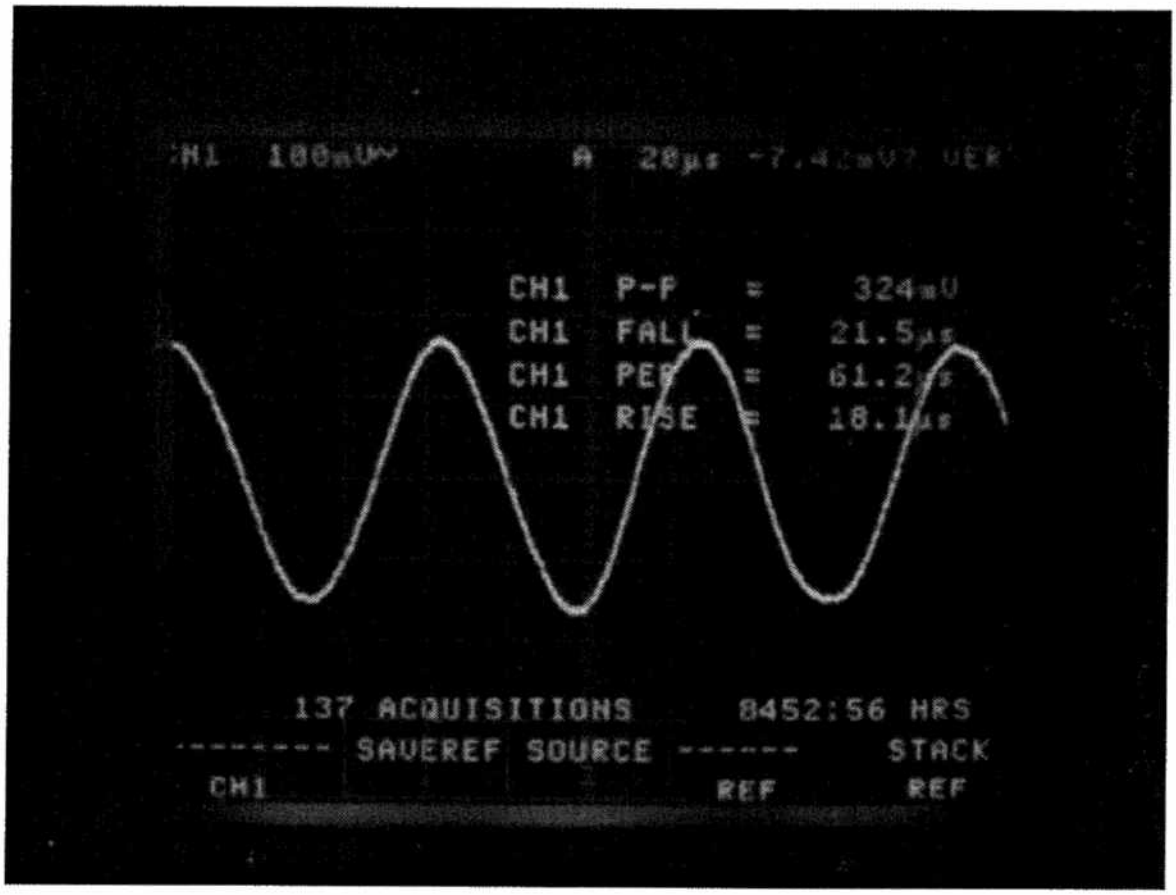

Fig. 4.35: Oscilloscope waveform for the CMOS µresonator oscillator.

4.5.1 Phase Noise Measurement

The phase noise performance of this oscillator was visibly of high quality when comparing the oscillator output spectrum seen on a dynamic signal analyzer with that of high grade instrumentation. The output spectrum of the 16.5 kHz CMOS micromechanical resonator oscillator prototype had a spectral purity (as seen by the close to carrier noise rolloff) between that of an HP 3314A Function Generator (synthesized output, i.e. phase-locked VCO) and the source of an HP 4195A Network Analyzer (high quality).

Measurement of the phase noise of a low frequency high-Q oscillator is a challenging task, since the noise levels at low frequencies are so low, as shown in Figs. 4.26 and 4.31. This is

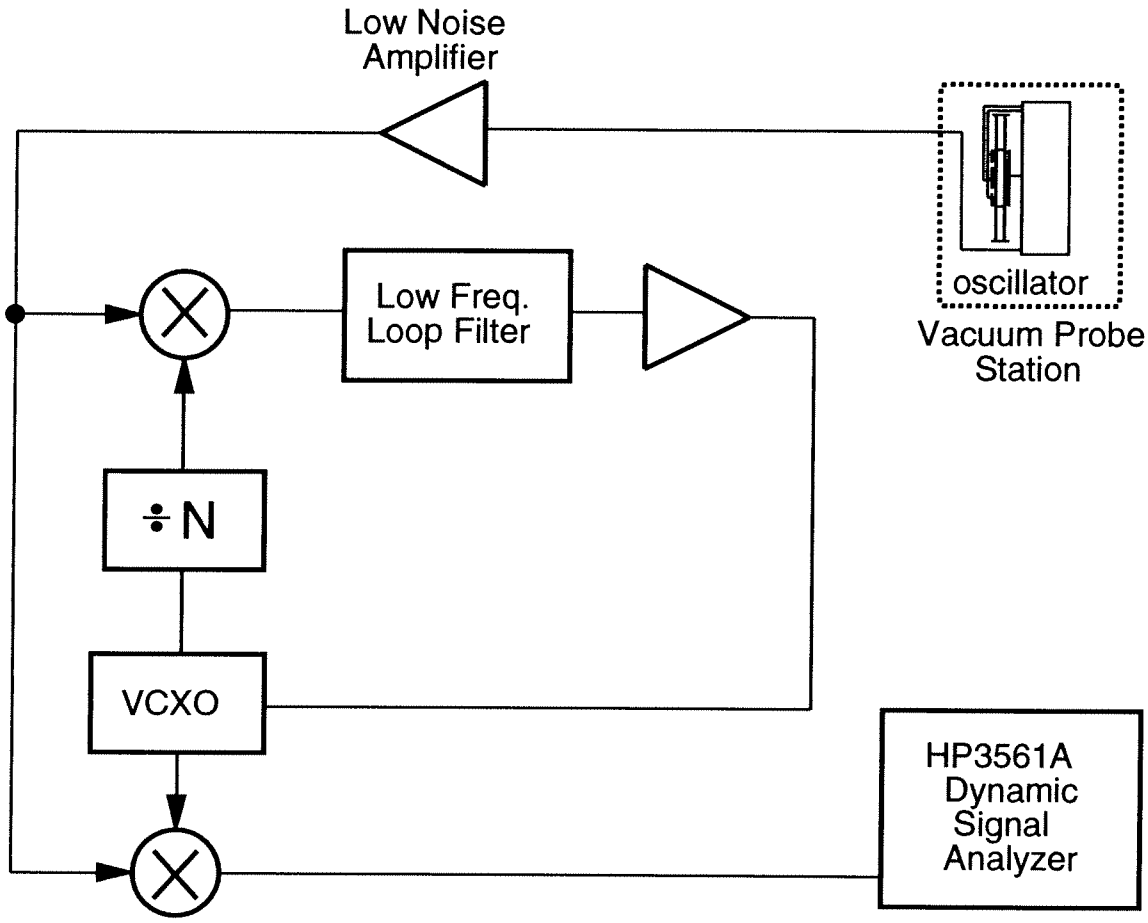

Fig. 4.36: Schematic of the system used to measure phase noise in the μresonator oscillator.

true for both superposed electronic noise and mass loading noise. A commercial phase noise measrement system was not available at this low frequency range, so a custom built unit was used.

The phase-lock loop-based measurement system used for measurement of phase noise for this work is summarized in Fig. 4.36. As shown, the system consists of a phase-lock loop, a voltage-controlled crystal oscillator (VCXO), a divide-by-*N* counter, a quiet multiplier, and an HP 3561A Dynamic Signal Analyzer. Similar to many other phase noise measurement systems, this system operates by eliminating the carrier power through quadrature multiplication of the microresonator oscillator signal and the signal generated by a high quality VCXO. Once the carrier power is eliminated, close to carrier noise may be measured reliably. As shown in the system, the output signal from the high quality VCXO is divided down before multiplying with the micromechanical resonator oscillator, which serves to further lower the phase noise of the VCXO. The

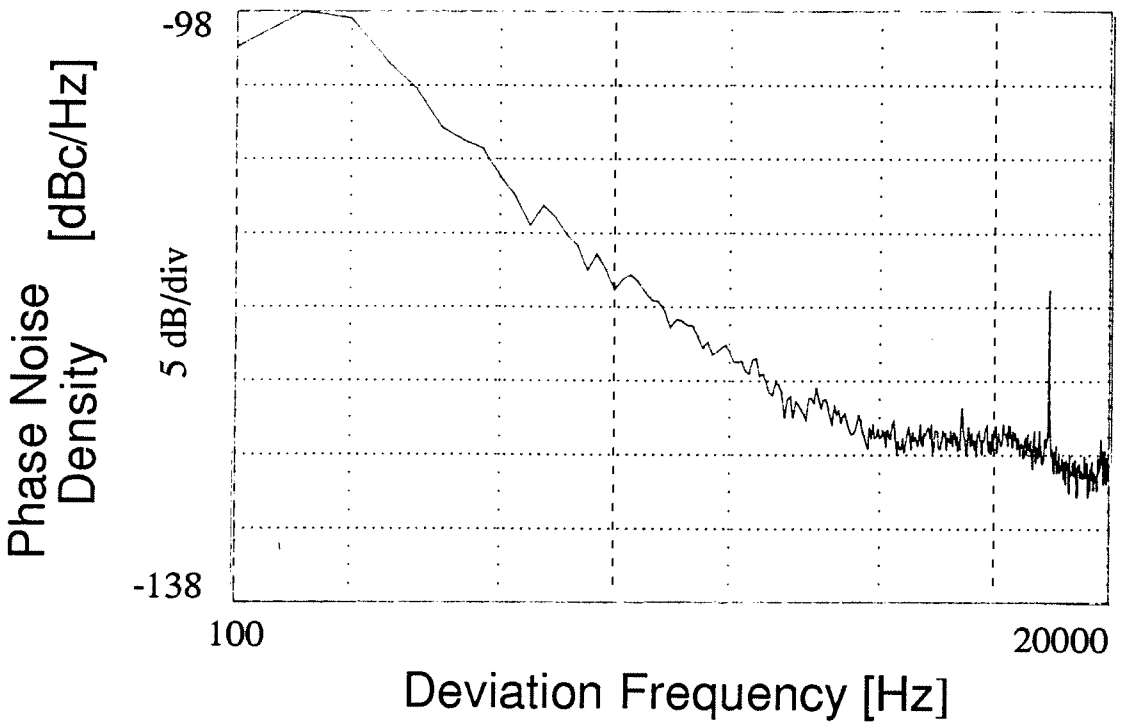

Fig. 4.37: The measured phase noise density spectrum for a 16.5 kHz microresonator oscillator as measured using the system of Fig. 4.36. It is believed that the noise floor of this system was not adequate to measure the phase noise of the oscillator.

oscillation frequency of the microresonator oscillator is pulled (via the dc-bias on the resonator) to match the frequency of the divided VCXO output.

The measured result of this set-up is shown in Fig. 4.37. Unfortunately, this result looks the same whether the micromechanical resonator oscillator is attached to the input or not, implying that the noise floor of this phase noise measurement system was not adequate for a reliable measurement. One could at least conclude, however, that the phase noise density spectrum for the resonator was at least as good as that shown in Fig. 4.37, which is already adequate for many communications applications.

In order to get a more reliable phase noise measurement, the multiplier used in the PLL and the output multiplier must be replaced by lower noise multipliers. The resources (both equipment and time) were not available for the duration of this degree. The author fully intends to make a measurement in the near future.

4.6 Conclusions

Completely monolithic, highly stable, high-Q oscillators utilizing surface-micromachined polysilicon mechanical resonators have been designed, fabricated, and tested with particular attention to amplitude control and phase noise performance. Due to the novelty of the process and the devices, conservative measures were taken for the designs, and oscillators up to only 20 kHz were fabricated. Designs up to a few megaHertz are feasible using folded-beam resonator designs, and higher frequencies (tens of MHz) should be feasible using more advanced designs aimed at maximizing resonator quality factor, which may otherwise degrade with increasing frequency. Both material and architectural improvements should be possible to increase μresonator Q.

The consequences associated with miniaturization of high-Q elements were addressed via this oscillator. High series resistance, which limits the maximum carrier power (and hence, limits the maximum phase noise density-to-carrier ratio) and mass loading were identified as phenomena which become increasingly important contributors to phase noise as resonator dimensions shrink. According to theory, mass loading-induced phase noise can be substantially reduced by operating the miniature μmechanical resonator under very low pressures. For this reason, integrated vacuum encapsulation techniques may play an important role in the future. Other techniques were also proposed to reduce mass loading noise.

Of the parameters which determine oscillator designability and performance, the series motional resistance of the micromechanical resonator is perhaps the most important. The large size of this resistance for present-day microresonators limits the usable oscillator topologies and the maximum power output of the oscillator. Techniques which lower the series motional resistance, such as smaller gaps for capacitive transduction, may be required when attempting to stretch the frequency range of these oscillators into the VHF range and further (if possible).

CHAPTER 5 *High-Q CMOS Micromechanical Resonator Filters*

In addition to applications as the reference element in high-Q oscillators, micromechanical resonators have great potential as resonator elements in high-Q micromechanical filters. Such filters could be applied to a great number of products, from speech recognition systems, which often require audio frequency, low-power filters, to communications or radar systems, where they may serve as IF or RF filters. Their range of applicability is, of course, determined by the frequency range of micromechanical filters, which in turn is dependent upon the highest frequency for which the structural material still has high Q. High-Q mechanical resonance has been measured for polysilicon micromechanical resonators in the frequency range from 100 Hz to 30 MHz [94,27,4,6]. This already covers the range of frequencies from ELF to VHF, and the highest frequency attainable by micromechanical resonators that still shows high Q is still unknown. Perhaps it is not unreasonable that even the UHF range may be accommodated by micromechanical resonators.

Although crystal and SAW filters are similar, the closest macroscopic analog to the micromechanical filters to be discussed in this chapter are the macroscopic mechanical spring-coupled resonator filters [33,35], which have a frequency range from 300 Hz to 600 kHz. The low-frequency range is generally implemented by tuning fork mechanical filters, while the higher frequencies are commonly realized utilizing disk flexure, torsional rod, or extensional rod mechanical filters. The frequency limits of these filters are determined by the size (mass) of the constituent resonators, which become too small for reasonable construction tolerances around 600 kHz. The fre-

quency range above 600 kHz, of course, is easily accommodated by ceramic ladder networks, crystal lattice or ladder networks, and/or SAW filters.

Several architectures are available for macroscopic mechanical filters, including spring-coupled series ladders and parallel ladders. These architectures are very popular for such filters because they minimize losses in the filter response. Despite the difference in attainable electromechanical coupling and frequency range, these architectures are also quite applicable to integrated microresonator filters [95], and they are, thus, the focus of this work. It should be understood, however, that many other architectures are available which use a variety of electrical or mechanical couplings between resonators, each with its own susceptibility to parameter tolerances and with its own tuning and frequency characteristics. For example, capacitively-coupled crystal filter architectures are just as applicable to micromechanical resonator filters as are the traditional mechanical filter architectures to be pursued, here.

This chapter details the design and implementation of electronic filters based upon micromechanical resonators. Single resonator second-order bandpass filters are addressed first, with particular emphasis on noise performance and methods by which their bandwidths may be controlled. The discussion then proceeds to the design of higher order filters based upon spring-coupled micromechanical resonators, with emphasis on termination design, which will be seen to be a challenging prospect for micro-scale filters. A prototype, 455 kHz, 5-resonator filter is then summarized and measured results for Q-controlled filters are presented.

5.1 Single Microresonator Biquads

Single high-Q microresonator biquads may find applications as pilot-tone filters for FM or pulse-based communications, or for low-power frequency selection in analog speech recognition systems. With comparatively simple designs, such resonator-based filters can easily outperform filters built in traditional integrated technologies in terms of selectivity and possibly center frequency. The high selectivity of vacuum-operated single micromechanical resonators is explicitly demonstrated by the measured spectrum presented in Fig. 2.7, where the measured quality factor is 50,000. With this degree of selectivity, and given a reasonable tuning range, such a device could easily be used to lock onto and separate a stable pilot-tone signal from information signals surrounding it.

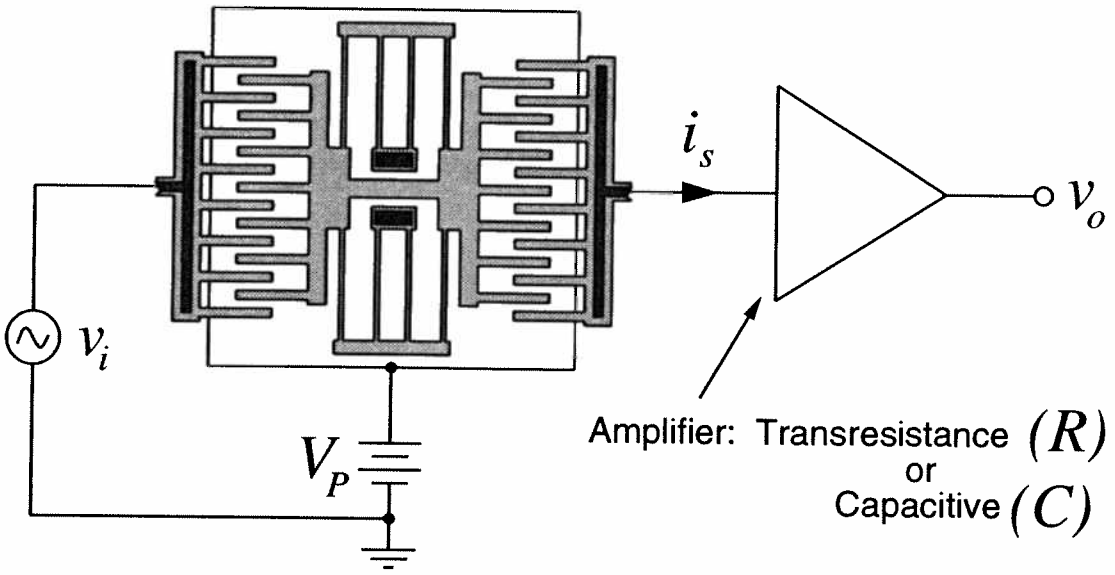

Fig. 5.1: Circuit schematic for a single-microresonator, open-loop, biquad filter. Here, a folded-beam, comb-driven resonator is used. The sense amplifier may be transresistance or capacitive.

In many cases, however, a filter with $Q = 50{,}000$ is too selective, and methods by which the Q may be reduced are required. Thus, after a detailed discussion of the design and performance of single resonator filters, the following sections address electronic methods by which the Q of microresonators may be adjusted.

5.1.1 Open-Loop μResonator Filters

Figure 5.1 shows the schematic for a single microresonator, open-loop, biquad, filter. In Fig. 5.1, the sense amplifier can be either transresistance or capacitive, and the comments of Section 2.7 apply here, as well. Referring then to Fig. 2.33, when capacitive detection is used, the voltage output represents the position of the resonator, and the transfer function is that of a low-pass biquad stage:

$$\frac{v_o}{v_i}(s) = \frac{\omega_o}{QC}\frac{1}{s^2 + \left(\frac{\omega_o}{Q}\right)s + \omega_o^2} \tag{5.1}$$

For the case of resistive detection, as shown in Fig. 2.34, the velocity of the resonator is detected, and the transfer function is that of a bandpass biquad:

$$\frac{v_o}{v_i}(s) = \frac{\omega_o}{QR}\frac{s}{s^2 + \left(\frac{\omega_o}{Q}\right)s + \omega_o^2} \tag{5.2}$$

Figures 2.33 and 2.34 depict filter transfer functions for the cases of relatively low Q filters. For pilot-tone applications, where Q values in the thousands will most likely be utilized, the magnitude transfer functions for both filters will be largely similar near resonance, with the only difference being that the capacitively detected frequency spectrum will be asymmetrical. The phase versus frequency plots (also shown in Fig. 1.2), however, will differ by 90°. In addition, some applications require absolute symmetry of filters. For these applications, capacitive detection can be used only if two stage amplifiers are used, both shifting the signal phase by 90°.

Resistive versus capacitive sensing of resonator motion was discussed at length in Chapter 2. Each has its own advantages for different applications. As will be shown in this chapter, many of the filter applications utilizing resonators utilize positive or negative feedback architectures, in which the detection electronics is required to provide an output signal that is either in phase, or 180° out of phase with the resonator input signal. Although this could be achieved using capacitive detection, followed by a 90° phase shifting second stage, it is more directly implemented using resistive detection methods. In addition, automatic gain control strategies are easier to implement resistively, than capacitively. For these reasons, most of the electronics used in this work are transresistance amplifiers, rather than integrators.

5.1.1.1 Noise in Single Resonator Filters

The equivalent voltage and current noise generators will be now be determined for an open-loop single resonator filter. For this purpose, the schematic for a general single resonator filter with sense electronics and appropriate noise generators is shown in Fig. 5.2. In this figure, $\overline{v_{ia}^2}$ and $\overline{i_{ia}^2}$ are the equivalent voltage and current noise generators at the input of the amplifier (which has input impedance z_{ia}), and $\overline{v_{R_x}^2}$ is voltage noise generator arising from thermal (Brownian) noise in the microresonator.

Using Fig. 5.2, shorting inputs and equating the output noises of the circuits in (a) and (b), the input voltage noise generator is found to be

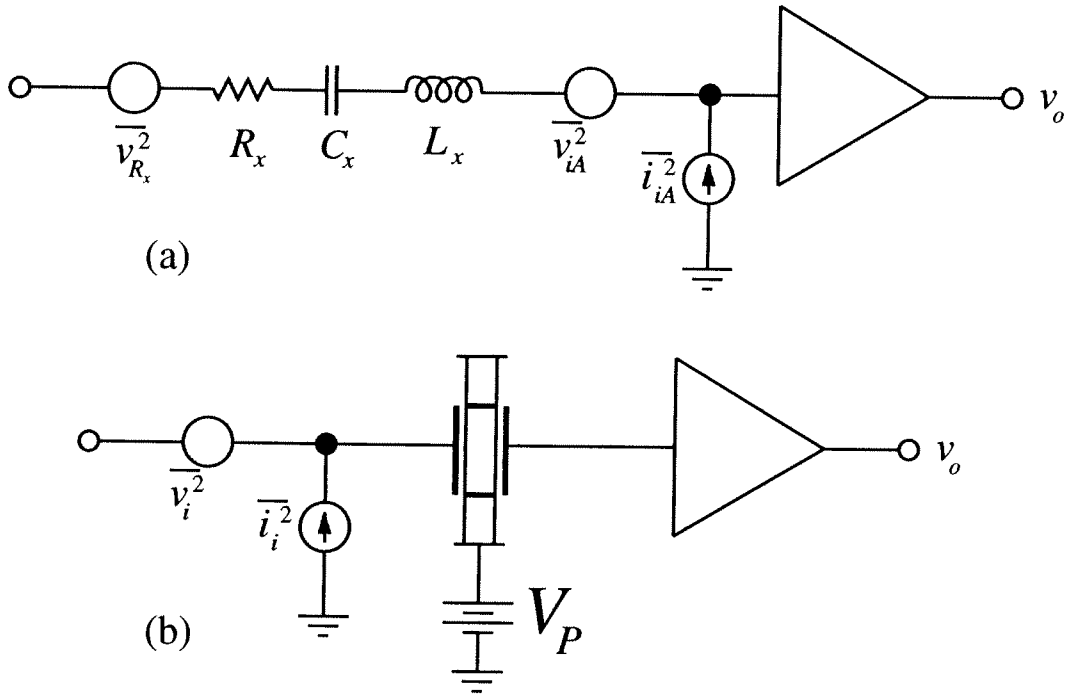

Fig. 5.2: Equivalent noise diagrams for the filter circuit schematic of Fig. 5.1. (a) Detailed noise diagram. (b) Noise diagram with noise referred to the input. Here, the micromechanical resonator circuit element diagram is used. The correspondence between this circuit element and an actual two-port resonator should be obvious.

$$\overline{v_i^2} = \overline{v_{R_x}^2} + \overline{v_{iA}^2} + \overline{i_{iA}^2} R_x^2 . \tag{5.3}$$

Note that if the series resistance of the microresonator is large (which is the case for today's micromachined designs), the input voltage noise generator will be dominated by this resistance. Equivalently, the input noise voltage of a single resonator filter is dominated by the Brownian motion noise of the resonator. Once again, the importance of reducing the equivalent series motional resistance of a micromechanical resonator is paramount.

Open circuiting inputs and equating outputs, the input current noise generator is found to be

$$\overline{i_i^2} = \overline{i_{iA}^2} . \tag{5.4}$$

Thus, the current noise generator consists of only amplifier current noise.

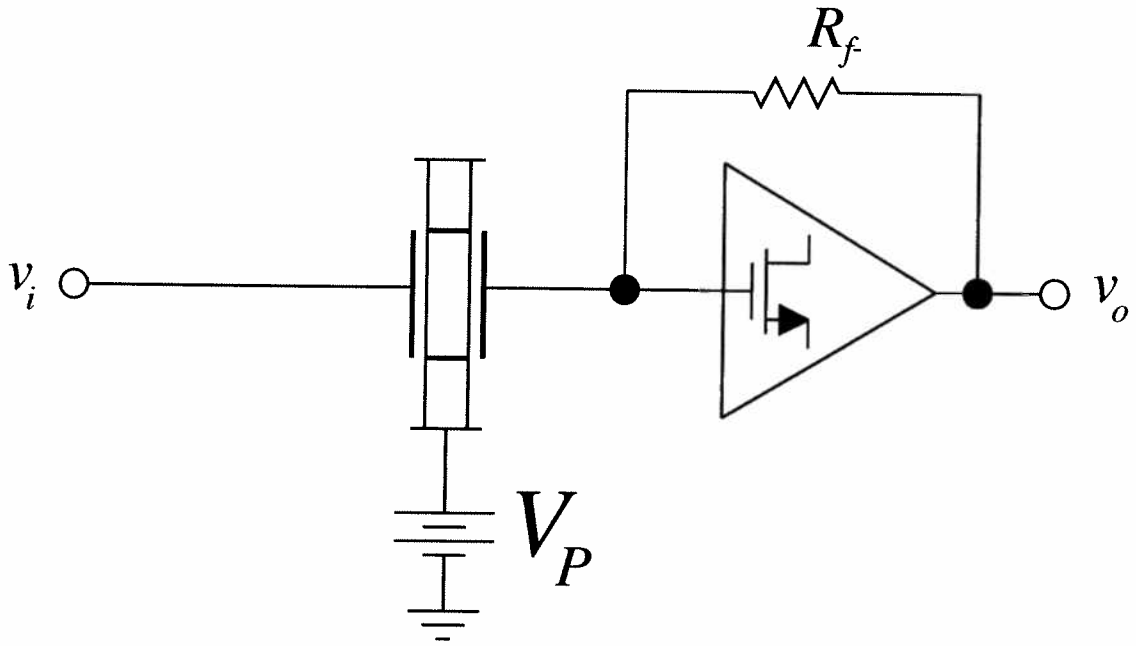

Fig. 5.3: Single-microresonator filter utilizing a transresistance sense amplifier.

In communications, noise figure is a common figure of merit by which amplifiers may be compared. A general equation for noise figure is

$$F = 1 + \frac{\overline{v_i^2}}{4kTR_s\Delta f} + \frac{\overline{i_i^2}}{4kT\frac{1}{R_s}\Delta f}. \tag{5.5}$$

In the following sections, the input noise generators and noise figures for specific single resonator filters will be derived and evaluated for typical resistive and capacitive detection techniques.

5.1.1.2 Noise in Single Resonator Resistively Sensed Filters

For this section, we take as an example, the transresistance amplifier of Section 4.2, which is shown in a single-resonator filter configuration in Fig. 5.3. The equivalent feedback loading diagrams with noise generators, which in general can be used to derive the equivalent input noise generators for any feedback circuit [80], are shown in Fig. 5.4. The input voltage and current noise generators of at the input to M_1 of the imbedded amplifier are

$$\overline{v_{ia}^2} = \alpha\left[4kT\frac{2}{3}\frac{1}{g_m} + \frac{K_f}{WLC_{ox}f}\right]\Delta f \tag{5.6}$$

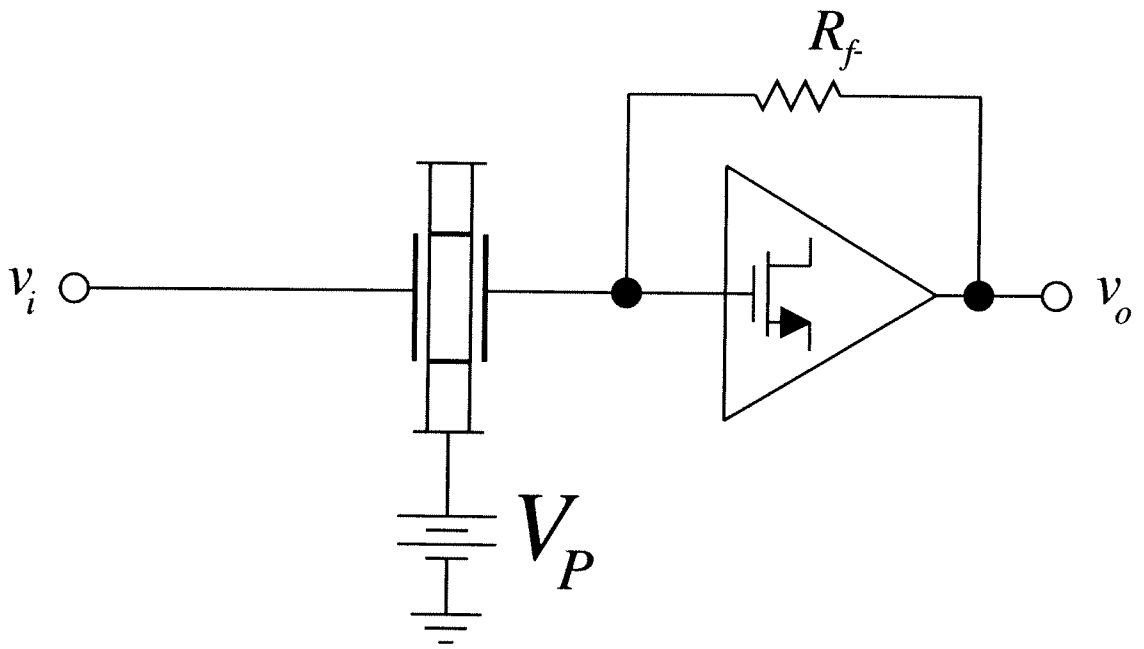

Fig. 5.4: Equivalent feedback loading diagrams with noise generators for the circuit of Fig. 5.3. In (a), noise is represented by individual noise generators for each element, whereas, in (b), the equivalent input referred noise generators are used.

$$\overline{i_{ia}^2} = 2qI_G\Delta f + \omega^2 C_{gs}^2\left[4kT\frac{2}{3}\frac{\alpha}{g_m} + \frac{\alpha K_f}{WLC_{ox}f}\right]\Delta f \tag{5.7}$$

where the constant α has been introduced to model contributions to input voltage noise from the input MOS transistor and the biasing and load transistors. (α is not necessarily 4 anymore, since there may not be a requirement for 50% duty cycle in this design.)

It is insightful to evaluate the voltage and current noise generators at intermediate frequencies, where $1/f, f$, and f^2 noise may be neglected. Thus, shorting inputs and equating outputs of the circuits in Fig. 5.4, we obtain the input voltage noise generator:

$$\begin{aligned}\overline{v_i^2} &= \left(1+\frac{R_x}{R_f}\right)^2\overline{v_{ia}^2} + \overline{i_{ia}^2}R_x^2 + \left(\frac{R_x}{R_f}\right)^2\overline{v_f^2} + \overline{v_{R_x}^2} \\ &= \left(1+\frac{R_x}{R_f}\right)^2 4kT\frac{2}{3}\frac{\alpha}{g_m}\Delta f + 4kT\frac{R_x^2}{R_f}\Delta f + 4kTR_x\Delta f\end{aligned} \tag{5.8}$$

where $1/f$, f, and f^2 noise has been neglected, and $\overline{i_{ia}^2} = 0$ for an MOS transistor input at these intermediate frequencies. Opening inputs and equating outputs, the equivalent current noise generator, again neglecting $1/f$, f, and f^2 noise, is found to be

$$\begin{aligned} \overline{i_i^2} &= \overline{i_{ia}^2} + \overline{i_f} + \frac{\overline{v_{ia}^2}}{R_f^2} \\ &= 4kT\frac{1}{R_f}\Delta f + 4kT\frac{2}{3}\frac{\alpha}{g_m R_f^2}\Delta f \end{aligned} \tag{5.9}$$

Again, in present-day capacitively transduced resonators, the series resistance is large, on the order of 100 kΩ. For this case, the voltage noise generator as given by Eq. (5.8) is dominated by Brownian noise from the resonator. To reduce the value of the voltage noise generator, R_x must be reduced, and this again emphasizes the importance of reducing the series motional resistance.

Using (5.8) and (5.9) in Eq. (5.5), the noise figure is given by

$$F = 1 + \left(1 + \frac{R_x}{R_f}\right)^2 \frac{2}{3}\frac{\alpha}{g_m R_s} + \frac{R_x}{R_s} + \frac{R_x^2}{R_f R_s} + \frac{R_s}{R_f} + \frac{2}{3}\frac{R_s}{R_f^2}\frac{\alpha}{g_m} \tag{5.10}$$

Equation (5.10) is plotted as a function of source resistance for an assumed microresonator series resistance of $R_x = 100$ kΩ in Fig. 5.5. From this plot we see that the noise figure is minimized when the source resistance has a value close to R_x.

For the case of single resonator micromechanical filters, the input-referred voltage noise predicted by Eq (5.8) will still be quite small, despite the large thermal noise contribution from the resonator. This is because the effective noise bandwidth of a high-Q resonator is extremely small, and this offsets the large value of R_x. Thus, these filters are still relatively quiet, and quite usable in many communication systems (as say, pilot-tone filters). For larger bandwidth filters, however, the series resistance will have to be dealt with. Larger bandwidth filters are covered later in this chapter.

5.1.1.3 Noise in Single Resonator Capacitively Sensed Filters

For capacitively sensed microresonators, the noise bandwidth is similar to that for resistive detection only for very high-Q situations. If the Q is low, then the noise bandwidth includes

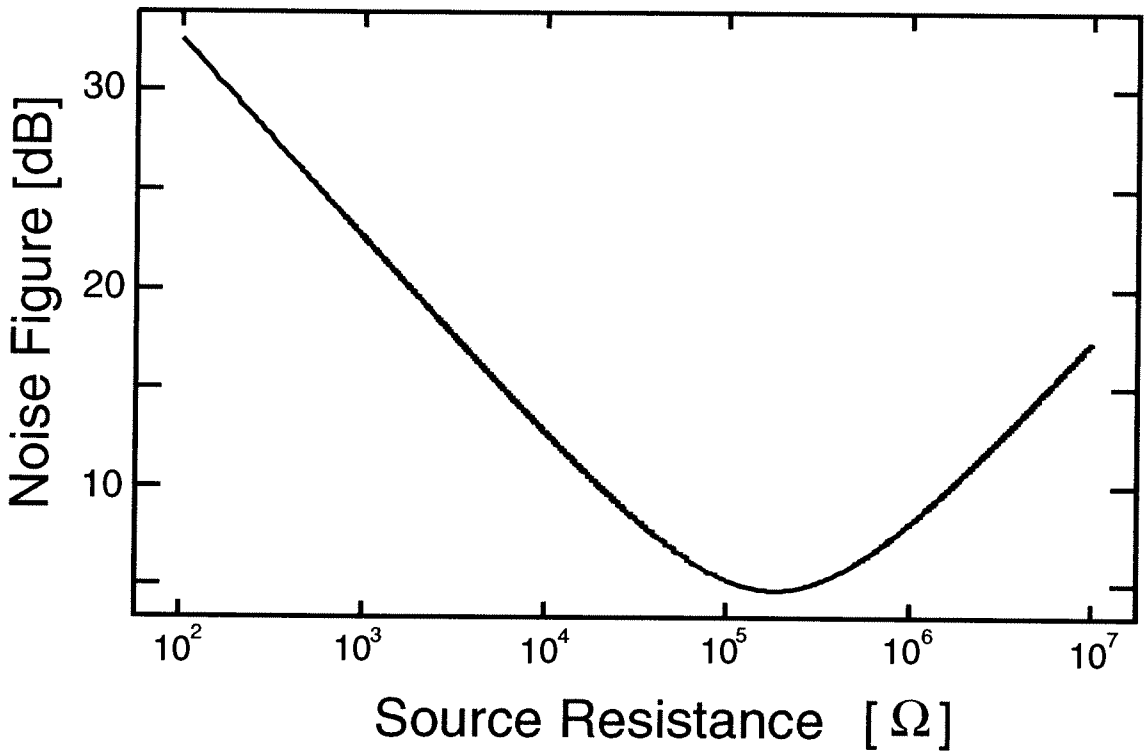

Fig. 5.5: Plot of noise figure versus source resistance for the circuit of Fig. 5.3 with $R_x = 100\ \text{k}\Omega$.

low frequencies as well, and the total noise power will be increased, especially when $1/f$ noise components become involved. Since this section focuses upon high-Q single resonator filters, the noise bandwidth will be assumed equal to that for resistively detected filters.

For this case, the input noise of capacitively detected single resonator filters may be found in a similar manner to that in Section 5.1.1.2. A schematic for a single resonator filter using a capacitive amplifier for detection (with a diode biasing device) is shown in Fig. 5.6, along with applicable noise generators. The reverse-biased diode in Fig. 5.6 is required to bias the amplifier input node, since it would otherwise be floating. As a noise source, the reverse-biased diode is similar to a huge resistor and will be modelled as such. (Any other noise sources associated with the diode are neglected in this analysis.) The amplifier noise generators will depend upon the specific amplifier design. For simplicity, and for consistency with the transresistance amplifier analysis in Section 5.1.1.2, we assume a capacitive amplifier with MOS inputs and with input noise characteristics identical to that of the (voltage gain) amplifier used for the transresistance amplifier. With this assumption, the amplifier noise generators are also given by Eqs. (5.6) and (5.7).

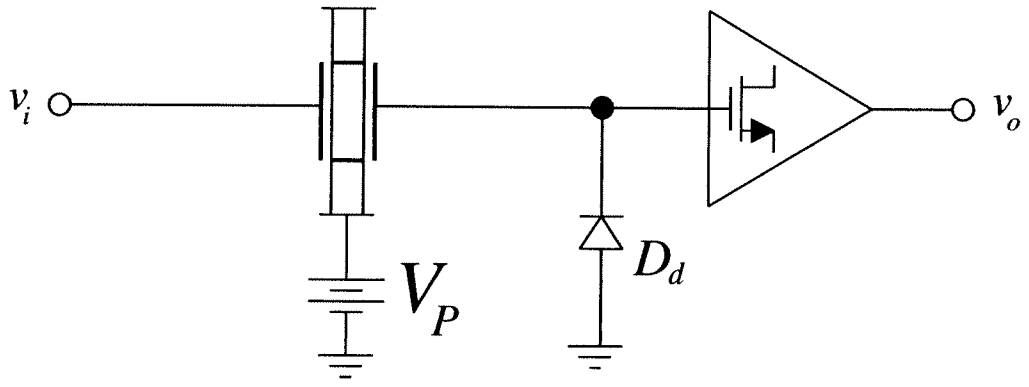

Fig. 5.6: Schematic of a single resonator filter using a capacitive amplifier for detection.

Note that the schematic for the capacitively sensed single-resonator filter is identical to the feedback loading diagram for the transresistance amplifier, except for element values. Thus, the equivalent input noise generators and noise figure F can be written by inspection:

$$\overline{v_i^2} = \left(1+\frac{R_x}{R_d}\right)^2 4kT\frac{2}{3}\frac{\alpha}{g_m}\Delta f + 4kT\frac{R_x^2}{R_d}\Delta f + 4kTR_x\Delta f \tag{5.11}$$

$$\overline{i_i^2} = 4kT\frac{1}{R_d}\Delta f + 4kT\frac{2}{3}\frac{\alpha}{g_m R_d}\Delta f \tag{5.12}$$

$$F = 1+\left(1+\frac{R_x}{R_d}\right)^2\frac{2}{3}\frac{\alpha}{g_m R_s} + \frac{R_x}{R_s} + \frac{R_x^2}{R_d R_s} + \frac{R_s}{R_d} + \frac{2}{3}\frac{R_s}{R_d^2}\frac{\alpha}{g_m} \tag{5.13}$$

The only difference between Eqs. (5.11) - (5.12) and Eqs. (5.8) - (5.9) is the replacement of the feedback resistor R_f with the reverse-biased diode resistance R_d. Normally, $R_d \gg R_f$, so that better noise performance should be achievable when using capacitive detection, for situations where Brownian motion noise from the resonator does not dominate. A situation where Brownian noise does not dominate is presently difficult to achieve, but is conceivable in more advanced technologies where resonator series motional resistance R_x may be reduced. Even when R_x is small enough, this noise advantage must be weighed against design complexity, which increases due to the requirement for 90° phase-shifters (as will be seen). For these reasons, the electronics of this work are transresistance.

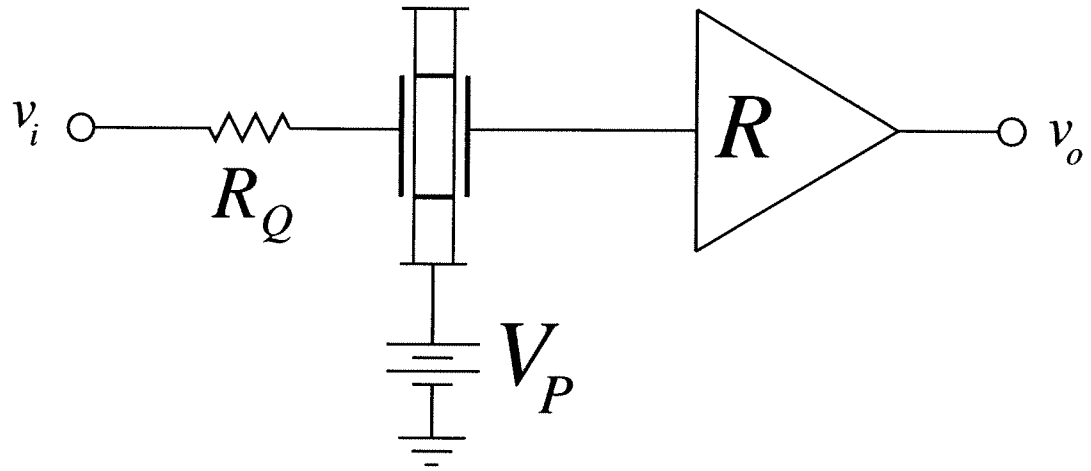

Fig. 5.7: Method for controlling the Q of a single resonator filter by placing a resistor in series with the resonator. (not recommended)

5.1.2 Q-Control of Micromechanical Resonators

For many applications, such as RF filters, the quality factor of a micromechanical resonator is too large. For example, at 100 MHz, the required quality factor to achieve a 3dB-down bandwidth of 200 kHz (used in broadcast FM radio) is only 500. This value is well out of the range of transistor-based integrated technologies, but may well be within the range of the micromechanical filters of this work. However, if the Q of a microresonator is larger than 500 at 100 MHz, some method for reduction of resonator Q must be used. This section discusses several methods by which this problem may be addressed.

5.1.2.1 Passive Q-control

The simplest way to control resonator Q is to place a resistor in series with the resonator, as shown in Fig. 5.7, which shows a single resonator filter using this Q-control strategy. The transfer function for the filter of Fig. 5.7 is found to be

$$\frac{v_o}{v_i}(j\omega) = \frac{R}{R_x + R_Q} \frac{1}{1 + 2jQ'\left(\frac{\omega}{\omega_o} - \frac{\omega_o}{\omega}\right)} \tag{5.14}$$

where

$$Q' = \frac{\omega_o L_z}{R_x + R_Q} = \frac{\omega_o L_x}{R_x} \frac{1}{1 + (R_Q/R_x)} = \frac{Q}{1 + (R_Q/R_x)} \tag{5.15}$$

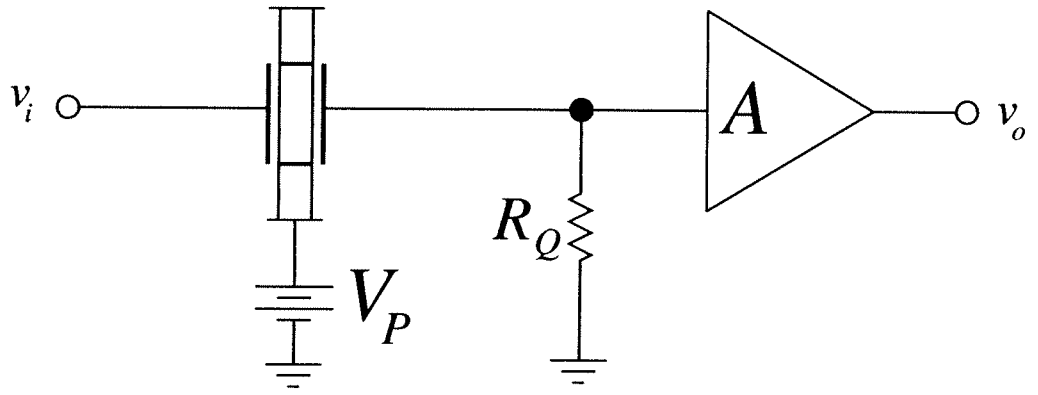

Fig. 5.8: Method for controlling the Q of a single resonator micromechanical filter by placing a resistor in shunt with the output node and sensing with a buffer (voltage amplifier).

One disadvantage of this technique is immediately apparent from Eq. (5.14): The gain is directly dependent upon R_Q, and thus, is dependent upon the controlled value of quality factor, Q'. Another equally significant drawback is that the input noise voltage generator is now dominated by $R_{eff} = R_x + R_Q$, which can be much larger than the original R_x. Specifically, to reduce the quality factor by a factor a, the value of R_Q should be

$$R_Q = (a-1)R_x, \tag{5.16}$$

which means the series resistance-dominated equivalent input voltage noise power will be (a - 1) times larger.

Fortunately, other Q-control schemes are available which avoid both of the above problems. One such configuration is shown in Fig. 5.8, where now the Q-controlling resistor R_Q is placed in shunt with the resonator output, and the signal is detected by a buffer with gain A. The transfer function for this filter is now given by

$$\begin{aligned}\frac{v_o}{v_i}(j\omega) &= \frac{AR_Q v_i}{R_Q + R_x(1 + 2jQ(\omega/\omega_o - \omega_o/\omega))} \\ &= \frac{AR_Q v_i}{R_Q + R_x + 2jR_xQ(\omega/\omega_o - \omega_o/\omega)} \\ &= \frac{R_Q}{R_Q + R_x}\frac{Av_i}{1 + 2jQ'(\omega/\omega_o - \omega_o/\omega)} \approx \frac{Av_i}{1 + 2jQ'(\omega/\omega_o - \omega_o/\omega)}\end{aligned} \tag{5.17}$$

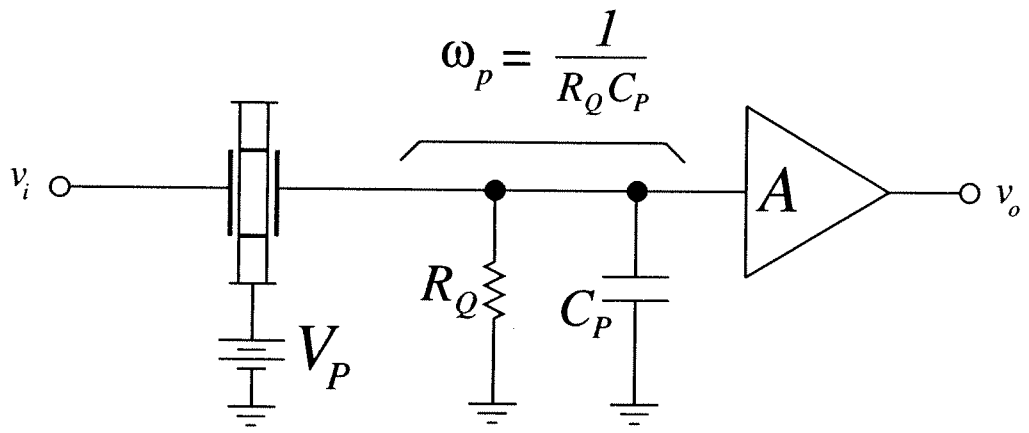

Fig. 5.9: Schematic showing the problem with parasitic capacitance in parallel with the shunt Q-controlling resistor in the implementation of Fig. 5.8.

where

$$Q' = \frac{Q}{1 + (R_Q/R_x)}, \tag{5.18}$$

and the last form of Eq. (5.17) applies for $R_Q \gg R_x$. Note that for large values of R_Q, which will usually be the case, the gain of this filter at resonance is the gain of the voltage-to-voltage amplifier A.

Furthermore, the noise schematic for this configuration is identical in form to that in Fig. 5.3. Thus, the equivalent input noise generators may be written as

$$\overline{v_i^2} = \left(1 + \frac{R_x}{R_Q}\right)^2 \overline{v_{ia}^2} + \overline{i_{ia}^2} R_x^2 + \left(\frac{R_x}{R_Q}\right)^2 \overline{v_f^2} + \overline{v_{R_x}^2} \tag{5.19}$$

$$\overline{i_i^2} = \overline{i_{ia}^2} + \overline{i_f} + \frac{\overline{v_{ia}^2}}{R_Q}, \tag{5.20}$$

which are much smaller than those for the configuration of Fig. 5.7.

Thus, the Q-control scheme of Fig. 5.8 outperforms that of Fig. 5.7 in both designability (gain-setting) and noise. However, one drawback against the Q-control scheme of Fig. 5.8 is depicted in Fig. 5.9, where the parasitic capacitance at the resonator output node, from the resonator and amplifier, are included. This capacitance is usually quite small, but can be significant if R_Q

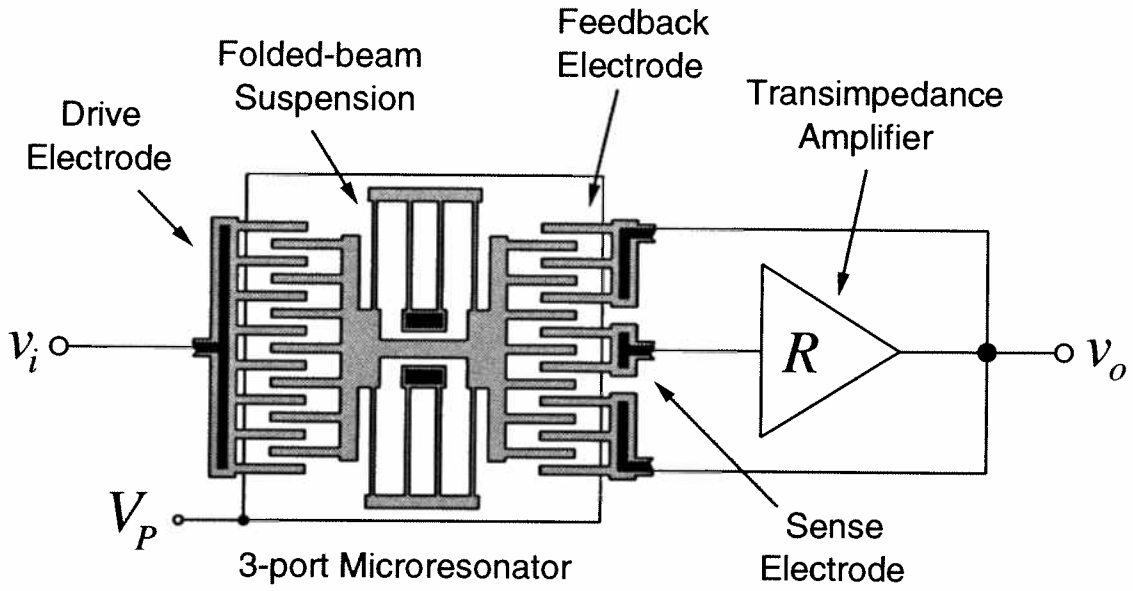

Fig. 5.10: Schematic showing an implementation of active Q-control for a three-port micromechanical resonator.

is large, which will usually be the case for the present high series resistance resonators. As will be seen shortly, the parallel combination of a huge R_Q and parasitic capacitance results in phase shifts large enough to heavily distort the passbands of higher order filters.

5.1.2.2 Three-Port Active Q-Control

To minimize the phase shift problem described above, an equivalent effective resistance R_Q must be implemented without using a large amount of "real" resistance. One way to achieve this is to realize the effective R_Q actively, via the circuit schematic shown in Fig. 5.10. Here, a three-port micromechanical resonator is shown, where the output current from the sense port is amplified by a transresistance amplifier to a voltage, which is then directed back to a feedback port situated on the same side as the output port. This feedback voltage produces a force which directly opposes the input force at resonance and provides phased opposition to the input force off resonance. In effect, the microresonator sums the input and negative feedback signals, closing a negative feedback loop which reduces its own original Q.

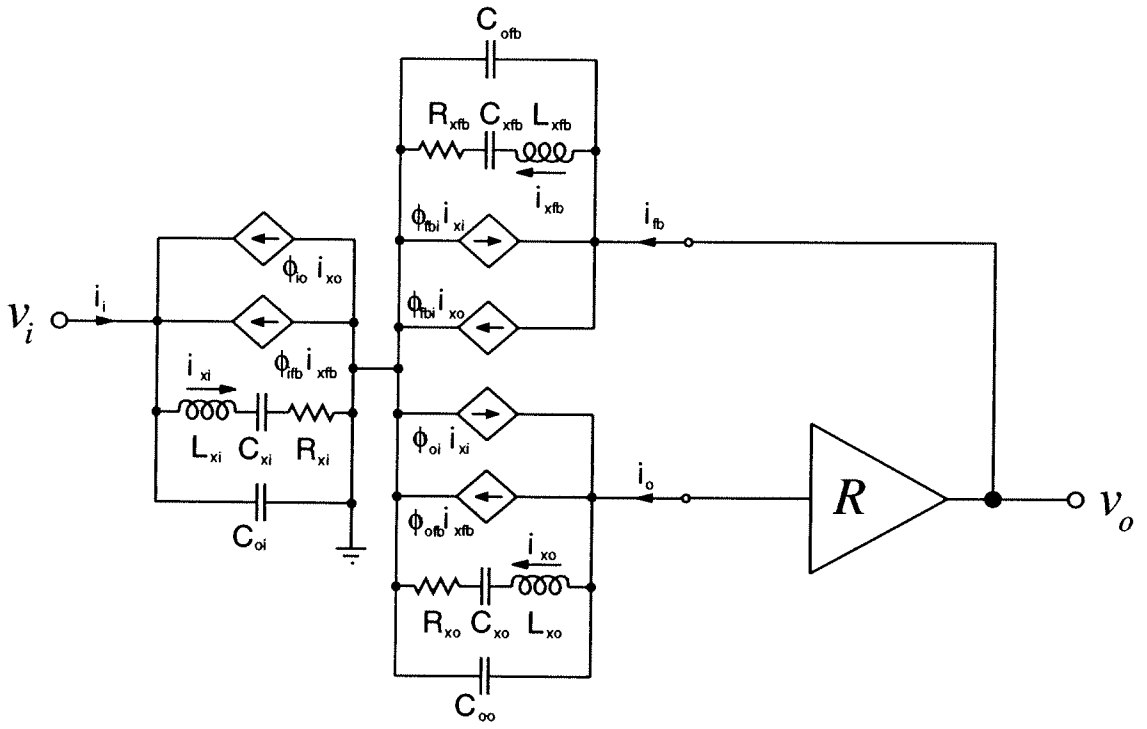

Fig. 5.11: Equivalent circuit for the active Q-control circuit of Fig. 5.10.

To derive the transfer function for the circuit of Fig. 5.10, one may use its equivalent small signal circuit, presented in Fig. 5.11. Here, the three -port resonator has been replaced with the equivalent small signal circuit derived in Section 2.5.3.

To analyze this circuit, we first write the output voltage v_o in terms of currents input to the transresistance amplifier:

$$v_o = (-i_{xo} - \phi_{ofb} i_{xfb} + \phi_{oi} i_{xi})\, R = (-\phi_{ofb} i_{xfb} + \phi_{oi} i_{xi})\, R \tag{5.21}$$

where the fact that i_{xo} is effectively grounded out is used. (The transresistance amplifier is assumed ideal, with input resistance equal to zero.) Referring to Fig. 5.11, the value for i_{xi} is given by

$$i_{xi} = \frac{v_i}{R_{xi}} \frac{1}{1 + 2jQ\,(\omega/\omega_o - \omega_o/\omega)}\,, \tag{5.22}$$

and i_{xfb} is given by

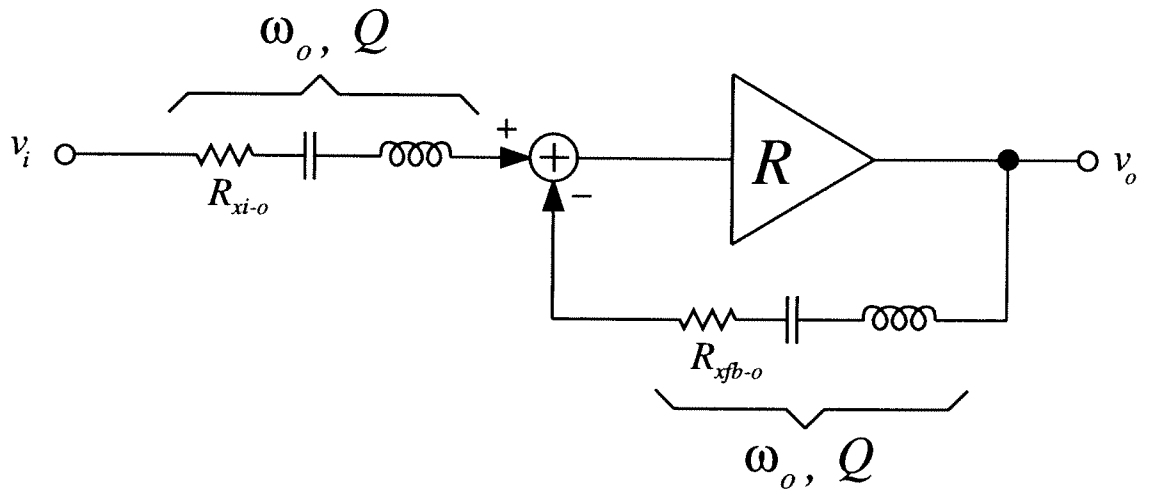

Fig. 5.12: Simplified alternative equivalent circuit for the filter of Fig. 5.10.

$$i_{xfb} = \frac{v_o}{R_{xfb}} \frac{1}{1 + 2jQ\,(\omega/\omega_o - \omega_o/\omega)}. \tag{5.23}$$

Using Eqs. (5.22) and (5.23) in Eq. (5.21), the transfer function is found to be:

$$\begin{aligned} v_o &= \frac{\phi_{oi}R}{R_{xi}} \frac{v_i}{1 + 2jQ\,(\omega/\omega_o - \omega_o/\omega)} - \frac{\phi_{ofb}R}{R_{xfb}} \frac{v_o}{1 + 2jQ\,(\omega/\omega_o - \omega_o/\omega)} \\ v_o\left(1 + \frac{\phi_{ofb}R}{R_{xfb}}\right)\left(1 + 2jQ'\left(\frac{\omega}{\omega_o} - \frac{\omega_o}{\omega}\right)\right) &= \frac{\phi_{oi}R}{R_{xi}} v_i \\ \frac{v_o}{v_i}(j\omega) &\approx \frac{R_{xfb}}{\phi_{ofb}} \frac{\phi_{oi}}{R_{xi}} \frac{1}{1 + 2jQ'\,(\omega/\omega_o - \omega_o/\omega)} \end{aligned} \tag{5.24}$$

where

$$Q' = \frac{Q}{1 + (\phi_{ofb}R)/R_{xfb}}. \tag{5.25}$$

For the final form of Eq. (5.24), it is assumed that the loop gain, $A_l = \dfrac{\phi_{ofb}R}{R_{xfb}}$, is large.

From a conceptual point of view, and to explicitly show this resonator system as a traditional feedback circuit, Fig. 5.11 can be simplified to the circuit shown in Fig. 5.12. Here, we introduce the effective input-to-output resistance, defined by

$$R_{xi\bullet o} = \frac{v_i}{i_o}, \tag{5.26}$$

and the effective feedback -to-output resistance, defined by

$$R_{xfb\bullet o} = \frac{v_{fb}}{i_o}, \tag{5.27}$$

where in both Eqs. (5.26) and (5.27) all ports in resonator equivalent circuit in Fig. 5.11 are grounded except the port which takes the drive signal (either v_i or v_{fb}).

To find an expression for $R_{xi\bullet o}$, the resonator equivalent circuit of Fig. 5.11 is first driven at the input port i with all other ports grounded. At resonance, we have

$$i_o = \phi_{oi} i_{xi} \quad \text{and} \quad i_{xi} = \frac{v_i}{R_{xi}}. \tag{5.28}$$

Applying (5.28) to (5.26) yields

$$R_{xi\bullet o} = \frac{R_{xi}}{\phi_{oi}}. \tag{5.29}$$

A similar analysis yields

$$R_{xfb\bullet o} = \frac{R_{xfb}}{\phi_{ofb}}. \tag{5.30}$$

Through feedback analysis of Fig. 5.12, the transfer function is found to be:

$$\begin{aligned} \frac{v_o}{v_i}(j\omega) &= \frac{(R/R_{xi\bullet o})}{1+(R/R_{xfb\bullet o})} \frac{1}{1+2jQ'(\omega/\omega_o - \omega_o/\omega)} \\ &\approx \frac{R_{xfb\bullet o}}{R_{xi\bullet o}} \frac{1}{1+2jQ'(\omega/\omega_o - \omega_o/\omega)} \end{aligned} \tag{5.31}$$

where

$$Q' = \frac{Q}{1+(R/R_{xfb\bullet o})}, \tag{5.32}$$

which is identical to Eq. (5.24).

5.1.2.2.1 Active *Q*-Control Stage Gain

The gain at resonance can be expanded from either Eq. (5.24) or (5.32) using the equivalent circuit element values summarized in Fig. 5.12 as follows:

$$\left.\frac{v_o}{v_i}(j\omega)\right|_{\omega=\omega_o} = \frac{R_{xfb\bullet o}}{R_{xi\bullet o}} = \frac{R_{xfb}}{\phi_{ofb}}\frac{\phi_{oi}}{R_{xi}} = \frac{(\partial C/\partial x)_i}{(\partial C/\partial x)_{fb}} \tag{5.33}$$

Thus, the gain is determined by resonator geometry and is independent of variables which determine the controlled Q. Equation (5.33) applies to any general three-port resonator (where the ports could be parallel-plate-transduced, comb-transduced, etc...) in the configuration of Fig. 5.10. For the specific case of a microresonator where all ports consist of comb transducers, (5.33) reduces to

$$\left.\frac{v_o}{v_i}(j\omega)\right|_{\omega=\omega_o} = \frac{N_i}{N_{fb}}, \tag{5.34}$$

where N_i and N_{fb} are the number of input and feedback fingers, respectively. (Note that Eq. (5.34) assumes identical finger gaps and thicknesses for both ports.) The fact that the gain of a Q-controlled, three-port, comb-transduced micoresonator is determined by a ratioed quantity is well suited to integrated manufacturing, where absolute values are difficult to achieve, but ratioed quantities can be implemented with 0.1% accuracy. The accuracy limit for the gain is largely determined by the matching tolerances of finger-to-finger capacitance. Since many fingers are usually present at each port, statistical mismatches are expected to average out. Systematic mismatches, however, may not average out.

5.1.2.2.1 Noise in Active *Q*-Control

The equivalent input noise generators for the active Q-control configuration of Fig. 5.10 are now derived. For this purpose, the equivalent noise diagram showing appropriate voltage and current noise generators is presented in Fig. 5.13. Note in Fig. 5.13 that of the three resistors associated with the equivalent circuit for the three-port microresonator, only one of these is given a noise generator, in this case, R_{xi}. One, and only one, noise generator is required, because the equivalent circuit is structured such that the current-controlled current sources will distribute the noise proportionately to all other ports. The resistors at other ports (in this case, R_{xo} and R_{xfb}) are purely

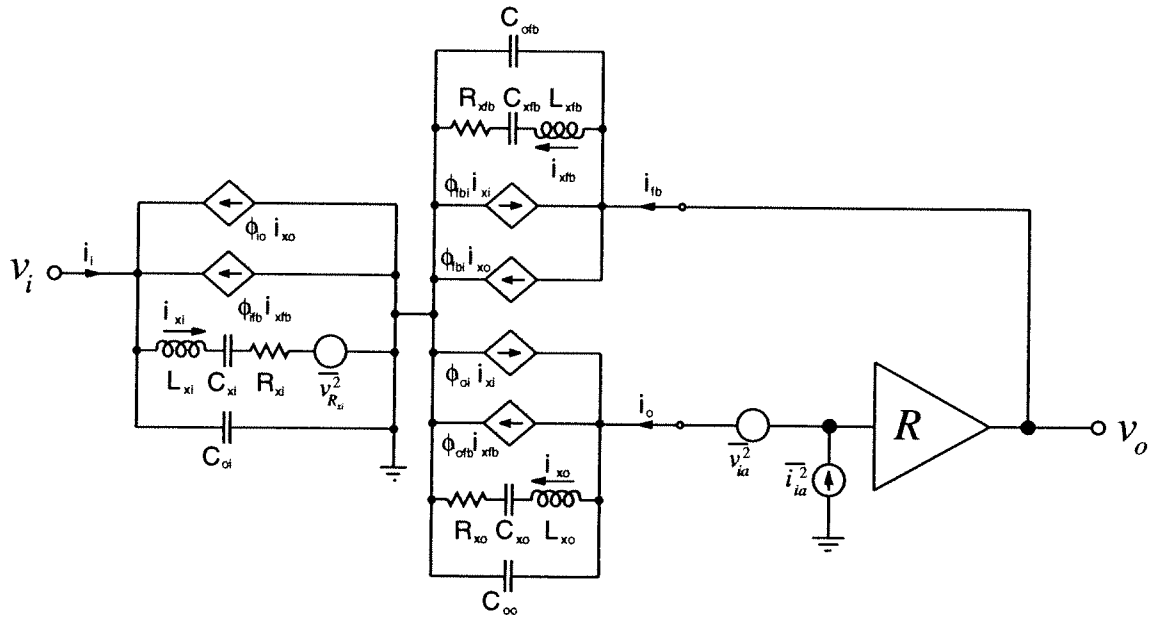

Fig. 5.13: Equivalent noise diagram for the active Q-controlled resonator of Fig. 5.10, showing appropriate voltage and current noise generators.

functional, and do not generate noise. Note that the choice of R_{xi} as the noise generating resistance is purely arbitrary; either one of R_{xo} or R_{xfb} could have been chosen with the same results.

With this, we now proceed with the noise derivation, addressing first the equivalent input noise voltage generator. Shorting inputs for both circuits in Fig. 5.13, the output voltages due to each noise generator can be found individually by shorting all other voltage sources and opening all other current sources. The rms output voltage is related to the $\overline{v_i^2}$ and $\overline{v_{R_{xi}}^2}$ generators through the transfer function, and can be written for each generator by inspection as follows:

$$\overline{v_i^2}: \qquad v_o = \frac{R_{xfb\bullet o}}{R_{xi\bullet o}} \frac{v_i}{1 + 2jQ'(\omega/\omega_o - \omega_o/\omega)} \tag{5.35}$$

$$\overline{v_{R_x}^2}: \qquad v_o = \frac{R_{xfb\bullet o}}{R_{xi\bullet o}} \frac{v_{R_x}}{1 + 2jQ'(\omega/\omega_o - \omega_o/\omega)} \tag{5.36}$$

The rms output voltage contribution from the $\overline{v_{ia}^2}$ noise generator can be obtained by first writing the expression for the output voltage in terms of output port currents (using Fig. 5.13):

$$v_o = (-i_{xo} - \phi_{ofb} i_{xfb} + \phi_{oi} i_{xi}) R = (-i_{xo} - \phi_{ofb} i_{xfb}) R, \tag{5.37}$$

where $i_{xi} = 0$ has been used. (This holds because the input is shorted as explained above.) The expressions for i_{xo} and i_{xfb} are obtained from Fig. 5.13 as

$$i_{xo} = -\frac{v_{ia}}{R_{xo}} \frac{1}{1 + 2jQ\,(\omega/\omega_o - \omega_o/\omega)} \tag{5.38}$$

$$i_{xfb} = \frac{v_o}{R_{xfb}} \frac{1}{1 + 2jQ\,(\omega/\omega_o - \omega_o/\omega)} \tag{5.39}$$

Inserting Eqs. (5.38) and (5.39) in (5.37) yields

$$\begin{aligned} v_o &= \frac{R}{R_{xo}} \frac{v_{ia}}{1 + 2jQ\,(\omega/\omega_o - \omega_o/\omega)} - \frac{\phi_{ofb} R}{R_{xfb}} \frac{v_o}{1 + 2jQ\,(\omega/\omega_o - \omega_o/\omega)} \\ v_o\left(1 + \frac{\phi_{ofb} R}{R_{xfb}}\right)&(1 + 2jQ'\,(\omega/\omega_o - \omega_o/\omega)) = \frac{R}{R_{xo}} v_{ia} \end{aligned} \tag{5.40}$$

which reduces to (assuming a large loop gain, i.e. $(R/R_{xfb\bullet o}) \gg 1$)

$$\overline{v_{ia}^2}: \qquad v_o = \frac{R_{xfb\bullet o}}{R_{xo}} \frac{v_{ia}}{1 + 2jQ'\,(\omega/\omega_o - \omega_o/\omega)} \tag{5.41}$$

A similar analysis leads to the expression for v_o in terms of the input current noise generator of the transresistance amplifier:

$$\overline{i_{ia}^2}: \qquad v_o = i_{ia} R_{xfb\bullet o} \frac{1 + 2jQ\,(\omega/\omega_o - \omega_o/\omega)}{1 + 2jQ'\,(\omega/\omega_o - \omega_o/\omega)} \tag{5.42}$$

Equating the output voltage for the circuit of Fig. 5.13 with that for an identical circuit with noise represented by input-referred noise generators (and with input shorted), and using Eqs. (5.35), (5.36), (5.41), and (5.42), the equivalent input-referred voltage noise generator for the actively Q-controlled, single-resonator filter is found to be

$$\overline{v_i^2} = \overline{v_{R_x}^2} + \overline{v_{ia}^2}\left(\frac{R_{xi\bullet o}}{R_{xo}}\right)^2 + \overline{i_{ia}^2} R_{xi\bullet o}^2 \left|1 + 2jQ\,(\omega/\omega_o - \omega_o/\omega)\right|^2 . \tag{5.43}$$

Again, if the resonator series motional resistance is large, $\overline{v_i^2}$ will be dominated by Brownian motion noise.

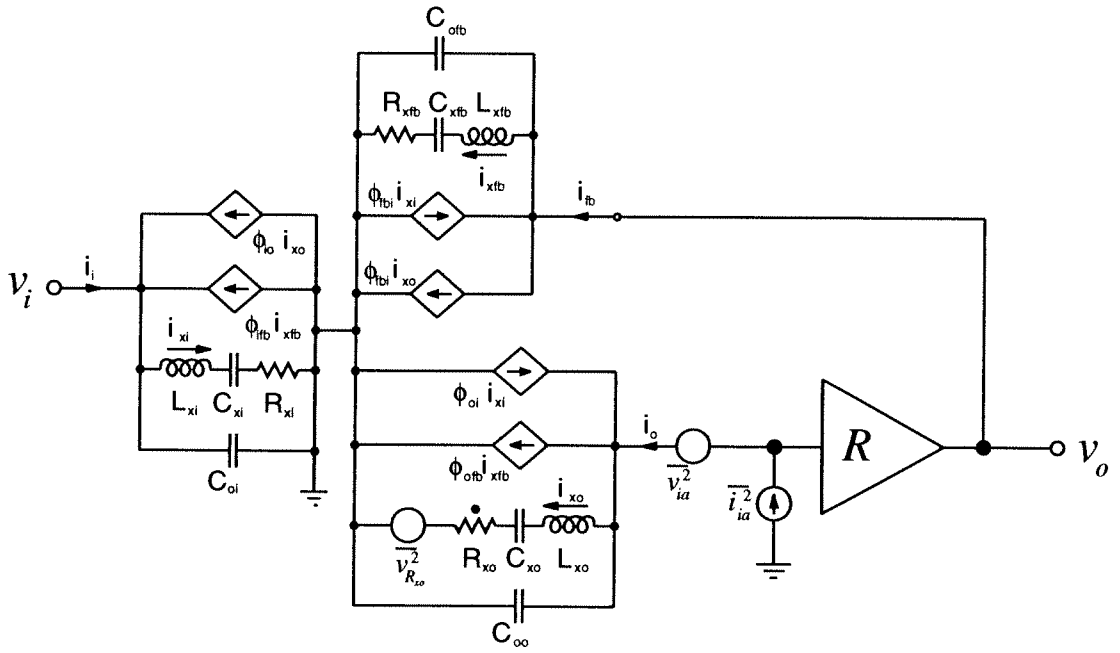

Fig. 5.14: Alternative equivalent noise diagram for the active Q-controlled resonator of Fig. 5.10, showing appropriate voltage and current noise generators. This time the noise in the resonator is represented by a noise voltage generator associated with R_{xo}.

To obtain the input current noise generator, the inputs of Fig. 5.13 are open circuited, and the output voltages due to each noise generator are again determined in a similar manner to the above. The noise contribution due to the micromechanical resonator is easily found when using the noise voltage generator associated with R_{xi}, $\overline{v_{R_{xi}}^2}$. Since the LCR branch of port 1 is open circuited, no current can arise from $\overline{v_{R_{xi}}^2}$, and thus, the contribution from this noise generator to v_o is zero.

It is instructive to verify this result by selecting another resistor in the three-port resonator equivalent circuit to serve as the noise generator. For this purpose, then, let us choose R_{xo}, with noise voltage generator $\overline{v_{R_{xo}}}$. Referring now to Fig. 5.14, we begin by writing the expression for the output voltage v_o in terms of currents at the output port:

$$v_o = (-i_{xo} - \phi_{ofb} i_{xfb} + \phi_{oi} i_{xi}) R = (-\phi_{ofb} i_{xfb} + \phi_{oi} i_{xi}) R \quad , \tag{5.44}$$

where $i_{xo} = 0$ has been used. From Fig. 5.14, the expression for the LCR branch current i_{xi} at the input port is given by

$$i_{xi} = \phi_{ifb} i_{xfb} - \phi_{io} i_{xo} = \phi_{ifb} i_{xfb}, \tag{5.45}$$

where $i_{xo} = 0$ has again been used. Inserting (5.45) in (5.44) yields

$$\begin{aligned} v_o &= (-\phi_{ofb} i_{xfb} + \phi_{oi}\phi_{ifb} i_{xfb}) R \\ &= (-\phi_{ofb} i_{xfb} + \phi_{ofb} i_{xfb}) R = 0 \end{aligned} \tag{5.46}$$

which agrees with the previous result. (i.e. the microresonator does not contribute to the input-referred current noise.)

Proceeding with similar analyses for each of the remaining noise generators, the output voltages in terms of each generator are summarized as follows:

$$\overline{i_{ia}^2}: \qquad v_o = i_{ia} R \tag{5.47}$$

$$\overline{v_{ia}^2}: \qquad \text{no output} \tag{5.48}$$

$$\overline{v_{R_{xo}}^2}: \qquad \text{no output} \tag{5.49}$$

Equating the total output voltage for the circuit of Fig. 5.14 (as given by the sum of Eqs. (5.47) through (5.49)) to that for an identical circuit with noise represented by input-referred noise generators (and input open), the input-referred equivalent current noise generator is given by

$$\overline{i_i^2} = \overline{\phi_{io}^2}\,\overline{i_{ia}^2}. \tag{5.50}$$

Thus, the input-referred current noise depends only upon the amplifier, and not on the microresonator.

To summarize, active Q-control performs similarly to the passive Q-control of Fig. 5.8, in both Q-reduction and noise performance. It, however, has the advantage of being able to realize a large Q-reduction factor without requiring a large physical resistor, which can introduce passband distorting phase-shifts when in parallel with parasitic capacitance. For example, to realize a transresistance of $R = 5\ \text{M}\Omega$, the amplifier of Fig. 4.4 in Chapter 4 requires only a 100 kΩ resistor with a second stage voltage gain of 50. Furthermore, since the input impedance of a properly designed transresistance amplifier is small, capacitance due to the resonator electrode overlap (effectively seen at the amplifier input) will have a much smaller effect on the phase-shift performance of the amplifier than on a large passive 5 MΩ resistor.

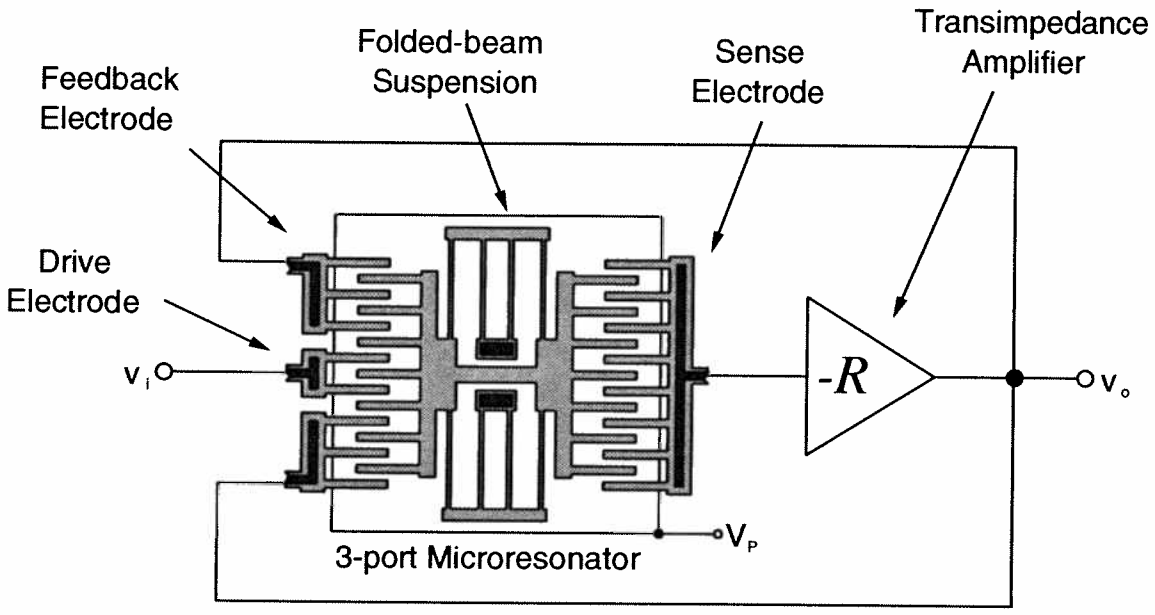

Fig. 5.15: Alternative implementation of active Q-control for a three-port micromechanical resonator. Here, an inverting transresistance amplifier is utilized.

5.1.2.2.1 Other Active Q-control Architectures (Two-Port Q-control)

The active Q-reduction architecture shown in Fig. 5.10 is only one of several possibilities. For example, if the position of the feedback electrodes is switched to the side of the drive electrode, then Q-reduction may be achieved by using an inverting transresistance amplifier, as shown in Fig. 5.15. Furthermore, in each of Figs. 5.10 and 5.15, the direction of the transresistance amplifier may be flipped without changing the amount of Q-reduction achieved. In other words, the feedback and sense electrodes may be interchanged without changing the final system Q'. (Note, however, that the total gain of the Q-reduction stage will change if the number of sense and feedback fingers differ; the gain, in fact, will become the reciprocal of the original gain.) In addition, active Q-reduction utilizing resonators with more than three-ports is also available, and in fact, sometimes advantageous.

A reduction in the number of ports required for Q-reduction is also feasible. Figure 5.16 shows the schematic for Q-reduction of a two-port micromechanical resonator, where now a summing amplifier is used to sum feedback and input signals. The transfer function for the Q-control scheme of Fig. 5.16 is

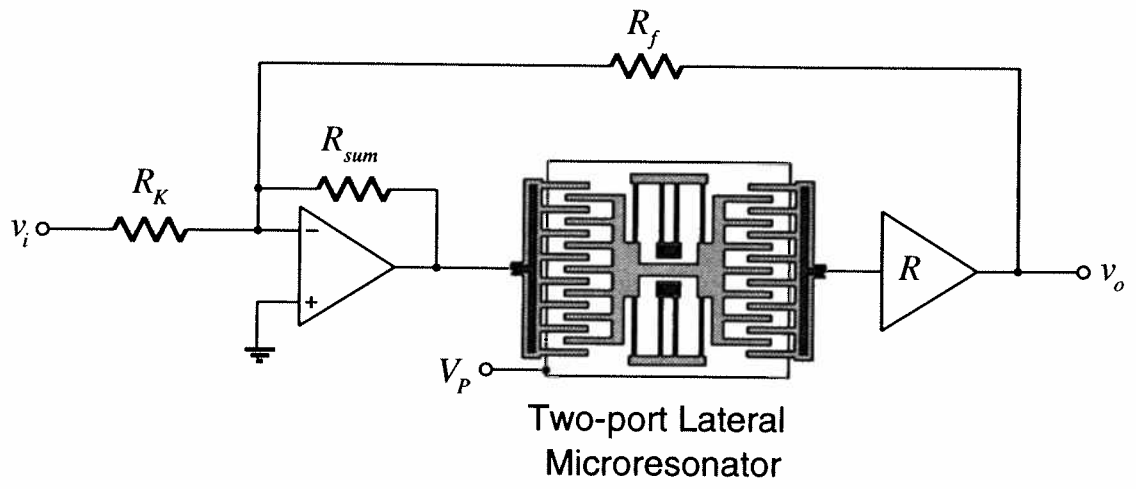

Fig. 5.16: An implementation of active Q-control for a two-port micromechanical resonator.

$$v_o = \frac{\frac{R_{sum}}{R_K}\frac{R}{R_x}}{1+\frac{R_{sum}}{R_Q}\frac{R}{R_x}} \frac{v_i}{1+2jQ'(\omega/\omega_o-\omega_o/\omega)} \approx \frac{R_Q}{R_K}\frac{v_i}{1+2jQ'(\omega/\omega_o-\omega_o/\omega)} \tag{5.51}$$

where

$$Q' = \frac{Q}{1+\frac{R_{sum}}{R_Q}\frac{R}{R_x}} \tag{5.52}$$

where the last expression in Eq. (5.51) holds for a large loop gain (i.e. $\frac{R_{sum}}{R_Q}\frac{R}{R_x} \gg 1$).

Through a noise analysis similar to that of the previous section, the input-referred voltage and current noise generators are found to be

$$\begin{aligned}\overline{v_i^2} = {} & \overline{v_{R_x}^2} + \left(\frac{R_K}{R_{sum}}\right)^2\left(\overline{v_{R_x}^2}+\overline{v_{iR}^2}+\overline{v_{R_{sum}}^2}\right) + \left(1+\frac{R_K \| R_Q}{R_{sum}}\right)^2\overline{v_{iA}^2} + \left(\frac{R_K}{R_Q}\right)^2\overline{v_{R_Q}^2} \\ & + \left(\frac{R_x R_K}{R_{sum}}\right)^2\left|1+2jQ(\omega/\omega_o-\omega_o/\omega)\right|^2\overline{i_{iR}^2} + R_K^2\overline{i_{iA}^2}\end{aligned} \tag{5.53}$$

$$\overline{i_i^2} = \frac{1}{R_{sum}^2}\left(\overline{v_{R_x}^2} + \overline{v_{iR}^2} + \overline{v_{R_{sum}}^2}\right) + \left(\frac{R_Q + R_{sum}}{R_Q R_{sum}}\right)^2 \overline{v_{iA}^2} + \frac{\overline{v_{R_Q}^2}}{R_Q^2} + \left(\frac{R_x}{R_{sum}}\right)^2 \left|1 + 2jQ\left(\omega/\omega_o - \omega_o/\omega\right)\right|^2 \overline{i_{iR}^2} + \overline{i_{iA}^2} \tag{5.54}$$

Note that if the resonator R_x is large and dominates the noise, then its contributions to both the voltage and current input-referred generators may be reduced by increasing the value of R_{sum}. For the case of voltage noise, the gain of the input branch to the summing amplifier should be maximized.

5.1.2.3 Independence of Controlled Q on Initial Resonator Q

Because of squeeze-film damping, Couette flow, or similar fluid-based damping mechanisms, the quality factor of a micromechanical resonator is strongly dependent upon the ambient pressure in which it operates. In addition, the intrinsic Q of a μresonator is a function of material properties, surface roughness, temperature, and anchor design, all of which influence energy dissipation in the μresonator. For lateral electrostatic-comb driven resonators, the Q ranges from under 50 in atmosphere to over 50,000 in 10 mTorr vacuum. Because the Q of a microresonator is not easily predictable, a Q-control method independent of the original Q of the resonator is desirable.

The controlled Q's in all of the proposed schemes in the above sections were governed by expression with a common form:

$$Q' = \frac{Q}{1 + (R/R_x)}. \tag{5.55}$$

Using this expression, the value of Q' can be shown to be independent of the original resonator Q (and thus, of ambient pressure, among other factors) by inserting the expression for equivalent series resistance derived in the Chapter 2 (Eq. (2.62)) and assuming sufficient loop gain (i.e. $R/R_x \gg 1$). Doing this yields

$$Q' = \frac{QR_x}{R} = \frac{\sqrt{mk}}{V_P^2\left(\frac{\partial C}{\partial x}\right)^2 R}. \tag{5.56}$$

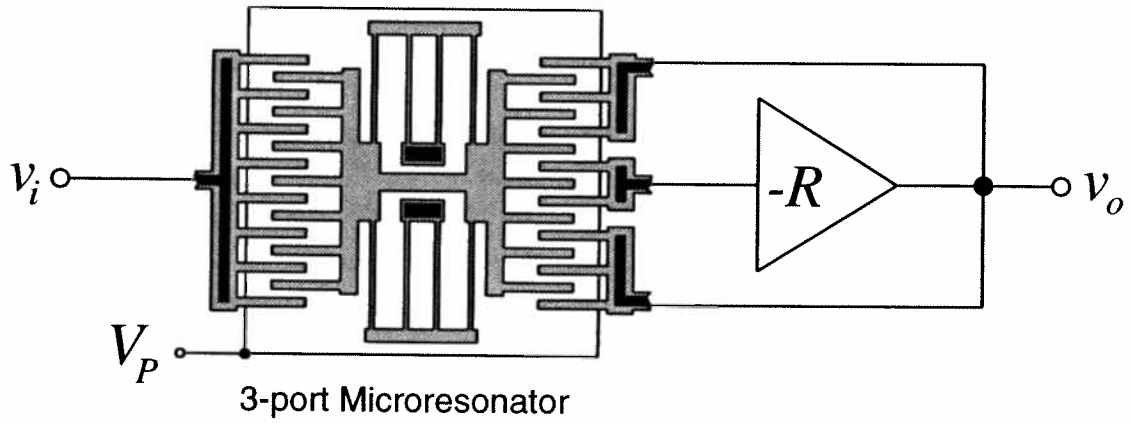

Fig. 5.17: An implementation of microresonator Q-enhancement via positive feedback.

Note that the controlled quality factor Q' depends only upon the transresistance amplification R, the bias voltage V_P, and μresonator geometry, and has no dependence on the original Q provided there is sufficient loop gain.

5.1.2.4 Active Q-enhancement Via Positive Feedback

By using positive feedback (or, in effect, a negative resistor), the effective quality factor of a given resonator may be increased. Figure 5.17 shows one possible implementation of Q-enhancement. This schematic is obtained by simply replacing the transresistance amplifier of Fig. 5.10 by an inverting one, with a gain magnitude chosen such that the total loop gain of the positive feedback system does not exceed unity. (Otherwise, an oscillator would result.) In general, all of the active Q-reduction schemes described above may be converted to Q-enhancement by replacing the transresistance amplifier with one that outputs a 180° phase-shifted signal relative to the original.

The transfer function for the circuit of Fig. 5.17 is given by

$$\frac{v_o}{v_i}(j\omega) = \frac{(R/R_{xfb\bullet o})}{1-(R/R_{xi\bullet o})}\frac{1}{1+2jQ'(\omega/\omega_o-\omega_o/\omega)} \tag{5.57}$$

where

$$Q' = \frac{Q}{1-(R/R_{xi\bullet o})}. \tag{5.58}$$

In Eqs. (5.57) and (5.58), the loop gain $R/R_{xi\bullet o}$ must be less than unity to avoid oscillation.

5.1.3 Practical Implementations of Q-Controlled Single-μResonator Filters

The Q-control implementations of Section 5.1.2 all required either a passive resistor or an active amplifier which effectively provides a transresistance transfer function (whether its input is capacitive or not). Since typical series motional resistances of present-day vacuum-operated capacitively driven μmechanical resonators are over 100 kΩ, very large resistors are required to achieve practical Q-reduction factors. The expression for the resistance R_Q required to achieve a given Q-reduction factor $a = Q/(Q')$ was given as Eq. (5.16), and is repeated here

$$R_Q = (a-1)R_x, \tag{5.59}$$

where R_x represents the appropriate equivalent series motional resistance involved for the type of Q-control implemented. For example, for the passive Q-control architectures discussed, this would be the R_x coupling the input and output ports of a resonator, whereas for the active Q-control architectures, it would be $R_{xfb\bullet o}$, coupling the feedback and output ports. Given an initial μresonator series resistance of $R_x = 100\ \text{k}\Omega$ and an initial $Q = 50,000$, Eq. (5.59) predicts that the resistance required to reduce the quality factor to $Q' = 500$ is 9.9 MΩ. Such values of resistance are readily available as off-chip components. However, depending upon the available technology, this value of resistance is difficult to achieve on-chip.

One might think that by reducing the initial quality factor of the μresonator, one may reduce the Q-reduction factor a, therefore reducing the required value of Q-controlling resistance R_Q. This thinking, however, is fundamentally flawed. This is immediately apparent when writing out Eq. (5.59) in explicit form:

$$\begin{aligned} R_Q &= \left(\frac{Q}{Q'} - 1\right)\frac{\sqrt{km}}{QV_P^2(\partial C/\partial x)^2} \\ &\approx \frac{Q}{Q'}\frac{\sqrt{km}}{QV_P^2(\partial C/\partial x)^2} = \frac{\sqrt{km}}{Q'V_P^2(\partial C/\partial x)^2} \end{aligned} \tag{5.60}$$

where for simplicity it has been assumed that the ports coupled by R_x have identical $\partial C/\partial x$ and bias voltage V_P. Note that Eq. (5.60) is independent of the initial microresonator quality factor Q.

In fact, one may conceptually think of the Q-controlled stage as an open-loop single-resonator stage in which the resonator has been replaced by one with series resistance R_Q.

Getting back to the problem of implementing a large resistance on-chip, several techniques may be attempted. One approach is to solve the problem with "brute force", using passive on-chip resistor technologies, such as thin-film or diffused resistors. Another approach would be to use active transistor resistors, such as MOS channels, for which the value of resistance may be controlled via the gate voltage. The problem of implementing on-chip resistors was addressed in brief in Chapter 4, where transresistance amplifiers were utilized as sustaining amplifiers. We now take a more detailed look at these issues.

5.1.3.1 Passive Integrated Resistors

As previously stated, and as will be made much clearer in succeeding sections, the use of stand-alone passive resistors in the Q-control configuration of Fig. 5.8 is impractical with present-day high series resistance microresonators. This has to do with excessive phase-shifts introduced by parasitic (or intrinsic resonator) capacitance in parallel with the large Q-controlling resistors. Excessive phase shifts leads to filter passband distortion, as will be shown.

Thus, for present-day microresonators, active Q-control using transresistance amplifiers is most appropriate. Passive resistors may still play a role in these implementations as the feedback resistor in a shunt-shunt configuration. They could conceivably be used in filters to some advantage over MOS resistors, since they are more linear than their MOS counterparts. An MOS resistor, however, has the advantage of tunability, which is a very significant attribute when considering that elements may need to be tweaked to satisfy the matching specifications of very high Q filters.

In terms of bandwidth and amplifier stability, the applicability of a resistor for use in a shunt-shunt transresistance amplifier design, such as that of Fig. 4.5, is measured by two main characteristics which limit amplifier performance: (1) linearity; and (2) distributed capacitance over the length of the resistance. Most integrated passive resistors satisfy item (1) fairly well.

Item (2), however, warrants further investigation. Its importance is immediately apparent from the discussion of Section 4.2.2.4, where it was shown that excessive distributed capacitance across the shunt resistor can severely compromise the stability of and limit the bandwidth of a

TABLE 5.1. Available Passive Resistors in the MICS Process

Resistor Type	$\Omega/\square$	$C/\square$	D_R
Gate Polysilicon	20	0.2 fF	1×10^{17}
Nwell Diffusion	10 000	3.4 fF	2.9×10^{18}
MOS Resistor with μC_{ox} = 15 μA/V² V_{GS} = 2.5 V V_t = 0.7 V t_{ox} = 500 A°	37 000	17.2 fF	2.1×10^{18}

transresistance amplifier. Table 5.1 presents data for several possible resistors available for use in CMOS technologies, and available in the CMOS technology used for this work: thin film resistors, constructed from gate polysilicon; diffused resistors, consisting of well diffusion; and the previously discussed MOS resistors. The table shows data for both sheet resistance R_{sh}, and the effective sheet capacitance C_{sh}, and a figure of merit D_R, defined by

$$D_R = \frac{R_{sh}}{C_{sh}}. \tag{5.61}$$

D_R measures the applicability of a given resistor R for use as the feedback resistor in a transresistance amplifier. The higher the value of D_R, the better.

In constructing Table 5.1, it was assumed that the minimum square for the gate polysilicon was $2\mu \times 2\mu$, that for the nwell diffusion $10\mu \times 10\mu$, and that for the MOS resistor $5\mu \times 5\mu$. In addition, the oxide thickness between gate polysilicon and substrate over the field regions was taken as 7000 Å. As an example, let us take the thin-film gate polysilicon resistor. Given that the minimum width of such a resistor is 2 μm in the CMOS technology of this work, a square of resistance is a 2 x 2 μm^2 section of gate poly. Thus, the length of a 1 MΩ resistor would be

$$L = \frac{1\ \text{M}\Omega}{R_{sh}} \bullet (2\ \mu\text{m}) = 1 \times 10^5\ \mu\text{m} = 0.1\ \text{m}, \tag{5.62}$$

which is rather long (to say the least). The total distributed capacitance over this resistor is

$$\left(\frac{0.1}{2\times 10^{-6}}\right)(2\times 10^{-16}) \;=\; 10\ \text{pF} \tag{5.63}$$

which is somewhat large. According to Table 5.1, the MOS resistor can do better, and it has the added convenience of tunability. Also, although the nwell resistor has the highest D_R, it has an undesirable susceptibility to substrate noise. We now look at MOS resistors in more detail.

5.1.3.2 MOS Resistors

The use of the channel resistance from the drain to source of an MOS transistor as the feedback element in a transresistance amplifier was addressed in Chapter 4. There, the value of resistance as a function of gate voltage was given to first order as

$$R_3 = \left[\mu_n C_{ox}\frac{W}{L}(V_{GS}-V_t-V_{DS})\right]^{-1}. \tag{5.64}$$

The sheet resistance and sheet capacitance were also given in Chapter 4 as (assuming $V_{DS}=0$)

$$\begin{aligned} R_S &= [\mu_n C_{ox}(V_{GS}-V_t)]^{-1} \\ C_S &= W^2 C_{ox} \end{aligned}, \tag{5.65}$$

which yields a figure of merit

$$D_{RMOS} = \left[\mu_n W^2 C_{ox}^2 (V_{GS}-V_t)\right]^{-1}. \tag{5.66}$$

The value of D_{RMOS} can be tailored to a large range of values by simply adjusting the gate width W of the MOS transistor and the gate bias voltage V_{GS}.

Equation (5.66) shows that the figure of merit D_R is inversely proportional to the square of the gate capacitance C_{ox}. Since the current technology trend is to shrink the gate oxide thickness as dimensions shrink to yield faster devices, the advantages of using MOS resistors versus passive resistors may disappear. For example, the ω_{pk} for the case of a passive resistor will probably improve as the gate oxide thickness decreases, and as general transistor dimensions shrink. This can be shown by deriving the expression for ω_{pk} using Eq. (4.28) as follows:

$$\omega_{pk} = \sqrt{\frac{g_m}{R_{pass}C_{pass}^2}}, \tag{5.67}$$

where it has been assumed that the passive resistance value R_{pass} and its total distributed capacitance are independent of gate oxide thickness. Equation (5.67) shows that as g_m is increased (perhaps by decreasing the gate oxide thickness), the peak frequency of a transresistance amplifier increases. In actuality, the increase in peak frequency will not be as good as Eq. (5.67) predicts, since as technologies scale, the thickness of the field oxide between the gate poly and the substrate generally decreases as well. Still, there is probably a scaling where polysilicon resistors perform better with respect to amplifier bandwidth.

Still, however, MOS resistors are tunable, which has significant implications for automatic-gain control and trimming of micromechanical/electronic circuits. Regardless of the value of D_R, this advantage in itself may well justify the use of MOS resistors for the transresistance amplifiers in this work. If not for their nonlinearity, it would be hard to justify using other resistor types in place of MOS resistors.

5.1.3.2.1 Nonlinearity in MOS Resistors

Equation (5.64), giving the channel resistance of a linearly-operated MOS transistor, is a linear approximation to the actual value. A more complete derivation that emphasizes the actual nonlinearity of the resistor is achieved by starting with a more complete description of the drain current for an MOS transistor [14]. From [96], a more accurate expression for the drain current I_D of an NMOS transistor is given by

$$I_D = \mu_n C_{ox} \frac{W}{L} \{ \langle V_G - V_{FB} - 2|\phi_p| - \frac{1}{2}v_D - \frac{1}{2}v_S \rangle (v_D - v_S) - \frac{2}{3}\gamma [(2|\phi_p| + v_D - v_B)^{3/2} - (2|\phi_p| + v_S - v_B)^{3/2}] \} \quad (5.68)$$

where V_G is the gate bias voltage, V_{FB} is the flat band voltage, ϕ_p is the potential in the neutral bulk of the p-type silicon substrate (relative to surface potential = 0), v_D is the drain voltage, v_S is the source voltage, and v_B is the bulk voltage. As used previously, μ_n is the electron mobility in the channel, C_{ox} is the gate-to-channel capacitance, and W and L are the dimensions of the MOS transistor.

The first term in the brackets of Eq. (5.68) may be expanded as follows

$$\left\langle V_G - V_{FB} - 2|\phi_p| - \frac{1}{2}v_D - \frac{1}{2}v_S \right\rangle (v_D - v_S) = (V_G - V_{FB} - 2|\phi_p|)(v_D - v_S) - \frac{1}{2}(v_D^2 - v_S^2) \tag{5.69}$$

Using the binomial expansion, the second term may be expanded as

$$\begin{aligned} -\frac{2}{3}\gamma(2|\phi_p| + v_D - v_B)^{3/2} &= -\frac{2}{3}\gamma(2|\phi_p| - v_B)\left(1 + \frac{v_D}{2|\phi_p| - v_B}\right)^{3/2} \\ &= -\frac{2}{3}\gamma(2|\phi_p| - v_B)^{3/2} - \gamma(2|\phi_p| - v_B)^{1/2}v_D \\ &\quad -\frac{1}{4}\gamma(2|\phi_p| - v_B)^{-1/2}v_D^2 + \frac{1}{12}\gamma(2|\phi_p| - v_B)^{-3/2}v_D^3 \end{aligned} \tag{5.70}$$

and in a similar manner, the third as

$$\begin{aligned} \frac{2}{3}\gamma(2|\phi_p| + v_S - v_B)^{3/2} &= \frac{2}{3}\gamma(2|\phi_p| - v_B)^{3/2} + \gamma(2|\phi_p| - v_B)^{1/2}v_S \\ &\quad + \frac{1}{4}\gamma(2|\phi_p| - v_B)^{-1/2}v_S^2 - \frac{1}{12}\gamma(2|\phi_p| - v_B)^{-3/2}v_S^3 \end{aligned} \tag{5.71}$$

Combining Eqs. (5.69) through (5.71), the expression for drain current becomes

$$I_D = K\{a_1(v_D - v_S) + a_2(v_D^2 - v_S^2) + a_3(v_D^3 - v_S^3) + \ldots\} \tag{5.72}$$

where

$$K = \frac{1}{2}\mu_n C_{ox}\frac{W}{L} \tag{5.73}$$

$$a_1 = 2(v_G - V_T) \tag{5.74}$$

$$a_2 = -\left(1 + \frac{1}{2}\gamma(2|\phi_p| - v_B)^{-1/2}\right) \tag{5.75}$$

$$a_3 = \frac{1}{6}\gamma(2|\phi_p| - v_B)^{-3/2}. \tag{5.76}$$

Equation (5.72) is a general expression relating the drain and source voltages across a linearly operated MOS transistor to the resulting nonlinear drain current, for a given value of gate bias. For the purposes of this work, a (largely) linear microresonator output current is converted to a voltage via a transresistance amplifier of the form shown in Fig. 5.18. For this case, the expression for the drain and source voltages (V_2 and V_1, respectively, in Fig. 5.18) in terms of drain current is required. This can be obtained by first recognizing that, given enough gain in the amplifier,

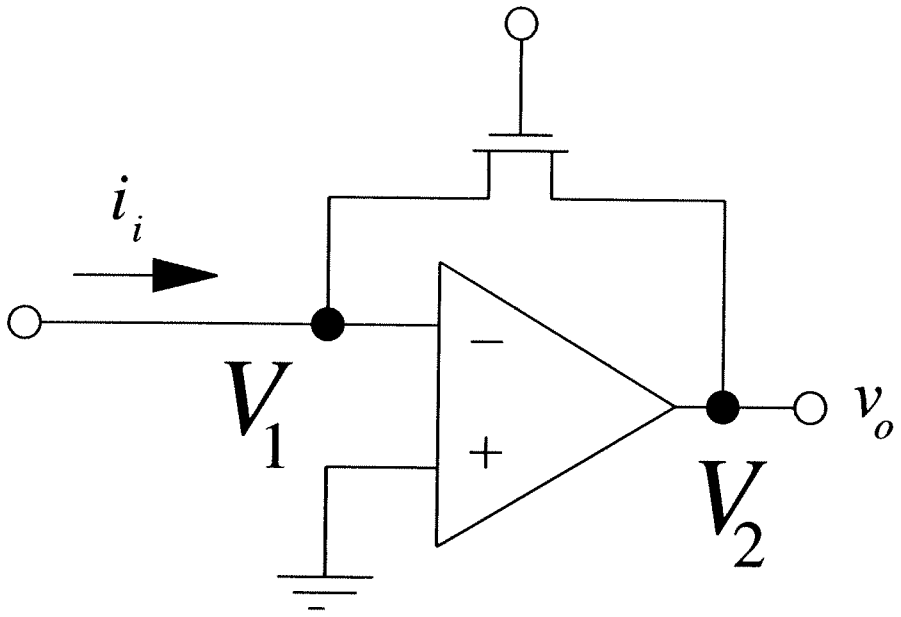

Fig. 5.18: Transresistance amplifier utilizing an MOS resistor.

the input node to the circuit of Fig. 5.18 is a virtual ground, so V_1 is effectively zero. Thus, Eq. (5.72) becomes

$$I_D = b_1 V_2 + b_2 V_2^2 + b_3 V_2^2 + \ldots, \tag{5.77}$$

where the K of Eq. (5.73) has been combined with the a_n coefficients to form the b_n coefficients. A series reversion of Eq. (5.77) yields

$$V_2 = c_1 I_D + c_2 I_D^2 + c_3 I_D^2 + \ldots \tag{5.78}$$

where

$$c_1 = \frac{1}{b_1} = \left[\mu_n C_{ox} \frac{W}{L} (V_{GS} - V_T)\right]^{-1} \tag{5.79}$$

$$c_2 = -\frac{b_2}{b_1^3} \tag{5.80}$$

$$c_3 = \frac{2b_2^2}{b_1^5} - \frac{b_3}{b_1^4} \tag{5.81}$$

and where the last two are not expanded to avoid cluttering. For the case of voltage-to-current conversion by an MOS resistor (Eqs. (5.74) through (5.76)), the second harmonic term dominates over all others. The third harmonic term is quite small. Thus, balanced circuit topologies which cancel even-ordered harmonics, are popular when using MOS resistors as voltage-to-current converters (as in an integrator).

For the case of current-to-voltage conversion (Eqs. (5.79) through (5.80)), however, although the second harmonic still dominates, the third harmonic is also quite large, and balanced circuit topologies will not cancel this. Thus, if an MOS resistor-based transresistance amplifier is to be used as an output amplifier for a mechanical filter, some other way must be devised to alleviate the third order nonlinearity. Of course, however, if the amplifier were used for Q-control and only Q-control (and the signal never reaches the output), the nonlinearity in the amplifier would not be a problem, since the resonator will filter out distortion components before they reach an output.

5.1.3.3 Experimental Demonstration of Q-Control

Using the set-up shown in Fig. 5.19, Q-control for a three-port micromechanical resonator was demonstrated. In this experimental set-up, the resonator is operated in a vacuum probe station (actually, an MMR probe station), which lowers the operating pressure to 10 mTorr and insures a high initial Q for the microresonator. The results are presented in Fig. 5.20, where the transconductance spectra for the three-port resonator are plotted for different values of R_{amp}, clearly demonstrating active control of the system quality factor.

The dependence of controlled Q on ambient pressure was also investigated by varying the pressure in the vacuum probe station. Figure 5.21 presents experimental verification that the value of the controlled Q is invariant under changing ambient pressures, being dependent only on the Q-controlling feedback set by R_{amp}.

5.1.4 Low-Pass Resonator Biquads

As mentioned earlier in this chapter, and briefly in Chapter 2, the force versus position transfer function has the form of a lowpass biquad function. Such filtering characteristics can be extracted. via capacitive detection of resonator motion. Among the useful applications for lowpass

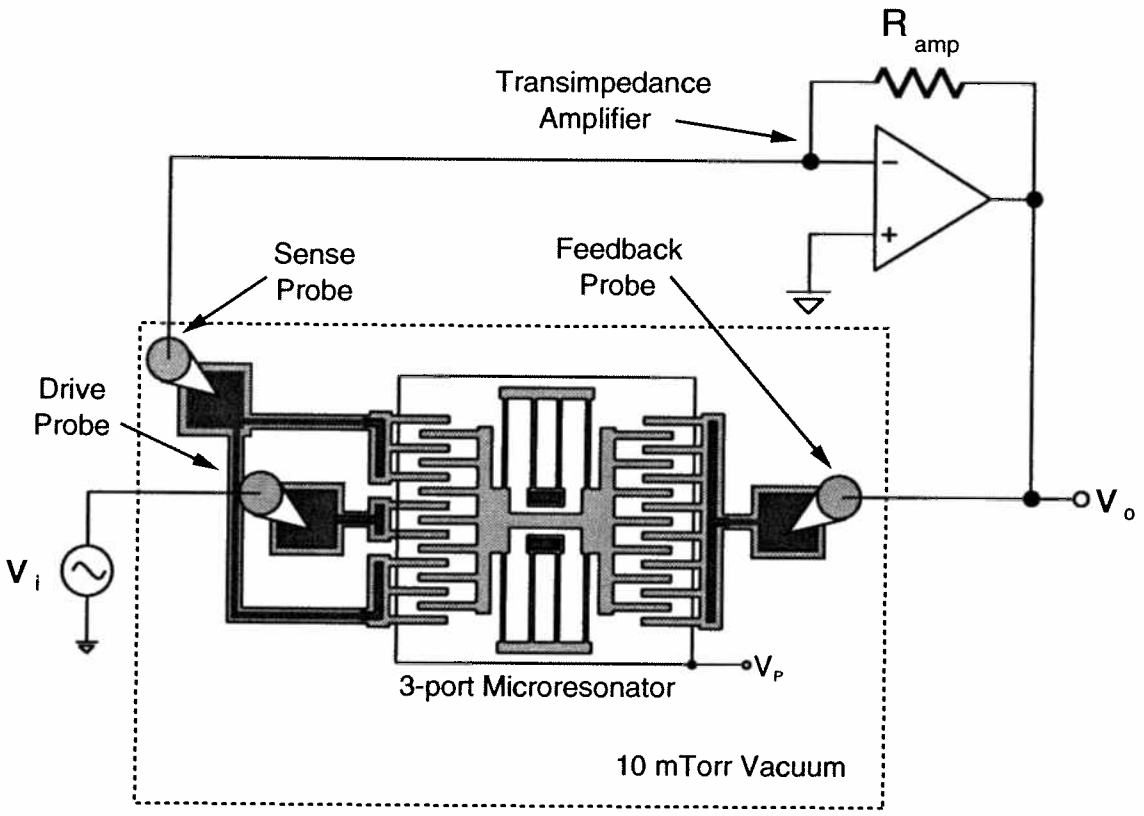

Fig. 5.19: Schematic of the experimental set-up used to implement Q-control.

biquad filters are some speech recognition systems. Lowpass biquads made using quasi-passive micromechanical resonators have the advantage in that they are more stable than their transistor-based counterparts, because they do not require positive feedback to implement the required peaking. Since the focus of this work is on bandpass filters for communications, lowpass biquad filters constructed from micromechanical resonators will not be addressed in detail.

5.2 Coupled-Biquad Filter Designs

Although single-resonator second-order biquad filters are useful in their own right, there is considerable need for higher order filters, which require many more poles and zeros than obtainable from a single resonator. Such filters are generally implemented via a building block approach, where several biquad blocks are combined and coupled either electrically or mechanically. For example, the majority of bandpass filters implemented in integrated transistor technologies (switched-capacitor, MOSFET-C, g_m-C) utilize coupled-biquad architectures, such as the popular

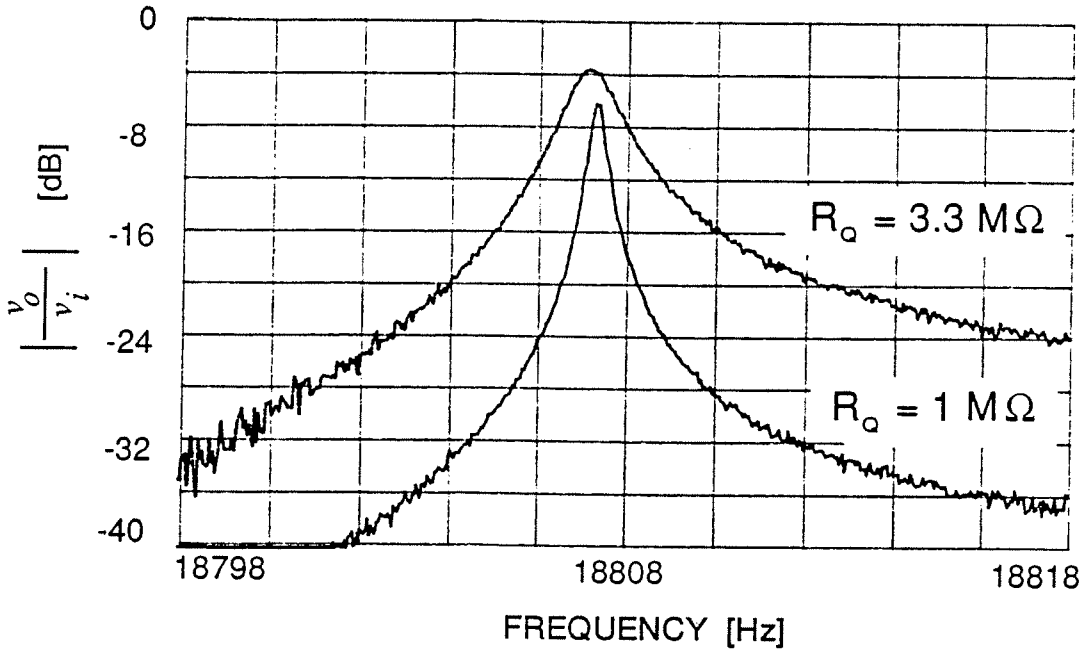

Fig. 5.20: Experimental demonstration of Q-control using the set-up of Fig. 5.19. Each microresonator transconductance spectrum corresponds to a different value of R_{amp}. The measured values of Q are 53,000 for R_{amp} = 1 MΩ and 17,000 for R_{amp} = 3.3 MΩ.

leap frog design, where biquads and couplings are implemented in the electrical domain, exclusively. Coupled-biquad architectures are also utilized in purely mechanical filter designs, as well, such as single blank crystal filters and spring-coupled mechanical filters. In addition, there are designs where mechanical biquads are used with electrical coupling, such as discrete crystal filters.

Since a bandpass or lowpass biquad transfer function is completely determined by a resonance frequency ω_o, a quality factor Q, and a gain factor K (Eq. (5.1)), the Q-controlled single-resonator filters of the previous section should be able to implement nearly any bandpass or lowpass biquad function within the frequency and Q range of a designed microresonator, and with potentially improved selectivity performance, and possibly lower power dissipation. With this capability, a large variety of coupled-biquad resonator-based filter architectures are available, both purely mechanical or mechanical biquads with electrical coupling. Spring-coupled designs with architectures similar to existing macroscopic examples immediately come to mind. In addition, leap frog or follow-the-leader-feedback architectures, where micromechanical resonator biquads are cou-

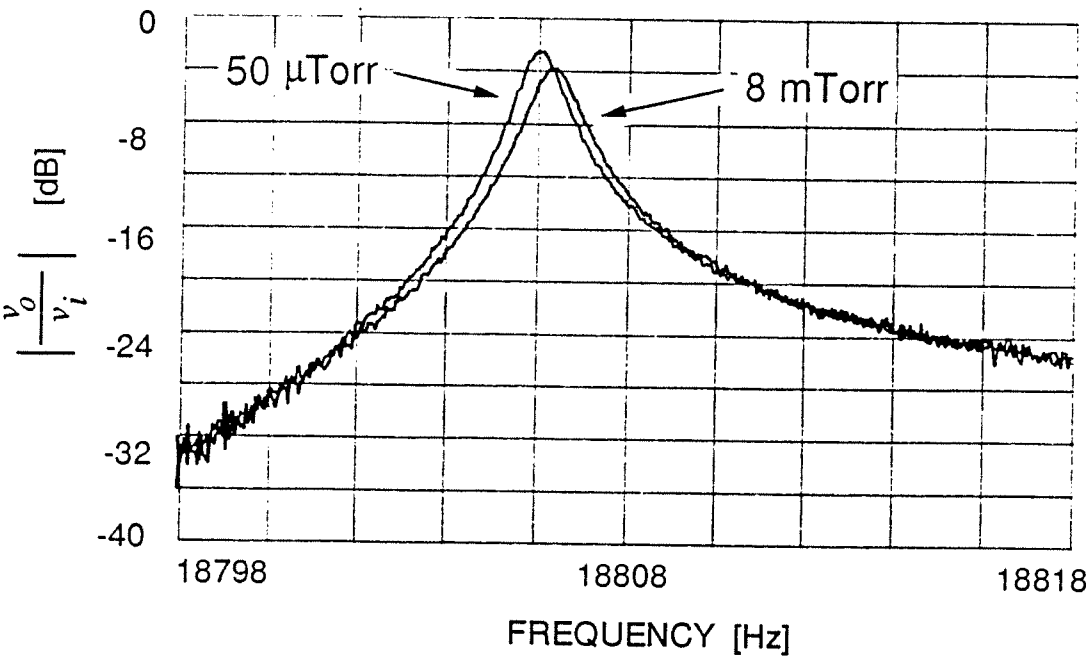

Fig. 5.21: Transconductance spectrum for a micromechanical resonator subjected to Q-control with R_Q = 3.3 MΩ and with varying ambient pressure. Without Q-control, the original Q at 8 mTorr is 53,000 and that at 50 μTorr is 84,000. With Q-control, the Q for both cases is 17,000.

pled via electronics, are also feasible. Reference [97], in fact, details the design of a frequency and bandwidth controllable FLF filter based upon micromechanical resonators.

In the interest of reasonable brevity, this report will not detail the design of electrical/mechanical filters, where both mechanical and electrical domains are utilized for either biquad realization or for coupling. Rather, the focus will be on the more traditional purely mechanical spring-coupled designs common for macroscopic filters. The small size and comparatively small electromechanical coupling characteristic of micromechanical resonators already makes this a challenging prospect. The reader is referred to [97] for specific design details of an FLF version.

5.3 Spring-Coupled Ladder Filters

As discussed in Chapter 1, classic macroscopic mechanical filters are commonly designed via spring-coupling of mechanical resonators. One possible advantage of this architecture, as opposed to crystal architectures which use crystal resonators coupled electrically (via capacitive networks), is that only two electromechanical energy conversions are required: one at the input and one at the output. The majority of filter processing is done in the mechanical domain. The

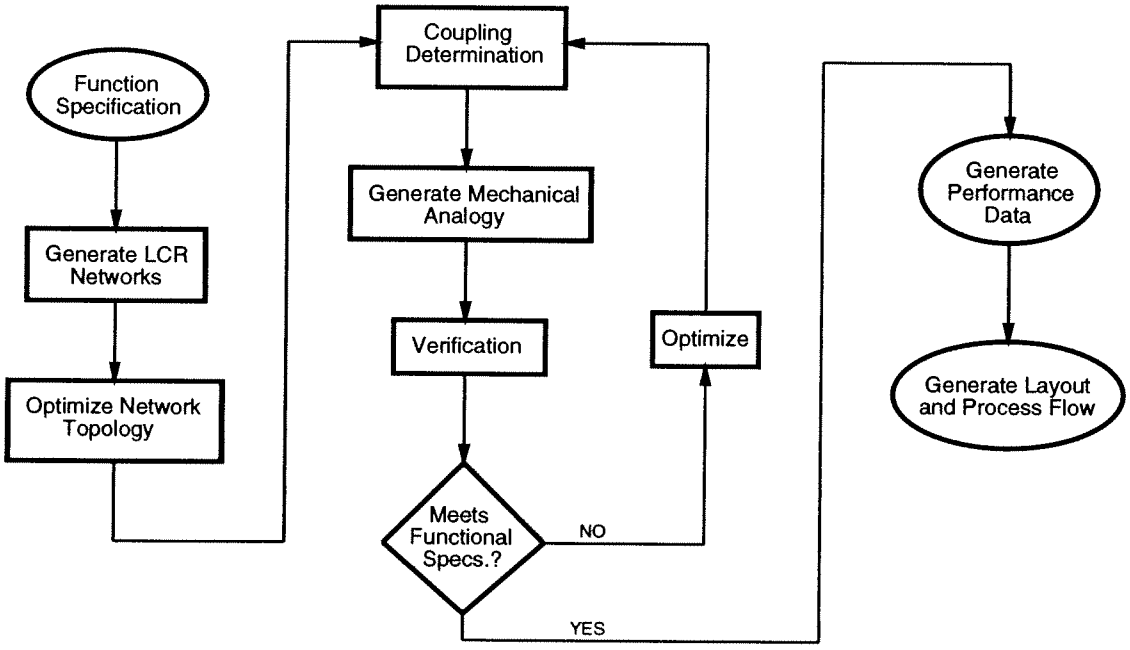

Fig. 5.22: Flow chart describing the design procedure for a micromechanical resonator filter.

advantage here is that there are fewer losses with fewer energy conversions. One advantage of a discretely coupled crystal filter over this spring-coupled approach, however, is that spurious mechanical resonance modes can be suppressed when using electrical coupling. However, these spurious modes can be suppressed in the spring-coupled approach, as well, by proper resonator design.

The general design procedure for a spring-coupled micromechanical resonator usually follows the flow chart presented in Fig. 5.22. As shown, the procedure begins with the specification of the desired filtering function. Appropriate LCR networks are then generated, followed by some optimization to achieve the best topology. Next, electromechanical analogies (current or mobility) are utilized to specify a coupled mechanical geometric design for a given method of transduction. Some optimization will be necessary, here, to account for second-order effects in transduction and in distributed mass. Next, loading of the filter is determined, which is important for achieving the specified passband shape. Following verification by simulation, the layout and process flow may then be generated, and filter subsequently fabricated.

The following sections detail each step in the design procedure of Fig. 5.22.

5.3.1 LC Ladder Design

A filter response is perhaps most conveniently specified graphically via a plot of attenuation versus frequency. In such descriptions, reasonable filter bounds are also drawn in, corresponding to the boundaries which must be achieved by the designed filter. Such a description immediately conveys the passband cut-off frequencies, the dB/decade roll-off, the maximum attenuation in the passband (amount of acceptable passband ripple), and the minimum acceptable attenuation in the stopband (or amount of acceptable stopband ripple).

General methods for synthesizing LC ladder filters are well documented For a given filter specification, an equivalent LC ladder may be achieved by first approximating the attenuation function by an nth order polynomial function. For attenuation functions with monotonically increasing attenuation outside the passband, an all pole polynomial is required, expressed by the transfer function

$$T(s) = \frac{1}{s^n + a_{n-1}s^{n-1} + \ldots + a_o} \tag{5.82}$$

where s is the complex frequency, and where there are zeros only at infinite frequencies. Attenuation functions with ripples in the stopband are described by polynomials with finite zeros, given by transfer functions of the form

$$T(s) = K\frac{b_n s^n + b_{n-1}s^{n-1} + \ldots + b_o}{s^n + a_{n-1}s^{n-1} + \ldots + a_o}. \tag{5.83}$$

An LC ladder circuit which approximates a given polynomial function may be synthesized using pole and zero removal techniques [98], where the ladder is constructed one element at a time. The resulting ladder structure is not unique, and in fact, several LC ladder networks may be synthesized from a single polynomial function, depending upon the path taken in the element-by-element synthesis procedure. Usually, several canonical versions are available, and these are usually selected for implementation via active RC designs. For the case of integrated switched-capacitor or g_m-C leap frog architectures, a canonical LC network for which all integrator-based resonators are identical is typically implemented, with the intent of suppressing dependences on absolute values and relying more heavily on matched values.

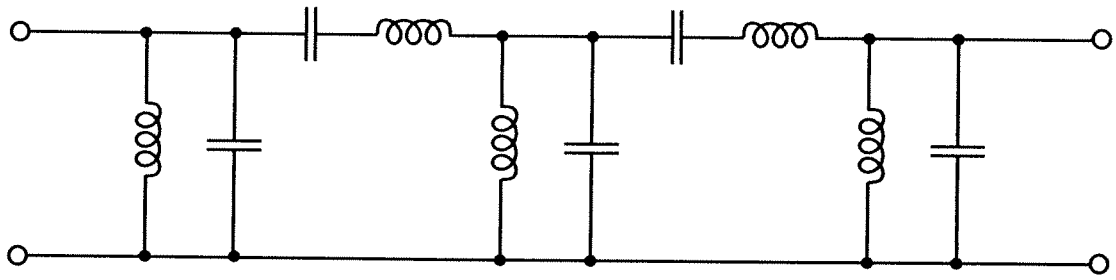

Fig. 5.23: LC ladder for an all-pole bandpass filter.

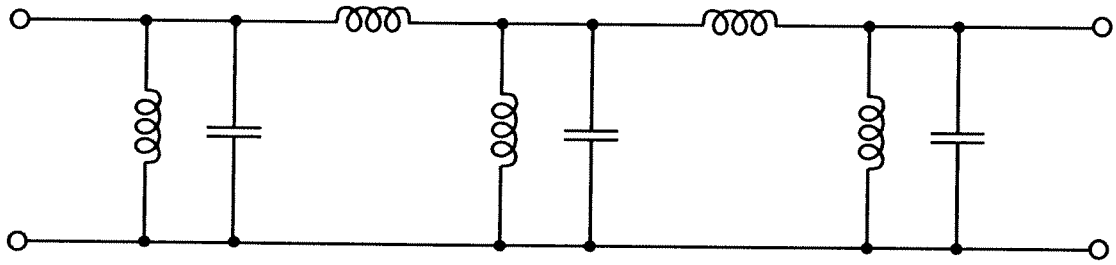

Fig. 5.24: Resulting LC ladder when the narrowband approximation is applied to Fig. 5.23.

For the case of mechanical spring-coupled filters, the most appropriate LC ladder network for a given polynomial function generally requires more elements than a canonical equivalent. In addition, since mechanical filters are generally highly selective, the narrow bandwidth approximation is frequently used their design. With these in mind, a typical LC ladder configuration suitable for implementation of all-pole mechanical filters is presented in Fig. 5.23. This figure shows the ladder network as it looks immediately after synthesis from the describing polynomial. Application of the narrow bandwidth approximation yields the ladder network shown in Fig. 5.24. The network of Fig. 5.24 is now directly transformable to an equivalent mechanical circuit, as will be shown in the next section.

5.3.1.1 Electromechanical Analogies

Since they generally consist of a large number of elements (resonators and couplers), mechanical filters are relatively complex mechanical systems, with complexities approaching that of electronic circuits. For this reason, it is usually advantageous to simplify a given mechanical filter system and convert it to a lumped-parameter model, in a manner similar to that done for electronic circuits. As with electrical circuits, such a design approach not only simplifies the design procedure, it also may potentially provide more insight into the operation of mechanical filters.

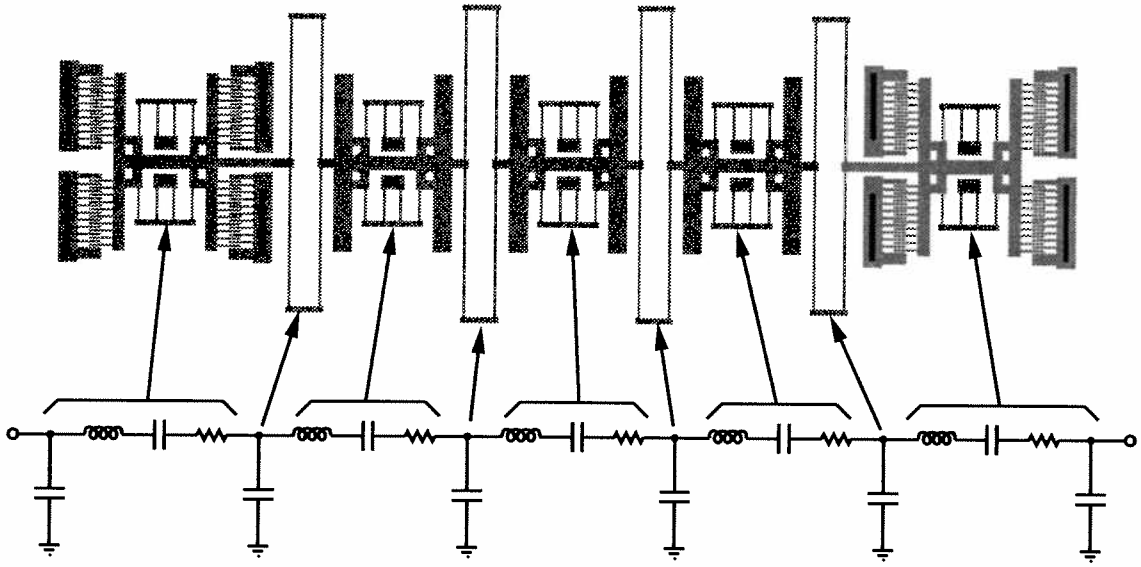

Fig. 5.25: Current analogy equivalence between a micromechanical filter and an electrical LCR network.

Using the current (voltage-to-force) analogy, which equates force (F) to voltage (V) and velocity ($\dot{x}$) to current (I), the mechanical-to-electrical circuit correspondence is shown in Fig. 5.25 for a five resonator spring-coupled micromechanical filter. As shown, each mechanical resonator corresponds to a series LCR circuit in the electrical domain, while each coupling spring corresponds to a coupling capacitor. Note that in reality, the mechanical filter shown has an infinite number of resonances. A lumped circuit approximation such as shown in Fig. 5.25, however, is an adequate representation for the case of a narrowband filter.

The mechanical-to-electrical element correspondence may be obtained by equating differential or Laplace equations for the mechanical and electrical domains. Doing so, one finds that in the current analogy, mass (m) corresponds to inductance (L), stiffness (k) relates inversely to capacitance (C), and damping (d) corresponds to resistance (R). The expressions relating these quantities were already given in Chapter 2 as Eqs. (2.60) to (2.63). Since for actual filter design one generally first synthesizes an LCR circuit that corresponds with the desired filtering function, then finds the corresponding masses and stiffness coefficients required for implementation in the mechanical domain, the inverse relations to Eqs. (2.60) to (2.63) are needed for design. These are given as follows:

$$m = \eta^2 L \tag{5.84}$$

$$k = \frac{\eta^2}{C} \tag{5.85}$$

$$d = \frac{\sqrt{km}}{Q} = R\eta^2 \tag{5.86}$$

where

$$\eta = V_P \frac{\partial C}{\partial x}. \tag{5.87}$$

Given an appropriate LC ladder, Eqs. (5.84) through (5.87) may be used to produce the required mechanical resonators and couplings which realize the specific filter response.

5.3.2 Filter Termination

The majority of available algorithms for filter synthesis assume lossless inductors and capacitors, or nearly lossless. The general assumption in these algorithms is that the filter elements, be they inductors, capacitors, or resonators, have much higher quality factor than the filter quality factor, defined by

$$Q_{fltr} = \frac{f_o}{BW}, \tag{5.88}$$

where f_o is the center frequency of a bandpass filter (or cutoff frequency of a lowpass or highpass filter), and BW is the bandwidth of the filter (3dB-down bandwidth for Butterworth types). In order to insure nondistorted filter design using these algorithms, the Q of the resonators implementing a given filter should be at least ten times higher than Q_{fltr}.

Predistorted filter synthesis techniques also exist and are necessary when the above criterion is not met. However, whether predistorted or nondistorted filter synthesis techniques are applied, every such filter design requires a given terminating impedance, to add controlled amounts of loss and increase the effective bandwidth of the constitutive resonators. The amount of termination resistance required is dependent on the value of the lossless elements constituting the filter, and is usually derived as part of the filter synthesis procedure.

A ball park estimate of the required termination resistance R_S, however, can be inferred from the following equation:

$$R_S \approx \frac{1}{\omega_m C_n Q_{fltr}}, \tag{5.89}$$

where C_n is the motional capacitance of one of the terminating resonators in the filter, and

$$\omega_m = \sqrt{\omega_1 \omega_2} \tag{5.90}$$

is the geometric mean frequency of the bandpass filter, where ω_1 and ω_2 are the lower and upper cut-off frequencies of the filter, respectively.

Given that an achievable value of motional capacitance for the capacitively transduced microresonators of this work is 20 aF, the terminating resistance for a 455 kHz bandpass micromechanical filter with a bandwidth of 4 kHz constructed from such resonators, should be in the range of 25 MΩ. Needless to say, this is a very large value of resistance. It's value could be decreased by increasing the electromechanical coupling factor, η. This would require either an increase in the dc-bias voltage V_P applied to the capacitively transduced resonator, or an increase in the value of $\partial C/\partial x$. The former will be a challenging prospect, since even the current values of V_P are larger than acceptable in most CMOS technologies. The latter will most likely require a technology that can achieve small gaps between conductors, on the order of 500 A or less. A technology which can achieve this is plausible, since CMOS gate oxides are already far below this value.

Nevertheless, the technology presently available for this work cannot achieve such gaps. Thus, large terminating resistors will have to be dealt with.

5.3.2.1 Passband Distortion by Parasitics

One of the more damaging consequences of a large terminating resistance is excessive phase lag due to the parallel combination of this resistance and any parasitic capacitance, or even intrinsic resonator gap capacitance. Note that the ideal circuit network for a resonator-based bandpass ladder filter, shown in Fig. 5.24, does not include a shunt capacitor at the input and output nodes. In reality, however, there will always be a shunt capacitor at the input and output nodes due to interconnect parasitics. For LC ladder filters or macroscopic ladder filters, this parasitic shunt

capacitance is generally not a problem. However, as seen in Fig. 5.29, mechanical filters (macroscopic or micro-scale) have an intrinsic shunt capacitance that must be dealt with. The actual circuit for a properly terminated mechanical filter is shown in Fig. 5.26.

The effect of this phase lag is explicitly shown in the simulations of Fig. 5.27. In these figures, the frequency response of a five resonator Chebyshev bandpass filter with structure shown in Fig. 5.26 is simulated with varied values of input/output capacitance $C_{i/o}$. Figure 5.27(a) shows the filter characteristic with $C_{i/o} = 0$ fF. Here, there is no phase lag, and the filter characteristic is as designed. Figure 5.27(b) shows the same filter, but now with only 3 fF of input/output capacitance, which is a typical value for the intrinsic electrode-to-resonator dc capacitance on the micro-scale. Some amount of distortion in the filter passband is already visible. Finally, Fig. 5.27(c) shows the filter characteristic with $C_{i/o} = 500$ fF. The distortion for this case is tremendous. Note that of all the capacitance values used in the simulation, 500 fF may be the most realistic. For example, this amount of capacitance is in the range of typical values expected at the drain or source of an MOS resistor.

Two solutions to this problem immediately come to mind. One has already been mentioned: Increase the electromechanical coupling factor in the transduction, to reduce the value of

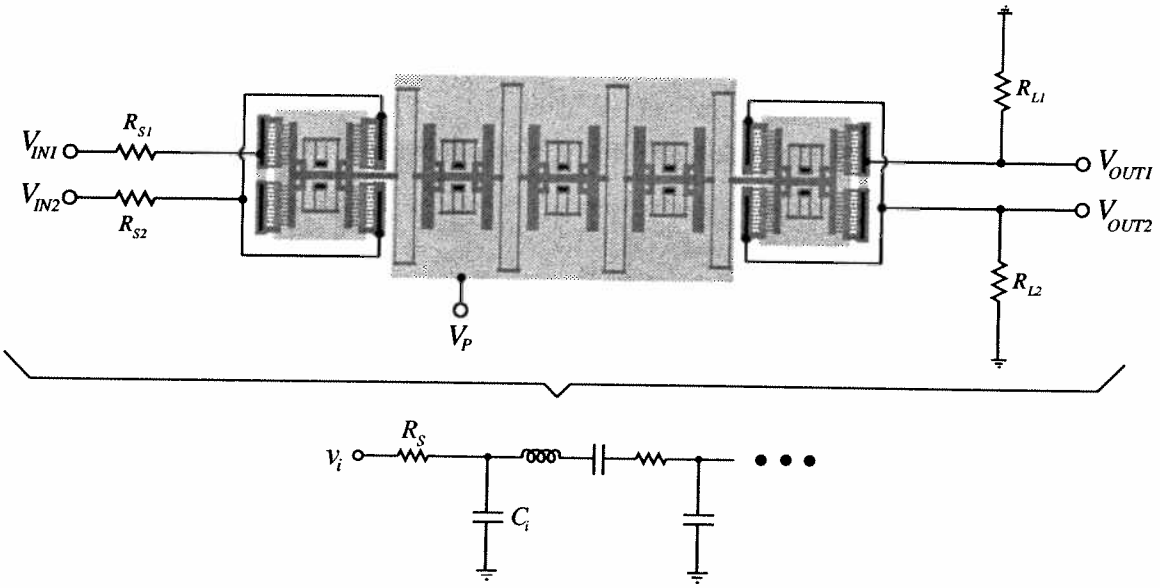

Fig. 5.26: Schematic and input circuit diagrams for a properly terminated micromechanical spring-coupled filter.

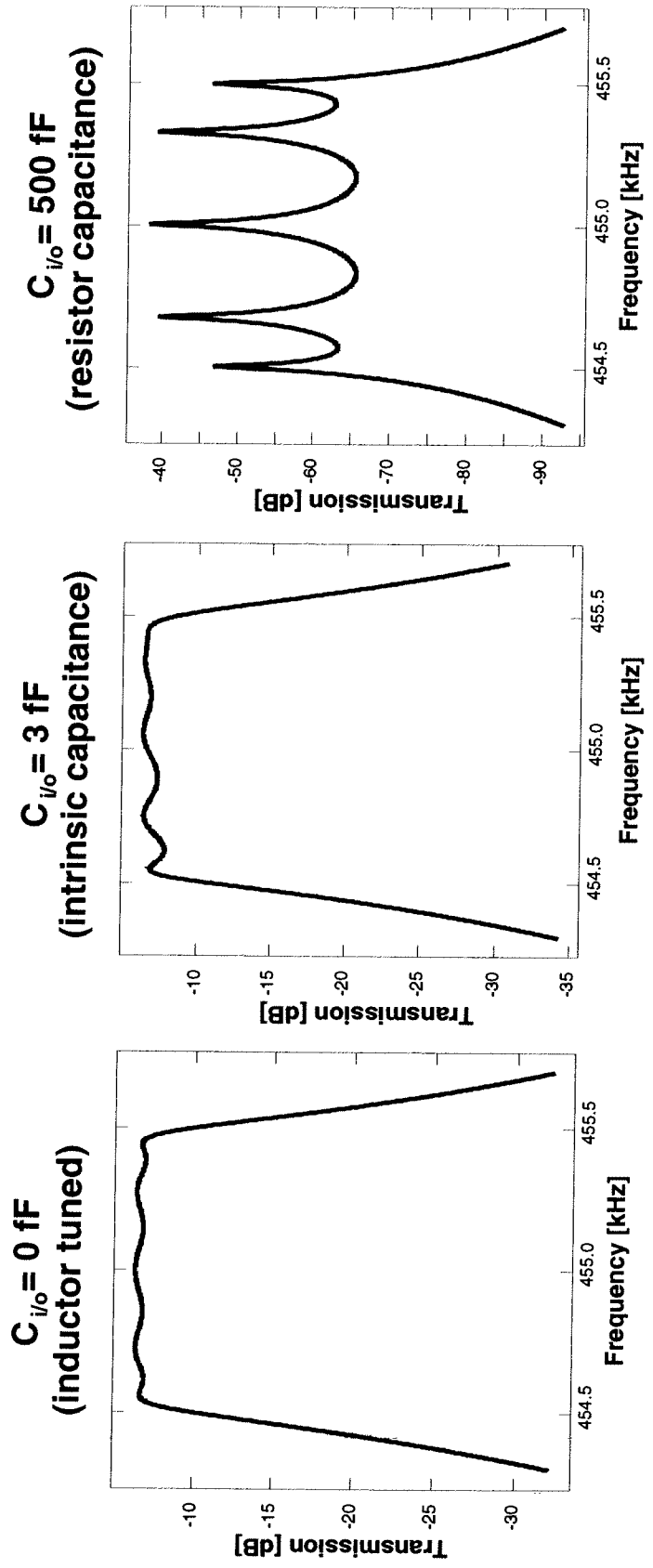

Fig. 5.27: Simulations of the passband frequency response for a typical present-day high series resistance micromechanical filter with differing values of shunt input/output capacitance.

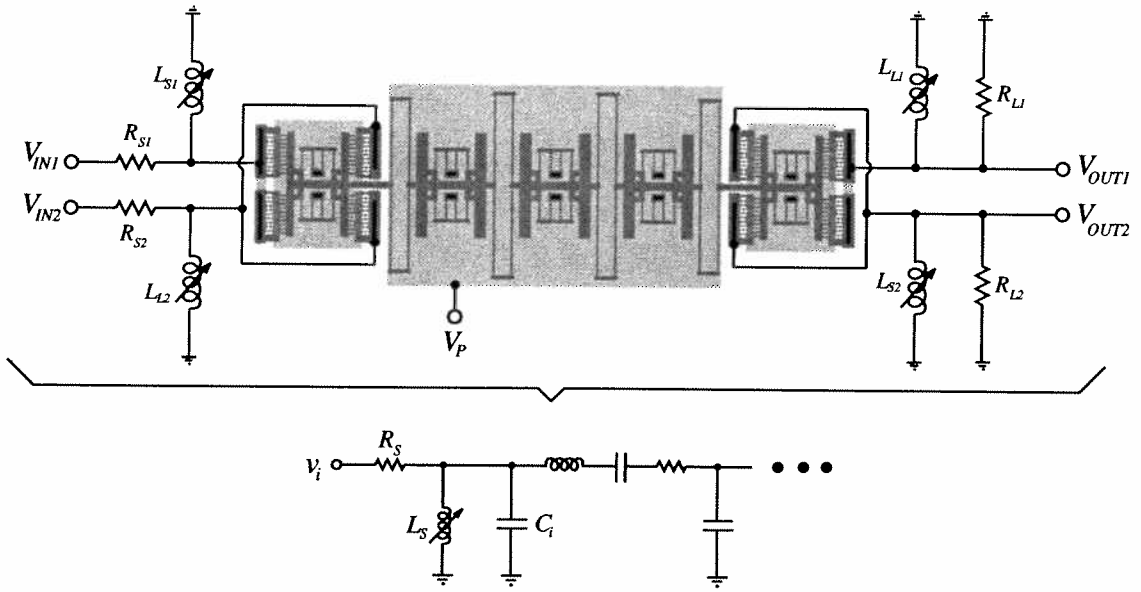

Fig. 5.28: Eliminating shunt input/output capacitance via a tuning inductor.

terminating resistance required, thus, reducing the phase shift resulting from combination of this resistor and parallel capacitance. As mentioned, this would most likely require technological improvements, either to increase the usable dc-bias voltage, V_P, or to decrease achievable gap spacings. Although achievable in the next few years, this technology is not ready for this work.

Another approach to eliminating passband distorting phase-shift involves tuning out of the parasitic capacitance via a tuning inductor, shown in Fig. 5.28. This, in fact, is a common procedure used for macroscopic mechanical filters [35], Since current integrated inductor technologies can achieve only small values of inductance, this technique is presently not practical when attempting to realize a fully monolithic high-Q micromechanical filter. Thus, some other technique is required to alleviate the passband distortion.

As if passband distortion were not enough, another perhaps more significant problem accompanies a large terminating resistance: Noise! In situations where the input termination is provided by simply placing a huge source resistance in series with the filter, the voltage noise of this resistor appears in series with that of the resonator. From Eq. (5.3), we see that voltage noise from this resistor directly contributes to the input referred voltage noise generator of the whole filter. Due to the large size of the resistor, this noise will dominate. Thus, termination in series with the filter input should be avoided.

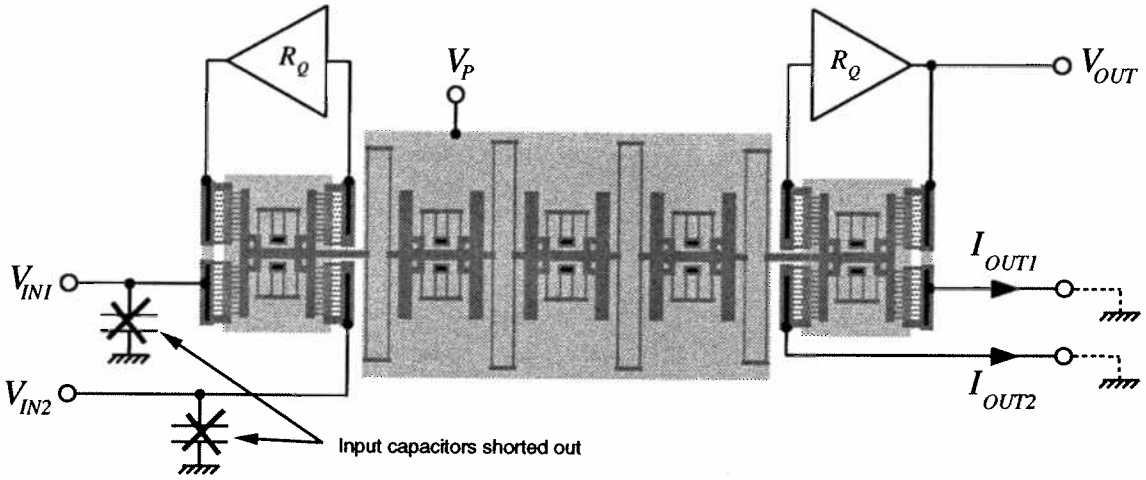

Fig. 5.29: A five resonator micromechanical filter employing active Q-controlling terminations, which alleviate termination-derived passband distortion.

5.3.2.2 Active Q-controlling Termination

The purpose of the large terminating resistors at the input and output of a spring-coupled micromechanical filter is merely to lower the quality factor of the end resonators. Such Q lowering could also be achieved by other techniques, such as changes in the material of the end resonators or increasing fluid damping on them. Perhaps, however, the most convenient method for doing this is through the active Q-reduction methods discussed in Section 5.1.2 of this chapter.

One implementation of this Q-control technique to a five resonator micromechanical filter is shown in Fig. 5.29, where extra ports have been added to allow for Q-control. Here, the value of transresistance required by the amplifier is equal to the value of termination resistance required by this design; in other words,

$$R_Q = R_S, \tag{5.91}$$

where R_S is the designed value of terminating resistance.

This technique will improve the filter characteristics only if the phase shift of the amplifier is smaller than that of the alternative large resistor in parallel with the input/output capacitance $C_{i/o}$. This is usually achievable when using a two-stage transresistance amplifier, where a transresistance amplification on the order of only 200 kΩ is required, followed by a second stage with a

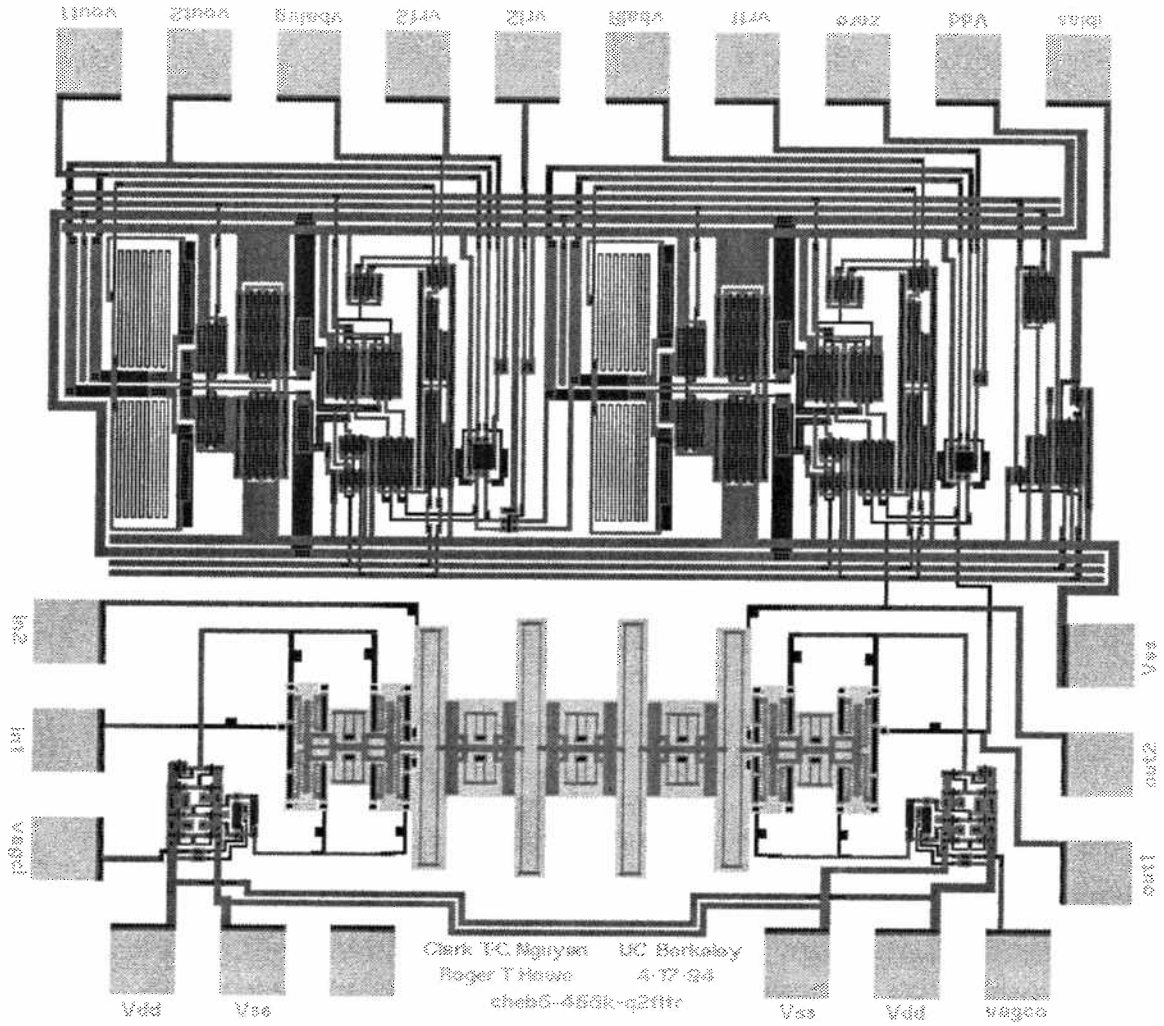

Fig. 5.30: Layout for a 455 kHz five-resonator spring-coupled micromechanical filter with supporting Q-control and signal conditioning electronics.

voltage gain of around 100. Such a transresistance amplifier will be detailed later in this Chapter, when a specific filter design is presented.

5.3.3 A 455 kHz Filter Design

The layout for a 455 kHz spring-coupled micromechanical filter with Q-controlling and sense electronics is presented in Fig. 5.30. The SPICE simulated transfer characteristic for this design is shown in Fig. 5.31. At the time of this writing, this filter is still undergoing fabrication.

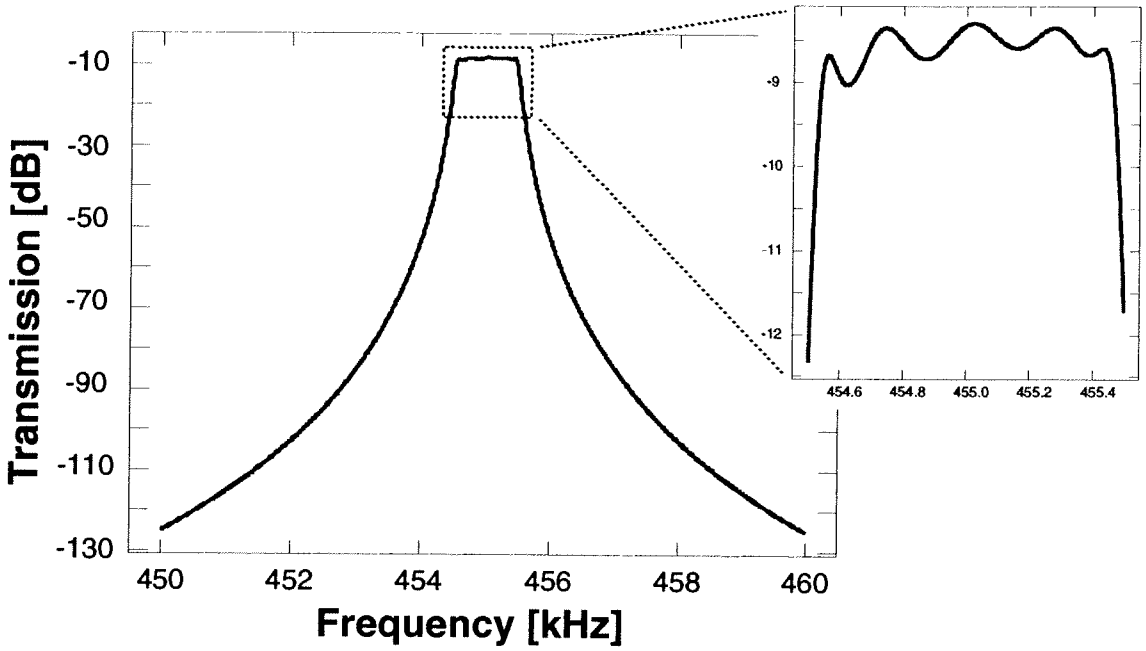

Fig. 5.31: Simulated frequency response spectrum for the filter of Fig. 5.31.

Thus, the details of its design and performance will not be discussed here, but rather, will be deferred to a later publication.

5.4 Experimental Demonstration of a Spring-Coupled Micromechanical Filter

In order to test the active Q-controlled termination concept, passive micromechanical filters with multi-port end resonators were fabricated. The scanning electron micrograph (SEM) of a two-resonator spring-coupled filter is presented in Fig. 5.32.

Attempts at filter termination simulation using off-chip transresistance amplifiers were not successful, due to the large interconnect (bonding) parasitics present, which axed the bandwidths of off-chip components. Some Q-controlling effect was visible, however, although not enough to achieve a flat passband.

In order to lower the Q of the resonators to provide adequate terminations, the fabricated filters were operated in an MMR vacuum probe station, which allowed control of the pressure in the MMR chamber via the admission of controlled amounts of nitrogen. By using this system to

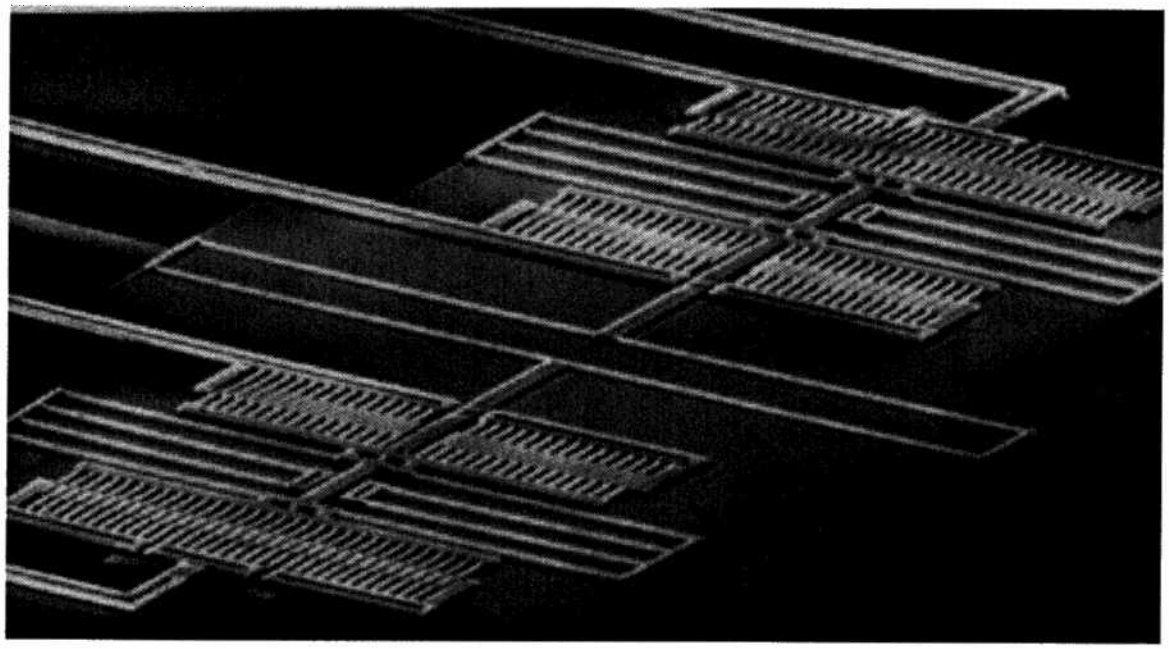

Fig. 5.32: SEM of a spring-coupled micromechanical resonator filter with three-port end resonators for implementation of Q-controlling termination.

tweak the operating pressure, the quality factor of the filter end resonators were controllable, and could be tweaked (within the accuracy of the pressure control) to yield relatively flat passbands. The spectrum for a two-resonator filter terminated using this strategy is shown in Fig. 5.33.

5.5 Parallel Micromechanical Resonator Filters

Given that hundreds, perhaps thousands of micromechanical resonators may be fabricated onto a single silicon chip, systems which use massive parallel banks of bandpass filters are conceivable. Such banks of filters have, in fact, been used for FDM-based communications in the past, and may find application in some speech recognition architectures. One convenient method for implementing banks of fourth order filters utilizing single resonator filters is shown in Fig. 5.34. Here, the outputs of two microresonators spaced in frequency by a designed amount are combined to yield a higher order bandpass or notch filter.

Whether a bandpass or a notch filter results depends upon the respective phases of the outputs of the two resonators. If the phase difference for the inputs to the resonators is 180°, the response spectra for the individual resonators are in phase in the frequency interval between the

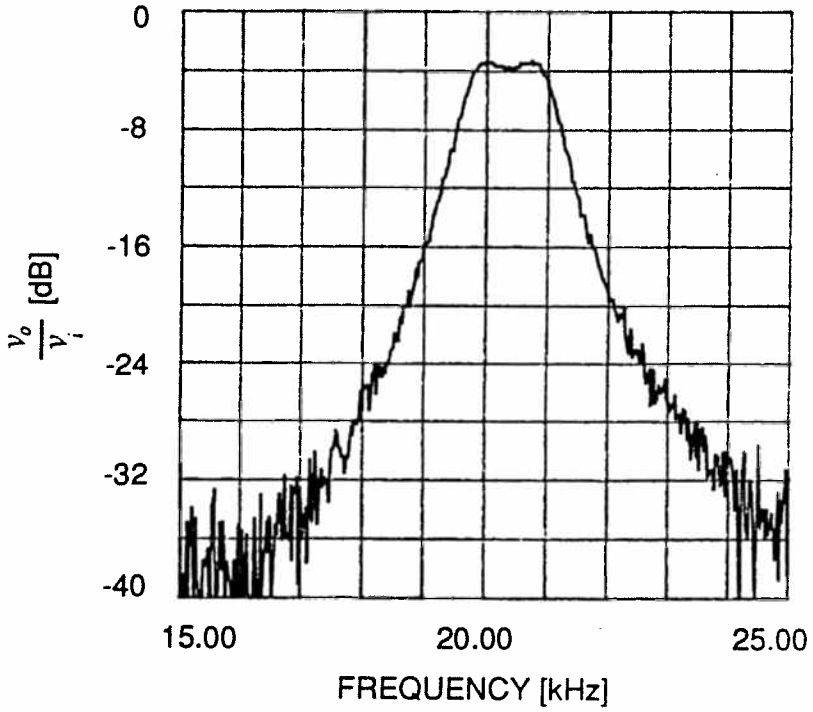

Fig. 5.33: Spectrum of a two-resonator micromechanical filter.

resonance frequencies. Thus, they combine here, creating a flat passband between resonators. In the stopband (i.e., frequencies not between the resonances), the outputs are out of phase, and subtract, creating a sharper rolloff. In effect, a bandpass filter response is implemented. In Fig. 5.34, the bandpass filter is implemented when the switch is set at 1, which includes the analog inverter. A pictorial representation of the mechanism behind this filter is shown in Fig. 5.35(a).

For the notch filter, the phasing scheme is reversed as shown in Fig. 5.35(b). Here, there is subtraction between the resonances and addition outside. The notch filter is implemented when the switch is set at 2 in Fig. 5.34.

Figure 5.34 shows the implementation of a two-resonator filter. With the addition of more such resonator pairs, a parallel bank of fourth-order filters can easily be envisioned.

5.6 Conclusions

High-Q electronic signal processing filters have been investigated and demonstrated utilizing polysilicon micromechanical resonators. Particular attention was focused upon noise and designability. Due to inadequate electromechanical coupling in present-day micro-scale capaci-

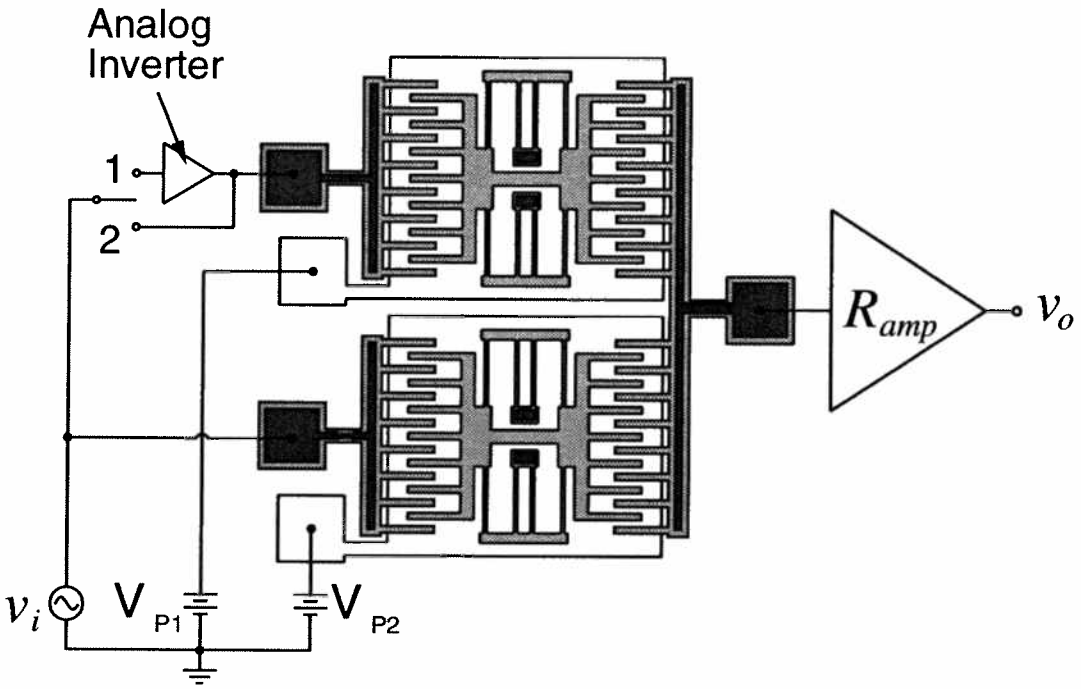

Fig. 5.34: Schematic of a parallel microresonator filter. When the switch is set at 1, the analog inverter provides a 180° phase shift and a bandpass filter results. When the switch is set at 2, a notch filter is implemented.

tively transduced resonators, the series motional resistance of such resonators is quite large, on the order of 100 kΩ on up, for reasonable dc-bias voltage values and capacitor gaps. This large series resistance impacts the feasibility of micromechanical filters in two ways:

6. The equivalent noise resistance of a system using such filters at the front end is equal the resistance of the microresonator R_x. Large R_x means more input referred voltage noise.
7. Large R_x (and correspondingly large series inductance L_x), leads to the requirement for large terminating resistors for spring-coupled ladder filters, which in turn makes a given filter more susceptible to passband distortion by parasitics.

In many ways, active Q control can alleviate some of the above problems. Active Q-control has been shown to be an effective method for terminating micromechanical resonators (i.e., for lowering the Q of such resonators), while avoiding passband distortion, and with very little added noise.

With smaller capacitor gaps or larger dc-bias voltages (or higher Q's), the series motional resistance of micromechanical resonators may be reduced, making the design and performance of

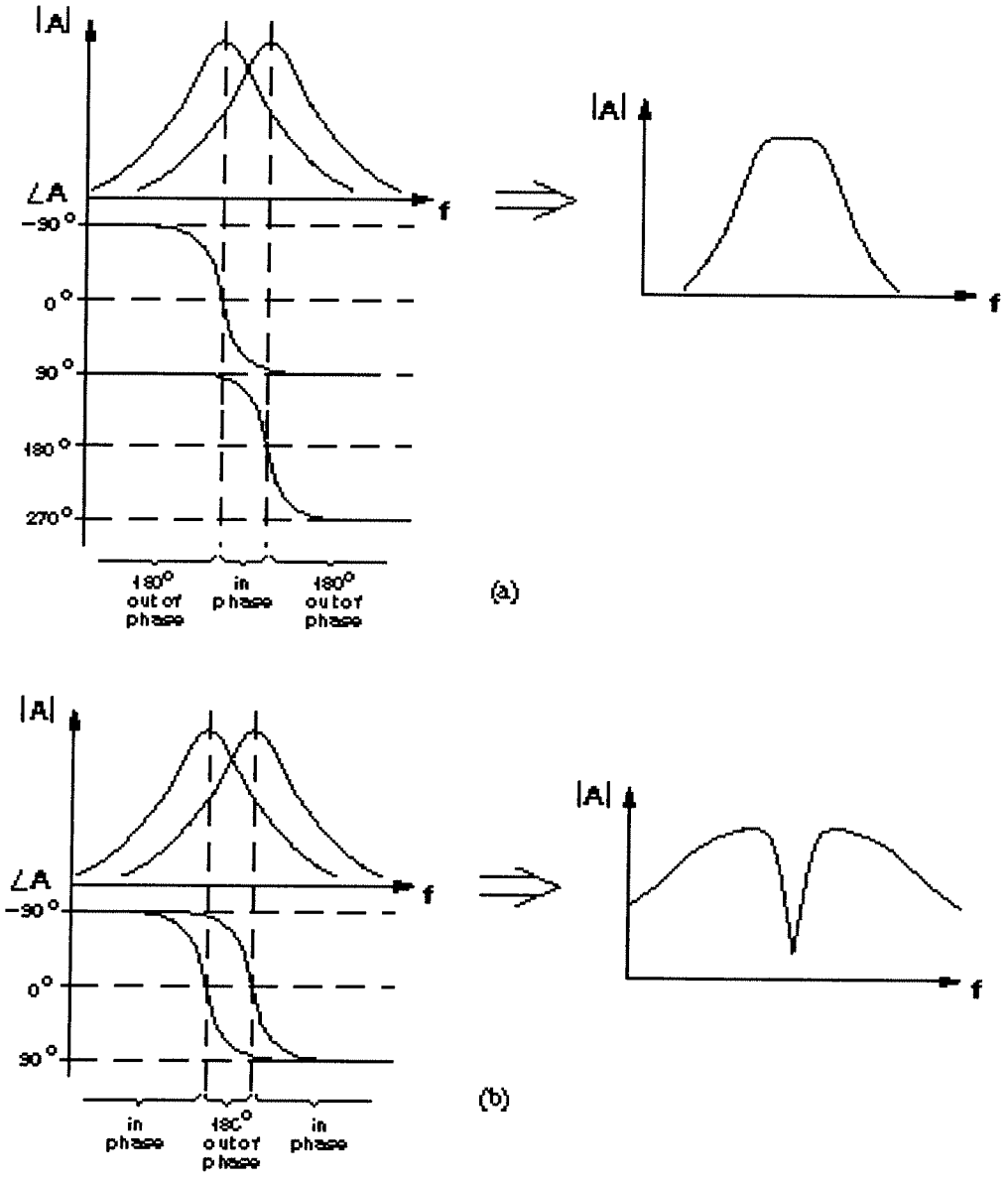

Fig. 5.35: Mechanism behind parallel microresonator filters for the case of (a) a bandpass filter; and (b) a notch filter. In (a), microresonator currents at frequencies between the resonances of the microresonators are in phase, and thus, add. Those at frequencies outside this interval are 180° out of phase, and thus, subtract, leading to improved roll-off. In (b), everything in (a) is turned around.

micromechanical filters much impressive; equal to, or perhaps better, than present-day macroscopic filters. Thus, series resistance reduction will very likely be a topic for future research.

CHAPTER 6 *Mixing and Modulation Via Micromechanical Resonators*

In Chapter 2, the "normal" bias and excitation configuration for capacitively driven micromechanical resonators was presented as Fig. 2.11 or Fig. 2.16. These, in fact, are the preferred configurations for filters where parasitic feedthrough from input to output is not a problem. Such filters usually operate at lower frequencies, or are extremely selective (i.e. they have very high Q). For filters which operate at high frequencies, or which are heavily damped (i.e. low Q), parasitic feedthrough currents may often mask motional currents, which, as shown in Chapter 2, can be very small.

In this Chapter, methods by which the output motional current of a micromechanical resonator (filter) can be separated from parasitic feedthrough in the frequency domain will be detailed. The basic techniques involve the application of a carrier frequency to the mechanical resonator (in addition to the dc-bias) to amplitude modulate the output current to higher frequencies away from interfering parasites, or to allow excitation of the resonator with frequencies different from the its resonance frequency. All techniques are detailed in this chapter, and applications, such as communications up- and down-conversion (heterodyning) using a single micromechanical resonator (or filter composed of resonators) and quadrature modulators using microresonators.

6.1 Parasitic Feedthrough Interference

The intrinsic transconductance spectrum for a two-port micromechanical resonator biased, excited, and sensed as in Fig. 2.14 is as shown in Fig. 2.7. For many filtering applications, the

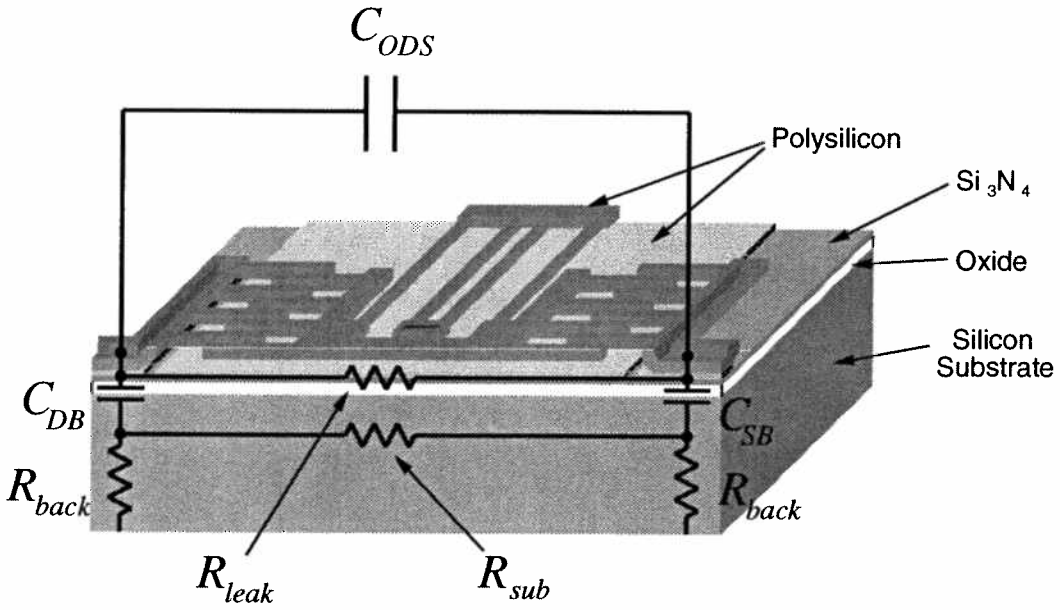

Fig. 6.1: Perspective view of a micromechanical resonator and the parasitic elements which influence its electrical characteristics.

symmetry of this spectrum is very desirable. Unfortunately, this symmetry is not always achievable in the face of parasitics, which can dominate over the tiny motional currents typical for micro-scale capacitively transduced resonators. Specifically, feedthrough currents which flow through port-to-port dc parasitic capacitors shown in Fig. 6.1 are at the same frequency as the excitation voltage and resonator motional current, and can be large enough to mask the motional current and distort the frequency spectrum of the resonator by adding a parallel resonance.

6.1.1 *Q*- and Frequency-Dependence of Parasitic-Induced Passband Distortion

The parasitic dc capacitance of concern for two-port resonators is identical to the dc capacitance intrinsic to quartz crystals or one-port resonators. It, thus, effects the passband in an identical manner: It adds a parallel resonance peak at a slightly higher frequency than the series resonance peak.

There are several sources of parasitic feedthrough currents which compete with the motional current from a dc-biased oscillating resonator. These sources are summarized in Fig. 6.1 for a folded-beam comb-driven microresonator. In this figure, C_{ODS} represents the capacitance

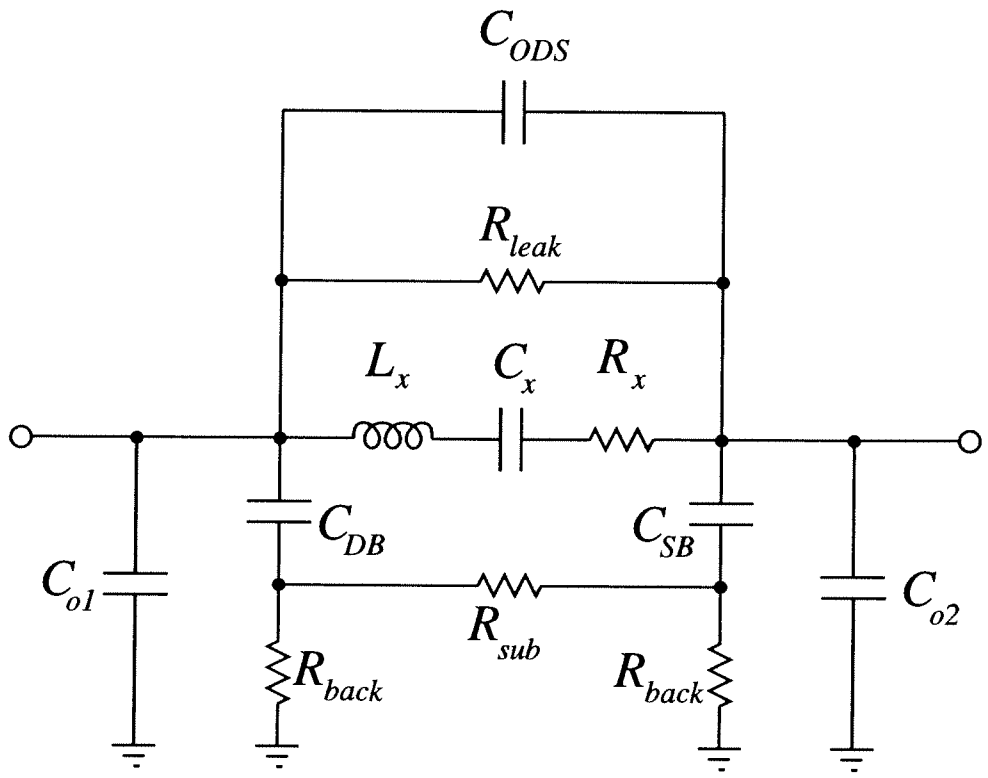

Fig. 6.2: Equivalent circuit, including parasitics, for the symmetrical micromechanical resonator of Fig. 6.1.

coupling the drive electrode to the sense electrode over the resonator. C_{DB} and C_{SB} denote electrode-to-substrate capacitors, which could significantly couple the drive and sense electrodes if the substrate resistance R_{sub} is small and uncontacted. Finally, R_{leak} represents leakage current components due to moisture on the substrate or any other impurities which resistively couple the drive and sense electrodes.

These parasitics combined with the port-to-port equivalent circuit of a micromechanical resonator (shown in Fig. 2.23) yield the equivalent circuit shown in Fig. 6.2 (where the LCR equivalent for a port-symmetrical resonator is used for convenience). As before, C_{o1} and C_{o2} represent electrode-to-ground plane and electrode-to-shuttle capacitance. As derived in Chapter 2, the motional current of the micoresonator is given by

$$i_x = \omega \frac{Q}{k} V_P^2 \left(\frac{\partial C}{\partial x}\right)^2 v_i, \tag{6.1}$$

where we assume that $V_D = V_S = 0$ and that $(\partial C/\partial x)_d = (\partial C/\partial x)_s = (\partial C/\partial x)$ for notational convenience. Assuming for now that the leakage resistance R_{leak} is large enough to be neglected, the parasitic feedthrough current is capacitive, and is given by

$$i_P = j\omega C_P v_i, \tag{6.2}$$

where C_P is the total effective parasitic capacitance coupling the drive and sense electrodes. Using Eqs. (6.1) and (6.2), the magnitude ratio of motional current to parasitic feedthrough current is

$$\phi_{xp} = \left|\frac{i_x}{i_P}\right| = \frac{\frac{Q}{k}V_P^2\left(\frac{\partial C}{\partial x}\right)^2}{C_P} = \frac{\eta^2 Q}{kC_P}, \tag{6.3}$$

where as in Chapter 2, η is the electromechanical coupling factor, and k is the system spring constant. A large value of ϕ_{xp} corresponds to little interference from parasitics, whereas a small value indicates significant interference.

From Eq. (6.3) we see that ϕ_{xp} increases with increasing quality factor Q and decreasing spring constant k. Thus, for a low frequency microresonator operated under vacuum, for which k is small and Q is large, interference from parasitics should be negligible. However, as the frequency of the resonator increases, k usually gets larger and Q is expected to decrease, resulting in an overall decrease in ϕ_{xp}. Thus, interference from capacitive feedthrough parasitics is expected to be a problem for high frequency microresonators.

6.1.1.1 Shielding Techniques

There are two obvious approaches to minimizing feedthrough along the path from drive electrode to substrate, then substrate to sense electrode. One approach would be to make the substrate as resistive as possible in an effort to minimize current flow. This works well when the resonator (filter) has high Q, and the drive voltage amplitude need only be a few milliWatts to instigate adequate vibration amplitude. For low Q applications, where drive voltages of 1 V or more are required, substantial current may still pass through even large substrate resistors. For example, one volt applied across a substrate resistor of $10^9\ \Omega$ would result in 1 nA of feedthrough current, which is already comparable to the expected resonator current. In addition, if electronics are also inte-

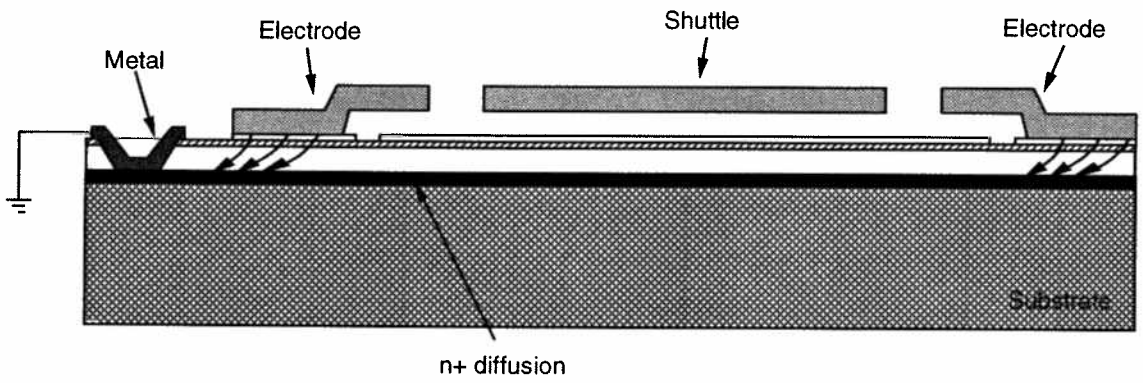

Fig. 6.3: Strategy for reduction of parasitic feedthrough current. Here, a grounded, heavily doped substrate ground plane is used to soak up parasitic feedthrough currents, steering them away from the sense electrode.

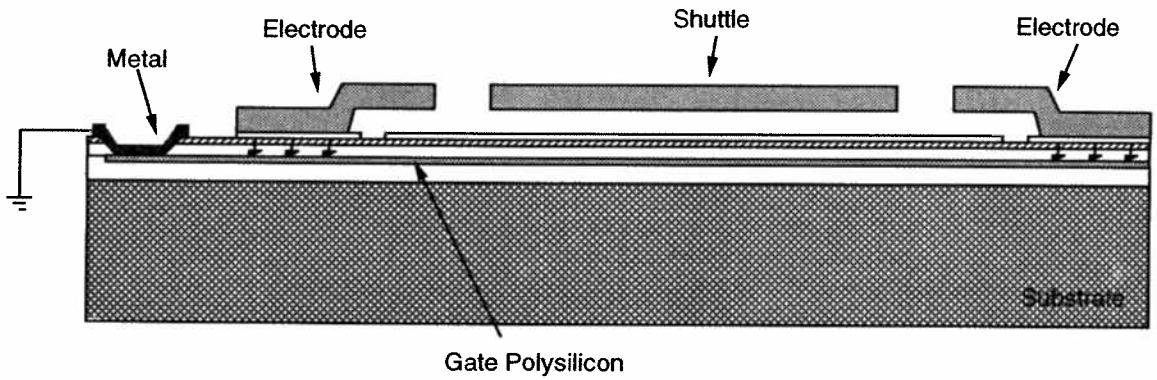

Fig. 6.4: Strategy for reduction of parasitic feedthrough current. Here, the gate polysilicon in the merged CMOS plus microstructures process serves as a ground plane which steers parasitic feedthrough currents away from the sense electrode.

grated onto the same substrate (as in this work), the resistance of the substrate cannot be tailored to an arbitrarily large value. Thus, the strategy of increasing substrate resistivity is not optimal.

Another approach is to make the substrate conductive and ground it out. This way current feeding through from the drive electrode to the substrate can be steered away from the sense electrode, greatly minimizing substrate drive-to-sense feedthrough. This can be practically implemented by heavily doping the substrate, as shown in Fig. 6.3, or by putting a zero-level ground plane under the entire microresonator or microfilter, as shown in Fig. 6.4, where the gate polysilicon of the merged CMOS + Microstructures process is used for this purpose. By careful placement

of grounding contacts to this blanket ground plane, the parasitic feedthrough under the resonator may be substantially reduced.

For the 455 kHz micromechanical filter design of Section 5.3.3, overhead drive-to-sense electrostatic coupling is not a big problem, since the distance between input and output ports is comparatively large, and the filter structure effectively serves as a ground plane, soaking up would be coupling field lines. For higher frequency filters, however, the dimensions are much smaller, and the drive and sense electrodes are close enough that overhead electrostatic coupling becomes a problem. Much of this coupling could be eliminated by a conductive microshell, which could also provide vacuum encapsulation. Without microshell technology, there are, of course, a wide variety of geometric strategies that could be used to minimize overhead coupling.

Although the shielding techniques above can substantially reduce the amount of feedthrough coupling from the input to the output of a microfilter, this still may not be enough in many situations. Thus, some other strategy which separates motional current from parasitic feedthrough may be required.

6.2 Gated Sinusoid Excitation and Detection

Separation of motional current from parasitics can be done in either the time or frequency domains. One available time domain technique involves gated sinusoid excitation and detection (GSED), which is summarized in Fig. 6.5. Here, excitation and detection of the microresonator are done in separate (clock) phases. As shown in Fig. 6.5, the microresonator is first driven by a sinusoidal excitation signal over the first phase. The excitation is then abruptly cut-off, at which point, motional current is detected by sense electronics. The magnitude of motional current detected is a function of the quality factor of the resonator and of the time difference between cessation of the drive signal and the start of sensing.

Since this chapter concentrates on frequency domain techniques, the GSED method will not be discussed in detail. More information on this technique can be found in [99].

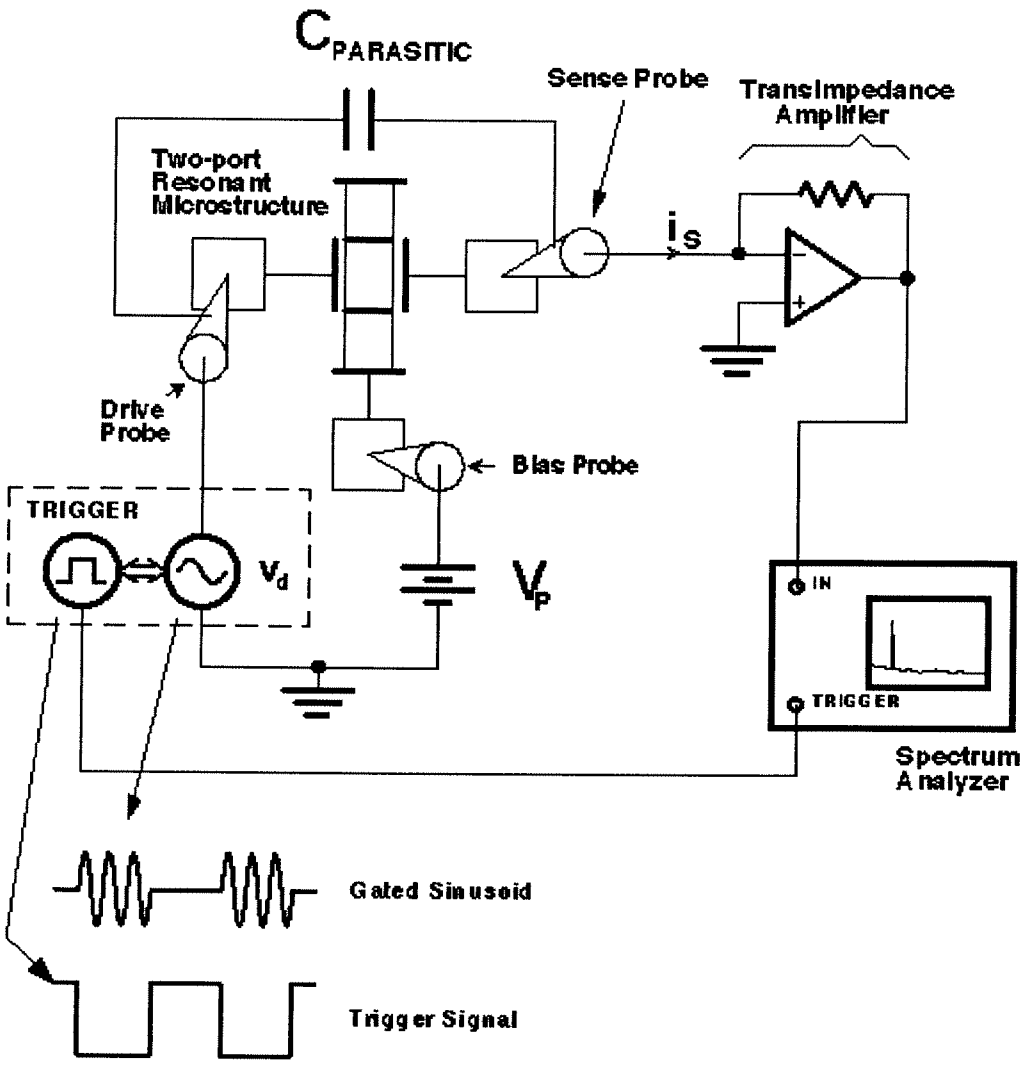

Fig. 6.5: Schematic of the gated sinusoid excitation and detection (GSED) method for separating motional current from parasitic feedthrough in the time domain.

6.3 Electromechanical Amplitude Modulation (EAM)

There are two methods by which motional current can be separated from parasitic feedthrough in the frequency domain: (1) drive the resonator with an ac voltage at the resonance frequency and sense motional current at a frequency other than the resonance frequency; or (2) drive the resonator with an ac voltage not equal to the resonance frequency and sense motional current at the resonance frequency. Method (2) will be discussed in Section 6.4.

One way to implement method (1) is to first recognize the main difference between motional current and parasitic feedthrough: motional current arises from ac capacitors, while parasitic feedthrough flows through dc capacitance. Thus, if a carrier signal at frequency ω_c were introduced into the system that gets modulated only by signals derived from ac capacitors, and not by those derived from dc capacitors, then motional and parasitic feedthrough currents may be separated in the frequency domain. Motional currents would be mixed to sidebands around the carrier frequency ω_c, while parasitics would remain at the drive frequency ω_c. Upon subsequent demodulation, motional current would end up at ω_d, while feedthrough and carrier components would be at much higher (or lower, depending on ω_c) frequencies.

The above technique will be termed electromechanical amplitude modulation (EAM). Injection of the carrier signal may be accomplished via the schematic shown in Fig. 6.6, where the device symbol for a two-port folded-beam micromechanical resonator is used. The principle difference from the drive configurations shown previously lies in the biasing of the microstructure, which now includes an ac carrier signal, as well as the dc-bias. The latter is still necessary, since it both amplifies the drive force (Eq. (2.12)) and allows this force to be at the same frequency as the drive voltage. Qualitatively, the carrier signal and its time-derivative are multiplied by capacitive elements of microstructure motion, resulting in motional current, frequency-shifted to sidebands around the carrier frequency and separated from dc parasites still at the driving frequency. The end result of the EAM technique, after demodulation, is an effective nulling of all dc feedthrough capacitors, including any dc capacitors intrinsic to the microresonator. The principle mechanisms involved in electromechanical amplitude modulation will now be derived.

6.3.1 The EAM Sidebands

The Fourier spectrum for the sense current i_s in Fig. 6.6 will now be derived for the case of a two-port electrostatic-comb driven lateral microresonator. This current is given by (refer to Fig. 6.6)

$$i_s = C_{PD}\frac{dV_d(t)}{dt} + C_{PC}\frac{dV_s(t)}{dt} + C_s(t)\frac{dV_s(t)}{dt} + V_s(t)\frac{dC_s(t)}{dt} \tag{6.4}$$

where

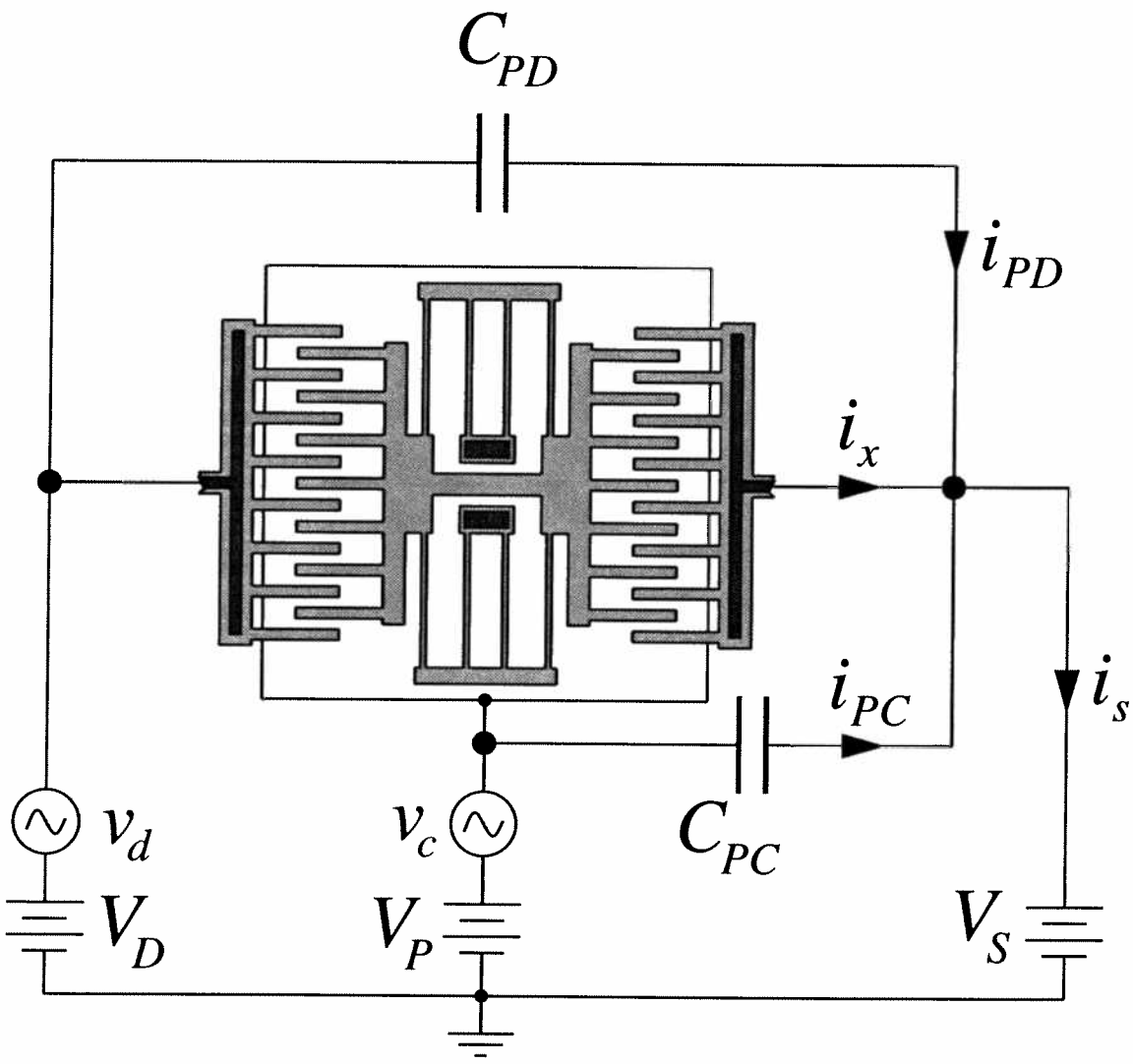

Fig. 6.6: Bias and excitation configuration which implements electromechanical amplitude modulation (EAM). Here, the device symbol for a two-port folded-beam micromechanical resonator is used.

$$
\begin{aligned}
v_d(t) &= |v_d| \cos \omega_d t \\
v_c(t) &= |v_c| \cos \omega_c t \\
V_d(t) &= V_{PD} + v_d(t) \\
V_s(t) &= V_{PC} + v_c(t) \\
V_{PD} &= V_P - V_D \\
V_{PC} &= V_p - V_C
\end{aligned}
\tag{6.5}
$$

and

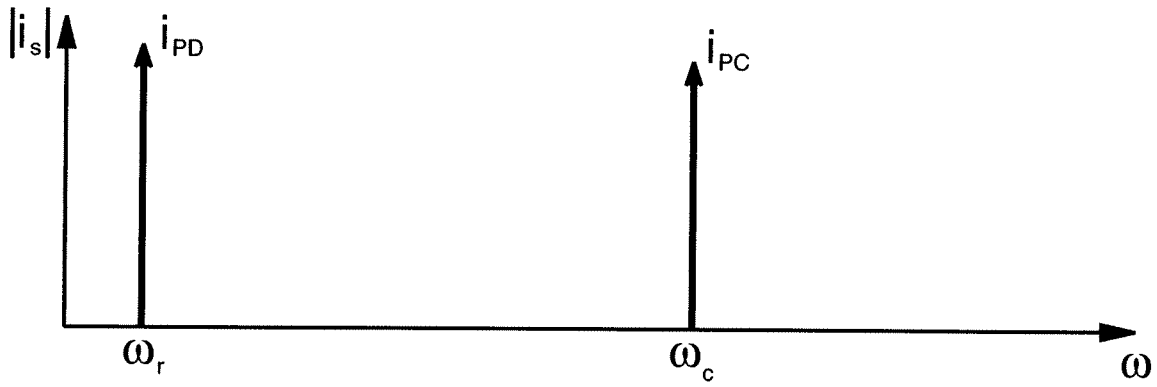

Fig. 6.7: Fourier spectrum of the sense current i_s of Fig. 6.6 for off resonance drive frequencies.

$$C_s(t) = \begin{cases} \approx C_{os} & \text{off resonance} \\ C_{os} + C_{ms}(t) & \text{at resonance} \end{cases} \tag{6.6}$$

$$C_{ms}(t) = |C_{ms}| \sin \omega_r t \tag{6.7}$$

where $C_s(t)$ represents the microresonator finger-overlap capacitance at the *sense port*, C_{os} is the dc value of this capacitance, $C_{ms}(t)$ is the motional (ac value of) capacitance at the sense port, and C_{PD} and C_{PC} are parasitic capacitors coupling the microresonator ports. Solving Eq. (6.4) using the off resonance condition of Eq. (6.6) the current entering the sense port during nonresonance periods is found to be

$$i_p = -(\omega_d C_{PD} |v_d| \sin \omega_d t + \omega_c (C_{PC} + C_{os}) |v_c| \sin \omega_c t) \, . \tag{6.8}$$

This current is composed predominantly of parasitic components, and thus, it is given the subscript *P*. The Fourier spectrum for i_s off resonance, predicted by Eq. (6.8), is shown in Fig. 6.7.

At resonance, Eq. (6.4) with the appropriate condition of Eq. (6.6) and setting $\omega_d = \omega_r$ (*r* for resonance), yields

$$\begin{aligned} i_r = {} & i_P + \omega_r V_{PS} |C_{ms}| \cos \omega_r t \\ & -\frac{1}{2} (\omega_c - \omega_r) |C_{ms}| |v_c| \cos (\omega_c - \omega_r) t \\ & +\frac{1}{2} (\omega_c + \omega_r) |C_{ms}| |v_c| \cos (\omega_c + \omega_r) t \end{aligned} \tag{6.9}$$

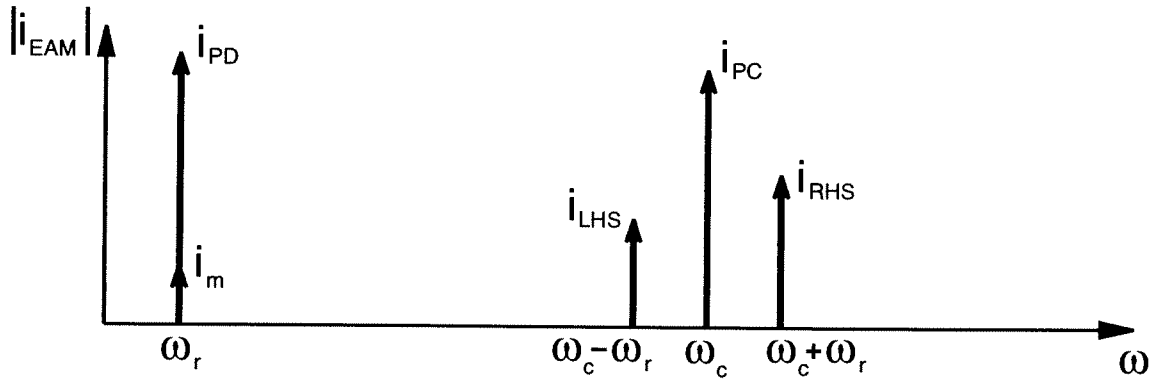

Fig. 6.8: Fourier spectrum for $i_s = i_{EAM}$ of Fig. 6.6 at resonance.

The current peaks (in the Fourier spectrum) due to motion of the microstructure are those containing the time-varying capacitance amplitude term, $|C_{ms}|$. The motional currents of interest, however, are only those at frequencies ($\omega_c - \omega_r$) and ($\omega_c + \omega_r$), since the motional current at ω_r is inaccessible due to masking by feedthrough currents. The amplitudes of these sidebands are readily seen from Eq. (6.9) to be given by

$$|I_{LHS}| = \frac{1}{2}(\omega_c - \omega_r)|C_{ms}||v_c| \tag{6.10}$$

$$|I_{RHS}| = \frac{1}{2}(\omega_c + \omega_r)|C_{ms}||v_c| \tag{6.11}$$

These equations show that the left-hand and right-hand sidebands of motional current are not equal in amplitude. The Fourier spectrum corresponding to Eq. (6.9) for i_s at resonance is presented in Fig. 6.8.

Equations (6.10) and (6.11) may be converted to useful transconductance equations, relating phasor sense current I_s to phasor drive voltage V_d, given an expression for $|C_{ms}|$. Thus, defining the displacement x of the microstructure at resonance by

$$x = |x| \sin \omega_r t \tag{6.12}$$

we can obtain an expression for $|C_{ms}|$ through the time-derivative of C_{ms} (Eq. (6.7))

$$\frac{\partial C_{ms}(x,t)}{\partial t} = \frac{\partial C_s(x,t)}{\partial x}\frac{\partial x}{\partial t}. \tag{6.13}$$

Converting to phasor form and cancelling jω terms gives

$$|C_{ms}| = \left(\frac{\partial C}{\partial x}\right)_s X. \tag{6.14}$$

The expression for the transfer function relating phasor displacement X to phasor drive voltage V_d for an electrostatic-comb driven lateral resonant structure at resonance was given in Chapter 2 as Eq. (2.58), and is repeated here for convenience:

$$\frac{X}{V_d}(j\omega) = \frac{k^{-1}V_{PD}\left(\frac{\partial C}{\partial x}\right)_d}{1-(\omega/\omega_r)^2+j(\omega/Q\omega_r)}, \tag{6.15}$$

where Q is the loaded quality factor of the resonator, k is the system spring constant, and $(\partial C/\partial x)_d$ is the resonator-to-electrode capacitance change per unit displacement at the drive port. Inserting (6.15) in (6.14), the expression for $|C_{ms}|$ is found to be

$$|C_{ms}| = \left|\frac{k^{-1}V_{PD}\left(\frac{\partial C}{\partial x}\right)_d\left(\frac{\partial C}{\partial x}\right)_s V_d}{1-(\omega/\omega_r)^2+j(\omega/Q\omega_r)}\right| \tag{6.16}$$

Substitution of (6.16) in Eqs. (6.10) and (6.11) yields the transconductance functions at resonance relating phasor sense current I_s and phasor drive voltage V_d for each sideband of motional current:

$$\frac{I_{LHS}}{V_d}(\omega_c-\omega) = -\frac{1}{2}\frac{j(\omega_c-\omega)|v_c|V_{PD}k^{-1}\left(\frac{\partial C}{\partial x}\right)_d\left(\frac{\partial C}{\partial x}\right)_s}{1-(\omega/\omega_r)^2+j(\omega/Q\omega_r)} \tag{6.17}$$

$$\frac{I_{RHS}}{V_d}(\omega_c+\omega) = \frac{1}{2}\frac{j(\omega_c+\omega)|v_c|V_{PD}k^{-1}\left(\frac{\partial C}{\partial x}\right)_d\left(\frac{\partial C}{\partial x}\right)_s}{1-(\omega/\omega_r)^2+j(\omega/Q\omega_r)}. \tag{6.18}$$

The transconductance function for a dc-biased (*no ac*) electrostatic-comb driven lateral microresonator was given in Chapter 2 by Eq. (2.64), which is repeated here for convenience

$$\frac{I_s}{V_d}(j\omega) = \frac{j\omega k^{-1}V_{PD}V_{PS}\left(\frac{\partial C}{\partial x}\right)_d\left(\frac{\partial C}{\partial x}\right)_s}{1-(\omega/\omega_r)^2+j(\omega/Q\omega_r)} \tag{6.19}$$

Comparison of (6.19) with Eqs. (6.17) and (6.18) shows that motional current produced via EAM contains a $(1/2)(\omega_c \pm \omega_r)$ factor replacing the ω_r term of oscillating dc-biased structures. Thus, when $\omega_c \gg \omega_r$ motional current produced via EAM is amplified over that produced by an oscillating dc-biased (*only*) structure by a factor of approximately $\frac{\omega_c}{2\omega_r}\frac{|v_c|}{V_{PS}}$, which can be very large for high carrier frequencies.

6.3.2 Demodulation of EAM Motional Current

In order to view the transconductance spectrum of the microresonator under a network analyzer, the EAM motional current i_{EAM} must be post-processed by *off-chip* electronics. Figure 6.9 summarizes the required signal processing.

The first step (Fig. 6.9(a)) involves a (transimpedance) amplification and bandpass filtering to eliminate the parasitic feedthrough component at the drive frequency ω_r (assuming resonance). Next (Fig. 6.9(b)), the EAM components of current i_{RHS} and i_{LHS} must be demodulated back down to the resonance frequency ω_r, yielding finally, the Fourier spectrum shown in Fig. 6.9(c). Note that the bandpass filtering in Fig. 6.9(a) would not be necessary if the demodulation in Fig. 6.9(c) were ideal, since parasitic components at the resonance frequency would effectively be mixed to higher frequencies However, since the actual mixer is not perfectly linear, some fraction of the parasitic components may remain at the resonance frequency, and may still be large enough to distort the transconductance spectrum. (Remember, the parasitics may have been orders of magnitude larger than the motional current to begin with, so a fraction of this will still dominate.)

The spectrum in (c) is suitable for input to a network analyzer even without the lowpass filtering shown. (The lowpass filter is, of course, necessary for communications applications or for viewing via an oscilloscope.)

Let us now focus on the demodulation of the EAM motional current back to the original microstructure oscillation frequency. As with any amplitude-modulated signal, this can be achieved by multiplication with a sinusoid of the carrier frequency ω_c. To obtain an expression for

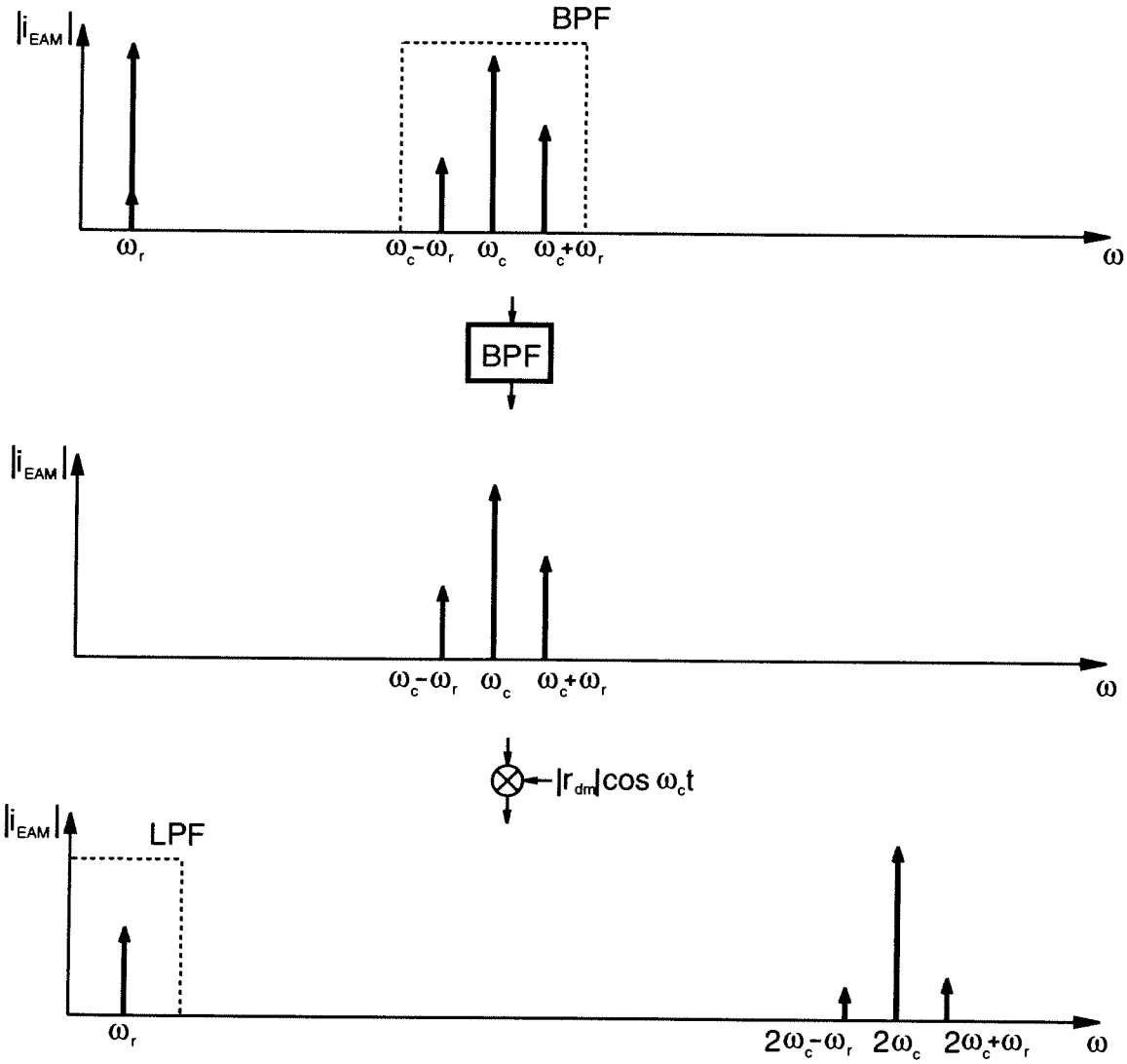

Fig. 6.9: Schematic flow diagram of the post-processing necessary to prepare the EAM current i_{EAM} for in put to a network analyzer. (a) A bandpass filter is used to filter out the components at the drive frequency. This filtering also improves the signal-to-noise ratio of the system. (b) The sidebands are demodulated back down to the drive frequency with a sinusoid at the carrier frequency ω_c and with adjustable phase. (c) Final EAM output suitable for input to a network analyzer. For viewing with an oscilloscope, the lowpass filter will be necessary.

the signal at the output of the demodulator v_{dm}, let us first assume a demodulating sinusoid with resistive amplitude $|r_{dm}|$[8] [and *in phase* with the original carrier:

$$r_{dm} = |r_{dm}| \cos \omega_c t \tag{6.20}$$

Multiplication of Eq. (6.9) with (6.20), then, yields the following:

$$\begin{aligned} v_{dm} &= i_r r_{dm} \\ &= -\frac{1}{2}\omega_d C_{PD}|v_d||r_{dm}|\,[\sin(\omega_r-\omega_c)\,t+\sin(\omega_r+\omega_c)\,t] \\ &\quad -\frac{1}{2}\omega_c C_{PC}|v_c||r_{dm}|\sin 2\omega_c t \\ &\quad +\frac{1}{2}\omega_r V_{PS}|C_{ms}||r_{dm}|\,[\cos(\omega_c-\omega_r)\,t+\cos(\omega_c+\omega_r)\,t] \\ &\quad -\frac{1}{4}(\omega_c-\omega_r)\,|v_c||C_{ms}||r_{dm}|\,[\cos(2\omega_c-\omega_r)\,t+\cos\omega_r t] \\ &\quad -\frac{1}{4}(\omega_c+\omega_r)\,|v_c||C_{ms}||r_{dm}|\,[\cos(2\omega_c+\omega_r)\,t+\cos\omega_r t] \end{aligned} \tag{6.21}$$

The term at the resonance frequency ω_r is usually of most interest. From Eq. (6.21),

$$v_{EAM} = \frac{1}{2}\omega_r|v_c||C_{ms}||r_{dm}|\cos\omega_r t\,. \tag{6.22}$$

The output voltage after amplification and demodulation is, thus, of the same order of magnitude as the voltage that would be sensed from a dc-biased (*no ac*) oscillating microstructure with $V_{PS} = |v_c|$ (Eq. (6.19)). Thus, demodulation by a sinusoid *in phase* with the original carrier negates the $\omega_c/2\omega_r$ amplification originally provided by EAM.

Fortunately, however, the EAM amplification can be retrieved by proper selection of the phase of the demodulating carrier r_{dm}. To see this, let us now obtain an expression for the amplitude of v_{EAM} as a function of the phase θ of r_{dm}, generalized as

$$r_{dm} = |r_{dm}|\cos(\omega_c t+\theta) \tag{6.23}$$

Multiplication of Eq. (6.23) with (6.9) and taking only motional current terms yields:

---

[8] A resistance is used to be consistent with the current-to-voltage electronics used in previous chapters. Note that capacitive detection could also be used as long as phase considerations are preserved.

$$
\begin{aligned}
v_{dm} &= i_r r_{dm} \\
&= \ldots - \frac{1}{4}(\omega_c - \omega_r)\,|v_c||C_{ms}||r_{dm}|\,\{\cos[(2\omega_c - \omega_r)\,t + \theta] + \cos(\omega_r t + \theta)\} \\
&\quad + \frac{1}{4}(\omega_c + \omega_r)\,|v_c||C_{ms}||r_{dm}|\,\{\cos[(2\omega_c + \omega_r)\,t + \theta] + \cos(\omega_r t + \theta)\}
\end{aligned}
\tag{6.24}
$$

Taking terms at ω_r,

$$
v_{EAM} = \frac{1}{4}|v_c||C_{ms}||r_{dm}|\,\{-(\omega_c - \omega_r)\cos(\omega_r t + \theta) + (\omega_c + \omega_r)\cos(\omega_r t - \theta)\} \tag{6.25}
$$

Converting to phasor form, we have

$$
v_{EAM} = \frac{1}{2}|v_c||C_{ms}||r_{dm}|\,\{\omega_r \cos\theta - j\omega_c \sin\theta\} \tag{6.26}
$$

Expressing the above in terms of magnitude and phase,

$$
V_{EAM} = |V_{EAM}|\exp(\angle V_{EAM}) \tag{6.27}
$$

where

$$
|V_{EAM}| = \frac{1}{2}|v_c||C_{ms}||r_{dm}|\sqrt{\omega_r^2\cos^2\theta + \omega_c^2\sin^2\theta} \tag{6.28}
$$

$$
\angle V_{EAM} = \tan^{-1}\left(-\frac{\omega_c \sin\theta}{\omega_r \cos\theta}\right) \tag{6.29}
$$

The θ corresponding to the maximum V_{EAM} amplitude can be found by setting the derivative of $|V_{EAM}|$ to zero and solving for θ, yielding:

$$
\frac{\partial|V_{EAM}|}{\partial\theta} = \frac{2(\omega_c^2 - \omega_r^2)\sin\theta\cos\theta}{\sqrt{\omega_r^2\cos^2\theta + \omega_c^2\sin^2\theta}} = 0 \quad \Rightarrow \quad (\omega_c^2 - \omega_r^2)\sin\theta\cos\theta = 0 \tag{6.30}
$$

From Eq. (6.30), $|V_{EAM}|$ is maximized when $\theta = 0^\circ$ or 90°, depending upon which of ω_c and ω_r is larger.

For the usual case where $\omega_c \gg \omega_r$, $|V_{EAM}|$ is maximized for $\theta = 90^\circ$, as can be seen in the $|V_{EAM}|$ vs. θ plot shown in Fig. 6.10. Evaluating Eq. (6.28) at $\theta = 90^\circ$, the maximum v_{EAM} is found to be

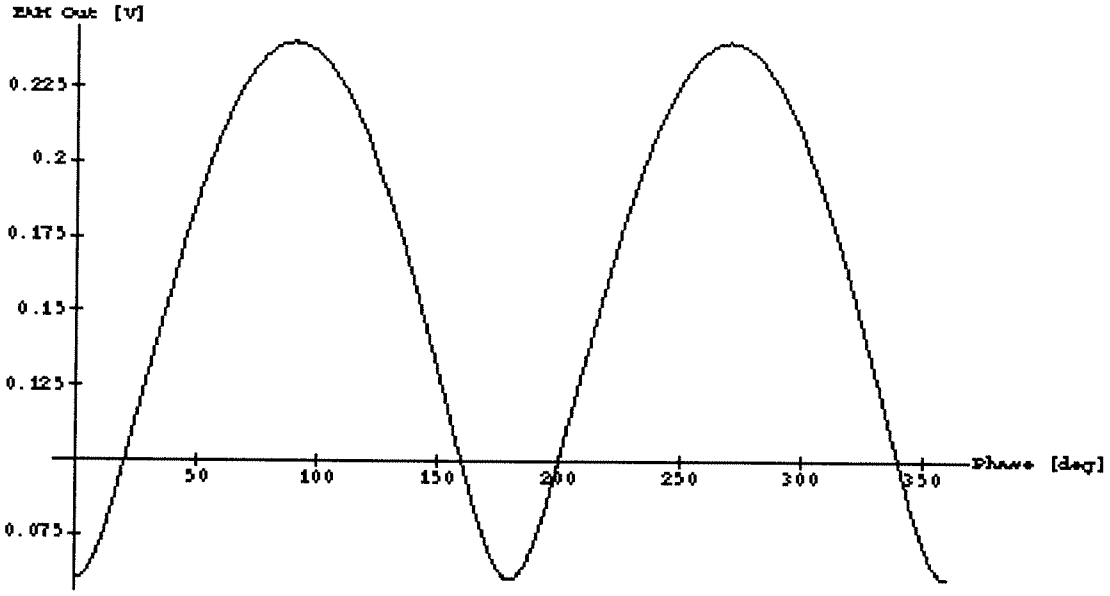

Fig. 6.10: Amplitude of EAM output voltage $|V_{EAM}|$ vs. the phase of the demodulating signal, θ, for the case of $\omega_c > \omega_r$. The plot is made specifically for the case of $|C_m| = 2.0 \times 10^{-10}$ F/m, $|v_c| = 3.0$ V, $|r_{dm}| = 10^4$, $\omega_c = 80$ kHz, and $\omega_r = 20$ kHz.

$$v_{EAM} = \frac{1}{2}\omega_c |v_c||C_{ms}||r_{dm}| \sin\omega_r t \tag{6.31}$$

Note that the maximum output signal is amplified over the output obtained directly from a dc-biased (only) microresonator by $\frac{\omega_c |v_c|}{2\omega_r V_{PS}}$, assuming identical transimpedance amplification for both cases. In addition, unlike the output from a dc-biased (only) microresonator, the EAM demodulator output is 90° phase-shifted from the input signal v_d.

In summary, to maximize the output of the EAM demodulator, a demodulation signal 90° phase-shifted from the EAM carrier $r_{dm} = |r_{dm}| \sin \omega_c t$ is required. Such a demodulation signal yields an output with amplitude proportional to the carrier frequency and with phase 90° shifted from the drive signal. Using Eqs. (6.22) and (6.31), effective transfer functions may be proposed for the output voltage (for the case of 0° and 90° phase-shifted carrier):

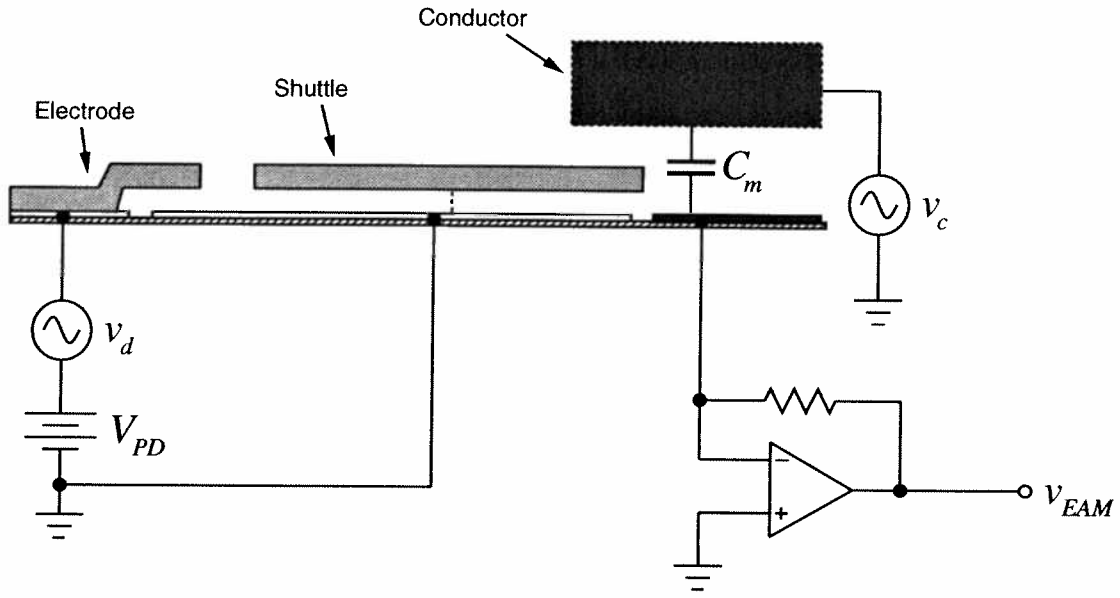

Fig. 6.11: Schematic of an implementation of remote carrier EAM.

$$\frac{V_{EAM}}{V_d}(\omega) = \frac{1}{2}\frac{j\omega k^{-1} V_{PD}|v_c||r_{dm}|\left(\frac{\partial C}{\partial x}\right)_d\left(\frac{\partial C}{\partial x}\right)_s}{1-(\omega/\omega_r)^2+j(\omega/Q\omega_r)} \tag{6.32}$$

$$\frac{V_{EAM}}{V_d}(\omega) = \frac{1}{2}\frac{\omega_c k^{-1} V_{PD}|v_c||r_{dm}|\left(\frac{\partial C}{\partial x}\right)_d\left(\frac{\partial C}{\partial x}\right)_s}{1-(\omega/\omega_r)^2+j(\omega/Q\omega_r)}. \tag{6.33}$$

6.3.3 Remote Carrier EAM

The electromechanical amplitude modulation technique can detect and determine *any* ac capacitance, and thus, it can serve a very general role in detection of motional current for any conductive resonator. One prime example of this is the availability of *remote carrier EAM*, in which the carrier signal is remotely, rather than directly, coupled to microresonator motion through a nearby noncontacting conductor. Remote carrier EAM senses microresonator motion without direct application of a carrier to the resonant shuttle or any excitation electrode.

A typical design which implements remote carrier EAM is shown in Fig. 6.11, where noncontacting conductors are placed such that the capacitance between them is chopped by the oscillating resonator. Here, one of the noncontacting conductors supplying the carrier is a third poly plate. The movable shuttle of the microresonator (which is electrically connected to the microreso-

nator ground plane) is grounded. The second noncontacting conductor is a sense plate, halfway covered by the shuttle under off resonance conditions. This plate and the third poly upper plate form the terminals of a capacitor which varies as the microresonator oscillates. This is the motional capacitance to be detected. EAM is instigated in this system by applying the carrier v_c to the noncontacting probe (effectively, across the motional capacitance). Demodulation of the resulting EAM current can be achieved as before (with the same post-processing electronics).

6.3.4 Experimental Implementation of EAM

In addition to direct communications applications, EAM may also find use in characterization (i.e. extraction of parameters, such as resonance frequency, quality factor, and $\partial C/\partial x$) of micromechanical resonators through the resonator's transconductance spectrum. An experimental set-up implementing EAM for determination of the transconductance spectrum for a microresonator is presented in Fig. 6.12.

The post-processing electronics shown follow closely that described in the previous section and in Fig. 6.9. A sample spectrum obtained using the set-up of Fig. 6.12 is presented in Fig. 6.13 for a microresonator with properties summarized in the inset. The shape of the spectrum corresponds to pure series resonance, indicating an effective nulling of dc capacitance, both parasitic and intrinsic. Resonance frequency (f_r), quality factor (Q), and peak magnitude (P_{NA}) are easily obtainable from the spectrum. From these three variables, the equivalent circuit model for the resonator may be extracted.

To facilitate the extraction process, we define an effective EAM series resistance R_{EAM90}, for the case where a 90° phase-shifted demodulating signal is used. To obtain R_{EAM90}, Eq. (6.31) (which applies at resonance) is first expanded:

$$T_{NA} = \left|\frac{v_{EAM}}{v_i}\right| = \frac{1}{2}\omega_c \frac{Q}{k} V_{PD} |v_c| |r_{dm}| \left(\frac{\partial C}{\partial x}\right)_d \left(\frac{\partial C}{\partial x}\right)_s \sin \omega_r t \,. \tag{6.34}$$

From (6.34), the effective EAM current-to-voltage ratio magnitude is given by

$$\left|\frac{i_{EAM}}{v_i}\right| = \frac{T_{NA}}{|r_{dm}|} = \frac{1}{2}\omega_c \frac{Q}{k} V_{PD} |v_c| \left(\frac{\partial C}{\partial x}\right)_d \left(\frac{\partial C}{\partial x}\right)_s , \tag{6.35}$$

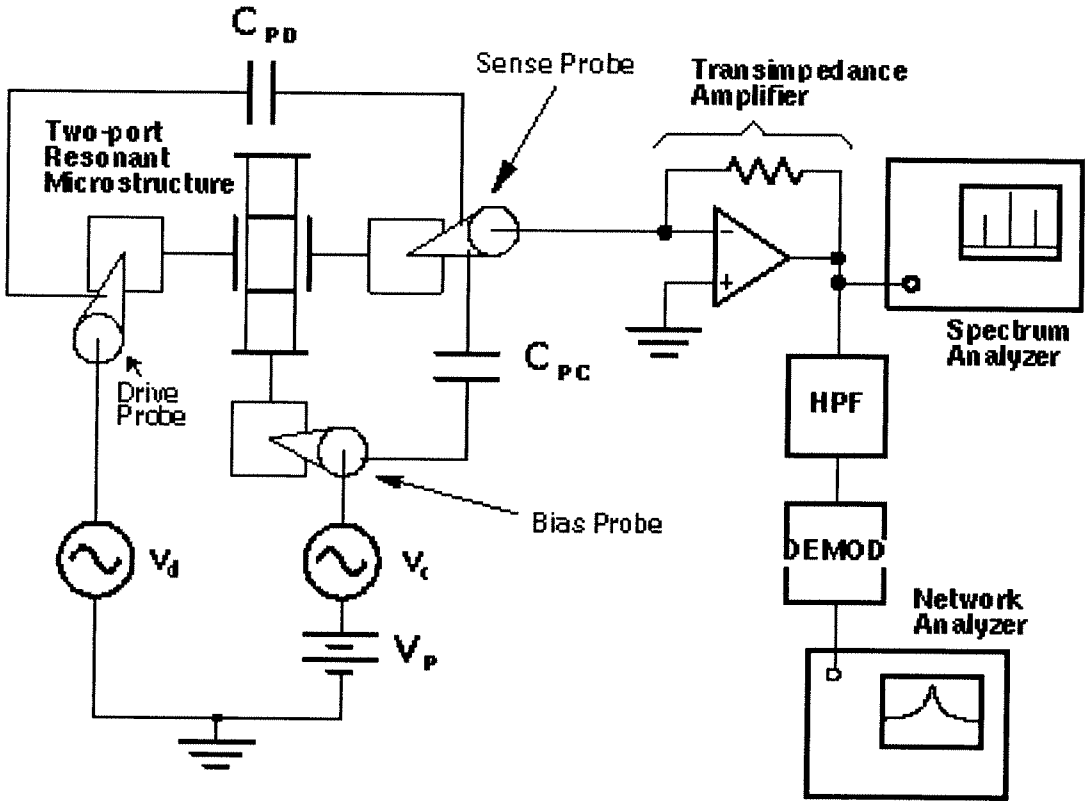

Fig. 6.12: Experimental (probe station) set-up implementing EAM for determination of the transconductance spectrum for a microresonator.

and R_{EAM90} is the inverse of (6.35):

$$R_{EAM90} = \frac{|r_{dm}|}{T_{NA}} = \frac{2k}{\omega_c Q |v_c| V_{PD} \left(\frac{\partial C}{\partial x}\right)_d \left(\frac{\partial C}{\partial x}\right)_s}. \tag{6.36}$$

Comparing Eq. (6.36) with (2.62), the series resistance of a microresonator may be related to R_{EAM90} by

$$R_x = \frac{1}{2}\frac{|v_c|}{V_{PS}}\frac{\omega_c}{\omega_r} R_{EAM90} = \frac{1}{2}\frac{|v_c|}{V_{PS}}\frac{\omega_c}{\omega_r}\frac{|r_{dm}|}{T_{NA}}. \tag{6.37}$$

Given R_x, L_x and C_x follow readily through the expressions

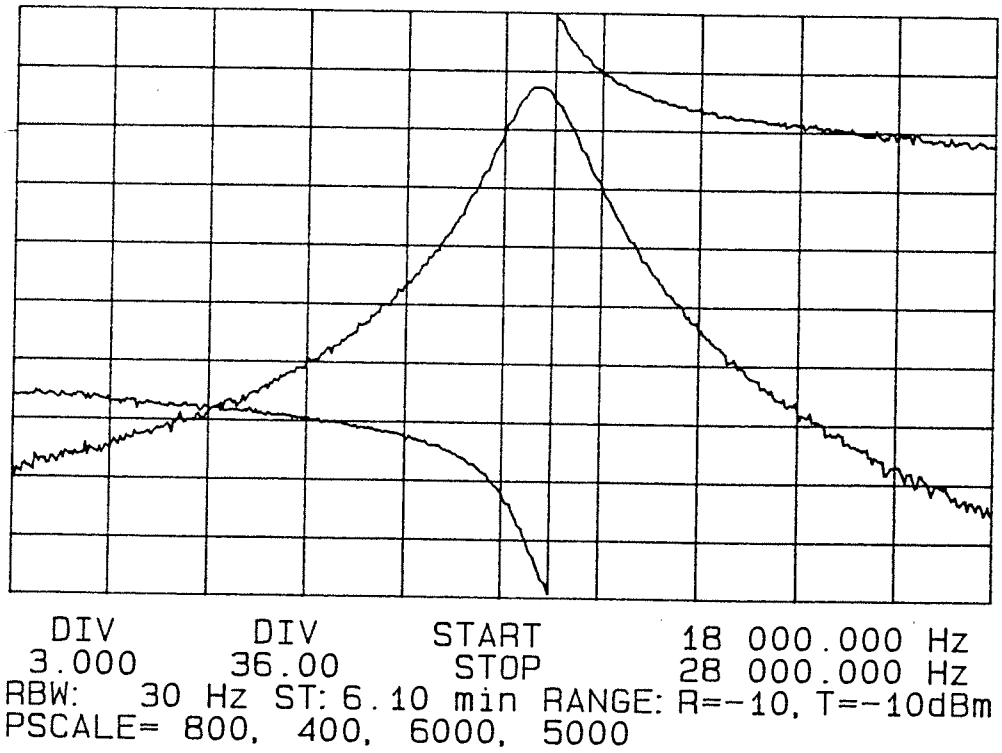

Fig. 6.13: Transconductance spectrum for a folded-beam, comb-driven lateral micromechanical resonator as determined by the EAM technique.

$$L_x = \frac{QR_x}{\omega_r} \tag{6.38}$$

$$C_x = \frac{1}{\omega_r Q R_x}. \tag{6.39}$$

Also of importance for resonator design is the value of $\partial C/\partial x$, which largely determines the electromechanical coupling coefficient of transduction. $\partial C/\partial x$ is most easily obtained using EAM when $(\partial C/\partial x)_d = (\partial C/\partial x)_s = \partial C/\partial x$. For this case, $\partial C/\partial x$ is given by

$$\frac{\partial C}{\partial x} = \left[\frac{2kT_{NA}}{\omega_c Q V_{PD} |v_c||r_{dm}|}\right]^{1/2}. \tag{6.40}$$

In cases where the resonator cannot be contacted, remote carrier EAM may prove most useful for characterization purposes. One set-up for doing this uses a tungsten probe to serve as the upper noncontacting electrode and is shown in Fig. 6.14. With the exception of the addition of the probe, operation of the system is the same as described above.1

The magnitude of capacitance variation between the probe or upper electrode and the sense electrode might be of interest for certain applications, and this can be determined from the resulting transconductance spectrum by taking the EAM output voltage magnitude $|V_{EAM}|$ at resonance and using

$$|C_m| = \frac{2|V_{EAM}|}{\omega_c |v_c| |r_{dm}|} \tag{6.41}$$

6.3.5 EAM for One-Port Microresonators

EAM has been detailed extensively above for the case of a two-port microresonator, but with a slight modification in the biasing scheme, it also can be applied to one-ports. Figure 6.15 shows the experimental set-ups necessary to implement EAM for one-ports for (a) a one-port par-

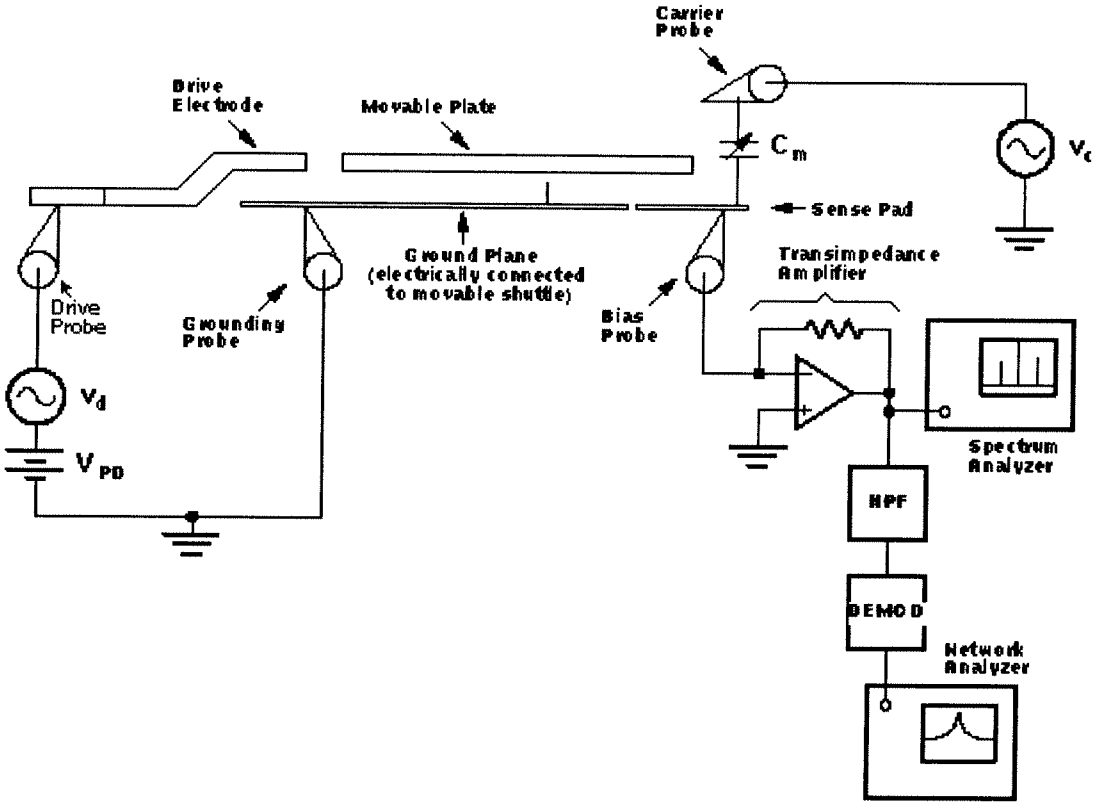

Fig. 6.14: Schematic of an experimental implementation of remote carrier EAM. Here, the noncontacting tungsten probe serves as one terminal of the time-varying capacitance to be measured and as the probe with which the carrier is introduced.

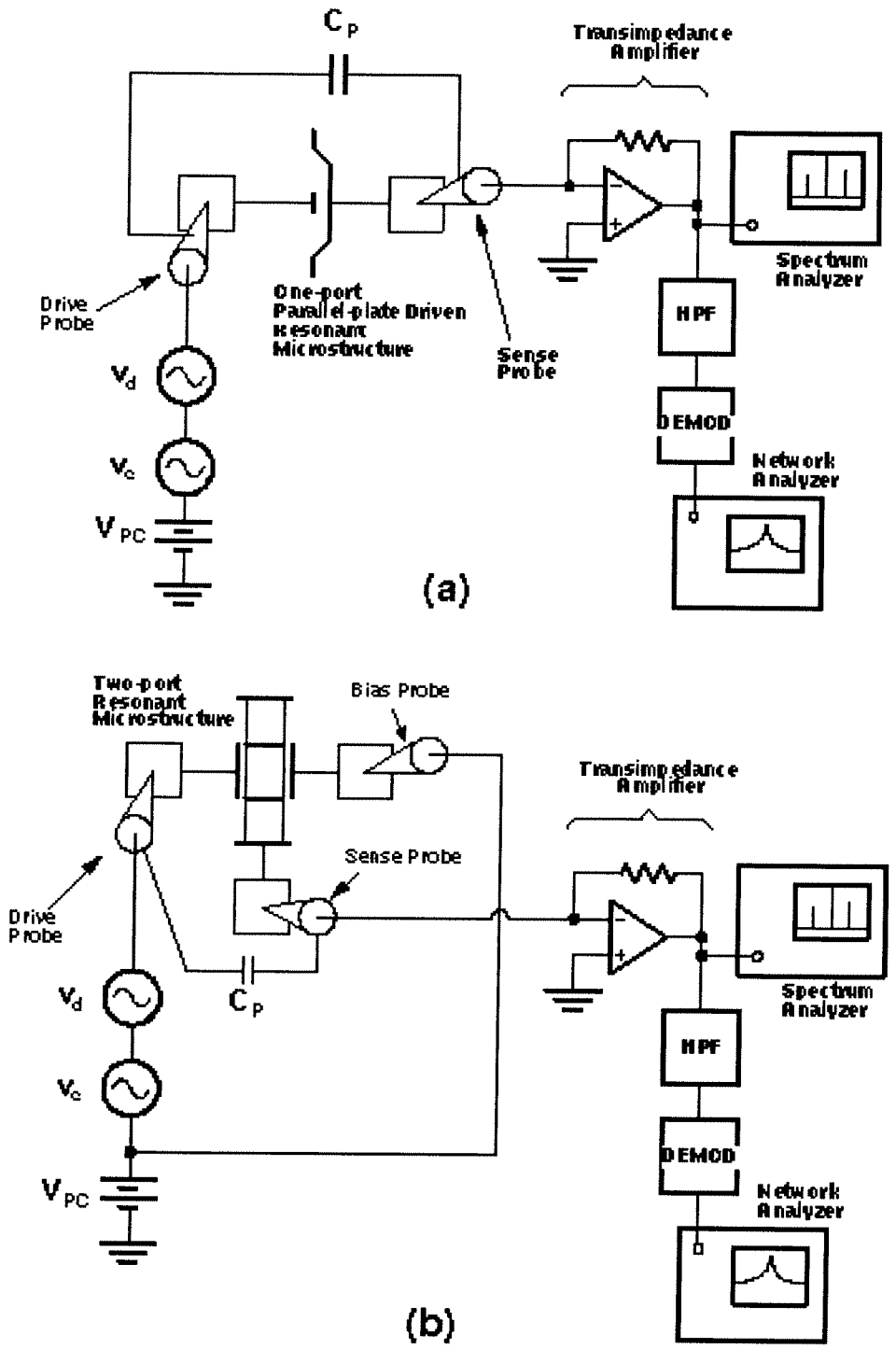

Fig. 6.15: Experimental set-ups necessary to implement EAM for one-ports for (a) a one-port parallel-plate driven micromechanical resonator and (b) a two-port electrostatic comb-driven microresonator used as a one port.

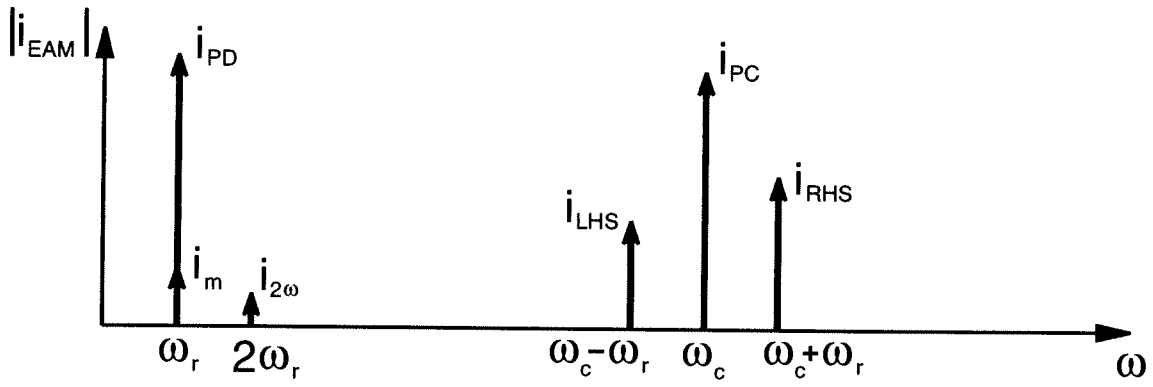

Fig. 6.16: Fourier spectrum for the current seen at the summing node of the amplifier of Fig. 6.15 at resonance.

allel-plate driven microresonator and (b) a two-port electrostatic-comb driven microresonator used as a one-port. The EAM current resulting at the summing node of the transimpedance amplifier can be found in the same manner as in Section 6.3.2. Thus, referring to Fig. 6.15,

$$
\begin{aligned}
i_r &= C_P\frac{dV_d(t)}{dt} + C(t)\frac{dV_d(t)}{dt} + V_d(t)\frac{\partial C(t)}{\partial t} \\
&= \underbrace{(C_P + C_o)\frac{dv_c}{dt}}_{\sin\omega_c t} + \underbrace{(C_P + C_o)\frac{dv_d}{dt}}_{\sin\omega_r t} + \underbrace{V_P\frac{\partial C}{\partial t}}_{\cos\omega_r t} + \underbrace{C_m(t)\frac{dv_c}{dt}}_{(\sin\omega_r t)\,(\sin\omega_c t)} + \underbrace{C_m(t)\frac{dv_d}{dt}}_{(\sin\omega_r t)^2} \\
&\quad + \underbrace{v_c\frac{dv_c}{dt}}_{(\cos\omega_c t)\,(\cos\omega_r t)} + \underbrace{v_d\frac{dv_d}{dt}}_{(\cos\omega_r t)^2}
\end{aligned}
\tag{6.42}
$$

where the effective frequency contributions of each component are indicated. The Fourier spectrum of Eq. (6.42) is shown in Fig. 6.16. The terms of interest are, again, those at $(\omega_c \pm \omega_r)$, and these terms are found to be identical to those in Eq. (6.10) and (6.11). Thus, the sidebands of the EAM current for the systems of Fig. 6.15 can be described as before. Demodulation of this current is also achieved in the same manner as for two-ports.

The only difference between the i_r of one-port EAM and that for two-port EAM is the presence of the frequency-doubled term. This term is masked by feedthrough of the drive signal second harmonic, anyway, so actually, there is practically no difference between the two. Incidentally, when selecting a carrier frequency for EAM, one should chose ω_c such that crossing by the

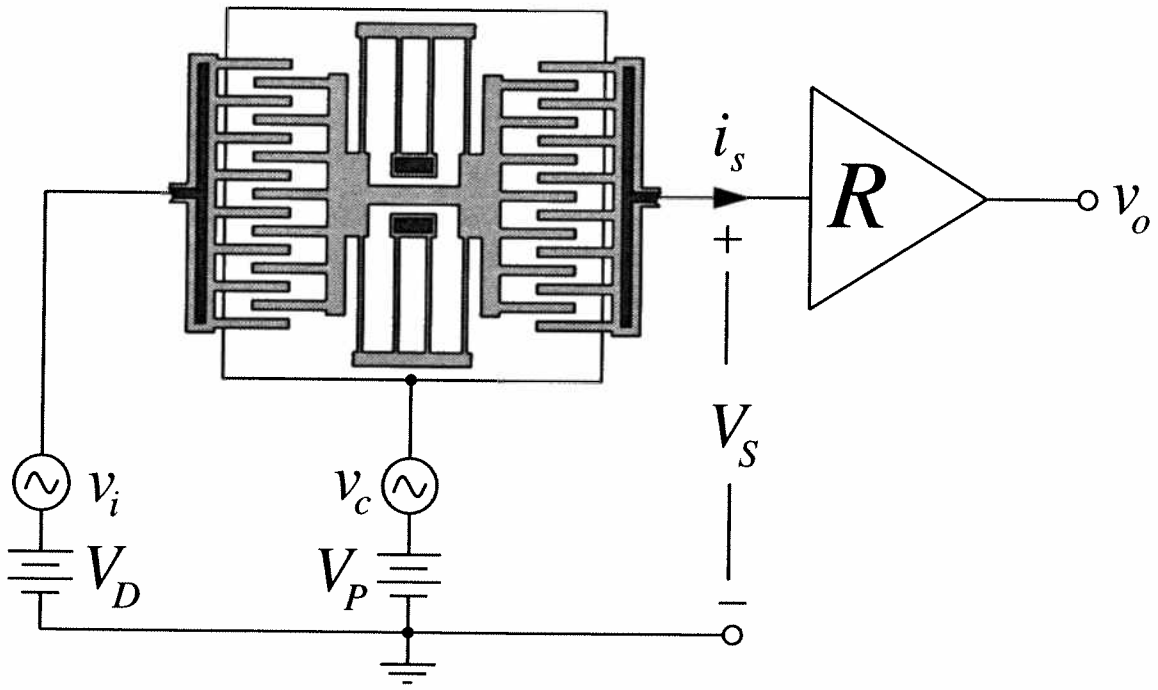

Fig. 6.17: Circuit schematic showing the bias and excitation required to implement a mixer+filter function utilizing a mechanical resonator.

frequency-doubled component and the ω_c - ω_d term is avoided. Otherwise, a sharp glitch in the transconductance spectrum will appear.

6.4 Micromechanical Mixer+Filters

As seen in the previous section, the output spectrum of a micromechanical resonator (filter) can be amplitude modulated to extremely high frequencies by the simple application of a carrier signal to the resonator. The implications for transmitter designs based upon microresonators with injected carriers are already far reaching. Even so, the usefulness of carrier injection goes well beyond up-conversion for transmission: It, in fact, can be used for down-conversion as well.

Figure 6.17 shows the bias and excitation configuration required for achieving a mixer+filter function from a single micromechanical resonator (or filter constructed from such resonators). Note that the configuration is identical to that of Fig. 6.6 for EAM up-conversion! The only difference between the two figures is the value of the excitation voltage, v_i. For the case of EAM, v_i was near the resonance frequency of the resonator. For the case of mixer+filter implemen-

tation shown in Fig. 6.17, the frequency of v_i which causes oscillation is equal to the sum or difference of the resonance and carrier frequencies, ω_r and ω_c, respectively.

6.4.1 Voltage-to-Force Mixing

The mixer+filtering phenomenon comes about because proper combination of carrier and excitation signals, v_c and v_i, respectively, can give rise to force components near the center frequency of the resonator. For the excitation configuration of Fig. 6.17, the drive force f_d may be found using the procedure of Section 2.4.1:

$$\begin{aligned} f_d &= \frac{1}{2}v_D^2\left(\frac{\partial C}{\partial x}\right)_i \\ &= \frac{1}{2}(V_{PD}+v_c-v_i)^2\left(\frac{\partial C}{\partial x}\right)_i \\ &= \frac{1}{2}\{\frac{|v_i|^2}{2}+\frac{|v_c|^2}{2}+V_{PD}^2+\frac{|v_i|^2}{2}\cos 2\omega_i t+\frac{|v_c|^2}{2}\cos 2\omega_c t-2V_{PD}|v_i|\cos\omega_i t \\ &\quad +2V_{PD}|v_c|\cos\omega_c t-|v_i||v_c|\,[\cos(\omega_c-\omega_i)t+\cos(\omega_c+\omega_i)t]\,\}\left(\frac{\partial C}{\partial x}\right)_i \end{aligned} \tag{6.43}$$

where $(\partial C/\partial x)_i$ is the change in capacitance per unit displacement at the input (drive) port. Assuming a reasonably large resonator quality factor, the force components which will excite resonance are those close to the resonance frequency, ω_r. Such components arise when

$$\omega_i = \omega_r \quad \Rightarrow \quad |f_d| = V_{PD}|v_i|\left(\frac{\partial C}{\partial x}\right)_i \tag{6.44}$$

$$\omega_i = \omega_c - \omega_r \quad \Rightarrow \quad |f_d| = \frac{1}{2}|v_i||v_c|\left(\frac{\partial C}{\partial x}\right)_i \tag{6.45}$$

$$\omega_i = \omega_c + \omega_r \quad \Rightarrow \quad |f_d| = \frac{1}{2}|v_i||v_c|\left(\frac{\partial C}{\partial x}\right)_i \tag{6.46}$$

The case where $\omega_i = \omega_r$ corresponds to the bias and excitation scheme previously used for mechanical resonators in Chapters 2 through 5.

The $\omega_i = \omega_c \pm \omega_r$ case corresponds to the mixer+filter function. When the drive signal has frequency approaching $\omega_c \pm \omega_r$, a drive force f_d with frequency approaching ω_r arises, and the resonator oscillates around its resonance frequency, ω_r. In other words, the resonator is driven by a signal at frequency $\omega_c \pm \omega_r$, but oscillates (and provides an output signal) at frequency ω_r—an IF

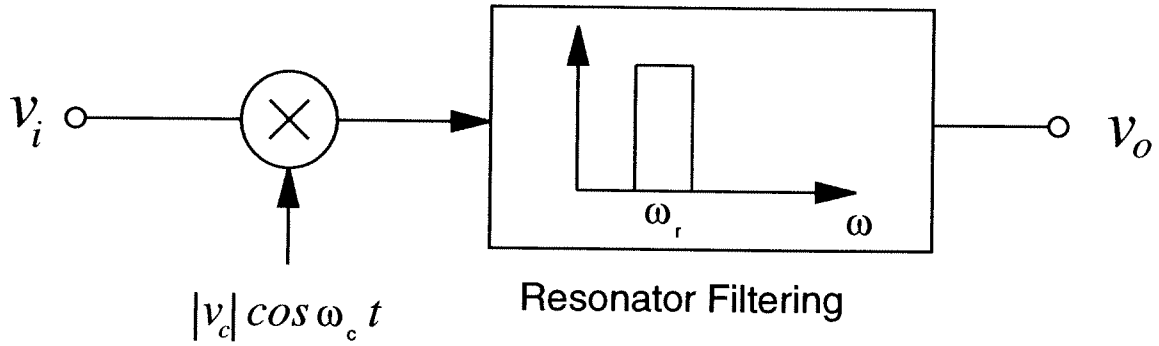

Fig. 6.18: Equivalent block diagram schematic for the scheme of Fig. 6.17.

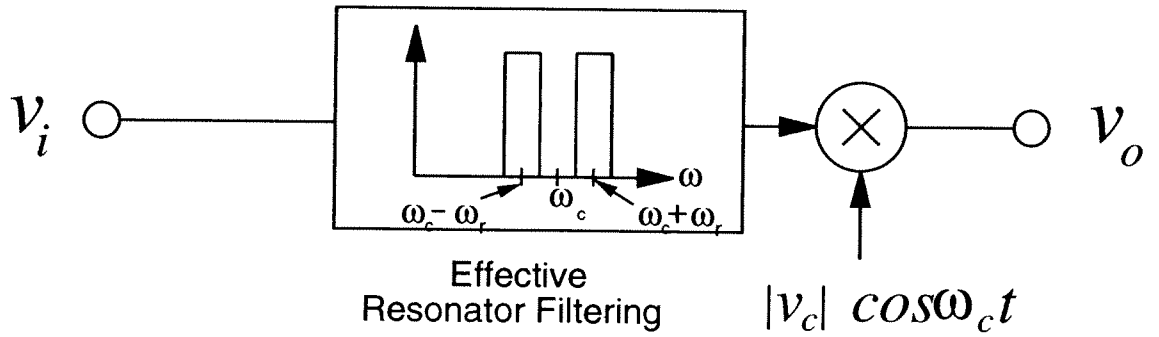

Fig. 6.19: Block diagram schematic showing an alternative, but equivalent, view of the mixer+filter function, with the filtering first. This view shows more clearly which components around ω_c are actually collected.

frequency. In effect, a signal at frequency $\omega_c \pm \omega_r$ can be mixed down to IF and filtered using a single resonator in the configuration of Fig. 6.17. Figure 6.18 explicitly shows the equivalence between the resonator configuration of Fig. 6.17 and a mixer+filter function in block diagram form. Alternatively, this function may viewed as first a high frequency filtering at $\omega_c \pm \omega_r$, and then a subsequent mixing to the IF frequency, as shown in the block diagram of Fig. 6.19. This view shows more clearly which frequency components are actually collected and processed to the output. Note that two frequency components are collected: the desired component and an image.

The phasor equations describing resonator output current as a function of phasor input voltage are

$$I_s(\omega-\omega_c) = \frac{1}{2}\frac{j(\omega-\omega_c)k^{-1}V_{PD}V_iV_c\left(\frac{\partial C}{\partial x}\right)_i\left(\frac{\partial C}{\partial x}\right)_o}{1-\left(\frac{\omega-\omega_c}{\omega_r}\right)^2+j\left(\frac{\omega-\omega_c}{Q\omega_r}\right)} \tag{6.47}$$

for $\omega = \omega_c + \omega_i$; and

$$I_s(\omega_c-\omega) = \frac{1}{2}\frac{j(\omega_c-\omega)k^{-1}V_{PD}V_iV_c\left(\frac{\partial C}{\partial x}\right)_i\left(\frac{\partial C}{\partial x}\right)_o}{1-\left(\frac{\omega_c-\omega}{\omega_r}\right)^2+j\left(\frac{\omega_c-\omega}{Q\omega_r}\right)} \tag{6.48}$$

for $\omega = \omega_c - \omega_i$. For a signal with both sidebands, the output current is equal to the sum of Eqs. (6.47) and (6.48).

The above theory has been developed using a single resonator. However, it also applies to any resonator system, such as a spring-coupled micromechanical resonator filter or a Q-controlled microresonator filter. An explicit excitation and bias configuration for the case of the spring-coupled mechanical filter is shown in Fig. 6.20. For the case of the Q-controlled resonator filter of Fig. 5.30, the above mixer+filtering function can be achieved by applying the carrier frequency to the resonator closest to the input.

6.4.2 Micromechanical Quadrature Modulators

The above mixer+filter device, as shown in Fig. 6.17, can be used to replace the mixer and IF amplifier in the receiver system of Fig. 1.1, as shown in Fig. 6.21.

Figure 6.21 depicts the architecture of a relatively low frequency communication system. For systems with much higher carrier frequencies, such as satellite networks, double heterodyning is often employed, where two IF stages are required. In general, the noise performance (and thus, the range) of a given heterodyning communication system can be improved by decreasing the number of heterodyning steps. Thus, a given system can be improved by replacing all amplifiers, RF and IF, by a single mixer+filter device, as shown in Fig. 6.22. The problem with doing this is that the image frequency, as well as the desired information frequency, will reach the output of the resonator, as shown in Fig. 6.23. This can be seen more easily in Fig. 6.19, which more explicitly shows which components are collected through filtering. Thus, a mechanism which suppresses the image frequency is required.

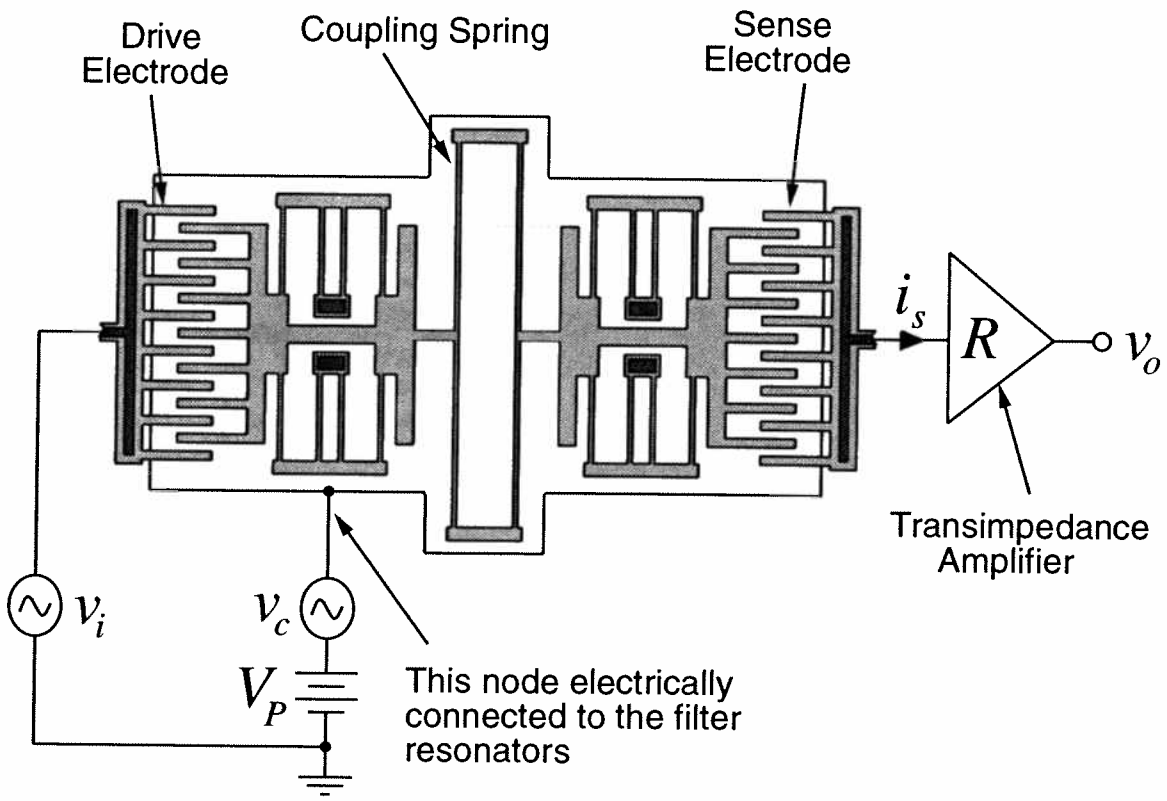

Fig. 6.20: Resonator mixing+filtering applied to a spring-coupled microelectromechanical filter. The two-port input plus carrier configuration of Fig. 3(b) may also be used here.

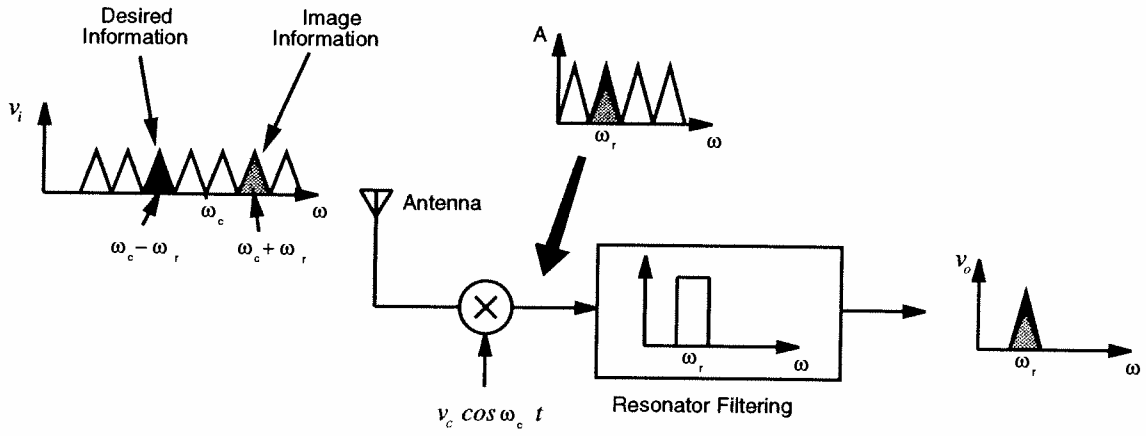

Fig. 6.23: Operation of the mixer+filter device, showing how both the desired information and its image reach the output.

One way to achieve this image suppression is through the use of quadrature mixing [100].

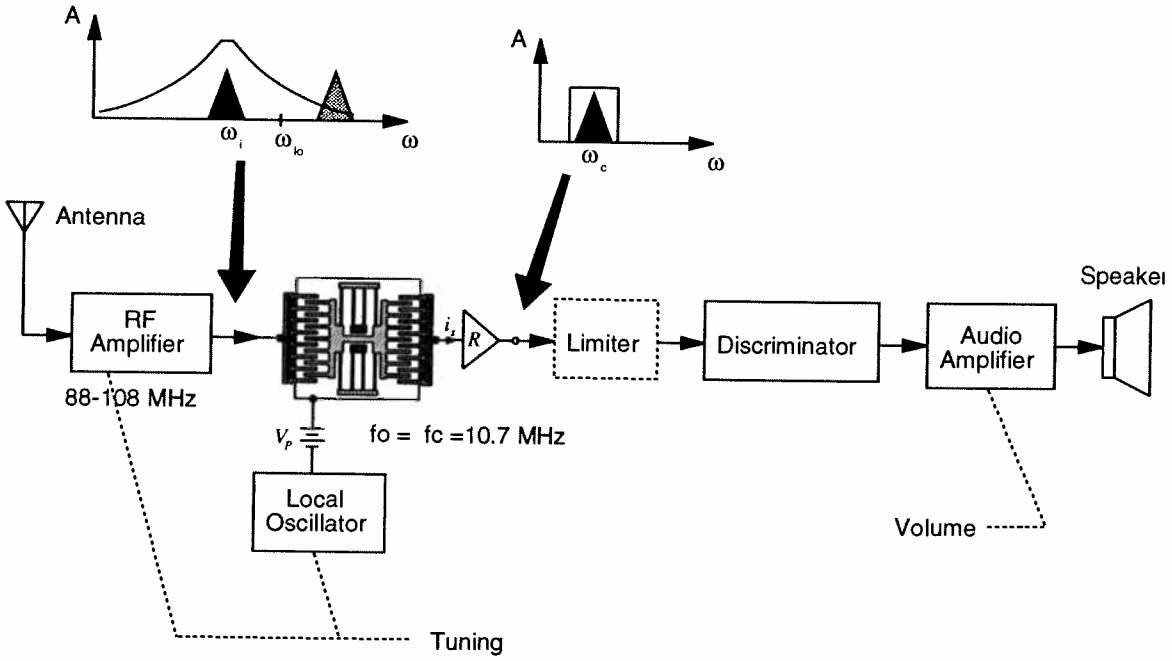

Fig. 6.21: Schematic block diagram of a commercial FM receiver utilizing mixer+filter micromechanical resonator. (The single resonator could be replaced by higher order filter using multiple resonators.) Note that the local oscillator can be implemented utilizing a microresonator oscillator, multiplied if necessary.

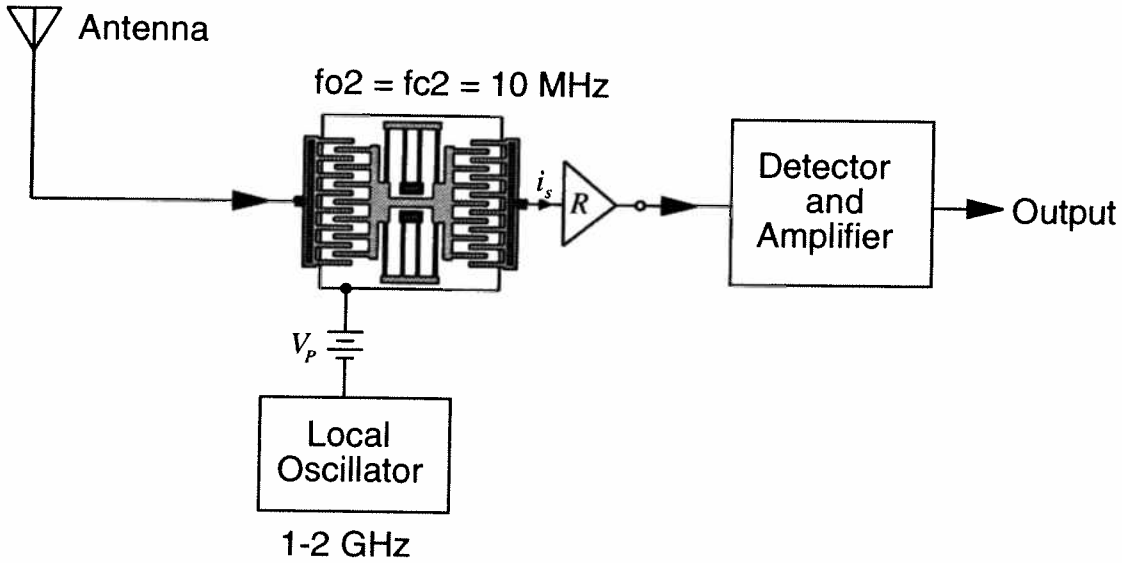

Fig. 6.22: Schematic block diagram of a receiver attempting to utilize the mixer+filter in a single heterodyning step. This configuration is not optimum, since the image frequency, and well as the information frequency, would reach the output.

For micromechanical mixer+filters, quadrature mixing can be implemented as shown in Fig. 6.24.

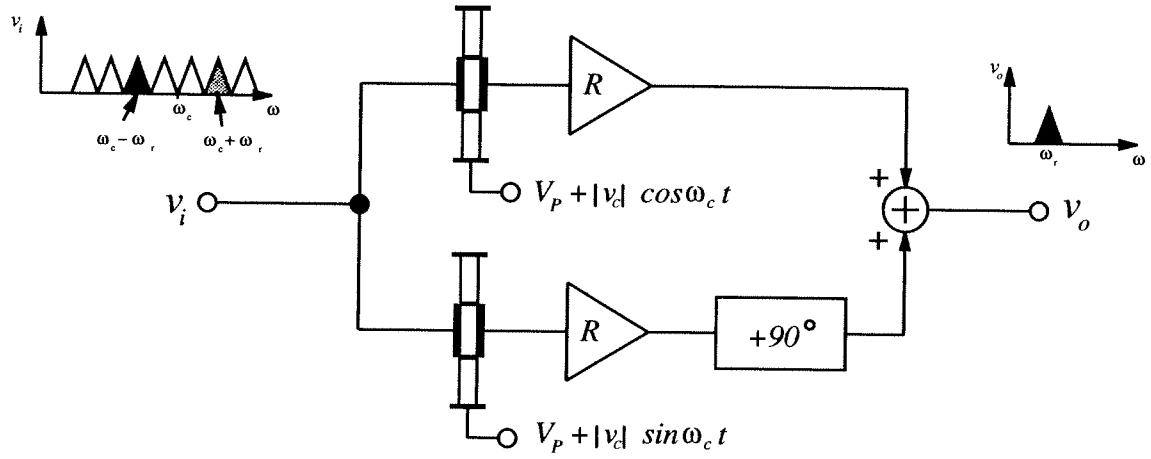

Fig. 6.24: A quadrature technique for suppression of the upper band image frequency component in the mixer+filter.

Here, the input signal is applied to two mixer+filters in parallel. The mixer+filters are identical in construction and in passband response, but operate slightly differently in that their applied carrier signals are 90^o out of phase. For the mixer+filter with an applied cosine carrier, the relevant force components are

$$\omega_i = \omega_c - \omega_r \quad \Rightarrow \quad f_d = \frac{1}{2}|v_i||v_c|\left(\frac{\partial C}{\partial x}\right)_i [\cos\omega_r t + \cos(2\omega_c - \omega_r)t] \tag{6.49}$$

$$\omega_{im} = \omega_c + \omega_r \quad \Rightarrow \quad f_d = \frac{1}{2}|v_{im}||v_c|\left(\frac{\partial C}{\partial x}\right)_i [\cos\omega_r t + \cos(2\omega_c + \omega_r)t] \tag{6.50}$$

where ω_i is the frequency of the desired information, ω_{im} is the frequency of its image, $|v_i|$ is the amplitude of the information signal, and $|v_{im}|$ is the amplitude of the image signal. For the mixer+filter with an applied sine carrier

$$\omega_i = \omega_c - \omega_r \quad \Rightarrow \quad f_d = \frac{1}{2}|v_i||v_c|\left(\frac{\partial C}{\partial x}\right)_i [\sin\omega_r t - \sin(2\omega_c - \omega_r)t] \tag{6.51}$$

$$\omega_{im} = \omega_c + \omega_r \quad \Rightarrow \quad f_d = \frac{1}{2}|v_{im}||v_c|\left(\frac{\partial C}{\partial x}\right)_i [-\sin\omega_r t - \sin(2\omega_c + \omega_r)t] \tag{6.52}$$

In the above equations, only the components at ω_r are important, as the other frequency components will be filtered out by the resonator. Given this, the significant components at the outputs of the transresistance amplifiers in Fig. 6.24 are, at node 1:

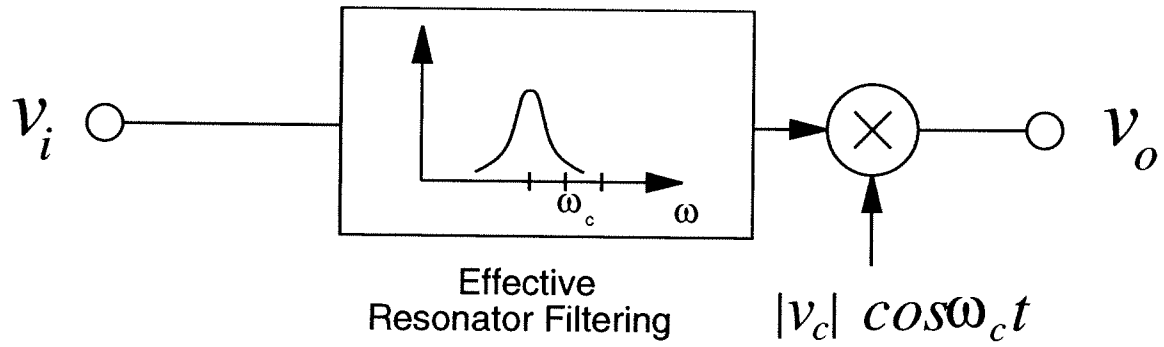

Fig. 6.25: Equivalent block diagram for the system of Fig. 6.24.

$$v_1 = \frac{1}{2}\omega_r|v_c|V_{PO}\left(\frac{\partial C}{\partial x}\right)_i\left(\frac{\partial C}{\partial x}\right)_o\frac{Q}{k}(|v_i| + |v_{im}|)\cos\omega_r t \tag{6.53}$$

and at node 2:

$$v_1 = \frac{1}{2}\omega_r|v_c|V_{PO}\left(\frac{\partial C}{\partial x}\right)_i\left(\frac{\partial C}{\partial x}\right)_o\frac{Q}{k}(|v_i| - |v_{im}|)\sin\omega_r t \tag{6.54}$$

where $(\partial C/\partial x)_o$ is the capacitance change per unit displacement at the output ports, Q is the quality factor, and k is the system spring constant of the resonators. The output of the sine carrier mixer+filter then goes through a 90^o phase shifter, after which the voltage at node 3 is

$$v_1 = \frac{1}{2}\omega_r|v_c|V_{PO}\left(\frac{\partial C}{\partial x}\right)_i\left(\frac{\partial C}{\partial x}\right)_o\frac{Q}{k}(|v_i| - |v_{im}|)\cos\omega_r t \tag{6.55}$$

Combination of v_1 and v_3 through a summer, then yields:

$$v_o = v_1 + v_3 = \omega_r|v_i||v_c|V_{PO}\left(\frac{\partial C}{\partial x}\right)_i\left(\frac{\partial C}{\partial x}\right)_o\frac{Q}{k}\cos\omega_r t \tag{6.56}$$

where the image component with magnitude $|v_{im}|$ has been suppressed.

From a block diagram point of view, the system of Fig. 6.24 is equivalent to Fig. 6.25, where the mixing/filtering order has been reversed (but the system equivalency retained) to show the suppression more clearly. Note that the image filtering, which would occur a frequency ω_r higher than the carrier frequency ω_c, is now suppressed. To collect information at the higher frequency and suppress the lower frequency image, the system of Fig. 6.26 may be used.

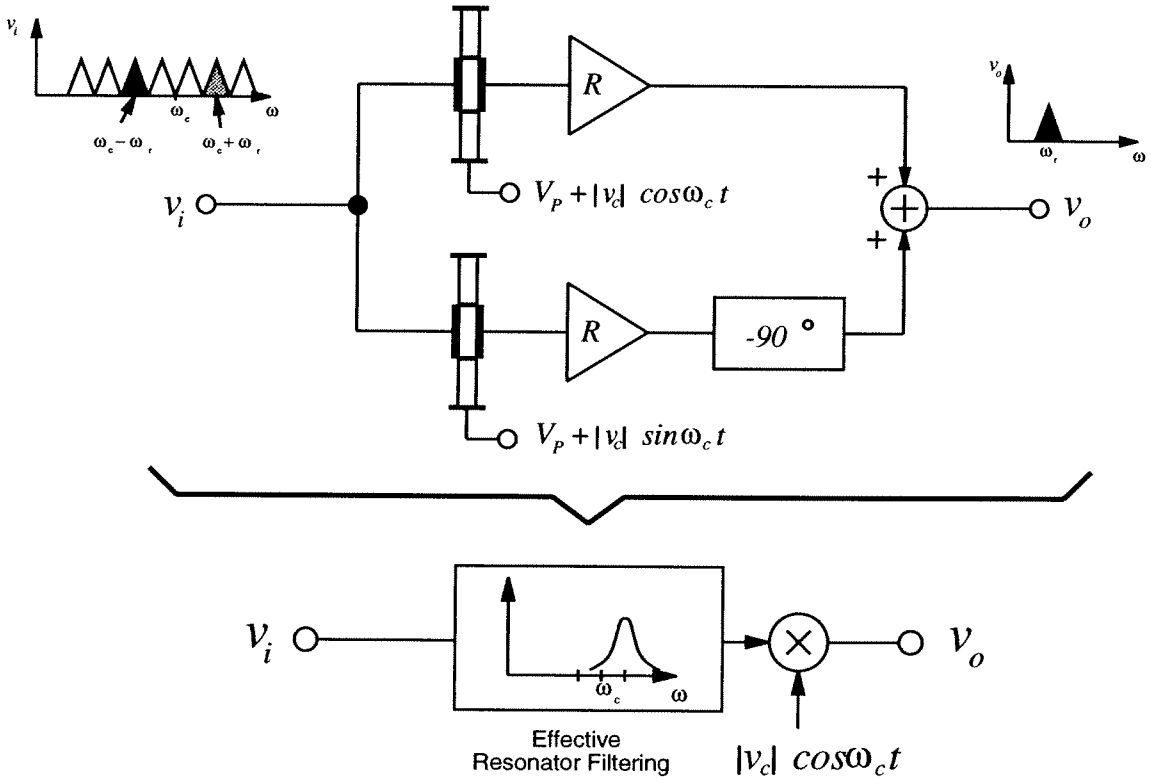

Fig. 6.26: A quadrature technique for suppression of the lower band image frequency component in the mixer+filter. The equivalent block diagram is also shown.

Using the above image suppression scheme, a feasible single-heterodyne high frequency receiver system would then appear as in Fig. 6.27. As with all quadrature mixers, the performance of the receiver in Fig. 6.27 will strongly depend upon matching of components (in this case, resonators) and on how accurately the 90^0 phase shifts can be implemented.

6.5 Maximum Carrier Frequency

Given the obvious commercial application of EAM and mixer+filters to communications, it is instructive to study the limitations of these methods. The most important limitation is possibly how high the carrier frequency can be since this determines the range of FCC frequency allocations available.

To answer this question, the parasitic capacitors, resistors, and inductors associated with the complete resonator must be scrutinized. In particular, the transduction time constant, from

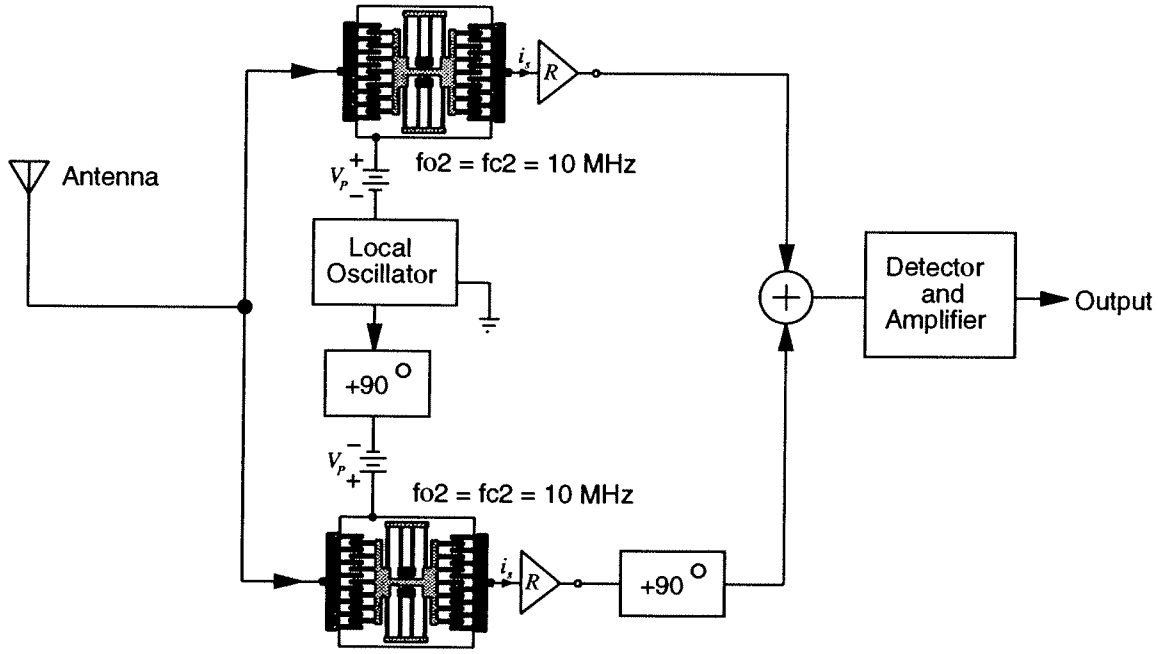

Fig. 6.27: Schematic block diagram of a receiver utilizing a micromechanical mixer+filter in with single mixing step.

voltage (charge) to force will probably come into play. Since the capacitance C_{oi} at the input port to a typical micromechanical resonator is rather small (on the order of femtoFarads for present-day technologies), the RC time constant should be extremely small (i.e., the bandwidth should be large). Assuming a source resistance of 50 Ω and an input capacitance of 1 fF, the frequency bandwidth for acceptable carrier inputs should be on the order of teraHertz!

To date, the mixer+filtering function has been demonstrated on a 20 kHz comb-transduced folded-beam polysilicon resonator, for carrier frequencies up to 200 MHz (which was the highest function generator frequency I could find that day). We suspect that the highest attainable frequency is much higher.

6.6 Conclusions

As the frequency of operation gets higher, parasitic feedthrough interference is expected to have a greater influence on filter performance. This is especially true for high series resistance resonators, which source very small output currents. The desired motional current may be sepa-

rated from feedthrough parasitics in both the time and frequency domain. For continuous-time applications, frequency domain techniques are most attractive.

An amplitude modulation technique which translates resonator motional current to higher frequencies via electromechanical amplitude modulation (EAM) was demonstrated. The basic methodology involves the application of a carrier frequency signal to the resonator (on top of the dc-bias). This carrier frequency interacts multiplicatively with the motional current at the sense port, heterodyning the motional current to frequencies far away form local parasites. In effect, an AM modulator is implemented via a single micromechanical resonator or filter made up of such microresonators. The only extra hardware required for implementing EAM is a local oscillator.

Alternatively, the exact same bias and excitation configuration (i.e., carrier applied to resonator) can be used to mix carrier frequency input signals down to the IF frequency of the resonator, where it gets filtered by the resonator. In effect, a mixing+filtering function is implemented via a single micromechanical resonator or filter made up of such microresonators. By operating two identical resonators in quadrature, one can envision a quadrature modulator based upon micromachined components.

The frequency limits to these modulation techniques are as yet, undetermined, but are expected to be quite high.

CHAPTER 7 *Micro Oven Stabilization*

In the preceding chapters, high-Q polycrystalline silicon mechanical resonators have been demonstrated to be useful as stable oscillators and highly selective filters for use in communications systems and timekeepers. The high Q of the polysilicon resonator is instrumental in establishing the performance boundaries in both of these applications. For the case of the oscillator application, the phase noise density-to-carrier ratio was found to be inversely proportional to the square of the unloaded Q. In filter applications, the minimum achievable bandwidth was found to be proportional to Q.

Another equally important performance criterion, however, is the temperature stability of the oscillator or filter. Temperature stability is especially important in single-sideband equipment, where frequency shifts greater than 100 Hz may result in either poor carrier rejection or a loss of the audio response. For a 445 kHz IF frequency, the above requires a fractional frequency variation of less than 220 ppm over the operating temperature range.

A measured frequency versus temperature plot for a polysilicon folded-beam comb-driven microresonator was presented in Fig. 2.8, and is repeated here as Fig. 7.1 for convenience. The extracted temperature coefficient is -10 ppm/°C over the measured temperature range. This equates to a fractional frequency variation of 1000 ppm over a -20°C to 80°C temperature range. Although much better than achievable by other integrated filter technologies (e.g. switched-capacitor or transconductance-C), this is still poorer than for conventional quartz oscillators and

mechanical filters. For example, a typical AT-cut quartz crystal may exhibit an uncompensated fractional frequency variation of only 60 ppm over the a -20°C to 80°C temperature range [79]. The limit for quartz is 20 ppm over this temperature range [79]. Materials used for macroscopic mechanical filters also exhibit better temperature performance. For example, Ni-Span-C (thermelast 4002), when properly constructed, has a typical fractional frequency variation of only 80 ppm over a -25°C to 75°C range [7].

Thus, some means of temperature compensation or control is required to achieve, on the micromechanical scale, a temperature independence similar to that of currently available macroscopic oscillators and filters. This chapter details an initial investigation of frequency stabilization against varying temperature through micro-oven control. In brief, the micromechanical resonator is fabricated on a suspended platform, which is thermally isolated from the surrounding substrate. The temperature of the platform is controllable through on-board heating and temperature sensing

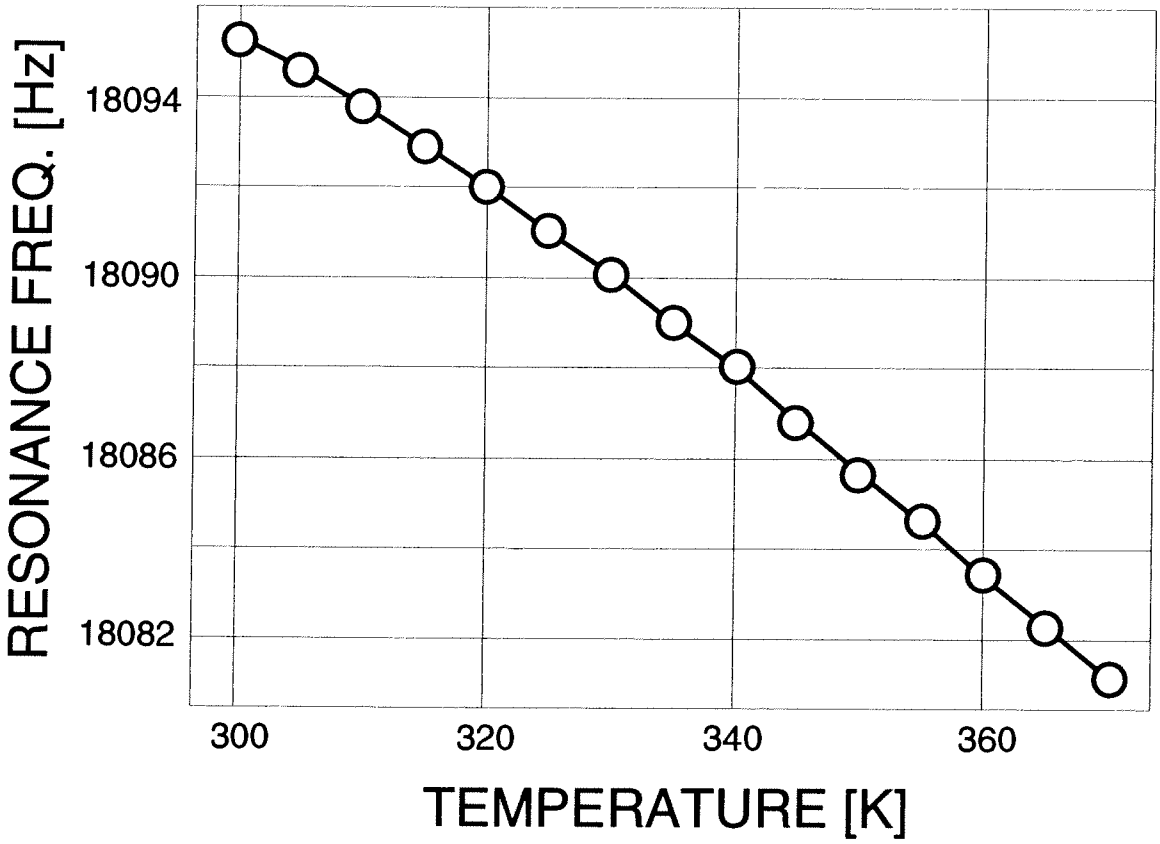

Fig. 7.1: Measured fractional frequency versus temperature curve for an 18 kHz folded-beam, comb-driven polysilicon micromechanical resonator.

resistors and feedback electronics. Using this technique, the temperature coefficient of the resonator is reduced to -2 ppm/°C—5 times less than the uncompensated coefficient of -10 ppm/°C.

After an initial discussion of strategies for temperature compensation or control that have been utilized for quartz crystal oscillators, this chapter proceeds into details of micro-oven control, including fabrication, thermal modelling, and experimental results.

7.1 Strategies for Frequency Stabilization Against Temperature

Much of the previous work on frequency stabilization of mechanical resonators has concentrated on quartz crystals used in extremely stable oscillators. The majority of methods used can be classified into two distinct categories: (1) temperature compensation, where circuit techniques are utilized to counteract temperature-induced frequency variations; and (2) temperature control, where an oven with feedback electronics is utilized to keep the temperature of the resonator (crystal) stable, thus, eliminating temperature dependence at its source.

7.1.1 Temperature Compensation

Due to its simplicity relative to alternative methods, temperature compensation has by far been the most predominant TC_f reduction strategy used for quartz crystal oscillators. Using compensation methods, quartz crystals with temperature stabilities in the range of ±10 to ±0.5 ppm over a -20°C to 80°C temperature range.

A schematic diagram summarizing the requirements of temperature compensation is shown in Fig. 7.2. As shown, some method for pulling the frequency of the crystal is required; in the case of Fig. 7.2, a variable capacitor C_v is placed in series with the crystal is utilized for this purpose. Usually, this variable capacitor is implemented as a varactor diode, for which the value of capacitance is controllable by the voltage applied across its terminals. In temperature compensation, a temperature dependent circuit provides a voltage which controls the value of C_v such that it pulls the crystal frequency by precisely the amount that it drifted under a given change in temperature, but in the opposite direction.

The temperature-dependent voltage generating circuit is generally implemented using either an analog thermistor network or a digital PROM combined with a temperature sensor. In the

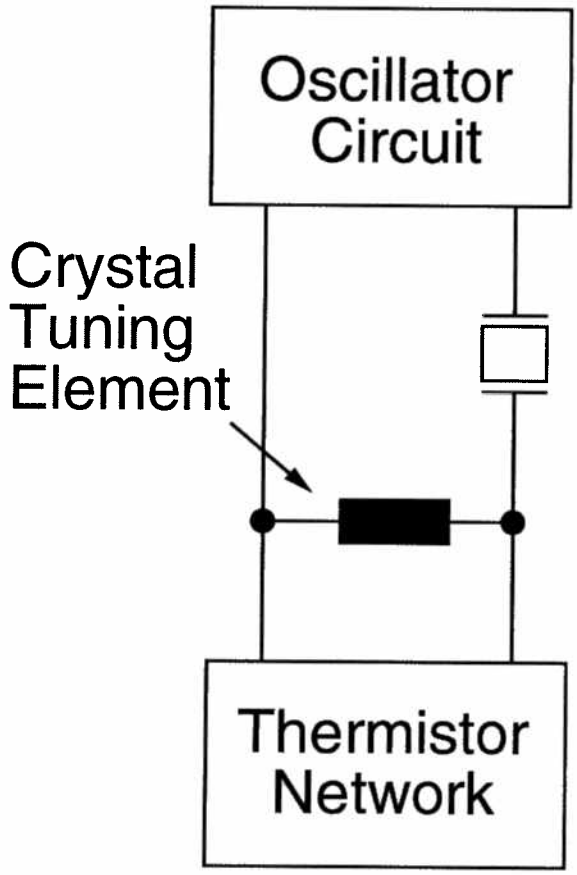

Fig. 7.2: Schematic diagram showing a typical implementation of temperature compensation for a quartz crystal oscillator.

former, the thermistor network is usually constructed such that its voltage output approximate the frequency versus temperature curve the quartz crystal, which generally follows a cubic equation of the form [79]

$$f = A_1 (t - t_0) + A_2 (t - t_0)^2 + A_3 (t - t_0)^3, \tag{7.1}$$

where f is the frequency between the reference temperature t_0 and the temperature t. For the case of digital compensation, a temperature sensor feeds temperature information to a ROM, which then outputs a voltage as given by Eq. (7.1). Digital compensation requires great circuit complexity, since A/D and D/A converters are required, as well as a PROM.

As shown in Fig.7.1, the resonance frequency of a folded-beam comb-driven resonator seems to vary linearly with temperature in a monotonically decreasing fashion. The temperature dependence, then, may be described simply by

$$f = A_1 (t - t_0) \ . \tag{7.2}$$

The thermistor network required to match this temperature dependence should be relatively simple when compared to those required to compensate quartz crystals. The problem is further simplified if a linear frequency pulling method is available.

7.1.2 Temperature (Oven) Control

Despite the potential simplicity involved with temperature compensating a micromechanical resonator oscillator, this work does not pursue this direction. The reason for this is the potential for oven control on a micro-scale to achieve frequency stabilities (against temperature) orders of magnitude better than achievable via compensation. This, in fact, is the case for macroscopic quartz crystal oscillators, where frequency stabilities in the range of $\pm 1 \times 10^{-8}$ are typical over the temperature range -55°C to 105°C, and even stabilities of parts per 10^{10} have been achieved with double ovens. Another reason for pursuing oven-control initially, is that it applies equally well to a complex system of resonators, such as a mechanical filter consisting of several resonators. Temperature compensation of a filter may require separate circuits for groups of resonators or springs.

A schematic diagram depicting the fundamentals behind temperature control of a crystal oscillator via an oven is shown in Fig. 7.3. Here, a crystal oscillator is shown embedded in a thermally insulated container, along with temperature sensing and heating resistors. These resistors are embedded in the loop path of a feedback circuit, which maintains a constant temperature within the insulating container. Ideally, the temperature of the container is independent of outside temperature variations. Because of thermal losses, this ideal condition is, of course, not achievable, but some systems come very close.

Despite their superior performance, oven controlled macroscopic oscillators are much less used than their temperature compensated counterparts. This is due to several drawbacks associated with oven controlled macroscopic oscillators:

1. A relatively large container volume is required due to the need for thermal insulation.
2. A warm-up time is required, typically on the order of from 5 to 30 minutes.
3. A large amount of power is required to maintain the oven temperature. The exact amount is determined by the degree of thermal loss, and is usually in the range of from 1 to 10 Watts.

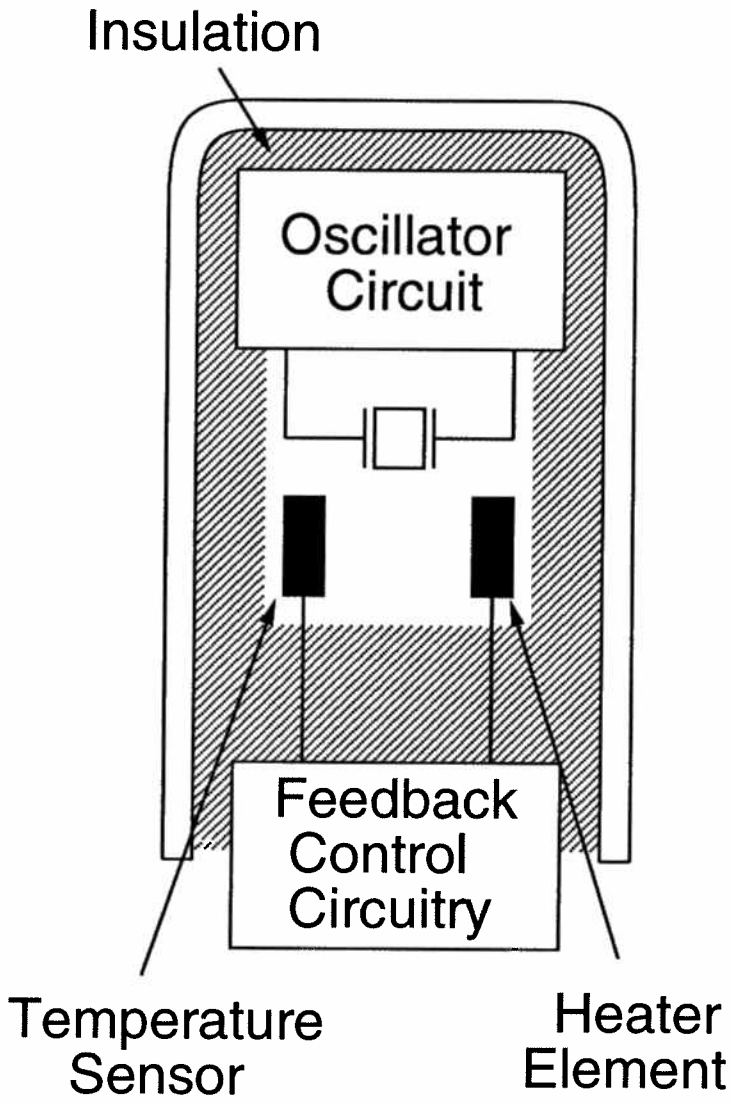

Fig. 7.3: Schematic depicting a typical implementation of oven control for a quartz crystal oscillator.

4. Operation of the crystal under elevated temperatures may accelerate aging, and thus, may degrade the long-term stability of the oscillator.

The above drawbacks make temperature compensation preferable to oven-control for many applications which do not absolutely require the performance advantages of oven-control (but which could benefit from them).

As will be shown, miniaturization of oscillators and oven-control eliminates the first three of the above drawbacks. Item (1) is eliminated for obvious reasons, while items (2) and (3) are substantially alleviated by the large degree of thermal isolation achievable on the micro-scale. This thermal isolation is such that heating (and cooling) time constants are on the order of only milli-seconds (rather than 30 minutes), and micro-oven power dissipation is on the order of milliWatts (as opposed to 10 Watts).

7.2 Micro-Oven Structure

The design of the micro-oven centers upon achieving sufficient thermal insulation to insure that the oven can be heated to the desired temperature with minimal power dissipation. Of the heat loss mechanisms involved, heat conduction is the most directly addressable by oven geometry and construction.

An overhead schematic of the micro-oven control system with cross-section is presented in Fig. 7.4, along with dimensional design data. Here, a polysilicon μresonator is suspended above a nitride platform, which in turn, is suspended above the substrate via long, thin struts. The suspending struts, which can be polysilicon or a poly/nitride sandwich (shown in Fig. 7.4), provide thermal isolation of the platform from the substrate, as well as conductive interconnect between these media. These struts are folded in order to relieve post fabrication stress, preventing possible buckling of the platform. The residual stress could be either compressive or tensile, depending upon the composition of the poly/nitride struts and the deposition conditions for the silicon-rich nitride. In addition to providing stress relief, folding also increases the effective length of the struts, increasing the conductive thermal resistance from the platform to the substrate.

Platforms supported by straight beams were also designed for comparison. A typical overhead view and cross-section for this design is presented in Fig. 7.5.

Devices on the platform include the μresonator, plus two polysilicon resistors, which serve to heat the platform and sense its temperature.

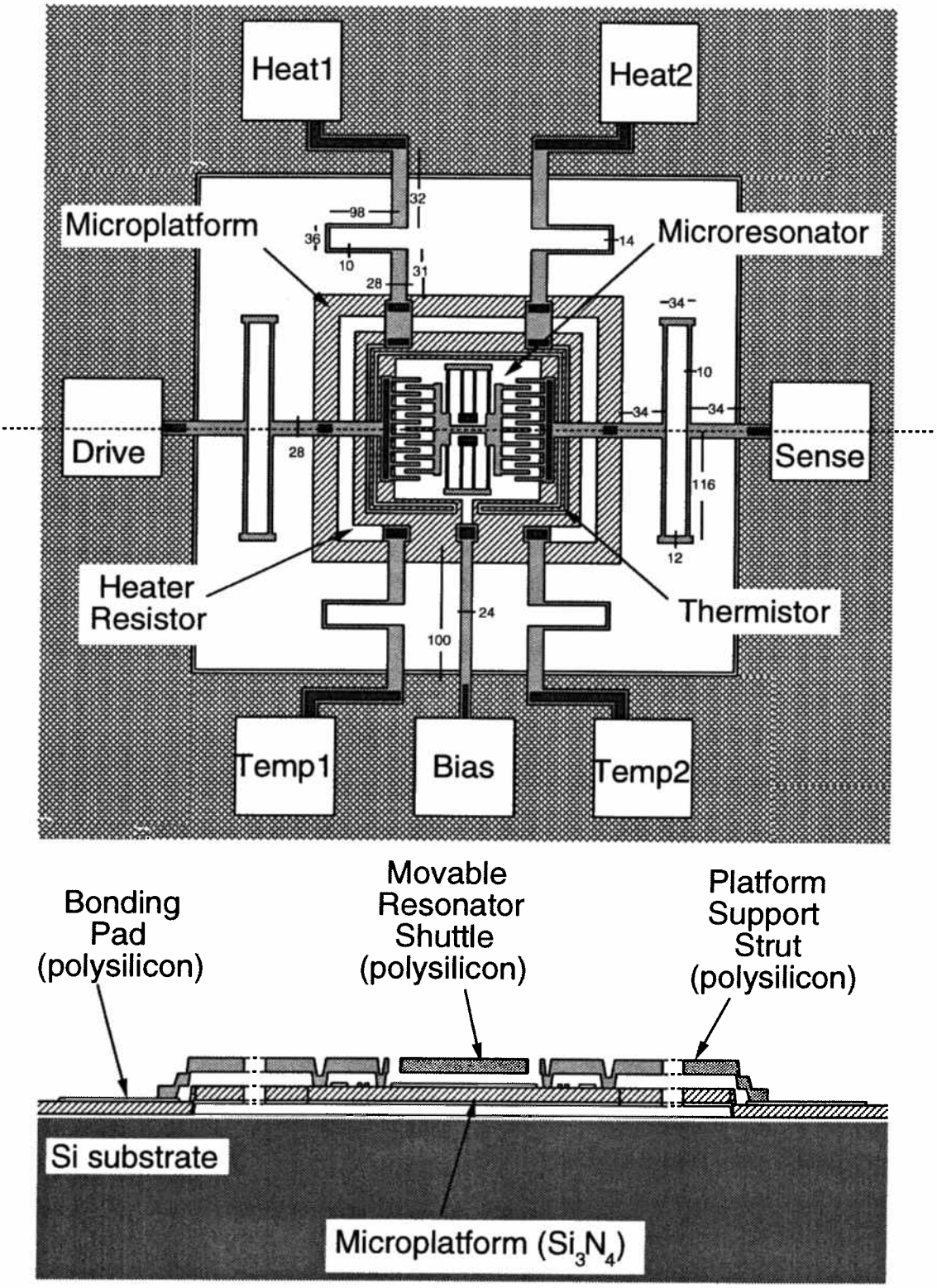

Fig. 7.4: Overhead schematic and cross-sectional view of the micro-oven control system, showing a μresonator situated on top of a nitride platform, which in turn, is suspended above the substrate. The platform is attached to the substrate via long, thin beams, which provide thermal isolation from the substrate. This design uses folded-beam supports to relieve post-fabrication residual stress and possible thermal stresses.

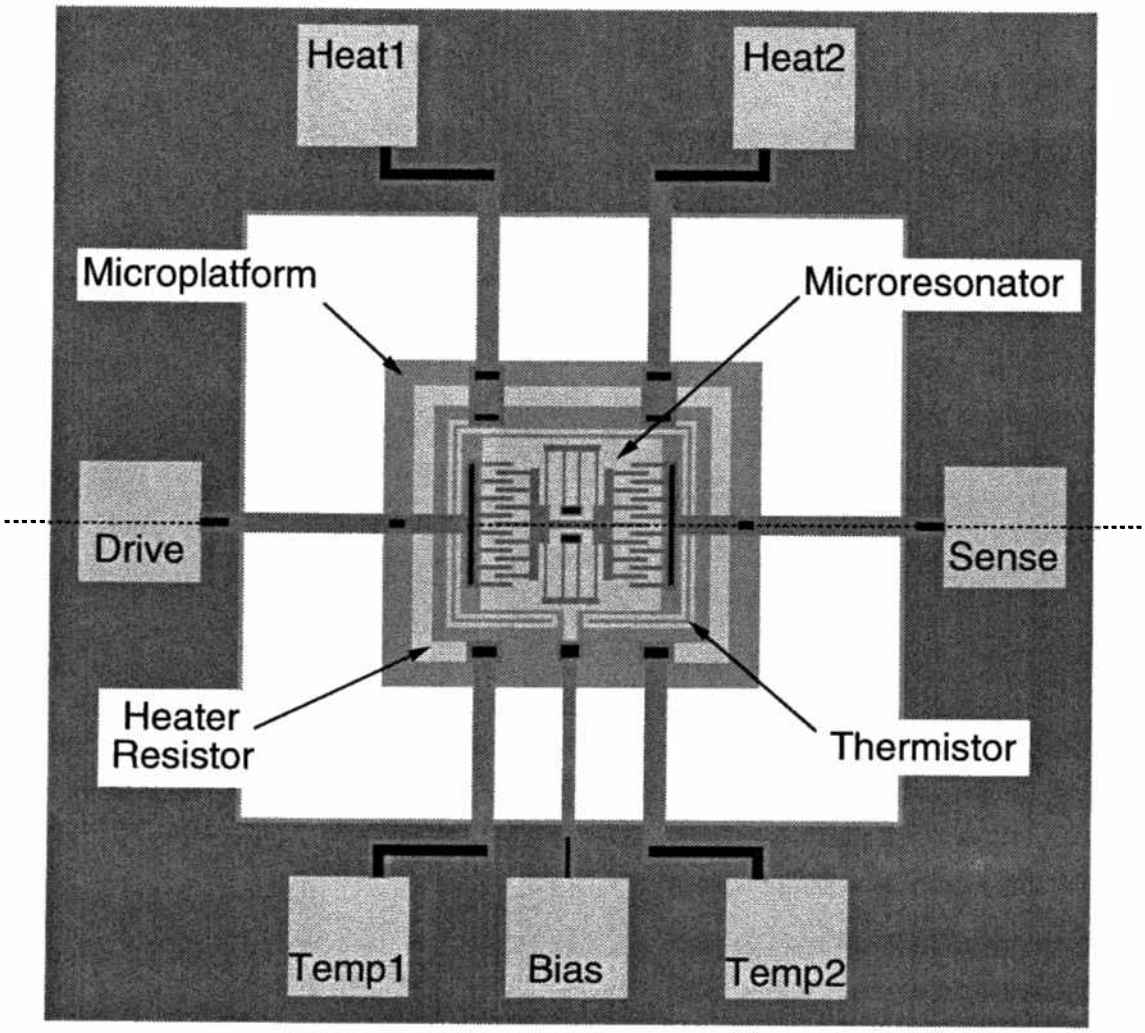

Fig. 7.5: Overhead schematic view of the micro-oven control system, where in this design, straight supporting beams are used for comparison with the design of Fig. 7.4.

7.3 Micro Oven Fabrication

This demonstration of micro-oven control was implemented without on-chip electronics, but using a process largely compatible with the MICS process detailed in Chapter 3. The process utilizes surface micromachining procedures, exclusively, and is summarized in Fig. 7.6 and 7.7.

The process begins with the blanket deposition of a conductive ground plane via an in *situ* phosphorous-doped low-pressure chemical vapor deposition (LPCVD) of polycrystalline silicon. This polysilicon is deposited in a tube where the temperature is controlled to vary from 604°C to

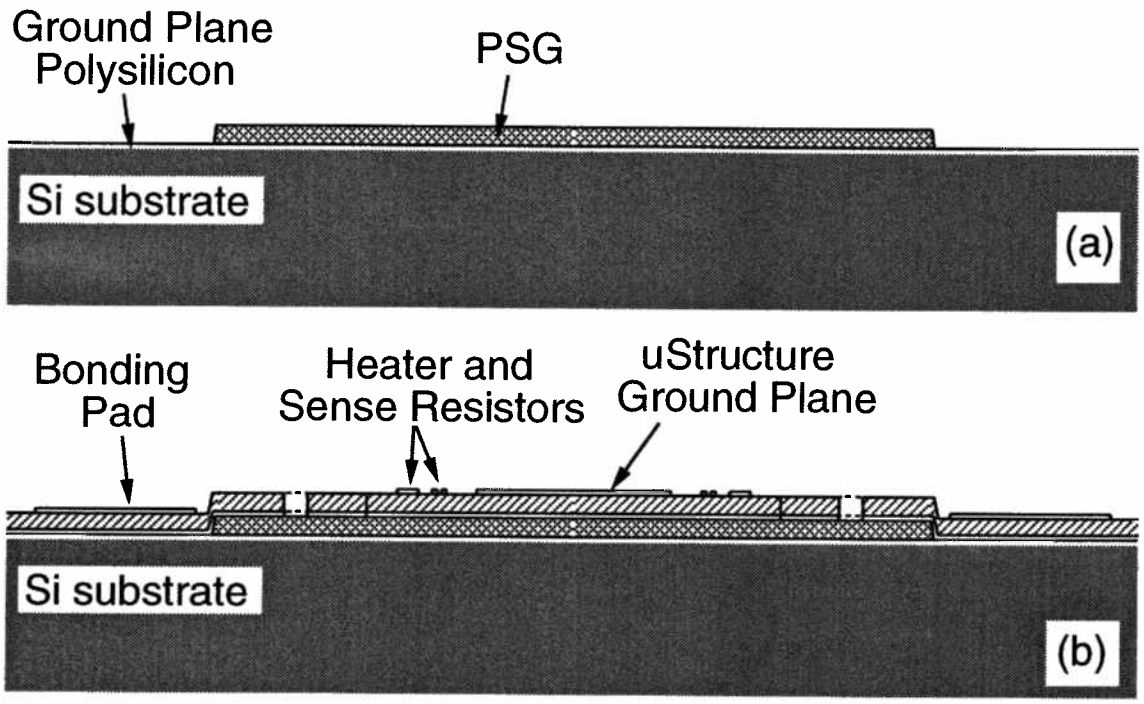

Fig. 7.6: Micro oven fabrication process. (Cross sections taken through the line indicated in Fig. 7.4.)

implant step or an anneal in $POCl_3$. The polysilicon deposition is immediately followed by the LPCVD deposition of a 2 μm-thick layer of phosphosilicate glass (PSG, 8% phosphorous), which serves as the sacrificial layer for the silicon-rich nitride platform. The PSG is then patterned via a CF_4/CHF_3-based plasma etch to define the platform anchor points. At this point, the cross-section is as shown in Fig. 7.6 (a).

Next, a polysilicon/silicon-rich nitride/polysilicon sandwich of layers is deposited via LPCVD in thicknesses of 4000Å/1μm/4000Å. For the process of this work, the nitride was deposited at 835 °C with a 5:1 SiH_2 Cl_2:NH_3 ratio. These deposition conditions yield a slightly tensile film. Both layers of polysilicon in the sandwich are in-situ phosphorous-doped. The top layer of polysilicon is patterned using a Cl_2-based plasma etch to form bonding pads, the μresonator ground plane, and the heating and sensing resistors. The patterns for the nitride platform and supporting beams are then etched into both the silicon-rich nitride layer and bottom film of polysilicon using an SF_6-based plasma etch. At this juncture, the cross-section looks as shown in Fig. 7.6 (b). The bottom layer of polysilicon is in electrical contact with the substrate and serves as a conduc-

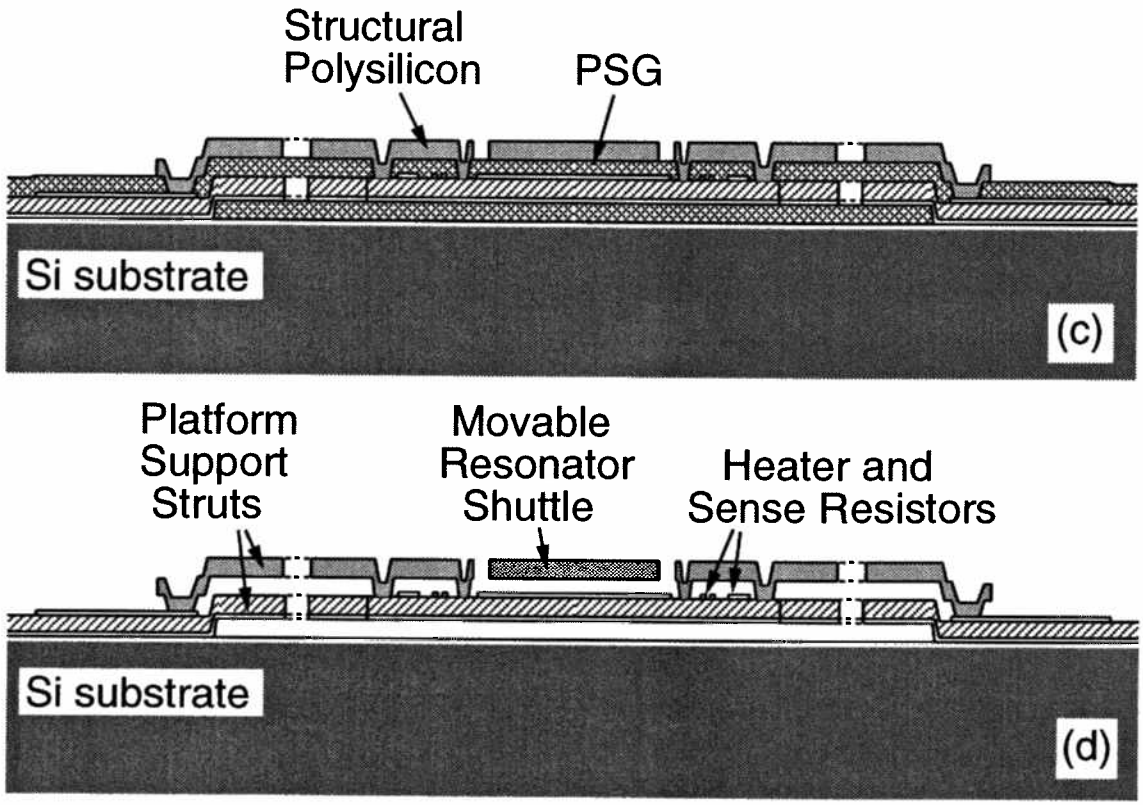

Fig. 7.7: Micro oven fabrication process (continued). (Cross sections taken through the line indicated in Fig. 7.4.)

tive shield preventing electrostatic attraction between platform devices and the substrate, which tends to pull the platform down.

Next, a second sacrificial PSG layer 2 μm-thick is deposited and patterned to define the microstructure anchors. In situ phosphorous-doped polysilicon is then deposited via LPCVD at ~625°C 2μm-thick to serve as the microstructural layer, and this is followed by an oxide etch mask (similar to that discussed in Chapter 3). The polysilicon is deposited doped for consistency with the MICS process. The (oxide mask and) structural polysilicon is patterned to form the resonator (Fig. 7.6(c)), then rapid thermal annealed (RTA'ed) for 1 minute at 1100°C to relieve overly compressive residual stress in the polysilicon caused by an excessive amount of phosphorous in the lattice and between grains. Even after the anneal, clamped-clamped beams with lengths over 200 μm are buckled. However, folded-beam resonators remain unbuckled because most of the residual strain is released in this structure.

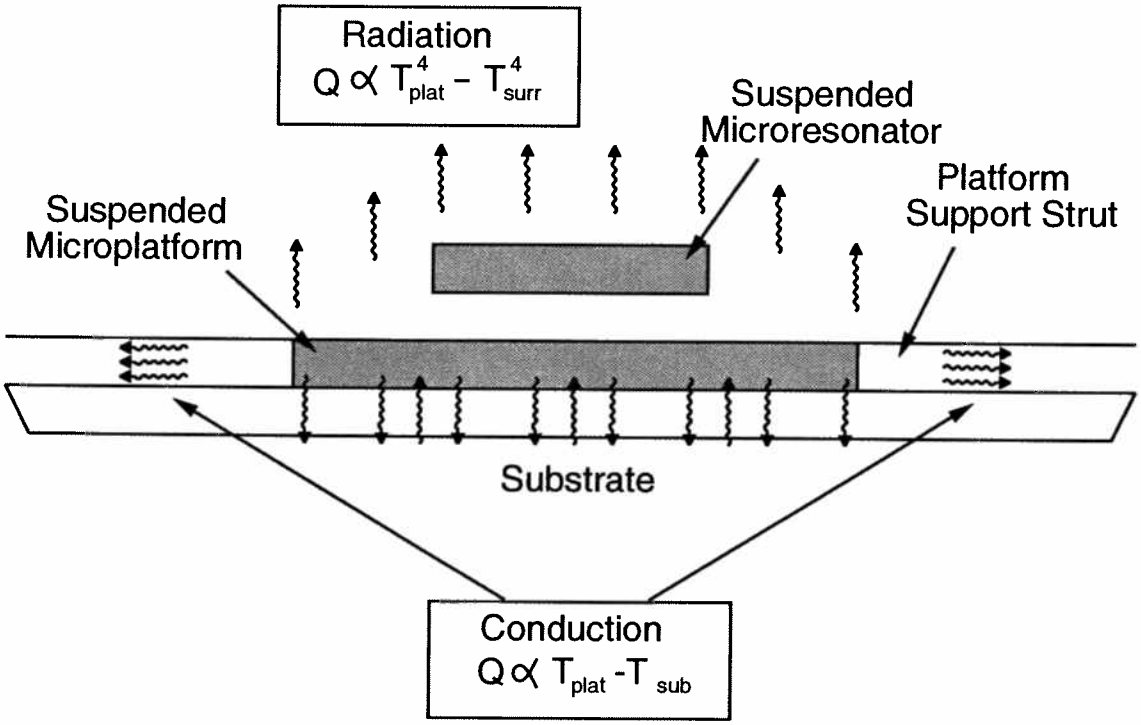

Fig. 7.8: Schematic of the microplatform, showing the relevant heat loss mechanisms in a vacuum environment.

After RTA, suspended structures are released via a sacrificial PSG etch using 48.8 wt. % hydroflouric acid, after which the cross-section is as shown in Fig. 7.6(d). Since the HF is highly concentrated, the release etch takes less than 3 minutes, even for 300x400 μm^2 platforms suspended only 2 μm above the substrate (with no etch holes).

A detailed process flow for the micro-oven and resonator is presented in Appendix C.

7.4 Thermal Modelling

The main concern in design of this microplatform is the degree of thermal isolation achieved, since this dictates the power required to sustain a given temperature and the time required to change it [101]. Since the μresonator is normally operated in vacuum to achieve high Q, thermal loss through convection can be neglected. For this reason, this analysis considers only conductive and radiative loss mechanisms. The loss mechanisms of interest, then, are summarized in Fig. 7.8.

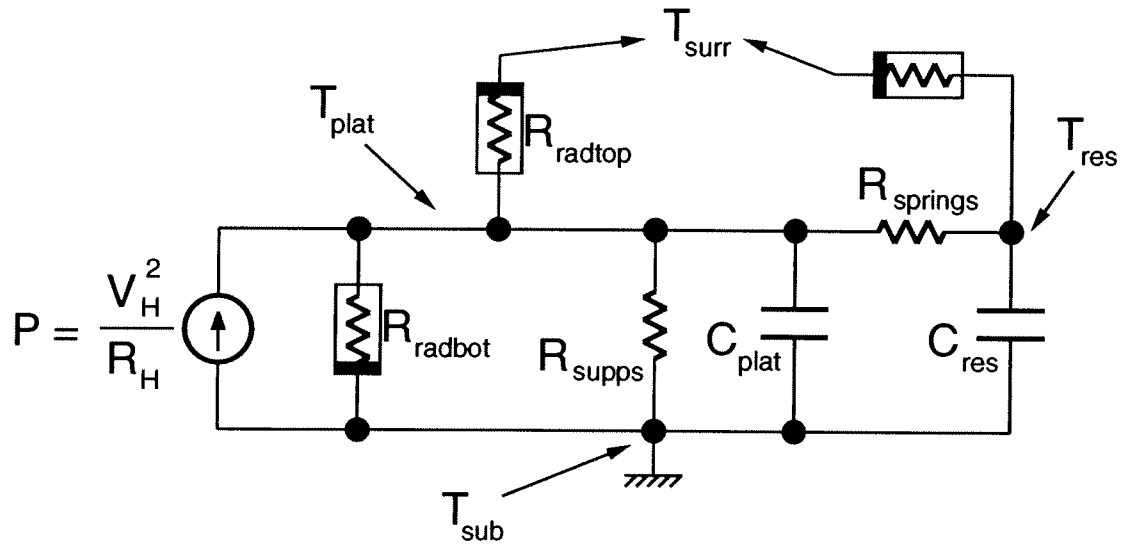

Fig. 7.9: Equivalent thermal circuit schematic for micro-oven control systems of Figs. 7.4 and 7.5.

For this structure, power and transient information can be conveniently attained using a simple lumped-parameter model where the supporting struts are represented by equivalent thermal resistances (thermal C neglected), while the platform and resonator shuttle are modeled with thermal capacitors (thermal R neglected). Loss due to radiation may be modeled via nonlinear thermal resistors. Using this lumped parameter model, the equivalent thermal circuit for the micro-oven is as shown in Fig. 7.9.

The expression for conductive thermal resistance is given by [102]

$$R_{thermal} = \sum_{j=1}^{m} \left[\sum_{i=1}^{n} k_i \left(\frac{A_i}{l_j} \right) \right]^{-1} \tag{7.3}$$

where k_i is the thermal conductivity of the i^{th} layer, A_i is the cross sectional area of the i^{th} layer, and l_j is the length of the j^{th} beam in the support strut. Thermal capacitance can be found using [102]

$$C_{thermal} = \sum_{i=1}^{n} \rho_i V_i c_{pi} \tag{7.4}$$

where ρ_i is the density of the i^{th} layer, V_i is the volume of the i^{th} layer, and c_{pi} is the specific heat of the i^{th} layer.

Two components of radiative thermal loss must be considered: one component for the top surface of the μplatform where heat radiates to free space; and one for the bottom surface, for which there is significant thermal reflection with the silicon substrate just 2 μm below. Top surface radiation can be modeled by [102]

$$P_{radtop} = \sigma A_{top} \varepsilon_{pSi} (T_{plat}^4 - T_{surr}^4) \tag{7.5}$$

where P_{radtop} is the power radiated from the platform at temperature T_{plat} to the surroundings (room or enclosed probe station compartment) at temperature T_{surr}, A_{top} is the top surface area, ε_{pSi} is the thermal emissivity for polysilicon, and σ is the Stefan-Boltzmann constant. ε_{pSi} is used since the top of the platform is mostly polysilicon (resistors, ground plane, and resonator). The bottom polysilicon surface and polysilicon-coated substrate may be approximated as infinite parallel planes, for which radiative thermal loss from the μplatform is given by [102]

$$P_{radbot} = \frac{\sigma A_{bot} (T_{plat}^4 - T_{sub}^4)}{2/\varepsilon_{pSi} - 1} \tag{7.6}$$

where P_{radbot} is power, A_{bot} is the bottom surface area, and T_{sub} is the substrate temperature.

The total steady-state power dissipation required to maintain a constant temperature T_{plat} on the platform is given by (referring to Fig. 7.9)

$$P = \frac{T_{plat} - T_{sub}}{R_{supps}} + P_{radtop} + P_{radbot} \tag{7.7}$$

where T_{sub} is the substrate temperature and R_{supps} is the parallel combination of the thermal resistances of all the supporting struts. Again, referring to Fig. 7.9, the thermal time constants by which the platform and resonator temperatures may be adjusted can be approximated by

$$\tau_{plot} \approx R_{supps} C_{plat} \tag{7.8}$$

$$\tau_{res} \approx R_{supps} C_{plat} + R_{springs} C_{res} \tag{7.9}$$

Table 7.1 summarizes important constants, measured and theoretical, required by the expressions in this section. Using typical dimensions for the micro-oven control system (total platform strut lengths of 320 μm, platform dimensions of 300 x 400 μm^2, 67 μm resonator spring lengths), and assuming that the struts and microplatform are composed of a 1 μm-thick silicon-rich nitride sandwiched between two layers of polysilicon (4000 Å- and 2 μm-thick), the expected power requirement and thermal time constants to maintain a platform/resonator temperature of 120°C are $P = 1.4$ mW, $\tau_{plat} = 21$ ms, and $\tau_{res} = 41$ ms. Note that the required power and warm-up time are several orders of magnitude smaller than those required by similar oven-control methods applied to crystal oscillators (1–10 W and from 5 to 30 minutes [79]), and herein lies a major incentive for miniaturizing frequency-stable, crystal-based oscillators.

TABLE 7.1. Relevant Thermal Data for the (Folded-Beam) Micro Oven

Parameter	Value	Units
Density of Silicon Nitride ρ_{nit}	3.0	gm/cm^3
Density of Polysilicon ρ_{pSi}	2.3	gm/cm^3
Specific Heat of Silicon Nitride c_{pnit}	0.7	J/(gm K)
Specific Heat of Polysilicon c_{pSi}	0.77	J/(gm K)
Thermal Conductivity of Si Nitride k_{nit}	0.032	W/(cm K)
Thermal Conductivity of Polysilicon k_{Si}	0.3	W/(cm K)
Stefan-Boltzmann constant σ	5.67×10^{-8}	
Top or Bottom Surface Area of Platform A_{plat}	300×400	μm^2
Temperature of Surroundings T_{surr}	300	K
Heater Resistance R_h	1150	Ω
Temperature Coefficient of Resonator Resonance Frequency TC_{f_r}	-12	ppm/K

7.5 Experimental Results

Figure 7.10 shows the scanning electron micrograph (SEM) of a fabricated micro-oven. Figure 1.10 shows angled-light photomicrographs of two microplatforms, one suspended by folded beams, another by straight beams. The concentric circular rings on the straight-beam platform are visible even under direct light, and they clearly indicate buckling due to compressive stress. Ripples are fewer and farther apart for the folded-beam suspended platform and can only be seen under angled light, indicating partial stress relief via folded beams.

7.5.1 Frequency Control and Power Dissipation

By applying a voltage across the on-platform heating resistor (1150 Ω), the temperature of the platform and resonator may be adjusted. Figure 7.12 presents a plot of resonance frequency versus applied heating voltage, comparing experiment with prediction based on the theory of Section 7.4 and physical constants summarized in Table 7.1. Note that for a 1% change in center

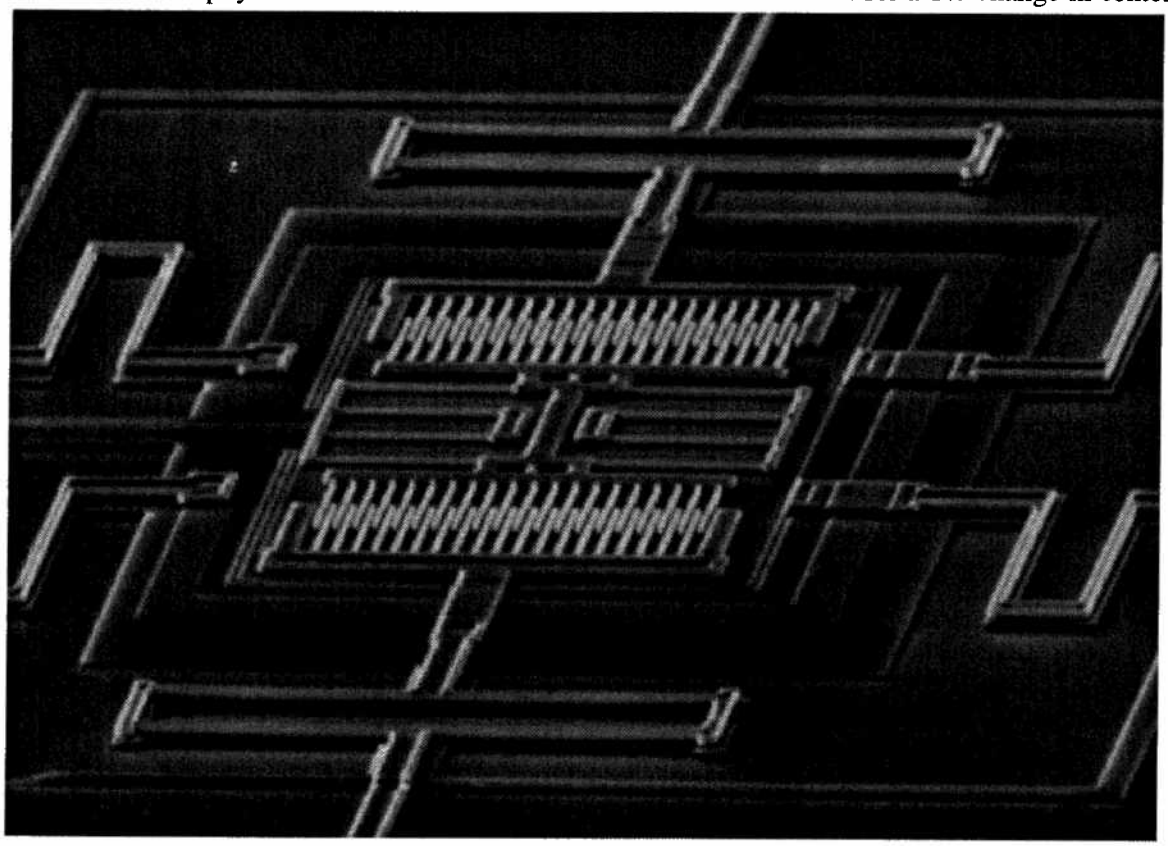

Fig. 7.10: SEM of a fabricated micro-oven with on board micromechanical resonator, plus heating and sensing resistors.

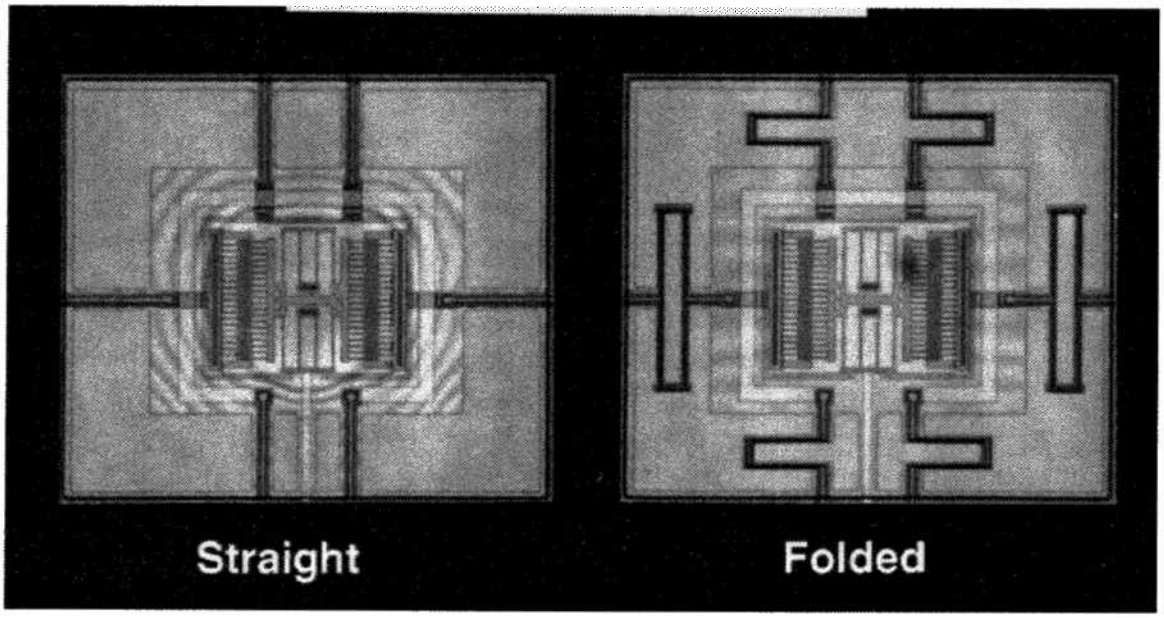

Fig. 7.11: Angled-light photomicrographs of microplatforms suspended by (a) straight beams; and (b) folded-beams. The concentric rings on the platform of (a) indicates post-fabrication compressive stress, which is partially relieved via folded-beams in (b).

frequency, only 5 V need be applied to the heater resistor, which corresponds to 22 mW of power and a platform temperature over 750° C. The power required to achieve a specified temperature on the microplatform is summarized in Fig. 7.13, which plots the measured platform temperature versus the power applied to the heater resistors which achieves that temperature. Also shown, for comparison, is the theoretical prediction of Section 7.4. The measured τ_{plat} = 20 ms, which agrees very well with the values obtained from Eq. (7.8).

7.5.2 Micro Oven Stabilization

Frequency stabilization through feedback control was then demonstrated using the feedback circuit shown in Fig. 7.14 In this scheme, the voltage V_{th} is initially low and causes the amplifier to supply current to the heating resistors. As the temperature rises, the thermistor (a polysilicon resistor of about 12 kΩ) resistance increases, causing V_{th} to rise to the optimum value V_{ref}, where the feedback loop attempts to stabilize V_{th}. The bias temperature of the system is, thus, set by V_{ref}. For purposes of maximizing frequency stability, this temperature is chosen at the point of minimum TC_{fr}.

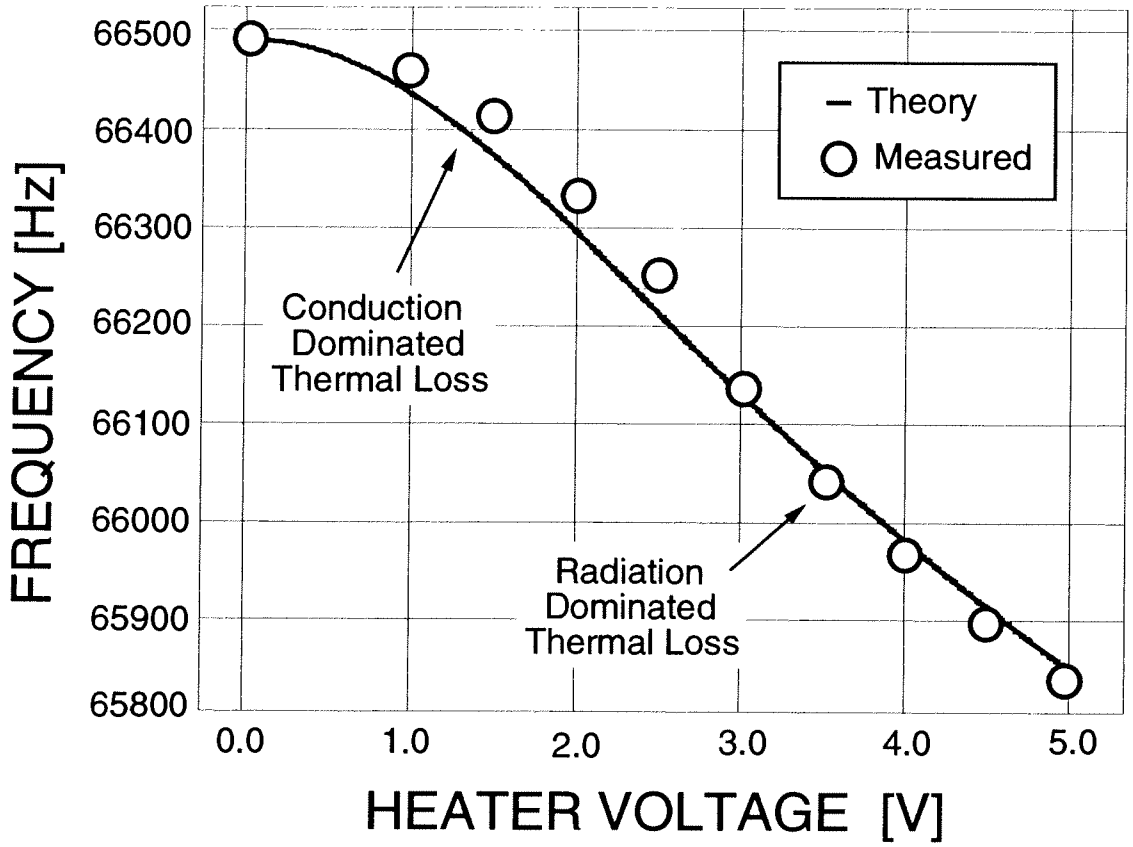

Fig. 7.12: Plot of resonance frequency vs. voltage applied to the heater resistor on the microplatform.

Unfortunately, there is no turning point or zero slope point in the frequency versus temperature plot of Fig. 7.1 where the system can be biased for maximum stability. Rather, the TC_{fr} stays relatively constant along the whole curve (from 300 to 370 K), so any elevated bias temperature in this range would be as good as another for oven-stabilization tests. For this report, the bias temperature was 160° C. The frequency versus temperature curve under micro-oven stabilization using the circuit of Fig. 7.14 is shown in Fig. 7.15. The TC_{fr} is now only 2 ppm/°C. Again, a much smaller TC_{fr} might be achieved through μoven-control if the resonator can be designed to have a turning point or zero slope point at which the temperature may be biased.

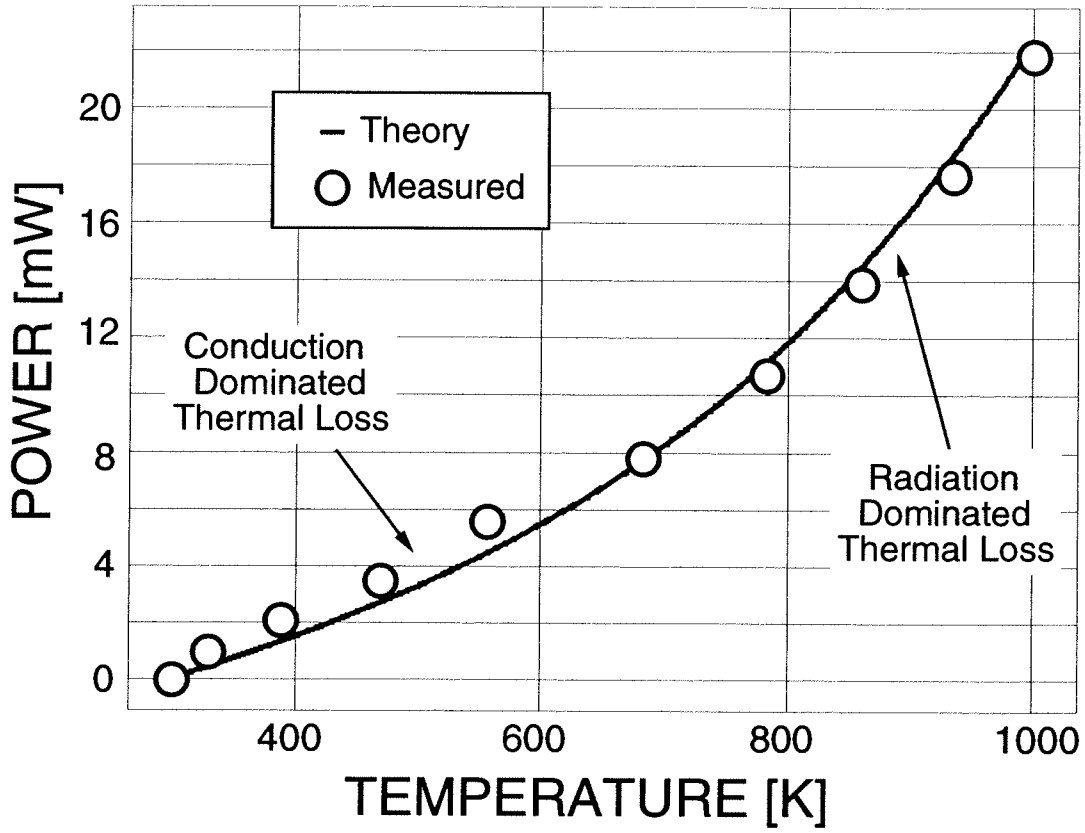

Fig. 7.13: Plot of platform temperature versus power applied to the heater resistor.

7.6 Conclusions

Due to the large volume required for thermal insulation, the long warm-up time needed (around 30 minutes), and the excessive power requirements (1–10 Watts), there has been a tendency to avoid oven control techniques for *macroscopic* crystal oscillators, and rather, use circuit compensation techniques, which are less effective than oven control [9,79]. However, as have been discussed, orders of magnitude improvement in power dissipation and thermal time constant can be obtained through micro-miniaturization. Because of this, oven control of a frequency reference becomes much more practical on a micron scale, and an oven-controlled μresonator oscillator becomes a much more viable approach for achieving a stable, completely monolithic frequency reference, for use in sensors or in signal processing environments.

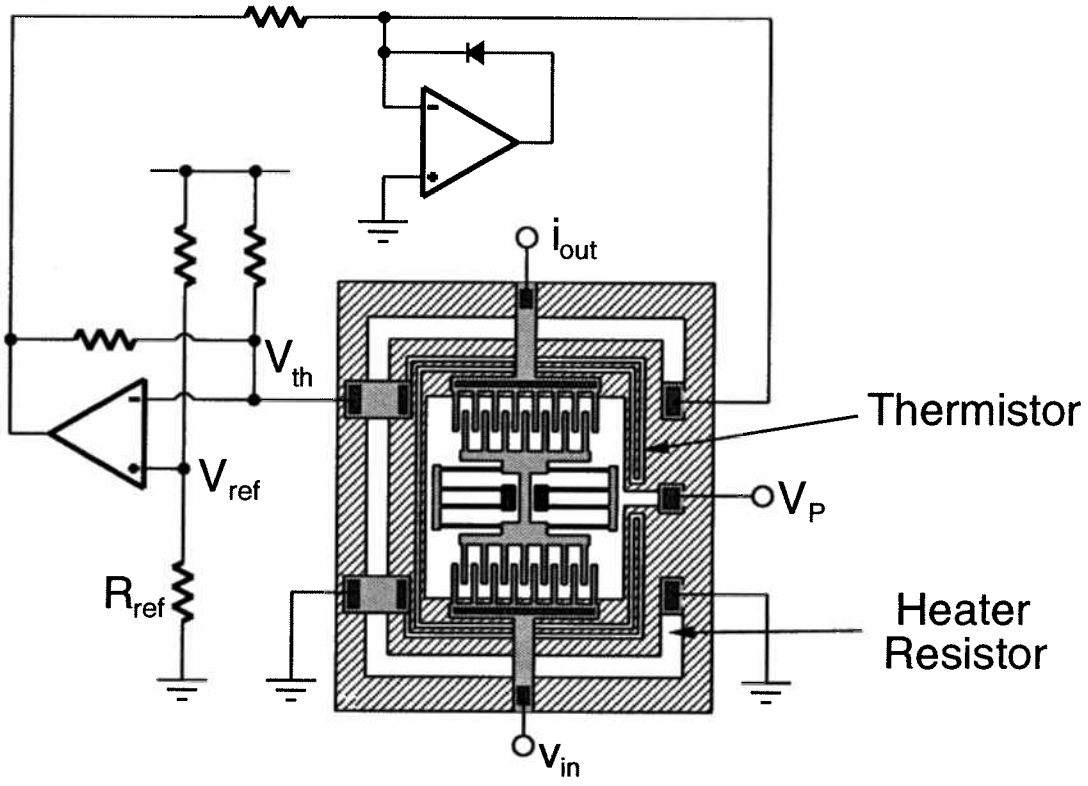

Fig. 7.14: Feedback circuitry for stabilizing the temperature of the microplatform.

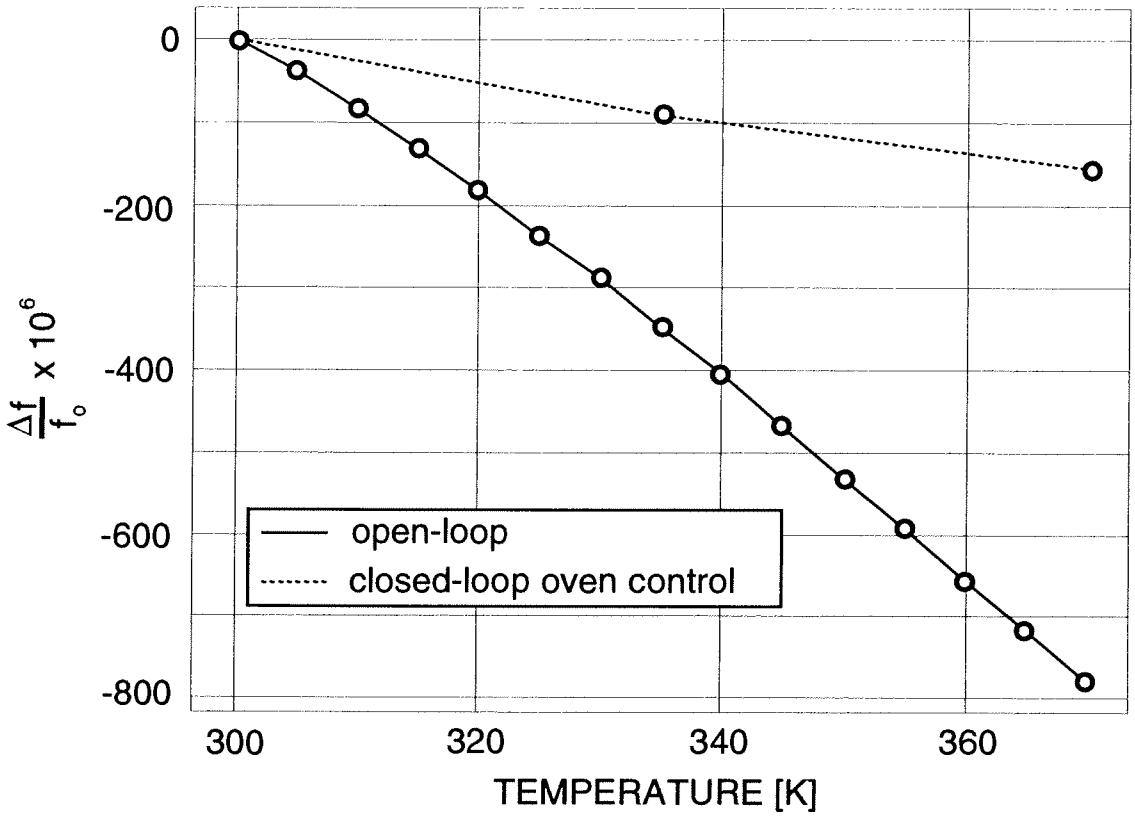

Fig. 7.15: Plot of ppm change in resonance frequency vs. temperature for a μresonator on a thermally isolating μplatform, comparing the case where on-platform controlling resistors are unused to that where resistors are connected in an active temperature controlling feedback loop.

CHAPTER 8 *Conclusions*

By lowering the price and abundance of compact sensors, which use mechanical elements as physical-to-electrical transducers, micromachining technologies as applied to sensors are strongly impacting the evolution of industrial societies. The contents of this dissertation are aimed at applying micromechanics to yet another field/industry that makes heavy use of the properties of mechanical devices: the communications industry, where high-Q bulk-mode quartz crystals, ceramic resonators, and SAW resonators are regularly used for IF and RF filtering in almost all systems. Given that the communications industry—which makes possible radio, television, telephone, among others—is among the most influential products of technology today, the ability to replace the macroscopic mechanical elements used in communication systems with integrable miniaturized equivalents should have enormous economic and cultural impact.

In this day, when almost every imaginable signal processing function can be implemented using analog or digital transistor technologies, micromechanical elements may still find use in signal processing applications for the same reasons that macroscopic elements are still used: (1) they can achieve much higher quality factor (Q) than their electronic counterparts; (2) they are generally much more stable with respect to temperature; and (3) they age at much slower rates. One f the direct consequences of item (1) to communications applications is that filters based upon mechanical elements can be much more selective than electronic versions, and oscillators referenced to mechanical elements are many times more stable and less noisy. In short, quartz and

ceramic resonators are used in communication systems because they simply outperform their electronic counterparts, nevermind the cost and space they require.

But how good are they when miniaturized? One must be careful not to assume that miniaturized versions of these components will be as good! This is the single most important question addressed by this dissertation. In effect, one of the main purposes of this work was to investigate the consequences of miniaturizing the mechanical signal processors used in today's (and yesterday's) communications systems.

Before addressing this question, however, one must first be sure that the technology which realizes these novel devices is feasible. To this end, a process which merged CMOS electronics and polycrystalline silicon surface micromachining technologies was developed. Development of the fabrication technology was based upon the philosophy that a modular process, in which the CMOS and the micromechanics were processed in separate, flexible modules, was most economically sensible. The economic advantages result from the fact that true modularity allows one to upgrade each technology (CMOS or structural) independently of one another.

As one might expect, true modularity is an idealization; a technology can be modular only to the extent that its modules will allow. Almost invariably, each module will impose certain constraints on the other. In the process developed, here, CMOS was fabricated in the first module, followed by a microstructural processing module. The deficiencies of this modular process were immediately discernible:

1. One could not use just any CMOS process. Due to high temperature processing (> 835°C), Al metallization could not be used. The process of this work used tungsten metallization with $TiSi_2$ contact barriers.
2. One could not use just any microstructural process. Processing temperatures were limited to less than 835°C for long time periods. High temperatures were possible, however, but only when doing rapid-thermal annealing

Despite these deficiencies in modularity, the process was functional.

The novelty of the fabrication technology had a huge influence on the scope of this work. Designs were made simple and robust, so that deficiencies in either the CMOS (e.g, V_t's wrong,

horrendous matching tolerances) or the micromechanics (e.g., excessive residual stress, sticking) could not deny results. For these reasons, replica biasing circuit topologies were utilized, as were folded-beams. Capacitive transduction was used exclusively, to simplify process complexity and predictability.

Given a working technology, the first communications device investigated was a fully monolithic high-Q oscillator, with oscillation frequency referenced to a micromechanical resonator, and with oscillation sustained by active CMOS electronics—seemingly very much like a quartz crystal oscillator. A tenth of the way into the design, however, the differences are immediately apparent. To start, the series motional resistance of present-day micromechanical resonators is quite large, from 100 kΩ on up, for reasonable capacitor gap spacings and resonator dc-biasings. This is a direct consequence of the micro-scale of this technology: Since dimensions are small, the overlap capacitance which determines the electromechanical coupling factor of most capacitively transduced designs, is likewise small. A small electromechanical coupling factor leads to a large series resistance (through an inverse proportionality). This large series resistance excluded many parallel oscillator architectures, including the ever popular Pierce design, since these parallel architectures are more difficult to implement when the series resistance of the high-Q element is large. Thus, a series resonant oscillator architecture was used in this work. Series resonant architectures minimize Q-loading when the series resistance of a resonator is high.

Through theoretical analysis, one of the major consequences of miniaturization of the high-Q element in the oscillator was revealed: The short-term stability becomes more susceptible to such phenomena as mass loading of the resonator. Mass loading noise refers to frequency fluctuations brought about by instantaneous differences in the rates of adsorption and desorption of contaminant molecules to and from the surface of a micromechanical resonator, which causes in instantaneous variations in resonator mass, which in turn causes fluctuations in resonance frequency. Mass loading is found to be dependent upon the following:

1. Adsorption and desorption rates of contaminant molecules.
2. Contaminant molecule size and weight.
3. Pressure.
4. Temperature.

5. Inversely proportional to the number of sites (i.e., the smaller the surface area, the larger the noise due to mass loading)

The pressure and temperature dependence of phase noise due to mass loading are particularly interesting. For both, the noise peaks at some intermediate value of the parameter. For both, this phase noise peak becomes larger as the dimensions of the mechanical resonator shrink. Since high frequency micromechanical resonators will most likely be less massive, this suggests that mass loading noise makes larger and larger contributions to the total phase noise performance as the frequency of a given oscillator goes up. The theory of this dissertation predicts that phase noise due to mass loading will even dominate over that due to superposed electronic noise at high enough frequencies.

Another significant consequence of miniaturization, which will be seen to be a constant problem through these conclusions, is again the large series resistance of the microresonator. Firstly, this large resistance limits the total power capacity of the oscillator, thus limiting the phase noise density-to-carrier ratio at frequencies close to the carrier. Secondly, the large resistance allows the oscillator to limit through nonlinearities in the resonator, rather than in the sustaining amplifier. This feature may prove convenient at some times, since it allows the amplitude of oscillation to be controlled through the dc-bias applied to the resonator. It may also, however, prove disastrous, since in some regimes, chaotic behavior of the resonator has been observed.

Despite the above potential problems, the (audio-frequency protoype) CMOS microresonator oscillator did display adequate phase noise performance experimentally. (The phase noise density, in fact, was too low to be measured by a custom-built measuring instrument.) One would question how the oscillator would perform at much higher frequencies. Read on.

Next, microelectromechanical filters were investigated, with particular attention to designability and noise performance. The ever returning problem of high series motional resistance in present-day micromachined resonators was again a limiting factor, here. For single and multiple resonator filters, the equivalent input noise resistance was dominated by the large series motional resistance of the microresonator(s). In effect, the noise performance of such filters is dominated by Brownian motion noise. The noise levels are not a big problem for IF filters, since dynamic ranges higher than 80 dB are feasible when active driving stages with matched output impedances are

used. For use as RF filters, however, the series resistance of these resonators must be reduced, via smaller capacitor gaps or via larger dc-bias voltages—both technology solutions.

On top of these noise problems, the high series resistance of these micro-scale resonators leads to the requirement for large terminating loads. Such large loads are more susceptible to interaction with parasitic capacitance, which causes phase lag, which in turn leads to passband distortion in bandpass filters. Fortunately, an active (and very quiet) Q-controlling termination technique was proposed to alleviate passband distortion problems. Audio frequency filters with acceptable performance were experimentally demonstrated.

The next signal processing element investigated was the mixer+filter device, which consisted of a single resonator, or filter made up of such resonators, in which an ac component is added to the dc-bias of the resonator. This powerful technique could both amplitude modulate an information signal to very high frequencies (with power gain), and mix an incoming signal down to the IF frequency and filter it as well. Adding this device to the group above, all components at the front end of a receiver (before the discriminator) have been shown to be realizable via micromechanical elements.

In addition to implementing and studying the above devices, this dissertation addresses a more fundamental materials issue: thermal stability of devices based upon micromechanical resonators, particularly those constructed of polycrystalline silicon. The temperature coefficient of the resonance frequency of a typical polysilicon, folded-beam, comb-driven, micromechanical resonator was measured to be -10 ppm/^{o}C. Since this is much larger than that for quartz, an oven control technique was implemented to stabilize this temperature dependence. Full advantage was taken of the excellent thermal isolation attainable through surface micromachining technologies, and power dissipations of only 2 mW were required to adequately heat a micro-oven to a reasonable stabilization temperature. The temperature coefficient of the resonance frequency was reduced to -2 ppm/^{o}C using active oven-control methods. More advanced strategies should be able to reduce this even further.

In summary, miniaturization of high-Q mechanical signal processors yields in large part, devices with performance adequate for present-day communications applications at the low frequencies of the prototypes designed in this work. Thus, the answer to the question, "Are they good

enough?": YES, at low (VF to MF) frequencies. What the micromechanical performance will be at higher frequencies is still unclear and is certainly a question ripe for further research.

8.1 Future Research Directions (Solving the Problems)

In the course of investigating micromechanical signal processors, this research has literally opened up a can of worms. Numerous questions have been raised and problems identified, including technology merging, mass loading noise, and high series motional resistance in micro-scale resonators. A multitude of other questions not mentioned in these conclusions (but mentioned in the text) also need to be addressed (e.g. How does the quality factor vary with frequency? with surface roughness? What other methods are available to improve thermal stability?). This section suggests some solutions to a subset of some of the explicitly mentioned problems.

8.1.1 Mass Loading

Solutions to mass loading noise were already suggested in Chapter 4, and are repeated here:

5. Encapsulate the microresonator under very low pressure vacuum ($< 10^{-6}$ Torr). (Note that high pressures are unreasonable, since these will severely degrade the quality factor of the mechanical resonator.)
6. Operate the microresonator under more optimal temperatures as determined by curves such as Figs. 1.37 and 1.38. One low power method for doing this could be through the micro-oven techniques of Chapter 7.
7. Treat the surface of the resonator to tailor the desorption energies of contaminant molecules such that the peaks of mass loading occur at pressures and temperatures far removed from the operating point.
8. Tailor an encapsulation process such that only contaminants with molecular weights and desorption energies that create mass loading-derived phase noise peaks far removed from the operating point are used.
9. Increase the surface area of the resonator.

Thus, there are many solutions to mass loading. It should not be a debilitating phenomenon.

Item 1 may be the most convenient method for controlling mass loading noise, given that the resonator must be operated under vacuum anyway, to attain high Q. It may be the case that the very low pressures required to eliminate mass loading noise can only be attained through integrated encapsulation methods. Whatever the case, problems arising from mass loading of microresonators combined with the necessity for vacuum to attain high Q both underline the important role that vacuum encapsulation technologies will play in future implementations of micromechanical signal processors, and resonant sensors alike.

8.1.2 High Series Resistance

High series motional resistance R_x in the microresonator equivalent circuit has been identified through this dissertation as a major detriment to the performance and designability of micromechanical signal processors. Among the many consequences of high R_x are:

1. Large Brownian motion noise generator associated with the micromechanical resonator.
2. Compromised designability. For example, in oscillators, a large gain is required to sustain oscillation, and limiting occurs in the resonator (which may lead to instability, and thus, may require automatic-level control circuitry). In addition, large R_x leads to a requirement for large terminating resistors for mechanical filters, which in turn leads to passband distortion.
3. For a given circuit technology, R_x may limit the highest attainable frequency for a given application.

Thus, methods which reduce the value of R_x must be pursued. Some insight into how this can be done is obtained by examining the expression for R_x, given in Chapter 2, and repeated here:

$$R_x = \frac{\sqrt{mk}}{QV_P^2\left(\frac{\partial C}{\partial x}\right)^2} \tag{8.1}$$

Thus, the following strategies can reduce the value of series motional resistance:

1. Minimize mass.

2. Maximize Q. This emphasizes the importance of research on maximizing the quality factor of micromachined resonators, whether by material approaches, anchoring approaches, or others.
3. Increase the resonator dc-bias V_P. This is a technology limited option.
4. Increase the capacitance change per unit displacement at the transducer ports. One way to do this is to reduce the gaps between electrodes and resonator. As mentioned in Chapter 2 gaps of 1000 Å or less are not unreasonable, given that MOS gate oxide thicknesses are already much thinner than this. In essence, this approach can be thought of as fighting the problems of miniaturization with further miniaturization.

Research on the above or on other techniques for reducing series motional resistance in micro-scale resonators will most likely be extremely important for improving the performance of micro-mechanical signal processors.

8.1.3 Trimming

As mentioned in Chapter 2, the absolute tolerance of the resonance frequency depends strongly upon the fabrication technique. For the *in situ* doped polycrystalline silicon resonators of this work, the resonance frequency was usually within 5% of the predicted value, usually within 3%. Obviously, some trimming will be required for oscillator and filtering applications. Practical trimming methods have been available for quartz crystals for a long time. Thus far, however, very few practical trimming methods which can tune over a 3% range have been implemented for micromechanical resonators. This is an area for further research.

Also mentioned in Chapter 2, the matching tolerance for folded-beam surface micromachined polysilicon mechanical resonators in close proximity was on the order of 0.4%. Thus, as with integrated transistor-capacitor filters, the use of ratioed designs is encouraged.

8.2 Extending the Frequency Range

With the current interest in wireless communications, and the current congestion in the FCC-regulated frequency allocations, applications for micromechanical resonator filters will inevitably require higher and higher frequencies. Thus far, the highest reported frequency was 30 MHz for a silicon resonator operated in vacuum with $Q > 10{,}000$. This is a very promising figure, since

it implies that the IF frequency range (70 to 200 MHz) of wireless communications applications might in fact be attainable with acceptable Q by micromechanical resonators.

What limits the highest attainable frequency? As seen in Chapter 2, it will probably not be lithography. Typical dimensions for the tines of a DETF operating at 100 MHz are 2μm x 2μm x 15μm, which is well within the capabilities of present-day fabrication equipment.

It is also unlikely that, even though resonator dimensions get smaller when going to high frequencies, mass loading noise will seriously limit the frequency range, since there are a variety of methods by which this noise source can be reduced.

High series resistance may pose a significant problem, since R_x increases with spring constant k, and the higher the frequency of a resonator, the higher the required spring constant. (Yes, the mass generally gets smaller, but the increase in required spring constant more than compensates for this.) Perhaps, however, continually decreasing gap spacings can offset this phenomena.

Possibly the most important determinant of the ultimate frequency limit for micromechanical resonators is quality factor. In quartz crystals, the quality factor rolls off proportionately with frequency; i.e., the ωQ product is often modelled as a constant. Whether this is also the case for micromechanical flexural mode resonators, which operate on a fundamental mode, is yet to be seen. Research on micromechanical resonator quality factor is needed to answer the question of the ultimate frequency limit.

8.3 Concluding Remarks

To summarize, prototype micromechanical signal processors based upon polycrystalline silicon micromechanical resonators have been demonstrated in this dissertation. Many of the consequences of miniaturization of high-Q components have been identified and solutions proposed. In the final analysis, micromechanical signal processors show much promise for one day being the enabling components of compact, inexpensive, high performance communication devices.

Bibliography

[1] K. Petersen, P. Barth, J. Poydock, J. Brown, J. Mallon, Jr., J. Bryzek, "Silicon fusion bonding for pressure sensors," *Rec. of the IEEE Solid-State Sensor and Actuator Workshop*, 1988, pp. 144-147.

[2] Ko, W. H., M.-H. Pao, and Y.-D. Hong, "A high-sensitivity integrated-circuit capacitive pressure transducer," *IEEE Trans. Electron Devices*, vol. ED-29 (1), pp. 48-56, January, 1982.

[3] W. Yun, R. T. Howe, and P. R. Gray, "A surface micromachined digitally force-balanced accelerometer with integrated CMOS detection circuitry," *Technical Digest,* IEEE Solid-State Sensor and Actuator Workshop, Hilton Head Island, South Carolina, June 21-25, 1992, pp. 122-125.

[4] R. T. Howe and R. S. Muller, "Resonant microbridge vapor sensor," *IEEE Trans. Electron Devices*, ED-33, pp. 499-506, 1986.

[5] D. G. Hafeman, J. W. Parce, H. M. McConnell, "Light-addressable potentiometric sensor for biochemical systems," *Science*, vol. 240. pp. 1182-1185, May 1988.

[6] D. Burns, announced at the *IEEE Solid-State Sensor and Actuator Workshop*, 1994.

[7] R. A. Johnson, *Mechanical Filters in Electronics*, New York: John Wiley & Sons, 1983.

[8] M. Konno and H. Nakamura, "Equivalent electrical network for the transversely vibrating uniform bar," *J. Acoust. Soc. Amer.*, 38, pp. 614-622 (Oct. 1965)

[9] E. A. Gerber, A. Ballato, Editors, *Precision Frequency Control, Volume 2: Oscillators and Standards*. New York: Academic Press, Inc., 1985.

[10]A. I. Zverev, *Handbook of Filter Synthesis*, New York: John Wiley & Sons, 1967.

[11]W. H. Horton and R. C. Smythe, "On the trapped-wave criterion for AT-cut quartz resonators with coated electrodes," *Proc. IEEE*, pp. 598-599, April 1967.

[12]R. Gregorian and G. C. Temes, *Analog MOS Integrated Circuits for Signal Processing*. New York: John Wiley & Sons, 1986.

[13]B.-S. Song and P. R. Gray, "Switched-capacitor high-Q bandpass filters for IF applications," *IEEE J. Solid-State Circuits*, vol. SC-21, No. 6, pp. 924-933, Dec. 1986.

[14]M. Banu and Y. Tsividis, "Fully integrated active *RC* filters in MOS technology," *IEEE J. Solid-State Circuits*, vol. SC-18, No. 6, pp. 644-651, Dec. 1983.

[15]H. Khorramabadi and P. R. Gray, "High-frequency CMOS continuous-time filters," *IEEE J. Solid-State Circuits*, vol. SC-19, No. 6, pp. 939-948, Dec. 1984.

[16]J. Silva-Martinez, M. S. J. Steyaert, W. Sansen, "A 10.7-MHz 68-dB CMOS continuous-time filter with on-chip automatic tuning," *IEEE J. Solid-State Circuits*, vol. 27, No. 12, pp. 1843-1853, Dec. 1992.

[17]M. B. Ghaderi, G. C. Temes, and J. A. Nossek, "Switched-capacitor pseudo N-path filter," in *Proc. IEEE Int. Symp. Circuits and Systems*, pp. 519-522, April 1981.

[18]S. V. Krishnaswamy, J. Rosenbaum, S.Horwitz, C. Vale, and R. A. Moore, "Compact FBAR filters offer low-loss performance," Microwaves and RF, pp. 127-136, September, 1991.

[19]H. Nathanson, W. E. Newell, r. A. Wickstrom, and J. R. Davis, Jr., "The resonant gate transistor," *IEEE Trans. Electron Devices*, vol. ED-14, No. 3, pp. 117-133, March 1967.

[20]S. Timoshenko, D. H. Young, W. Weaver, Jr., Vibration Problems in Engineering, 4th Ed. New York: John Wiley & Sons, 1974.

[21]V. B. Braginskky, V. P. Mitrofanov, and V. I. Panov, *Systems With Small Dissipation.* Chicago: University of Chicago Press., 1985.

[22]A. Cheshmehdoost, M.J. Halliwell, B. E. Jones, and B. O'Connor, "Design and applications of double-ended tuning fork mechanical resonators for measurement of force"

[23]M. J. Halliwell and B. E. Jones, "Force transducer using a double-ended tuning fork mechanical resonator with optical fibre links," *Proc. of Conf. Eurosensors I*, Cambridge, pp. 145-147, Sept. 1987.

[24]Y. Tomikawa, S. Oyama, adn M. Konno, "A quartz crystal tuning fork with modified base-width for a high quality factor: finite element analysis and experiments," *IEEE Trans. Sonics Ultrason.*, vol. SU-29, No. 6, pp. 217-223, July 1982.

[25]Y. C. Tai, L. S. Fan, and R. S. Muller, "IC-processed micromotors: design, technology, and testing," *Technical Digest*, IEEE Micro Electro Mechanical Systems Workshop, Salt Lake City, Utah, February 20-22, 1989, pp. 1-6.

[26]R. A. Buser, "Theoretical and experimental investigations of silicon single crystal resonant structures," Ph.D. Thesis, Inst. of Microtechnology, University of Nauchatel, CH-2000 Neuchatel, Switzerland, July 1989.

[27]W. C. Tang, T.-C. H. Nguyen, and R. T. Howe, "Laterally driven polysilicon resonant microstructures," *Sensors and Actuators,* **20**, 25-32, 1989.

[28]W. C. Tang, T.-C. H. Nguyen, and R. T. Howe, "Laterally driven polysilicon resonant microstructures," *Proceedings*, IEEE Micro Electromechanical Systems Workshop, Salt Lake City, Utah, pp. 53-59, February 1989.

[29]T. V. Rozhart, "The effect of thermoelastic internal friction on the Q of micromachined silicon resonators," *Technical Digest* of the IEEE Solid-State Sensor and Actuator Workshop, Hilton Head, South Carolina, pp. 13-16, June 4-7, 1990.

[30]M. W. Judy, "Micromechanisms Using Sidewall Beams," Ph.D. Dissertation, Univeristy of California at Berkeley, Berkeley, CA, 1994.

[31]R. I. Pratt, G. C. Johnson, R. T. Howe, and J. C. Chang, "Micromechanical structures for thin film characterization," *Digest of Technical Papers*, 1991 International Conference on Solid-State Sensors and Actuators (Transducers'91), San Francisco, California, pp. 205-208, 1991.

[32]H. Guckel, *et al.*, "The mechanical properties of fine-grained polysilicon: the repeatability issue," Technical Digest, IEEE Solid-State Sensor and Actuator Workshop, Hilton Head Island, S. C., June 1988, pp. 96-99.

[33]J. C. Hathaway and L. F. Babcock, "Survey of mechanical filters and their applications," *Proc. IRE*, vol. 45, pp. 5-16, jan. 1957.

[34]D. F. Sheahan and R. A Johnson, "Crystal and mechanical filters," *IEEE Trans. Circuits and Syst.*, vol. CAS-22, pp. 69-89, Feb. 1975.

[35]R. A. Johnson, M. Borner, and M. Konno, "Mechanical filters—a review of progress," *IEEE Trans. Sonics Ultrason.*, vol. SU-18, pp. 155-170, July 1971.

[36]M. W. Putty, "Polysilicon resonant microstructures," M.S. Thesis, Dept. of Electrical Engineering and Computer Science, University of Michigan, Ann Arbor, Mich., September 1988.

[37]W. C. Tang, M. G. Lim, and R. T. Howe, "Electrostatically balanced comb drive for controlled levitation," *Technical Digest*, IEEE Solid-State Sensor and Acutator Workshop, Hilton

Head Island, S. C., June 4-7, 1990, pp.23-27.

[38]W. C. Tang, "Electrostatic Comb Drive for Resonant Sensor and Actuator Applications," Ph.D. Dissertation, Dept. of Electrical Engineering and Computer Sciences, University of California at Berkeley, Berkeley, CA, Sept. 1989.

[39]G. K. Fedder, "Simulation of Microelectromechanical Systems," Ph.D. Dissertation, University of California at Berkeley, Berkeley, CA, 1994.

[40]M.W. Judy and R. T. Howe, "Highly compliant lateral suspensions using sidewall beams," Digest of Technical Papers, The 7th International Conference on Solid-State Sensors and Actuators (Tranducers'93), Yokohama, Japan, pp. 54-57, June 7-10, 1993.

[41]F. S. Crawford, "Elementary derivation of the law of equipartition of energy," Am J. Phys., 55, pp. 180-182 (1987).

[42]Thomas B. Gabrielson, "Fundamental noise limits in miniature acoustic and vibration sensors," Phase Report, Report No.NADC-91113-50, Dec. 31, 1991.

[43]K. E. Petersen, "Silicon as a mechanical material," *Proc. IEEE*, vol. 70, no. 5, pp. 420-457, May 1982.

[44]S. Terry, "A miniature silicon accelerometer with built-in damping," *Technical Digest*, IEEE Solid-State Sensor and Actuator Workshop, Hilton Head Island, S. C., pp. 114-116, June 6-9, 1988.

[45]K. J. Ma and K. Najafi, "A new capacitive electro-chemical etch-stop technique," *Proceedings*, IEEE Micro Electro Mechanical Systems Workshop, Oiso, Japan, Jan. 25-28, 1994, pp.158-163.

[46]K. Petersen, D. Gee. F. Pourahmadi, R. Craddock, J. Brown, L. Christel, "Surface micromachined structures fabricated with silicon fusion bonding," *Digest of Technical Papers*, The 1991 International Conference on Solid-State Sensors and Acuators, June 24-27, 1991, pp. 397-399.

[47]E. S. Kim, r. S. Muller, and P. R. Gray, "Integrated microphone with CMOS circuits on a single silicon chip," *Technical Digest*, IEEE International Electron Devices Meeting, Washington, D. C., Dec. 1989, pp. 880-883.

[48]S. W. Wenzel and R. M. White, "A multisensor employing an ultrasonic lamb-wave oscillator," *IEEE Trans. Electron Devices, Special Issue on Microsensors and Microactuators*, vol. ED-35, pp. 735-743, June 1988.

[49]M. A. Schmidt, R. T. Howe, S. D. Senturia, and J. H. Haritonidis, "Design and calibration of a microfabricated floating-element shear-stress sensor," *IEEE Trans. Electron Devices*, vol. ED-35, pp. 750-757, 1988.

[50]W. Menz, W. Bacher, M. Harmening, A. Michel, "The LIGA technique—a novel concept for microstructures and the combination with Si-technologies by injection molding," Proceedings, IEEE Micro Electro Mechanical Systems Workshop, Oiso, Japan, Jan. 25-28, 1994, pp. 69-73.

[51]M. W. Putty and K. Najafi, "A micromachined vibrating ring gyroscope," Technical Digest, Solid-State Sensor and Actuator Workshop, Hilton Head Island, S. C., June 13-16, 1994, pp. 213-220.

[52]D. Moser, O. Brand, and H. Baltes, "A CMOS compatible thermally excited silicon oxide beam resosonator with aluminum mirror," *Digest of Technical Papers*, The 1991 International Conference on Solid-State Sensors and Acuators, June 24-27, 1991, pp. 547-550.

[53]J. B. Sampsell, "The digital micromirror device and its application to projection displays," *Digest of Technical Papers*, The 7th International Conference on Solid-State Sensors and

Actuators, Yokohama, Japan, June 7-10, 1993, pp. 24-27.

[54]A. Lal and R. M. White, "Micro-fabricated acoustic and ultrasonic source/receiver," *Digest of Technical Papers*, The 7th International Conference on Solid-State Sensors and Actuators, Yokohama, Japan, June 7-10, 1993, pp. 712-715.

[55]R. Ruby and P. Merchant, "Micromachined thin film bulk acoustic resonators," *Proceedings* of the 1994 IEEE International Frequency Control Symposium, Boston, MA, June 1-3, 1994, pp. 135-138.

[56]J. D. Zook, D. W. Burns, H. Guckel, J. J. Sniegowski, R. L. Engelstad, and Z. Feng, "Resonant microbeam strain transducers," *Digest of Technical Papers*, 1991 International Conference on Solid-State Sensors and Actuators, San Francisco, CA, June 24-27, 1991, pp. 529-532.

[57]W. Riethuller and W. Benecke, "Thermally excited silicon microactuators," *IEEE Trans. on Electron Devices*, ED-35, 1988, pp. 758-763.

[58]J. W. Judy, R. S. Muller, and H. H. Zappe, "Magnetic microactuation of polysilicon flexure structures," *Technical Digest*, Solid-State Sensor and Actuator Workshop, Hilton Head Island, S. C. June 13-16, 1994, pp. 43-48.

[59]Y. Gianchandani and K. Najafi, "Micron-sized, high aspect ratio bulk silicon micromechanical devices," *Proceedings*, IEEE Micro Electro Mechanical Systems Workshop, Salt Lake City, Utah, February 1989, pp. 208-213.

[60]M. J. Vellekoop, G. W. Lubking, P. M. Sarro, and A. Venema, "A multi-purpose smart acoustic lamb wave sensor system," *Digest of Technical Papers*, The 7th International Conference on Solid-State Sensors and Actuators, Yokohama, Japan, June 7-10, 1993, pp.1052-1055.

[61]S. J. Sherman, W. K. Tsang, t. A. core, R. S. Payne, E. E. Quinn, K. H.-L. Chau, J. A. Farash, and S. K. Baum, "A low cost monolithic accelerometer; product/technology update," *Technical Digest*, IEEE International Electron Devices Meeting, San Francisco, California, December 14-16, 1992, pp. 501-504.

[62]T. A. Core, W. K. Tsang, and S. J. Sherman, "Fabrication technology for an integrated surface-micromachined sensor," *Solid State Technology*, pp. 39-47, October 1993.

[63]R. A. Alley, G. J. Cuan, R. T. Howe, and K. Komvopoulos, "The effect of release-etch processing on surface microstructure stiction," *Proceedings*, IEEE Solid-State Sensor and Actuator Workshop, Hilton Head Island, S. C., June 21-25, 1992, pp. 202-207.

[64]H. Guckel, J. J. Sniegowski, T. R. Christenson, and F. Raissi, "The application of fine-grained, tensile polysilicon to mechanically resonant transducers," *Sensors and Actuators*, **A21**, pp. 346-351, 1990.

[65]C. H. Mastrangelo and G. S. Saloka, "A dry release based on polymer columns for microstructure fabrication," *Technical Digest*, IEEE Micro Electromechanical Systems Workshop, Ft. Lauderdale, FL, 1993, pp. 77-81.

[66]G. T. Mulhern, D. S. Soane, and R. T. Howe, "Supercritical carbon dioxide drying of microstructures," *Digest of Technical Papers*, The 7th International Conference on Solid-State Sensors and Actuators, Yokohama, Japan, June 7-10, 1993, pp. 296-299.

[67]C. T.-C. Nguyen and R. T. Howe, "CMOS micromechanical resonator oscillator," *Technical Digest*, IEEE International Electron Devices Meeting, Washington, D. C., pp. 199-202, December 5-8, 1993.

[68]C. T.-C. Nguyen and R. T. Howe, "Design and performance of CMOS micromechanical resonator oscillators," *Proceedings* of the 1994 IEEE International Frequency Control Symposium, June 1-3, 1994, pp. 127-134.

[69]G. K. Fedder and R. T. Howe, "Integrated test-bed for multi-mode digital control of suspended microstructures," Technical Digest, IEEE Solid-State Sensor and Actuator Workshop, Hilton Head Island, S. C., June 13-16, 1994, pp. 145-150.

[70]Signetics, *Linear Data Manual: Volume 1: Communications*, pp. 7-61—7-76.

[71]C. T.-C. Nguyen and R. T. Howe, "Quality factor control for micromechanical resonators," *Technical Digest*, IEEE International Electron Devices Meeting, San Francisco, California, December 14-16, 1992, pp. 505-508

[72]C. T.-C. Nguyen and R. T. Howe, "Microresonator frequency control and stabilization using an integrated micro oven," *Digest of Technical Papers*, the 7th International Conference on Solid-State Sensors and Actuators (Transducers'93), Yokohama, Japan, pp. 1040-1043, June 7-10, 1993.

[73]C. H. Mastrangelo and R. S. Muller, "Fabrication and performance of a fully integrated μ-pirani pressure gauge with digital readout," *Digest of Technical Papers*, 1991 International Conference on Solid-State Sensors and Actuators (Transducers'91), San Francisco, California, June 24-27, 1991, pp. 245-248.

[74]J. T. Kung, "Integrated Capacitive Sensors Using Charge-Redistribution Sense Techniques," Ph.D. Dissertation, Dept. of Electrical Engineering and Computer Sciences, Massachusetts Institute of Technology, Cambridge, Massachusetts, June 1992.

[75]J. Bustillo, G. K. Fedder, C. T.-C. Nguyen, and R. T. Howe, "Process technology for the modular inegration of CMOS and polysilicon microstructures," *Microsystems Technologies*, **1**, October 1994.

[76]W. P. Robins, *Phase Noise in Signal Sources*. London: Peter Peregrinus, Ltd., 1982.

[77]F. E. Nathanson, *Radar Design Principles*. New York: McGraw-Hill Book Company, 1969.

[78]Y. K. Yong and J. R. Vig, "Resonator surface contamination—a casue of frequency fluctuations?" *IEEE Trans. Utrason. Ferroelec. Freq. Contr.*, vol. 36, no. 4, pp. 452-458, March 1989.

[79]M. E. Frerking, *Crystal Oscillator Design and Temperature Compensation*. New York: Van Nostrand Reinhold, 1978.

[80]R. J. Matthys, *Crystal Oscillator Circuits*. New York: Wiley, 1983.

[81]P. R. Gray and R. G. Meyer, *Analysis and Design of Analog Integrated Circuits*, 2nd Ed. New York: John Wiley & Sons, 1984.

[82]F. L. Walls and J.-J. Gagnepain, "Environmental sensitivities of quartz oscillators," *IEEE Trans. Ultrason. Ferroelec. Freq. Contr.*, vol. 39, no. 2, pp. 241-249, March 1992.

[83]S. Timoshenko, D. H. Young, and W. Weaver, Jr., *Vibration Problems in Engineering*. New York: John Wiley & Sons, 1974.

[84]T. S. Parker and L. O. Chua, "Chaos: a tutorial for engineers," *Proceedings of the IEEE*, vol. 75, no. 8, pp. 982-1008.

[85]N. Slawsby, "Frequency control requirements of radar," *Proceedings* of the 1994 IEEE International Frequency Control Symposium, June 1-3, 1994, pp. 633-640.

[86]M. Prutton, *Surface Physics, 2nd ed.* Oxford: Clarendon Press, 1983.

[87]J. S. Bendat and A. G. Piersol, Random Data, Analysis, and Measurement Procedures, 2nd ed. Orlando: Academic Press, 1985.

[88]L. Lin, K. M. McNair, R. T. Howe, and A. P. Pisano, "Vacuum-encapsulated lateral microres-

onators," *Digest of Technical Papers*, the 7th International Conference on Solid-State Sensors and Actuators (Transducers'93), Yokohama, Japan, pp. 270-273, June 7-10, 1993.

[89]V. P. Zhdanov, "Arrhenius parameters for rate processes on solid surfaces," Surface Science Reports, **12**, pp. 183-242 (1991).

[90]R. C. Anderson, "Formation, Properties, and Applications of Porous Silicon," Ph.D. Dissertation, University of California at Berkeley, Berkeley, CA, April 1991.

[91]C. H. Mastrangelo, "Thermal Applications of Microbridges," Ph.D.Dissertation, Dept. of Electrical Engineering and Computer Sciences," Univeristy of California at Berkeley, Berkeley, CA, 1991.

[92]J. J. Sniegowski, "Design and Fabrication of th e Polysilicon Resonating Beam Force Transducer," Ph.D. Dissertation, Univeristy of Wisconsin-Madison, 1991.

[93]R. Legtenberg and H. A. C. Tilmans, "Electrostatically driven vacuum-encapsulated polysilicon resonators, Parts I and II," *Sensors and Actuators*, A45, pp. 57-84, 1994.

[94]M. W. Judy and R. T. Howe, "Highly compliant lateral suspensions using sidewall beams," *Digest of Technical Papers*, the 7th International Conference on Solid-State Sensors and Actuators (Transducers'93), Yokohama, Japan, pp. 54-57, June 7-10, 1993

[95]L. Lin, C. T.-C. Nguyen, R. T. Howe, and A. P. Pisano, "Micro electromechanical filters for signal processing," *Technical Digest*, IEEE Micro Electromechanical Systems Workshop, Travemunde, Germany, pp. 226-231, Feb. 4-7, 1992.

[96]R. S. Muller and T. I. Kamins, *Device Electronics for Integrated Circuits, 2nd ed.* New York: John Wiley & Sons, 1986.

[97]C. T.-C. Nguyen and R. T. Howe, "Tunable electronic filters utilizing coupled Q-controlled micromechanical resonators," U. S. Patent Application, UC Case No. B93-003-1, December 11, 1992.

[98]A. S. Sedra and P. O. Brackett, Filter theory and design: active and passive. Beaverton, Oregon: Matrix Publishers, Inc., 1978.

[99]C. T.-C. Nguyen, "Electromechanical Characterization of Microresonators for Circuit Applications," M. S. Report, Dept. of Electrical Engineering and Computer Sciences, University of California at Berkeley, April 1991.

[100]K. Yamamoto, K. Maemura, N. Andoh, and Y. Mitsui, "A 1.9-GHz-band GaAs direct-quadtrature modulator IC with a phase shifter," IEEE J. Solid-State Circuits, vol. 28, no. 10, pp. 994-1000, October 1993.

[101]M. A. Huff, S. D. Senturia, and R. T. Howe, "A thermally isolated microstructure suitable for gas sensing applications," *Technical Digest,* IEEE Solid-State Sensor and Actuator Workshop, Hilton Head Island, S. C., June 6-9, 1988, pp. 47-50.

[102]J. P. Holman, *Heat Transfer, 6th ed.* New York: McGraw-Hill, 1986.

APPENDIX A *EAM: A Step-By-Step Procedure*

The following comprises a step-by-step description of the practical procedures required for characterizing a resonator utilizing the EAM system described in Chapter 2. This section contains information specific to the EAM circuitry built for this dissertation, and thus, is most directly useful to future students/operators at the University of California at Berkeley. The methodology, however, as detailed in this appendix, can be generalized to a variety of EAM-based characterization systems, and should prove useful when designing future EAM systems.

The focus of this section is on procedure. As such, there will be no discussion pertaining to the detailed operation and construction of each EAM functional unit.

A.1 Check the Resonator

1. Check to make sure the device under test (DUT) is free to move. Preferably, use a probe-tip to displace the resonator by a reasonably large amount. (A 10 μm displacement is recommended for a 20 kHz comb-driven resonator. Obviously, the appropriate distance depends on resonator design.) For most resonator designs, every part of the resonator should move. When the probe-tip is removed, the resonator should spring back to its initial position.
2. Electrostatically drive the resonator into visible oscillation, using a simple set-up, if possible. One simple set-up for doing this is shown schematically in Fig. 2.14 of Chapter 2. By operating the resonator, one obtains knowledge of the resonance frequency, and more importantly, minimizes future set-up errors resulting from resonator drive problems.

A.2 The Drive End of EAM

3. Hook up the system as shown in Fig. A.1. The system comprises:

a. An HP4195A Network/Spectrum Analyzer, which provides the drive source and the end-detector of the EAM system. The HP4195A should be set-up as follows:

CONFIG: NETWORK (choose network analyzer, not spectrum analyzer)
PORT: T2/R1 (source from S1, reference at R1, sense at T2)
SOURCE AMPLTD: less than 0.09 V if using pre-amp, any setting if no pre-amp
TRIGGER MODE: MANUAL mode
FREQUENCY CENTER: resonance frequency of resonator
FREQUENCY SPAN: depends upon Q of resonator
REF (amplitude): -50 dB (for this system)
dB/DIV: 3 dB

b. An optional pre-amplifier with a voltage-to-voltage gain of 100. This is required since the HP4195A cannot provide a drive voltage larger than 1.26 V. Most resonators operated in air (or under any other low Q conditions) will required larger voltages to resonate. In vacuum, however, required drive voltages are quite small, and the pre-amplifier is unnecessary.

c. HP3314A function generator, which provides the carrier signal and the demodulation signal signal. The HP3314A should be set-up as follows:

MODE: ϕ-lock (F_{in} x N) (N=1)
TRIGGER: internal
TIME: .007 ms (which corresponds to 142.8 kHz)
AMPTD: 4 V (any voltage amplitude can be used...4 V is a common choice)
PHASE: 30^{o} (this will vary with different systems)
OUTPUT: sinusoid

Note that the output of the HP3314A serves as the EAM carrier, which is applied to the resonator, along with the dc-bias. The TRIGGER output of the HP3314A will be phase-shifted by 30^{o} from the EAM carier, and (as will be seen) will serve as the demodulating input to the EAM system.

d. A battery (- and + terminals of a power supply). The voltage range varies from 5 V to over 100 V, as required for the specific DUT. For example, in air, a lateral comb-driven resonator with a 20 kHz center frequency will require over 40 V of dc-bias and a 10 V amplitude drive sinusoid for visible resonance. The same resonator driven under 20 mTorr pressure will require as little as 5 V dc-bias and as little as 10 mV drive sinusoid amplitude. (This, of course, comes about to due differences in Q: Q=27 in air, Q=50000 in vacuum are typical.)

e. The DUT on a probe station or comparable apparatus which allows electrical connection to the DUT (i.e. a packaged resonator will suffice).

4. Drive the resonator into visible resonance using the system of Fig. A.1.

A.3 The Sense End of EAM

5. The complete EAM system, including additions for the sense end, are as shown in Fig. A.2, where the front end connections have been dulled to identify what has already been done. The electronics associated with the sense end include:

a. Transresistance Amplifier: Gain ~ 1 MΩ Bandwidth > 150 kHz.

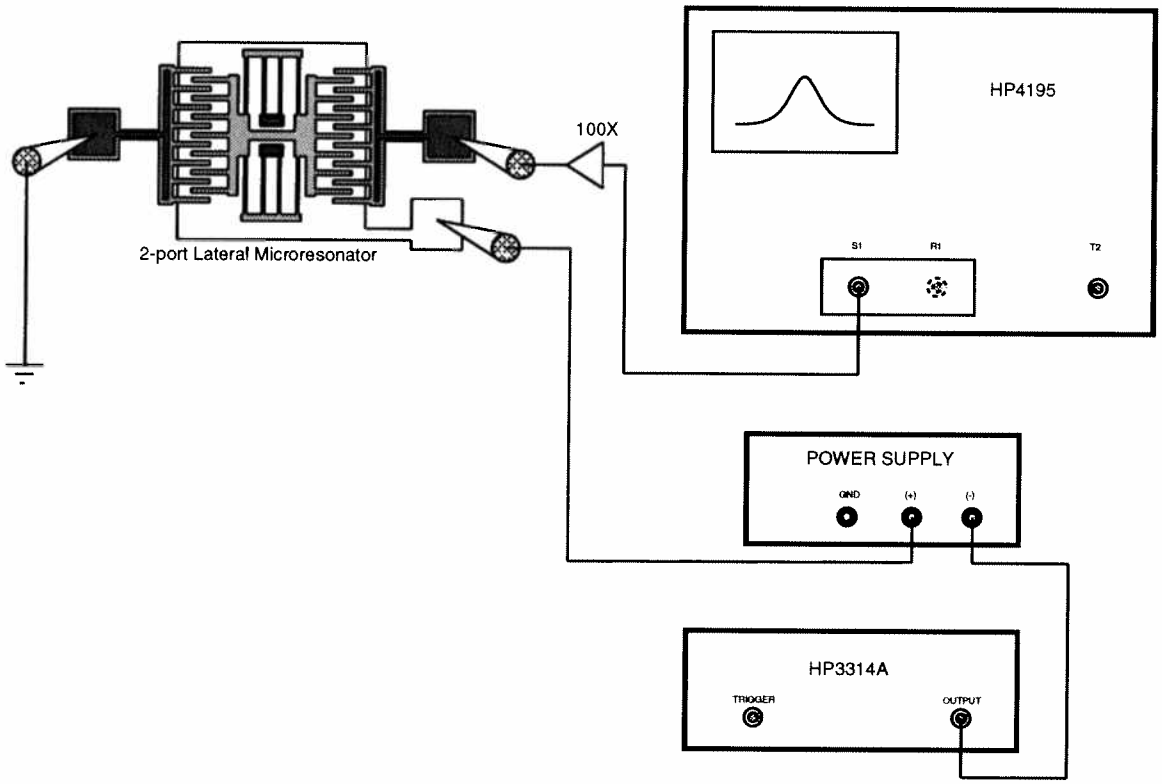

Fig. A.1: The drive end set-up for EAM. In the above, all electronics have the same

b. EAM Box: The detailed contents of this box are given in the Appendix B. The inputs and outputs are labelled and should be hooked up exactly as shown in Fig. A.2.

c. HP4195A: The same one as used for the drive above. It's still set-up as described in the drive section, except for the following (which you should change):

TRIGGER MODE: SINGLE mode (the WAIT TRIG bulb should now light up)

d. HP3314A: Here, the trigger output is used as the demodulating signal for the EAM box.

6. Start a sweep by pushing the TRIG/RESET button on the HP4195A. A resonator spectrum should be traced out slowly.
7. What? No resonator spectrum? It's NOT a problem with the EAM box, guaranteed!!! (It has NEVER been.) It's more likely a problem with one of the connections. Read on....

A.4 Trouble-Shooting Ideas

1. Make sure everything is grounded to the same ground....drive electronics...sense electronics...probe-station....everything should be grounded to a common point. Make sure you use the special connector built for the probe-station to insure common grounds.

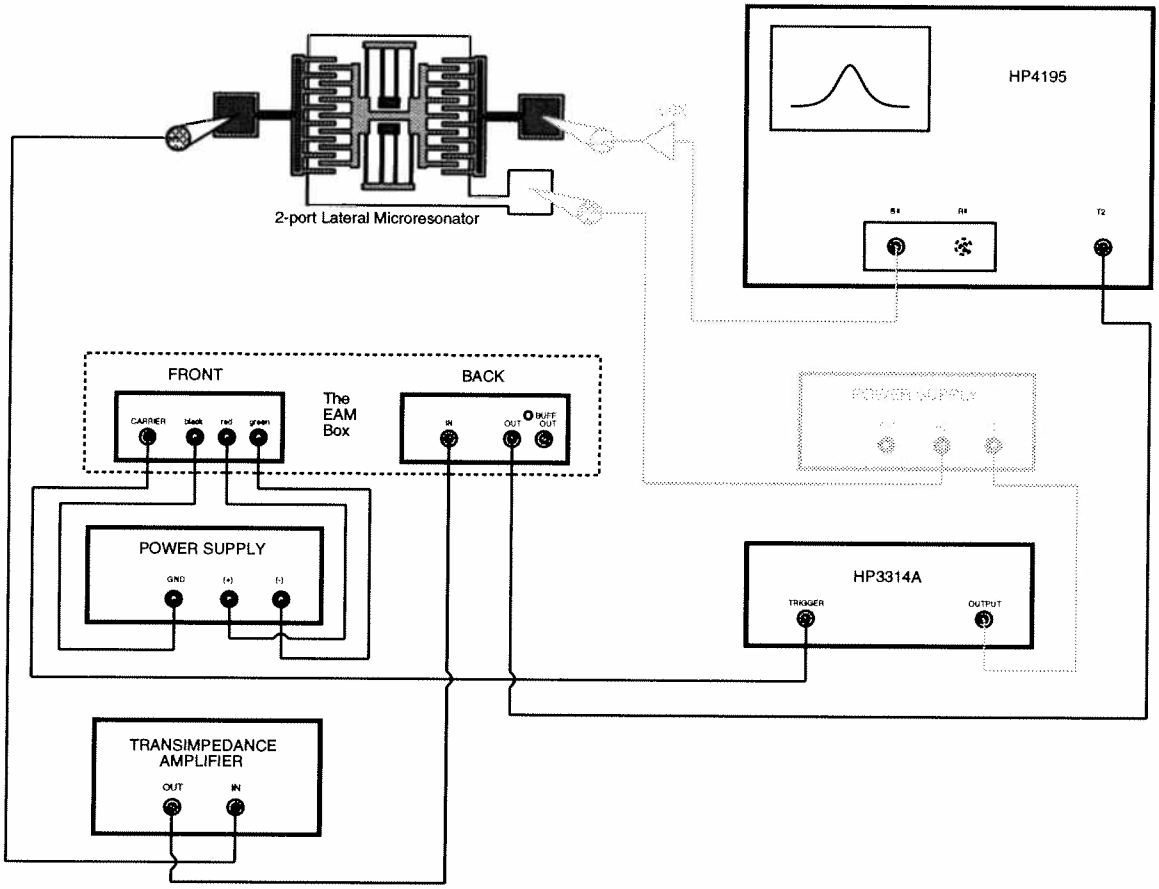

Fig. A.2: The complete EAM system. Here, front end components have been dulled to distinguish back end components.

2. Reverify that you can resonate the DUT using the current set-up. Start a sweep under SINGLE TRIGGER MODE (which you should be in now) and watch the resonator move under the microscope when the frequency goes across the resonance frequency. If the resonator resonates, you've greatly narrowed down the error possibilities. If it doesn't, you know you have a drive problem. In this case:

a. Look at the drive voltage (after the pre-amplifier, if used) to make sure it's a sinusoid at the desired level.

b. Look at the carrier+dc-bias voltage on an oscilloscope. Measure it using a probe on the ground plane of the reaonator to make sure it is reaching the resonator.

3. Check all coaxial connections to all boxes.

4. Check all connections to the probe-tips (if using a probe-station). Don't just look at them (you lazy slob!!!). Get a multi-meter and measure the resistances between points. Recheck coax connectors using a multimeter as well.

The above measures have solved 99% of all problems with EAM. If they still don't work, try the following:

5. Verify functionality of the transresistance amplifier. Measure its spectrum using the HP4195A. The settings on the HP4195A for this test should be as follows:

   CONFIG: NETWORK (choose network analyzer, not spectrum analyzer)
   PORT: T2/R1 (source from S1, reference at R1, sense at T2)
   SOURCE AMPLTD: 0 dBm
   TRIGGER MODE: SINGLE mode
   FREQUENCY START: 100 Hz
   FREQUENCY STOP: 10 MHz
   DISPLAY TYPE: log plot (in frequency)
   REF (amplitude): 10 dB
   dB/DIV: 10 dB

   The spectrum should show a low frequency level of around 0 dB and should have a -3 dB roll-off frequency close to or higher than 150 kHz. Verify stability of the amplifier by looking at its output on an oscilloscope while driving it with the HP4195A sinusoidal source (or any source, such as the HP3314A).

6. Could it be that the EAM box is defunct? What a ridiculous question! Go back through the above trouble-shooting steps. And this time, don't skimp on any step.

7. The EAM box may be defunct, eh? Contact Clark Nguyen or, if he's left, your local EAM expert.

APPENDIX B *MICS Process Outline*

The following comprises a step-by-step outline of the MICS process, as run for the devices of this dissertation.

```
      Modular Integration of CMOS and uStructures (MICS) Process
                        Version 1.0 (9/27/1991)
       3 um, P-well, double poly-Si, single metal, poly capacitors
      1 or 2 um substrate gap, 2um thickness, In Situ Doped poly-Si


-------------------------------------------------------------------------
0.0 Starting Wafers:  8-12 ohm-cm, n-type, <100>
    Control Wafers: PWELL (n-type), PCH (n-type)
    Sribe lot and wafer number on each wafer, including controls.
    Measure bulk resistivity (ohm-cm) of PWELL on Sonogage.
-------------------------------------------------------------------------
1.0 Initial Oxidation:  target = 1000 A
-------------------------------------------------------------------------
    1.1  TCA clean furnace tube.
-------------------------------------------------------------------------
    1.2  Standard clean wafers, include both controls:
         piranha clean for 10 min, 10/1 HF dip, spin-dry.
-------------------------------------------------------------------------
    1.3  Wet oxidation at 1000 C:
```

```
              5 min dry O2
             11 min wet O2
              5 min dry O2
             20 min dry N2
             Measure tox=
-------------------------------------------------------------------------
2.0 N- (Punch-Through) Implant:
    Blanket implant of phosphorous at 145 keV, 1.2E12/cm2
    Include both controls.
-------------------------------------------------------------------------
3.0 Well Photo Mask: PWELL-CWP (chrome-df)
    Control wafers are not included in the photoresist steps.
    (PWELL proceeds to Step 4.0,  PCH to Step 5.2)
-------------------------------------------------------------------------
    3.1  Standard clean wafers.
         Dehydrate in furnace for 5 min. at 750 C.
-------------------------------------------------------------------------
    3.2  Spin, expose, develop, inspect, descum, hard bake.
         Standard I-line process.
-------------------------------------------------------------------------
4.0 Well Implant: boron (B11), 3E12/cm2, 80 keV
    (Resist is left on wafers.) Include PWELL control (no resist).
-------------------------------------------------------------------------
5.0 Well Drive-In:  target  xj = 4 um, tox = 3000 A
-------------------------------------------------------------------------
    5.1  TCA clean furnace tube.
-------------------------------------------------------------------------
    5.2  Etch pattern into oxide in 5/1 BHF.
         Strip oxide off of both controls and measure Rs.
         RsPWELL=                  RsPCH=
-------------------------------------------------------------------------
    5.3  Remove resist and piranha clean wafers and controls.
-------------------------------------------------------------------------
    5.4  Standard clean wafers and controls.
-------------------------------------------------------------------------
    5.5  Dry oxidation and well drive at 1150 C:
               4 hrs dry O2
               5 hrs dry N2
         a) Measure oxide thickness on work wafer: in well and outside.
         b) Strip oxide and measure Rs on both controls.
            RsPWELL=                RsPCH=
            (PWELL proceeds to Step 6.3, PCH to Step 15.2)
-------------------------------------------------------------------------
6.0 Locos Pad Oxidation/Nitride Deposition:
    target = 200 A SiO2 + 1000 A Si3N4
-------------------------------------------------------------------------
    6.1  TCA clean furnace tube.
-------------------------------------------------------------------------
    6.2  Remove all oxide in 5/1 BHF until wafers dewet.
-------------------------------------------------------------------------
    6.3  Standard clean wafers, include PWELL control.
-------------------------------------------------------------------------
    6.4  Dry oxidation at 950 C:
               28 min dry O2
               20 min dry N2 anneal.
         a) Measure tox=             on PWELL control.
```

```
          b) Strip oxide off of PWELL control.
-------------------------------------------------------------------------
    6.5  Deposit 1000 A of Si-nitride immediately:
         Dep.time = 22 min., temp.= 800 C.
         a) Include PWELL control.
         b) Measure nitride thickness on PWELL cont.
         c) PWELL control proceeds to Step 12.1
-------------------------------------------------------------------------
7.0 Active Area Photo Mask: ACTIVE-CAA (emulsion-cf)
    Spin, expose, develop, inspect, descum, hard bake.
-------------------------------------------------------------------------
8.0 Nitride Etch: in Technics-c plasma etcher, SF6/He at 50 Watts
    Do not etch oxide, do not remove resist. Hard bake again.
-------------------------------------------------------------------------
9.0 Field (P-) Implant
-------------------------------------------------------------------------
    9.1 Photo Mask: PWELL-CWP (chrome-df)
        Spin, expose, develop, descum, hard bake.(Second photo)
        Inspect! Field inside well is open, active areas are covered
             with Si3N4 and photoresist.
-------------------------------------------------------------------------
    9.2 Measure resist thickness on active area with profilometer.
        Wafers cannot be passed unless pr is 0.8 um thick .
-------------------------------------------------------------------------
    9.3 Field (P-) Ion Implantation: boron (B11), 100 keV, 1E13/cm2
-------------------------------------------------------------------------
    9.4 Remove resist and piranha clean wafers.
-------------------------------------------------------------------------
10.0 Field (N-) Implant
-------------------------------------------------------------------------
    10.1  Standard clean and bake wfrs for 5 min at 750 C in N2.
-------------------------------------------------------------------------
    10.2  Photo mask: CWPi (NFIELD) mask (emulsion-cf, inverse of PWELL)
          Spin, expose, develop, descum, hard bake.
          Inspect! Well area is covered with pr,active areas with Si3N4.
-------------------------------------------------------------------------
    10.3  Phosphorous implant, 40 keV, 5E12/cm2.
-------------------------------------------------------------------------
    10.4  Remove resist and piranha clean wafers.
-------------------------------------------------------------------------
11.0 Locos Oxidation: target = 6500 A
-------------------------------------------------------------------------
    11.1  TCA clean furnace tube.
-------------------------------------------------------------------------
    11.2  Standard clean wafers; dip until field area dewets.
-------------------------------------------------------------------------
    11.3  Wet oxidation at 950 C:
               5 min dry O2
               4 hrs 40 min wet O2
               5 min dry O2
              20 min N2 anneal
          Measure tox=          on a device wafer in the field area.
-------------------------------------------------------------------------
12.0 Nitride Removal
-------------------------------------------------------------------------
    12.1  Dip in 10/1 HF for 1 min., include PWELL control.
```

(To remove thin oxide on top of the nitride)

12.2 Etch nitride off in hot phosphoric acid: 145 C, 30 min.

13.0 Sacrificial Oxide: target = 200 A

13.1 TCA clean furnace tube.

13.2 Standard clean wafers, include PWELL control.

13.3 Dry oxidation at 950 C:
28 min dry O2
20 min N2 anneal
Measure tox= on PWELL control.

14.0 Threshold Implant:
Blanket implant boron (B11) at 30 keV, 1.2E12-1.5E12/cm2.
Include PWELL control.

15.0 Gate Oxidation/Poly-Si Deposition:
target = 500 A SiO2 + 4500 A poly-Si

15.1 TCA clean furnace tube; reserve poly-Si deposition tube.

15.2 Standard clean wafers, include both controls, plus two CONTCTRLs.

15.3 Dip off sacrificial oxide (dewet) in 10/1 HF (approx. 1 min).

15.4 Dry oxidation at 950 C:
2 hr. 10 min. dry O2
20 min N2 anneal.
tox(PWELL)= tox(PCH)=
(Controls proceed to Step 17.2)

15.5 Immediately after oxidation deposit 4500 A of phos.doped poly-Si.
time = 2 hr. 15 min., temp.= 650 C
Do not include PWELL, PCH controls.
Include a new control with 1000 A thermal SiO2 on it. tpoly=
(POLY control proceeds to Step 17.2)

16.0 Gate Definition Mask: POLY-CPG (emulsion-cf)

16.1 Spin, expose, develop, inspect, descum, hard bake.

16.2 Plasma etch poly-Si in Lam1 etcher, inspect.
(CCl4/He/O2 at 300 Watts, 280 mtorr)

16.3 Remove resist, piranha clean wafers.

17.0 Reoxidation: target=800 A on poly-Si, 500 A on S/D

17.1 TCA clean furnace tube.

17.2 Standard clean wafers, include all 5 controls, PWELL,PCH,POLY,

```
          2 CONTCTRLs.
          From here on: only 10 sec dip in 25/1=H2O/HF after piranha.
-------------------------------------------------------------------------
    17.3  Dry oxidation at 950 C:
               30 min dry O2
               10 min N2 anneal.
          tox(PWELL) =                tox(PCH) =
          (PWELL proceeds to Step 19.1, PCH to Step 20.2,
      POLY proceeds to Step 23.2)
-------------------------------------------------------------------------
18.0 N-Channel Source/Drain Photo Mask: NII-CSP (emulsion-cf)
     Spin, expose, develop, descum, do not hard bake.
     Inspect! P+ active areas are covered. Cap. oxide is not covered.
-------------------------------------------------------------------------
19.0 N+ Source/Drain Implant
-------------------------------------------------------------------------
    19.1  Implant arsenic at 160 keV, 5E15/cm2, incl. PWELL cont.
-------------------------------------------------------------------------
    19.2  Remove resist and piranha clean wafers (no dip here).
-------------------------------------------------------------------------
20.0 N+ S/D Anneal
-------------------------------------------------------------------------
    20.1  TCA clean furnace tube.
-------------------------------------------------------------------------
    20.2  Standard clean wafers (10 sec dip), include both controls.
-------------------------------------------------------------------------
    20.3  Anneal wafers and controls in N2 at 925 C for 1hr 15min.
          (PWELL proceeds to Step 23.2, PCH to 22.1)
-------------------------------------------------------------------------
21.0 P-Channel Source/Drain Photo Mask: PII-CSP (chrome-df)
     Spin, expose, develop, descum, hard bake.
     Inspect! All areas are coverd except P-ch devices.
-------------------------------------------------------------------------
22.0 P+ S/D Implant
-------------------------------------------------------------------------
    22.1  Implant B11 at 50 keV, 2E15/cm2, include PCH control.
-------------------------------------------------------------------------
    22.2  Remove resist and standard clean wafers (no dip).
-------------------------------------------------------------------------
23.0 Capacitor Formation: SiO2 target = 800 A
-------------------------------------------------------------------------
    23.1  TCA clean furnace tube; reserve poly-Si deposition tube.
-------------------------------------------------------------------------
    23.2  Standard clean wafers (10 sec dip).
      Include PWELL, PCH, POLY controls.
-------------------------------------------------------------------------
    23.3  Capacitor oxidation at 950 C:
          30 min dry O2, 10 min N2 anneal
          Include CONTCTRLs.
          tox(PWELL)=                 tox(PCH)=
          (These controls proceed to Step 26.3)
      Etch step into oxide on POLY control, tox(POLY)=
      (Save POLY control in "completed controls" box.)
-------------------------------------------------------------------------
    23.4 Second Poly-Si deposition: target = 3000 A
         Immediately after oxidation deposit 4500 A of phos.doped
```

```
        poly-Si: approx.time = 1 hr.30 min, temp.= 650 C
        Include only a new control with 1000 A SiO2. tpoly2=
    (Do not save this control.)
-------------------------------------------------------------------------
24.0 Capacitor Photo Mask: CAP-CEL (emulsion-cf)
-------------------------------------------------------------------------
    24.1 Spin, expose, develop, inspect, descum, hardbake.
-------------------------------------------------------------------------
    24.2 Plasma etch poly-Si in Lam1 etcher. Inspect.
         Do not remove resist.
-------------------------------------------------------------------------
25.0 Reflow Glass: target = 7000 A
-------------------------------------------------------------------------
    25.1  Standard clean wafers (10 sec dip).
          Include one new, PSG control, and both CONTCTRLs.
-------------------------------------------------------------------------
    25.2  Deposit PSG : use 3LAYRLTO program.
          Include PSG control.
          Layers: 1000 A undoped LTO (~5 min.)
                  5000 A PSG (PH3 flow at 10.3) (~25 min.)
                  200 A undoped LTO (~1 min.)
          time = (approx) 31 min. total (check current dep rates)
          temp. = 450 C
          tPSG=              on PSG cont.
      (Use this control for contact etch test.)
-------------------------------------------------------------------------
     25.3  Densify glass in tube 2 at 950 C:
           Include PWELL, PCH controls.
           5 min dry O2, 30 min wet O2, 5 min dry O2
-------------------------------------------------------------------------
     25.4  Do wet oxidation dummy run afterwards to clean tube:
           1 hr wet oxidation at 950 C.
-------------------------------------------------------------------------
     25.5  Strip oxide off from controls and measure Rs.
           RsPWELL(nmos S/D)=          RsPCH(pmos S/D)=
           Save conrols in "completed controls" box.
-------------------------------------------------------------------------
26.0  Contact Photo Mask: CONTACT-CCA (chrome-df)
     Spin, expose, develop, inspect, descum, hard bake.
-------------------------------------------------------------------------
27.0 Contact Etch
-------------------------------------------------------------------------
    27.1  Plasma etch in Lam2 in CHF3/O2.
          Etch at 850/750 Watts, pressure ~300 mtorr.
-------------------------------------------------------------------------
    27.2  Remove photoresist in O2 plasma, piranha clean (no dip).
-------------------------------------------------------------------------
    27.4  Do a 20 sec. 25/1 HF dip just before metallization.
-------------------------------------------------------------------------
28.0 TiSi2 Formation
-------------------------------------------------------------------------
    28.1  Titanium Metallization:  target =
          CPA:  pressure = 20 mTorr, power = 2 kW, track speed = 20 cm/s
-------------------------------------------------------------------------
    28.2  RTA for TiSi2 Formation
          Heatpulse1:  time = 30 sec, pressure = 50 mTorr N2,
```

```
                        temp.= 600 C
-------------------------------------------------------------------------
     28.3  Strip Titanium
           Soak wafers in 3:1 NH3OH:H2O2 for a few minutes.
-------------------------------------------------------------------------
     28.4  RTA for contact resistance reduction
           Heatpulse1:  time = 10 sec, pressure = 50 mTorr N2,
                        temp.= 1000 C
-------------------------------------------------------------------------
29.0 Tungsten Metallization:  target = 6000 A
      CPA:  pressure = 20 mTorr, power = 2 kW, track speed = 7 cm/s
-------------------------------------------------------------------------
30.0 Metal Photo Mask:  CMF (emulsion-cf)
-------------------------------------------------------------------------
     30.1  Dehydrate:  VWR Oven for 30 min. @ 120 C
-------------------------------------------------------------------------
     30.2  Spin resist on Eaton: Kodak 820, 4600 RPM,
           25 seconds, soft bake at 120 C, 45 seconds. (prog. 10)
-------------------------------------------------------------------------
     30.3  Expose:  GCA 6200-10X wafer stepper
-------------------------------------------------------------------------
     30.4  Develop in MTI-Omnichuck:
           Kodak 932/H O=1:1, 60 seconds.
-------------------------------------------------------------------------
     30.5  Descum in Technics-C: O  plasma, 50 Watts, 1 minute.
-------------------------------------------------------------------------
     30.6  Hard bake in VWR oven: 120 C, 20 minutes. in oven.
-------------------------------------------------------------------------
     30.7  Etch W in lam3 (or teagal, once it comes up)
-------------------------------------------------------------------------
     30.8  Inspect:  should see oxide color (pink & green on edges)
           or use IV probe station:  make sure field is nonconductive.
-------------------------------------------------------------------------
     30.9  Sintering:  400 C for 20 min. in forming gas.
           No ramping, use SINT400 program.
-------------------------------------------------------------------------
31.10 Probe Testing:
       CMOS test devices...get Vt.
-------------------------------------------------------------------------
32.0 CMOS Passivation
-------------------------------------------------------------------------
     32.1  Std. Tungsten clean:  Acetone rinse for 30 min. + DI rinse
           in sink7.  Blow dry with N2 gun.
           Also, clean NITCTRL1 and NITCTRL2 in sink6.
-------------------------------------------------------------------------
     32.2  PSG Deposition:  target = 3500 A
           tylan12, VDOLTOC
           Flows (sccm):  SiH4 = 60, PH3 = 0 (entered), O2 = 90
           time = 17 minutes (~1000 A per 5 min.)
           Include NITCTRL1 and NITCTRL2 and a tox ctrl.
           tox =
-------------------------------------------------------------------------
     32.3  Nitride Deposition:  target = 1000 A
           tylan9, SNITC
           time = 22 min., temp.= 800 C
           ACK after 1 pass, to minimize total high temp. time.
```

```
            Include NITCTRL1 (not NITCTRL2) and thickness ctrls. (Si).
            tnit =
-------------------------------------------------------------------------
33.0 Inter CMOS-ustructure Contact Mask:  CNT (SNT) (chrome-df)
-------------------------------------------------------------------------
     33.1  Spin, expose, develop, inspect, descum, hard bake.
-------------------------------------------------------------------------
     33.2  Plasma etch nitride in technics-c.
-------------------------------------------------------------------------
     33.3  Plasma etch oxide in lam2.
-------------------------------------------------------------------------
34.0 uStructure Poly1 Deposition:  target = 3000 A
-------------------------------------------------------------------------
     34.1  Standard clean wafers (20 sec 10:1 HF dip)
-------------------------------------------------------------------------
     34.2  Phosphorous-doped polysilicon deposition:  tylan11, SDOPOLYG
           time = 1 hour 30 minutes, temp.= 650 C (~2000 A per hour)
           Include etching controls:  PLY1CTRL1, PLY1CTRL2
-------------------------------------------------------------------------
35.0 uStructure Poly1 Definition Mask:  CP1 (SP1) (emulsion-cf)
-------------------------------------------------------------------------
     35.1  Spin, expose, develop, inspect, descum, hard bake.
-------------------------------------------------------------------------
     35.2  Plasma etch poly-Si in Lam1 etcher, inspect.
           (CCl4/He/O2 at 300 Watts, 280 mTorr)
-------------------------------------------------------------------------
     35.3  Remove PR, piranha clean wafers along with PSG1CTRL1 and
           PSG1CTRL2.
-------------------------------------------------------------------------
36.0  Sacrificial PSG Deposition:  target = 2 um  (target = 1 um)
      tylan12, VDOLTOC
      Flows (sccm):  SiH4 = 60, PH3 = 10.3 (entered), O2 = 90
      time(2um) = 1 hour 40 minutes  (~1000 A per 5 min.)
      time(1um) = 50 minutes  (~1000 A per 5 min.)
      Include etching controls:  PSG1CTRL1 and PSG2CTRL2
-------------------------------------------------------------------------
37.0  Sacrificial PSG Densification
      RTA in Heatpulse1:  30 secs @ 950 C
      (also do PSG1CTRLs)
-------------------------------------------------------------------------
38.0  Dimple Photo Mask:  CD1 (SD1) (chrome-df)
-------------------------------------------------------------------------
     38.1  Spin, expose, develop, descum, hard bake.
-------------------------------------------------------------------------
     38.2  Timed wet etch in 5:1 BHF.  (E.R. ~ 3000 A per min.)
-------------------------------------------------------------------------
     38.3  Remove resist, piranha clean wafers.
-------------------------------------------------------------------------
39.0  uStructure Anchor Photo Mask:  CG1 (SG1) (chrome-df)
-------------------------------------------------------------------------
     39.1  Spin (double thickness for 2 um oxide, single for 1 um),
           expose, develop, descum, hard bake.
-------------------------------------------------------------------------
     39.2  Etch in lam2:
           For 1 um oxide:  etch as usual.
           For 2 um oxide:  [press = 2.8 Torr, power = 350 W,
```

```
            gap = 0.38 cm, CHF3 = 30 sccm, CF4 = 90 sccm,
            He = 120 sccm, time = 1 min.],[power = 0, same gases,
            time = 1 min.] 3X
            For both cases, overetch with 700 W recipe.
-------------------------------------------------------------------------
      39.3  Wet dip in 5:1 BHF for 10 secs.
-------------------------------------------------------------------------
      39.4  Remove resist, piranha clean wafers.
-------------------------------------------------------------------------
40.0  uStructure Poly2 Depostion:  target = 2 um
       Phosphorous-doped polysilicon deposition:  tylan11, SDOPOLYG
       time = 11 hours, temp.=650 C
       Include etching controls PLY2CTRL1 and PLY2CTRL2 (tylan11 cntrls).
-------------------------------------------------------------------------
41.0  Oxide Mask Deposition
       tylan12, VDOLTOC
       Flows (sccm):  SiH4 = 60, PH3 = 10.3 (entered), O2 = 90
       time = 25 minutes  (~1000 A per 5 min.)
       Include etching controls:  PSG2CTRL1 and PSG2CTRL2
-------------------------------------------------------------------------
42.0  RTA Anneal
       Heatpulse1:  1 min. @ 1100 C in 50 l/sec N2
-------------------------------------------------------------------------
43.0  uStructure Poly2 Definition Mask:  CP2 (SP2) (emulsion-cf)
       Align to ustructure poly1.
-------------------------------------------------------------------------
      43.1  Spin, expose, develop, inspect, descum, hard bake.
-------------------------------------------------------------------------
      43.2  Etch in oxide mask in lam2.
-------------------------------------------------------------------------
      43.3  (optional) Remove resist:
             technics-c, 10 min. O2 plasma @ 300 W
-------------------------------------------------------------------------
      43.4  Etch 2nd poly in lam1:  [press = 280 mTorr, power = 300 W,
            gap = 1.5 cm, CCl4 = 130 sccm, O2 = 15 sccm, He = 130 sccm,
            time = 1 min.] then [power = 0, same gases, time = 1 min.]
            5 or 6X, depending upon etch rate (E.R. usually ~ 4000 A
            per min.)
-------------------------------------------------------------------------
      43.5  If haven't already removed resist, remove resist.
            technics-c, 10 min. O2 plasma @ 300 W
-------------------------------------------------------------------------
44.0 Back Side Etch
-------------------------------------------------------------------------
     44.1 Spin photoresist (front side), do not expose; hard bake.
-------------------------------------------------------------------------
     44.2 Spin photoresist again, and hard bake.
-------------------------------------------------------------------------
     44.3 Etch back side of wafers as follows:
           a) Dip off oxide in BHF (ox. mask thickness).
           b) Wet etch poly-Si (structural poly2 thickness).
           c) Etch oxide off in BHF (sacrificial ox. thickness).
           d) Wet etch poly-Si (ground poly1 thickness).
           e) Etch Si3N4 in Technics-c.
           f) Etch oxide off in BHF (ox. over W + ox. over cap.).
           g) Wet etch poly-Si (cap. poly thickness).
```

```
          h) Etch oxide off in BHF (cap. ox. thickness).
          i) Wet etch poly-Si (gate poly thickness).
          j) Final dip in BHF until back dewets.
-------------------------------------------------------------------------
     44.4 Remove resist and piranha clean wafers (no dip).
          Measure oxide thickness in S/D area.
-------------------------------------------------------------------------
45.0  uStructure Release
-------------------------------------------------------------------------
      45.1  Piranha clean in sink8.
-------------------------------------------------------------------------
      45.2  Wet etch in 5:1 BHF (~6000 A per min.) in sink8.
            a) 10 min. BHF, std. DI rinses
            b) piranha clean in sink8 for 10 min., std. DI rinses
            c) 20 min. BHF, std. DI rinses
            d) spind dry, N2 gun dry, or IR lamp.
-------------------------------------------------------------------------


Clark Nguyen
9/27/91
last revision:  9/27/91
```

APPENDIX C *Micro Oven Process Outline*

The following comprises a step-by-step outline of the micro oven process, as run for the devices of this dissertation.

Micro-Oven uResonator Process
Version 1.0 (5/04/92)
1 or 2 um substrate gap, 2um thickness, In Situ Doped poly-Si

---

0.0 Starting Wafers: 8-12 ohm-cm, n-type, <100> prime or just n-type test wafers.

Control Wafers: PSG1F, PSG1B (Si)
NIT1F, NIT1B (Si)
POLY1F, POLY1B (tylan11 ctrl.)
PSG2F, PSG2B (Si)
POLY2F, POLY2B (Si)
PSG3F, PSG3B (Si)

```
1.0  n+ Diffusion
-------------------------------------------------------------------------
     1.1  Standard clean wafers
-------------------------------------------------------------------------
     1.2  n+ Diffusion
           tylan8, POCL3
           time = 2 hrs., temp.= 1000 C
-------------------------------------------------------------------------
                              (OR)
-------------------------------------------------------------------------
1.0  Substrate Ground Plane Poly Deposition:  target = 3000 A
-------------------------------------------------------------------------
     1.1  Standard clean wafers.
-------------------------------------------------------------------------
     1.2  Phosphorous-doped polysilicon deposition:
           tylan11, SDOPOLYG
           time = 1 hour 40 minutes, temp.= 650 C
           (Dep. Rate ~ 1800 A per hour)
-------------------------------------------------------------------------
2.0  Sacrificial PSG1 Deposition:  target = 3 um  (target = 2 um)
      (immediately after n+ diffusion)
      tylan12, VDOLTOC
      Flows (sccm):  SiH4 = 60, PH3 = 10.3 (entered), O2 = 90
      time(3um) = 2 hrs. 30 minutes  (~1000 A per 5 min.)
      time(2um) = 1 hour 40 minutes  (~1000 A per 5 min.)
      tox =
      Include etching controls:  PSG1F and PSG1B
-------------------------------------------------------------------------
3.0  uPlatform Anchor Photo Mask:  SNC (chrome-df)
-------------------------------------------------------------------------
     3.1  Spin (double thickness for 2 um oxide),
           expose, develop, descum, hard bake.
-------------------------------------------------------------------------
     3.2  Etch in lam2:
           For 2 um oxide:  [press = 2.8 Torr, power = 350 W,
           gap = 0.38 cm, CHF3 = 30 sccm, CF4 = 90 sccm,
           He = 120 sccm, time = 1 min.],[power = 0, same gases,
           time = 1 min.] 3X
           Overetch with 700 W recipe.
-------------------------------------------------------------------------
     3.3  Inspect under IV probe station:  check contact
-------------------------------------------------------------------------
     3.4  Wet dip in 5:1 BHF for 10 secs.
-------------------------------------------------------------------------
     3.5  Remove resist, piranha clean wafers.
-------------------------------------------------------------------------
4.0  Nitride Support Deposition:  target = 3 um
      Deposit silicon-rich low-stress nitride:
      tylan9, SNITC.V
      temp. = 835 C, Flows (sccm):  SiH2Cl2 = 64, NH3 = 16
      time = 14 hrs., (~2200 A per hour)
      tnit =
      Include etching controls:  NIT1F and NIT1B
-------------------------------------------------------------------------
4.0  uStructure Poly1 Deposition:  target = 3000 A
      (immediately after nitride support deposition)
```

Phosphorous-doped polysilicon deposition: tylan11, SDOPOLYG
time = 1 hour 40 minutes, temp.= 650 C (~1800 A per hour)
Include etching controls: POLY1F, POLY1B

5.0 uStructure Poly1 Definition Mask: CP1 (emulsion-cf)

5.1 Spin, expose, develop, inspect, descum, hard bake.

5.2 Plasma etch poly-Si in Lam1 etcher, inspect.
(CCl4/He/O2 at 300 Watts, 280 mTorr)

5.3 Remove PR, piranha clean wafers along with PSG2F and PSG2B.

6.0 Al Etch Mask Deposition: target = ~5000 A
Aluminum Metallization: target = ~5100 A
CPA: pressure = 6 mTorr, power = 4.5 kW, track speed = 16 cm/s

---

7.0 Microplatform Definition Mask: SNT (emulsion-cf)

7.1 Spin, expose, develop, inspect, descum, hard bake.

7.2 Plasma etch Al in lam3.

7.3 Inspect: use IV probe station: make sure field is nonconductive

---

7.4 Plasma etch nitride in Teagal etcher, inspect.

7.5 Remove PR, pirahna clean wafers

7.6 Strip Al in sink8 Al etch.

8.0 Sacrificial PSG Deposition: target = 2 um (target = 1 um)
tylan12, VDOLTOC
Flows (sccm): SiH4 = 60, PH3 = 10.3 (entered), O2 = 90
time(2um) = 1 hour 40 minutes (~1000 A per 5 min.)
time(1um) = 50 minutes (~1000 A per 5 min.)
Include etching controls: PSG2F and PSG2B

9.0 Sacrificial PSG Densification
RTA in Heatpulse1: 30 secs @ 950 C
(also do PSG2 ctrls)

10.0 (optional) Dimple Photo Mask: CD1 (chrome-df)

10.1 Spin, expose, develop, descum, hard bake.

10.2 Timed wet etch in 5:1 BHF. (E.R. ~ 3000 A per min.)

10.3 Remove resist, piranha clean wafers.

11.0 uStructure Anchor Photo Mask: CG1 (chrome-df)

11.1 Spin (double thickness for 2 um oxide, single for 1 um), expose, develop, descum, hard bake.

```
-------------------------------------------------------------------------
     11.2  Etch in lam2:
           For 1 um oxide:  etch as usual.
           For 2 um oxide:  [press = 2.8 Torr, power = 350 W,
           gap = 0.38 cm, CHF3 = 30 sccm, CF4 = 90 sccm,
           He = 120 sccm, time = 1 min.],[power = 0, same gases,
           time = 1 min.] 3X
           For both cases, overetch with 700 W recipe.
-------------------------------------------------------------------------
     11.3  Check contact using IV probe station.
-------------------------------------------------------------------------
     11.4  Wet dip in 5:1 BHF for 10 secs.
-------------------------------------------------------------------------
     11.5  Remove resist, piranha clean wafers.
-------------------------------------------------------------------------
12.0  uStructure Poly2 Depostion:  target = 2 um
       Phosphorous-doped polysilicon deposition:  tylan11, SDOPOLYG
       time = 11 hours, temp.=650 C
       Include etching controls POLY2F and POLY2B (tylan11 cntrls).
-------------------------------------------------------------------------
13.0  Oxide Mask Deposition
       tylan12, VDOLTOC
       Flows (sccm):  SiH4 = 60, PH3 = 10.3 (entered), O2 = 90
       time = 25 minutes  (~1000 A per 5 min.)
       Include etching controls:  PSG3F and PSG3B
-------------------------------------------------------------------------
14.0  RTA Anneal
       Heatpulse1:  1 min. @ 1100 C in 50 l/sec N2
-------------------------------------------------------------------------
15.0  uStructure Poly2 Definition Mask:  CP2 (emulsion-cf)
       Align to ustructure poly1.
-------------------------------------------------------------------------
     15.1  Spin, expose, develop, inspect, descum, hard bake.
-------------------------------------------------------------------------
     15.2  Etch in oxide mask in lam2.
-------------------------------------------------------------------------
     15.3  (optional) Remove resist:
           technics-c, 10 min. O2 plasma @ 300 W
-------------------------------------------------------------------------
     15.4  Etch 2nd poly in lam1:  [press = 280 mTorr, power = 300 W,
           gap = 1.5 cm, CCl4 = 130 sccm, O2 = 15 sccm, He = 130 sccm,
           time = 1 min.] then [power = 0, same gases, time = 1 min.]
           5 or 6X, depending upon etch rate (E.R. usually ~ 4000 A
           per min.)
-------------------------------------------------------------------------
     15.5  If haven't already removed resist, remove resist.
           technics-c, 10 min. O2 plasma @ 300 W
-------------------------------------------------------------------------
16.0  uStructure and uPlatform Release
-------------------------------------------------------------------------
     16.1  Piranha clean in sink8.
-------------------------------------------------------------------------
     16.2  Wet etch in 5:1 BHF (~6000 A per min.) in sink8.
           (14 min. or whatever is needed)
           Slowly agitate, rinse.
           Spin dry or N2 gun dry.
```

16.3 Piranha clean in sink8 for 10 min. Follow with standard DI rinses. No HF dip. Spin dry or N2 gun dry.

Clark Nguyen
5/04/92
last revision: 10/30/92